NUMERICAL STUDY OF VORTICITY-COMBUSTION INTERACTIONS IN SHEAR FLOW

by

ANANTHA KRISHNAN

B.E., Mechanical Engineering
Mangalore University
(1984)

M.S., Mechanical Engineering
Marquette University
(1986)

Submitted to the Department of
Mechanical Engineering
in Partial Fulfillment of the Requirements
for the Degree of

DOCTOR OF SCIENCE

at the

MASSACHUSETTS INSTITUTE OF TECHNOLOGY

September 1989

Signature of Author _____
Department of Mechanical Engineering
August, 1989

Certified by _____
Ahmed F. Ghoniem
Associate Professor, Mechanical Engineering
Thesis Supervisor

Accepted by _____
Ain A. Sonin
Chairman, Departmental Graduate Committee

NUMERICAL STUDY OF VORTICITY-COMBUSTION INTERACTIONS IN SHEAR FLOW

by

ANANTHA KRISHNAN

Submitted to the Department of Mechanical Engineering
in Partial Fulfillment of the
Requirements for the Degree of Doctor of Science
in Mechanical Engineering

ABSTRACT

Numerical methods are used to investigate turbulence-combustion interactions in shear flows. The reaction is governed by finite rate Arrhenius kinetics, the flow field is compressible and at high Reynolds number, heat release is moderate and molecular heat and mass diffusivities are finite. The scheme used in this study, the vortex element method, is grid-free, Lagrangian and adaptive, i.e., more computational elements are utilized to discretize the vorticity as a strong strain field develops in the flow. A similar Lagrangian scheme is formulated to compute the transport of scalars in the same field. This scheme, the transport element method, is based solely on the kinematical relations between the distortion of the flow map and the local scalar gradients. The numerical scheme is validated by applying it to study the evolution of the Kelvin-Helmholtz and the Rayleigh-Taylor instabilities in density stratified flows and comparing the results with the linear theory. In the non-linear range, the simulations are verified against experimental and theoretical observations.

Simulations were performed over a range of Damkohler numbers for premixed as well as non-premixed combustion in order to resolve the flow-combustion interactions and to understand the effects of this mutual feedback on the burning rate. The flow field affects the propagation of the flame through the mechanisms of entrainment and stretch while the reaction influences the flow through thermal expansion and the generation of baroclinic vorticity. Volumetric expansion due to heat release reduces the growth rate of the instability while the baroclinic vorticity generation enhances the entrainment of the low density fluid into the eddies and biases the motion of the structures in the direction of the heavy fluid. For a shear layer with non-premixed combustion, the reaction is extinguished in regions of large positive strain and the product concentration is maximum inside the large vortex structures. The total product formation increases with the Damkohler number. For a shear layer with premixed reactants, results indicate that the flame thickness is reduced in regions of positive strain leading to slower propagation speeds. However, the thickening of the flame due to entrainment within the large structures enhances product formation. In contrast to the non-premixed case, the product formation in premixed combustion approaches that of the laminar flame as the Damkohler number increases.

Thesis Committee: Prof. Ahmed F. Ghoniem (Chairman)
Prof. James C. Keck
Prof. Tau-Yi Toong
Prof. Michael B. Giles

ACKNOWLEDGEMENT

I am very thankful to Prof. Ahmed F. Ghoniem for introducing me to to the project and for guiding me during the course of my work. I am extremely grateful to him for supporting me as a research assistant which made it possible for me to do my graduate study here. I wish to acknowledge the committee members, Prof. James C. Keck, Prof. Tau-Yi Toong and Prof. Michael B. Giles, for their interest and assistance in my work.

Much of the initial and ground breaking work for this project was done by Ghassem Heidarinejad and I am indebted to him for his patience in helping me learn the ropes. I wish to thank Omar Knio for weeding out the 'bugs' in my work and for many enlightening discussions over the years. I am particularly grateful to him for helping me out with many odd jobs and for being a good friend. Luis-Filipe Martins provided me with much needed assistance in preparing for the qualifying exams. I am also thankful to him for sharing with me his rather unique philosophy on life and other abstract matters. Habib Najm was always there to help with the computer systems (hardware and software) and I thank him for his patience in dealing with my ignorance. I am greatly indebted to Gerard Payen and Bruno Mehlman for bringing much needed cheer and laughter (at their expense) into the group. Many thanks to Pat Condon, Tom Bress and Marios Soteriou for their part in making my stay here a pleasant and memorable experience.

I appreciate the efforts of Varad Acharya in providing me support, moral and financial, in times of dire need. And last, but not least, I acknowledge my parents for providing me with the invaluable gift that will continue to enrich me lifelong - a good education.

TABLE OF CONTENTS

I. INTRODUCTION

Turbulent reacting flows have been attracting increasing interest in recent years. The requirements of increased combustion efficiency and decreased pollutant emissions from a variety of devices, from power plants to jet engines, have led to the need for improved methods of analyzing and prediction for flows involving chemical reactions. It is important for any combustion system to release as large a fraction of the available chemical energy in the fuel as possible within the given volume of the combustion chamber. This can be achieved only by what is known as a turbulent burning process. Turbulent reactive flows occur in practically all combustion devices and in order to be able to control and optimise the burning process, it is necessary to have a clear understanding of the flow-combustion interactions and to be able to determine the effects of this interaction on the burning rate. Therefore turbulent flames have been studied intensively from both experimental and theoretical points of view. However turbulent combustion is now so multifaceted that there exists no complete or impartial review of it. Although a well understood theory has been developed for laminar flames [1,2,3,4], there has been little success in providing a better understanding or an accepted conceptual framework for turbulent flames. The need for a complete theoretical description of turbulent flames is strong because any progress in this direction would result in a better utilisation of scarce energy resources in the times to come.

Generally, experimental measurements in reacting flows involve significant difficulties and potential sources for error. As a consequence, the combustion literature contains important discrepancies among experiments that should apparently be in accord. Experimental difficulties frequently

limit the quantities accessible to comparison. While a theoretical analysis would yield distributions throughout the flow of all the aerothermodynamic variables, only a few of these can be experimentally measured and, perhaps, only at few spatial locations. Thus, accurate simulations of the flow may reveal very interesting aspects of the flow field and reaction that may not be obtained through conventional experimental techniques.

The difficulty in analyzing turbulent reactive flows arises due to their inherent unsteady nature. Moreover the complex nature of the interaction between flow and reaction has made the solution of the governing equations very difficult. The process of combustion is greatly influenced by the flow field through such effects as strain rate, flame elongation and curvature while the flow field in turn is affected by combustion through thermal expansion and the generation of baroclinic vorticity. This close feedback between the flow and the chemistry must be resolved in order to develop a theory for turbulent flames. These difficulties have led to the development of simplified models applicable only in certain regimes. The activation energy asymptotics model [4,5] is one such approach wherein the activation energy is assumed to be infinite, i.e., the flame thickness is very small compared to the length scales of the flow. This approach has yielded a great deal of insight into the problem and has been able to explain some of the phenomena that have been observed experimentally. Other attempts at modelling turbulent flames include the assumption of low heat release [6] or that of a constant density reaction and the use of a temperature independent reaction term [7]. While these models have been successful in identifying certain significant aspects of turbulent flame behavior, a great deal of work is still required in order to extend their predictive capabilities to other regimes.

The focus of this study is on the development of schemes for the numerical simulation of turbulent combustion. In this approach, accurate numerical methods are used to integrate the unsteady, unaveraged equations without modelling. Thus, the need for a priori assumptions about the flow is eliminated. Therefore, numerical simulation can be applied to study flow fields with complicated interactions in which prior knowledge about the physics of the problem is lacking. The validation of the numerical scheme is achieved by comparing the results of the simulations with available experimental data or with results of previous investigations. Once the validation of the scheme is complete, it can be used for obtaining predictions of different physical quantities as a function of time and space.

The numerical method used in this study is the vortex/transport element method. This scheme is Lagrangian and grid free and is based on discretizing the flow field in terms of the gradients of the primary variables. This has the advantage of optimizing the computational effort by distributing computational elements only in regions of large gradients. The governing equations for reacting flows are presented in section II. The development and formulation of the method is described in detail in section III. The scheme is then applied to study five different flow fields, of the kind found in most practical cases of interest. Section IV deals with the density stratified Kelvin-Helmholtz instability, section V is the study of the Rayleigh-Taylor instability in a gravitational field, section VI deals with the instability modes in a density stratified jet flow and sections VII and VIII present the results for jet diffusion flame and the premixed shear layer respectively. A general discussion and the conclusions of this work are presented in section IX.

II. FORMULATION

II.1. GOVERNING EQUATIONS

The non-dimensional governing equations for an unsteady, two dimensional reacting flow are summarized in Table 1. For all the cases considered in this study, it is assumed that the flow is at a very small Mach number. Therefore, the spatial pressure variation caused due to the acceleration or deceleration of the fluid is small in comparison to the total pressure and hence does not significantly affect the local density of the fluid. Under these conditions, the pressure term in the state equation can be assumed to be a function of time only and not of space. Expressed in different terms, the assumption of low Mach number flow states that the velocity of sound is much larger (infinite in the limit) than that of the flow and hence the pressure reaches equilibrium with inertial forces instantly across the flowfield [8,9]. Furthermore, if the flow is in an infinite domain, the pressure can be assumed to be independent of time and the simplified state equation can be expressed by Eqn. (1). Therefore, the pressure term in the energy equation is neglected in comparison to the other terms. Although the low Mach number assumption is used to decouple the density from spatial pressure variations, the pressure term is still retained in the equation of motion to balance the momentum changes in the flowfield. This is because the pressure term is of the same order of magnitude as the fluid acceleration and cannot be neglected in the momentum equation. The fluid is assumed to behave as a perfect gas with equal molecular weights and constant specific heats. The thermal and mass diffusivities are constants but not necessarily equal.

The Reynolds number is assumed to be high and hence the effect of viscosity is neglected.

TABLE 1

STATE $\rho T \sim$ constant (1)

VELOCITY $u = u_v + u_p + u_e$ (2)

ROTATION $\nabla^2 \psi = -\omega \quad ; \quad u_v = \nabla \times \psi$ (3)

EXPANSION $\nabla^2 \phi = -\frac{1}{\rho}\frac{d\rho}{dt} = \frac{1}{T}\frac{dT}{dt} \quad ; \quad u_e = \nabla\phi$ (4)

VORTICITY $\frac{d\omega}{dt} = \frac{1}{\rho^2}(\nabla\rho \times \nabla p) - \omega(\nabla \cdot u)$ (5)

PREMIXED FLAME:

Reactants $\xrightarrow{k = A \exp(-E/RT)}$ Products (6a)

ENERGY $\frac{dT}{dt} = \frac{1}{P_e}\nabla^2 T + A_f Q \dot{W}$ (7a)

SPECIES(R) $\frac{dC_R}{dt} = \frac{1}{P_e L_e}\nabla^2 C_R - A_f \dot{W}$ (8a)

SPECIES(P) $\frac{dC_P}{dt} = \frac{1}{P_e L_e}\nabla^2 C_P + A_f \dot{W}$ (9a)

REACTION RATE $\dot{W} = \rho^{n-1} C_R^{\,n} \exp(-T_a/T)$ (10a)

DIFFUSION FLAME:

Reactants (1) + Oxidizer (r) $\xrightarrow{k}$ Products (1+r) (6b)

ENERGY $\frac{dT}{dt} = \frac{1}{P_e}\nabla^2 T + (A_f/r) Q \dot{W}$ (7b)

$$\textbf{SPECIES(F)} \qquad \frac{dC_F}{dt} = \frac{1}{P_e L_e} \nabla^2 C_F - (A_f/r)\,\dot{W} \qquad (8b)$$

$$\textbf{SPECIES(O)} \qquad \frac{dC_O}{dt} = \frac{1}{P_e L_e} \nabla^2 C_O - A_f\,\dot{W} \qquad (8c)$$

$$\textbf{SPECIES(P)} \qquad \frac{dC_P}{dt} = \frac{1}{P_e L_e} \nabla^2 C_P + A_f\,(1+ 1/r)\,\dot{W} \qquad (9b)$$

$$\textbf{REACTION RATE} \qquad \dot{W} = \rho\, C_F\, C_O \exp\,(-T_a/T) \qquad (10b)$$

The definitions of the symbols are as follows: $d/dt = \partial/\partial t + \mathbf{u}\cdot\nabla$ is the Lagrangian derivative along a material line, t is time, ρ is the local fluid density, $\mathbf{u} = (u,v)$ is the fluid velocity, $\mathbf{x} = (x,y)$ is the space co-ordinate, x and y being the streamwise and cross-stream directions respectively. ϕ is a velocity potential, $\psi = \psi\,\mathbf{e}_z$ is a streamfunction defined such that $\mathbf{u}_\omega = \nabla \times \psi$ where $\omega = \nabla \times \mathbf{u}$ is the vorticity. $\mathbf{e}_z$ is the unit vector normal to the x-y plane and $\mathbf{u}_p$ is a potential velocity, $\nabla \cdot \mathbf{u}_p = 0$, added to satisfy the normal boundary conditions across the boundaries of the domain. ∇ and ∇^2 are the gradient and the laplacian operators respectively. All the variables are non-dimensionalized with respect to an appropriate combination of a characteristic velocity U_o and length L_o. These characteristic values depend on the problem and are assigned separately for each case. C is the concentration per unit mass normalized with respect to the free stream concentration values. The subscripts R, P, F and O refer to reactants, products, fuel and oxidizer respectively. k is the reaction rate for the chemical reaction and is of the Arrhenius type. T is the temperature and is non-dimensionalized with respect to T_o, the tempertaure of the unburned reactants or fuel. The Peclet number is defined as $Pe = U_o L_o/\alpha$ where α =

$\lambda_k/\rho C_p$ is the thermal diffusivity and λ_k the conductivity. Le= α/D is the Lewis number and D is the mass diffusivity.

For the premixed flame, A_f W is the rate of formation of products per unit mass per unit time and n is the order of reaction. Q is the specific enthalpy of reaction non-dimensionalized with respect to $C_p T_o$ where C_p is the specific heat at constant pressure. T_a is the activation energy ($E/R T_o$) non-dimensionalized with respect to $R T_o$ where R is the universal gas constant. A single step, first order, irreversible reaction is considered in which reactants go to products according to the rate constant k. For the diffusion flame, the rate constant is proportional to the product of the concentrations of the fuel and the oxidizer and exponentially dependent on the temperature. Therefore, the source term is of the second order for the diffusion flame. It is assumed that a unit mass of fuel combines with 'r' units of oxidizer to form (1+r) mass units of products.

With the assumption of low Mach number combustion, the state equation reduces to Eqn. (1). The velocity is decomposed into three components in accordance with the Helmholtz decomposition, the vortical velocity $\mathbf{u}_\omega$, the expansion velocity $\mathbf{u}_e$ and the potential component $\mathbf{u}_p$ added to satisfy the normal boundary conditions. $\mathbf{u}_\omega$ is obtained from Eqn. (3) and $\mathbf{u}_e$ from Eqn. (4). For a compressible, inviscid flow, the vorticity equation is as shown in Eqn. (5) [10]. The energy and species equations and the reaction rates for the premixed flame and the diffusion flame are given by Eqns. (6) to (10) respectively.

III. NUMERICAL SCHEMES

III.1. THE VORTEX METHOD

Vortex Methods are used to solve the equation of conservation of vorticity which is obtained by taking the curl of the Euler equations. The vorticity equation for a compressible flow in two dimensions is written as [10]:

$$\frac{\partial \omega}{\partial t} + \mathbf{u} \cdot \nabla\omega + \omega \nabla.\mathbf{u} = \frac{1}{\rho^2} (\nabla\rho \times \nabla p) \qquad (11)$$

Given an initial distribution of vorticity, Eqn. (11) is solved to obtain the vorticity as a function of time and space. The stream function ψ is found from the vorticity using the following equation:

$$\nabla^2 \psi = -\omega \qquad (12a)$$

If the domain is unbounded then the solution of ψ from the above equation can be written as:

$$\psi(\mathbf{x}) = \int G(\mathbf{x}-\mathbf{x}') \, \omega(\mathbf{x}') \, d\mathbf{x}' \qquad (12b)$$

where G is the Green's function of the Poisson equation. In two-dimensions, $G = -1/2\pi \, (\ln r)$ where $r^2 = x^2 + y^2$.

The solution of Eqn.(12) yields the streamfunction at all points in the flow field. The vortical component of the velocity is obtained from the streamfunction as follows:

$$u_\omega = \nabla \times \psi \tag{13a}$$

$$u_\omega (x) = \int K(x-x') \, \omega(x') \, dx' \tag{13b}$$

where $K = -1/2\pi r^2(-y,x)$ is the kernel of the Poisson equation. The above equations form the basis of the vortex method. The vortical component obtained from Eqn.(13) is complemented with the potential velocity (to satisfy the normal boundary conditions) and an expansion velocity (if the flow is compressible) to get the fluid velocity which is then used in Eqn.(11) to update the vorticity and the solution proceeds as before. One of the main advantages in solving the flow in terms of vorticity is that regions of vorticity are usually confined to a small part of the flowfield (especially so in highly turbulent flows) and all the computational effort can be used in resolving this region rather than solving the equations over the entire flow domain. Thus the numerical resolution for a given computational expense is maximized.

An important development in improving the accuracy and extending the application of vortex methods to highly unsteady flows with large strain rates, is the formulation of the vortex element method [11]. In this method, the vorticity is accurately discretized among finite elements that move along particle paths. Each of these elements transports a finite amount of vorticity. Therefore this scheme is Lagrangian in nature wherein the particles are followed in time and space. The main advantage in using a Lagrangian frame of reference is that it eliminates the necessity to deal with the non-linear convective terms explicitly. The distribution of vorticity associated with each element is described by a radially symmetric function, f_δ, with a characteristic radius δ such that most of the vorticity is concentrated within $r < \delta$ where r is the distance measured from the center of the element. Vortex elements are initially distributed over the area of

the flow where $|\omega| > 0$ such that the discretization error is less than a predetermined tolerance parameter ε. Typically ε is around 10^{-5}. A detailed discussion of the initialization is presented in Ghoniem et al [11,12,13]. The strength of the vortex element located at $\mathbf{X}_i$, denoted by ω_i, is obtained from the solution of the system of equations:

$$\omega(\mathbf{X},0) = \sum_{i=1}^{N} \omega_i h^2 f_\delta(\mathbf{X} - \mathbf{X}_i) \qquad (14)$$

where $\omega(\mathbf{X},0)$ is the vorticity distribution at t=0 . f_δ , the core function, is chosen to be a second order Gaussian given by $f_\delta(r) = (1/\pi\,\delta^2)\exp(-r^2/\delta^2)$. The importance of the core function in stabilizing vortex computations was realized, among others, by Chorin [14] and was shown to be necessary for the convergence of the method by Hald [15] and Beale and Majda [16]. Eqn.(14) is equivalent to expanding a function $\omega(\mathbf{x})$ in terms of a number N of kernel functions, f_δ, located at $\mathbf{X}_i$ and with weights $\Gamma_i = \omega_i h^2$. The accuracy of the discretization depends on: (1) the choice of the core function f; (2) the initial distribution of the particles which are used to transport the vorticity; (3) the method of determining the initial values of values of ω_i or Γ_i, i = 1, 2, ... , N; and, (4) the ratio δ/h. The selection of the core function for a particular accuracy was extensively discussed in the work of Leonard [17] and Beale and Majda [16], who show that a second-order Gaussian, which is used here, leads to a second-order discretization. Accurate discretization and long time accuracy of the computed flow field require that $\delta/h > 1$ (a recent review of the theory is given in Anderson and Greengard [18]). For an initially smooth distribution of vorticity, δ/h = 1.1-1.5 is sufficient to limit the discretization error to the desired value. Note that although the core function is constructed as a fast decaying

function, such as an nth order Gaussian, the fields of individual vortex elements are strongly overlapping due to the choice of δ/h. Thus, according to Eqn. (14), the local value of the vorticity at a point is determined by the contributions of many surrounding elements. Therefore, the vorticity at any point in the flowfield at any time is determined by:

$$\omega(\mathbf{x},t) = \sum_{i=1}^{N} \Gamma_i(t)\, f_\delta(\mathbf{x}-\chi_i(\mathbf{X}_i,t)) \tag{15}$$

where $\Gamma_i = \omega_i h^2$ is the total circulation of an element and is obtained as a function of time from the solution of the vorticity equation, i.e., Eqn.(11). h is the geometric average of the distance between the centers of neighboring elements in the two principal directions, $h^2=h_x h_y$. χ_i is the trajectory of the particle or the partcle path. The velocity field of a distribution of vortex elements is obtained by substituting Eqn.(15) into Eqn. (13) and the resulting expression is:

$$\mathbf{u}_\omega(\mathbf{x},t) = \sum_{i=1}^{N} \Gamma_i(t)\, \mathbf{K}_\delta(\mathbf{x}-\chi_i(\mathbf{X}_i,t)) \tag{16}$$

where

$$\mathbf{K}_\delta(\mathbf{x}) = -\frac{(y,\,-x)}{2\pi r^2}\, K\left(\frac{r}{\delta}\right) \tag{17}$$

$$K\left(\frac{r}{\delta}\right) = 1 - \exp(-r^2/\delta^2) \tag{18}$$

The velocity obtained from Eqn.(16) yields the vortical component. Depending on the nature of the flow domain, a potential component has to be added to $\mathbf{u}_\omega$ in order to satisfy the normal boundary conditions. For all the cases in this study, the flow is assumed to be infinite in the y-direction and infinitely periodic in the x-direction with a periodicity length λ .

Therefore, the potential component is obtained by taking into account the velocities generated by the infinite images in the x-direction for each ccputaional element in the domain. Therefore, the total velocity is given as:

$$u = \sum_{i=1}^{N} \left[\frac{\Gamma_i}{2\pi} \left\{ \sum_{j=0}^{\pm 1} \frac{(\Delta y, -(\Delta x + j\lambda))}{((\Delta x + j\lambda)^2 + \Delta y^2)} \exp\left(-\frac{((\Delta x + j\lambda)^2 + \Delta y^2)}{\delta^2} \right) \right.\right.$$

$$\left.\left. + \frac{\pi}{\lambda} \frac{(-\sinh(2\pi\,\Delta y/\lambda), \sin(2\pi\,\Delta x/\lambda))}{(\cosh(2\pi\,\Delta y/\lambda) - \cos(2\pi\,\Delta x/\lambda))} \right\} \right] + u_b \qquad (19)$$

where $\Delta x = x - x_i$, $\Delta y = y - y_i$, N is the total number of combutational elements in the domain $0 < x < \lambda$ and u_b is the boundary condition for the velocity. Since the core function, f_δ, is a fast decaying function, its effect is included only for the nearest images on both sides of the domain. If the flow is compressible, an expansion component u_e, has to be added to the velocity **u**. The computation of u_e is explained in the section describing the Transport Element method. The above expression is used to compute the velocity at the center of each computational element in order to displace the elements along the particle path according to:

$$\frac{d\chi_i}{dt} = u(\chi_i(\mathbf{x}_i, t), t) \qquad (20)$$

For a barotropic flow or an uniform density flow, the vorticity ω is conserved along the particle path and hence is independent of time for each element and hence $\omega_i(t) = \omega_i(0)$. The vortex elements are displaced according to the velocity calculated at the centers of the elements. As time progresses, the generation of strong strain with the growth of perturbations into the non-linear stage increases the distance between neighboring elements, $\delta\chi$, beyond the "target" value of h. Thus, the accuracy of spatial

discretization, which is governed by δ/h, is adversely affected. In the computations, deterioration of accuracy is observed in the form of generation of disorganized, random motion on the scale of h which grow as time progresses. To avoid this problem, more elements are introduced in areas where $\delta\chi > \beta h$ where $\beta \sim 1.5$, and the circulation of the original two elements is locally redistributed among the newly introduced elements. Since the circulation of each element is $\omega_i h^2$, and since the vorticity is conserved along a particle path, the redistribution of circulation is accomplished by dividing the value of h^2 of the original two elements equally among the newly generated elements and the original elements.

For consistency, and to minimize numerical diffusion, the value of δ^2 should also be adjusted so that the ratio of δ^2/h^2 is maintained constant in Eqn.(15). Thus, the core radius of an element is effectively decreased as the element is exposed to strong positive strain. By increasing the number of vortex elements, we insure that the underlying grid of computational elements can capture the instantaneous vorticity distribution as it evolves with the motion of the flow. The need to increase the number of elements becomes clear when realizing that as the flow develops strong strains, the streamlines become strongly convoluted and require more particles to describe their geometry accurately. On the other hand, reducing the size of the cores of vortex elements help in minimizing the numerical diffusion which may accumulate to unacceptable levels if the area on which the vorticity exists is allowed to grow far beyond its original size.

The redistribution of vorticity in the direction of maximum tensile strain requires maintaining a list of near neighbors in the direction of maximum strain, and updating this list each time step according to the changes in the vorticity distribution along the layer. This process is

equivalent to utilizing a one-dimensional Lagrangian grid along each individual layer of vortex elements to preserve the organization of the computations. It is also used to provide information about the flow map at any time step since, according to the condition of incompressibility, one can compute the changes in the length of the material layers normal to the layer of vortex elements by knowing the extension of the elements in the direction of maximum strain. Similar tricks were applied by Krasny [19] and by Zabuski et al [20] in numerical simulations of a similar nature.

For a compressible baroclinic flow, the vorticity is no longer conserved along the particle path. The interaction between the density gradient and the pressure gradient leads to the generation of baroclinic vorticity and the existing vorticity is further modified by the expansion term. Although the expansion term, $(\nabla.\mathbf{u})$, does indeed change the local vorticity, it is found that the circulation remains unaffected. This is because the circulation is the product of the vorticity and the material area and while expansion reduces the local vorticity, it increases the material area or volume by the same ratio such that the product, the circulation, remains constant. Therefore the expansion term does not appear explicitly in the circulation equation. However, the circulation is affected by the baroclinic term and the circulation equation is derived by using $\Gamma_i = \omega_i \, h_i^2$ in the vorticity equation:

$$\frac{d\Gamma_i}{dt} = - \frac{\nabla\rho_i}{\rho_i} \, h_i^2 \times (\nabla p)_i \qquad (21)$$

Thus the circulation of each element is a function of time and is found by integrating the above equation. The pressure gradient in the baroclinic term is replaced by the material acceleration from the momentum equation. Tthe

material acceleration of an element is computed by numerically differentiating its velocity between two time steps, and the local value of the density gradient and the density is computed using the transport element method. The computations of vorticity transport proceed in a fractional step scheme as follows: (1) vortex elements are transported according to the value of the velocity at their center without changing the circulation or the size of individual elements; (2) the elements that experience strong strain are split (or combined if the strain is negative) and their size and circulation are distributed among the new elements; and, (3) Eqn.(21) is integrated for each element according to the local acceleration, density and density gradient.

III.2. THE TRANSPORT ELEMENT METHOD

Another important development in the application of particle methods to reacting flows is the formulation of the transport element method to compute the scalar distributions in a Lagrangian form. In this scheme, the gradient of the scalar field is discretized into a number of finite elements using Eqn. (14) with ω replaced by $\mathbf{g} = \nabla s$ where s is a generalized scalar such as the temperature or species concentration. Similar to vortex elements, the transport elements are distributed where $|s| > 0$ and are displaced along the particle path with the velocity computed at the centers of the elements. Each transport element transports a finite value of the scalar gradient and the value of the scalar is recovered as a summation over all the particles. The strength or the scalar gradient transported by each element is updated by solving the gradient transport equation which is obtained by taking the gradient of the scalar transport equation. The conservation equation for a

generalized scalar (such as the temperature or the species concentration) can be written as:

$$\frac{\partial s}{\partial t} + \mathbf{u} \cdot \nabla s = \alpha \nabla^2 s + \dot{S} \tag{22}$$

where s is the generalized scalar, $\alpha\nabla^2 s$ is the diffusion term and S is the source term. The transport equation for the scalar gradient is obtained by taking the gradient of the above equation:

$$\frac{\partial g}{\partial t} + \mathbf{u} \cdot \nabla g + g \cdot \nabla u + g \times \omega = \alpha \nabla^2 g + \frac{d\dot{S}}{ds} g \tag{23}$$

where $g = \nabla s$ is the gradient of the scalar. Eqn. (23) is integrated for g as a function of time for each element. This can be done in fractional steps where the convective, diffusive and the source term effects on g are considered separately. The vorticity is obtained from the solution of the vorticity equation and ∇u is obtained by taking the gradient of Eqn. (19). The components of the velocity gradient tensor are given as:

$$\frac{\partial u}{\partial x} = \sum_{i=1}^{N} \left[\frac{\Gamma_i}{\pi} \left\{ \sum_{j=0}^{\pm 1} \frac{-(\Delta x + j\lambda)\,\Delta y}{r_j^2} \left(\frac{1}{r_j^2} + \frac{1}{\delta^2} \right) \exp\left(-\frac{r_j^2}{\delta^2} \right) + \frac{\pi^2}{\lambda^2} \frac{(\sinh(2\pi\,\Delta y/\lambda)\,\sin(2\pi\,\Delta x/\lambda))}{(\cosh(2\pi\,\Delta y/\lambda) - \cos(2\pi\,\Delta x/\lambda))^2} \right\} \right] \tag{24}$$

$$\frac{\partial u}{\partial y} = \sum_{i=1}^{N} \left[\frac{\Gamma_i}{\pi} \left\{ \sum_{j=0}^{\pm 1} \left(\frac{(\Delta x + j\lambda)^2 - \Delta y^2}{2r_j^4} - \frac{\Delta y^2}{r_j^2 \delta^2} \right) \exp\left(-\frac{r_j^2}{\delta^2} \right) + \frac{\pi^2}{\lambda^2} \frac{(\cosh(2\pi\,\Delta y/\lambda)\,\cos(2\pi\,\Delta x/\lambda) - 1)}{(\cosh(2\pi\,\Delta y/\lambda) - \cos(2\pi\,\Delta x/\lambda))^2} \right\} \right] \tag{25}$$

$$\frac{\partial v}{\partial x} = \sum_{i=1}^{N} \left[\frac{\Gamma_i}{\pi} \left\{ \sum_{j=0}^{\pm 1} \left(\frac{(\Delta x + j\lambda)^2 - \Delta y^2}{2r_j^4} + \frac{(\Delta x + j\lambda)^2}{r_j^2 \delta^2} \right) \exp\left(- \frac{r_j^2}{\delta^2} \right) + \frac{\pi^2}{\lambda^2} \frac{(1-\cosh(2\pi\,\Delta y/\lambda)\cos(2\pi\,\Delta x/\lambda))}{(\cosh(2\pi\,\Delta y/\lambda) - \cos(2\pi\,\Delta x/\lambda))^2} \right\} \right] \quad (26)$$

$$\frac{\partial v}{\partial y} = \sum_{i=1}^{N} \left[\frac{\Gamma_i}{\pi} \left\{ \sum_{j=0}^{\pm 1} \frac{(\Delta x + j\lambda)\,\Delta y}{r_j^2} \left(\frac{1}{r_j^2} + \frac{1}{\delta^2} \right) \exp\left(- \frac{r_j^2}{\delta^2} \right) - \frac{\pi^2}{\lambda^2} \frac{(\sinh(2\pi\,\Delta y/\lambda)\sin(2\pi\,\Delta x/\lambda))}{(\cosh(2\pi\,\Delta y/\lambda) - \cos(2\pi\,\Delta x/\lambda))^2} \right\} \right] \quad (27)$$

where $\Delta x = x - x_i$, $\Delta y = y - y_i$ and $r_j^2 = (\Delta x + j\lambda)^2 + \Delta y^2$. Therefore, the velocity gradients are obtained as a summation over all the elements in the domain. This process can be compuationally very expensive if the number of elements in the field becomes large. It can be shown that for very small values of the diffusion coefficient, the value of **g** can be evaluated without explicitly integrating Eqn. (23). The information obtained from the flow map is used to update **g**. This results in considerable saving of computation time since the velocity gradients, as given by the above expressions, need not be evaluated. This method is described below in detail [12,13]. For simplicity, the equation for a non-diffusive, non-reactive passive scalar is considered:

$$\frac{\partial s}{\partial t} + \mathbf{u} \cdot \nabla s = 0 \quad (28)$$

and the corresponding gradient equation is:

$$\frac{\partial \mathbf{g}}{\partial t} + \mathbf{u} \cdot \nabla \mathbf{g} + \mathbf{g} \cdot \nabla \mathbf{u} + \mathbf{g} \times \boldsymbol{\omega} = 0 \quad (29)$$

It is observed that while the scalar s is conserved along the particle path, its gradient **g** changes due to the action of the strainfield and the

local vorticity. If the material is exposed to a strong strain in the direction normal to the gradient, the value of g must increase by the same amount as the stretch in the material element. Fig. 1 (a) shows the schematic of a rectangular fluid material element with the initial scalar gradient perpendicular to the material length everywhere. Fig. 1 (b) shows the same element after it has been deformed by the flow field. Since the scalar is conserved, all material lines must be isoscalar lines, i.e., the gradient must still be perpendicular to the material lines everywhere. However, the magnitude of the gradient increases in regions of positive strain and decreases in regions of negative strain. Also, since the material lines are rotated due to the action of the flow field, the direction of the gradient is also rotated so as to maintain $\mathbf{g}$ perpendicular to the material lines. The direction and magnitude of $\mathbf{g}$ are indicated in Fig. 1 (b). The direction and magnitude of $\mathbf{g}$ can be calculated by deriving an equation that governs $g = |\mathbf{g}|$. To do this, Eqn. (29) is expanded in terms of $g\,\mathbf{n}$, implementing kinematical relations that describe the variations of $\mathbf{n} = \mathbf{g}/g$, the unit normal vector to the iso-scalar line. After some manipulations, the following expression is obtained:

$$\frac{dg}{dt} = -g\,\mathbf{n}\,.(\mathbf{n}\cdot\nabla\mathbf{u}) \tag{30}$$

Moreover, $\mathbf{g} = (d\rho/dn)\,\mathbf{n} \sim (\delta\rho/\delta n)\,\mathbf{n}$, where $\delta\rho$ is the variation of ρ across a small material line δn. Furthermore, according to Eqn. (28) a material line which is initially aligned with an iso-scalar line will remain aligned with the same iso-scalar line. The variation of a material vector element $\delta\mathbf{l}$ is governed by (Batchelor [21]):

$$\frac{d\,\delta\mathbf{l}}{dt} = \delta\mathbf{l}\cdot\nabla\mathbf{u} \tag{31}$$

where $\boldsymbol{\delta l} = \delta l\ \mathbf{l}$ and $\delta l = |\boldsymbol{\delta l}|$, $\mathbf{l}$ being the unit vector along the material line and perpendicular to $\mathbf{n}$. For an incompressible flow, i.e., $\nabla \cdot \mathbf{u} = 0$, it can be shown that the equation for δl is given by:

$$\frac{d\ \delta l}{dt} = -\ \delta l\ (\mathbf{n} \cdot (\mathbf{n} \cdot \nabla \mathbf{u})) \tag{32}$$

The equation governing the variation of δl is the same as that of g. Thus, it follows that $g/\delta l$ = constant along a particle path. Since $g \sim \delta\rho/\delta n$, the constant turns out to be $\delta\rho/h^2$ where $h^2 = \delta l\ \delta n$ is the material area of the fluid element. Therefore, the magnitude of $\mathbf{g}$ is proportional to the magnitude of δl and its direction is always normal to the vector $\mathbf{l}$. Since the Lagrangian calculations involve tracking the material interface, the magnitude and direction of δl are always known. Thus $\mathbf{g}$ is completely determined as a function of time without having to integrate Eqn. (29). For a compressible flow, $\nabla \cdot \mathbf{u} \neq 0$, it can be shown that:

$$\frac{d\ \rho\delta l}{dt} = -\ \rho\delta l\ (\mathbf{n} \cdot (\mathbf{n} \cdot \nabla \mathbf{u})) \tag{33}$$

Therefore, $g/(\rho\ \delta l)$ = constant along the particle path. Including the effect of the source term in the scalar transport equation, the gradient equation now becomes:

$$\frac{d\mathbf{g}}{dt} = -\mathbf{g} \cdot \nabla \mathbf{u} - \mathbf{g} \times \boldsymbol{\omega} + \frac{\dot{dS}}{ds}\ \mathbf{g} \tag{34}$$

and taking the dot product of $\mathbf{n}$ and the above equation:

$$\mathbf{n} \cdot \frac{d\mathbf{g}}{dt} = \frac{dg}{dt} = -\ g\ (\mathbf{n} \cdot (\mathbf{n} \cdot \nabla \mathbf{u})) + \frac{\dot{dS}}{ds}\ g \tag{35}$$

From Eqn. (33), :

$$-(\mathbf{n}.\ (\mathbf{n}.\nabla\mathbf{u})) = \frac{1}{\rho\delta l}\ \frac{d(\rho\ \delta l)}{dt} \tag{36}$$

substituting for $(\mathbf{n}.\ (\mathbf{n}.\nabla\mathbf{u}))$ into Eqn. (35):

$$\frac{d}{dt}\left(\frac{g}{\rho\delta l}\right) = \frac{\dot{dS}}{ds}\ \left(\frac{g}{\rho\delta l}\right) \tag{37}$$

From the scalar transport equation, it can also be written as:

$$\frac{d\ \delta s}{dt} = \frac{\dot{dS}}{ds}\ \delta s \tag{38}$$

where δs is a variation of the scalar. Comparing Eqns. (37) and (38):

$$\left(\frac{g}{\rho\ \delta l\ \delta s}\right) = \text{constant} \tag{39}$$

Therefore, it is observed that g is a function of δl, ρ and δs. The value of δs is updated in time by integrating Eqn.(38). It is interesting to note that the direction of the gradient is still perpendicular to the material lines inspite of the effect of the source term in the transport equation. This is because the source term is a function of the scalar and since material lines start out as isoscalar lines, the magnitude of the source term along the material line is also the same. Therefore, although the scalar changes as a function of time, this change is the same for all points on the material line thus maintaining g perpendicular to the material layers.

Therefore, a very general expression for the scalar gradient can be written as:

$$\mathbf{g}\ (t) = \frac{\rho(t)\ \delta s(t)\ \delta l(t)}{\rho(0)\ h^2(0)}\ \mathbf{n}\ (t) \tag{40}$$

where $\rho(0)\ h^2(0)$ is the initial mass at t=0 associated with the fluid element. These relations can be used to construct a scheme which is compatible with the vortex method to compute the evolution of the scalar field. The scalar gradient field is discretized among a number of elements which are transported along the particle path while the gradients vary according to Eqn.(40). Thus:

$$\mathbf{g}(\mathbf{x},t) = \sum_{i=1}^{N} \mathbf{g}_i(t)\ h_i^2\ (t)\ f_\delta(\mathbf{x} - \chi_i(\mathbf{X}_i,t)) \qquad (41)$$

where $\chi_i(\mathbf{X}_i,t)$ is, as before, the particle path. Eqn. (41) is based on the expansion of $\mathbf{g}$ in terms of the core functions f_δ. All the comments made before regarding the accuracy of such a representation apply to Eq. (41). Since an iso-scalar line is a material line in a non-diffusive field, $\delta\mathbf{l}_i$ can be updated as: $\delta\mathbf{l}_i(t) = (\chi_{i+1}-\chi_{i-1})/2$, while $\mathbf{n}_i \cdot \mathbf{l}_i = 0$. $\mathbf{l}$ is the unit vector in the direction of the material line and normal to the vector $\mathbf{n}$. Thus, it suffices to move the centers of the transport elements, while remembering the near neighbors at $t = 0$, to compute the scalar flux. When an element is inserted between two neighboring elements, the values of $\delta\mathbf{l}_i$ are redistributed between the three elements and h^2 and δ^2 are adjusted so that the total material area is conserved. The gradient for each element is updated in time according to:

$$\mathbf{g}_i(t) = \frac{\rho_i(t)\ \delta s_i(t)\ \delta l_i(t)}{\rho_i(0)\ h_i^2(0)}\ \mathbf{n}_i(t) \qquad (42)$$

where the subscipt i refers to the element i. This is a very general expression for evaluating $\mathbf{g}$. For a conserved scalar δs is independent of

time and is constant and for an incompressible flow, ρ is constant. In order to simulate the effect of the diffusion term in the scalar transport equation, the diffusion equation is written for each element:

$$\frac{\partial g_i}{\partial t} = \alpha \nabla^2 g_i \tag{43}$$

substituting Eqn.(41) into the above expression:

$$\frac{d\ \delta^2}{dt} = 4\ \alpha t \tag{44}$$

and the solution of this equation is:

$$\delta^2 = \delta_o{}^2 + 4\alpha t \tag{45}$$

where δ_o is the initial core radius of the element. Thus, the effect of diffusion is simulated by expanding the core radius as a function of time according to Eqn. (45). This is done without changing the shape of the core function or the value of g_i . If the diffusion coefficient is large, the direction of the gradient vector need not necessarily be perpendicular to the material lines and the above expressions for $\mathbf{g}$ become invalid. In this case it becomes necessary to directly integrate the equation for the gradient in order to obtain $\mathbf{g}$. Given the location and strength of the transport elements, the scalar concentration is computed by direct integration over the fields of the transport elements. The divergence of the vector $\mathbf{g}$ can be written as $\nabla^2 s = \nabla \cdot \mathbf{g}$. In analogy to the streamfunction ψ, the solution for s in an infinite domain is given by $s = \int \nabla \cdot \mathbf{g}\ G\ dx$ where $G = -1/2\ \pi\ \ln r$ is the Greens function of the Poisson equation. Thus, the transport elements act as sources of strength equal to the divergence of the scalar flux, $\nabla \cdot \mathbf{g}$. After integration by parts, it can be shown that $s = \int \mathbf{g} \cdot \nabla G\ dx$. The equation for $\mathbf{g}$, Eqn.(41), is substituted into the above expression to get:

$$s(\mathbf{x},t) = \sum_{i=1}^{N} g_i(t)\, h_i^2(t) \cdot \nabla G_\delta(\mathbf{x}-\chi_i(\mathbf{X}_i,t)) \tag{46}$$

where

$$\nabla G_\delta(\mathbf{x}) = \frac{(x,\ y)}{2\pi r^2} \quad \kappa\left(\frac{r}{\delta}\right) \tag{47}$$

where $\kappa(r/\delta)$ is as defined before. Including the effect of the images:

$$s(\mathbf{x},t) = \sum_{i=1}^{N} \left[\frac{g_i\, h_i^2}{2\pi} \left\{ \sum_{j=0}^{\pm 1} \frac{-((\Delta x+j\lambda),\ \Delta y)}{((\Delta x+j\lambda)^2 + \Delta y^2)} \exp\left(-\frac{((\Delta x+j\lambda)^2 + \Delta y^2)}{\delta^2} \right) + \frac{\pi}{\lambda} \frac{(\sin(2\pi\ \Delta x/\lambda),\ -\sinh(2\pi\ \Delta y/\lambda))}{(\cosh(2\pi\ \Delta y/\lambda) - \cos(2\pi\ \Delta x/\lambda))} \right\} \right] + S_b \tag{48}$$

where S_b is the boundary condition for the scalar. Note that this formulation is fully compatible with the vortex method since all the information needed to compute the scalar transport are already a part of the vortex computations, including all the expressions for the Green functions. The expansion field generated due to the reaction can also be simulated using the transport elements. The velocity field associated with the expansion can be described by:

$$\nabla^2 \phi_i = \frac{1}{T_i} \left(\frac{dT}{dt}\right)_i \tag{49}$$

where

$$\mathbf{u}_{ei} = \nabla \phi_i \tag{50}$$

This is similar to calculating the velocity from the vorticity field and hence the expansion velocity is calculated as:

$$\mathbf{u}_e(\mathbf{x},t) = \nabla\phi(\mathbf{x},t) = \sum_{i=1}^{N} \frac{1}{T_i} \left(\frac{dT}{dt}\right)_i h_i^2(t)\ \nabla G_\delta(\mathbf{x}-\chi_i(\mathbf{X}_i,t)) \tag{51}$$

and including the effect of the images:

$$u_e(x,t) = \sum_{i=1}^{N} \left[\frac{\nabla^2\phi_i \, h_i^2}{2\pi} \left\{ \sum_{j=0}^{\pm 1} \frac{-((\Delta x+j\lambda),\ \Delta y)}{((\Delta x+j\lambda)^2 + \Delta y^2)} \exp\left(-\frac{((\Delta x+j\lambda)^2 + \Delta y^2)}{\delta^2} \right) \right.\right.$$

$$\left.\left. + \frac{\pi}{\lambda} \frac{(\sin(2\pi\,\Delta x/\lambda),\ -\sinh(2\pi\,\Delta y/\lambda))}{(\cosh(2\pi\,\Delta y/\lambda) - \cos(2\pi\,\Delta x/\lambda))} \right\} \right] \qquad (52)$$

Thus the volume source strength of each element is given by $1/T\ dT/dt\ h^2$ for each element. This strength is obtained by numerically differentiating the values of the temperature at every time step. The material area of the element is updated according to the expansion term in order to maintain the mass of the element constant, i.e., $\rho_i\ h_i^2\ (t)$ = constant.

Therefore, the algorithm of the transport element method is as follows: (1) The velocity at the centers of the elements is calculated by summing the vortical, potential and expansion components. This velocity is used to displace the elements along the particle path. (2) The magnitude and alignment of $\delta\mathbf{l}_i$ is found for each element. If the transport equation has a source term , Eqn.(38) is integrated to find the new value of δs. Using this information, the new value of $\mathbf{g}$ is calculated from Eqn.(42). (3) The core radii of the elements are updated according to the diffusion coefficient as given by Eqn.(45). (4) The scalar is computed as a summation over all the elements according to Eqn.(48).

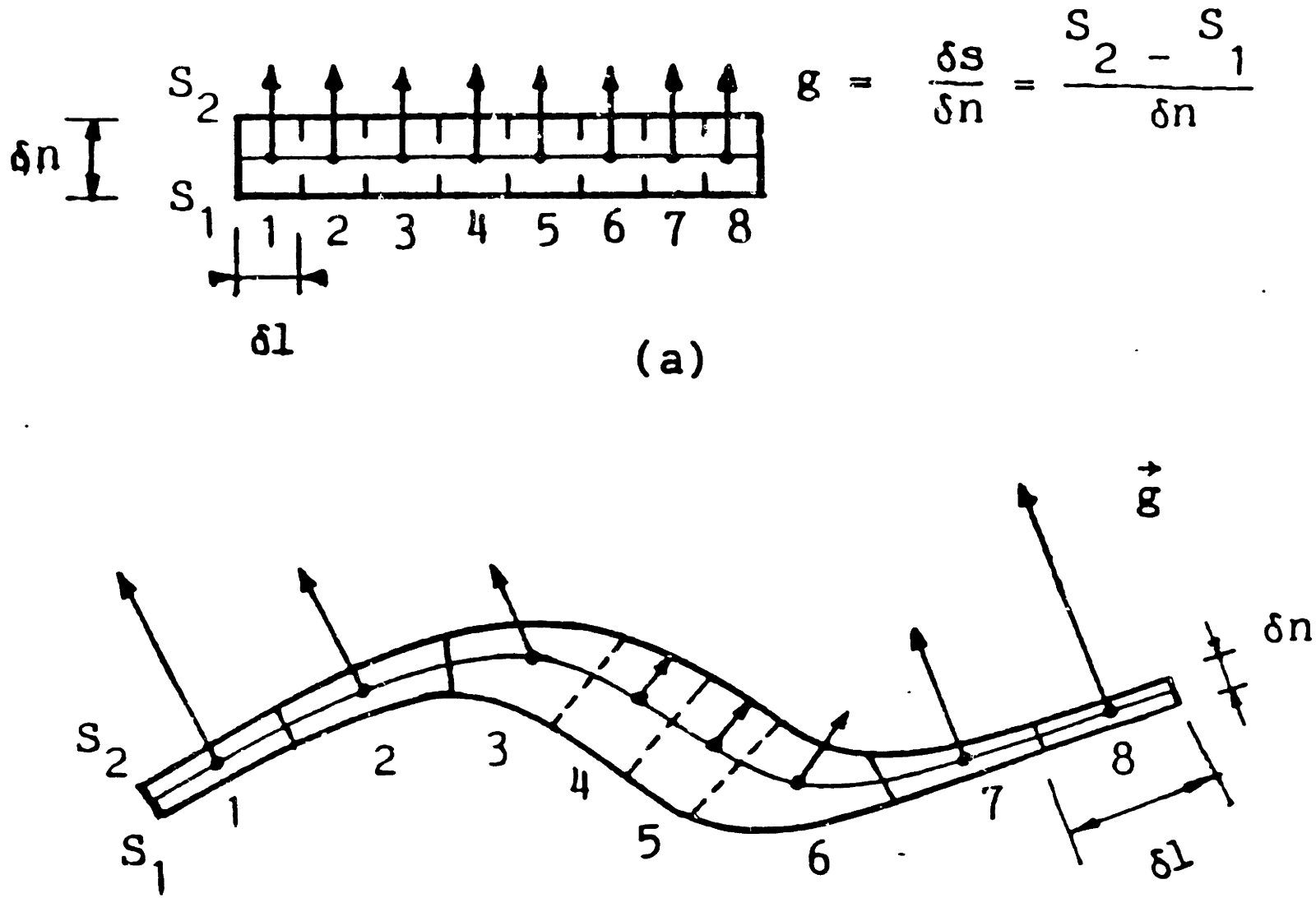
$g = \frac{\delta s}{\delta n} = \frac{S_2 - S_1}{\delta n}$
S_2
S_1
δn
1 2 3 4 5 6 7 8
δl
(a)
$\vec{g}$
δn
S_2
S_1
1 2 3 4 5 6 7 8
δl
(b)

Figure 1

IV. THE DENSITY STRATIFIED SHEAR LAYER

IV.1. INTRODUCTION

This section deals with the study of the dynamic effects of density stratification in shear flows. The presence of a density gradient is the first deviation from the incompressible, uniform density approximation and it is of great interest to study its effects on the flow stability, the growth of the coherent structures and fluid mixing. Flows with density variations have attracted considerable attention over the years [22]. Contrary to the homogeneous case, the evolution of pressure gradients in a density stratified flow leads to the generation of baroclinic vorticity which alters the dynamics of the flow. From a practical standpoint, this phenomenon has applications in combustion systems where the heat release establishes a density gradient in a highly unsteady flowfield. It is necessary to understand how baroclinicity affects flow stability and mixing and hence, the efficiency of burning.

IV.2. DESCRIPTION OF FLOW GEOMETRY

This study is an investigation of the effects of density stratification on the development of the temporal Kelvin-Helmholtz instability. Fig. 2(a) shows the schematic of a spatial shear layer formed due to two streams of unequal velocities coming together at the edge of a splitter plate. This flow becomes unstable downstream of the plate and the development of the characteristic large scale structures is observed. However, in order to minimize computational time and to simplify the problem, the governing

equations are solved in a frame of reference (or window) moving with the mean velocity of the free streams and periodic boundary conditions are applied in the x-direction [23,24,30]. The periodicity length is chosen to be the horizontal length of the window. Thus, the problem is reduced to one of temporal analysis wherein the spatial growth of a structure is approximated by a structure growing in time. Fig. 2(b) shows the schematic of the temporal shear layer. It can be shown that the temporal solution converges to the spatial solution as $\Delta U/U_m \rightarrow 0$, where $\Delta U=U_1-U_2$ and $U_m=0.5*(U_1+U_2)$. This means that the temporal solution is reasonably accurate as long as $\Delta U << U_m$. This condition is satisfied for most practical shear flows and hence the temporal analysis can be used to gain a good qualitative insight into the mechanism of the flow without having to expend too much computational time.

IV.3. GOVERNING EQUATIONS

The governing equations for the density stratified shear layer are shown below. The flow is assumed to be isentropic, i.e., all diffusion coefficients are zero and there is no reaction. The Mach number is assumed to be very small so that the effect of spatial pressure variations on the denisty are ignored and since the flow is in an open domain, the pressure term in the state equation is assumed to be constant with space and time. Under these conditions, the equation of transport of density is represented by Eqn. (53), i.e., the density is conserved along the material path. Thus, the flow is incompressible although there is a density gradient in the flowfield. This implies that at any time t, each fluid particle has the same density it had at t=0 even though the density of one fluid particle may differ from that of another.

$$\frac{d\rho}{dt} = 0 \tag{53}$$

$$\frac{d\omega}{dt} = -\frac{\nabla\rho}{\rho} \times \left(\frac{du}{dt}\right) \tag{54}$$

The equations are non-dimensionalized with the characteristic values U_o for velocity, L_o for length and ρ_o for density. U_o is defined as $0.5*\Delta U$ and L_o is the characteristic thickness ($=\sqrt{2}\,\sigma$, σ = std. deviation) of the initial Gaussian vorticity distribution. $\rho_o = \rho_1$, ρ_1 being the density of the upper stream. Subscripts 1 and 2 refer to the top and bottom streams respectively.

IV.4. LINEAR STABILITY THEORY

In this section, the linear stability theory for inviscid flows is reviewed and the modified Rayleigh equation which accounts for both the density stratification and the material acceleration is applied to study the evolution of the K-H instability. Results are then used to investigate the effect of the presence of a finite density gradient on the initial stages of evolution of the flow as a preliminary step to the numerical solution. These semi-analytical results are also be used to validate the results of the numerical simulations during the early times.

The governing equations of conservation of mass, momentum and entropy for the flow are written as:

$$\frac{\partial\rho}{\partial t} + \frac{\partial(\rho u)}{\partial x} + \frac{\partial(\rho v)}{\partial y} = 0 \tag{55}$$

$$\rho\left(\frac{\partial u}{\partial t} + u\frac{\partial u}{\partial x} + v\frac{\partial u}{\partial y}\right) + \frac{\partial p}{\partial x} = 0 \tag{56}$$

$$\rho\left(\frac{\partial v}{\partial t} + u\frac{\partial v}{\partial x} + v\frac{\partial v}{\partial y}\right) + \frac{\partial p}{\partial y} + \rho g_r = 0 \tag{57}$$

$$\frac{\partial s}{\partial t} + u\frac{\partial s}{\partial x} + v\frac{\partial s}{\partial y} = 0 \tag{58}$$

Gravity (g_r) is considered in the v-equation in order to make the derivation more general. The dependent variables, u,v,ρ,s and p, are expanded as a mean and a fluctuating component as follows [25]:

$$u(x,y,t) = U(y) + \tilde{u}(x,y,t) \tag{59}$$

$$v(x,y,t) = \tilde{v}(x,y,t) \tag{60}$$

$$s(x,y,t) = S(y) + \tilde{s}(x,y,t) \tag{61}$$

$$\rho(x,y,t) = R(y) + \tilde{\rho}(x,y,t) \tag{62}$$

$$p(x,y,t) = P(x) + \tilde{p}(x,y,t) \tag{63}$$

where the upper case letter indicates a mean and the tilde quantity denotes a fluctuation. By definition, the mean component of v is zero, while that of the pressure is P(x). The expanded variables are substituted into the governing equations, which are then linearized around the mean components to derive linear partial differential equations governing the fluctuating components. The linearization is done by ignoring the higher order terms involving the fluctuating quantities. Therefore the linearized equations are written as:

$$\frac{\partial\tilde{\rho}}{\partial t} + R\left(\frac{\partial\tilde{u}}{\partial x} + \frac{\partial\tilde{v}}{\partial y}\right) + U\frac{\partial\tilde{\rho}}{\partial x} + \tilde{v}\frac{\partial R}{\partial y} = 0 \tag{64}$$

$$R\left(\frac{\partial\tilde{u}}{\partial t} + U\frac{\partial\tilde{u}}{\partial x} + \tilde{v}\frac{\partial U}{\partial y}\right) + \frac{\partial\tilde{p}}{\partial x} = 0 \tag{65}$$

$$R\left(\frac{\partial\tilde{v}}{\partial t} + U\frac{\partial\tilde{v}}{\partial x}\right) + \frac{\partial\tilde{p}}{\partial y} + \tilde{\rho}\, g_r = 0 \tag{66}$$

$$\frac{\partial\tilde{s}}{\partial t} + U\frac{\partial\tilde{s}}{\partial x} + \tilde{v}\frac{\partial S}{\partial y} = 0 \tag{67}$$

Solutions are sought for the fluctuations in the form of propagating waves and the fluctuations can be expressed as follows:

$$\tilde{u}(x,y,t) = \hat{\mathbf{u}}(y)\ \exp[i\alpha(x-ct)] \tag{68}$$

$$\tilde{v}(x,y,t) = \hat{\mathbf{v}}(y)\ \exp[i\alpha(x-ct)] \tag{69}$$

$$\tilde{p}(x,y,t) = \hat{\mathbf{p}}(y)\ \exp[i\alpha(x-ct)] \tag{70}$$

$$\tilde{\rho}(x,y,t) = \hat{\boldsymbol{\rho}}(y)\ \exp[i\alpha(x-ct)] \tag{71}$$

$$\tilde{s}(x,y,t) = \hat{\mathbf{s}}(y)\ \exp[i\alpha(x-ct)] \tag{72}$$

where $i = \sqrt{-1}$, α is the wave number, $\alpha = 2\pi/\lambda$ where λ is the wavelength of the perturbation, $c = c_r + ic_i$ is the wave speed, c_r and c_i are the phase velocity and amplification rate divided by the wavenumber, respectively. The bold letters imply that the quantities are complex. In the temporal analysis, solutions are obtained for a real wave number, α, and a complex wave speed, c.

The expressions for the fluctuations are substituted into the linearized equations and the resulting ordinary differential equations for $\hat{\mathbf{u}}, \hat{\mathbf{v}}$, $\hat{\boldsymbol{\rho}}$ and $\hat{\mathbf{p}}$ are then reduced as follows:

$$i\alpha\,(U-c)\,\frac{\hat{\boldsymbol{\rho}}}{R} + R'\,\frac{\hat{\mathbf{v}}}{R} + i\alpha\,\hat{\mathbf{u}} + \hat{\mathbf{v}}' = 0 \tag{73}$$

$$i\alpha\,(U-c)\,\hat{\mathbf{u}} + U'\,\hat{\mathbf{v}} + i\alpha\,\frac{\hat{\mathbf{p}}}{R} = 0 \tag{74}$$

$$i\alpha\,(U-c)\,\hat{\mathbf{v}} + \frac{\hat{\mathbf{p}}'}{R} + \frac{\hat{\boldsymbol{\rho}}\,g_r}{R} = 0 \tag{75}$$

$$i\alpha\,(U-c)\,\hat{\mathbf{s}} + S'\,\hat{\mathbf{v}} = 0 \tag{76}$$

where the prime indicates a derivative with respect to y. Since the flow is incompressible, i.e., $\nabla.\mathbf{u} = 0$ and $d\rho/dt = 0$, the above expressions can be further simplified into the following expressions(the hats over the variables have been dropped):

$$i\alpha u + v' = 0 \tag{77}$$

$$i\alpha (U-c) \frac{\rho}{R} + R' \frac{v}{R} = 0 \tag{78}$$

$$i\alpha (U-c) u + U' v + i\alpha \frac{p}{R} = 0 \tag{79}$$

$$i\alpha (U-c) v + \frac{p}{R}' + \frac{\rho g}{R} r = 0 \tag{80}$$

Differentiating Eqn. (79) with respect to y and substituting into Eqn.(80) and using Eqns.(77) and (78), the above system can be reduced, after some manipulations, to the modified Rayleigh equation for a density-stratified flow with gravity:

$$v'' = -\frac{R'}{R} v' + \left(\frac{U''}{U-c} + \frac{R'U'}{R(U-c)} + \frac{R'g}{R(U-c)^2} + \alpha^2\right)v \tag{81}$$

where the double prime denotes a double differentiation with respect to y and U and R are the known mean streamwise velocity and density distributions. The solution of this eigenvalue problem depends strongly on satisfying the boundary conditions. For the K-H instability, gravitational effects are ignored. Therefore, the Rayleigh equation reduces to :

$$v'' = -\frac{R'}{R} v' + \left(\frac{U''}{U-c} + \frac{R'U'}{R(U-c)} + \alpha^2\right)v \tag{82}$$

Far from the instability, all mean derivatives decay to zero and Eqn. (82) can be simplified to $v'' = \alpha^2 v$. With proper boundary conditions at $\pm\infty$, namely that $v \to 0$, it can be shown that $v' = -/+\alpha v$ as $y \to +/- \infty$. If $v(-y_o) = v_o$, then $v'(-y_o) = \alpha v_o$ and from symmetry the value $\zeta = -1/\alpha (v'(y_o)/v(y_o))$ should be 1. The solution proceeds as follows: an arbitrary value of y_o is defined and v_o is taken as 1 and Eqn. (82) is integrated until y_o and the value of ζ is checked. If $\zeta \neq 1$, the solution of the eigenvalue problem continues by iteration to obtain the complex velocity c for each given wavenumber α.

Fig. 3(a) and (b) show the growth rate, αc_i, and the phase velocity, c_r, respectively, versus the wavenumber for the temporal K-H instability for different values of the density ratio. Calculations were made for a mixing layer with error function distributions for the streamwise velocity and density, with equal spreads in the y-direction. The spread, or the nominal layer thickness is defined as the standard deviation that characterizes the Gaussian curve describing the corresponding vorticity and density gradients within the layer. The top stream, moving to the right, is heavier than the bottom stream which is moving to the left. The continuous lines are results of the linear theory, while the symbols are obtained from the numerical simulations results using the schemes described in the previous section when the layer was perturbed by a sinewave with an initial amplitude $\varepsilon = 0.01 \lambda$. More on the numerical solution will be presented in the next section.

Results of the linear theory for the temporal shear layer indicate that the wavenumber of the most unstable mode depends weakly on the density ratio, and that the maximum growth rate is almost independent of the density stratification. As the density ratio across the shear layer increases, the most unstable mode, which corresponds to the most probable structure to be

shed, becomes smaller and is shed at higher frequency. The growth rate of the most unstable mode increases very slightly as the density ratio, $r_\rho = \rho_1/\rho_2$ increases, indicating that density stratification causes, at best, a very weak destabilization of the flow. Moreover, perturbations with longer/shorter wavelengths than that of the most unstable perturbation behave differently; they grow slower/faster as the density ratio increases. The results also suggest that the range of unstable waves increases as the density ratio is increased, indicating another destabilizing effect for the density stratification with shorter waves becoming more unstable as r_ρ increases. However, a cut-off wavenumber, which is a function of the density ratio, still exists though at higher values for higher r_ρ.

A more visible effect of the density ratio is in the phase velocity of the waves; for the same wavenumber the phase velocity increases with increasing density ratio. Thus, Kelvin-Helmholtz waves in a density-stratified flow are dispersive, with longer waves propagating at higher phase velocities in the direction of the heavy stream. For stable waves in the density stratified case, i.e., $\alpha > \alpha_c$ where α_c is the cut-off wavenumber, the phase speed is finite and approximately constant. The finite velocity is due to the finite generation of vorticity even if the wave does not grow. The fact that these waves are stable explains why their phase velocity, for a particular density ratio, is independent of the wavenumber. With a finite but growing deflection of the streamlines, a finite amount of vorticity is generated causing the finite propagation velocity of the structure. Evidence of vorticity generation will be shown in the numerical simulation results in the next section.

IV. 5. RESULTS OF NUMERICAL SIMULATIONS

The simulation of the Kelvin-Helmholtz instability in a density-stratified flow is based on the solution of Eqns. (53) and (54) using the vortex element and transport element methods described in Section III. Computations were done for density ratio $r_\rho = \rho_1/\rho_2 = 1, 2, 3, 4$ and 5. Results were obtained with the shear layer initially perturbed at a wavelength $\lambda = 13.2\ L_o$ using a sinewave displacement of the vortex elements with an amplitude $\varepsilon = 0.01\ \lambda$. This wavenumber is very close to the most unstable wavenumbers for all the density ratios considered, as seen from the results of the linear theory. The initial vorticity and density gradient distributions are Gaussians, i.e., the velocity and density distributions are error functions. In all cases, the high-density fluid is the top, fast stream, and the low density fluid is the bottom, slow stream. In this temporal analysis, the normalized value of the velocity of the top stream is 1 and that of the bottom stream is -1. Therefore if the density profile is inverted, i.e., the bottom stream is made the heavier stream, the consequent development of the eddy also takes place in an inverted reference frame. The initial number of elements in the field is N(t=0)=600 and the parameter β for the injection distance is 1.4 . The value of the time step used is $\Delta t = 0.1$ for $r_\rho = 1$ & 2 and $\Delta t = 0.05$ for $r_\rho = 3, 4$ & 5. A fourth-order Runge-Kutta scheme was used to integrate the equations.

Figs.4-8 show the location and velocity of all the vortex-transport elements used in the computations for the five values of the density ratio, respectively. The non-dimensional times are t= 5.5, 11.0, 16.5 and 22. In each case, the number of elements in the field increases with time as the interface is stretched due to the action of the strain field. The material

interface plots show that for all values of r_ρ, as shown before from the linear analysis, the vorticity layer is unstable to small perturbations. The growth of the initial vorticity perturbation leads to the roll-up of the vorticity layer into a coherent elliptical structure that entrains all the initial vorticity within the layer and, for $r_\rho > 1$, engulfs the newly generated vorticity. Contrary to the case of $r_\rho = 1$, the vorticity generated by baroclinicity, the only extra dynamic process in these computations, causes a definite asymmetry in the developing structures, and advances the structure at a finite velocity in the direction of the high-density stream. This phenomenon can be attributed to the pressure gradient that forms in the flow field due to the perturbation of the streamlines. For example, a negative pressure gradient on the top part of the interface would serve to accelerate the heavier stream and, assuming this pressure gradient is transmitted through the interface, its effect on the low density bottom stream would be more severe, i.e., the bottom stream would tend to reverse its direction. Therefore, in a density stratified flow, the heavier fluid tends to drag the structures along with it. This motion, also predicted by the linear analysis in the form of a finite phase velocity, indicates that the vorticity distribution within the structure does not exhibit the point-symmetric character observed in the uniform-density case. The motion indicates that the development of the instability occurs in time and in space simultaneously, i.e., a stationary structure like the case of $r_\rho = 1$ is not observed. It is also observed that this convective velocity is a strong function of r_ρ and increases with increasing density ratio. An interesting feature of the results for cases with large r_ρ revealed by the plots, is the strong concentration of vorticity around the outer edges of the large structure. In contrast to the case of $r_\rho = 1$ in which the elements are

almost uniformly distributed within the structure, an uneven distribution is observed with higher concentration of elements along the boundaries of the large eddies for $r_\rho > 1$. The development of waves, and small scale structures, along the boundaries of the large eddies during the final stages is associated with the growth of perturbations, numerically introduced, within these layers of intense vorticity. Furthermore, for $r_\rho > 1$, the material lines at the lower part of the eddy undergo a greater amount of distortion. The plots clearly indicate that, unlike the uniform density case, the density stratified eddy entrains fluid asymmetrically from the free streams. More of the low density, bottom stream fluid is entrained than that of the heavier top stream. This is shown by the presence of a deeper tongue of lighter fluid into the core than that of the heavy fluid. This asymmetric entrainment has been observed in experiments on shear layers in density-stratified flows [26,27]. It is also observed that the entrainment ratio or the degree of asymmetric entrainment between the two fluids increases with the density ratio. It should be noted that all these effects are dynamic consequences of the generation of vorticity by the baroclinic torque due to the interaction between the pressure field and the density gradient. A final observation to be made from the material line plots is that the instability appears to be stronger, particularly in the non-linear stages, for higher values of r_ρ.

Figs. 9-13 show the corresponding streamline contours for the five cases. The streamlines show the development of the eddy and also give a quantitative estimate of the volume of the fluid entrained within the eddy. The motion of the eddy, for $r_\rho > 1$, is clearly observed from the plots. The finite phase velocity of the structure in the linear range is obtained by calculating the mean motion of the stagnation point in the braid region over the time

interval $0<t<15$. A pattern similar to a "cat's eye" is formed due to the roll-up of the vorticity into a single coherent structure (see Corcos and Sherman [23]). Since, the domain over which the streamfunction is being calculated is the same for all values of r_ρ, the fluid entrainment rate in each case can be estimated by taking the difference between the minimum and the maximum value of the streamfunction. This quantity $\Delta\psi$ is calculated for each case at different time frames. The value of $\Delta\psi$ at $t=0$, i.e. $(\Delta\psi)_0$ is chosen as a reference value. Any increase of $\Delta\psi$ beyond this reference value is because of the entrainment of fluid into the structure. Therefore $\zeta = \Delta\psi - (\Delta\psi)_0$ is directly used as a measure of the volumetric entrainment into the eddy. In all cases, it is observed that the eddy grows by entraining fluid from the free streams, i.e., the value of ζ increases with time. The maximum volume of fluid entrained into the structure is reached with the maximum growth of the instability, around time $t = 20$ for the $r_\rho = 1$ case. Beyond this stage, fluid starts to leave the structure and rejoins the free streams. This collapse is associated with energy being fed back to the free streams due to the saturation of the instability [11]. At $t=22$, the values of ζ are 1.68, 2.21, 2.46, 2.77 and 2.96 for $r_\rho = 1$, 2, 3, 4 and 5, respectively. This supports the earlier observation that the degree of instability and hence the total volumetric entrainment into the eddy, increases with increasing density ratio. Also to be observed is the fact that the density stratified eddy appears to be "sinking" deeper into the low density fluid with increasing r_ρ. The aymmetric growth and the movement of the eddy into the low density stream have been observed in heterogeneous spatial shear layers [26]. Thus, the results of the simulations are consistent with the experimental observations. The reason for these phenomena will become clear from the vorticity contours for these flows.

Figs. 14-18 show the corresponding normalized temperature contours, $T = 1/\rho$, for the five cases at the same time frames as before. In all cases, the temperature contours are normalized between zero for the heavy, top stream and unity for the light, bottom stream. The formation of strong gradients due to the strong strain within the braids is shown in the plots. The relative entrainment of the fluid into the large structure is also clear from these plots. Since the formulation conserves the scalar, the temperature contours are essentially the same as the material line contours. The effect of molecular mixing can be investigated by including molecular diffusion in the governing equations. However, the temperature contours indicate that, barring very high diffusivities, there will still be inhomogeneity within the eddy even if molecular diffusion is active. This is apparent from the presence of large blobs of light fluid on both the upper and lower sides of the structure at the late stages of roll-up.

To complete the description of the flow, Figs. 19-23 show the plots of the corresponding vorticity contours for the five cases. The vorticity is calculated by summing over the effects of all the vortex elements as expresed by Eqn. (15). The vorticity is initially distributed in the form of a Gaussian in the y-direction with the peak value at the central layer. The vorticity decays from this peak value above and below this layer. Unfortunately, this configuration appears to be ill-conditioned as far as plotting the contours is concerned. The contour plotter draws the contours joining points of identical vorticity in the vertical direction rather than in the horizontal direction. This difficulty was eliminated for the uniform density shear layer since the vorticity is conserved along the particle path and the vorticity for each layer is completely determined from initial conditions. However, this argument is not applicable to the density

stratified cases. This is the reason for the appearance of a number of closed contours in the central part of the shear layer during the early stages of development of the eddy for the density stratified runs. Negative, clockwise vorticity is indicated by continuous lines while positive vorticity, which forms due to the action of the baroclinic torque, is shown by broken lines. The figure caption indicates the range of values of vorticity at the final time in each case. It is to be noted that the maximum of the absolute value of the negative increases with time, while the minimum of the absolute value decreases and then becomes positive. The contours reveal that as the eddy grows, a layer of intense negative vorticity forms on the lower side of the structure while positive vorticity, which leads to the reduction of the absolute value of the negative vorticity, forms on the upper side of the structure. The negative vorticity is constantly being entrained into the core of the eddy in a clockwise direction while the positive vorticity forms a "wing" on the top side of the eddy that penetrates the eddy core from the right-hand side. From these vorticity contours it is easy to formulate simple kinematical arguments as to why the eddy moves in the direction of the heavy stream and why it entrains more light fluid than heavy fluid by volume. The vorticity-concentration imbalance across the cross-stream direction, with a bias towards strong negative vorticity in the lower side and weak negative, or positive vorticity on the upper side leads to a net positive velocity component at the center of the eddy. It is also easy to see how the eddy retains its strength longer into the non-linear range. The increased intensity of vorticity in the eddy core helps in maintaining the coherence beyond the maximum entrainment stage.

As indicated by the linear analysis, the effect of the density gradient is felt as soon as a pressure gradient, or a material acceleration develops

during the growth of the instability. Concomitantly, a convolution of the iso-scalar lines produces a density gradient which is not aligned with the pressure gradient. The growth of the velocity perturbation, defined as $I = \int \int |u(x,t) - U(x)| \, dx$ where the integration is performed over a single wavelength in the x-direction and over $\infty \geq y \geq -\infty$, is shown in Fig. 24 for the same wavelength and for different values of the density ratio. It is to be noted that it is Log I that is plotted versus time. From the linear analysis, it is clear that the initial growth of the instability is exponential in nature and hence the slope of Log I versus time should directly yield the growth rate of the perturbation. The growth of the instability, as determined by the value of I, shows that: (1) the exponential growth rate within the linear range is almost the same at this wavelength for all density ratios, as shown by the results of the linear theory; (2) The non-linear growth of the density stratified cases reach higher values of I, indicating stronger total entrainment into the evolving structure; and, (3) the decay, or collapse of the density-stratified eddy is slower than that of a uniform density eddy. While the end of the linear range is identified better from the growth of the velocity perturbation, I, Figs. 4-8 indicate that it is closely related to the formation of a vertical interface at the center of the growing structure. The curves in Fig. 24 show that the stages of evolution of the large structure can be divided into three phases: (1) fast, exponential, small amplitude growth, the linear range, during which the streamlines and iso-scalar lines experience small deformation. This phase ends around $t = 10.0$; (2) moderate, almost linear, large amplitude growth, the non-linear range, during which entrainment is large and the streamline and iso-scalar experience strong deformation. This phase ends at t_m, where t_m increases with the density ratio; and (3) slow, almost linear, small

amplitude decay, the collapse range during which negative entrainment, or fluid leaving the structure and joining the free streams, is observed with the flattening of the streamlines. While the boundaries between these stages are not sharp and must be based on several aspects including the growth of the instability, it is useful to differentiate between these stages in the analysis and in drawing conclusions regarding the effect of baroclinicity on the flow development. The beginning of the non-linear phase and the collapse phase depend on the value of r_ρ. In all cases, the end of the non-linear growth while being a function of r_ρ, is around $t \sim 20$. It is also observed that a longer delay in both ranges accompanies larger density ratios (it should be mentioned that the exact value of the time when a range ends depends most strongly on the amplitude of the initial perturbation; in all of this analysis, the calculations were started with the same amplitude, $\varepsilon = 0.01\ \lambda$, which was shown by Ghoniem et al. [11] to lie within the linear range of instability for the uniform-density case. Since according to the linear analysis, density stratification slightly decreases the growth rate and delays the end of the linear range, this perturbation is still within this range for high density ratios across the layer). Fig. 24 indicates that for $r_\rho > 1$, there is a plateau after which the eddy reaches its maximum size or its point of maximum entrainment, t_m, before the collapse period starts. It is also observed that this plateau occurs later in time for higher density ratios. Thus, the vorticity generated due to acceleration, or baroclinic effects, leads to the formation of a stronger eddy that can entrain more fluid and survive longer before it collapses and fluid starts to leave the structure.

Another measure of the total entrainment into the large eddy is the mean length of the interface which is obtained as an average of the length of all

the material layers. This length 'L' is plotted as a function of time for different values of the density ratio in Fig. 25. The length of the interface remains almost constant during the linear range where the deformation of the streamlines is very small. The earlier and faster rise of L in the case r_ρ = 1 is due to the stronger linear instability of this flow over that of $r_\rho > 1$ (see Fig. 3). However, cases with $r_\rho > 1$ exhibit stronger non-linear instability and L reaches higher values as the density ratio increases. With higher L, more fluid is entrained into the large eddies, as indicated before by the streamline plots. The stronger non-linear instability is associated with the redistribution of the vorticity within the large structure by the action of the baroclinic torque.

To quantify the above arguements regarding the effect of baroclinicity, the generated circulation is plotted as a function of time in Fig. 26 for r_ρ = 1, 2, 3, 4 and 5 respectively. The generated circulation is obtained as $\Sigma(\Delta\Gamma_i)$ where $\Delta\Gamma_i = \Gamma_i(t)-\Gamma_i(t-\Delta t)$ and Σ represents summation over all the elements. The positive and the negative values are summed separately. It is observed that the generation of vorticity takes place right from the beginning although the amount generated is very small for $t<5.0$. For $t>5.0$, equal amounts of positive and negative circulation are generated thus maintaining the total circulation constant. For higher values of r_ρ, the amount of circulation generated at any given time is larger, particularly in the non-linear stages.

The cumulative circulation in the field, $\Gamma = \Sigma\ \Gamma_i$, was found to stay constant for all cases, indicating that the total positive circulation generated on the top side of the eddy is equal to the total negative circulation generated near the eddy core. Again, the positive and negative values of the circulation are summed separately. The total positive

circulation, $\Gamma^+ = \Sigma \Gamma_i$ if $\Gamma > 0$, and the total negative circulation, Γ^-, both plotted in Fig. 27, exhibit interesting trends: (1) both values change by the same amount so as to maintain the total circulation constant ; (2) both values rise sharply at the late stages of the non-linear regime; and (3) both values depend strongly on r_ρ in the non-linear regime. It is observed that for $r_\rho = 5$, the negative circulation in the flow field at the final time is almost five times the value at t=0. Fig. 28 shows the circualtion as a function of time for four individual material layers for $r_\rho = 3$. Layer 1 is the bottom most layer and layer 15 is the topmost layer (see transport element location plots). Again, positive and negative circulation along the layer are summed separately and the values are normalized with respect to the layer circulation at t=0. The topmost layer undergoes the least distortion and this is reflected in Fig. 28 where the generated circulation is the least for layer 15. The bottom and the middle layers undergo considerable distortion due to the rollup of the eddy and this leads to greater generation of vorticity along these layers. For layers 1 and 7, it is seen that the generated negative circulation at the final time is about three times the initial negative circulation. Figs. 29,30 and 31 show the vorticity along the interface for the material layers (for $r_\rho = 2$) 1,8 and 15 respectively at t=5.5,11,16.5 and 22. For layer 1 which is the bottom most layer, the generation effects are apparent only at t=22.0 when a large spike of negative vorticity is observed. For layer 8, which is the central layer, the vorticity along the interface undergoes a considerable amount of change indicating the severe distortion in the layer. The topmost layer, i.e., layer 15 shows very little change in vorticity since it undergoes the least distortion among the material layers. Thus , it is observed from the above results that the

generation of vorticity is directly related to the extent to which the material layer is twisted and stretched.

At later times, during the collapse stage, we observe the development of a number of small scale structures within the large eddies in the density-stratified cases. As mentioned before, the outer edges of the eddies, being zones of high-density gradients and strong strain, is where most of the baroclinic vorticity has been generated. This "layer of intense vorticity" is susceptible to an instability mechanism that is different from the K-H instability since these layers are exposed to strong planar strains. As indicated by Figs. 26-28, most of the vorticity is generated after the strong deformation of the streamlines and within the non-linear stages. Following this stage, the K-H instability matures and the eddy starts to flatten in the streamwise direction. This flattening produces a strain field which is almost aligned with these vorticity layers on the outer edges of the large eddies. The growth of perturbations along this layer under the effect of aligned strain leads to the formation of smaller scale structures within the large eddy. The plots of the vortex-transport elements at t = 24 for the five case presented before are shown in Fig. 32. The strength of the small scales is clearly indicated by the local concentration of vortex elements around the structures. The plot shows that the number and intensity of these small scales rises as r_ρ increases. The shapes of the small scales which form at the late stages of the instability are reminiscent of the mushroom structures computed by Corcos and Lin [28] for a strained, perturbed vorticity layer. The corresponding temperature and vorticity contours at t=24.0 for the five values of r_ρ are shown in Figs. 33 and 34 respectively. The temperature plots reveal the highly heterogeneous composition within the structure and the vorticity contours indicate the highly spotty nature of the

distribution. If molecular diffusion were to be included in the governing equations, the presence of high scalar gradients and many small scales inside the eddy provides the ideal environment for efficient mixing.

The large vortex structures which form as the K-H instability grows in a density-stratified shear layer move streamwise in the direction of the high-density fluid attaining a constant velocity. This velocity is slightly different from the phase velocity predicted from the linear analysis since it is dominated by non-linear effects. The computed velocity of the structure within the non-linear range is shown for various density ratios $s = \rho_2/\rho_1$ in Fig. 35. The structure convection velocity is calculated by measuring the mean motion of the core of the eddy (from the streamline contours or the transport element plots) over the time interval $15 < t < 24$, i.e., after the instability has matured and the structure has attained a constant velocity. These values are smaller than the phase speeds calculated in the linear range. The computed convection velocities are shown by dark circles. Applying Bernoulli's equation along a stagnation streamline in a reference frame moving with the eddies in a spatially-growing mixing layer, Dimotakis [26,27] derived the following formula for determining the structure velocity:

$$U_c = \frac{(1 + r_u\, s^{1/2})}{(1 + s^{1/2})} \tag{83}$$

where $r_u = U_2/U_1$ and $s = 1/r_\rho$ are the velocity ratio and density ratio across the spatial shear layer, respectively. This formula can be used to calculate the structure velocity in a temporal frame of reference by substituting $\Delta U = (U_1 - U_2)/2 = 1$ in the above expression . The resulting convection velocity in a temporal frame of reference is $U_{ct} = U_c - U_m$ (where $U_m = (U_1 + U_2)/2$) and is obtained by simplifying Eqn. (81):

$$U_{ct} = 1 - 2 \frac{s^{1/2}}{(1 + s^{1/2})} \tag{84}$$

This convective velocity is plotted as a function of $s = 1/r_\rho$ in Fig. 35 as a continuous line. The symbols represent the results of the numerical simulations. There is a good agreement between the predicted velocity and the measured velocity [29].

Dimotakis [26,27] also obtained an empirical expression for the volumetric entrainment ratio as a function of the density ratio and the velocity ratio in a spatial shear layer. This expression is given as:

$$E_v = s^{1/2} \left(1.0 + 0.68 \frac{(1 - r_u)}{(1 + r_u)}\right) \tag{85}$$

where E_v is defined as the ratio of volume of fluid entrained from the heavier top stream to that entrained from the lighter bottom stream. For a temporal shear layer the velocity ratio, r_u is unity and the above expression is reduced to [29]:

$$E_v = s^{1/2} \tag{86}$$

This expression is plotted as a function of $s=1/r_\rho$ in Fig. 36 by the continous line. The symbols represent the entrainment ratio estimated from the numerical simulations at a non-dimensional time of 24.0 after the maturation of the instability. The entrainment ratio is evaluated by integrating the concentration of the light fluid and the heavy fluid over the area of the eddy where the eddy itself is defined as the zone of non-zero gradients. This is calculated by considering the region where $|T-T_f| > 0.02$, where T is the normalised temperature and the subscript f refers to the free

stream value. Results of the numerical simulations compare very well with the empirical results. It is to be emphasized that the only effect of density stratification in this model is the generation of vorticity and that the entrainment asymmetry and the motion of the eddy are due to this effect.

IV. 6. CONCLUSIONS

The vortex-transport element method has been used to study the effect of density stratifictaion on the evolution of the K-H instability. The results obtained are validated using the linear theory in the initial stage of the growth of the perturbation and comparisons with experimental and theoretical work are used to support the results in the non-linear regime. The generation of vorticity due to baroclinicity in a density stratified temporal shear layer leads to the asymmetric development of the large scale structure and simultaneously imparts an extra convective velocity to the eddy in the direction of the heavier stream. The entrainment ratio and the convection velocity of the eddy calculated from the numerical simulations compare well with experimental results. Since the entrainment ratio is found to be a strong function of the density ratio, the effect of baroclinicity becomes very important in studying and understanding chemical reactions occuring in flows dominated by large scale structures. These structures serve to entrain the reactants and bring them into contact with each other thus promoting mixing and hence the reaction. Therefore the relative entrainment of the respective fluids will have an important effect on the reaction.

FIGURE CAPTIONS

Fig. 2. (a) A schematic of the density stratified spatial shear layer; (b) a schematic of the temporally growing shear layer with periodic boundary conditions.

Fig. 3. (a) Plot of the linear growth rate versus the wavenumber for different values of the density ratio; Curves 1,2,3,4 and 5 represent r_ρ=1,2,3,4 and 5 respectively. (b) the corresponding linear phase speeds versus the wavenumber. The phase speed for r_ρ=1 is zero for all wavenumbers. The symbols represent results of numerical simulations.

Fig. 4. Transport element location and velocity vectors for the temporal K-H instability for r_ρ = 1 at t=5.5, 11.0, 16.5 and 22.0 respectively.

Fig. 5. Transport element location and velocity vectors for r_ρ= 2 at t= 5.5, 11.0, 16.5 and 22.0 respectively.

Fig. 6. Transport element location and velocity vectors for r_ρ= 3 at t= 5.5, 11.0, 16.5 and 22.0 respectively.

Fig. 7. Transport element location and velocity vectors for r_ρ= 4 at t= 5.5, 11.0, 16.5 and 22.0 respectively.

Fig. 8. Transport element location and velocity vectors for r_ρ= 5 at t= 5.5, 11.0, 16.5 and 22.0 respectively.

Fig. 9. The streamline contours for r_ρ= 1 at t= 5.5, 11.0, 16.5 and 22.0 respectively.

Fig. 10. The streamline contours for r_ρ= 2 at t= 5.5, 11.0, 16.5 and 22.0 respectively.

Fig. 11. The streamline contours for r_ρ= 3 at t= 5.5, 11.0, 16.5 and 22.0 respectively.

Fig. 12. The streamline contours for r_ρ= 4 at t= 5.5, 11.0, 16.5 and 22.0 respectively.

Fig. 13. The streamline contours for r_ρ= 5 at t= 5.5, 11.0, 16.5 and 22.0 respectively.

Fig. 14. The normalised temperature contours ($T=1/\rho$) for r_ρ= 1 at t= 5.5, 11.0, 16.5 and 22.0 respectively.

Fig. 15. The normalised temperature contours ($T=1/\rho$) for r_ρ= 2 at t= 5.5, 11.0, 16.5 and 22.0 respectively.

Fig. 16. The normalised temperature contours ($T=1/\rho$) for r_ρ= 3 at t= 5.5, 11.0, 16.5 and 22.0 respectively.

Fig. 17. The normalised temperature contours ($T=1/\rho$) for r_ρ= 4 at t= 5.5, 11.0, 16.5 and 22.0 respectively.

Fig. 18. The normalised temperature contours ($T=1/\rho$) for $r_\rho = 5$ at t= 5.5, 11.0, 16.5 and 22.0 respectively.

Fig. 19. The vorticity contours for $r_\rho = 1$ at t= 5.5, 11.0, 16.5 and 22.0 respectively. The continuous lines represent the negative vorticity.

Fig. 20. The vorticity contours for $r_\rho = 2$ at t= 5.5, 11.0, 16.5 and 22.0 respectively. The continuous lines and the dashed lines represent negative and positive vorticity respectively.

Fig. 21. The vorticity contours for $r_\rho = 3$ at t= 5.5, 11.0, 16.5 and 22.0 respectively. The continuous lines and the dashed lines represent negative and positive vorticity respectively.

Fig. 22. The vorticity contours for $r_\rho = 4$ at t= 5.5, 11.0, 16.5 and 22.0 respectively. The continuous lines and the dashed lines represent negative and positive vorticity respectively.

Fig. 23. The vorticity contours for $r_\rho = 5$ at t= 5.5, 11.0, 16.5 and 22.0 respectively. The continuous lines and the dashed lines represent negative and positive vorticity respectively.

Fig. 24. Plot of $\log(I/I_0)$ versus time. Curves 1,2,3,4 and 5 represent values for $r_\rho = 1, 2, 3, 4$ and 5 respectively. I is defined as $I = \int\int |(\mathbf{u}(\mathbf{x},t)-\mathbf{U}(\mathbf{x}))| \, d\mathbf{x}$. $I_0^\rho = I$ at t=0.

Fig. 25. Plot of the average length of the interface versus time for $r_\rho = 1, 2, 3, 4$ and 5 respectively.

Fig. 26. Plot of the circulation generated as a function of time for $r_\rho = 1, 2, 3, 4$ and 5. The positive circulation and the negative circulation are shown separately.

Fig. 27. Plot of cumulative circulation versus time for $r_\rho = 1,2,3,4$ and 5. The positive and negative circulation are shown separately.

Fig. 28. Plot of circulation versus time for individual material layers 1, 7,9 and 15 for the case $r_\rho = 3$. The values are normalised by initial values and positive and negative circulation are shown separately.

Fig. 29. Plot of the vorticity along the interface for material layer number 1 for t=5.5,11.0,16.5 and 22.0. The density ratio is 2.0 and the interface length is normalized by its length at each time.

Fig. 30. Plot of the vorticity along the interface for material layer number 8.

Fig. 31. Plot of the vorticity along the interface for material layer number 15.

Fig. 32. Transport element location and velocity vectors for r_ρ = (a) 1, (b) 2, (c) 3, (d) 4 and (e) 5 at t= 24.0.

Fig. 33. The normalized temperature contours at t=24.0 for r_ρ = (a) 1, (b) 2, (c) 3, (d) 4 and (e) 5 respectively.

Fig. 34. The vorticity contours at t=24.0 for r_ρ = (a) 1, (b) 2, (c) 3, (d) 4 and (e) 5 respectively.

Fig. 35. Plot of eddy convective velocity versus s= $1/r_\rho$. The symbols represent results of numerical simulation and the continuous line is obtained from Eqn. (84).

Fig. 36. Plot of the entrainment ratio versus s=$1/r_\rho$. The symbols represent results of numerical simulations and the curve is obtained from Eqn. (86).

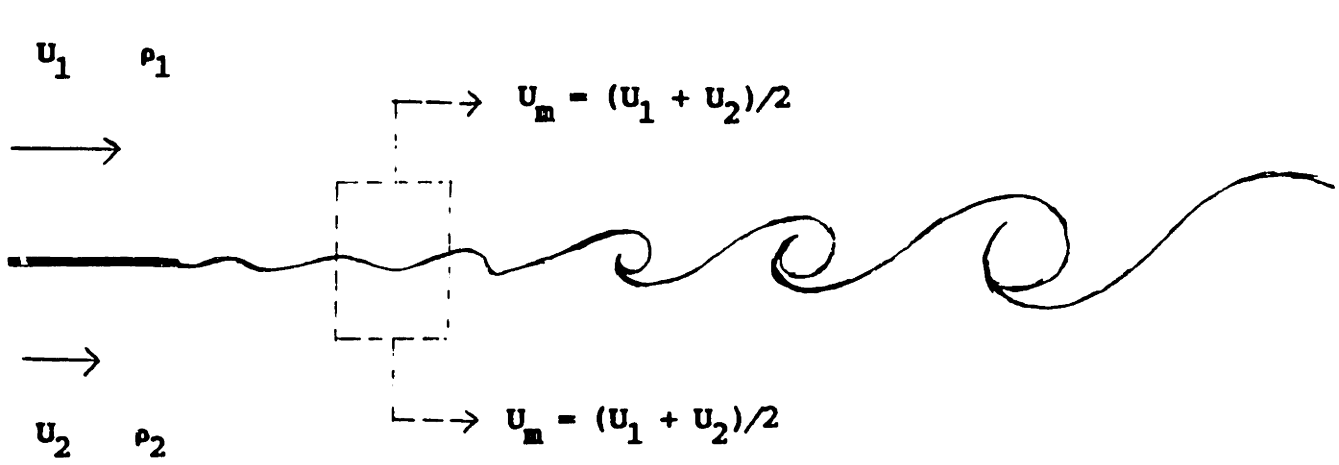
A SPATIAL SHEAR LAYER
U_1 ρ_1
$U_m = (U_1 + U_2)/2$
$U_m = (U_1 + U_2)/2$
U_2 ρ_2

(a)

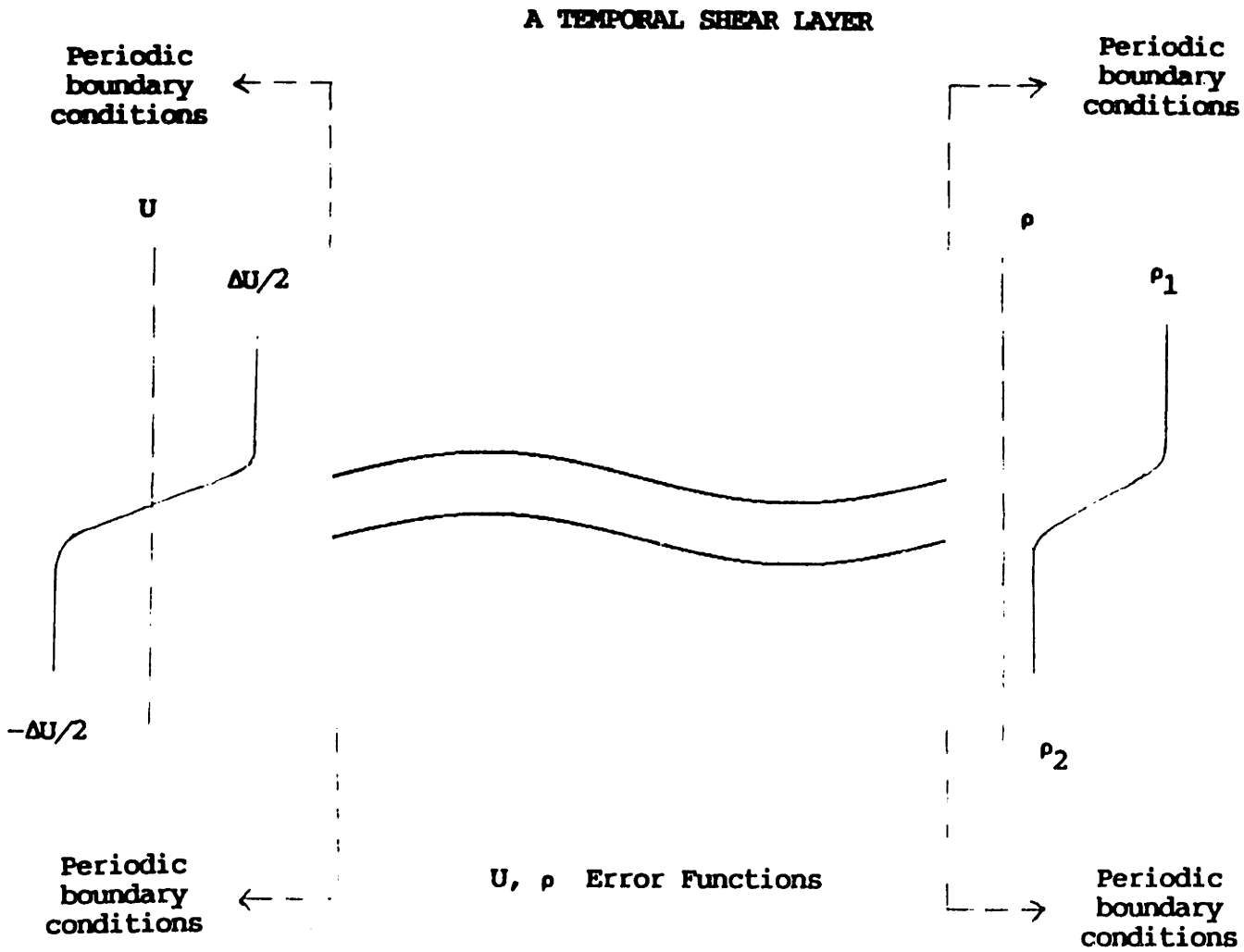
A TEMPORAL SHEAR LAYER
Periodic boundary conditions
Periodic boundary conditions
U
ΔU/2
ρ
ρ_1
-ΔU/2
ρ_2
Periodic boundary conditions
U, ρ Error Functions
Periodic boundary conditions

(b)

Figure 2

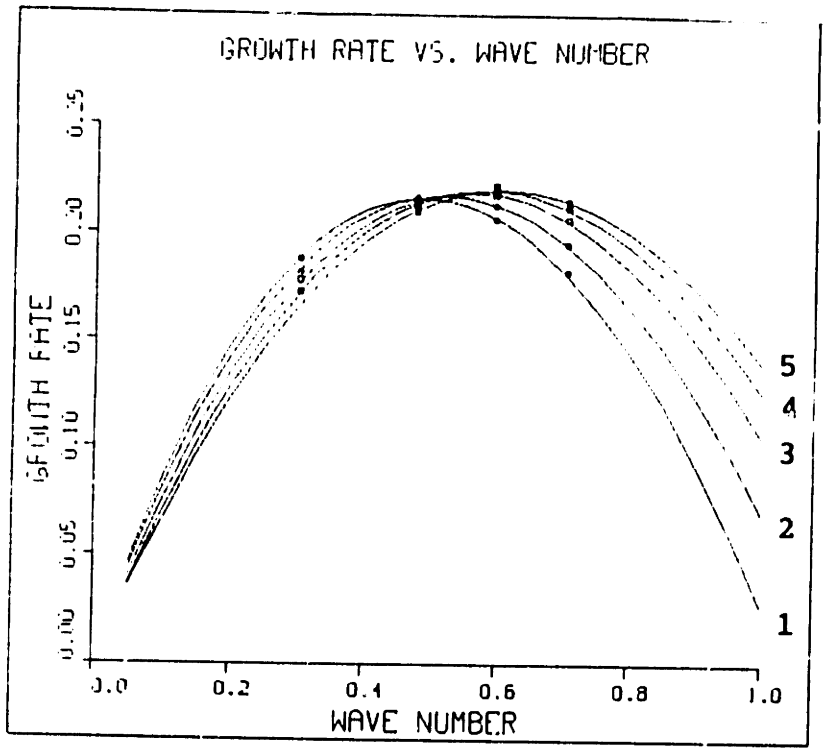
GROWTH RATE VS. WAVE NUMBER
GROWTH RATE
0.25
0.20
0.15
0.10
0.05
0.00
0.0
0.2
0.4
0.6
0.8
1.0
WAVE NUMBER
5
4
3
2
1

(a)

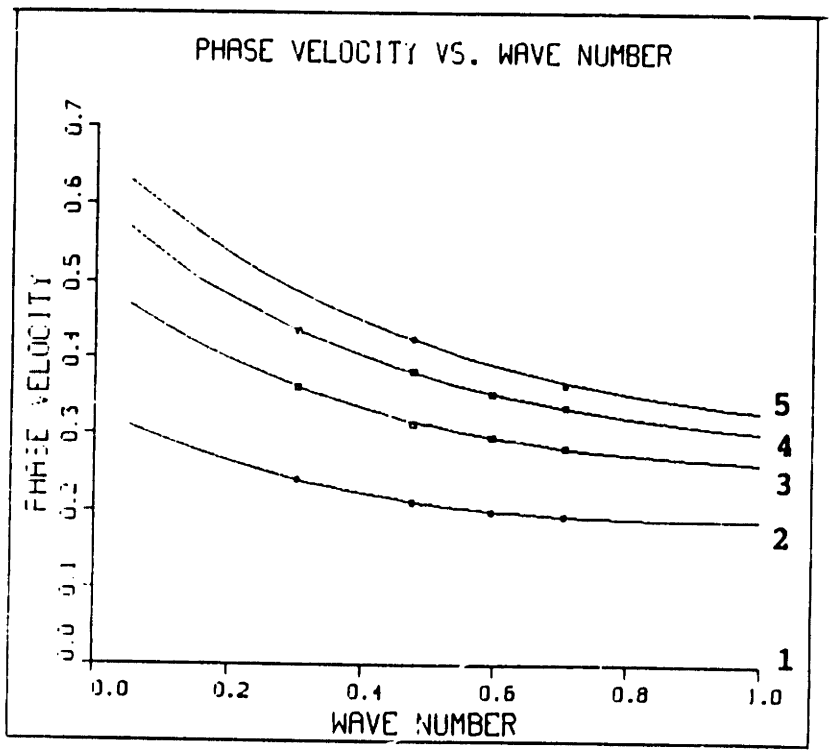
PHASE VELOCITY VS. WAVE NUMBER
PHASE VELOCITY
0.7
0.6
0.5
0.4
0.3
0.2
0.1
0.0
0.0
0.2
0.4
0.6
0.8
1.0
WAVE NUMBER
5
4
3
2
1

(b)

Figure 3

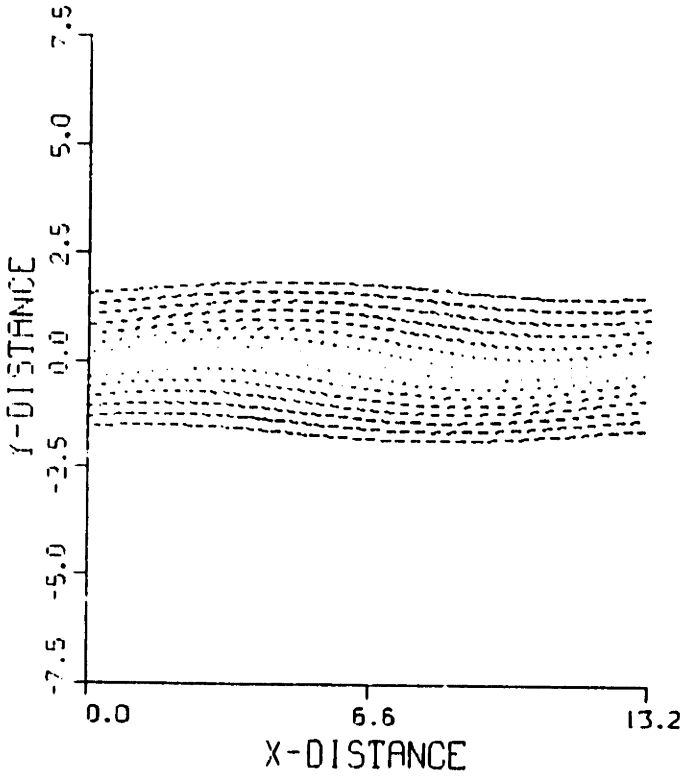

t = 5.5

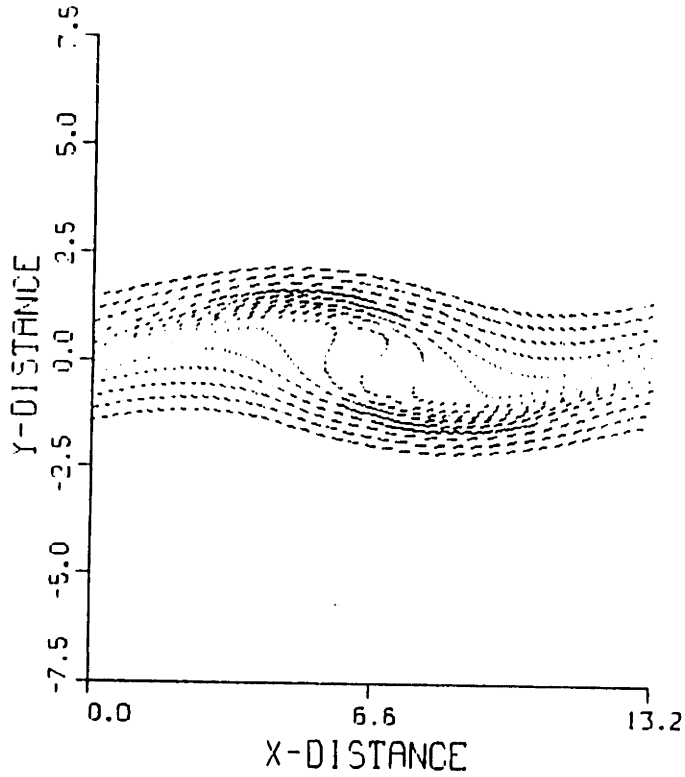

t = 11.0

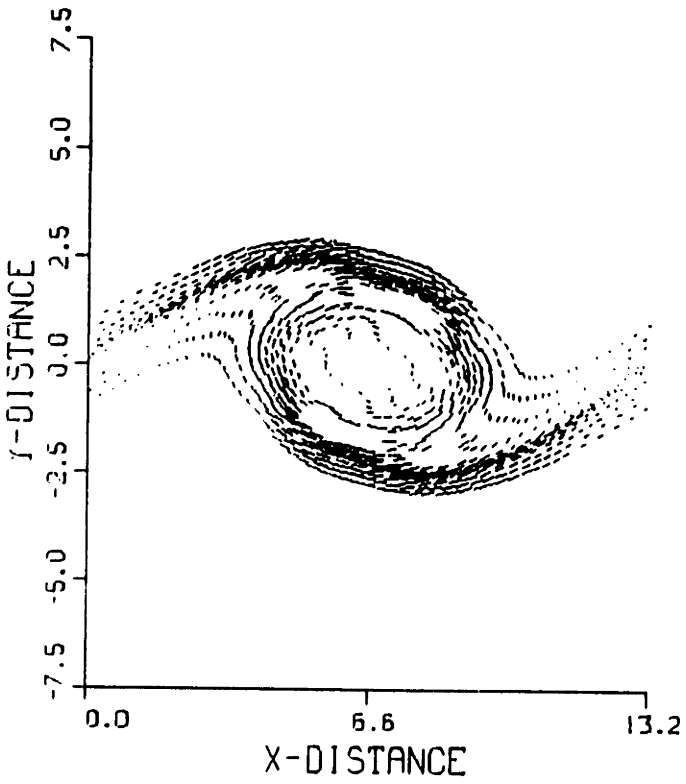

t = 16.5

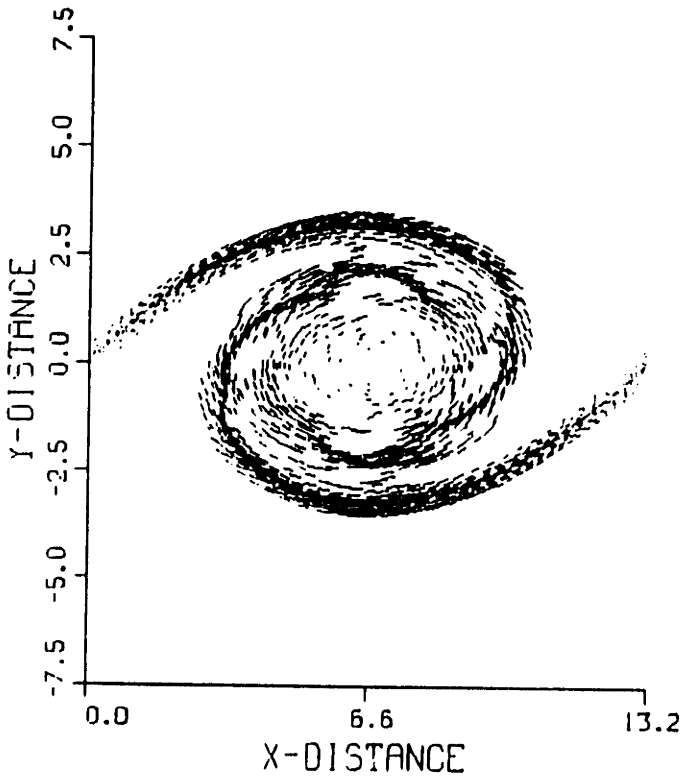

t = 22.0

Figure 4

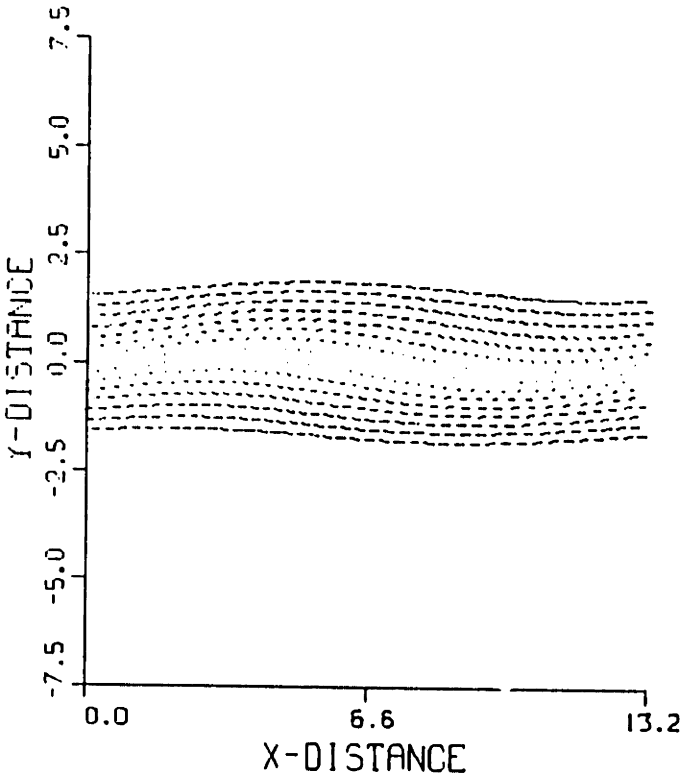

t = 5.5

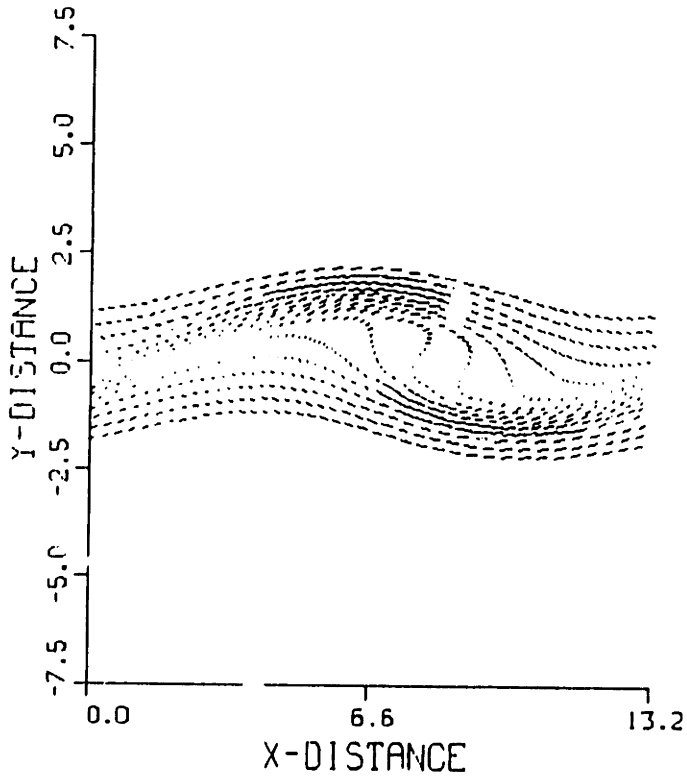

t = 11.0

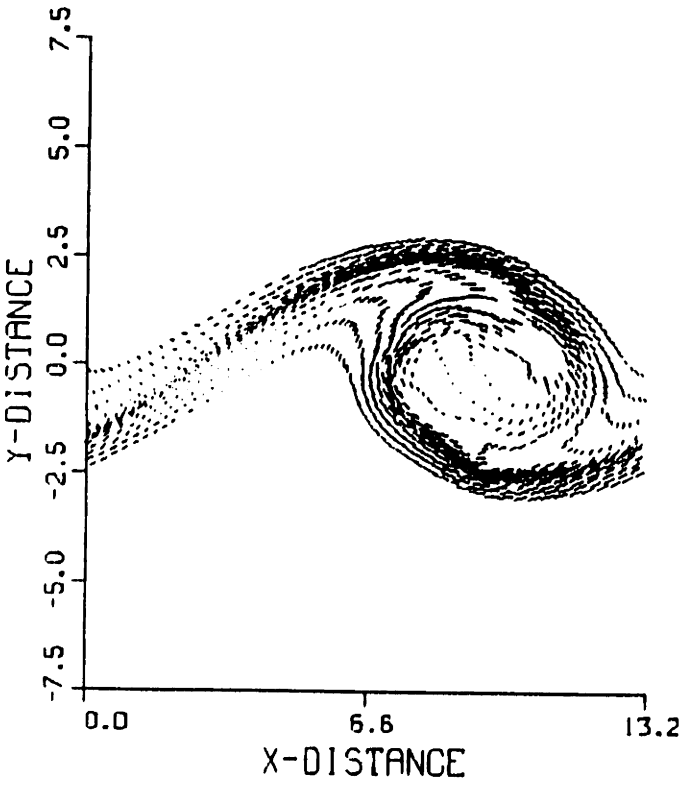

t = 16.5

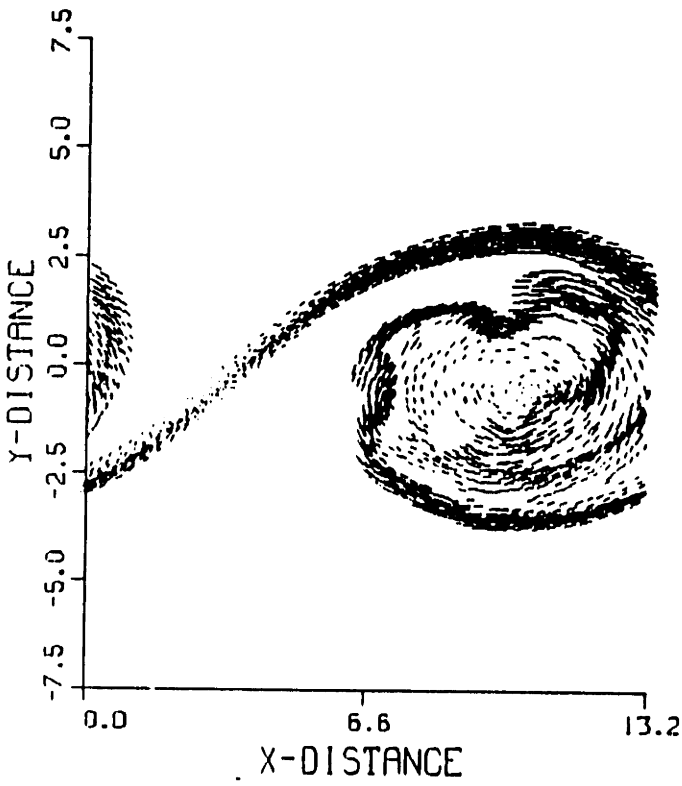

t = 22.0

Figure 5

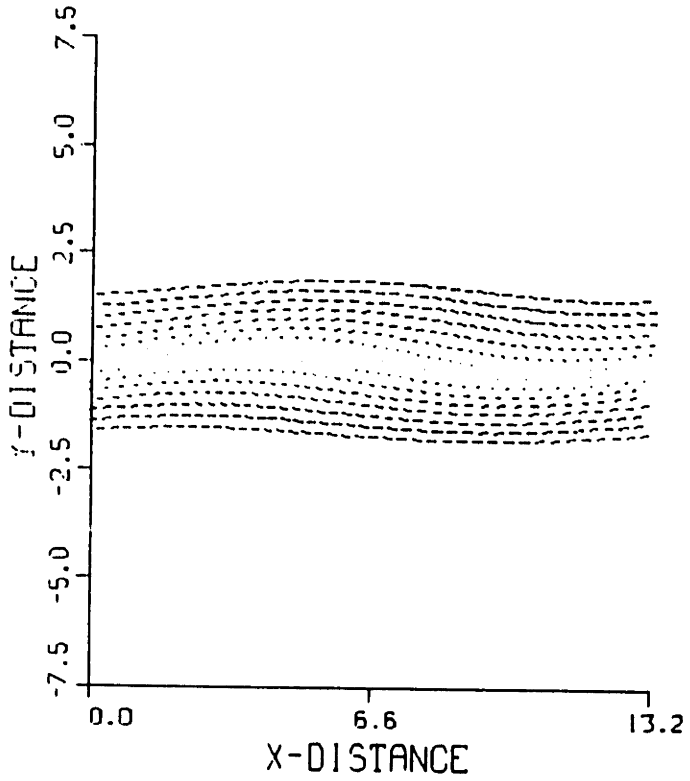

t = 5.5

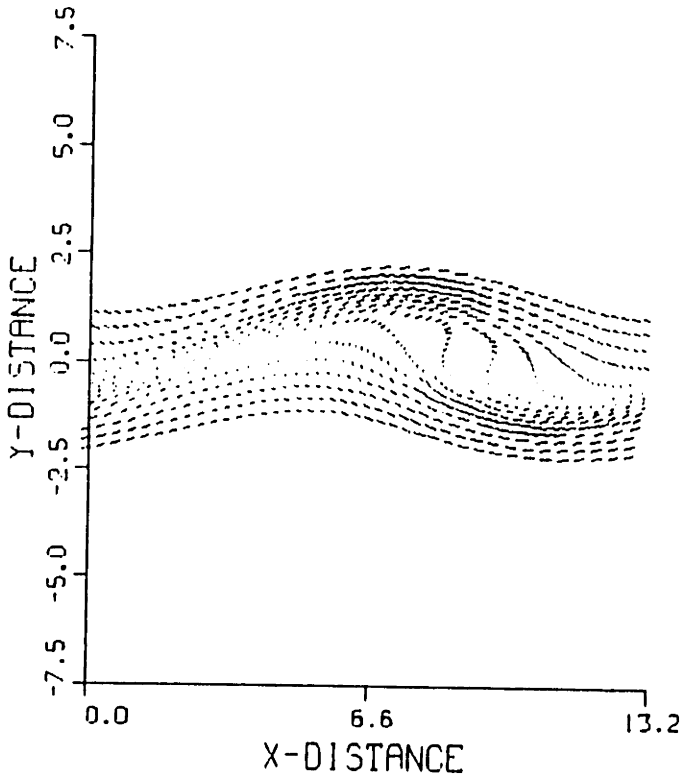

t = 11.0

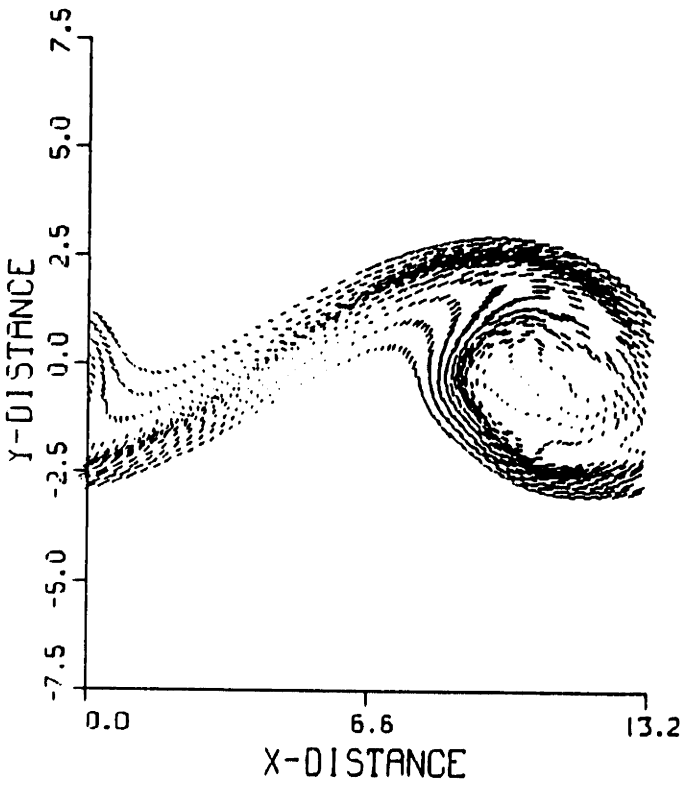

t = 16.5

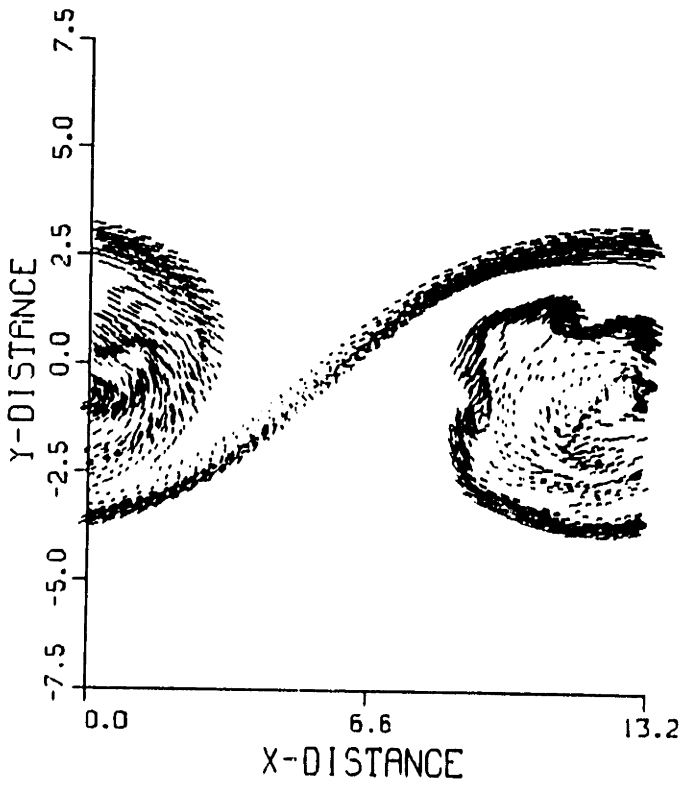

t = 22.0

Figure 6

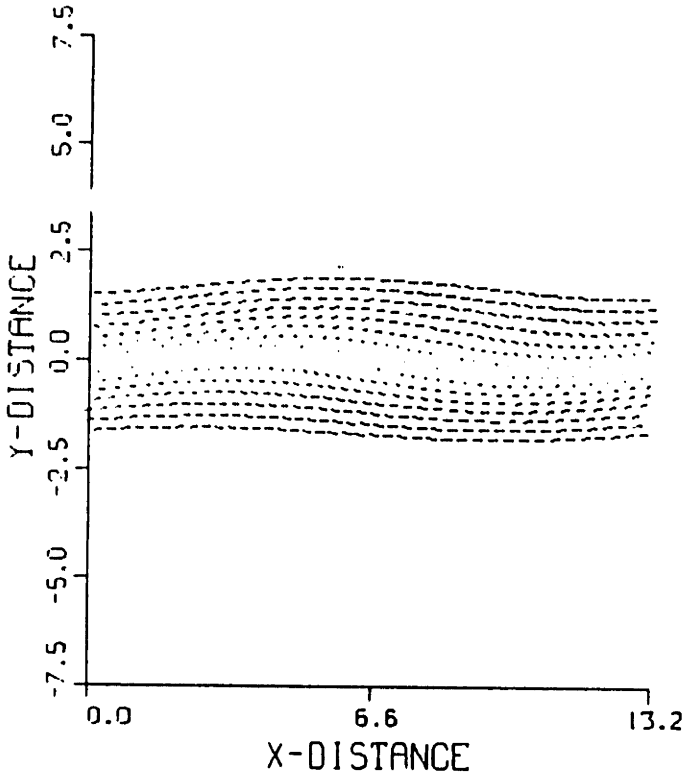

t = 5.5

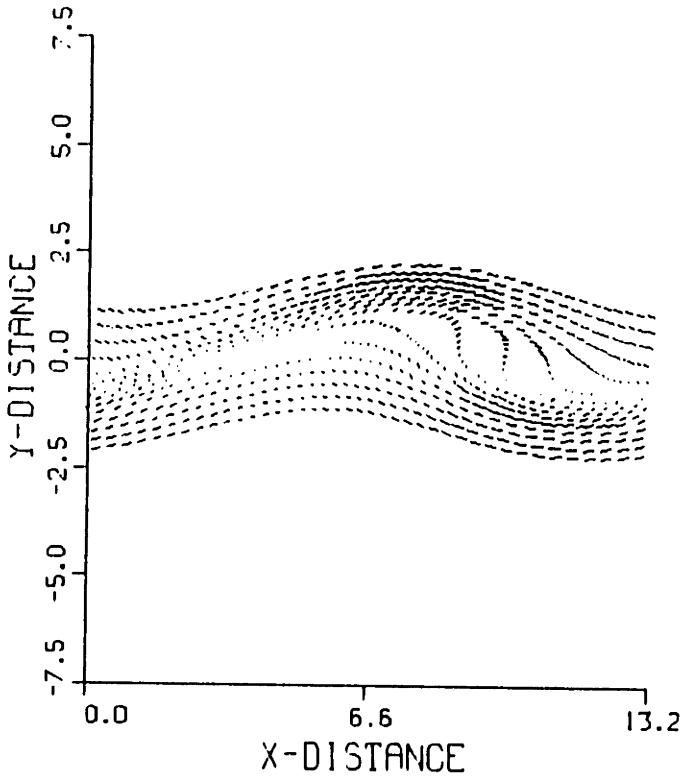

t = 11.0

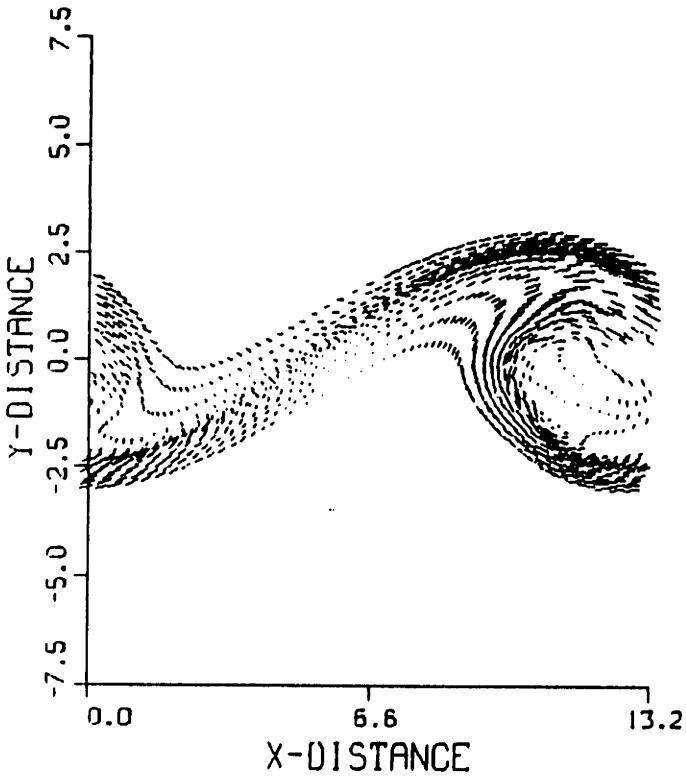

t = 16.5

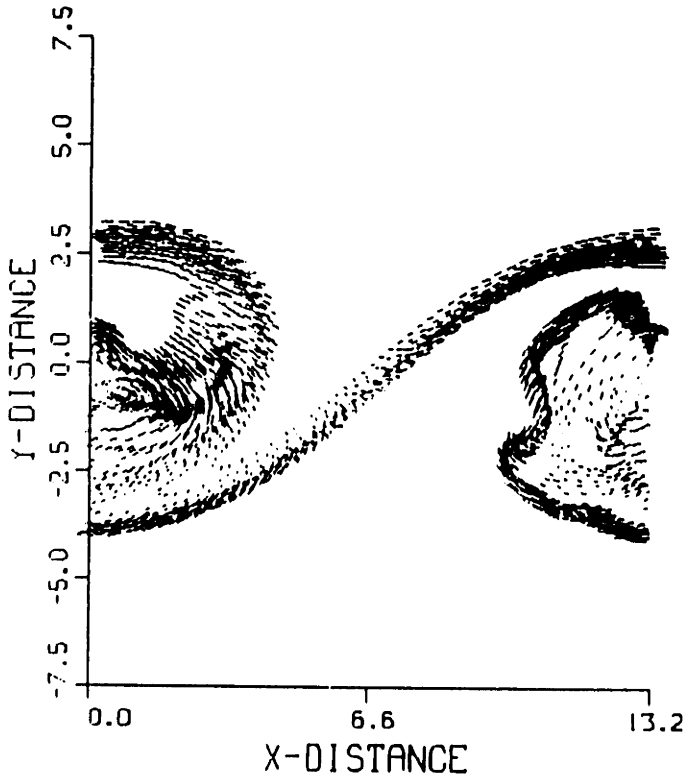

t = 22.0

Figure 7

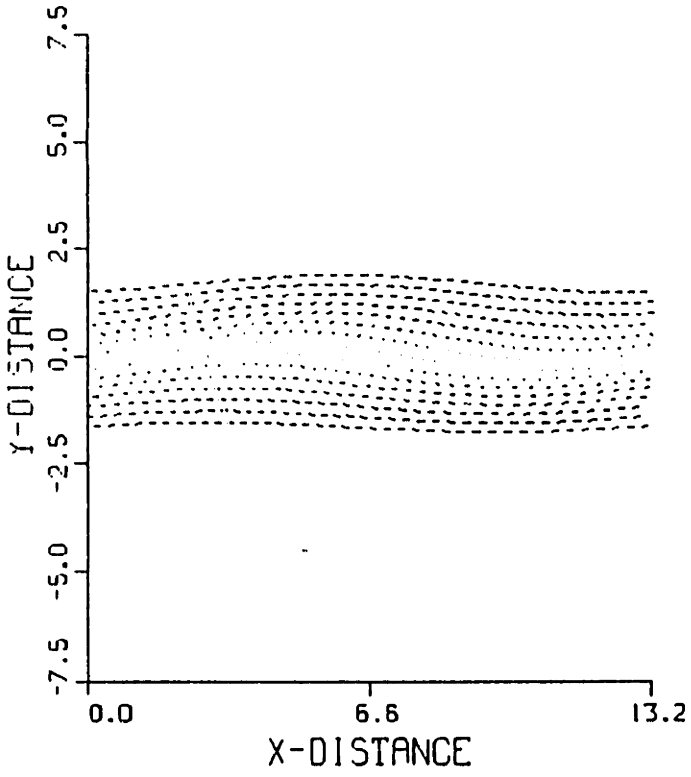

t = 5.5

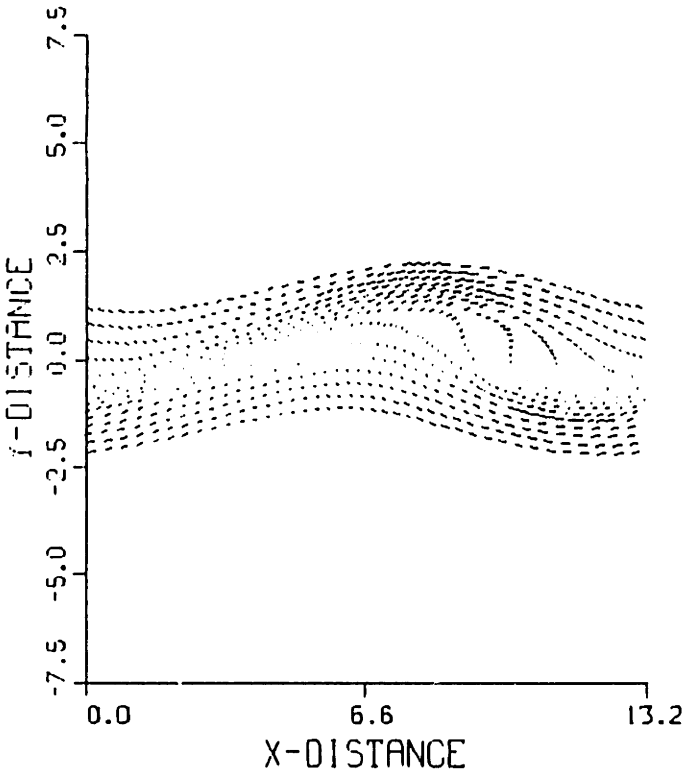

t = 11.0

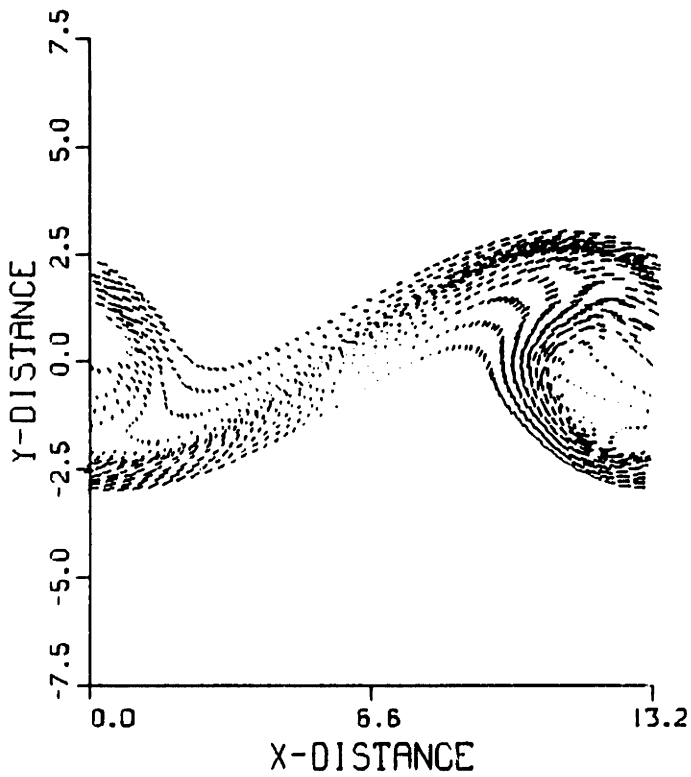

t = 16.5

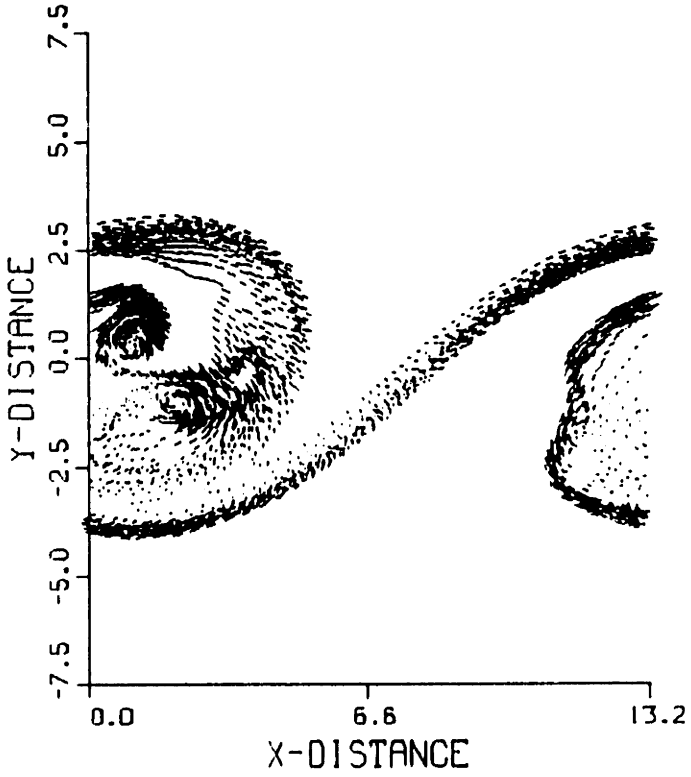

t = 22.0

Figure 8

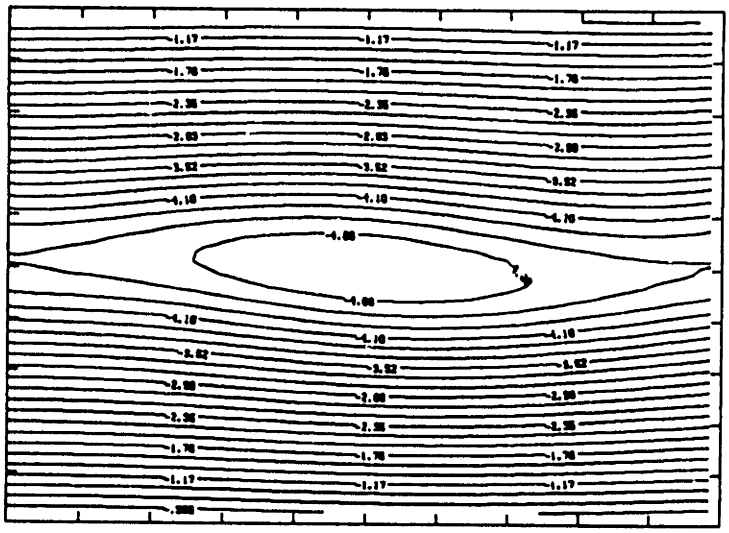

t = 5.5

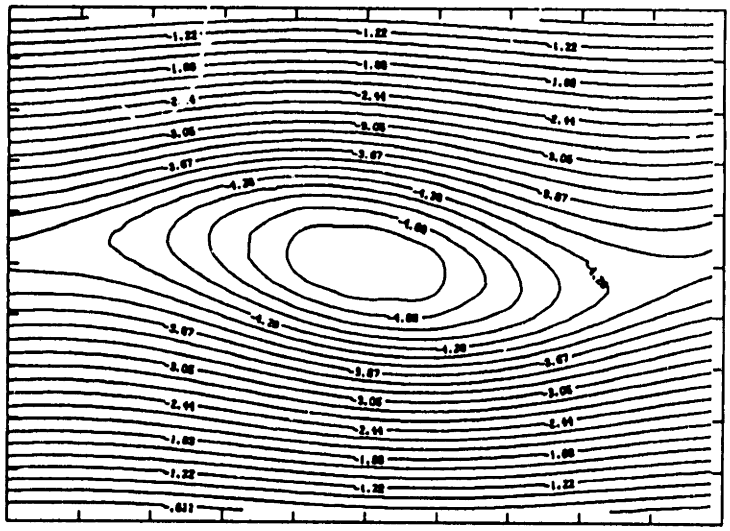

t = 11.0

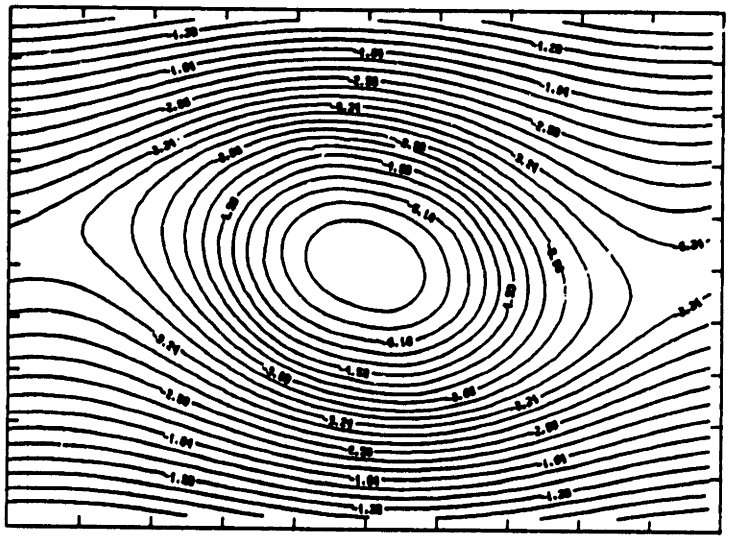

t = 16.5

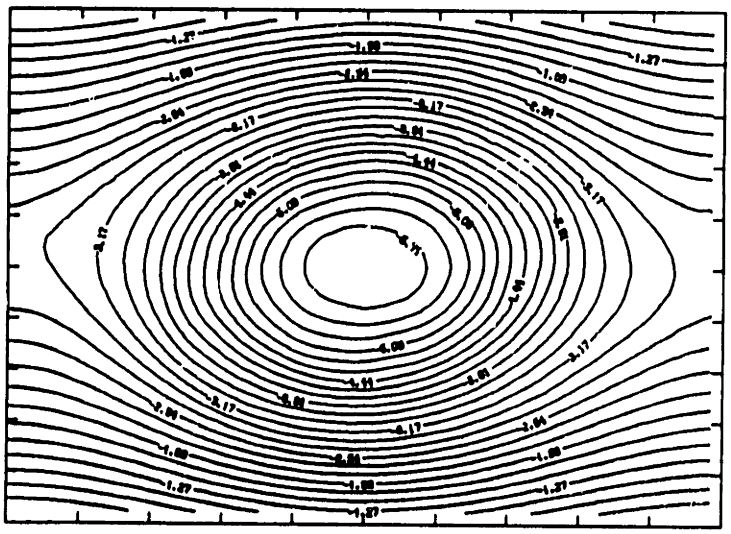

t = 22.0

Figure 9

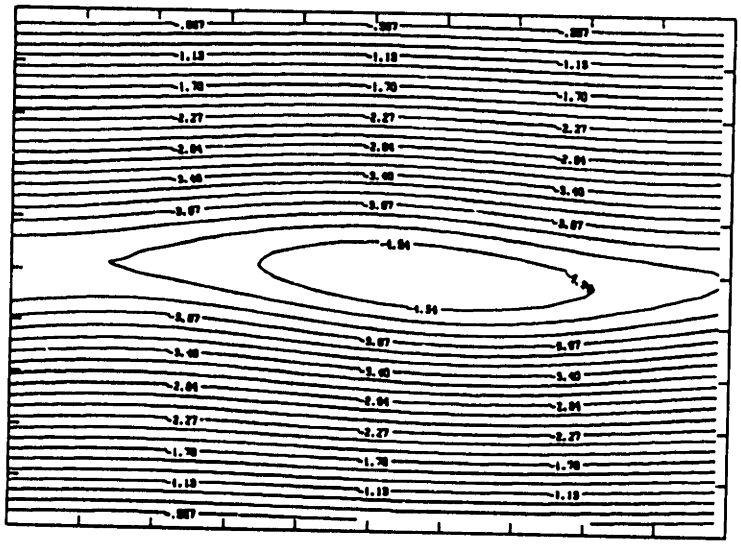

t = 5.5

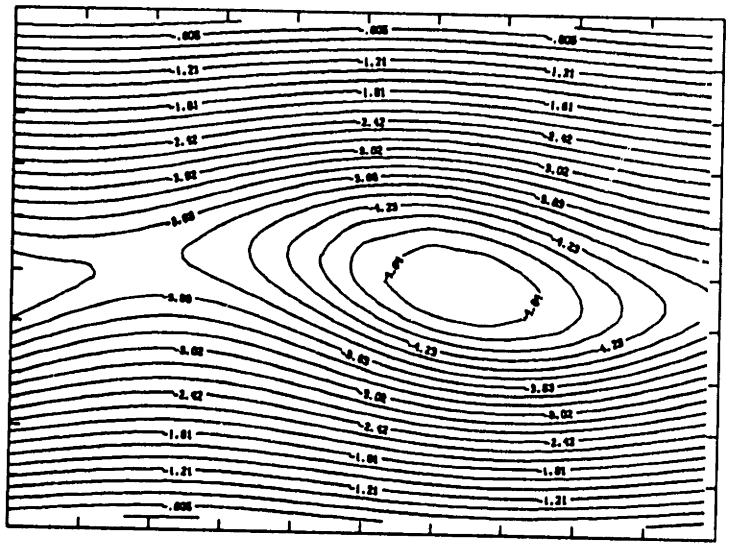

t = 11.0

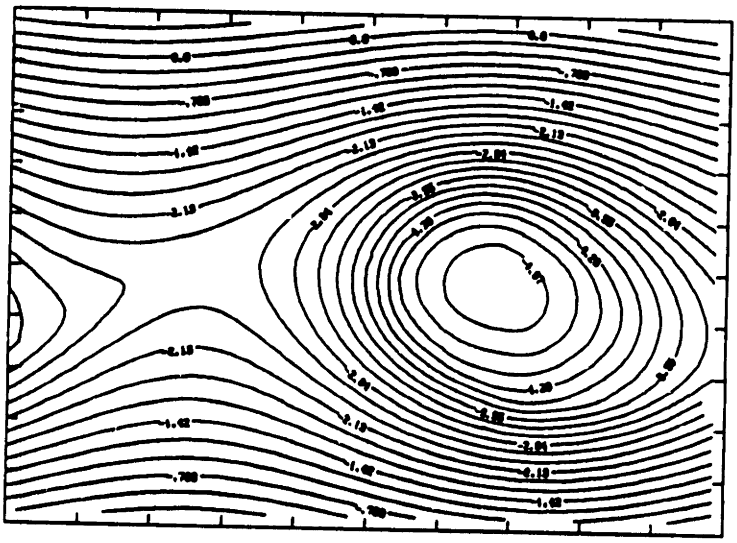

t = 16.5

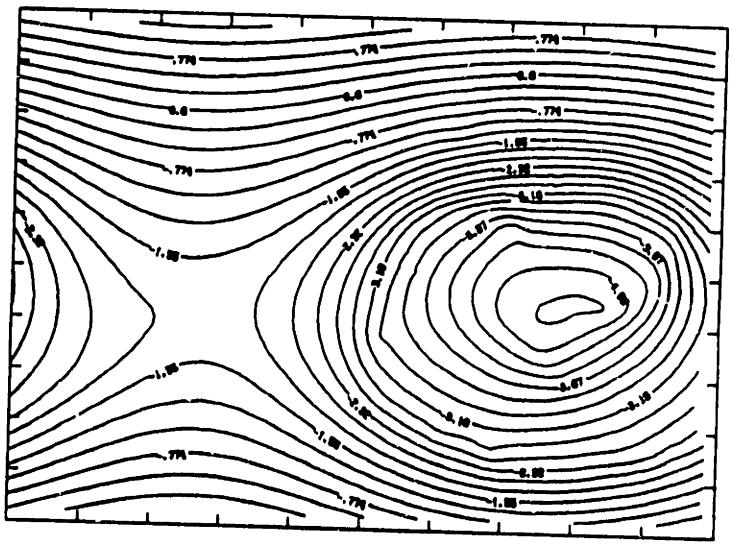

t = 22.0

Figure 10

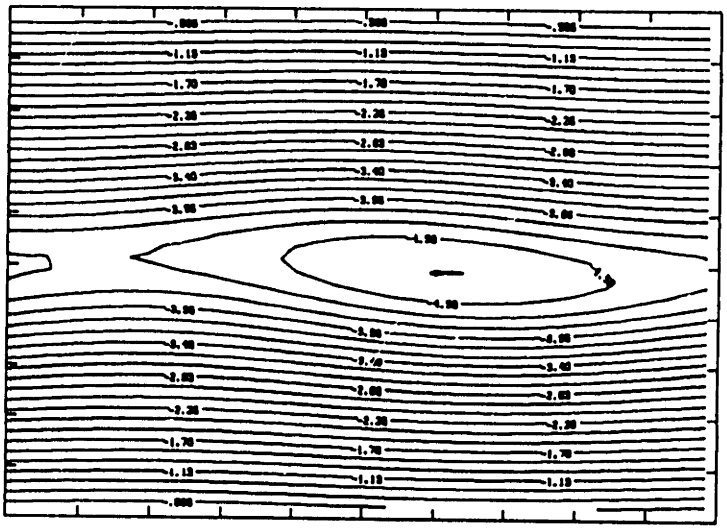

t = 5.5

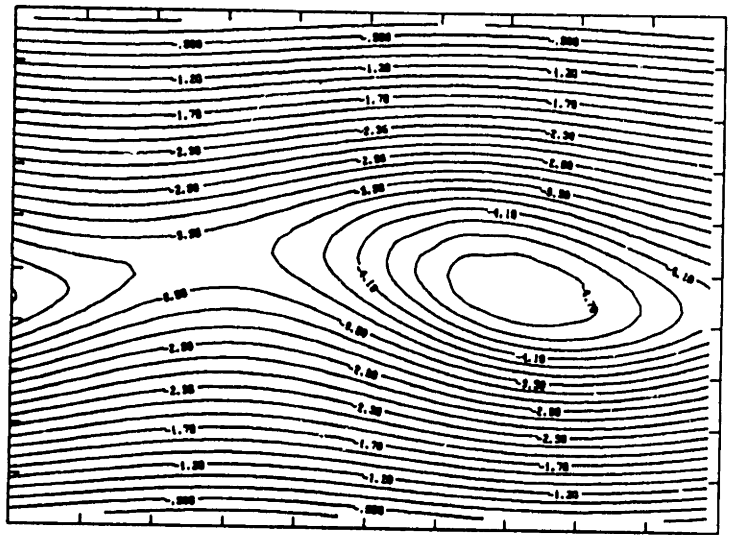

t = 11.0

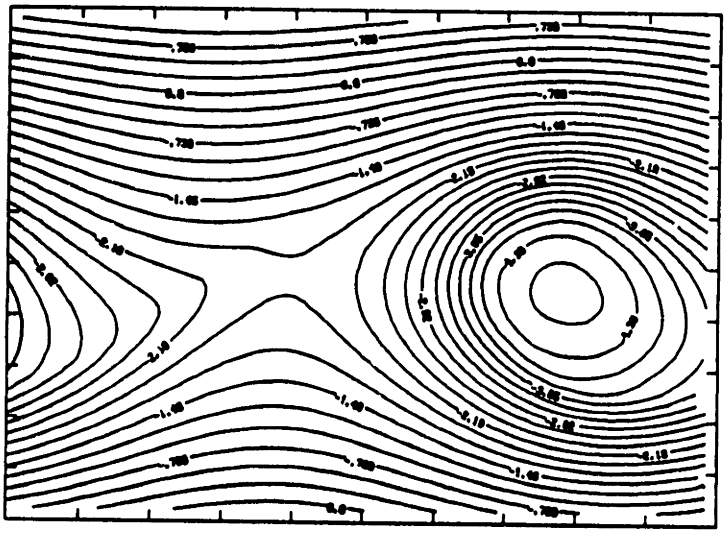

t = 16.5

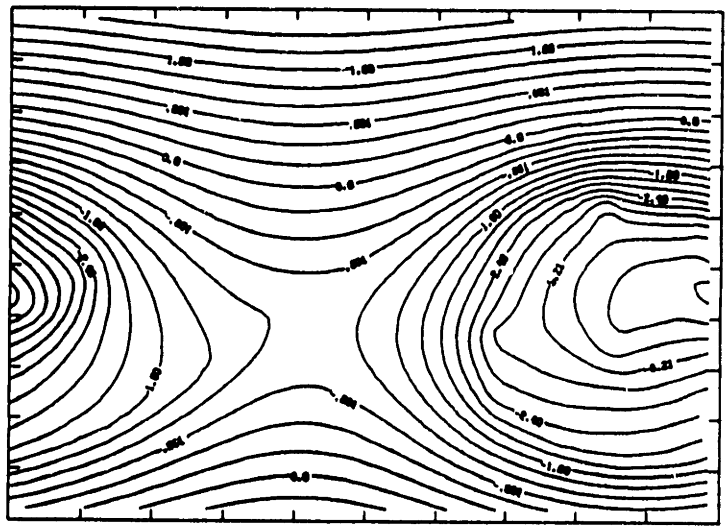

t = 22.0

Figure 11

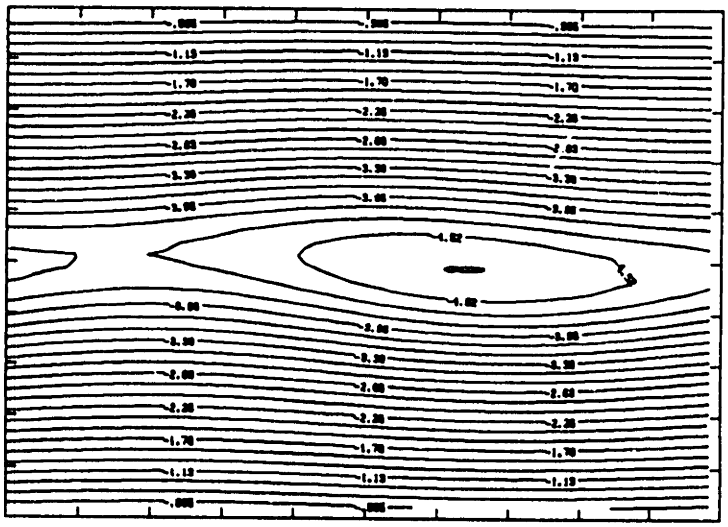

t = 5.5

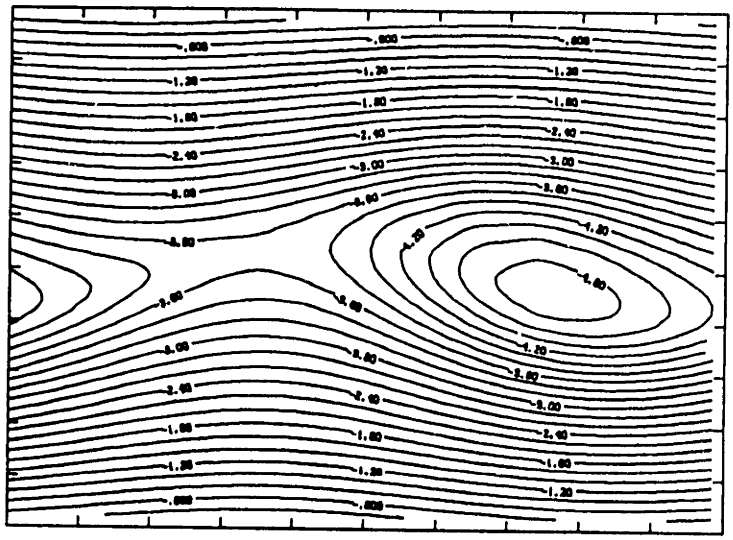

t = 11.0

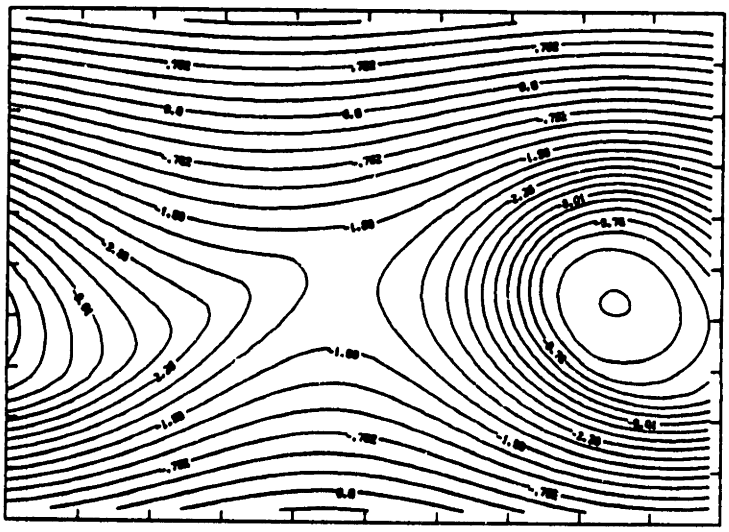

t = 16.5

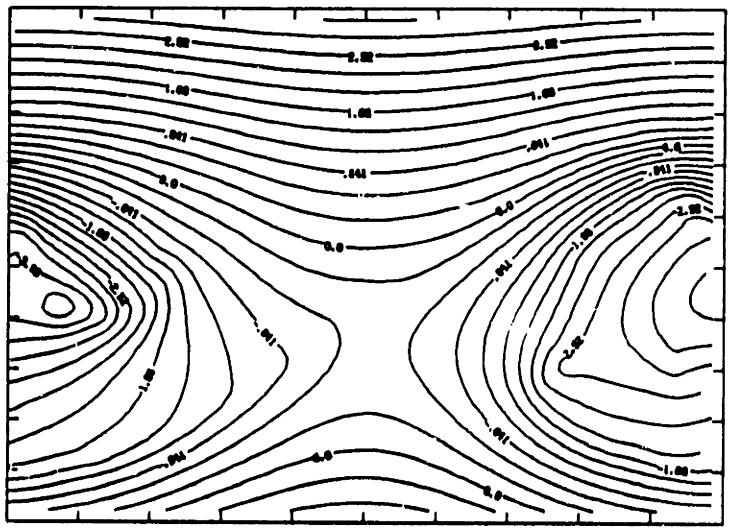

t = 22.0

Figure 12

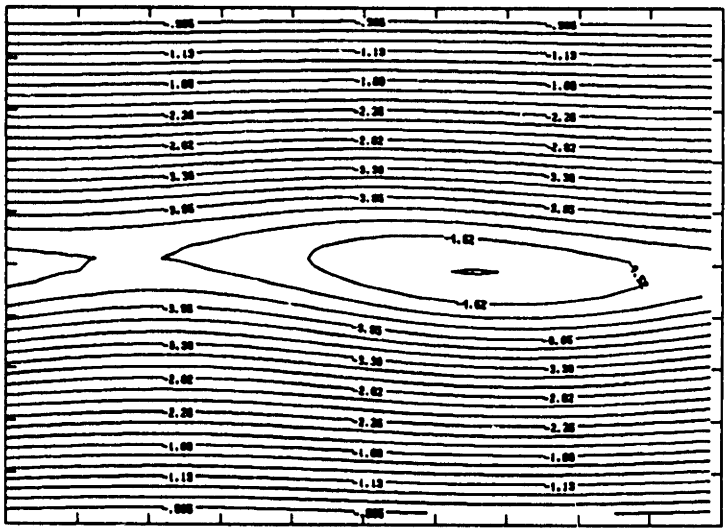

t = 5.5

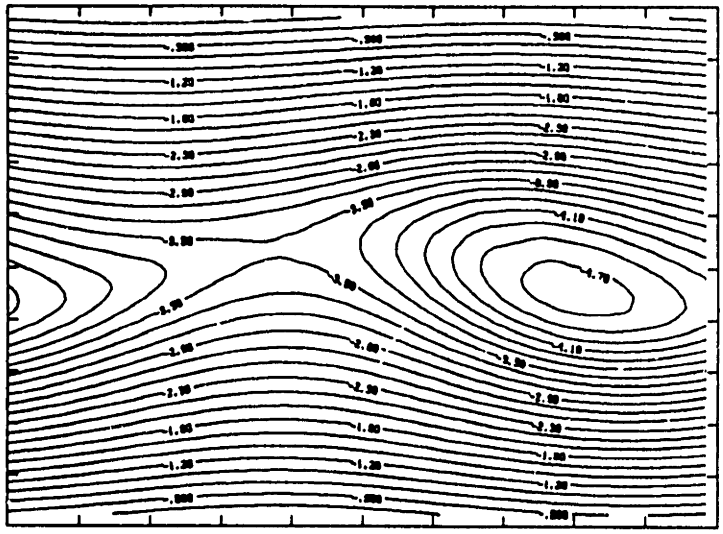

t = 11.0

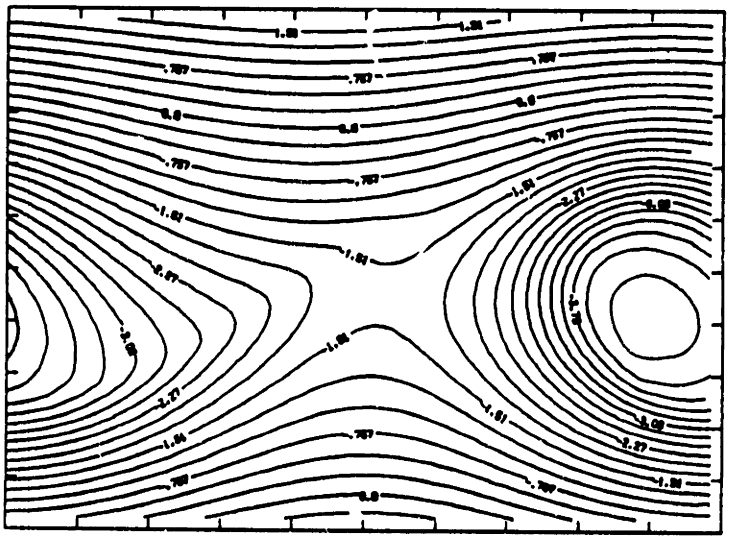

t = 16.5

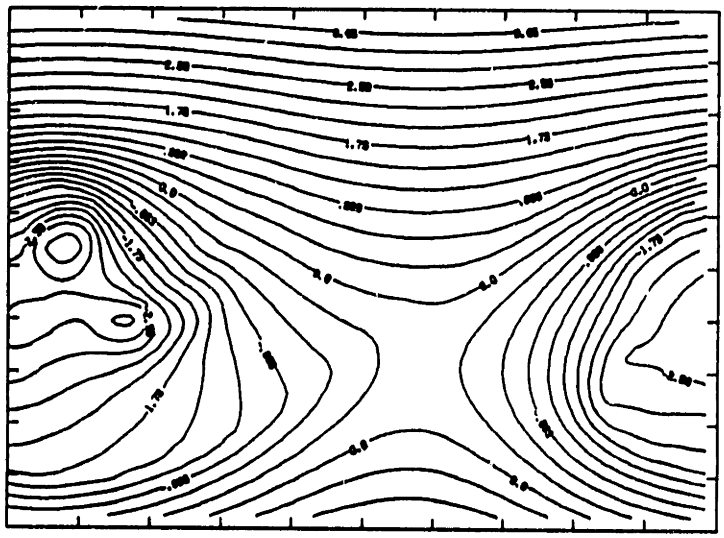

t = 22.0

Figure 13

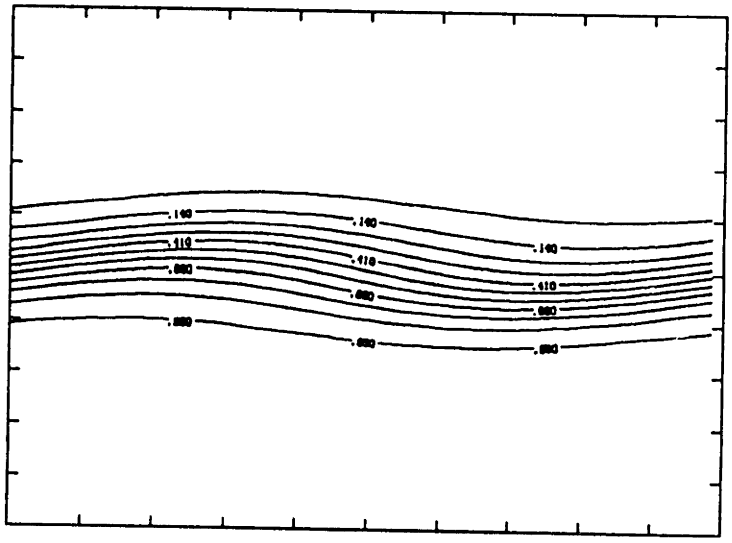

t = 5.5

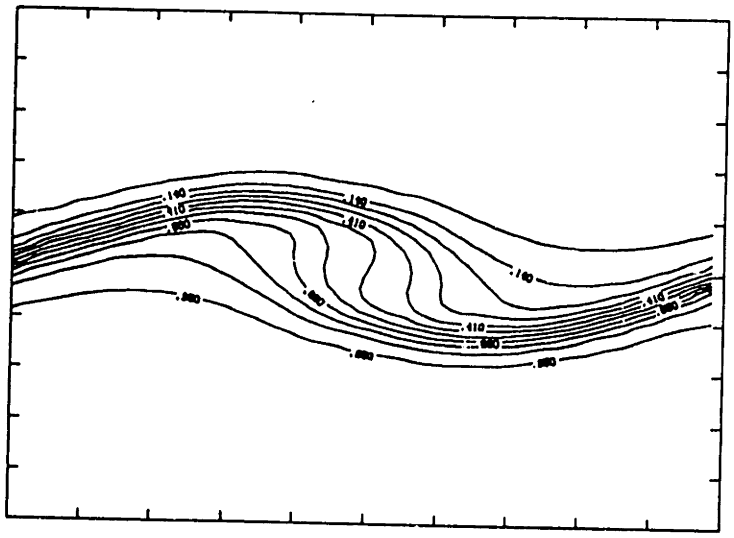

t = 11.0

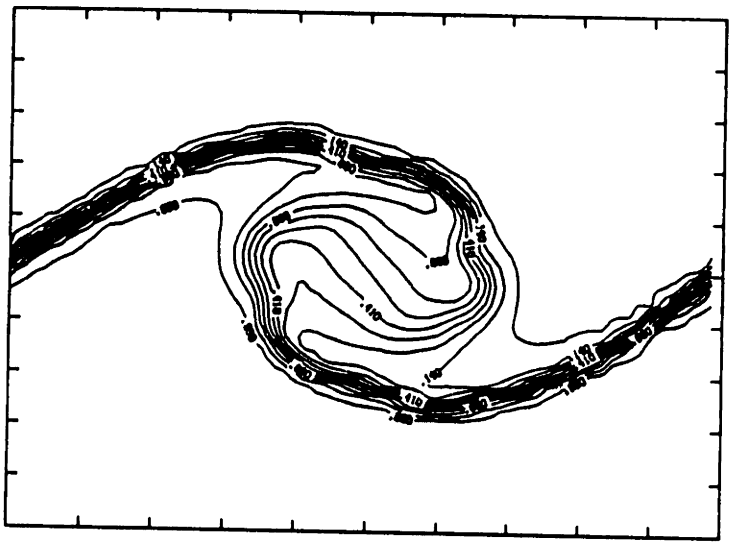

t = 16.5

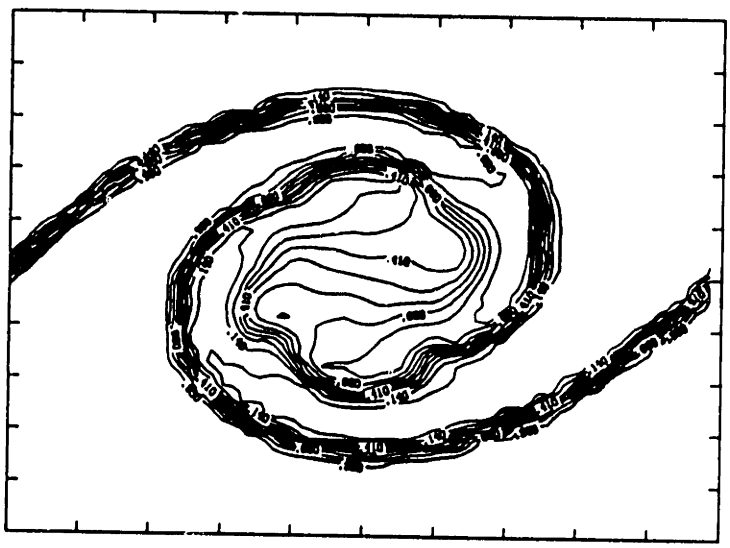

t = 22.0

Figure 14

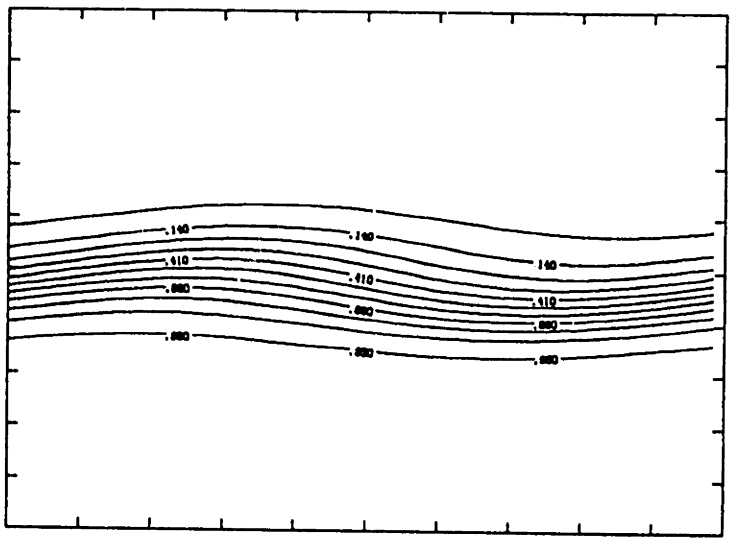

t = 5.5

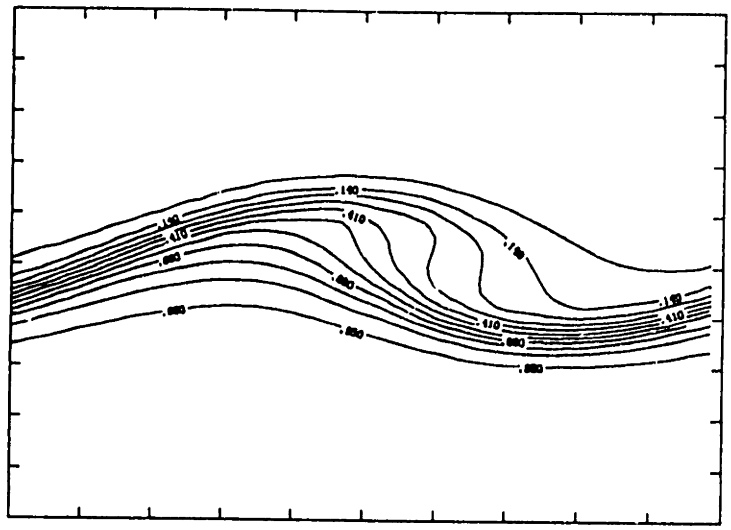

t = 11.0

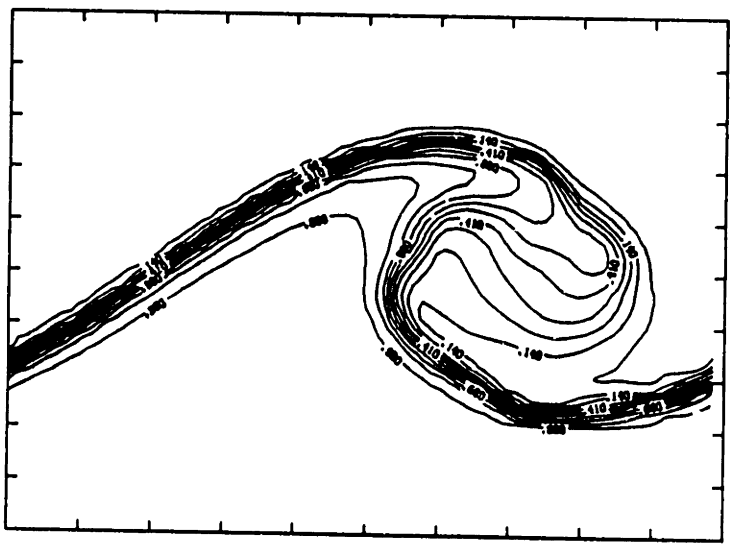

t = 16.5

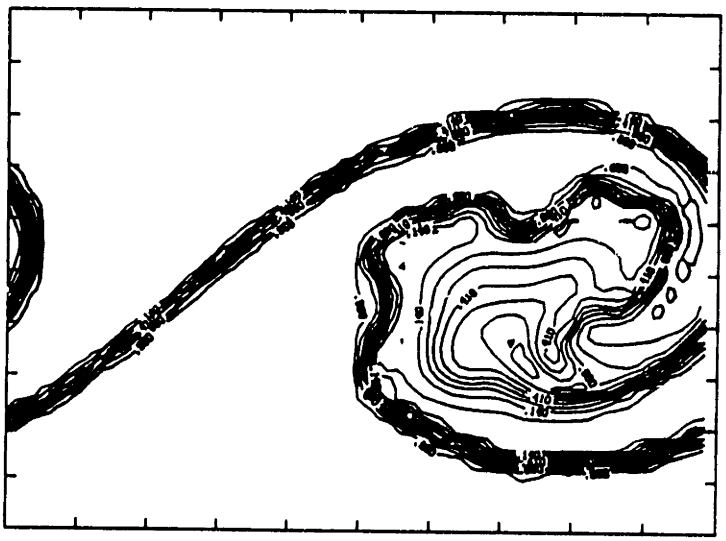

t = 22.0

Figure 15

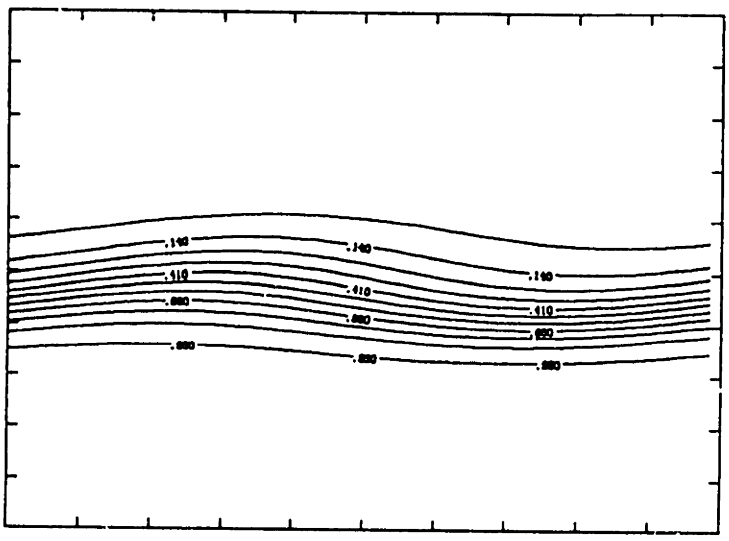

t = 5.5

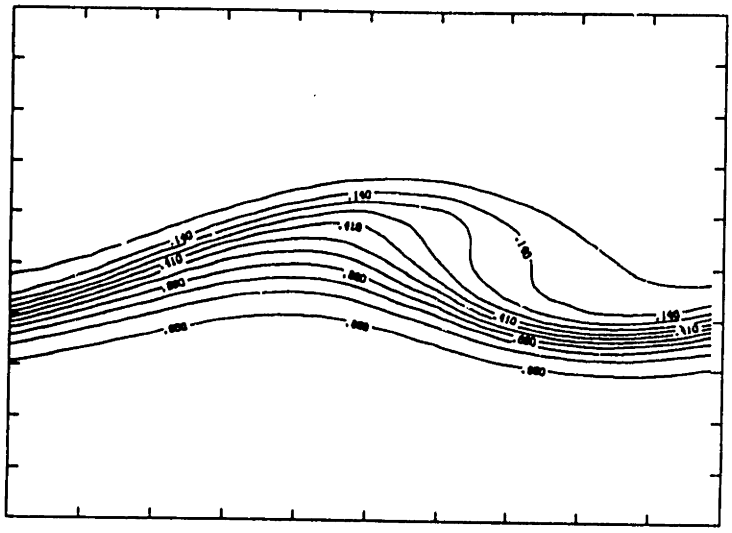

t = 11.0

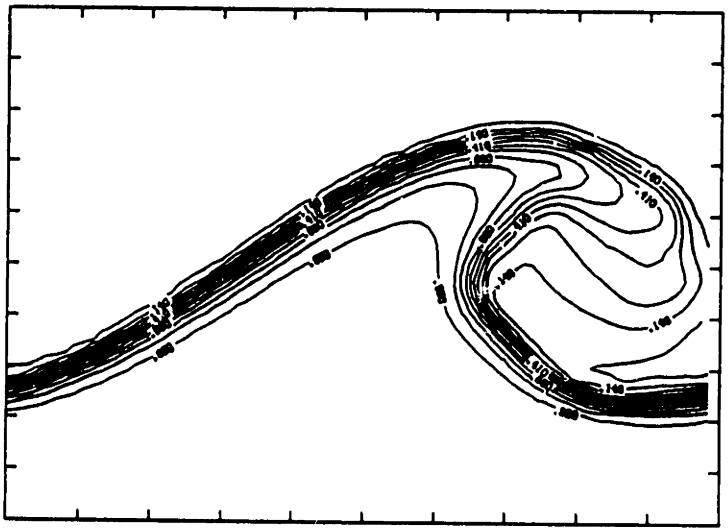

t = 16.5

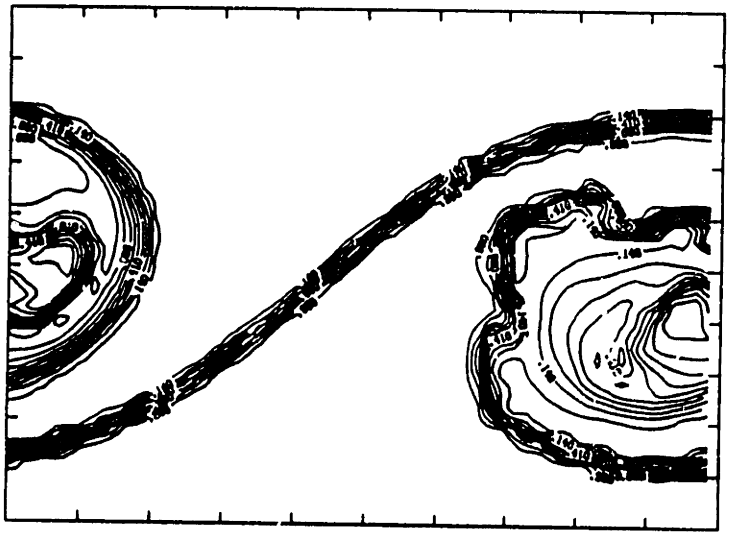

t = 22.0

Figure 16

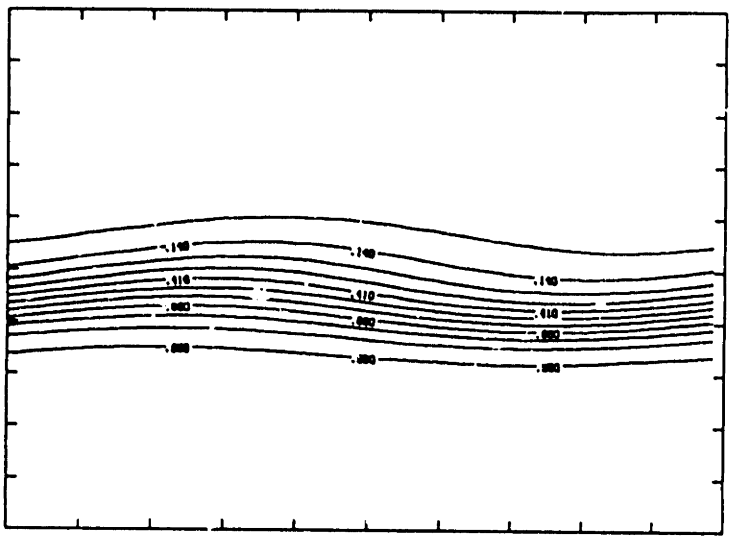

t = 5.5

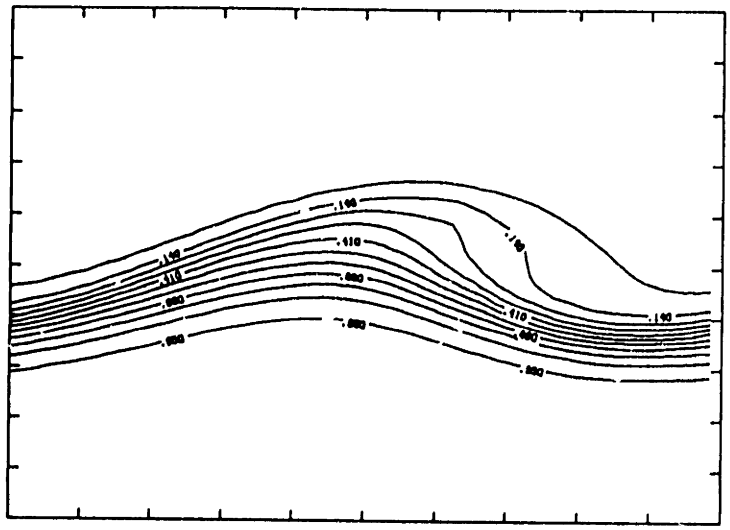

t = 11.0

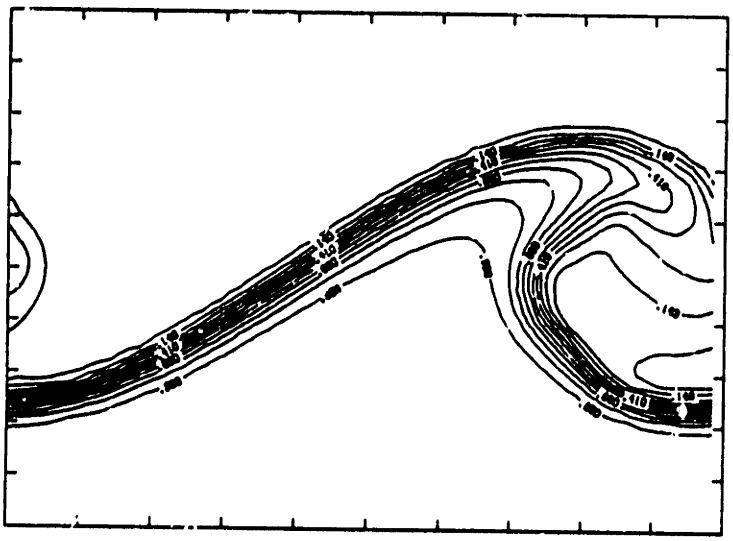

t = 16.5

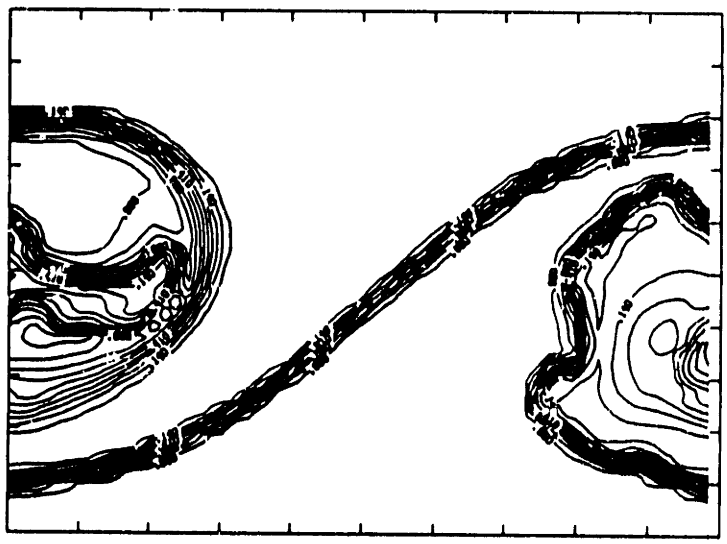

t = 22.0

Figure 17

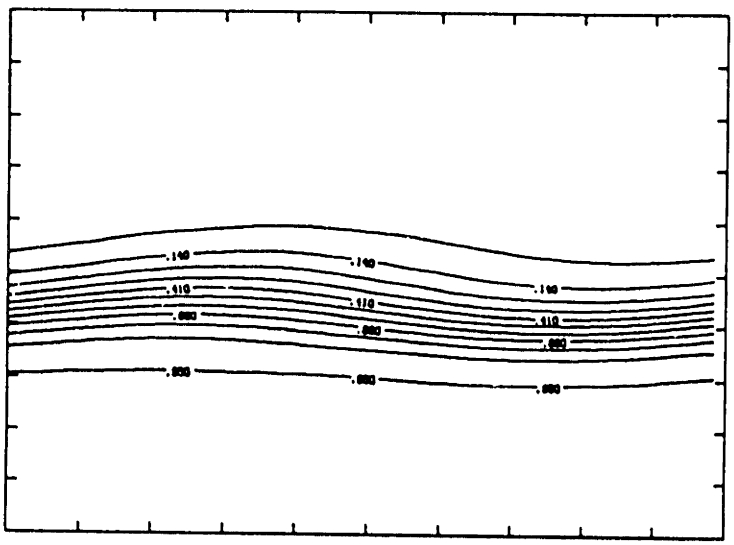

t = 5.5

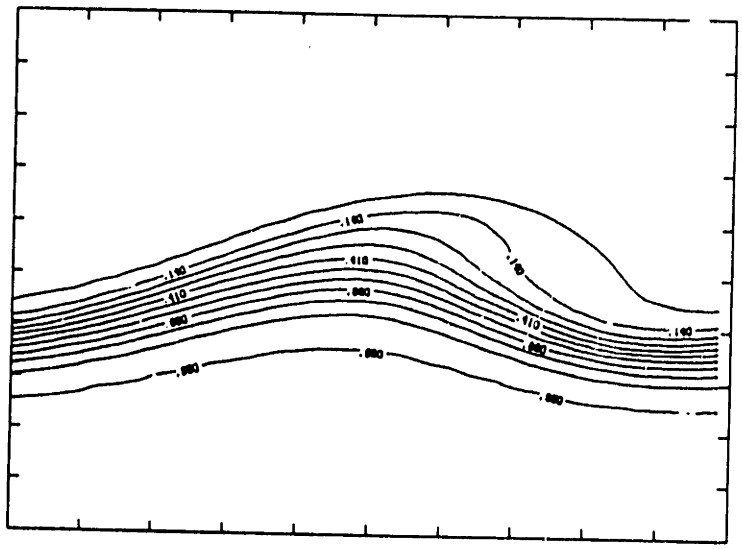

t = 11.0

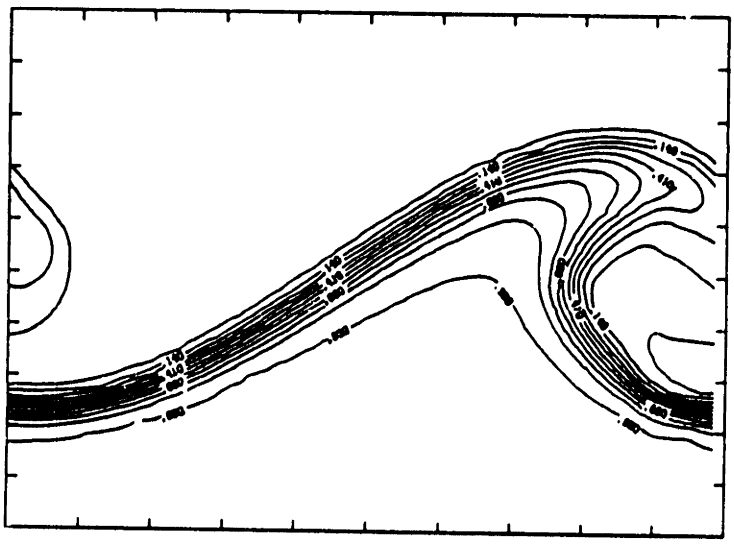

t = 16.5

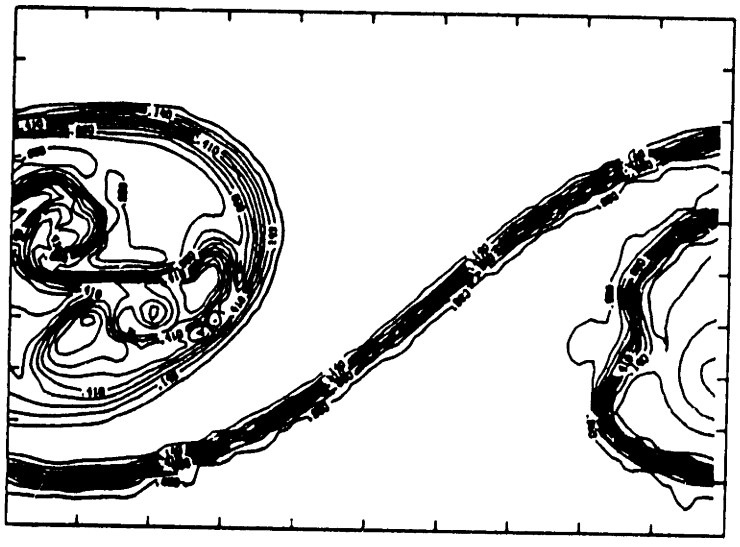

t = 22.0

Figure 18

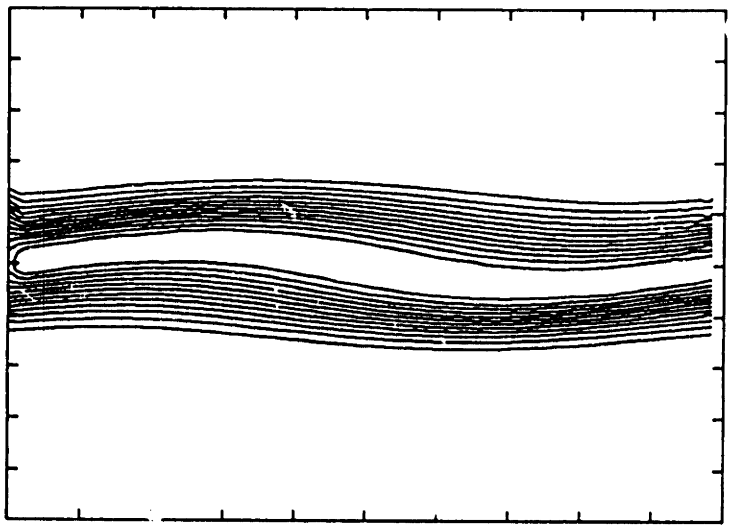

t = 5.5

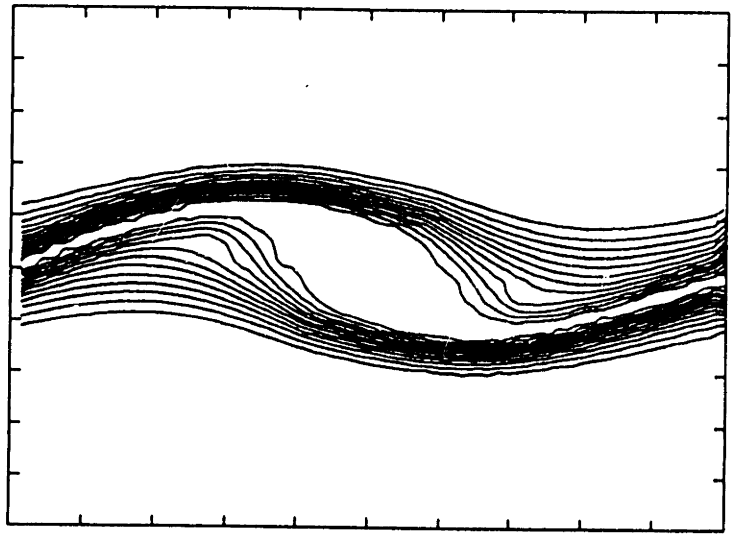

t = 11.0

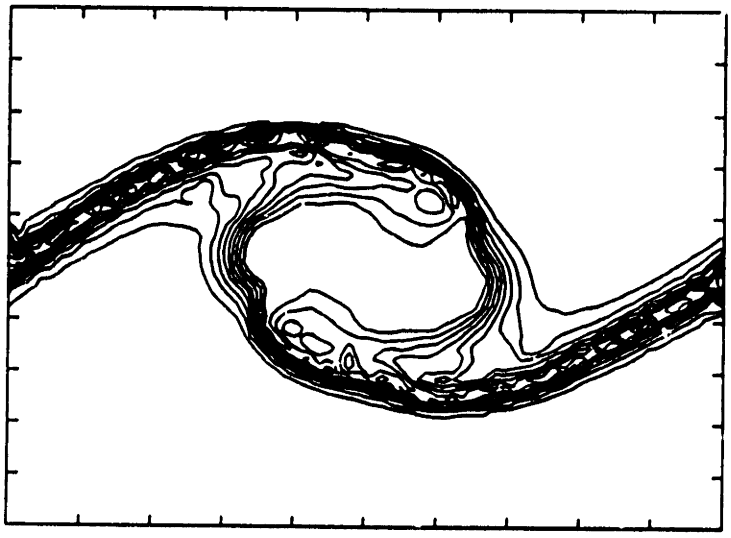

t = 16.5

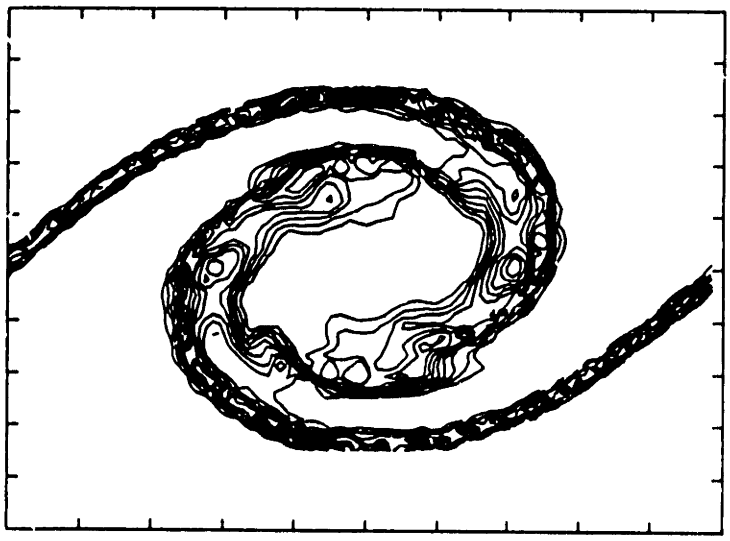

t = 22.0

Figure 19

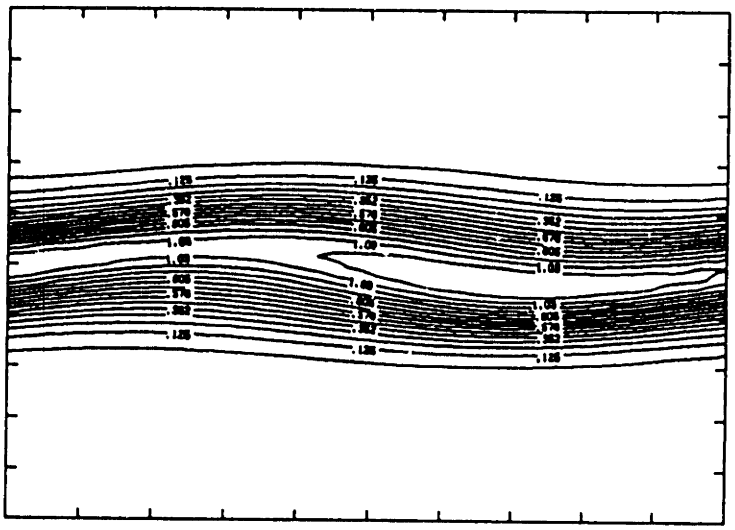

t = 5.5

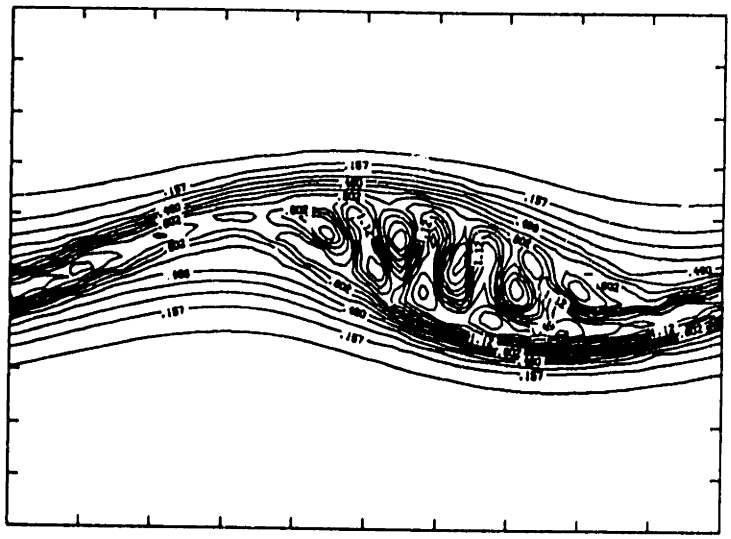

t = 11.0

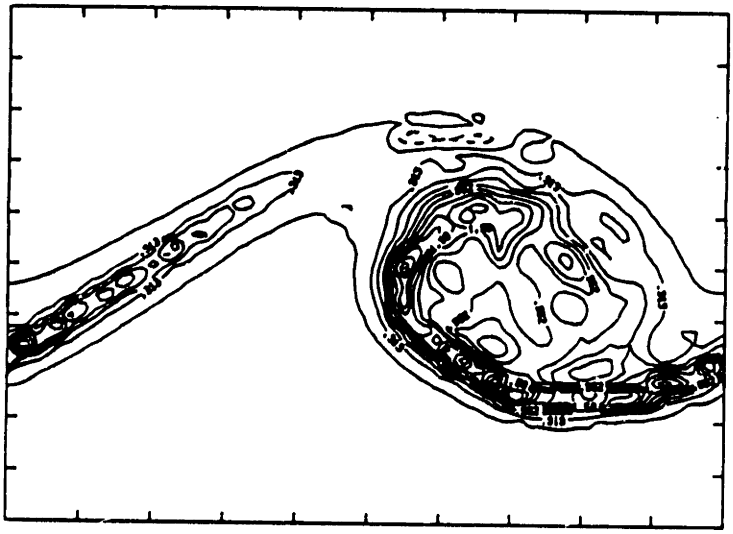

t = 16.5

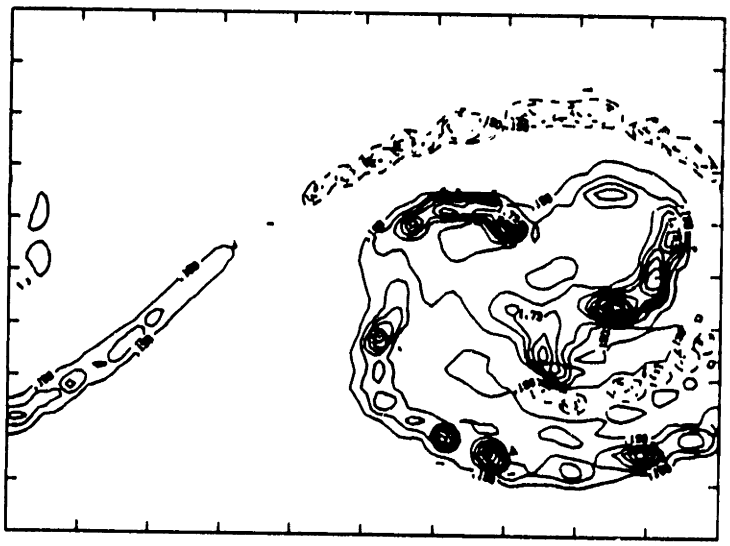

t = 22.0

Figure 20

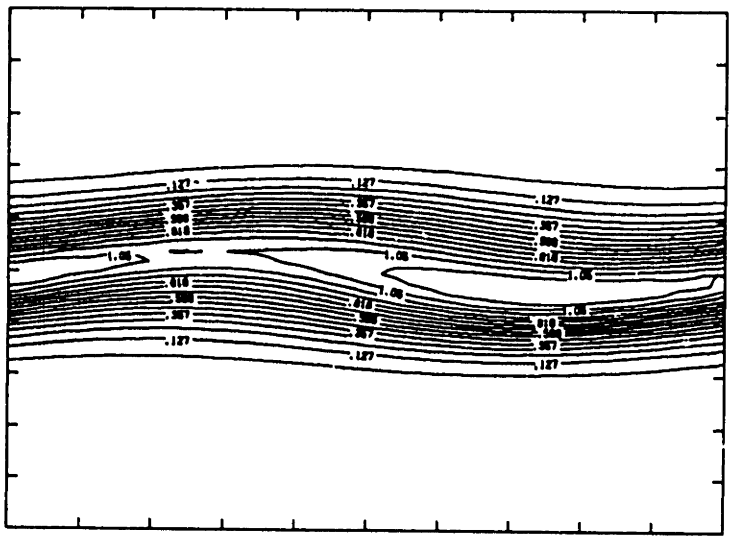

t = 5.5

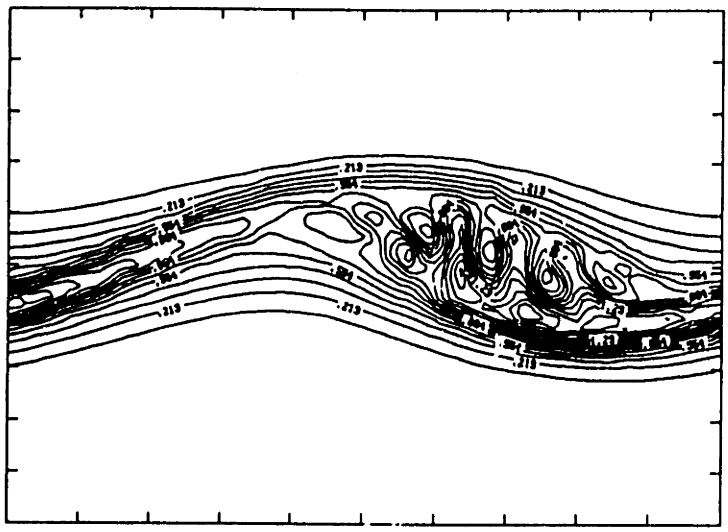

t = 11.0

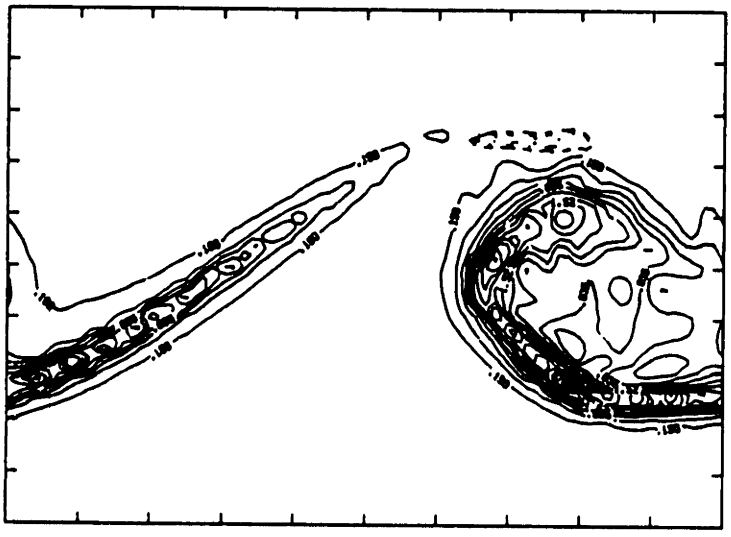

t = 16.5

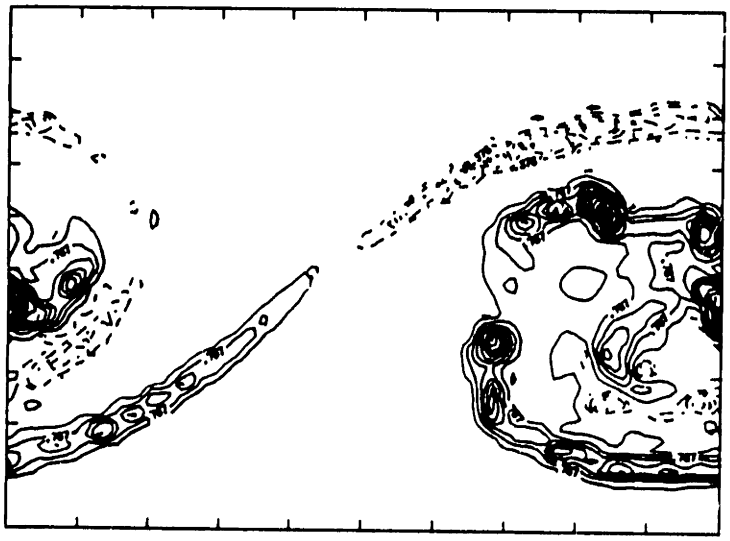

t = 22.0

Figure 21

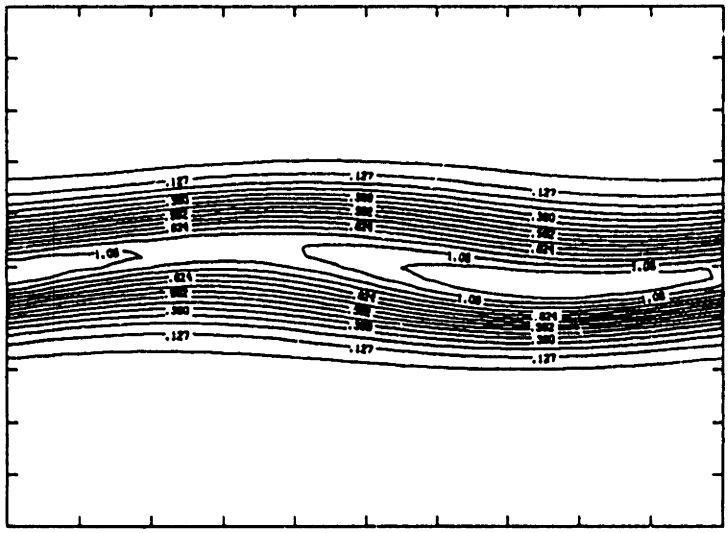

t = 5.5

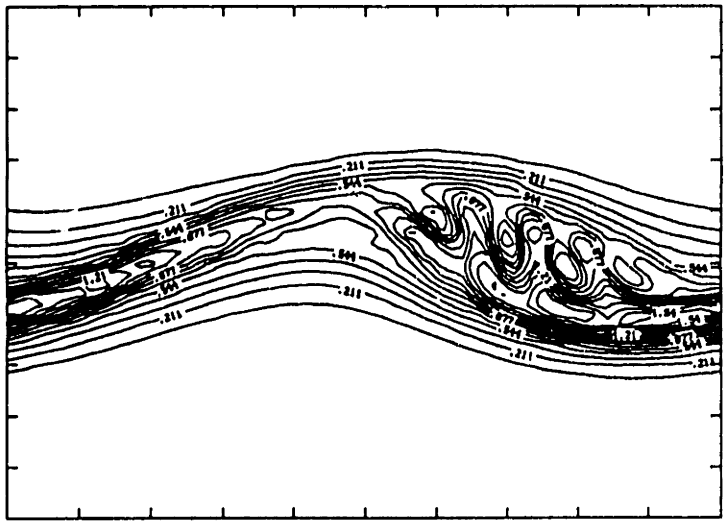

t = 11.0

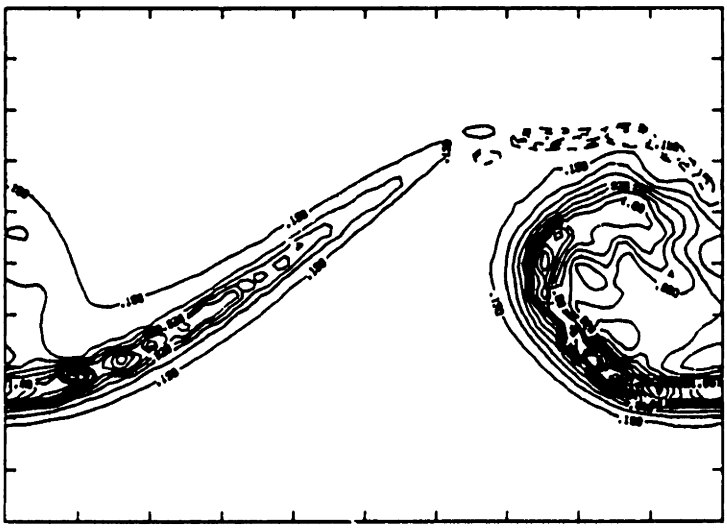

t = 16.5

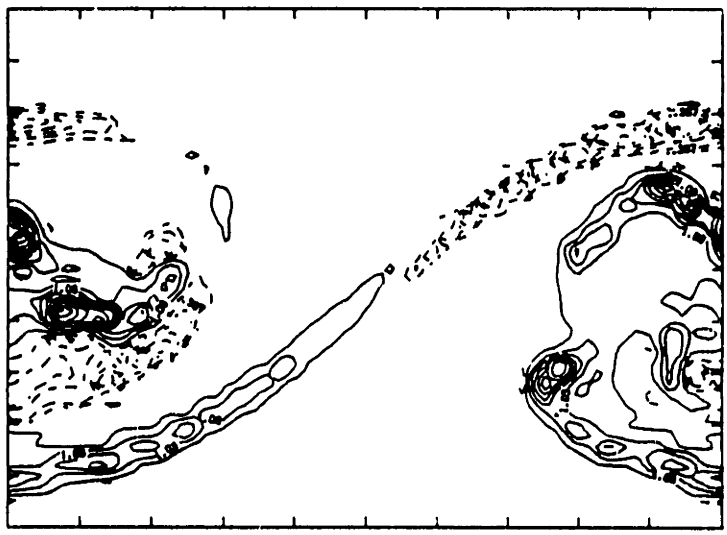

t = 22.0

Figure 22

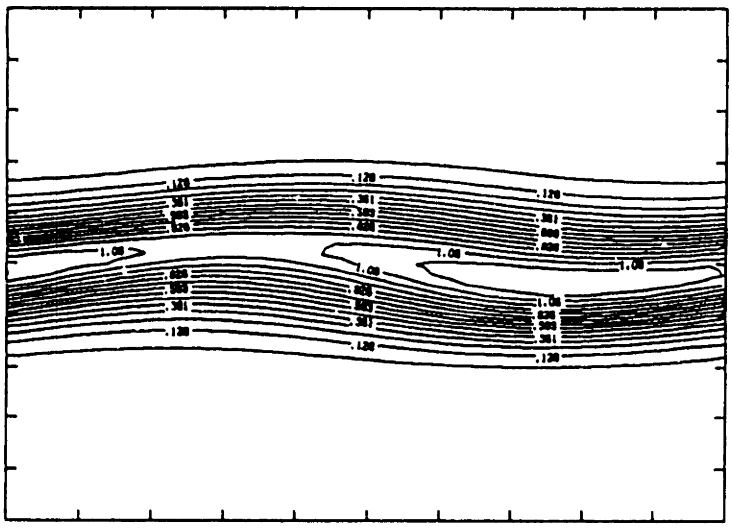

t = 5.5

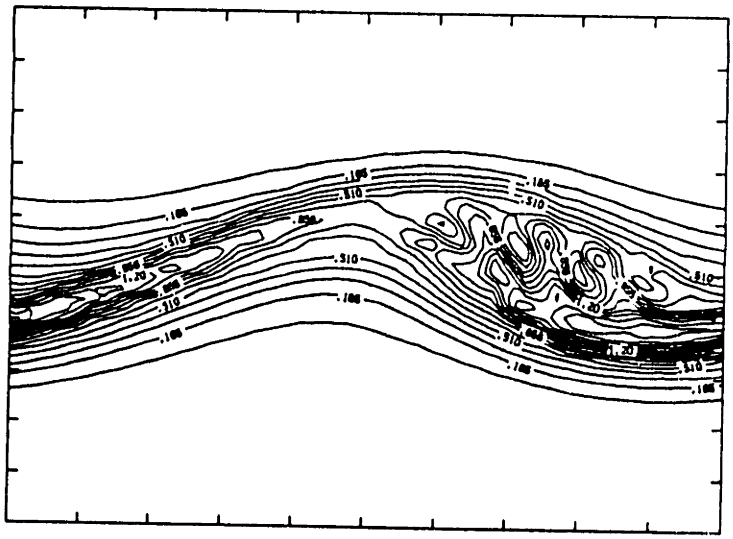

t = 11.0

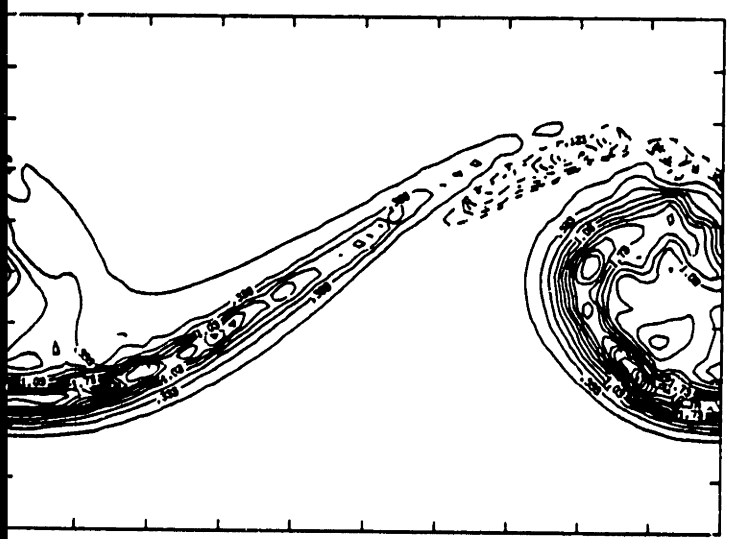

t = 16.5

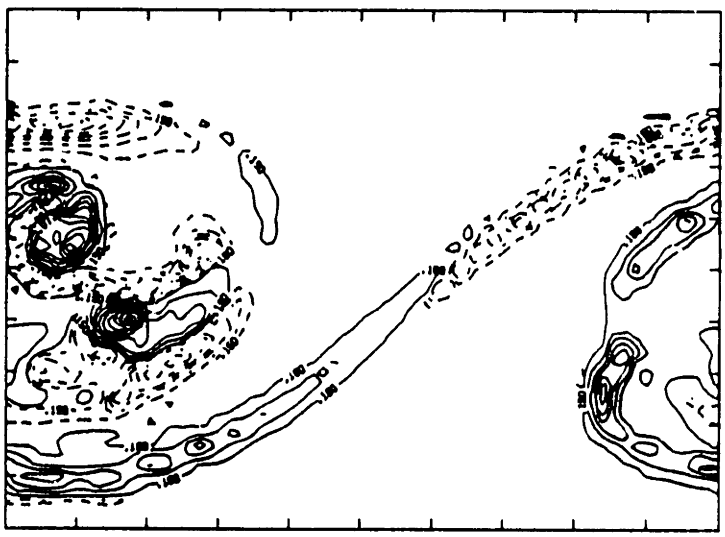

t = 22.0

Figure 23

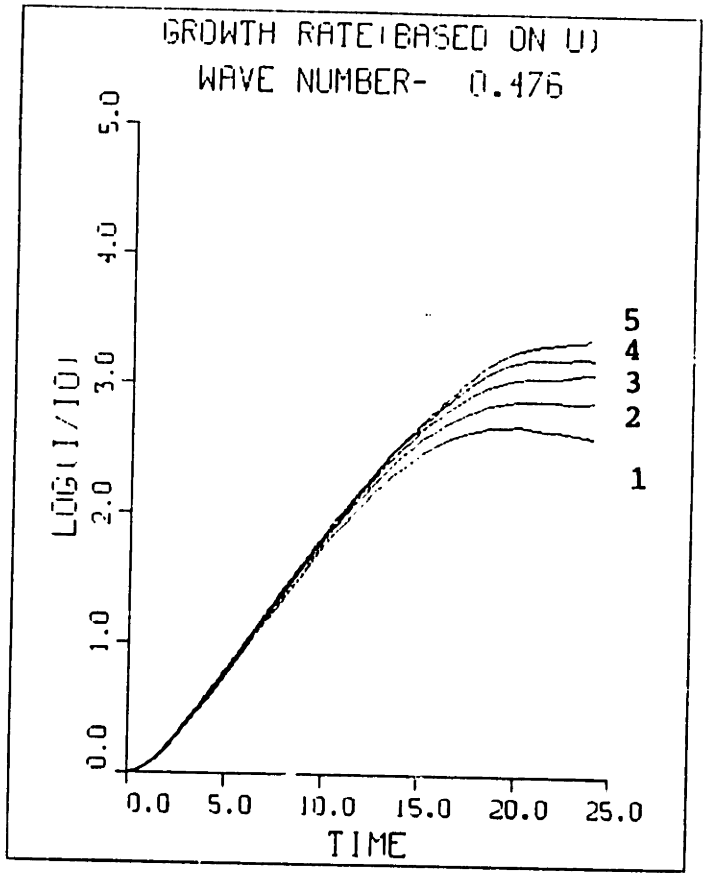

Figure 24

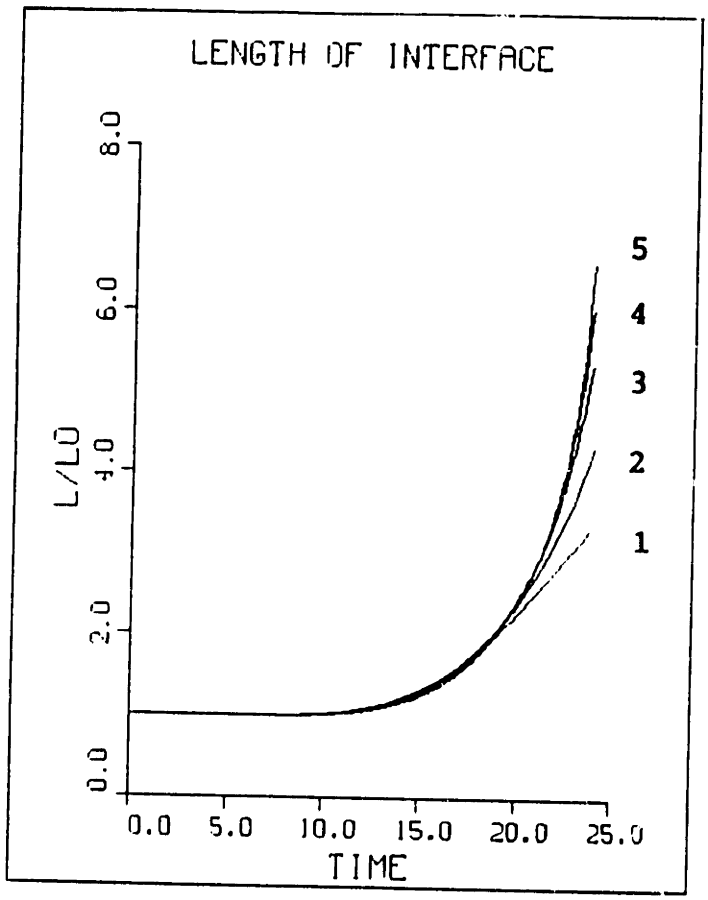

Figure 25

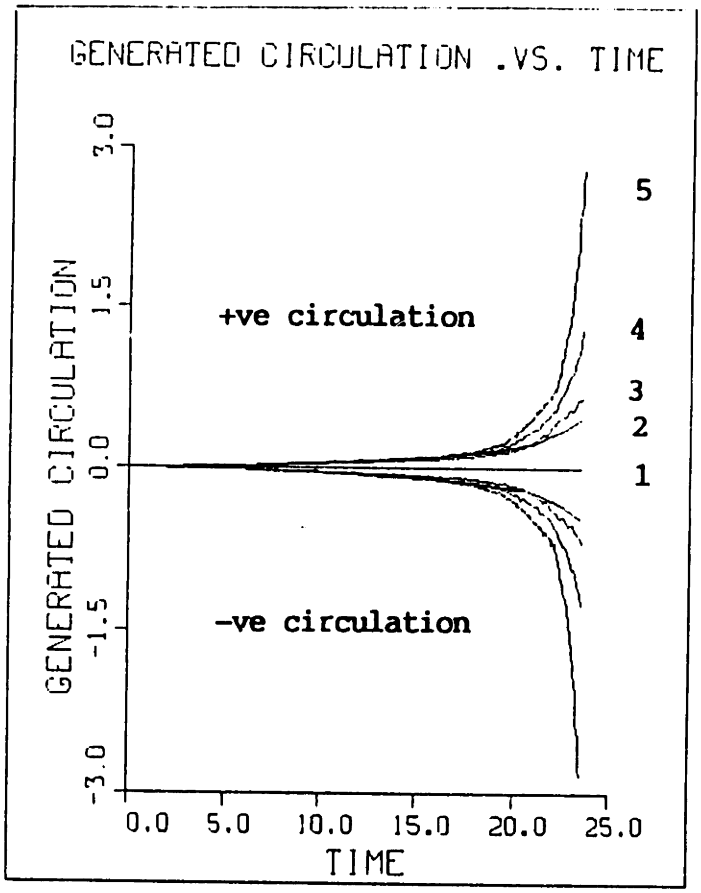

Figure 26

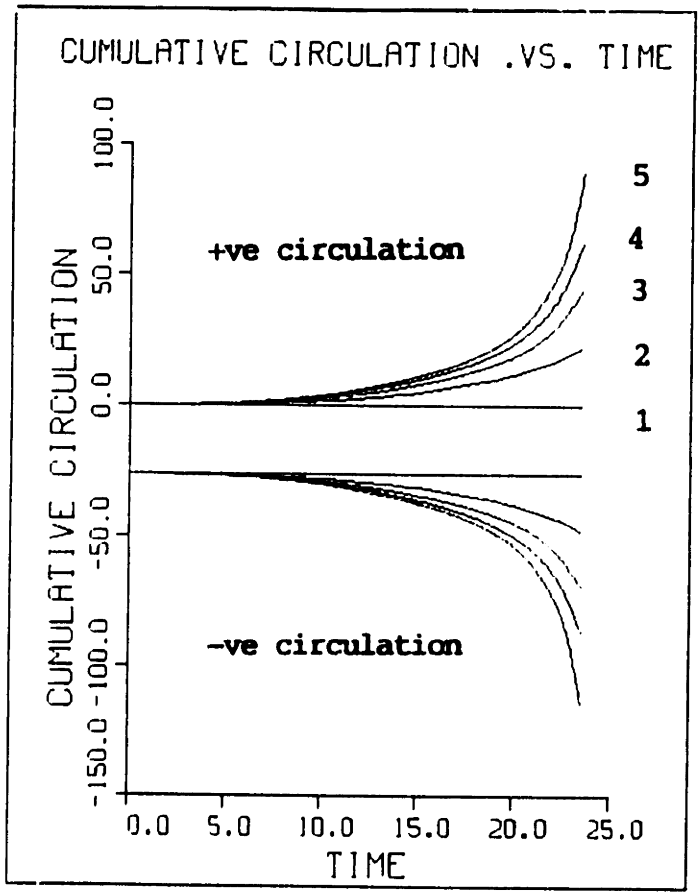

Figure 27

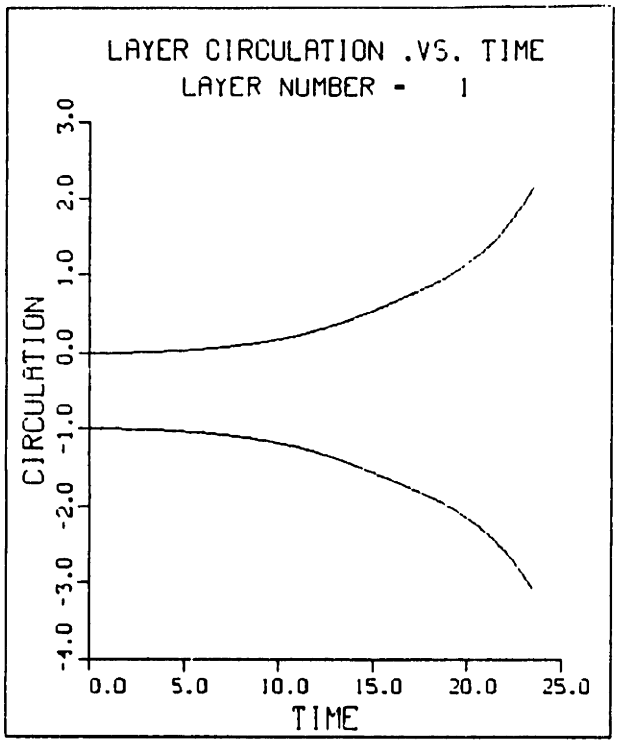

(a)

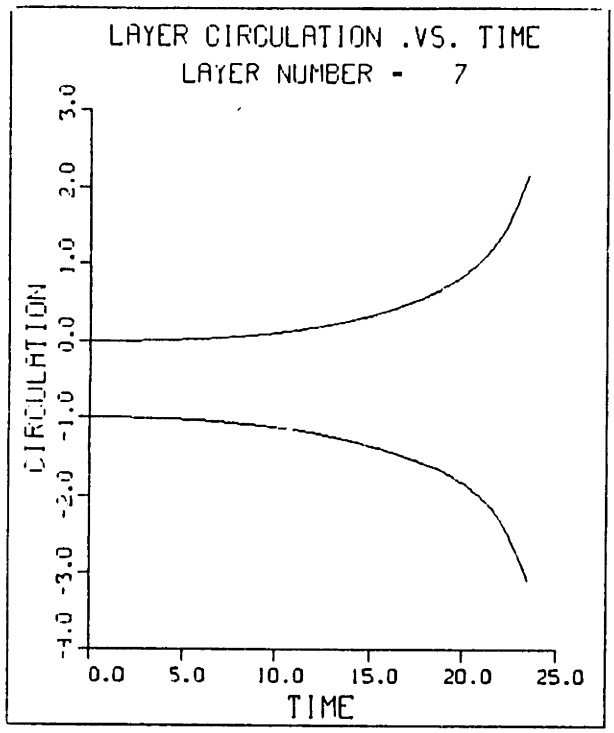

(b)

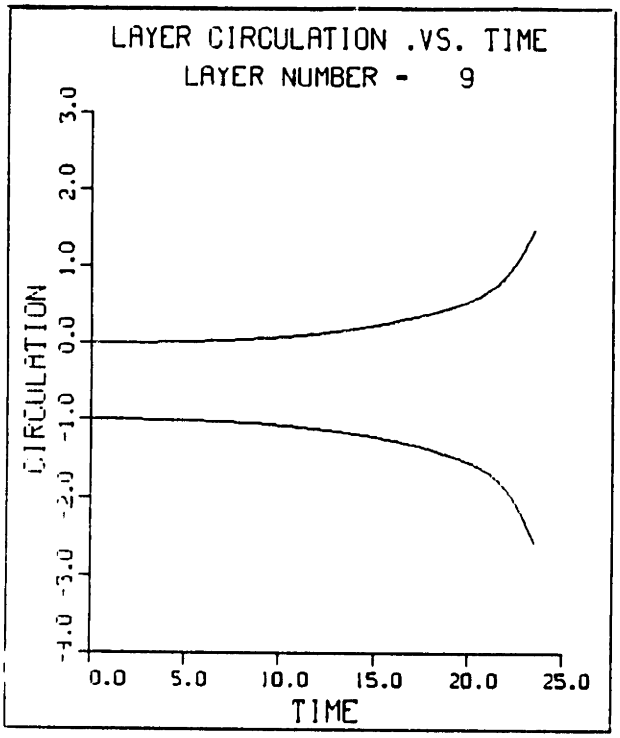

(c)

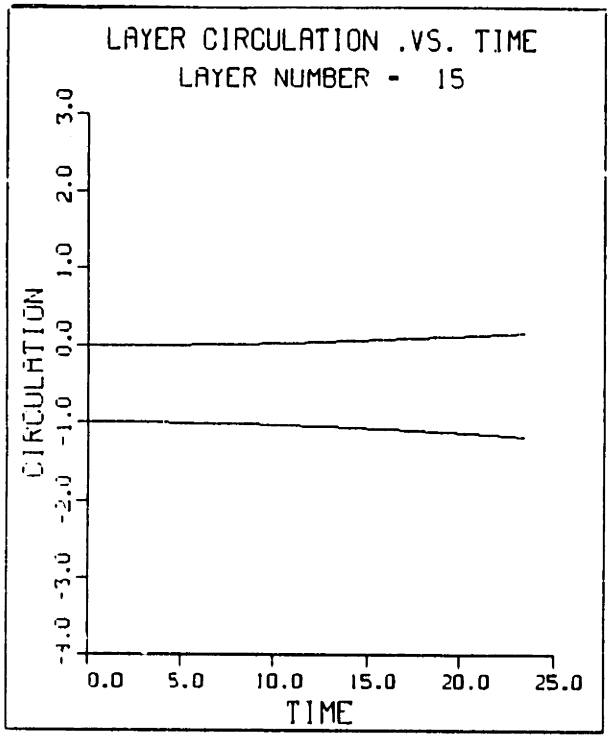

(d)

Figure 28

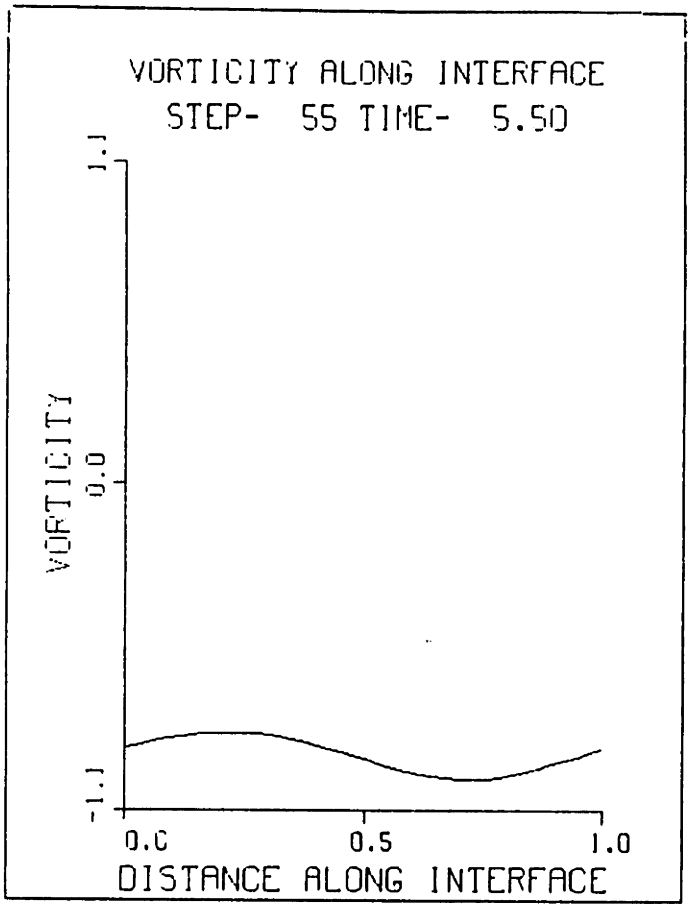
VORTICITY ALONG INTERFACE
STEP- 55 TIME- 5.50
VORTICITY
1.1
0.0
-1.1
0.0
0.5
1.0
DISTANCE ALONG INTERFACE

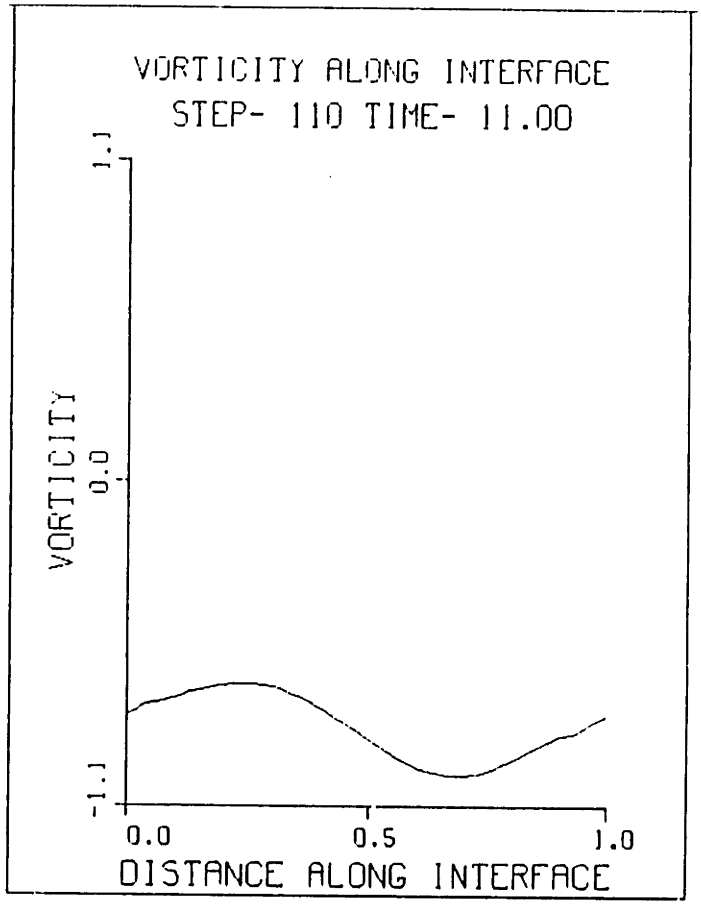
VORTICITY ALONG INTERFACE
STEP- 110 TIME- 11.00
VORTICITY
1.1
0.0
-1.1
0.0
0.5
1.0
DISTANCE ALONG INTERFACE

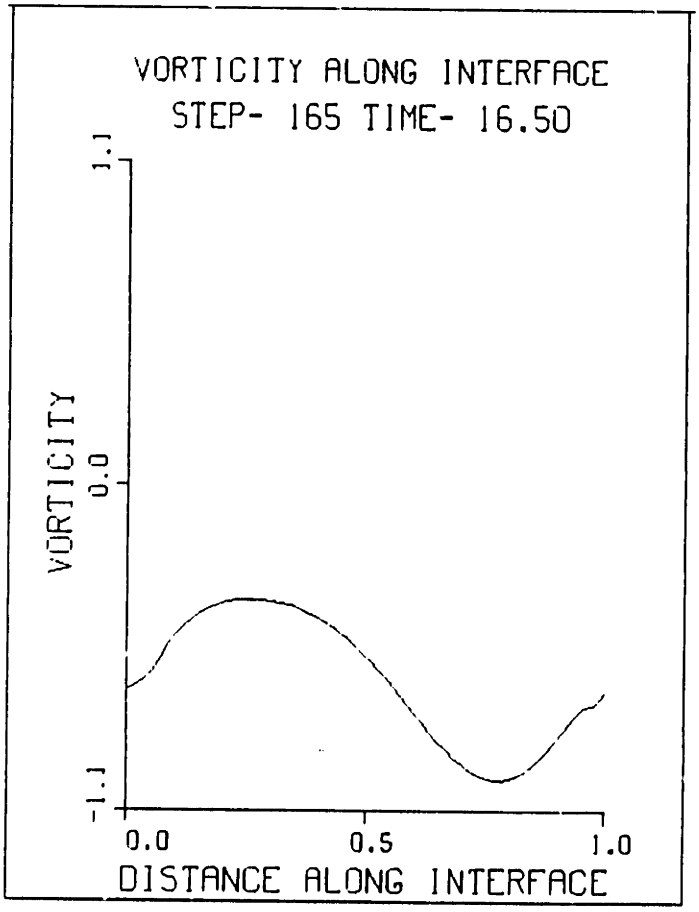
VORTICITY ALONG INTERFACE
STEP- 165 TIME- 16.50
VORTICITY
1.1
0.0
-1.1
0.0
0.5
1.0
DISTANCE ALONG INTERFACE

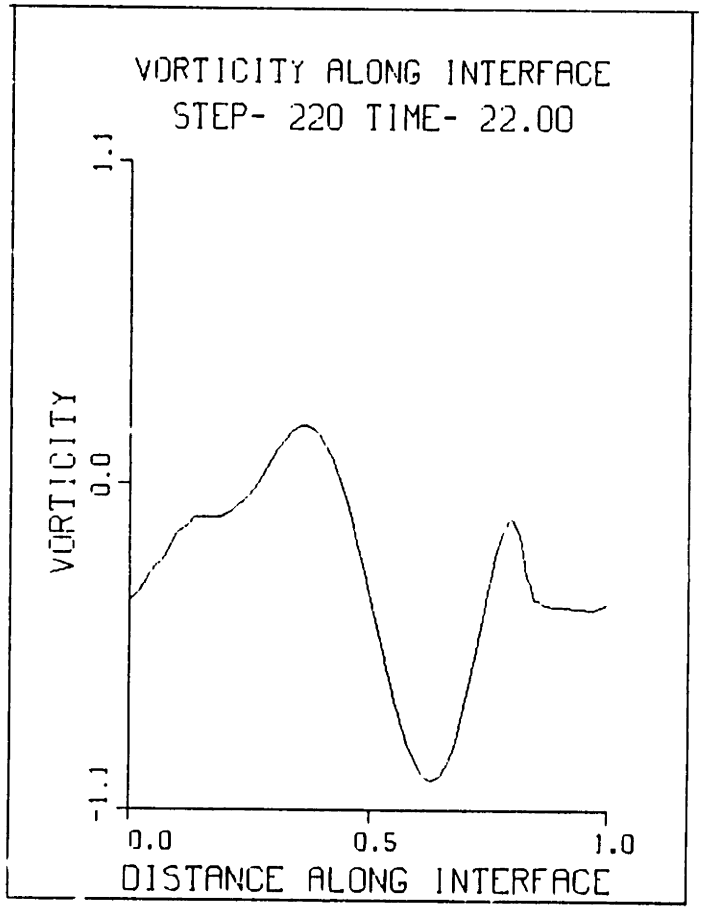
VORTICITY ALONG INTERFACE
STEP- 220 TIME- 22.00
VORTICITY
1.1
0.0
-1.1
0.0
0.5
1.0
DISTANCE ALONG INTERFACE

Figure 29

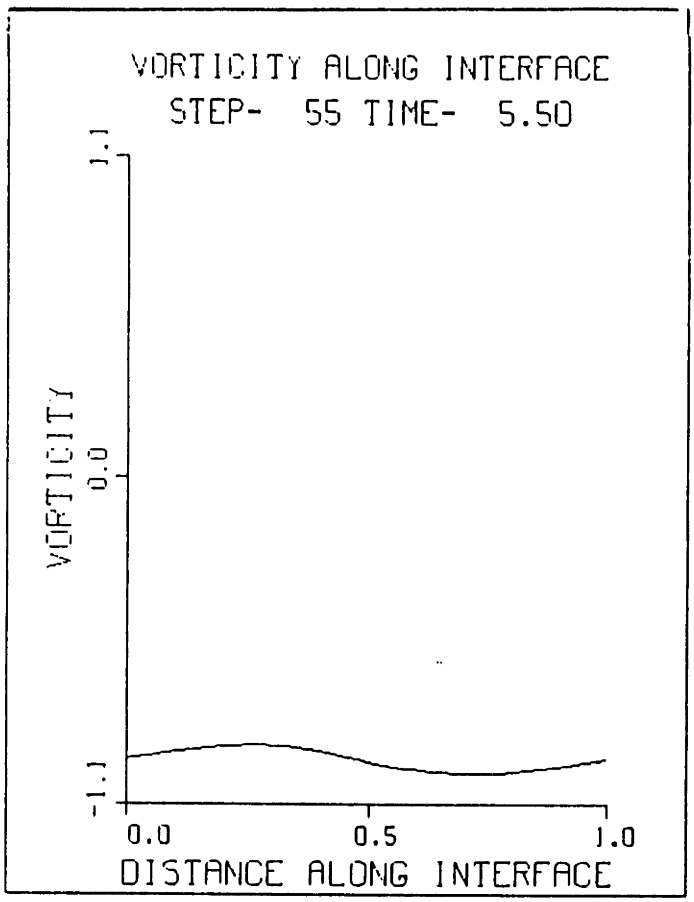
VORTICITY ALONG INTERFACE
STEP- 55 TIME- 5.50
VORTICITY
1.1
0.0
-1.1
0.0
0.5
1.0
DISTANCE ALONG INTERFACE

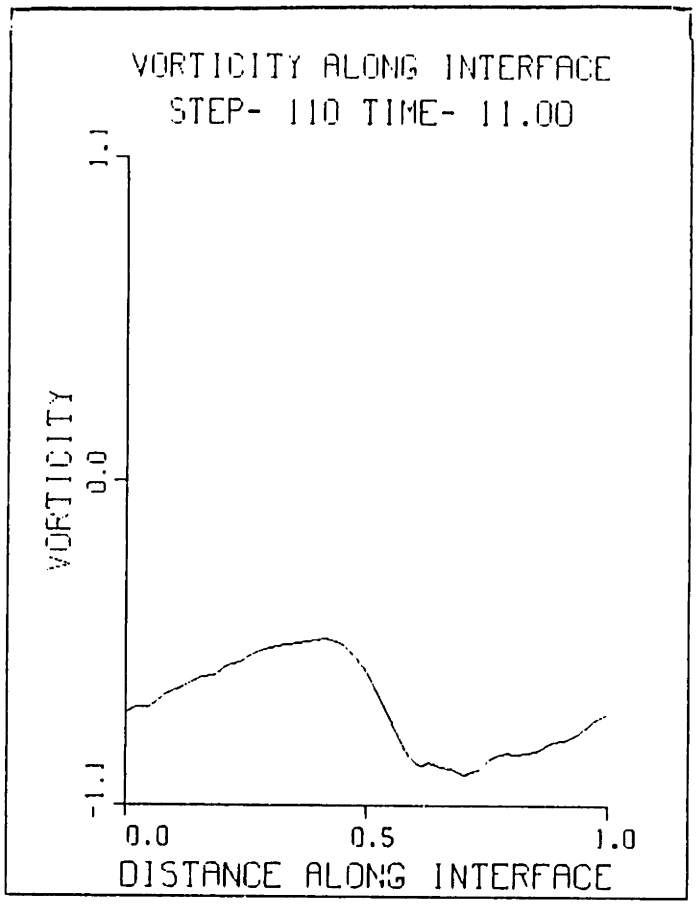
VORTICITY ALONG INTERFACE
STEP- 110 TIME- 11.00
VORTICITY
1.1
0.0
-1.1
0.0
0.5
1.0
DISTANCE ALONG INTERFACE

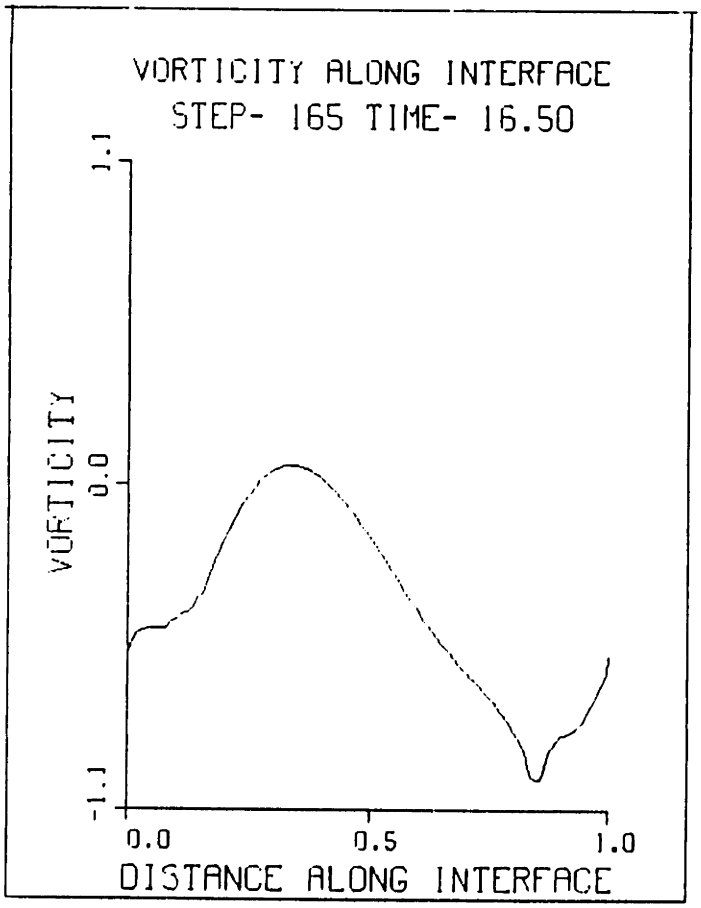
VORTICITY ALONG INTERFACE
STEP- 165 TIME- 16.50
VORTICITY
1.1
0.0
-1.1
0.0
0.5
1.0
DISTANCE ALONG INTERFACE

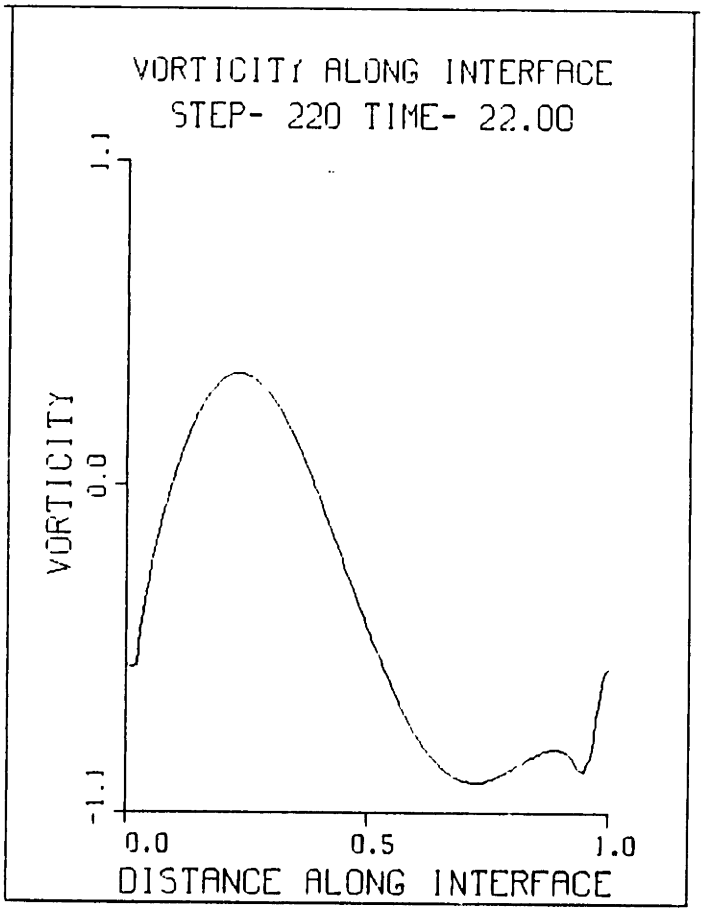
VORTICITY ALONG INTERFACE
STEP- 220 TIME- 22.00
VORTICITY
1.1
0.0
-1.1
0.0
0.5
1.0
DISTANCE ALONG INTERFACE

Figure 30

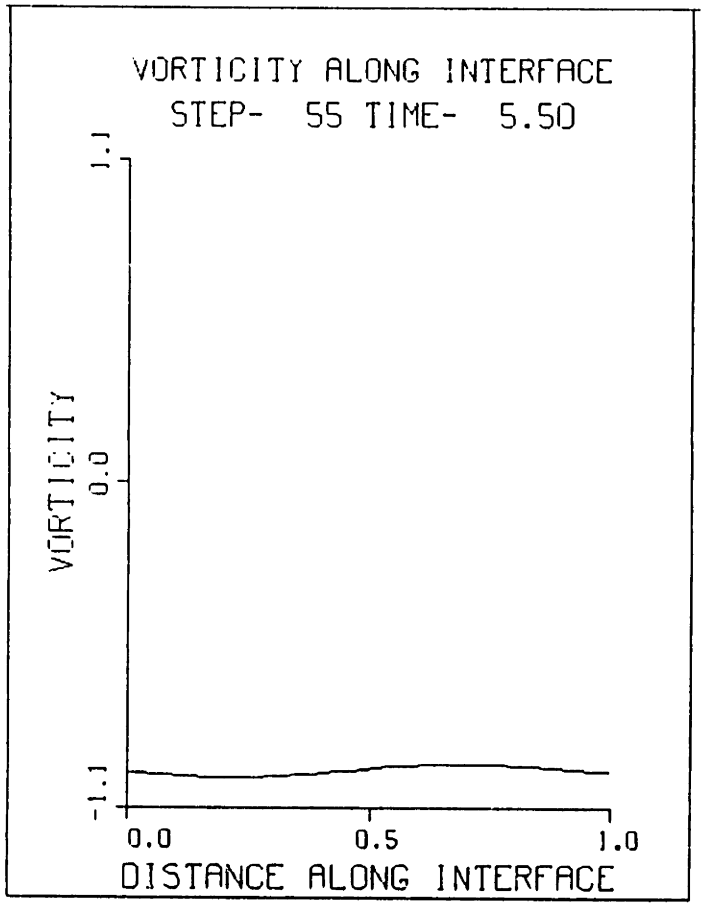
VORTICITY ALONG INTERFACE
STEP- 55 TIME- 5.50
VORTICITY
1.1
0.0
-1.1
0.0
0.5
1.0
DISTANCE ALONG INTERFACE

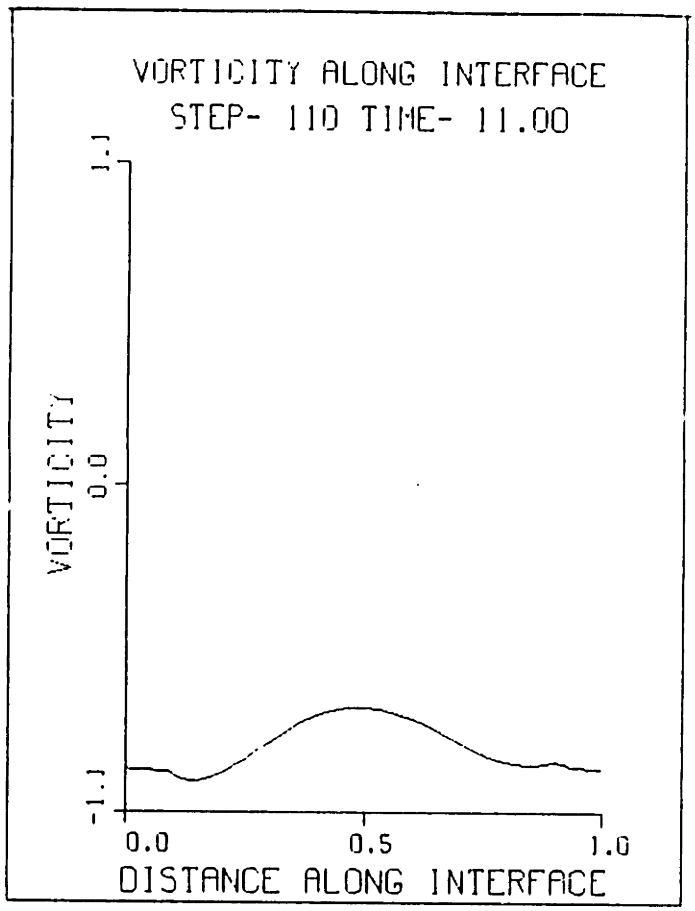
VORTICITY ALONG INTERFACE
STEP- 110 TIME- 11.00
VORTICITY
1.1
0.0
-1.1
0.0
0.5
1.0
DISTANCE ALONG INTERFACE

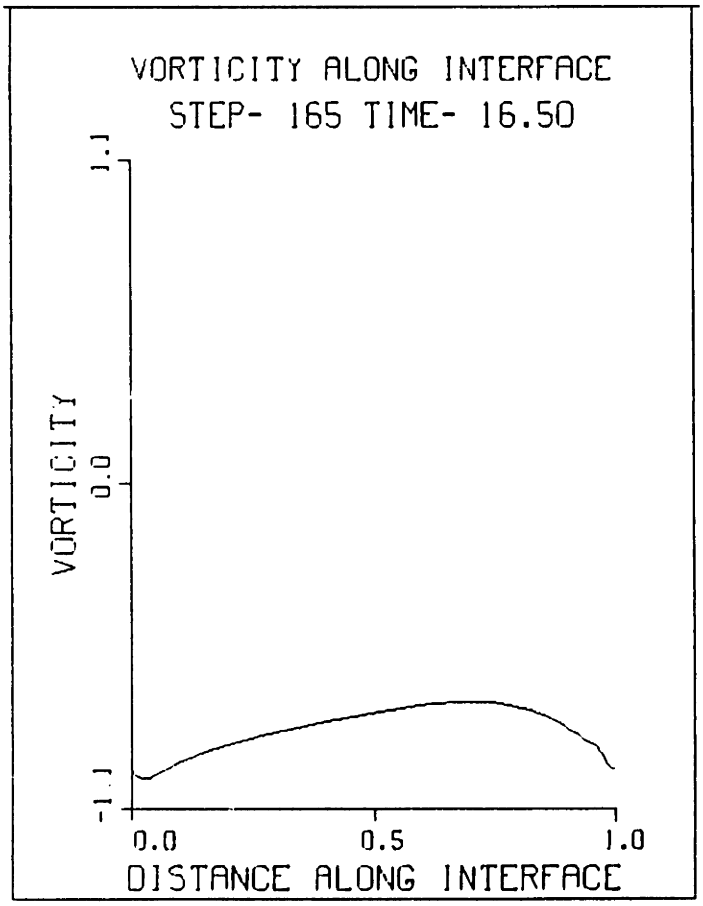
VORTICITY ALONG INTERFACE
STEP- 165 TIME- 16.50
VORTICITY
1.1
0.0
-1.1
0.0
0.5
1.0
DISTANCE ALONG INTERFACE

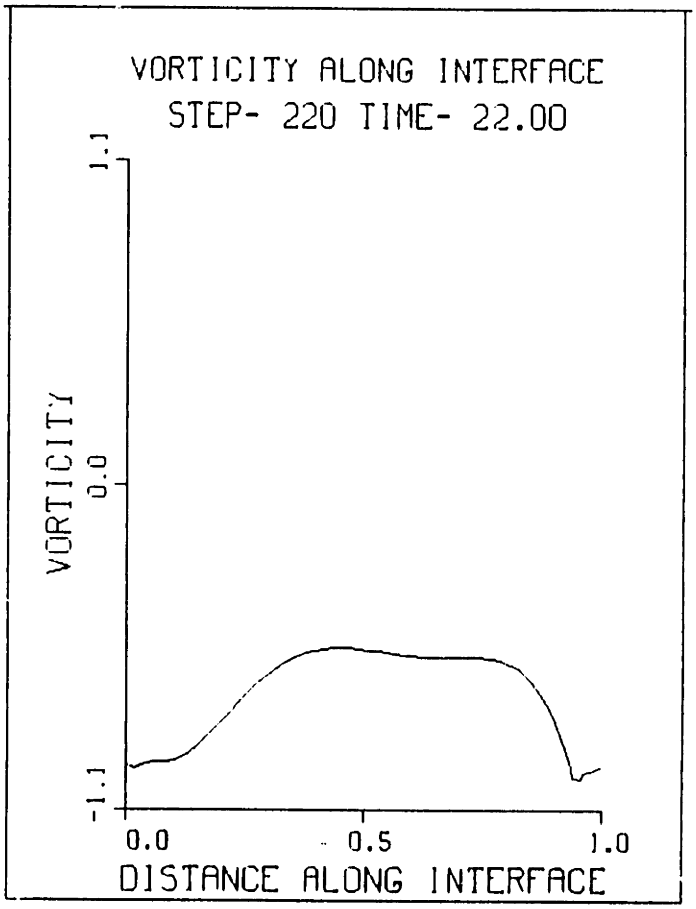
VORTICITY ALONG INTERFACE
STEP- 220 TIME- 22.00
VORTICITY
1.1
0.0
-1.1
0.0
0.5
1.0
DISTANCE ALONG INTERFACE

Figure 31

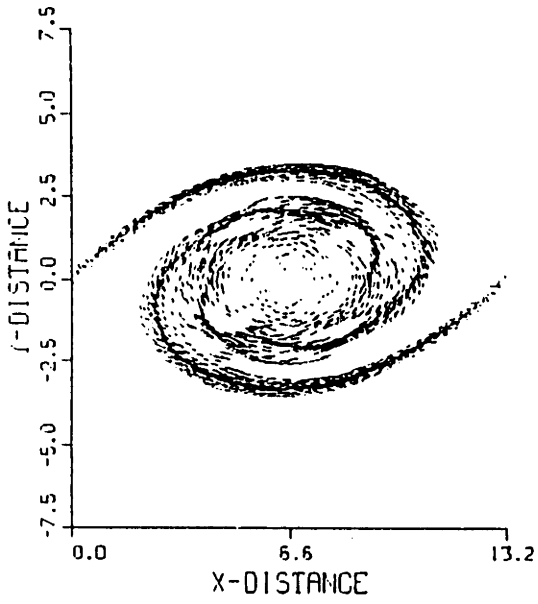

(a)

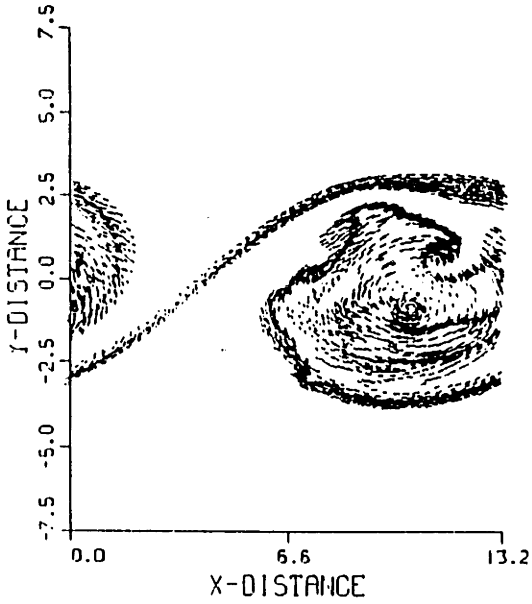

(b)

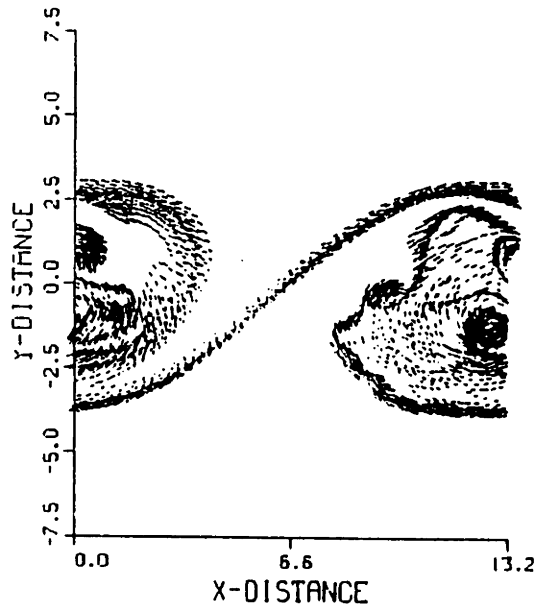

(c)

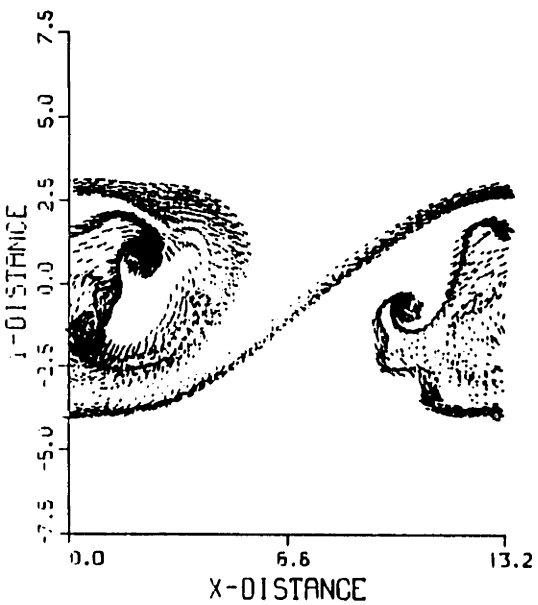

(d)

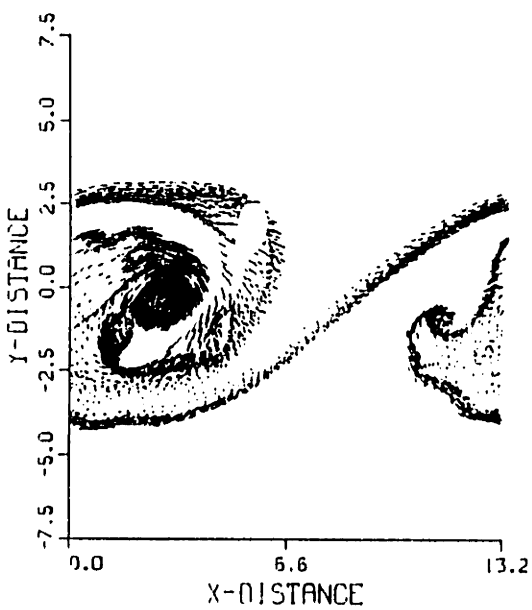

(e)

Figure 32

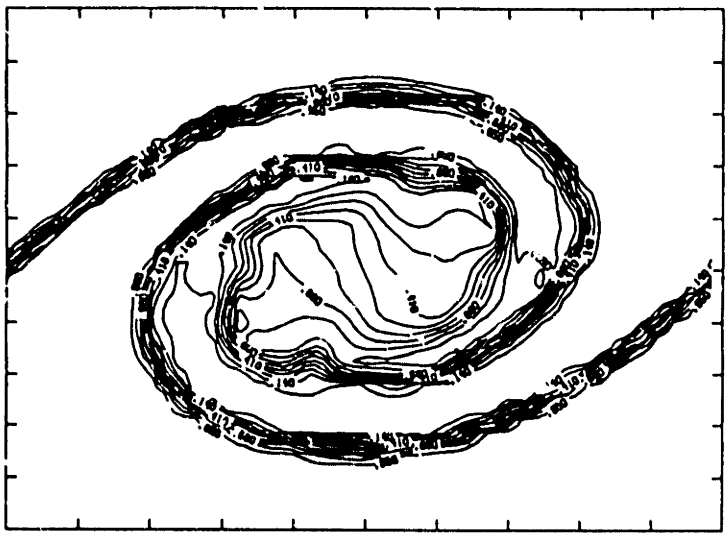

(a)

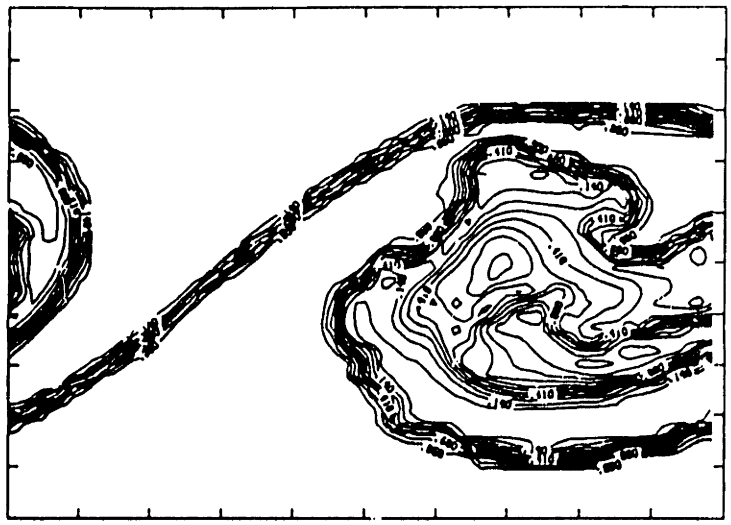

(b)

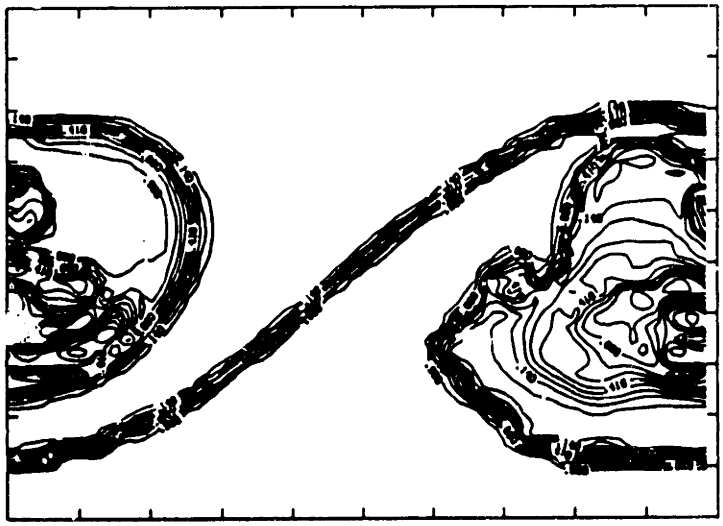

(c)

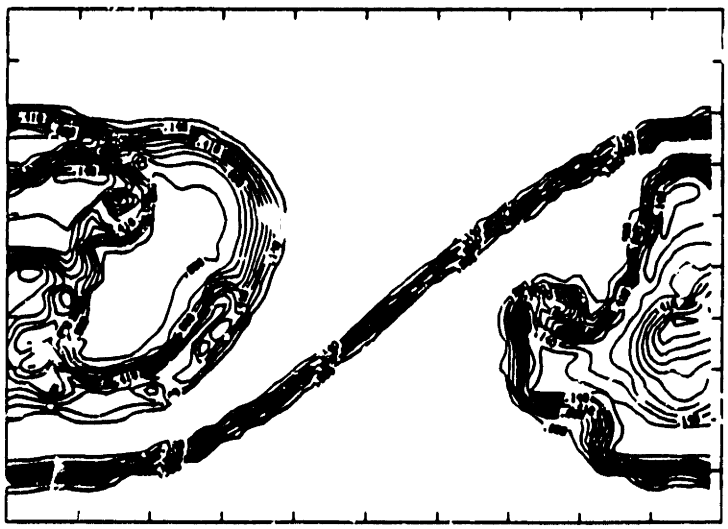

(d)

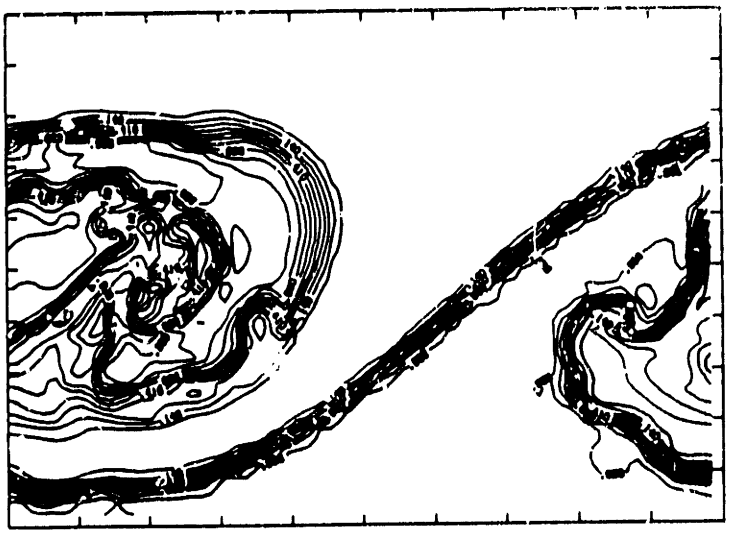

(e)

Figure 33

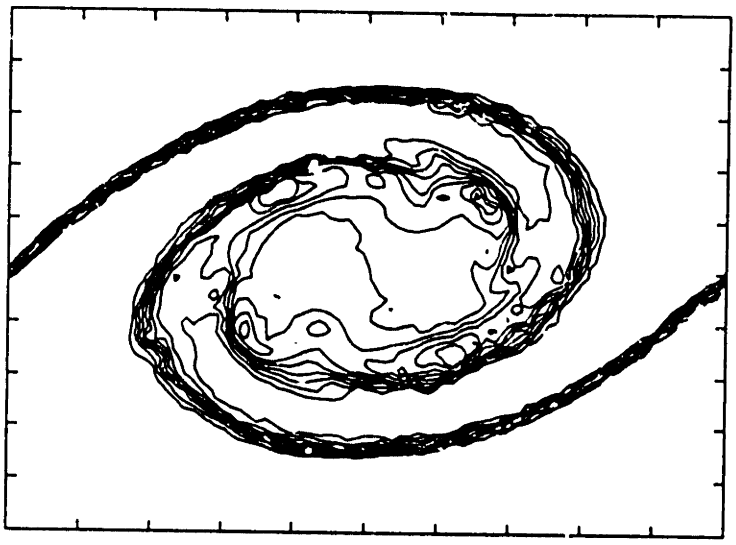

(a)

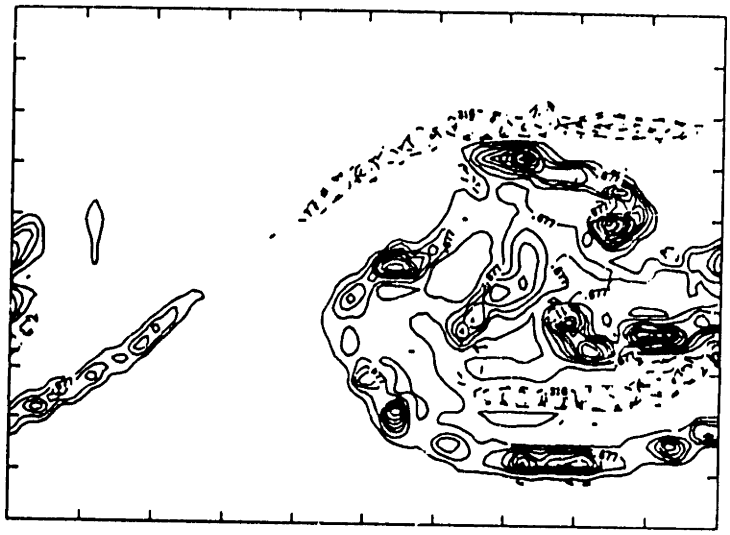

(b)

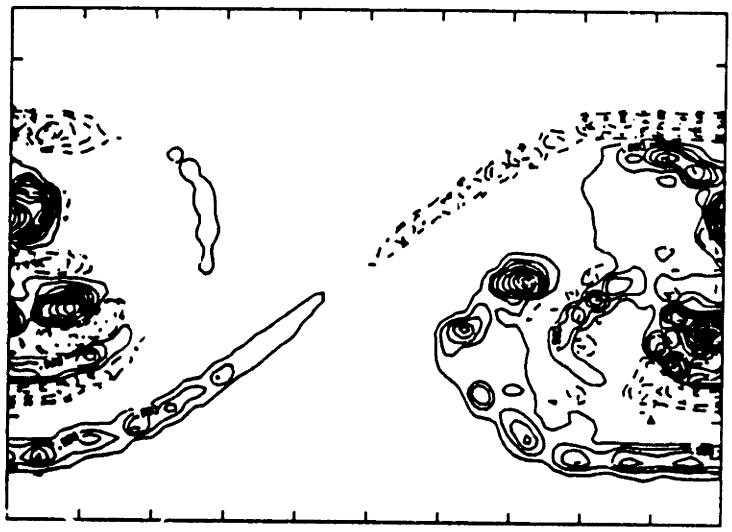

(c)

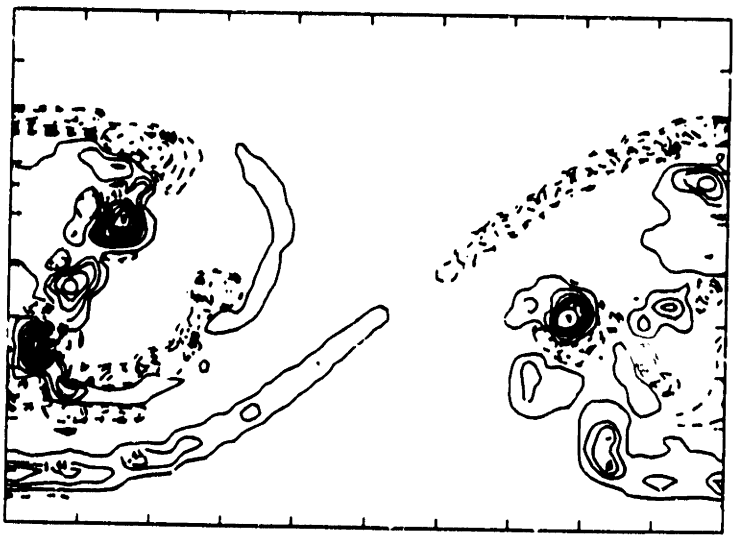

(d)

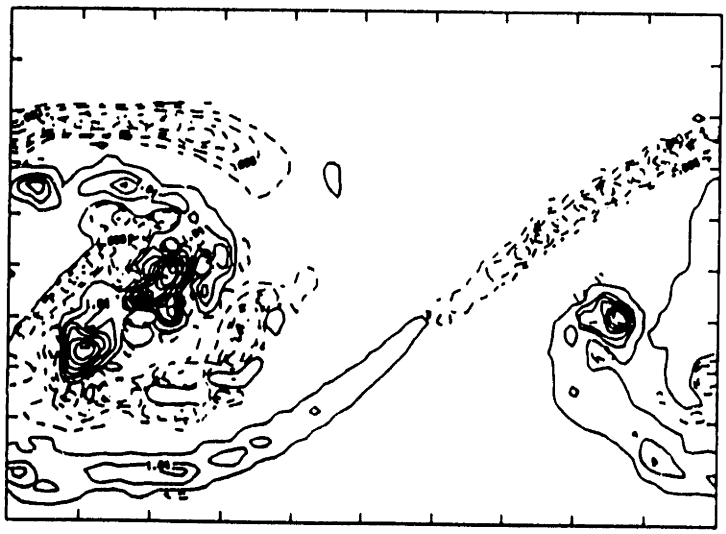

(e)

Figure 34

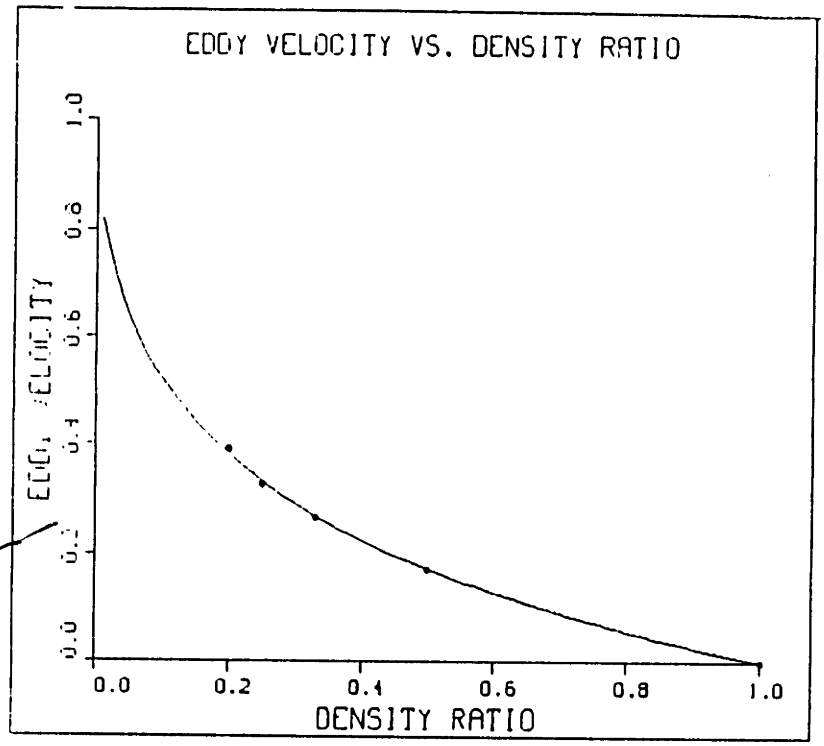

Figure 35

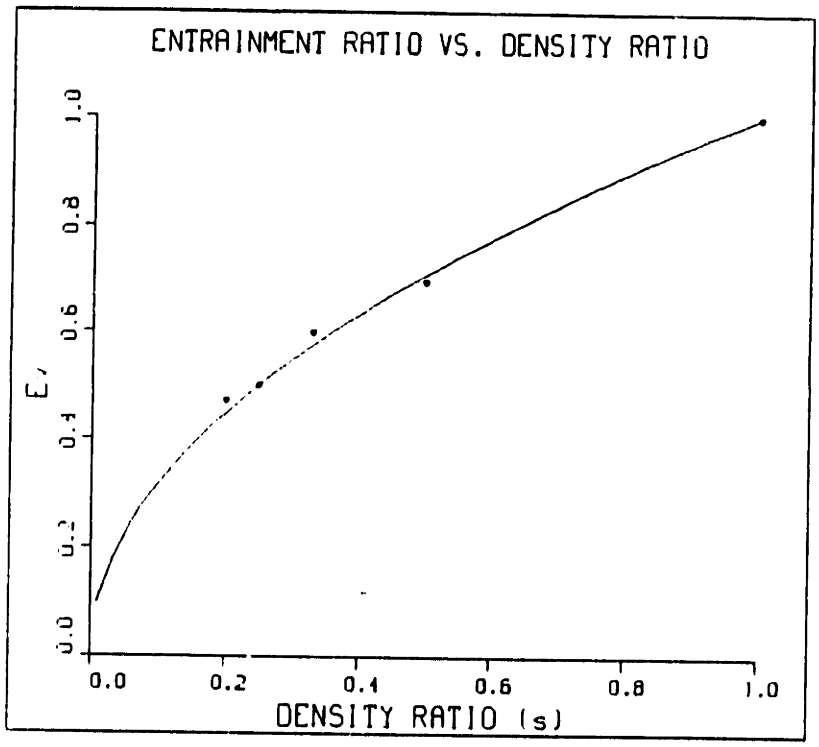

Figure 36

V. THE RAYLEIGH-TAYLOR INSTABILITY

V.1. INTRODUCTION

This section deals with the study of the Rayleigh-Taylor instability that develops when two fluids of different densities are unstably stratified in a gravitational field. This problem is of great practical importance and has wide ranging applications. Some of the phenomena involving the occurence of the R-T instability are (i) the establishment of a density gradient in the atmosphere, due to a temperature gradient, with the air near the earth being hotter than the air far from it. This results in a downwash of the heavier air leading to high levels of turbulence (ii) in fires and explosions where the enormous heat release results in strong density gradients. The familiar mushroom formation that is observed in nuclear explosions is the result of the R-T instability (iii) in buoyant jet diffusion flames when the flow is at low Froude numbers. Due to its far ranging applications, numerical simulation of buoyancy dominated flows are of considerable interest [31,32,33,34,35].

V. 2. DESCRIPTION OF FLOW GEOMETRY

The schematic for the R-T instability is shown in Fig. 37. The density of the top fluid is higher than that of the bottom fluid. The density varies as an error function in the y-direction. The fluid is stationary at t=0 and the initial vorticity is zero. The fluid interface is perturbed by a cosine wave as shown in the Fig. 37 . The gravitational force is acting in the negative y-direction. The flow is assumed to be periodic in the x-direction with the

periodicity length being equal to the wavelength of the pertubation. The flow domain is assumed to be infinite in the y-direction. The perturbation of the interface leads to the generation of vorticity due to the interaction between the density gradient and gravity and the flow becomes turbulent. The generation of vorticity represents the conversion of potential energy in the field into kinetic energy of the flow.

V. 3. GOVERNING EQUATIONS:

The governing equations for the problem are essentially the same as those for the density stratified K-H instability except for the inclusion of the gravity term in the vorticity equation. Again, the flow is assumed to be isentropic and at a low Mach number so that density is conserved along the particle path. Also included is the assumption that the hydrostatic variation in pressure does not affect the density. The fluid is a perfect gas with constant specific heats. This formulation allows the solution for large values of the density ratio without being limited by the Boussinesq approximation.

$$\frac{d\rho}{dt} = 0 \tag{87}$$

$$\frac{d\omega}{dt} = -\frac{\nabla\rho}{\rho} \times \left(\frac{du}{dt} + j \right) \tag{88}$$

The flow variables are non-dimensionalized with the characteristic values L_o for length, t_o for time and ρ_o for the density. The initial velocities are zero. L_o is the characteristic thickness ($= \sqrt{2}\ \sigma$) of the Gaussian distribution for the density gradient and t_o is given by $\sqrt{L_o/g_r}$, where g_r is

the gravitational acceleration. $\rho_o = \rho_1$, ρ_1 being the density of the top fluid. The subscripts 1 and 2 refer to the top and bottom fluid respectively.

V. 4. LINEAR STABILITY THEORY

The Rayleigh equation for the linear stability of the R-T problem is derived in the same manner as was done for the K-H instability except that the effect of gravity is included in the equation of motion. Using the fact that the initial velocity is zero everywhere in the domain, the Rayleigh equation is simplified as:

$$v'' = -\frac{R'}{R} v' + \left(\frac{R' g_r}{R c^2} + \alpha^2 \right) v \qquad (89)$$

where $\hat{v}$ is the fluctuating v-velocity and R is the mean cross stream density gradient. g_r is the gravitational acceleration and $c = c_r + ic_i$; in this case $c_r = 0$ since the initial velocity distribution is zero. For a given value of α, the solution for c ($= i\, c_i$) is obtained by iteration as was done in the case of the K-H instability.

The results of the linear stability theory are shown in Fig. 38 where the growth rate ($= -\alpha c_i$) is plotted as a function of the wavenumber α. Three cases are considered with the density ratio $r_\rho = 2, 3$ and 9 respectively. It is observed that the growth rate increases monotonically with the wavenumber. Therefore, in the absence of stabilizing mechanisms like viscosity or surface tension, the linear theory predicts that higher wavenumbers grow faster than smaller wavenumbers. In practice however, the effect of viscosity has to be considered as the wavenumbers become large and under these conditions, the growth rate decreases and a bell shaped curve is obtained. At low

wavenumbers, i.e., $\alpha < 0.5$, the effect of viscosity is negligible. The linear growth rates are also plotted for a zero thickness interface where the density distribution is a step function (i.e., a density jump) in the y-direction. The exact expression for the growth of a zero thickness interface is given as [36]:

$$n = \sqrt{A\, g_r\, k} \tag{90}$$

where n is the growth rate, A is the Atwood number, g_r is the non-dimensional gravitational acceleration (equal to unity in this study) and k is the non-dimensional wavenumber. The dashed curves in Fig.38 represent 'n' as a function of k. It is observed, for all values of r_ρ, that the effect of smoothening the density distribution leads to decreased values for the growth rate. At very small values of k, the solutions for the step function distribution and the error function distribution converge to the same values. This is to be expected since for k-->0, the wavelength λ --> ∞ and the ratio of the interface thickness to λ is almost zero. At moderate to high values of k, the finite thickness of the interface results in a viscous like effect and tends to increase the stability of the layer. The growth rate of the instability is also a function of the density ratio with the interface being more unstable for higher values of r_ρ. It is to be noted that the difference between the curves for different r_ρ decreases as r_ρ increases. The phase velocity c_r is zero for all the waves since the initial velocities in the domain are zero.

V. 5. RESULTS OF NUMERICAL SIMULATIONS

The simulation of the Rayleigh-Taylor instability was done, using the vortex/transport element method, for r_ρ = 2,3 and 9. The corresponding Atwood

numbers, defined as $A = (\rho_1-\rho_2)/(\rho_1+\rho_2)$, are 0.33, 0.5 and 0.8 respectively. The initial perturbation to the interface is in the form of a negative cosine function. The wavelength of the perturbation is taken to be $\lambda = 13.2\ L_o$ and the amplitude of the perturbation is $\varepsilon = 0.1\lambda$. Calculations were also done for very small amplitudes ($\varepsilon = 0.0005\ \lambda$) of perturbation in order to make appropriate comparisons with the linear theory. The results of the numerical simulations in the linear range are represented by the symbols in Fig. 38 . It is observed that the predictions of the numerical calculations compare very well with those of the linear theory.

(i) Case I : Density ratio = 2

The location and velocity of the vortex/transport elements are shown in Figs. 39 for $r_\rho = 2$ at t= 5.0, 8.0, 10.0 and 11.5 respectively. Since the elements are always on the material lines, these plots can be used to study the deformation of the material interface. The figures show the instability over two wavelengths in order to present a clear picture of the growth of the interface. It is observed that the initial perturbation of the interface is amplified due to the generation of baroclinic vorticity and the light fluid rises into the dense fluid while the dense fluid falls into the light fluid. The development of the familiar mushroom shaped instability is observed at the later stages with the interface rolling up to form two symmetric structures. The two eddies develop as a result of the Kelvin-Helmholtz instability and have opposite signs of vorticity and therefore the total vorticity in the domain is always zero. The part of the interface that moves into the dense fluid is referred to as the 'bubble' and the one that moves into the light fluid is referred to as the 'spike'. For all values of r_ρ, the

simulations were performed till the spike of the high density fluid reached a height of approximately -10.0 in non-dimensional units. Simulations beyond this point required a very large number of elements and a very small time step due to very large values for the strain rate and the material acceleration. It is clear from the material interface plots that the coherent eddy entrains more of the low density fluid by volume as was observed in the case of the density stratified shear layer. The bottom most material layer undergoes the most distortion due to the instability. It is also observed that the coherent structures form very close to the line y=0 in this case. Fig. 40 shows the corresponding streamline contours over a single wavelength of the instability for r_ρ=2. The streamlines show the development of the instability with time as more number of streamlines close around each other indicating increased volumetric entrainment. The central streamline is assigned a value of zero so that the streamfunction at the center of the structures can be used directly as a measure of volumetric entrainment. For r_ρ = 2, the non-dimensional streamfunction at the core of the eddy at t = 11.5 is calculated to be 7.85 .

Fig. 41 shows the normalized temperature (T= $1/\rho$) contours for the corresponding time frames. Since the scalar is non-diffusive and conserved, the temperature contours essentially follow the material lines. It is observed that most of the interface is experiencing large positive strain with negative strain occurring only in the cores of the eddies. Therefore, if a diffusion flame reaction was allowed to occur, it is obvious that all or most of the burning would be inside the coherent eddies since the flame would blow off in the regions of high positive strain. The scalar contours also indicate that more volume of the low density fluid is being entrained into the structures. The vorticity contours for this case are shown in Fig. 42.

At t=0, the vorticity is zero everywhere and the generation of vorticity takes place according to Eqn.(88). Positive vorticity is generated on the left side of the domain while negative voricity is generated on the right side. At later times, however, due to the effects of material acceleration, small amounts of negative/positive vorticity are also generated on the left/right part of the domain respectively. The dashed contours represent positive vorticity and the continuous lines the negative vorticity. For r_ρ = 2, it is observed that the vorticity that is generated on the braids between the eddies is entrained into the eddies leading to the rollup of the interface. The maximum values of vorticity are observed to be at the center of the coherent structures.

Fig. 51 (a) shows the cumulative circulation in the field as a function of time. Fig. 51 (b) shows the same plot on different scales for the circulation. The positive and the negative components are summed separately. Curve 1 represents the results for r_ρ =2 . It is observed that the circulation in the field increases from its initial value of zero to very large values at later times. Equal amounts of positive and negative circulation are generated so that the total circulation in the flow field is always zero. It is seen that the slope of the circulation curve increases with time indicating that the rate of generation of circulation (or destabilization of the flow) is increasing as time progresses. The length of the material interface is shown as a function of time by Curve 1 of Fig. 52 . The length is obtained as an average over the length of all the material layers used in the calculations. The material interface length is normalized by the length at t=0 . It is observed that the mean length of the interface increases as the instability develops in time. The final length of the interface is about seven times the initial length for r_ρ = 2. Also to be

observed is the fact that the slope of the curve also increases with time indicating that the rate of elongation is increasing with time. Fig. 53 shows the least squres fit of the vorticity distribution along the central layer for t= 5.0, 8.0, 10.0 and 11.5 respectively. The vorticity values and the locations along the layer are normalized by the corresponding maximum values at each time frame. It is observed that the vorticity distribution develops smoothly at the initial times with the peak values occurring at the edges of the coherent structures. The twin peaks of vorticity on the both halves of the domain occur due to the entrainment of vorticity from both sides of the eddy. It is observed that the peak close to the midsection of the domain is smaller than the peak at the edges of the domain. The reason for this phenomenon can be understood by looking at the material line plots. In one case the material acceleration term is in phase with the gravitational term, thus giving rise to strong local vorticity generation. This corresponds to the bigger peak. In the other case, the material acceleration term and the gravitational term are out of phase and thus oppose each other to reduce the amount generated. Hence a smaller peak is observed in this region.

The mean positions of the spike and the bubble are plotted as a function of time in Fig. 56 (a). The mean position of the bubble is calculated by taking the average of the topmost locations of all material layers and that of the spike is calculated by taking the average of all bottom most locations of all the material layers. Therefore, this represents the average location of the bubble and the spike respectively. For r_ρ=2, it is observed that the bubble and the spike grow almost symmetrically in time, i.e., the rise of the bubble is almost equal to the fall of the spike. Fig. 57 (a) shows the topmost and the lower most points of the bubble and the spike as a function of time. The positions of the lower most points on the bubble and the spike

are shown by the dashed curves and those of the topmost points by the continuous curves. At late times, it is observed that the dashed and continuous lines approach each other indicating that the total layer thicknesses at the tips of the bubble and the spike are becoming very small. It is also seen that different layers move with different velocities until the asymptotic value is reached. Curve 1 of Figs. 58 (a) and (b) shows the bubble and the spike velocities respectively as a function of time. The bubble velocity is estimated as the vertical velocity of the topmost point on the topmost material layer and the spike velocity is taken to be the vertical velocity of the lower most point on the bottom layer. Fig. 59 (a) and (b) show the average bubble and the spike velocities as a function of time. The average bubble velocity is obtained by taking the average of the velocities at the topmost points on all the material layers. The average spike velocity is obtained by averaging the velocities of the bottom most points on all the material layers. It is observed from Fig. 58 (a) and 59 (a) that the bubble velocity approaches an asymptotic value at late times. It can be shown that the spike velocity also has an aymptotic value (except for A=1.0 or $r_\rho = \infty$) although the calculations have to be continued for very long times in order for the spike velocity to approach this value. It is to be noted that the flow around the bubble and the spike is similar to a separated flow around a bluff body. Thus there is a certain amount of pressure drag on the bubble and the spike as they move into the dense fluid and the light fluid respectively [32]. This pressure drag is proportional to the size of the body (defined approximately by the radius of curvature), the density of the medium it is moving into and the velocity of the body. For $r_\rho = 2$, the size of the bubble is slightly larger than that of the spike and since the bubble is moving into a denser fluid, the pressure drag on the bubble is slightly larger than the

drag on the spike. Thus the bubble reaches its asymptotic value faster than the spike as is obvious from Curve 1 of Figs. 58 and 59. The calculations were stopped after the bubble reached its asymptotic velocity in order to limit the computational time. The velocities of the bubble and the spike for the R-T instability have been calculated by other investigators, in particular, Kerr [34] and Trygvasson [33]. The asymptotic velocities are usually normalized as $U_{bn} = U_b/(\sqrt{Ag_r}\,\lambda)$ which is similar to a non-dimensional Froude number. λ is the wavelength of perturbation, A is the Atwood number and g_r is the non-dimensional gravitational acceleration, equal to 1 in the present calculations. For an Atwood number of 0.5, the aymptotic value for the bubble velocity, U_b, is found to be 0.66 from the numerical simulations, which corresponds to $U_{bn} = 0.27$. Kerr [34] obtained a value of 0.27 for this quantity in his calculations of R-T instability using the vortex sheet method. The mean bubble asymptotic velocity from Fig. 59 (a) is obtained as $U_{bn} = 0.29$. The discrepancy between the tip value and the mean value for the bubble velocities can be attributed to the relative movement among the material layers during the growth of the instability. Experimentally, the asymptotic bubble velocity is measured to be between 0.2 and 0.3 [35]. It is observed from Curve 1 of Fig. 58 (b) that the spike accelerates from rest at t=0 and the velocity increases until the pressure drag becomes significant. The spike velocity overshoots its asymptotic value and starts decelerating to a velocity where the downward gravitational force on the spike is matched by the pressure drag. The peak value for the spike velocity from Fig. 58 (b) is 0.89 which corresponds to $U_{sn} = 0.43$. This peak occurs at t= 8.5 . Kerr [34] obtained a value of 0.44 for the peak spike velocity occurring at t=8.5 from his calculations.

(ii) Case II : Density ratio = 3

The location and velocity of the vortex/transport elements for r_ρ =3 is shown in Fig. 43 for t= 5.0, 7.0, 7.85 and 8.6 respectively. It is observed that the instability develops faster in time compared to Case I. The tip of the spike reaches y=-10.0 at t=8.6 as compared to a time of 11.5 for r_ρ=2. This is to be expected since the top fluid is heavier in this case and falls faster into the low density fluid. It is observed that the development of the K-H instability or the extent of the rollup is decreased with respect to Case I. Also, the size of the bubble in this case is much larger than that of the spike, i.e, the instability does not develop symmetrically with respect to y=0. Moreover, the coherent structures are formed at a lower elevation with respect to Case I. Again, it is obvious from the material line plots that more of the low density fluid by volume is being entrained into the eddies. Fig. 44 shows the streamline contours at the same time frames. The development of the streamlines is very similar to what was observed for Case I. However, the motion of the eddies into the low density fluid is clearly observed. The volumetric entrainment, as obtained from the value of the streamfunction at the center of the eddy, turns out to be 9.3 . This value is larger than that for Case I indicating that the entrainment currents set up by the development of the instability are larger for higher values of r_ρ . It is to be noted that the entrainment parameter is large inspite of the fact that the rollup has been significantly decreased. This is particularly important in studying fires since fire spread is determined by the intensity of circulation or entrainment currents that are set up in the flow field as a result of buoyancy.

Fig. 45 shows the normalized temperature contours at the respective times. The scalar contours reveal that the volumetric entrainment of the low density fluid is larger than that of the high density fluid. Also to be noted is the thickness of the scalar contours around the bubble and the spike. It appears that the scalar thickness in the region of the spike is smaller than that in the region of the bubble. This is contrary to Case I where the thicknesses were nearly the same. It will be shown later in this section that the reason for this phenomenon is the accumulation of vorticity in the lower part of the spike. This leads to smaller interface thickness in the region of the spike. The vorticity contours for r_ρ=3 are shown in Fig. 46 . The development of the K-H instability at a lower elevation is clearly observed. Once again, the vorticity that is generated at the braids is entrained by the eddies. The intensity of vorticity generation in this case is much higher than in Case I. This is because of the higher value for the $\nabla\rho$ term in the vorticity equation.

The generation of circulation in the flow field with time is shown in Fig. 51 (a) and (b) . Curve 2 represents the results for r_ρ = 3. Again, the results show a larger generation of circulation for r_ρ=3 as compared to r_ρ=2. The final slopes of the circulation curves are almost equal for Cases I and II although this slope is attained at an earlier time for Case II. Curve 2 of Fig. 52 shows the material interface length as a function of time. The faster development of the instability for r_ρ =3 is obvious from the fact that the curve is always above the curve for Case I. The final length of the interface is about five times the initial length. The slope of the curve is also increasing with time and it is interesting to note that the final slopes of the curves for Cases I and II are almost equal although this stage is reached earlier in time for Case II. Thus, for large values of r_ρ, a very

high rate of elongation of the interface is reached at earlier times as compared to the cases of low r_ρ. In other words, as r_ρ increases, the rate of destabilization of the flow also increases and therefore the calculations for large r_ρ have to be highly refined, i.e., a small time step and more elements, in order to resolve the large material acceleration and strain rate. Fig. 54 shows the least squares fit of the vorticity distribution along the central layer. The vortcity is normalized by its maximum value at each time frame and the distance along the layer is normalized by the total length of the layer. The same pattern of twin peaks, as was observed in the case of r_ρ=2, is also seen here. However, the relative size of the peak closer to the midsection of the is smaller than what was seen in the case of r_ρ=2. This can be attributed to larger values of the material acceleration term. Furthermore the larger peak appears to have shifted closer to x=0 .

Fig. 56 (b) shows the mean displacement of the bubble and the spike as a function of time. Unlike Case I, a near symmetric displacement of the bubble and the spike is no longer observed. It is clear that the spike is falling faster into the light fluid and the bubble is rising at a slower rate into the heavy fluid. Fig. 57 (b) shows the bubble and spike displacement in terms of the topmost and the lowermost points on the bubble and the spike as a function of time. The dashed curve represents the positions of the lowermost points on the bubble and the spike. Again, it is observed that the dashed and the continuous curves approach each other indicating that the total interface thickness at the edges of the bubble and the spike become smaller with time. However, it is seen that the interface thickness in the spike region is smaller than that in the bubble region. The bubble and the spike velocities are shown by Curve 2 in Figs. 58 and 59. Once again it is observed that the bubble reaches its asymptotic value earlier in time as

compared to the spike. Also to be noted ios the fact the bubble reaches its asymptotic value faster than in the case for r_ρ= 2. This is because the size of the bubble is much larger for r_ρ= 3 and it is moving into a relatively heavier fluid than in Case I. Thus the pressure drag on the bubble is higher than in Case I and hence it attains its asymtotic value faster in time. The spike on the other hand takes longer to reach its asymptotic value since, from the above arguments, the pressure drag on the spike is smaller than in Case I. For r_ρ =3, the value of U_{bn} for the bubble from Fig. 58 (a) is 0.255 which compares well with the value of 0.26 obtained by Trygvasson [33] in his simulations using the vortex-in-cell method. The mean bubble asymptotic velocity obtained from Fig. 59 (a) is 0.28. Although the calculations had to be stopped before the spike could attain its asymptotic velocity, the peak spike velocity from Fig. 58 (b) is obtained as 1.3 which corresponds to U_{sn}= 0.5 . The peak value for the spike velocity obtained by Trygvasson is 0.48.

(iii) Case III : Density Ratio = 9

The location and velocity of the vortex/transport elements are shown in Fig. 47 at t= 3.0, 4.25, 4.75 and 5.25 respectively. Due to the top fluid being much heavier, the interface falls faster into the light fluid as compared to Cases I and II. The spike reaches y=-10.0 at t= 5.25 in this case. It is observed from the material interface plots that the rollup is almost completely inhibited. Thus, at higher values of r_ρ, the faster growth of the spike into the light fluid allows very little time for the growth of the structures due to the K-H instability. As the density ratio goes to infinity, i.e., the case of a fluid falling freely into vaccum, the net pressure gradient and hence the baroclinic term would be zero everywhere in

the fluid and thus there would be no rollup of the interface. It is also observed that the bubble is now very large compared to the spike and the K-H instability forms at a lower elevation as compared to Cases I and II. As r_ρ increases, the spike becomes thinner than the bubble and falls faster into the light fluid. Fig. 48 shows the corresponding streamline plots for $r_\rho = 9$. Although there is very little rollup of the interface, the amount of entrainment or circulation of fluid in the flow field increases with r_ρ . The value of the streamfunction at the center of the structure at t= 5.25 is 9.75. This value is greater than what was calculated for Cases I and II. This indicates a greater destabilization of the flow. The migration of the structure to lower elevations is clearly observed from the streamline contours.

Fig. 49 show the contours for the normalized temperature at the corresponding times. Again, it is seen that the scalar thickness in the spike region is much smaller than in the bubble region. For r_ρ=9, the scalar thickness at the spike is about half that at the bubble. The intensification of scalar gradients in the spike region can lead to numerical complications if proper resolution is not provided. Fig. 50 shows the corresponding vorticity contours for $r_\rho = 9$. The vorticity that is generated in the upper part of the interface appears to be advected to the lower part of the spike. This is shown by the higher concentration of vorticity in the spike region. It is also observed that the vorticity concentration around the bubble is very small. This leads to the formation of a shock or a zone of very steep gradient of vorticity in the spike region, wherein the vorticity goes from a large negative value to a large positive value across a very small distance. This singularity makes it very difficult to continue the calculations very far in time. Some amount of diffusion or artificial viscosity has to be

introduced in order to stabilize the calculations beyond this point. Thus, for large values of r_ρ, one should expect the gradients of vorticity and the scalar in the vicinity of the spike to go to very large values and in the limit lead to a singularity in the calculations.

Curve 3 of Fig. 51 (a) and (b) shows the generation of circulation in the flow field as a function of time. It is observed from Fig. 51 (a) that the final slope of the curve is almost infinity. The amount of circulation generated is about five times that for Cases I and II. The same curve is shown in Fig. 51 (b) with the latter portion of the curve removed. The final slopes of all the three curves in Fig. 51 (b) are almost equal. The elongation of the material interface with the growth of the instability is plotted as a function of time in Curve 3 of Fig. 52 . As expected, the instability grows faster in time and the final length at t=5.25 is about four times the initial length. Again, it is observed that the slope of the curve at t=5.25 is almost the same as the final slopes for Cases I and II. Thus the same elongation rate is reached earlier in time with increasing r_ρ. Hence, the calculations for higher r_ρ have to be greatly refined, temporally as well as spatially. Fig. 55 shows the vorticity distribution along the central layer at t= 3.0, 4.25, 4.75 and 5.25 respectively. The vorticity is normalized by its maximum value at each time frame and the distance by the total length of the layer. In this case, it is seen that the smaller peak is much smaller relative to the larger peak than was observed for r_ρ=2 and 3. Also, the vorticity peaks for r_ρ =9 occur very close to x=0, i.e., the central portion of the spike. The formation of a very steep gradient in vorticity is clearly observed in the figure. Also to be noted is the fact that the vorticity in regions other than that of the spike is nearly zero. This is another evidence to the fact that the vorticity is being advected

into the lower portions of the spike. The advection of the vorticity takes place due to very large values for the material acceleration.

The mean positions of the spike and the bubble are plotted as a function of time in Fig. 56 (c). The spike falls at a very fast rate into the light fluid. The figure shows that the bubble and the spike grow very asymmetrically. Fig. 57 (c) shows the positions of the topmost and the lowermost points on the bubble and the spike as a function of time. The interface thickness in the region of the spike at late times is smaller than that in the region of the bubble. Curve 3 in Figs. 58 and 59 shows the bubble and the spike velocity plotted as a function of time. It is seen that the bubble tends to its asymptotic value at a much earlier time as compared to Cases I and II. This is because the pressure drag on the bubble is quite large since it is moving into a very dense fluid and the size of the bubble itself is very large. Although the tip of the bubble does not appear to have reached its asymptotiv velocity, it is observed that the mean bubble velocity from Fig. 59 has reached a constant value. Again, the discrepancies between the two values is due to the relative movement between the material layers. The velocity of the bubble at the final time from Fig. 58 (a) is obtained as 0.8 which correpsonds to $U_{bn} = 0.24$. The value obtained by Kerr [34] for $r_0 = 9$ is 0.23. The mean bubble asymptotic velocity from Fig. 59 (a) is 0.27 . On the other hand, it is observed that the size of the spike is very small and it is moving into a fluid of very low density and hence the pressure drag on the spike is very small. Therefore, the spike falls very fast in this case as is seen in Curve 3 of Fig. 58 (b). The downward gravitational force is matched by the pressure drag only at very large velocities of the spike and hence the approch to an asymptotic value for the spike velocity requires running the calculations for very long times. The calculations had to be

stopped long before the spike could even approach this value in order to limit the amount of computational time. In the limit of r_ρ going to infinity, the spike would have a constant acceleration equal to that of gravity, i.e., the slope of the curve would be unity. In fact, for r_ρ =9, the slope of the curve from Fig. 58 (b) is 0.94, suggesting that the pressure drag in the system is very small.

(iv) Case IV : Density Ratio= 3 (with Boussinesq Approximation)

Since these calculations were done for large values of the density ratio, the results are also compared with those obtained using the Boussinesq approximation in order to establish the limits of the approximation. This is implemented by neglecting the effects of material acceleration (du/dt), with respect to the gravitational acceleration, on the growth of the instability. The simulations were conducted for r_ρ=3 and the results for the locations and velocities of the transport/vortex elements are shown in Fig. 60 . The non-dimensional times are the same as in Fig. 43. Comparing the two cases (with and without the Boussinesq approximation), it is seen that the neglect of the inertial terms leads to a symmetric growth of the structures which remain centered at y=0. Equal volume of the heavy and the light fluid are being entrained into the eddies. This behavior is characteristic of the R-T instability at values of r_ρ close to unity. Thus, the results obtained using the Boussinesq approximation would be accurate only for low values of r_ρ. Fig. 61 shows the least squares fit of the vorticity distribution along the central layer. In this case it is observed that the peak closer to the midsection of the domain is slightly larger than the peak close to the edge of the domain. Although, one would expect the two peaks to be equal in

magnitude with the neglect of the inertial terms, it should be noted here that the difference in density between material layers leads to a small degree of asymmetry. In the Boussinesq approximation for the zero thickness interface, the density is approximated by the mean density, i.e., $\rho = (\rho_1+\rho_2)/2$. This leads to perfect symmetry in the growth of the structures. However, for the finite thickness interface, each layer has a different value for the density and the structures develop a small degree of asymmetry. The mean bubble and the spike displacement with time for this case is shown in Fig. 62 (a). Again, it is noted that the bubble and the spike grow almost symmetrically, i.e., they rise and fall by the same amount respectively. This is a characteristic feature of the R-T instability for low r_ρ . Fig. 62 (b) shows the topmost and the lowermost points on the bubble and the spike as a function of time. Again, a symmetric development is observed with the layer thicknesses at the tips of the bubble and the spike being equal. The mean bubble and spike velocities are plotted as a function of time in Fig. 62 (c). The curve on the top represents the velocity of the spike and the bottom curve represents the bubble. It is seen that the two velocities are almost equal for all times and have almost the same value for the asymptotic velocity. Thus the Boussinesq approximation is not able to predict the faster fall of the spike for moderate and large values of the density ratio. The symmetric development of the structures is observed only at very small values of r_ρ (e.g. $r_\rho < 2$) and in this regime the Boussinesq approximation may be used to yield reasonably accurate results for the growth of the instability. Therefore the inertial term plays an important role in the vorticity dynamics for moderate and large values of the density ratio and ignoring it can lead to erroneous predictions. The Boussinesq approximation is strictly valid only for small values of r_ρ .

V. 6. CONCLUSIONS

The results of the numerical simulations yielded accurate predictions for the growth of the R-T instability over a wide range of values for the density ratio. At high values of r_ρ, it is found that the K-H instability along the sides of the interface is completely inhibited. Although no significant rollup of the interface occurs, it is important to realize that the entrainment currents (as seen from the streamlines of the flow) set up by the instability are much larger than in the cases with low r_ρ. The generation of entrainment currents and fluid circulation is of great importance in analyzing fires and fire spread.

Also to be noted is the versatility of the vortex/transport element scheme in resolving flows with large strain rates. A crucial issue in the simulation of such problems is the accurate tracking of the material interface long after it has deformed and elongated far beyond its initial state. This scheme is able to preserve accuracy by the process of injection and simultaneous redistribution of material elements along the interface. The R-T instability is an ideal candidate problem to test the scheme, since it is highly non-linear and very sensitive to initial and boundary conditions. Furthermore, the linear growth of the R-T instability is well documented. The predictions of the linear growth rate from the numerical simulations compare well those of the linear theory. The characteristic features of the R-T instability in the non-linear range for different values of the density ratio, as predicted by the simulations are consistent with what has been observed in other investigations. The numerical values for the asymptotic bubble and spike velocities compare very well with previous results on the R-

T instability. The simulations were also used to check the accuracy of the Boussinesq approximation. It was found that this approximation does not correctly predict the advection of vorticity into the spike region, which is a dominant phenomenon, particularly at high Atwood numbers. Also the aymptotic bubble and spike velocities obtained using the Boussinesq approximation were almost equal and this behavior is true only at very low values of r_ρ. The spike velocity is much larger than that of the bubble at high r_ρ.

FIGURE CAPTIONS

Fig. 37. A schematic of the Rayleigh Taylor instability in a gravitational field. The density of the top fluid is greater than that of the bottom fluid.

Fig. 38. A plot of the linear growth rate of the R-T instability as a function of the wavenumber. The curves 1, 2 and 3 stand for r_ρ =2, 3 and 9 respectively. The continuous curve represents the results of the linear theory for a finite thickness interface. The dashed curves (1', 2' and 3') are the results of the linear theory for a zero thickness interface. The symbols are results of numerical simulations.

Fig. 39. The locations and velocities of the vortex/transport elements at t = 5.0, 8.0, 10.0 and 11.5 respectively for r_ρ = 2.

Fig. 40. The streamline contours at t= 5.0, 8.0, 10.0 and 11.5 respectively for r_ρ = 2.

Fig. 41. The normalized temperature contours (T= $1/\rho$) at t= 5.0, 8.0, 10.0 and 11.5 respectively for r_ρ = 2.

Fig. 42. The vorticity contours at t= 5.0, 8.0, 10.0 and 11.5 respectively for r_ρ =2. The dashed contours represent positive vorticity abd the continuous contours represent negative vorticity.

Fig. 43. The locations and velocities of the vortex/transport element methods at t= 5.0, 7.0, 7.85 and 8.6 respectively for r_ρ = 3.

Fig. 44. The streamline contours at t= 5.0, 7.0, 7.85 and 8.6 respectively for r_ρ = 3.

Fig. 45. The normalized temperature contours (T= $1/\rho$) at t= 5.0, 7.0, 7.85 and 8.6 respectively for r_ρ = 3.

Fig. 46. The vorticity contours at t= 5.0, 7.0, 7.85 and 8.6 respectively for r_ρ = 3. The dashed contours represent positive vorticity abd the continuous contours represent negative vorticity.

Fig. 47. The locations and velocities of the vortex/transport element methods at t= 3.0, 4.25, 4.75 and 5.25 respectively for r_ρ = 9.

Fig. 48. The streamline contours at t= 3.0, 4.25, 4.75 and 5.25 respectively for r_ρ = 9.

Fig. 49. The normalized temperature contours (T= $1/\rho$) at t= 3.0, 4.25, 4.75 and 5.25 respectively for r_ρ = 9.

Fig. 50. The vorticity contours at t= 3.0, 4.25, 4.75 and 5.25 respectively for r_ρ = 9. The dashed contours represent positive vorticity abd the continuous contours represent negative vorticity.

Fig. 51. (a) The cumulative circulation in the flow field as a function of time. The positive and the negative components are summed separately. Curves

1,2 and 3 represent r_ρ = 2, 3 and 9 respectively; (b) same figure as in (a) but on different scales.

Fig. 52. The mean length of the material layers as a function of time. Curves 1, 2 and 3 represent r_ρ = 2, 3 and 9 respectively.

Fig. 53. The least squares fit of the vorticity distribution along the central layer at t= 5.0, 8.0, 10.0 and 11.5 respectively for r_ρ = 2.

Fig. 54. The least squares fit of the vorticity distribution along the central layer at t= 5.0, 7.0, 7.85 and 8.6 respectively for r_ρ = 3.

Fig. 55. The least squares fit of the vorticity distribution along the central layer at t= 3.0, 4.25, 4.75 and 5.25 respectively for r_ρ = 9.

Fig. 56. The mean position of the bubble and the spike as a function of time for r_ρ = (a) 2, (b) 3 and (c) 9 respectively.

Fig. 57. The positions of the topmost and the lowermost points on the bubble and the spike as a function of time. The dashed curve represents the positions of the lowermost points. (a) r_ρ =2, (b) r_ρ = 3 and (c) r_ρ = 9.

Fig. 58. (a) The magnitude of the velocities at the topmost point on the bubble as a function of time. (b) the magnitude of the velocities at the lowermost point on the spike as a function of time. Curves 1, 2 and 3 represent r_ρ = 2, 3 and 9 respectively.

Fig. 59. (a) The magnitude of the mean velocity of the bubble as a function of time. (b) The magnitude of the mean velocity of the spike as a function of time. Curves 1, 2 and 3 represent r_ρ = 2, 3 and 9 respectively.

Fig. 60. The locations and velocities of the vortex/transport elements at t= 5.0, 7.0, 7.85 and 8.6 respectively for r_ρ= 3 with the Boussinesq approximation.

Fig. 61. The least squares fit of the vorticity distribution along the central layer at t= 5.0, 7.0, 7.85 and 8.6 respectively for r_ρ= 3 with the Boussinesq approximation.

Fig. 62. (a) The mean position of the bubble and the spike as a function of time for case IV; (b) the positions of the topmost and the lowermost points on the bubble and the spike as a function of time; (c) the mean bubble and spike velocity as a function of time.

THE RAYLEIGH TAYLOR INSTABILITY

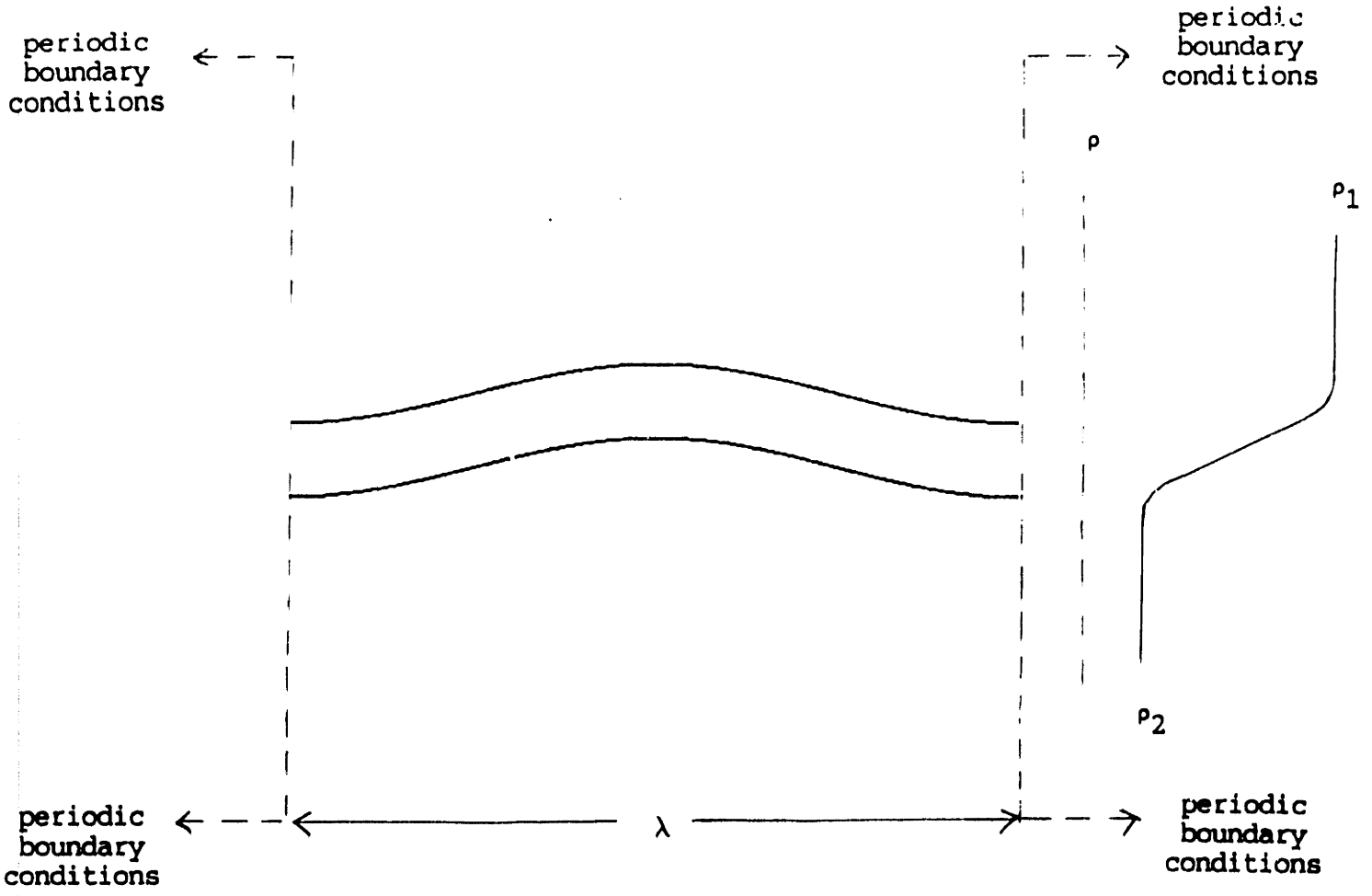

ρ Error Function Distribution

Figure 37

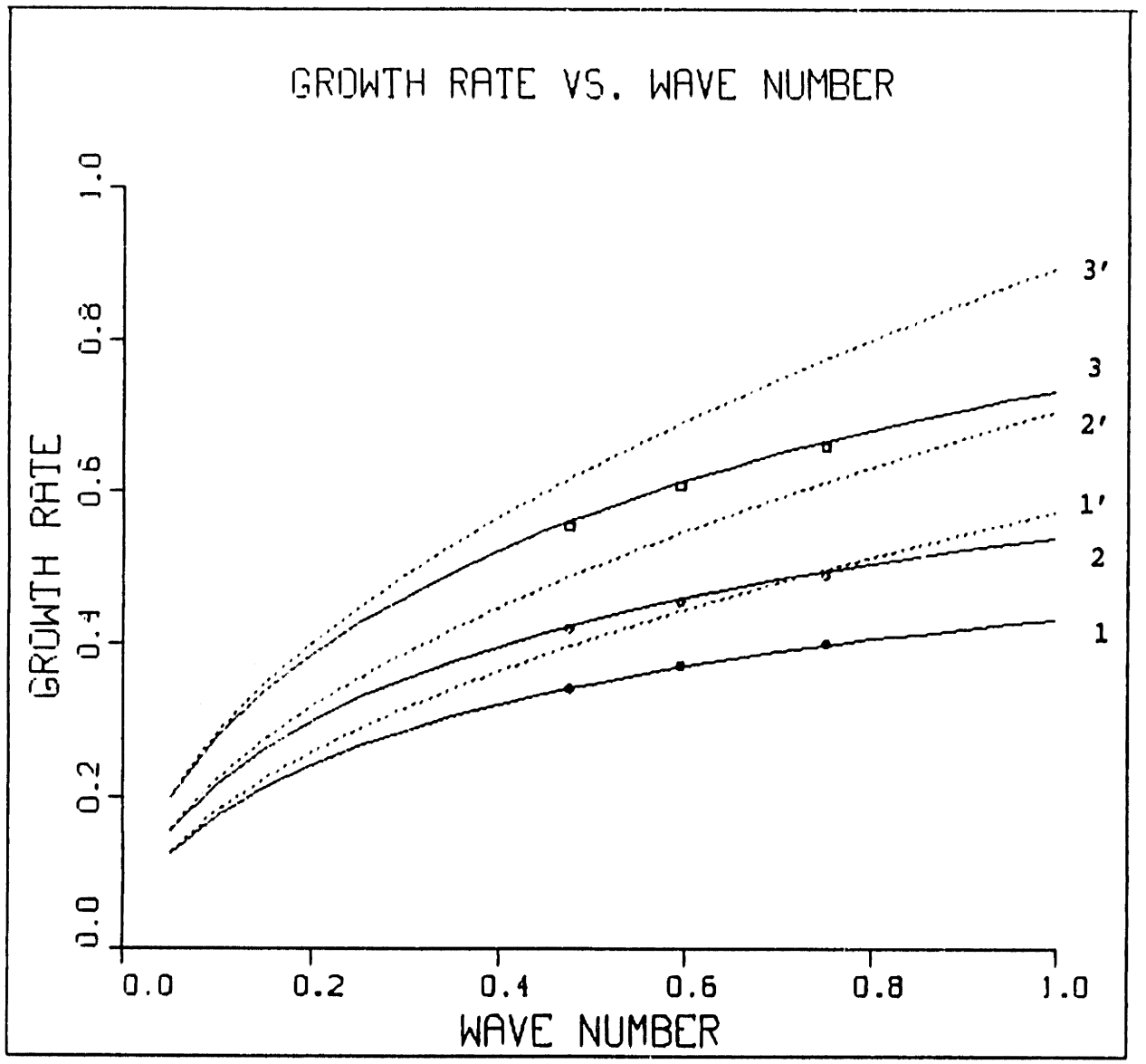
GROWTH RATE VS. WAVE NUMBER
GROWTH RATE
0.0
0.2
0.4
0.6
0.8
1.0
WAVE NUMBER
0.0
0.2
0.4
0.6
0.8
1.0
3'
3
2'
1'
2
1

Figure 38

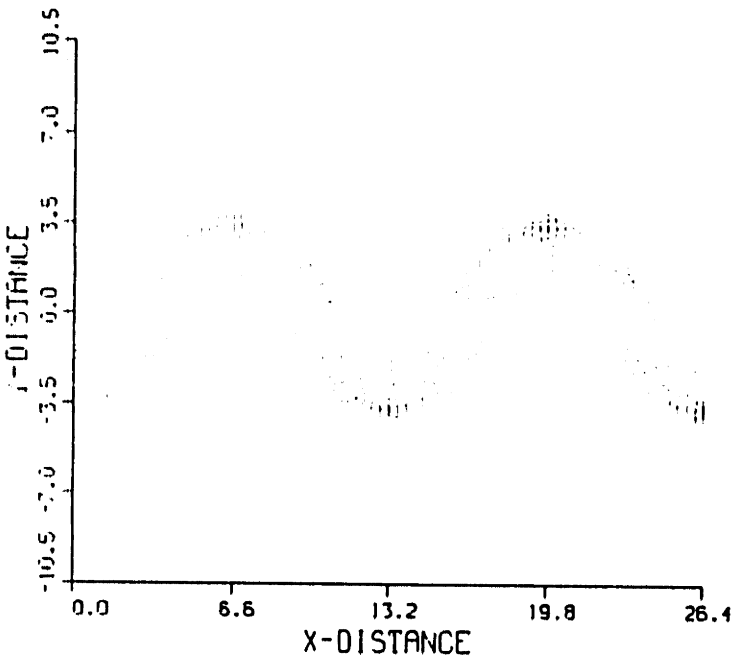

t = 5.0

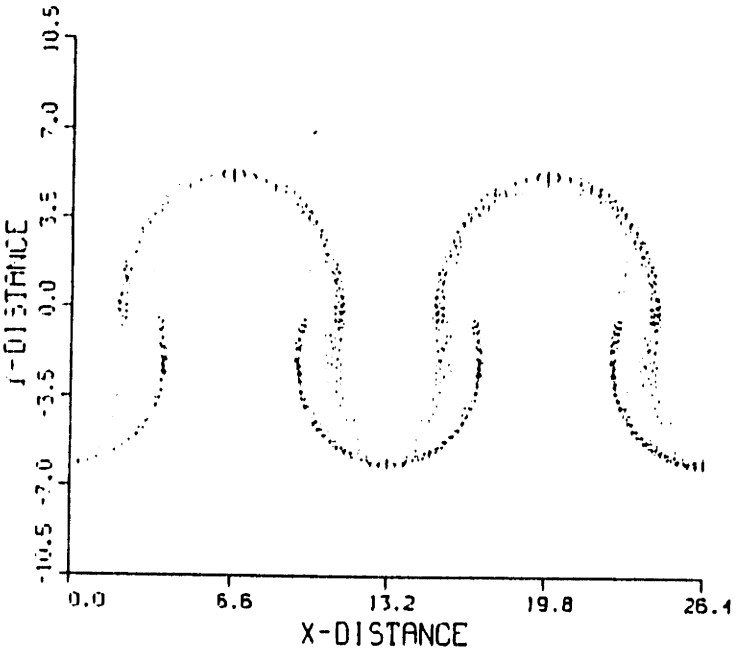

t = 8.0

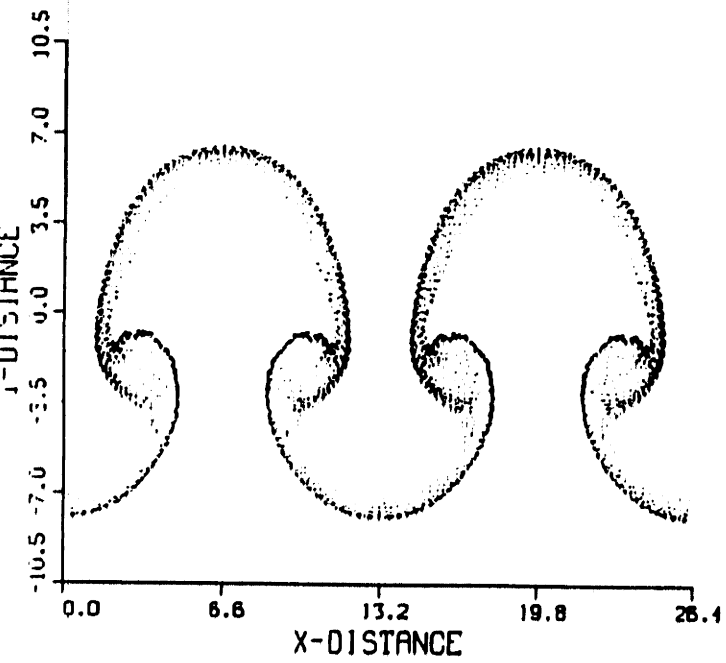

t = 10.0

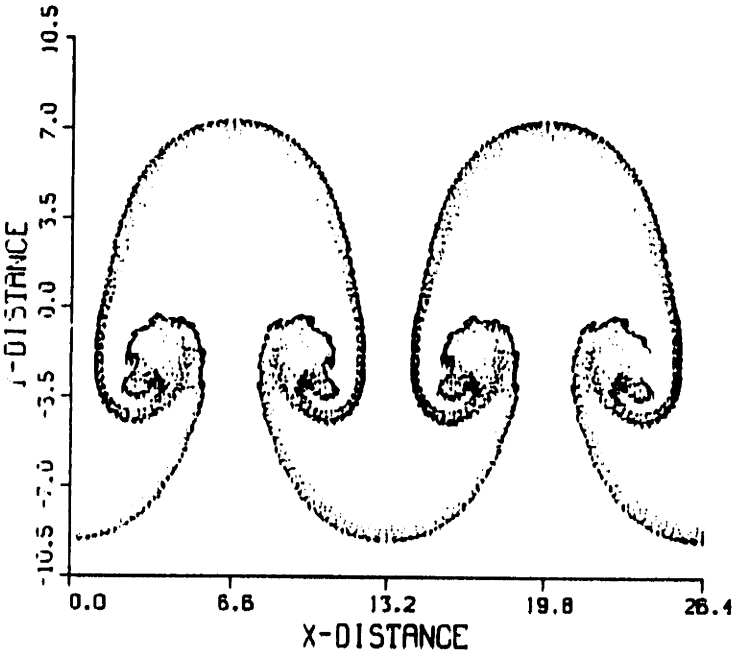

t = 11.5

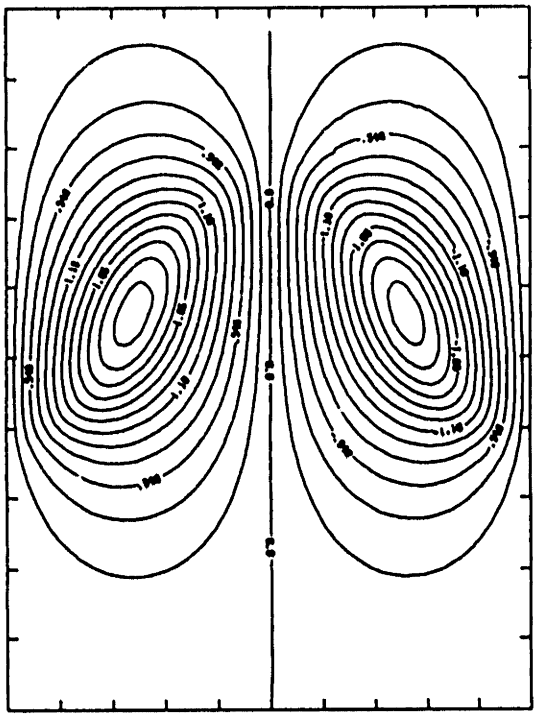

t = 5.0

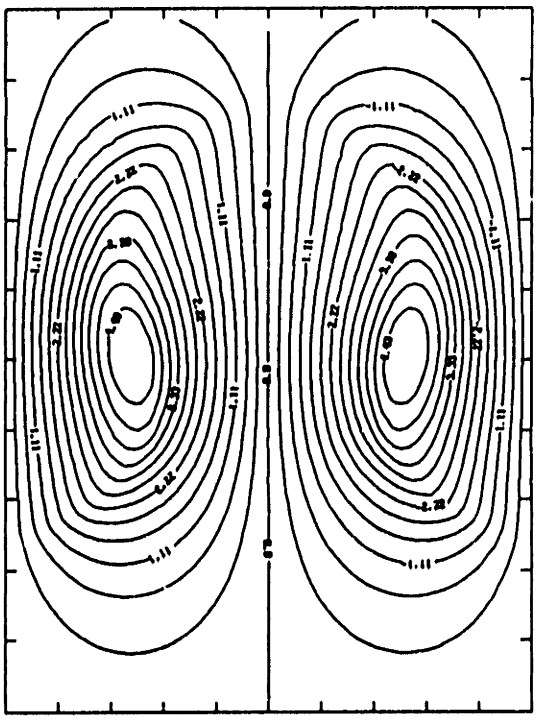

t = 8.0

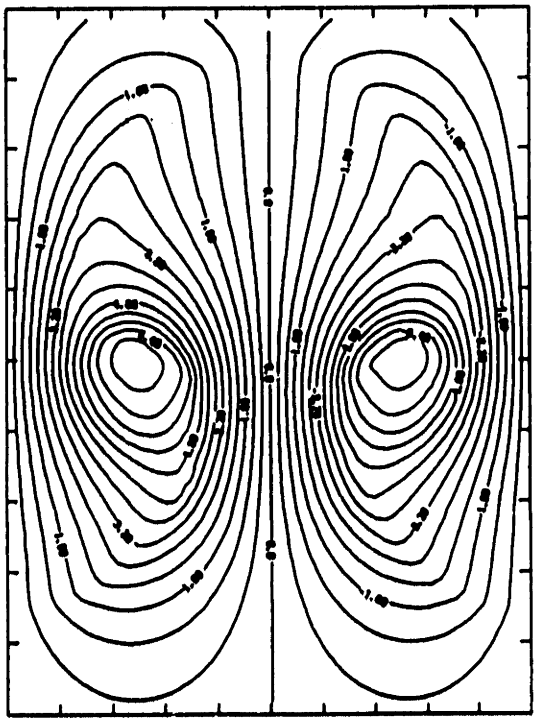

t = 10.0

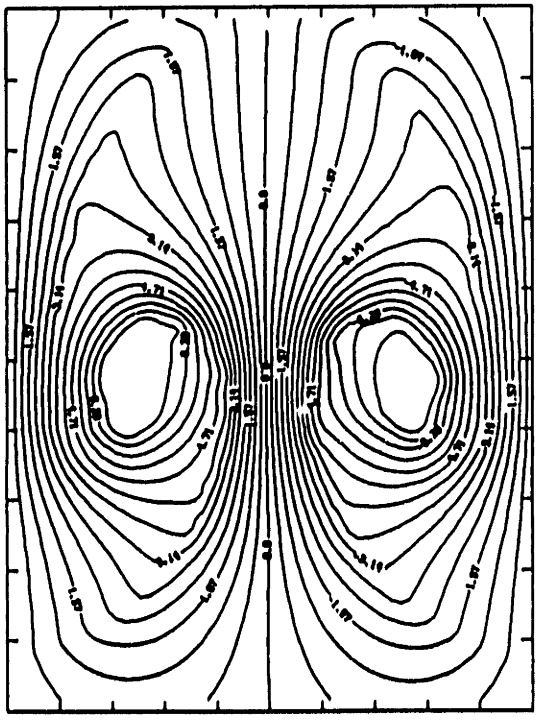

t = 11.5

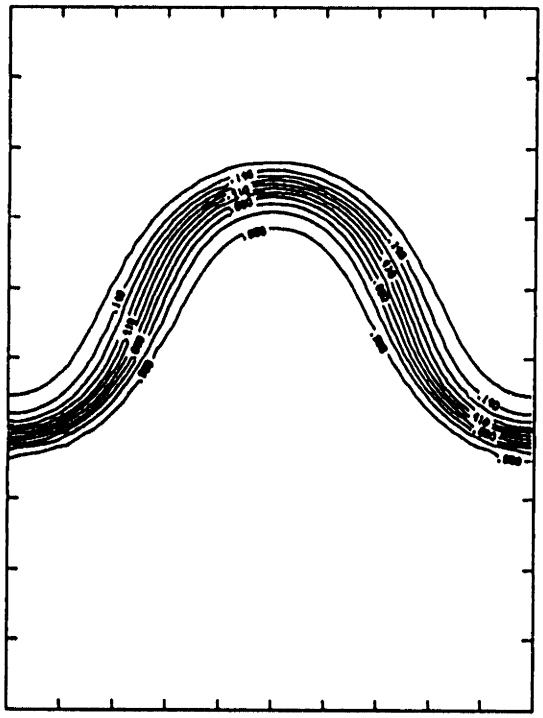

t = 5.0

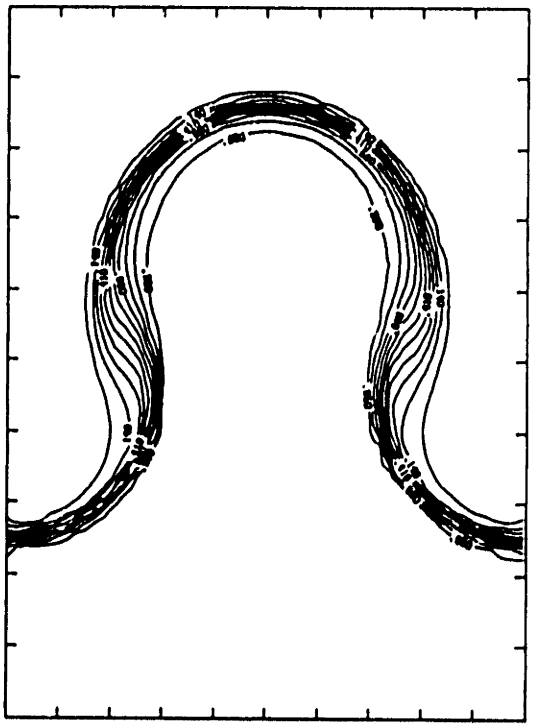

t = 8.0

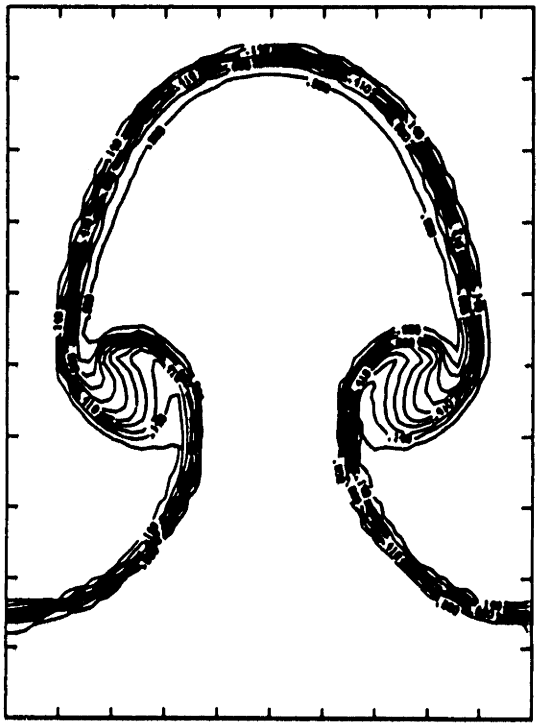

t = 10.0

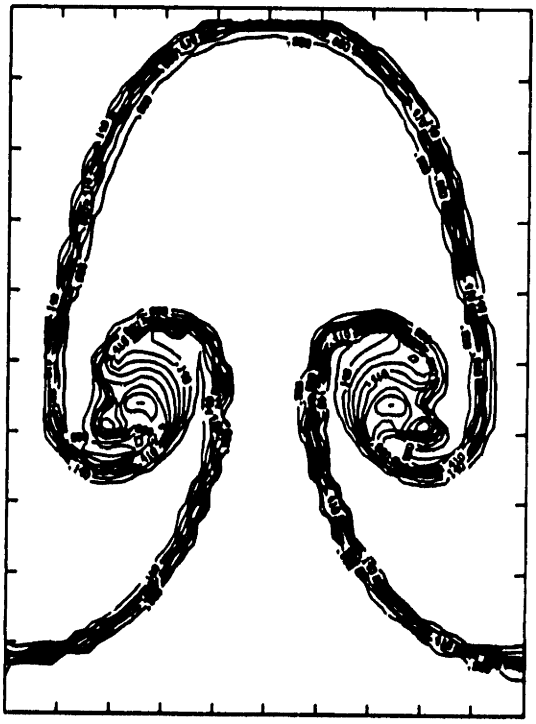

t = 11.5

Figure 41

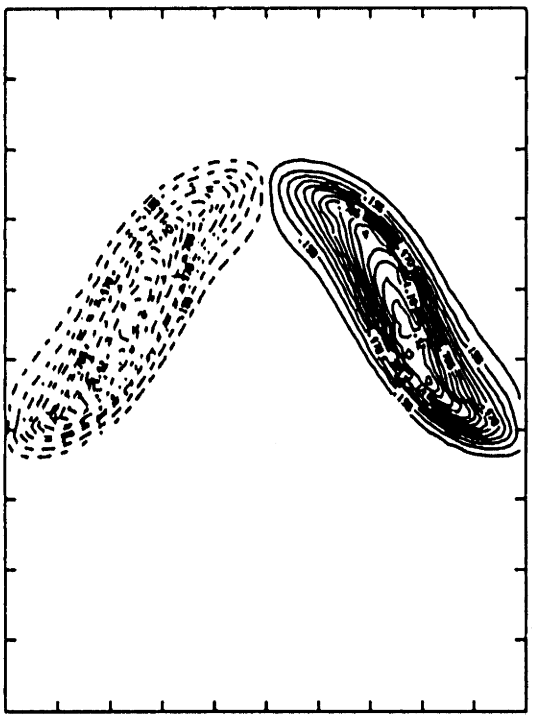

t = 5.0

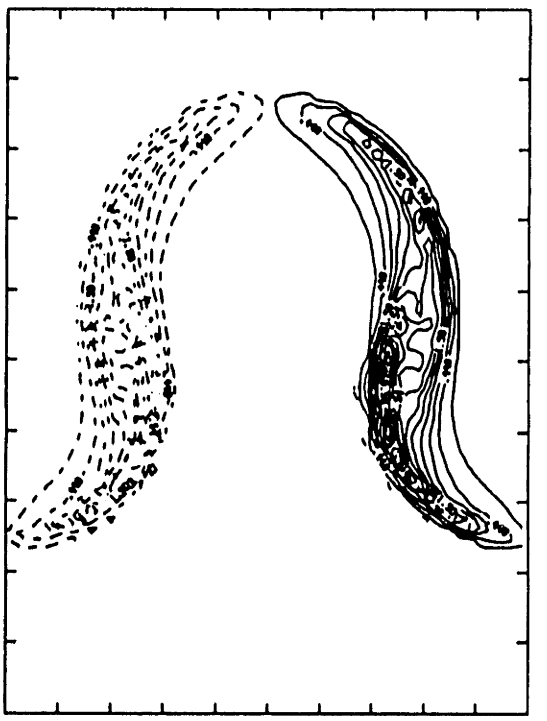

t = 8.0

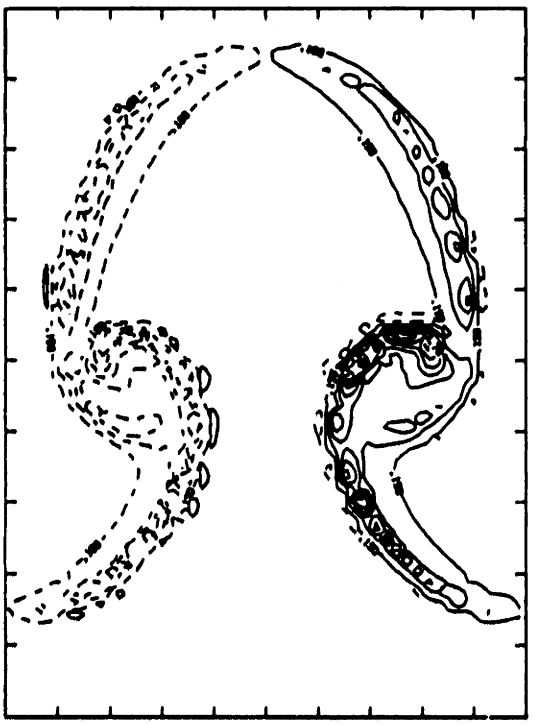

t = 10.0

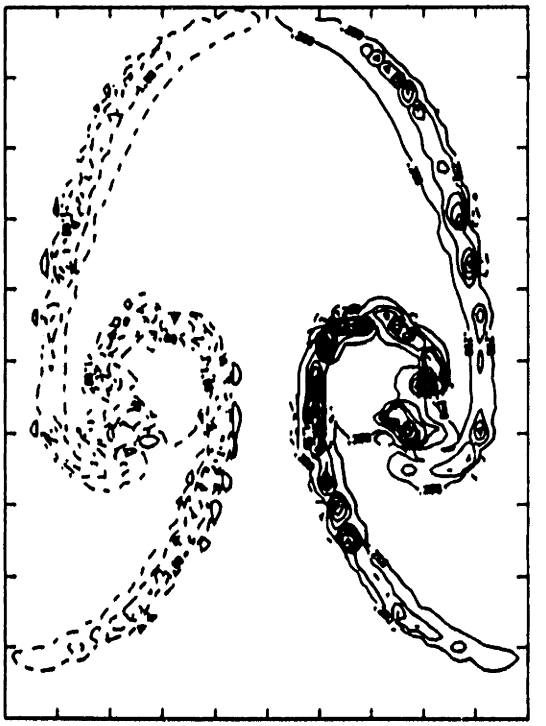

t = 11.5

Figure 42

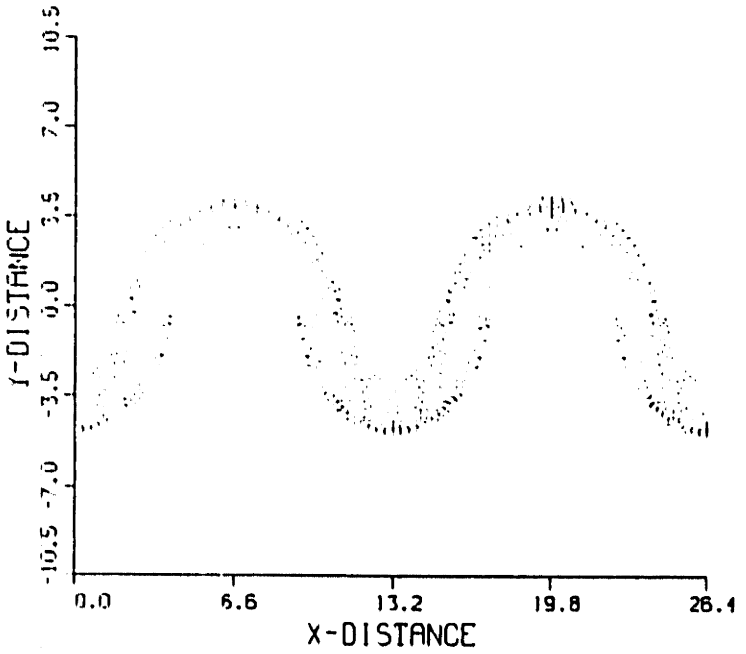

t = 5.0

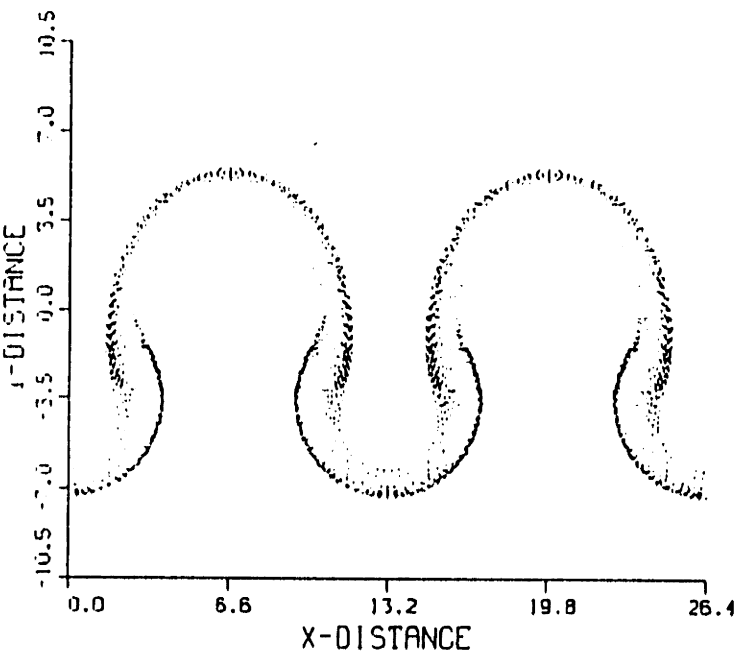

t = 7.0

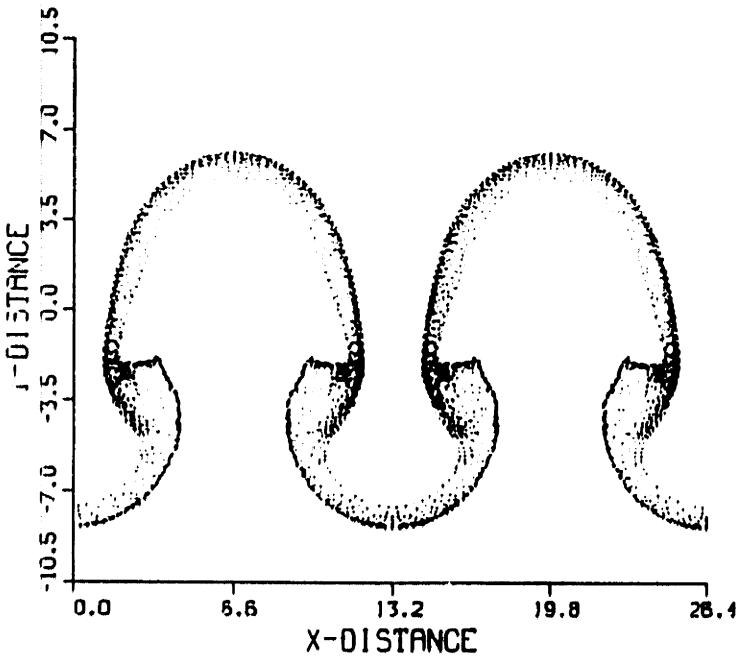

t = 7.85

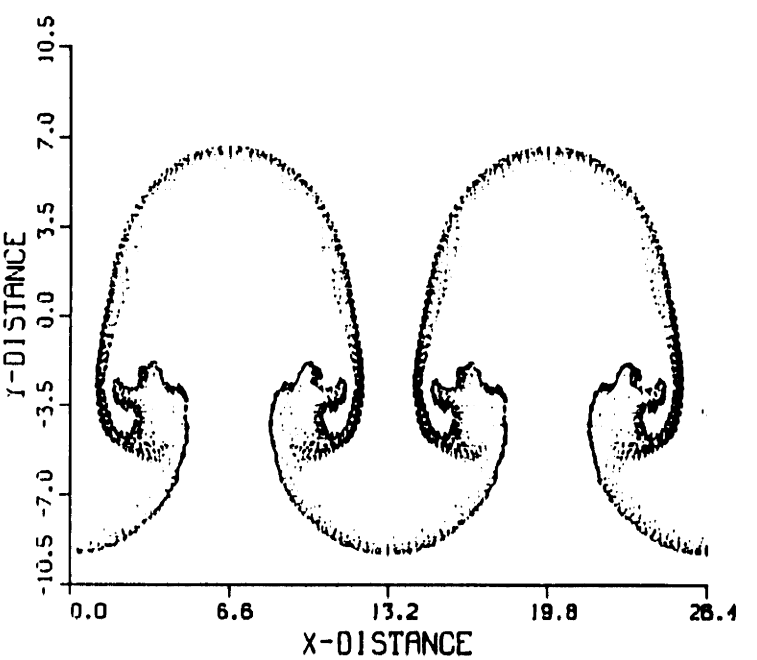

t = 8.6

Figure 43

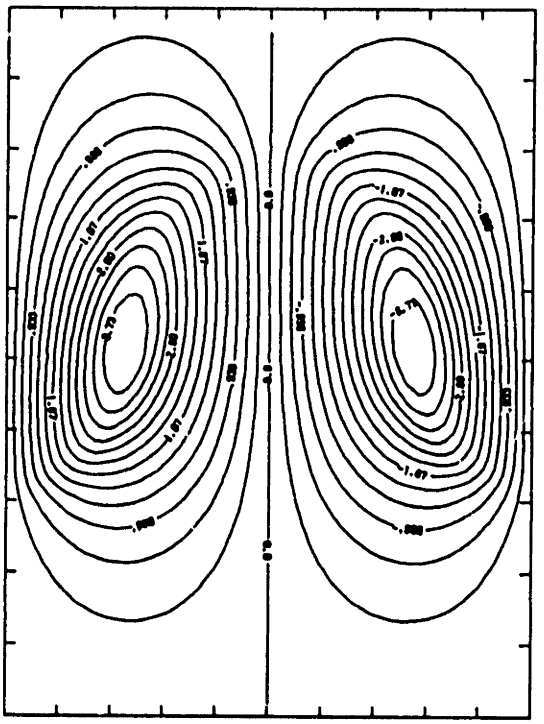

t = 5.0

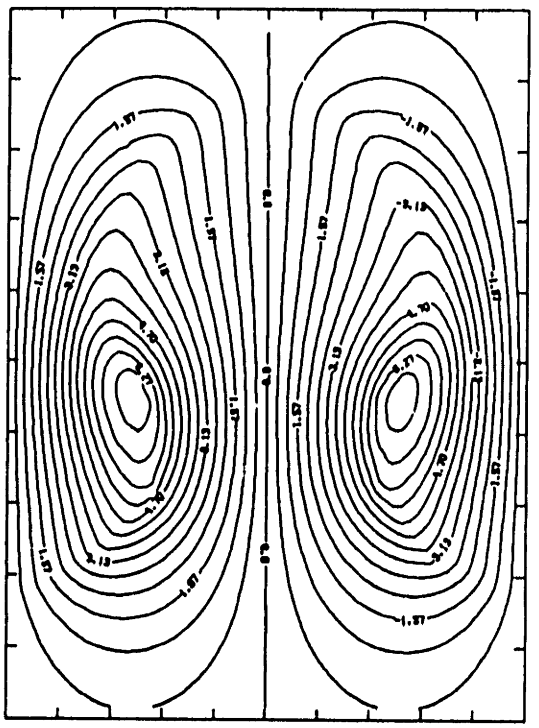

t = 7.0

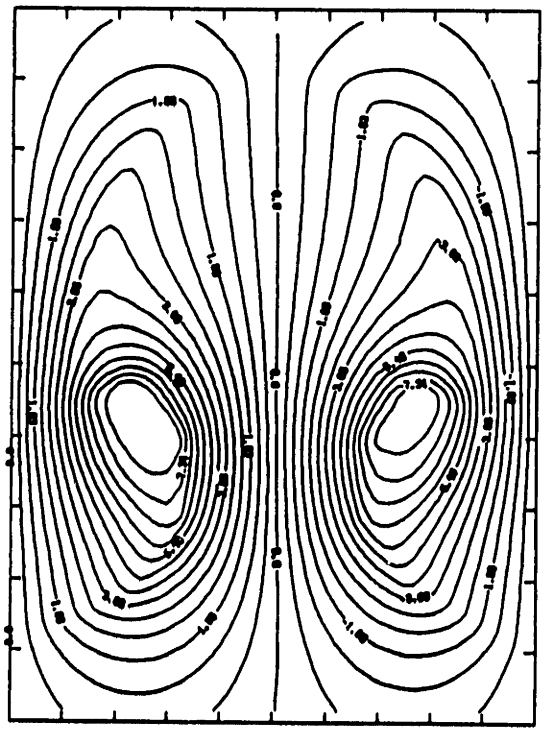

t = 7.85

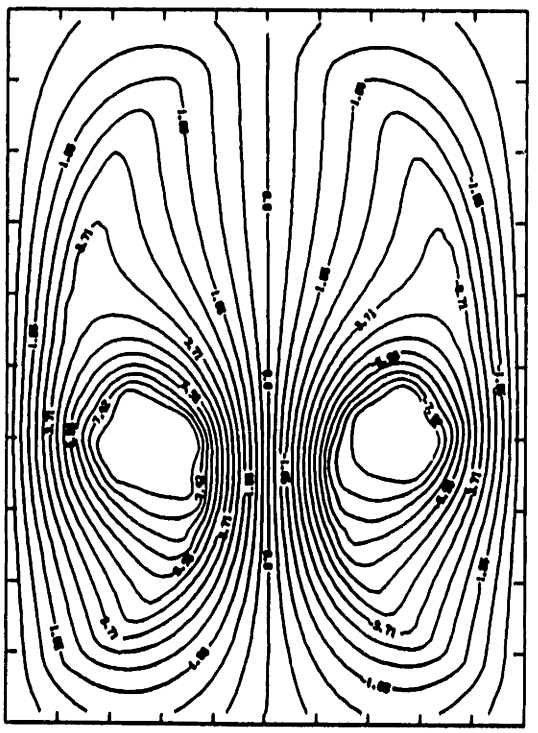

t = 8.6

Figure 44

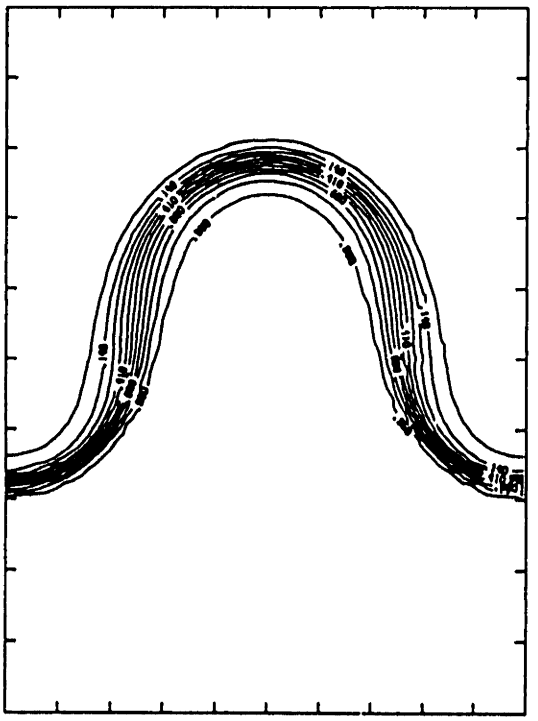

t = 5.0

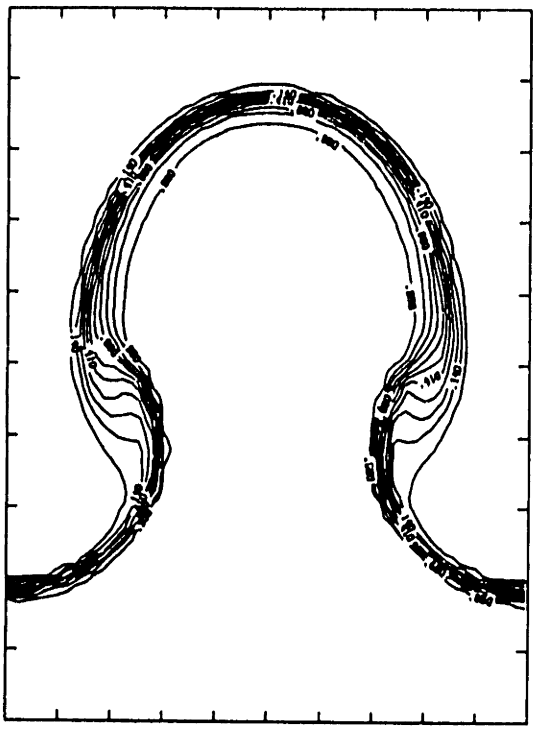

t = 7.0

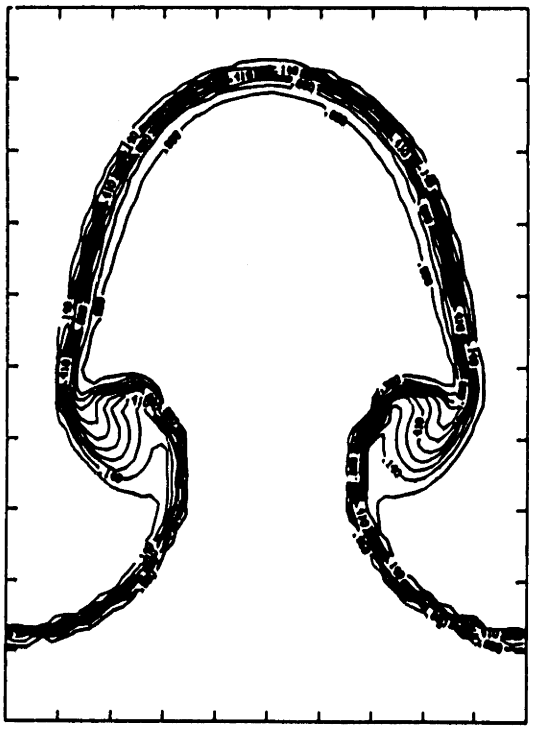

t = 7.85

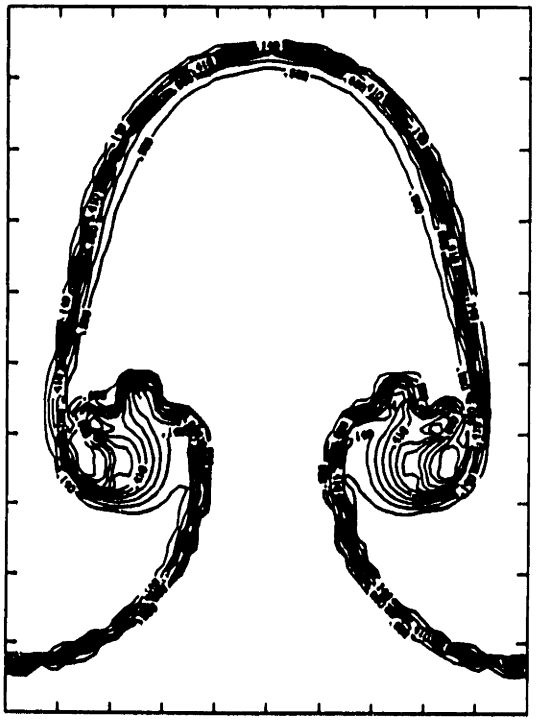

t = 8.6

Figure 45

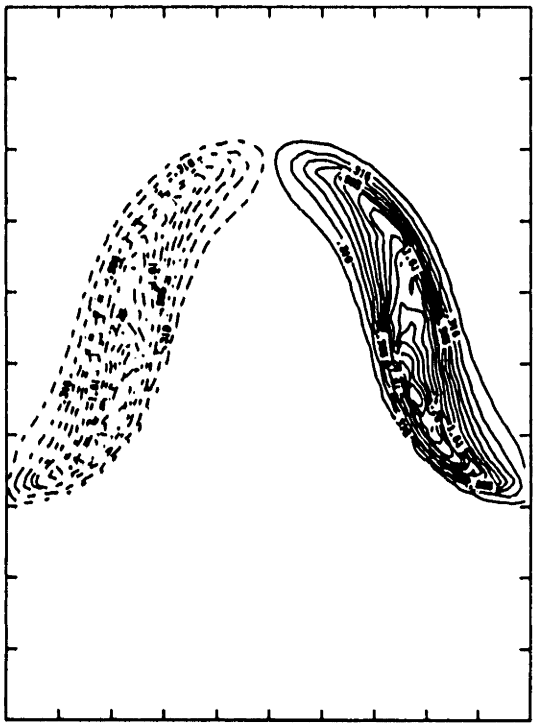

t = 5.0

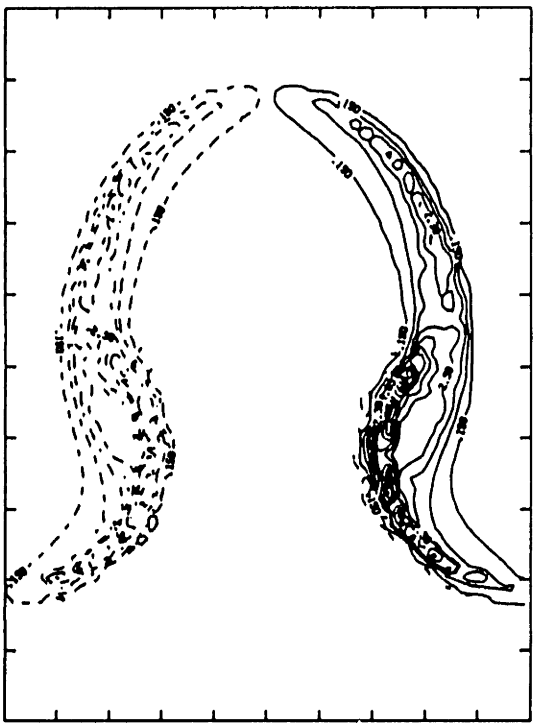

t = 7.0

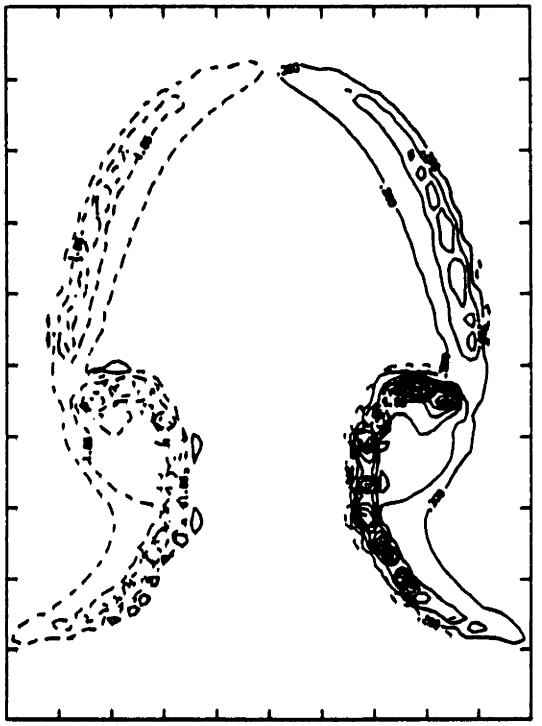

t = 7.85

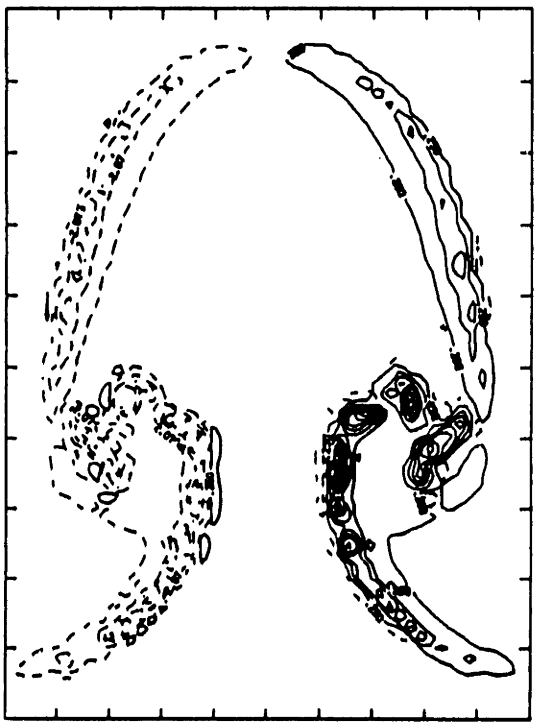

t = 8.6

Figure 46

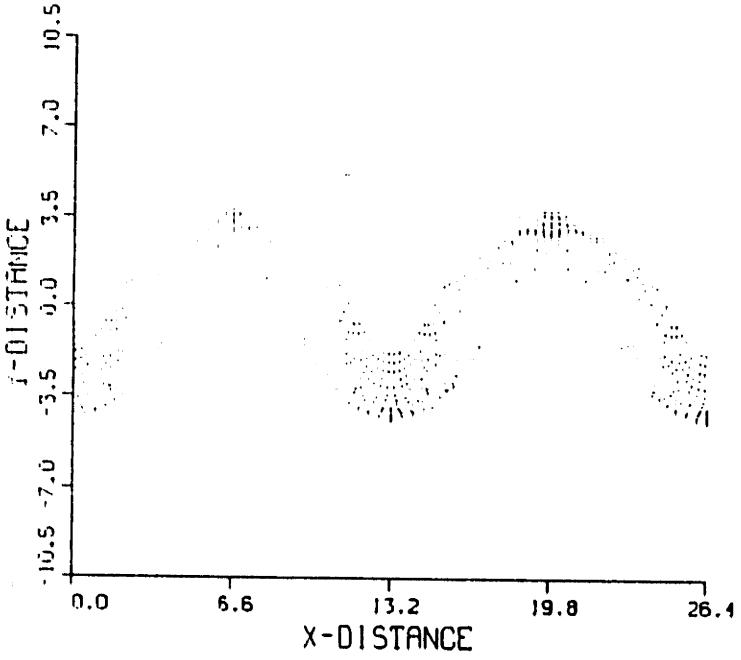

t = 3.0

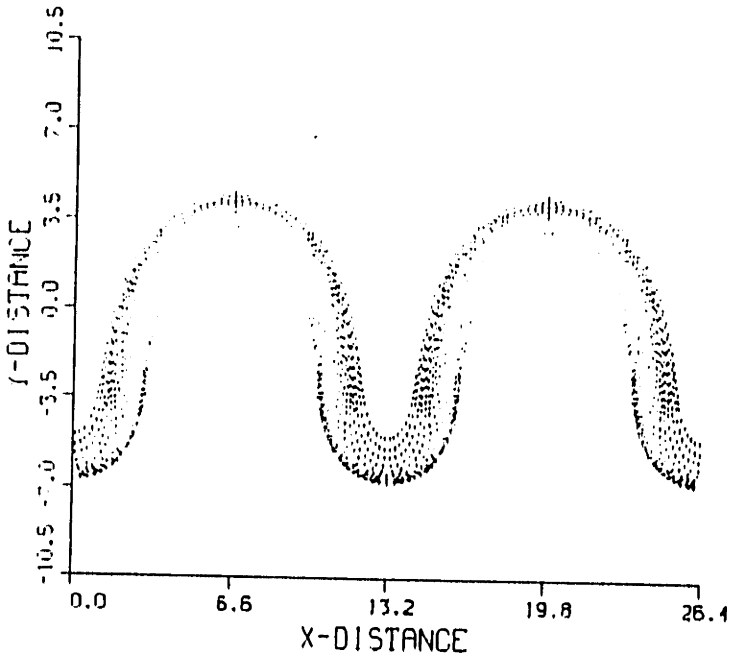

t = 4.25

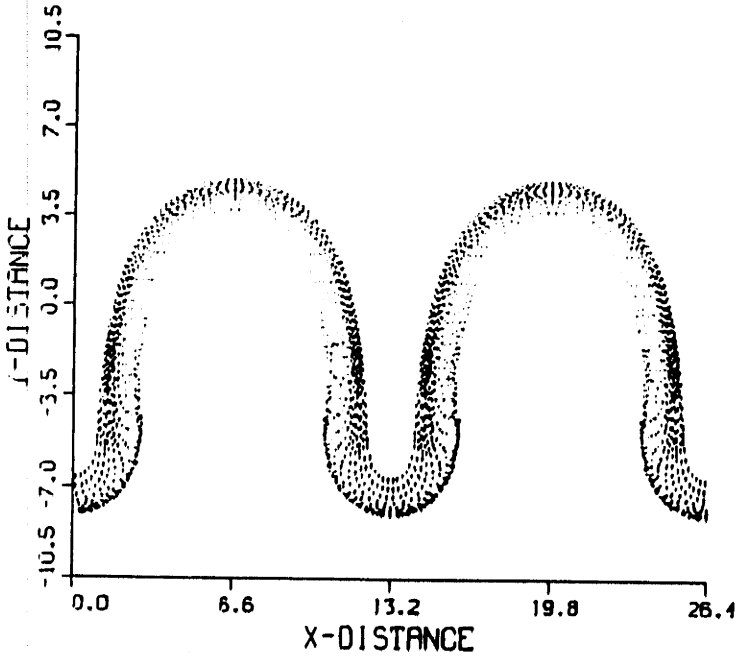

t = 4.75

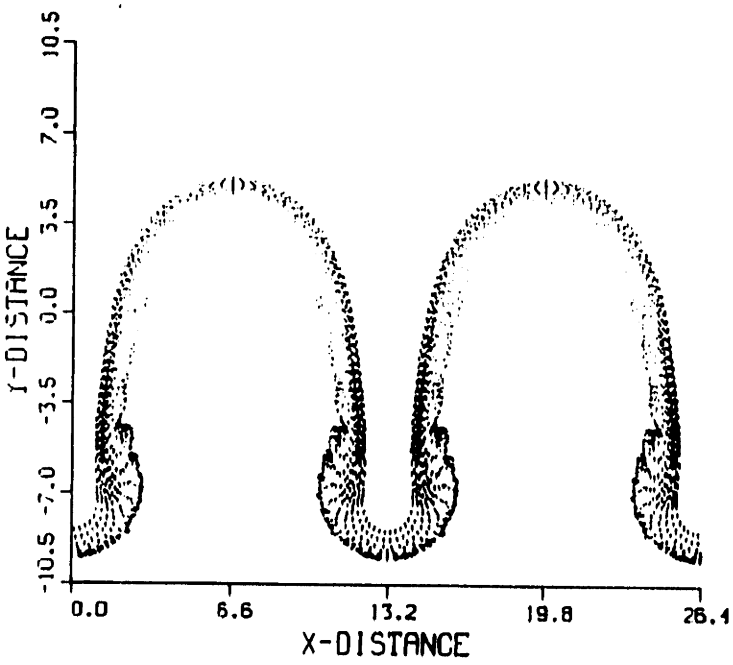

t = 5.25

Figure 47

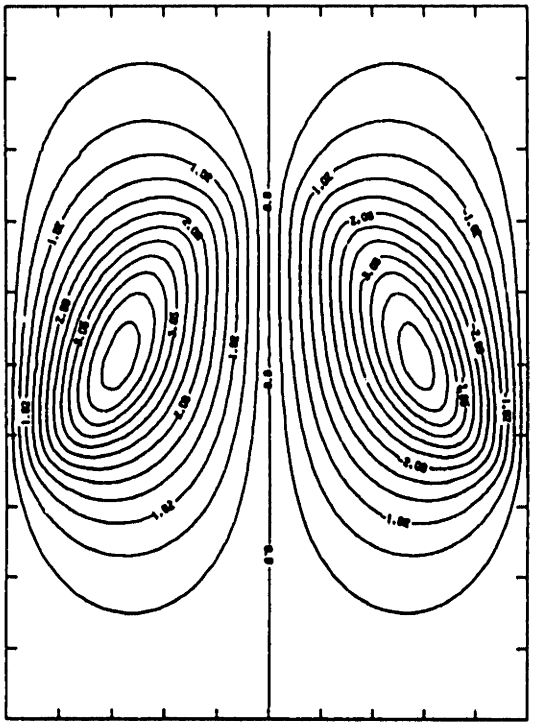

t = 3.0

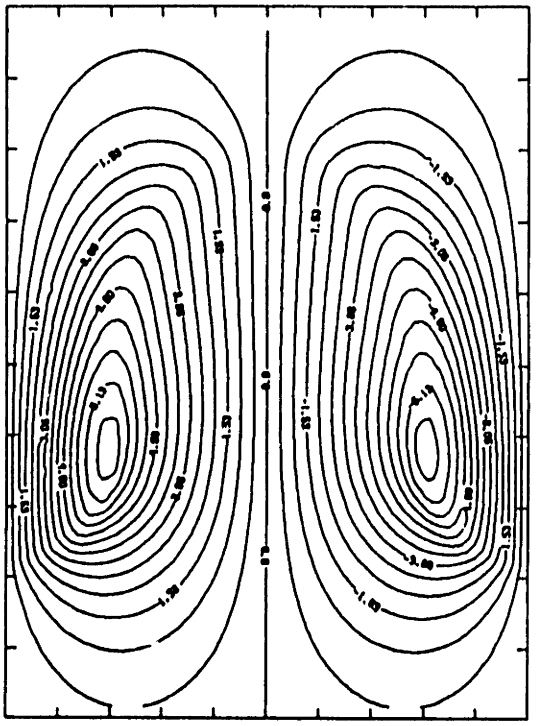

t = 4.25

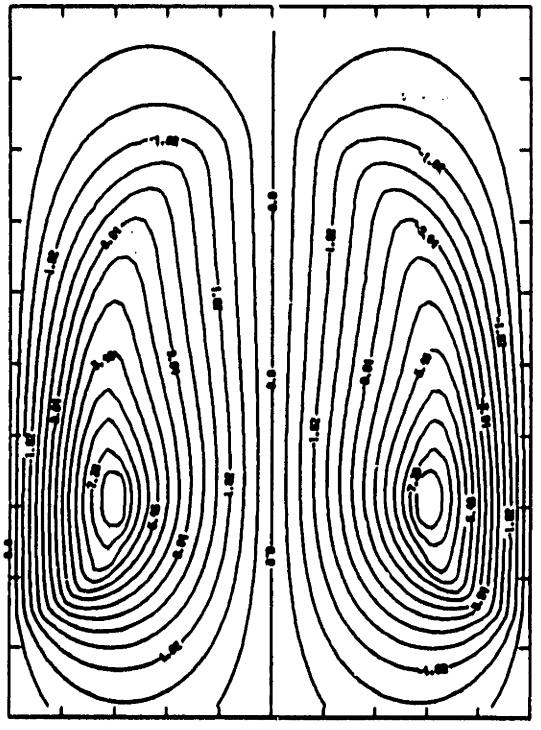

t = 4.75

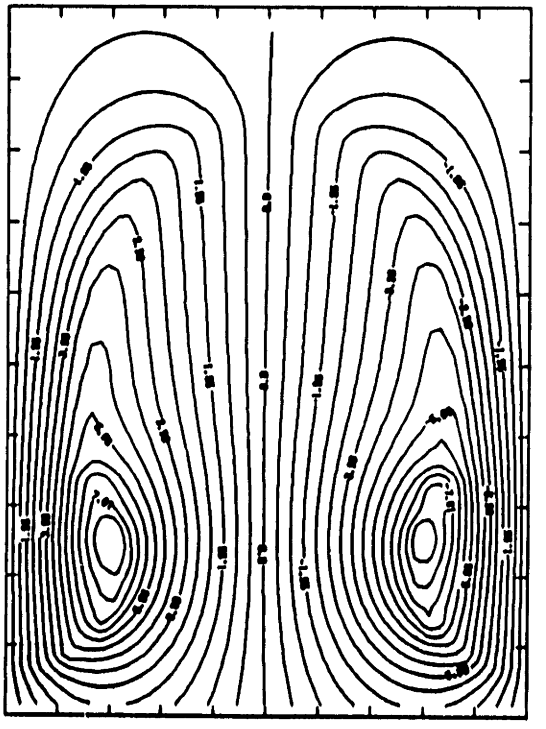

t = 5.25

Figure 48

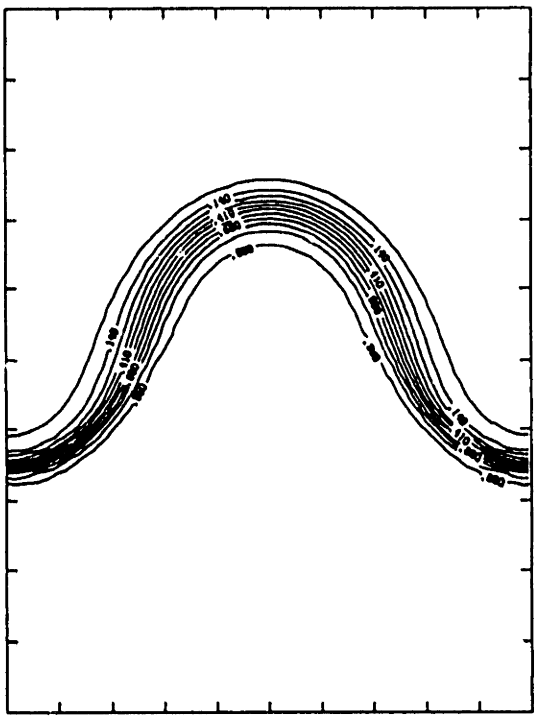

t = 3.0

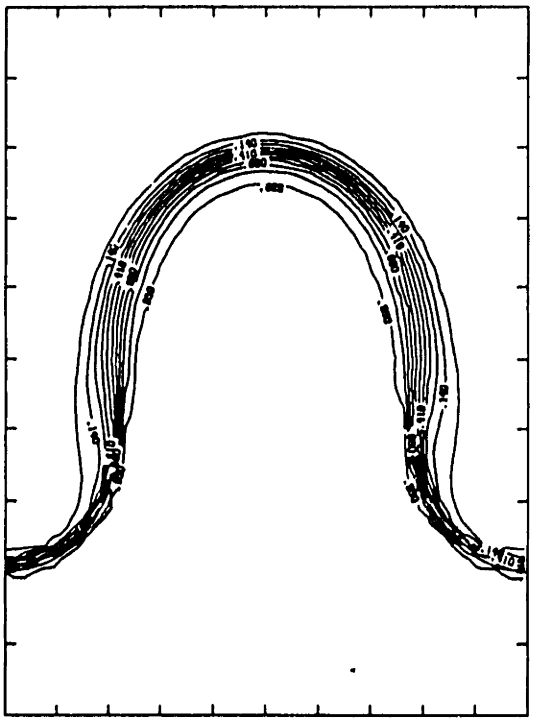

t = 4.25

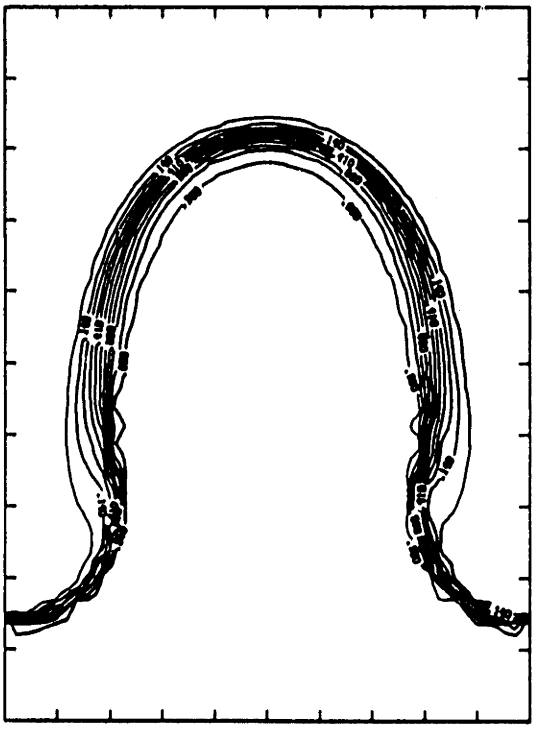

t = 4.75

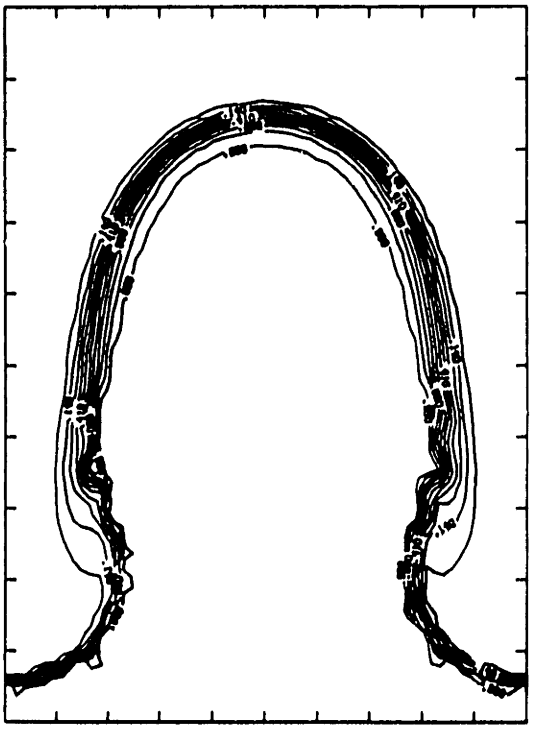

t = 5.25

Figure 49

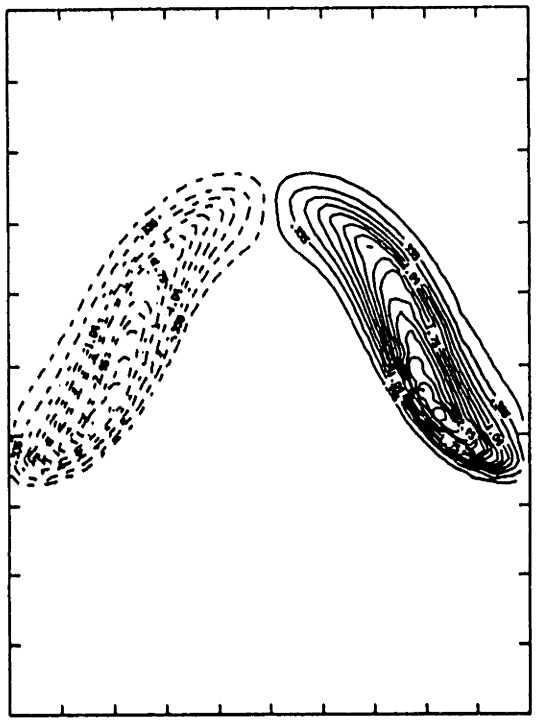

t = 3.0

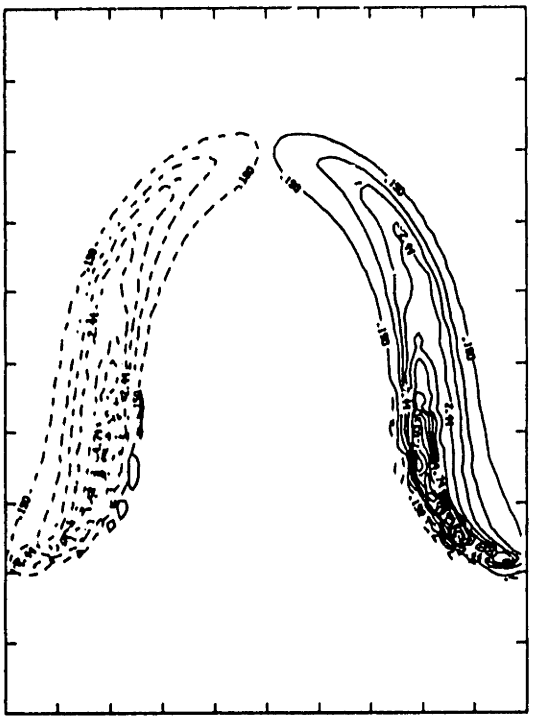

t = 4.25

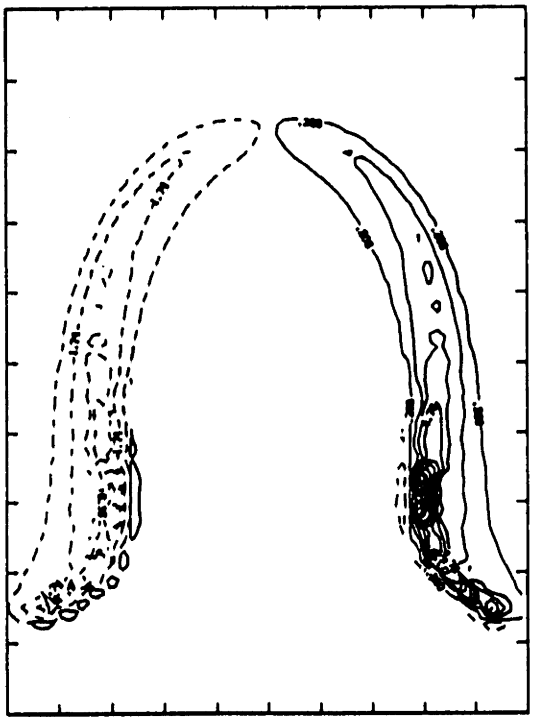

t = 4.75

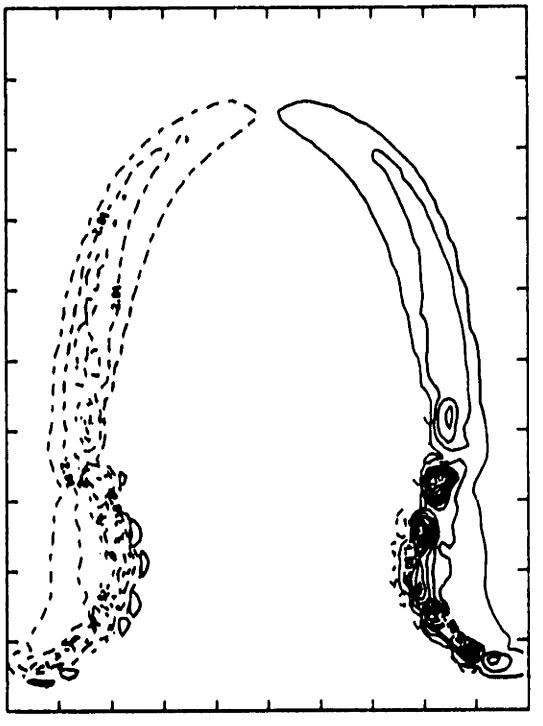

t = 5.25

Figure 50

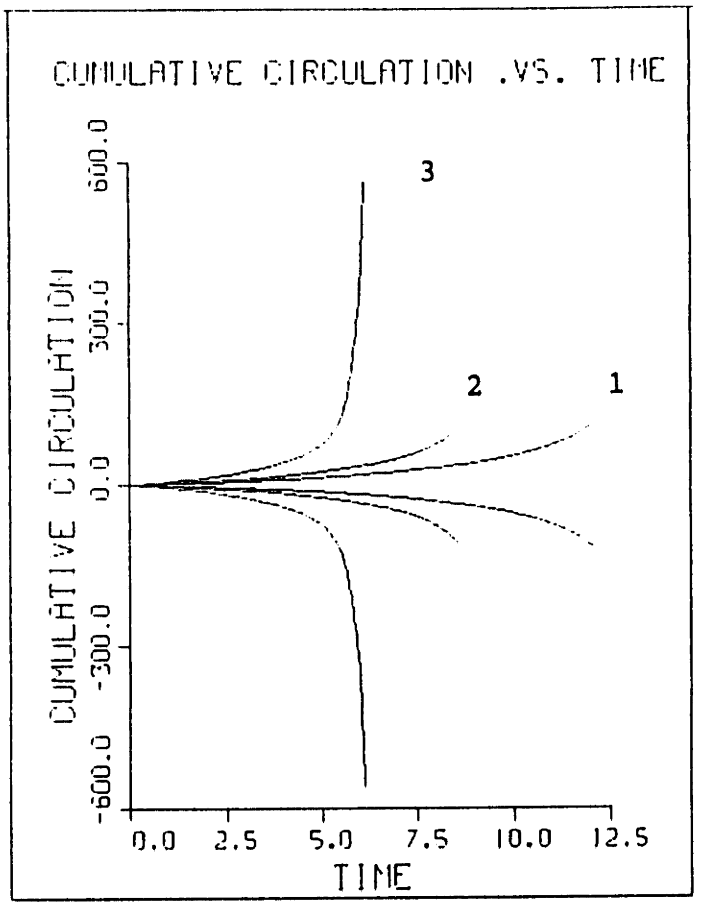

(a)

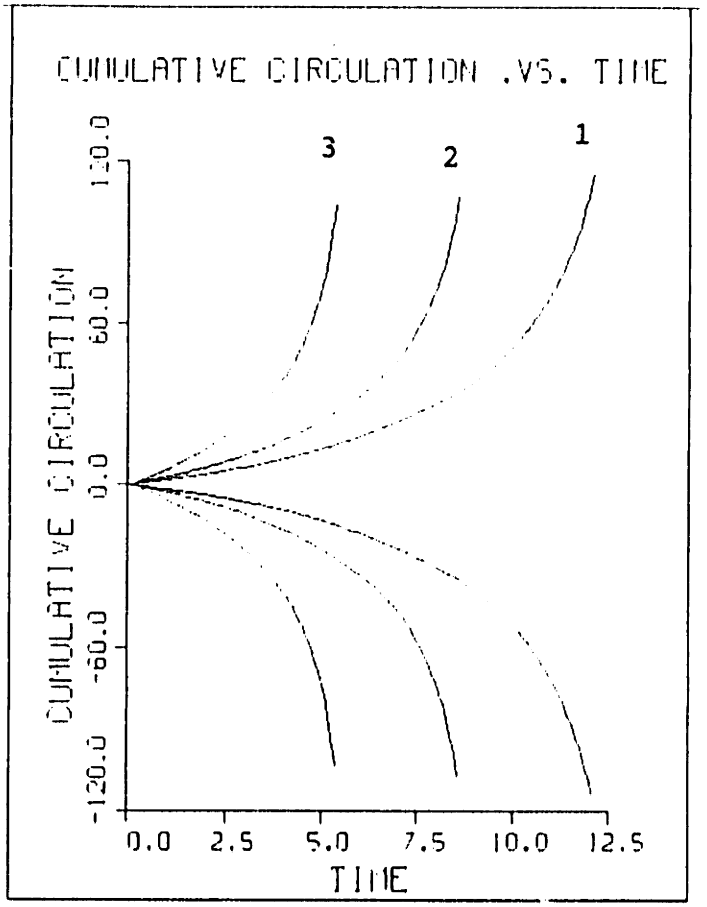

(b)

Figure 51

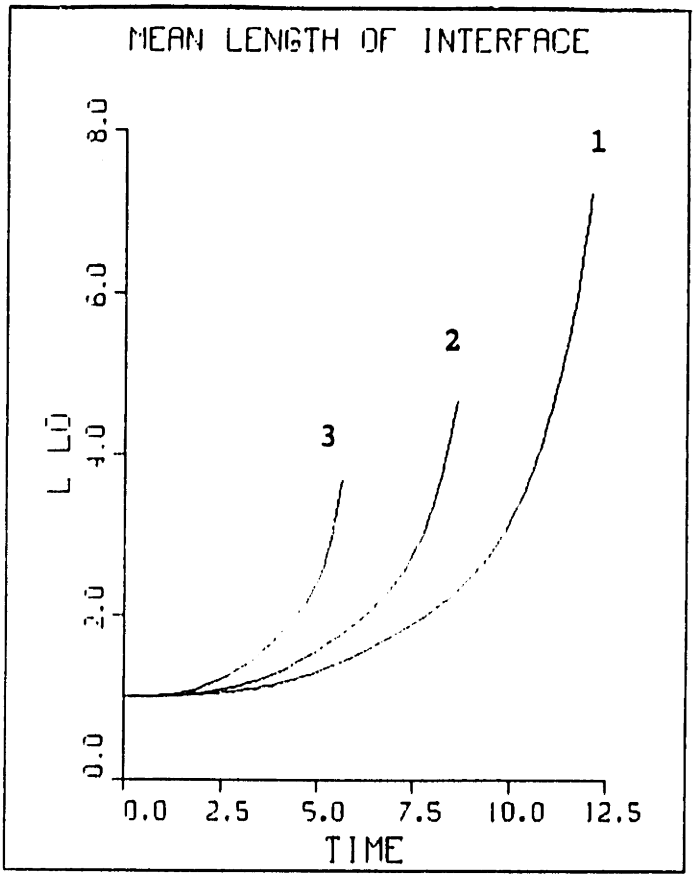

Figure 52

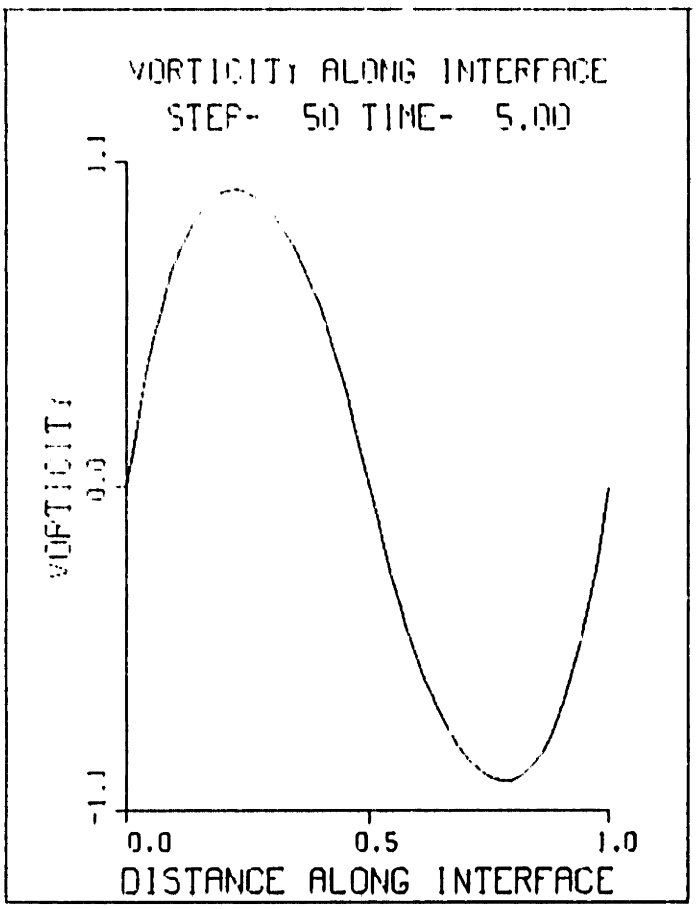
VORTICITY ALONG INTERFACE
STEP- 50 TIME- 5.00
VORTICITY
1.1
0.0
-1.1
0.0
0.5
1.0
DISTANCE ALONG INTERFACE

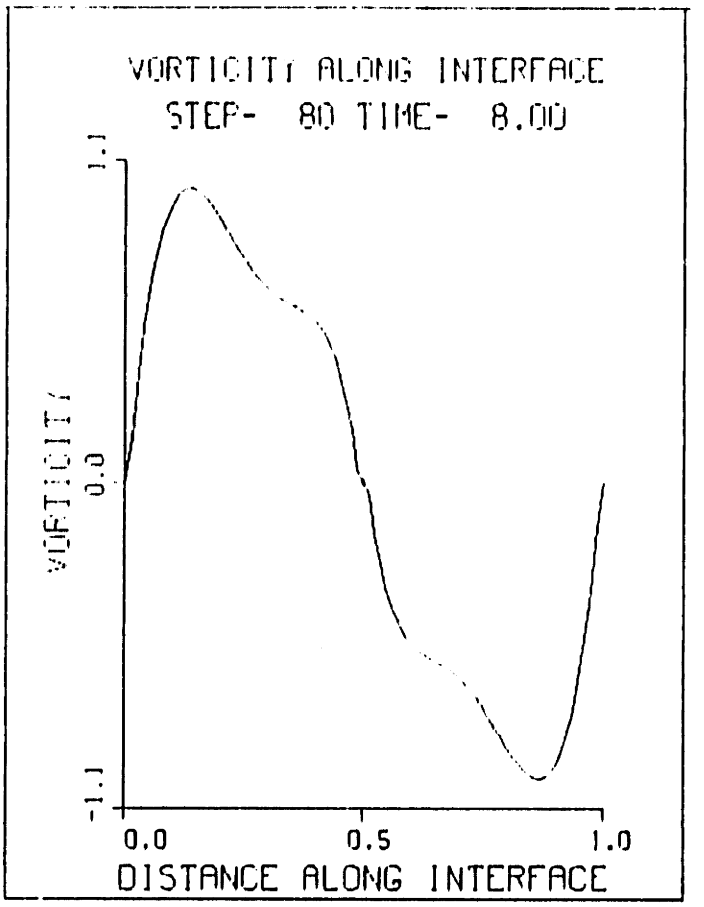
VORTICITY ALONG INTERFACE
STEP- 80 TIME- 8.00
VORTICITY
1.1
0.0
-1.1
0.0
0.5
1.0
DISTANCE ALONG INTERFACE

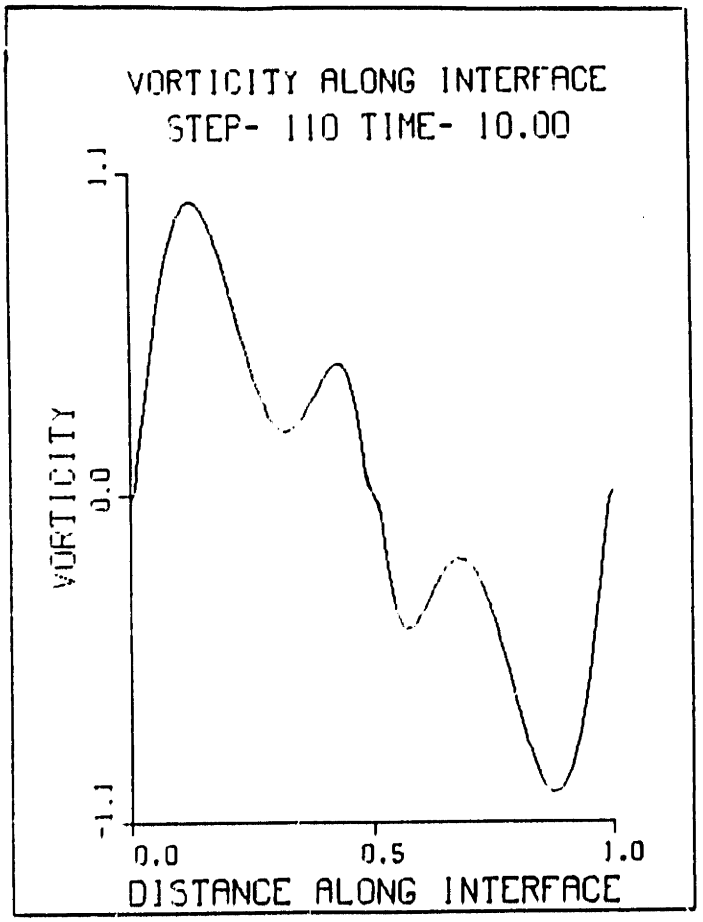
VORTICITY ALONG INTERFACE
STEP- 110 TIME- 10.00
VORTICITY
1.1
0.0
-1.1
0.0
0.5
1.0
DISTANCE ALONG INTERFACE

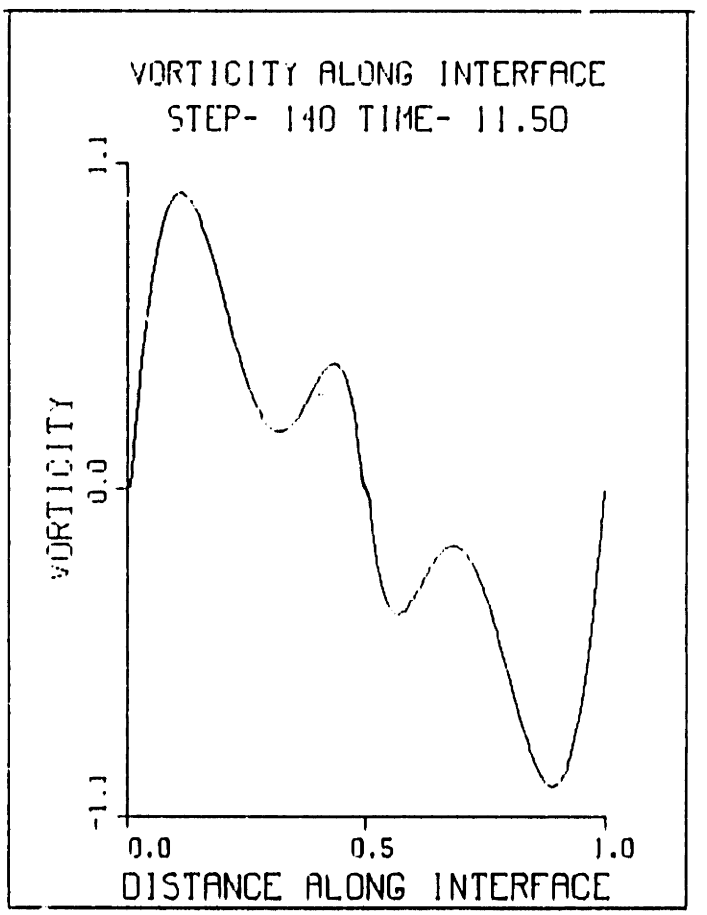
VORTICITY ALONG INTERFACE
STEP- 140 TIME- 11.50
VORTICITY
1.1
0.0
-1.1
0.0
0.5
1.0
DISTANCE ALONG INTERFACE

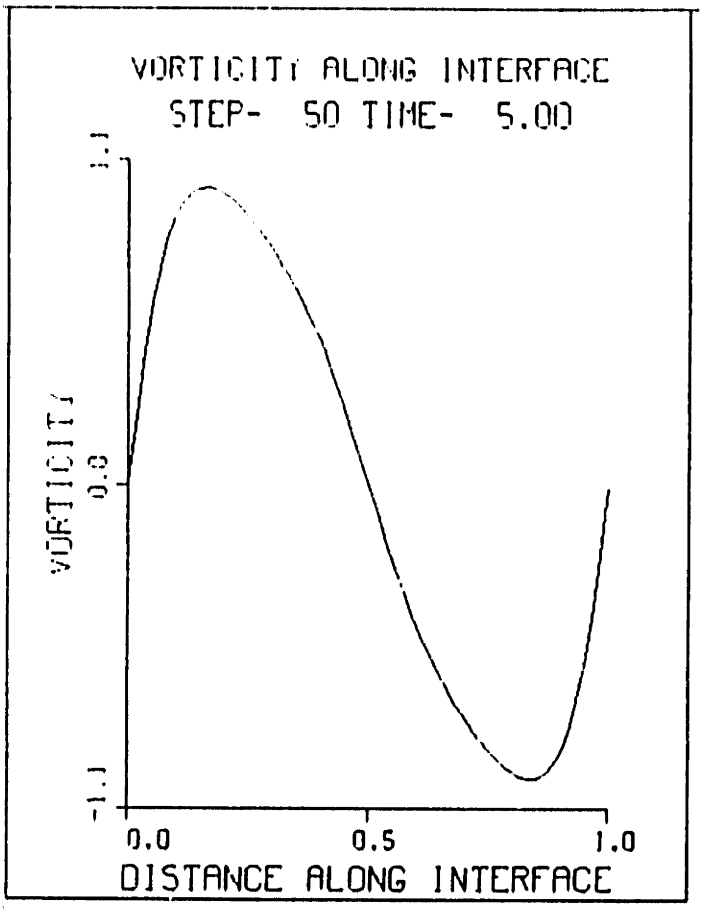
VORTICITY ALONG INTERFACE
STEP- 50 TIME- 5.00
VORTICITY
1.1
0.0
-1.1
0.0
0.5
1.0
DISTANCE ALONG INTERFACE

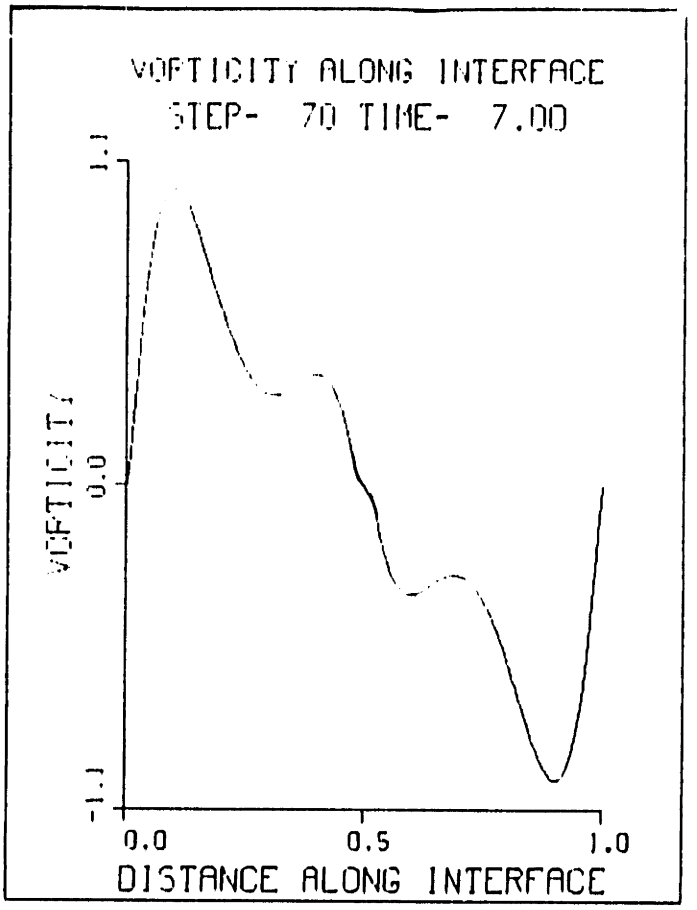
VORTICITY ALONG INTERFACE
STEP- 70 TIME- 7.00
VORTICITY
1.1
0.0
-1.1
0.0
0.5
1.0
DISTANCE ALONG INTERFACE

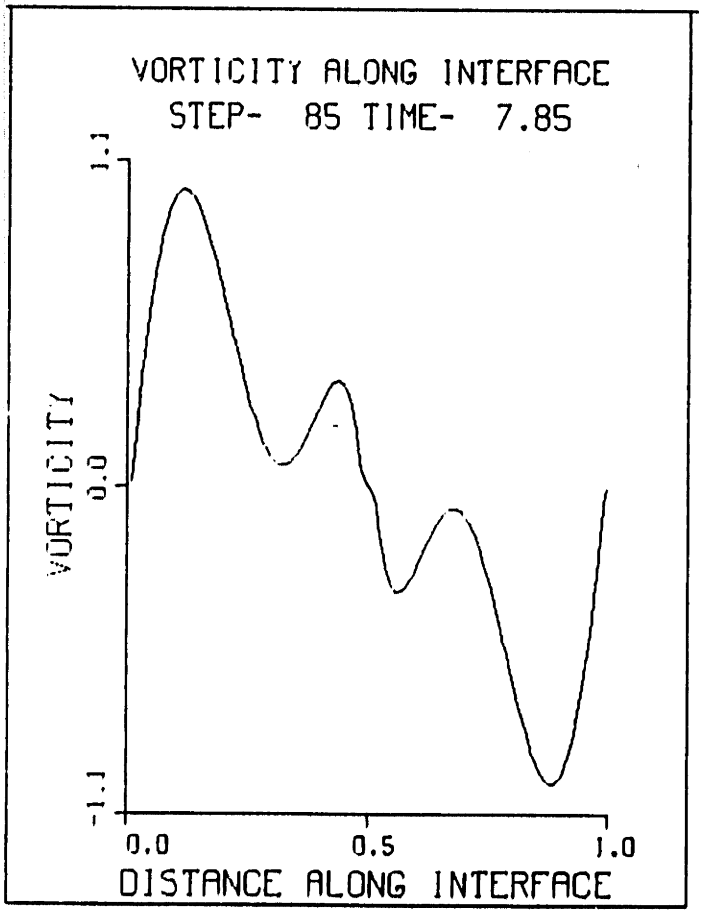
VORTICITY ALONG INTERFACE
STEP- 85 TIME- 7.85
VORTICITY
1.1
0.0
-1.1
0.0
0.5
1.0
DISTANCE ALONG INTERFACE

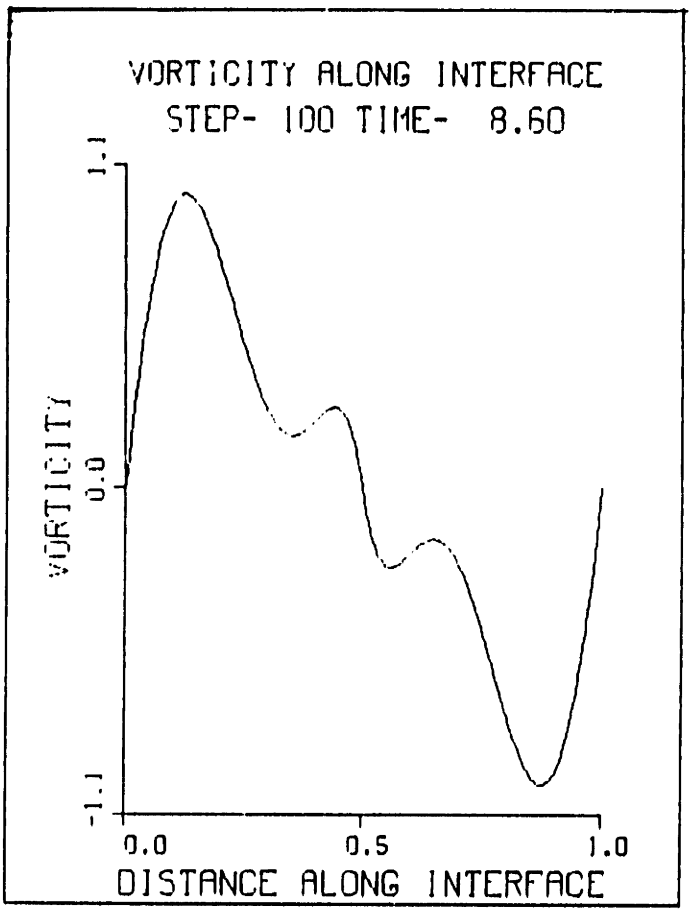
VORTICITY ALONG INTERFACE
STEP- 100 TIME- 8.60
VORTICITY
1.1
0.0
-1.1
0.0
0.5
1.0
DISTANCE ALONG INTERFACE

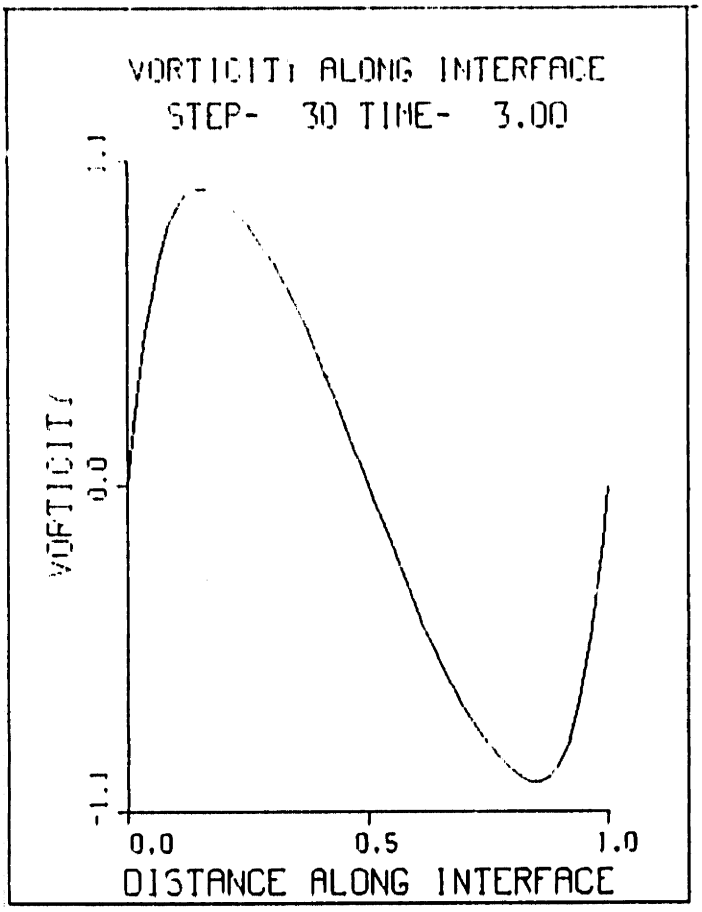
VORTICITY ALONG INTERFACE
STEP- 30 TIME- 3.00
VORTICITY
1.1
0.0
-1.1
0.0
0.5
1.0
DISTANCE ALONG INTERFACE

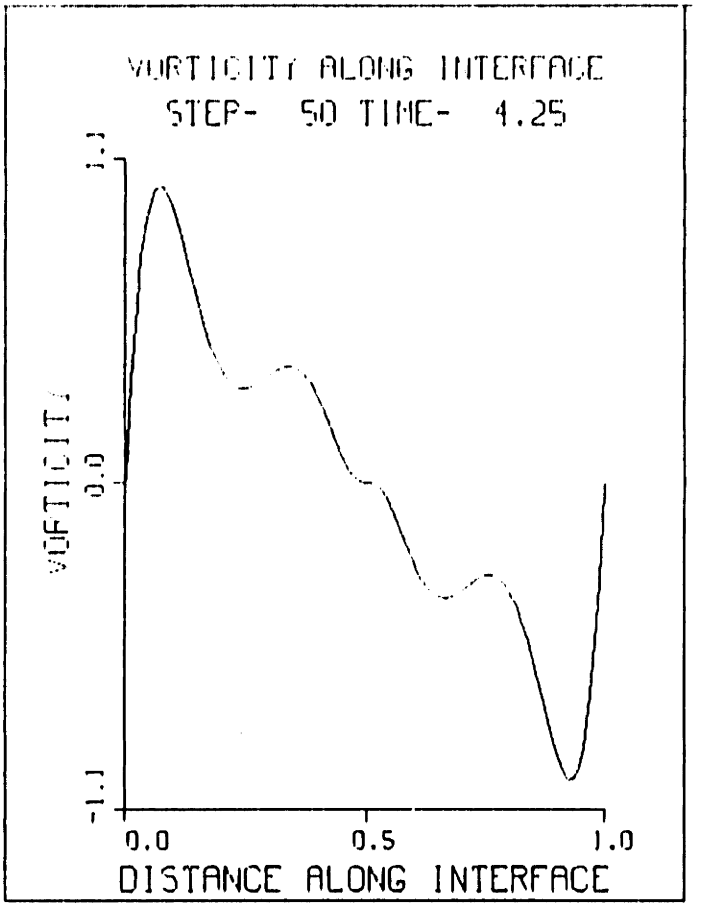
VORTICITY ALONG INTERFACE
STEP- 50 TIME- 4.25
VORTICITY
1.1
0.0
-1.1
0.0
0.5
1.0
DISTANCE ALONG INTERFACE

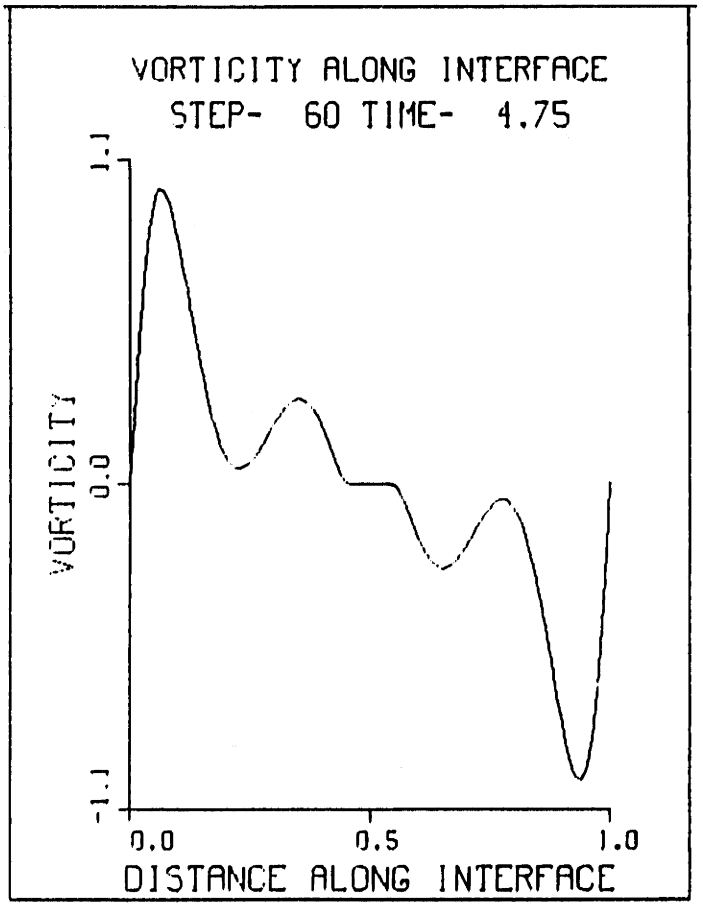
VORTICITY ALONG INTERFACE
STEP- 60 TIME- 4.75
VORTICITY
1.1
0.0
-1.1
0.0
0.5
1.0
DISTANCE ALONG INTERFACE

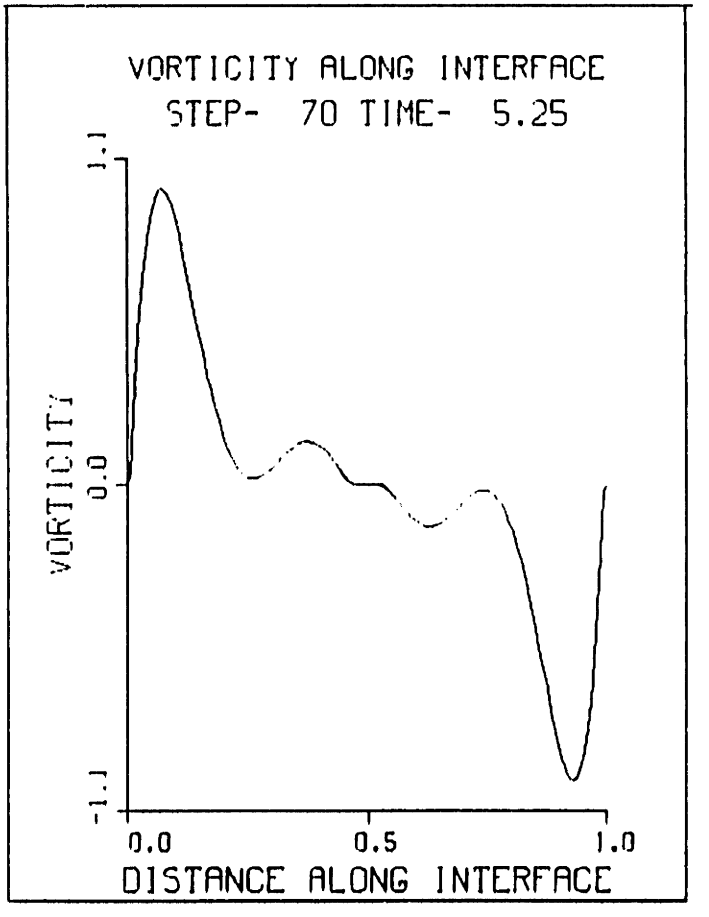
VORTICITY ALONG INTERFACE
STEP- 70 TIME- 5.25
VORTICITY
1.1
0.0
-1.1
0.0
0.5
1.0
DISTANCE ALONG INTERFACE

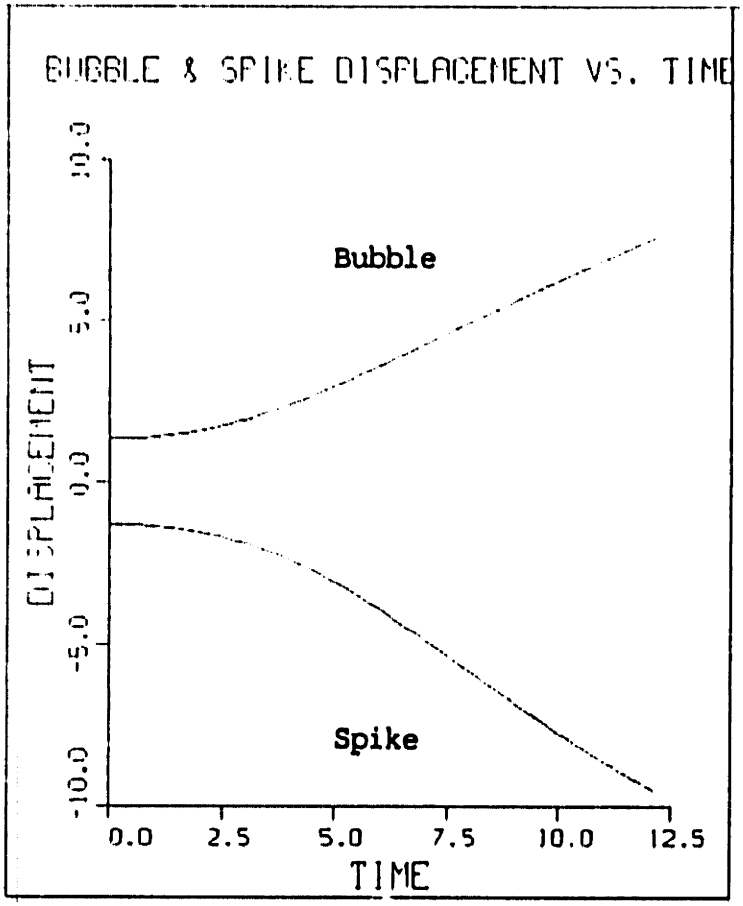
BUBBLE & SPIKE DISPLACEMENT VS. TIME
DISPLACEMENT
10.0
5.0
0.0
-5.0
-10.0
Bubble
Spike
0.0
2.5
5.0
7.5
10.0
12.5
TIME

(a)

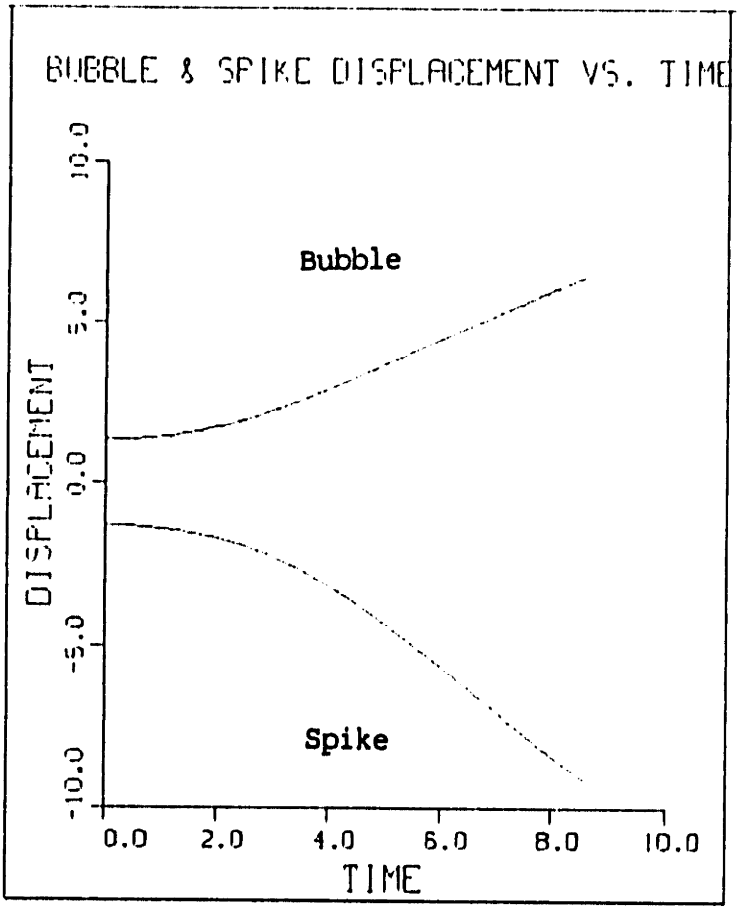
BUBBLE & SPIKE DISPLACEMENT VS. TIME
DISPLACEMENT
10.0
5.0
0.0
-5.0
-10.0
Bubble
Spike
0.0
2.0
4.0
6.0
8.0
10.0
TIME

(b)

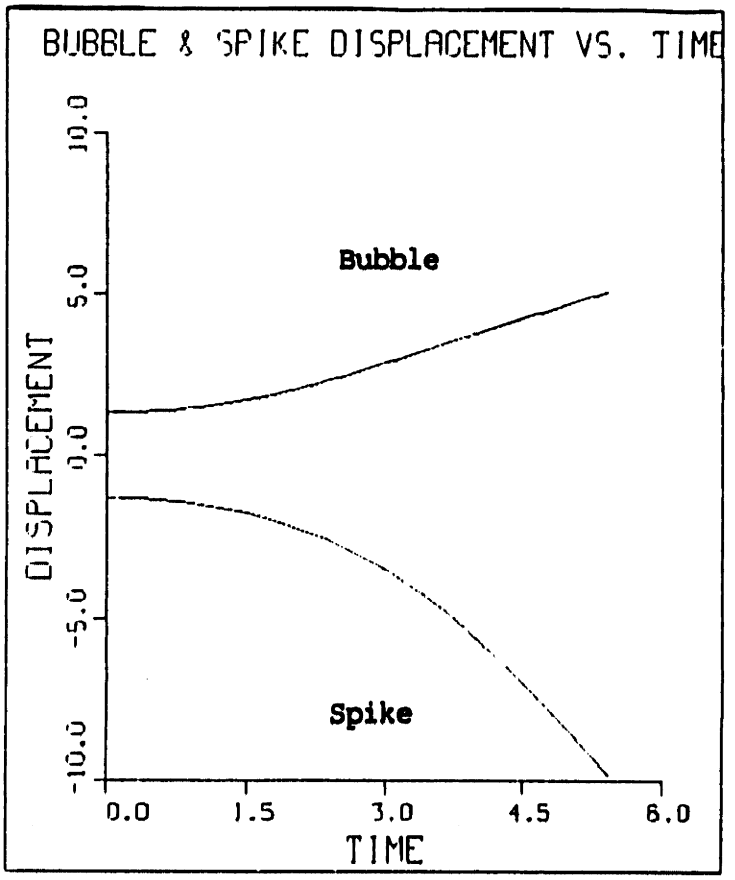
BUBBLE & SPIKE DISPLACEMENT VS. TIME
DISPLACEMENT
10.0
5.0
0.0
-5.0
-10.0
Bubble
Spike
0.0
1.5
3.0
4.5
6.0
TIME

(c)

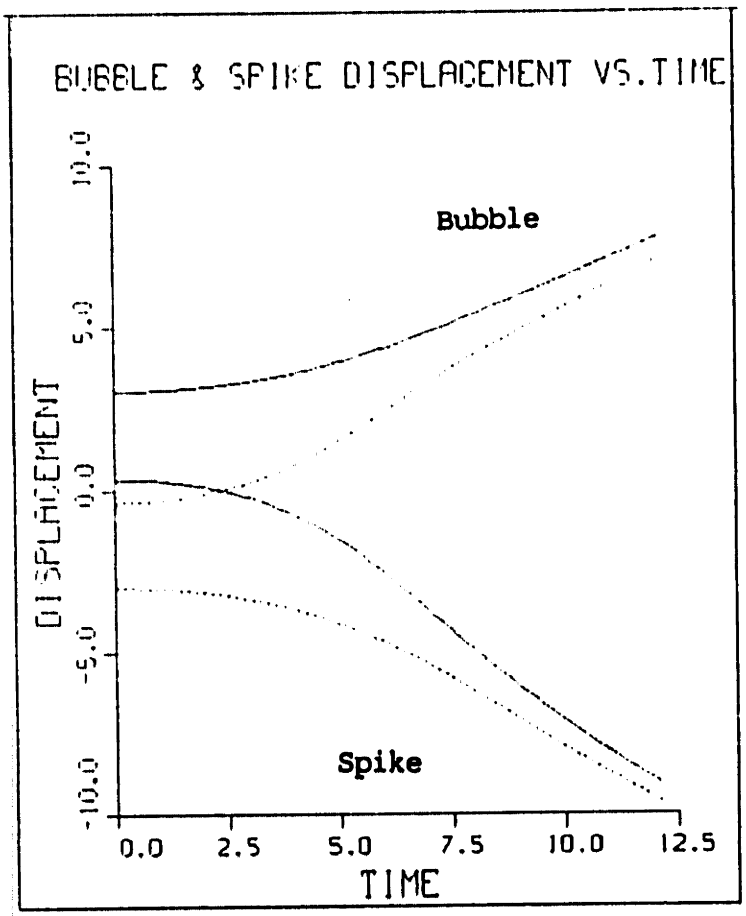
BUBBLE & SPIKE DISPLACEMENT VS.TIME
Bubble
Spike
DISPLACEMENT
TIME
10.0
5.0
0.0
-5.0
-10.0
0.0
2.5
5.0
7.5
10.0
12.5

(a)

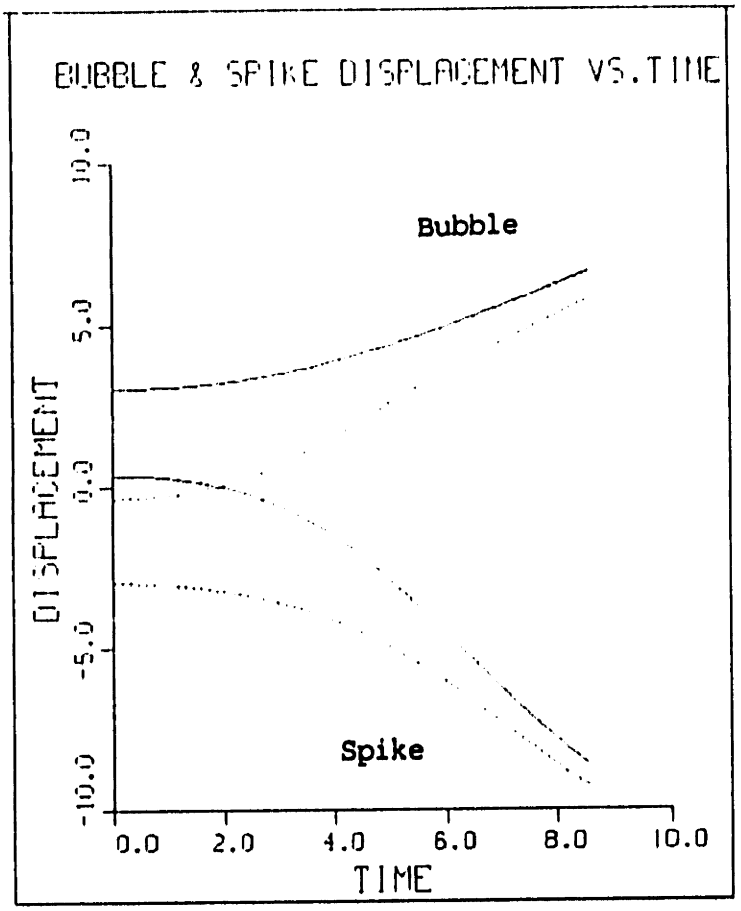
BUBBLE & SPIKE DISPLACEMENT VS.TIME
Bubble
Spike
DISPLACEMENT
TIME
10.0
5.0
0.0
-5.0
-10.0
0.0
2.0
4.0
6.0
8.0
10.0

(b)

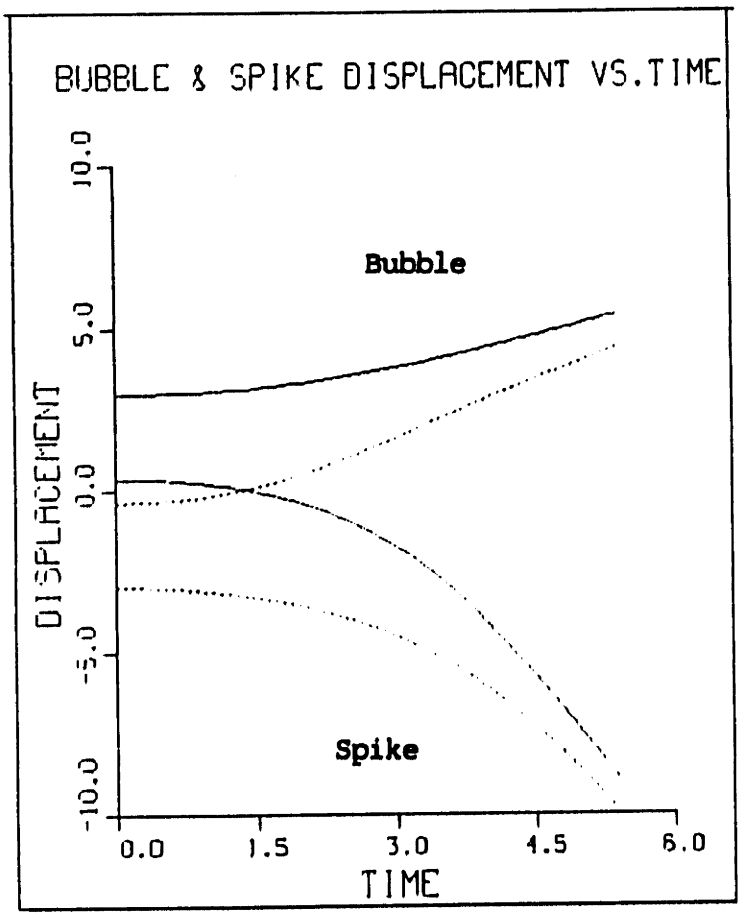
BUBBLE & SPIKE DISPLACEMENT VS.TIME
Bubble
Spike
DISPLACEMENT
TIME
10.0
5.0
0.0
-5.0
-10.0
0.0
1.5
3.0
4.5
6.0

(c)

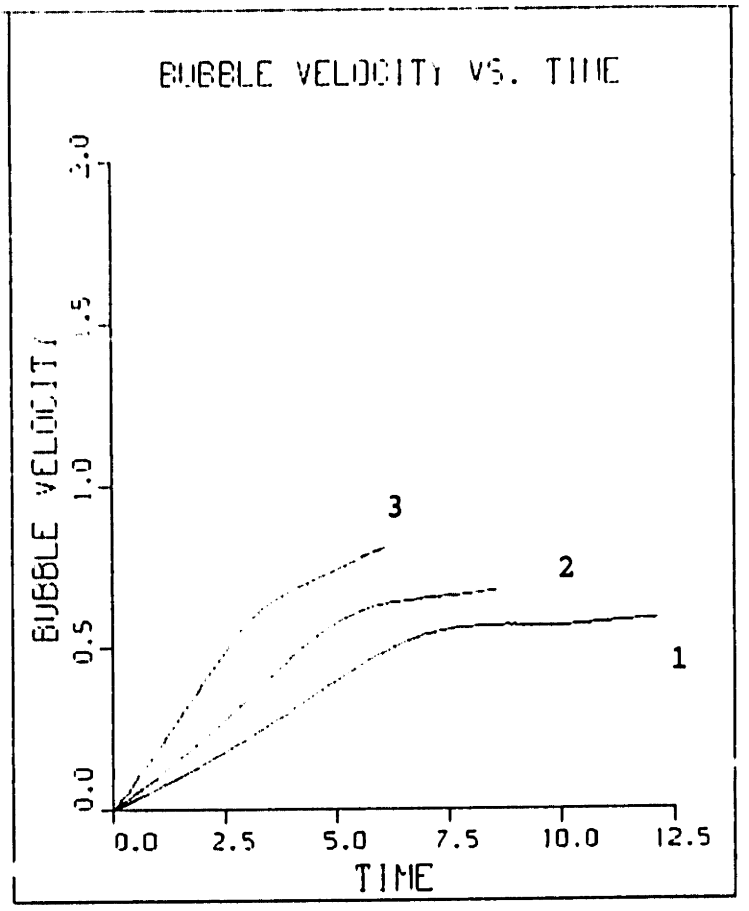
BUBBLE VELOCITY VS. TIME
BUBBLE VELOCITY
0.0
0.5
1.0
1.5
2.0
0.0
2.5
5.0
7.5
10.0
12.5
TIME
1
2
3

(a)

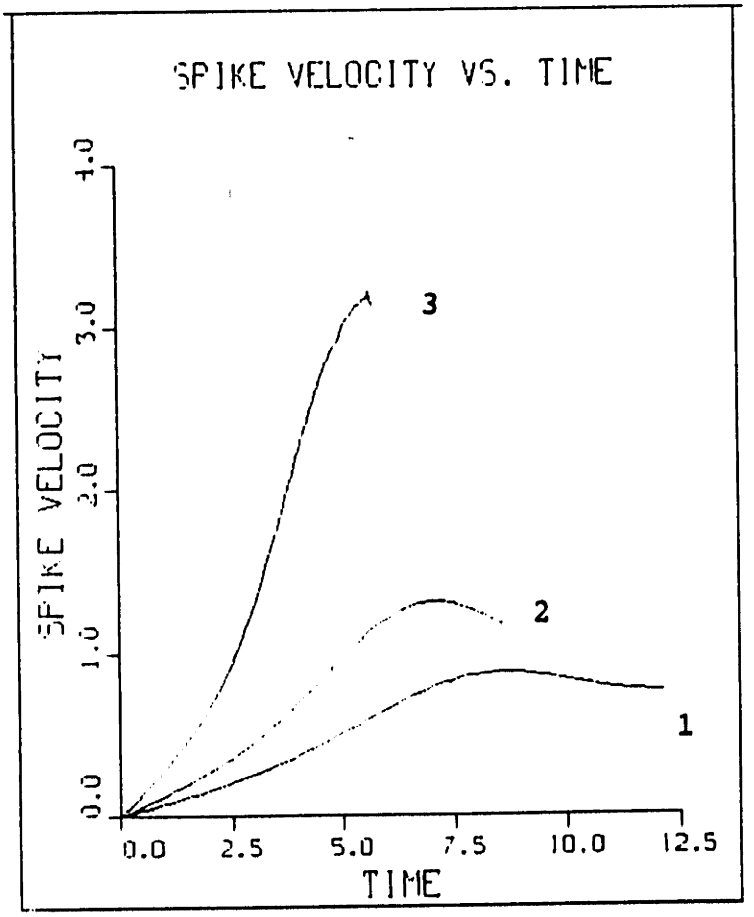
SPIKE VELOCITY VS. TIME
SPIKE VELOCITY
0.0
1.0
2.0
3.0
4.0
0.0
2.5
5.0
7.5
10.0
12.5
TIME
1
2
3

(b)

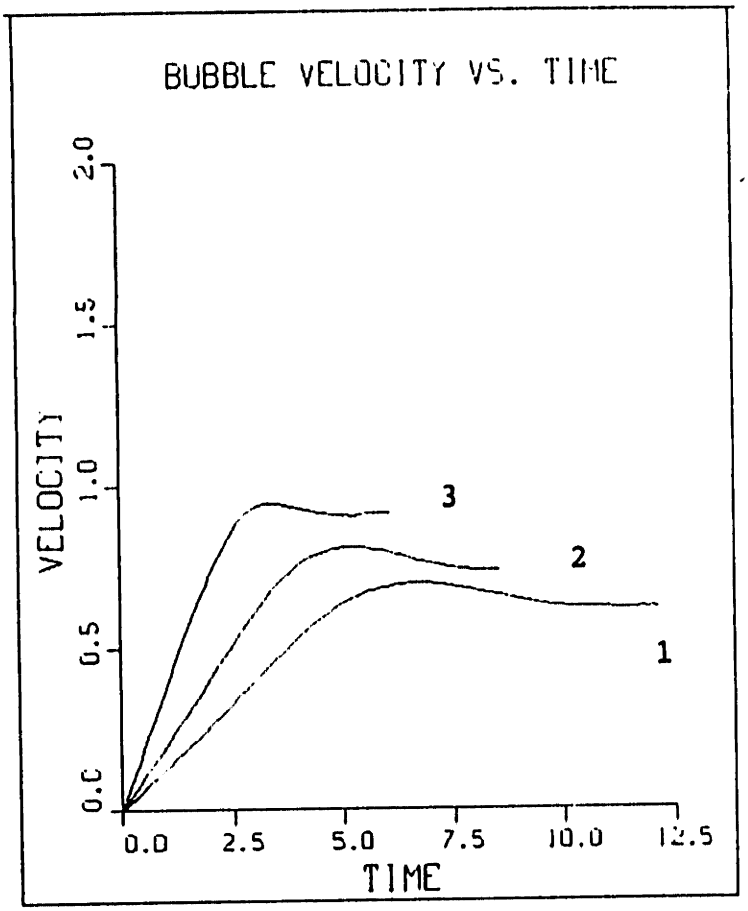
BUBBLE VELOCITY VS. TIME
VELOCITY
0.0
0.5
1.0
1.5
2.0
0.0
2.5
5.0
7.5
10.0
12.5
TIME
1
2
3

(a)

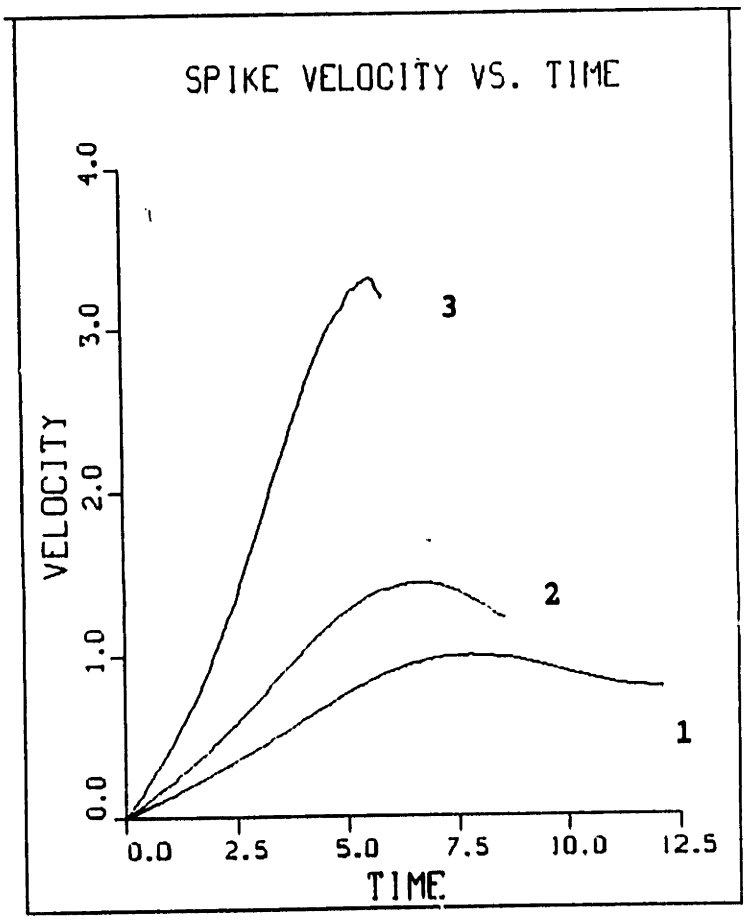
SPIKE VELOCITY VS. TIME
VELOCITY
0.0
1.0
2.0
3.0
4.0
0.0
2.5
5.0
7.5
10.0
12.5
TIME
1
2
3

(b)

Figure 53

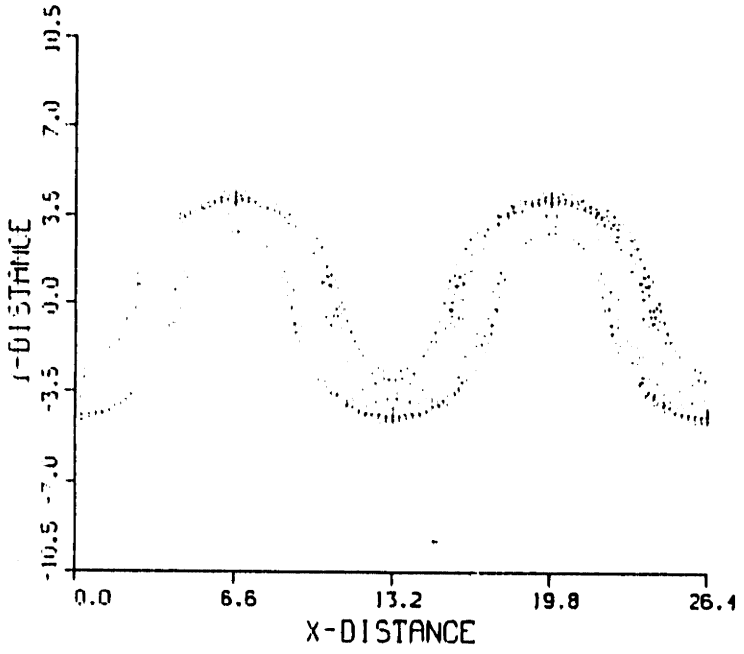

t = 5.0

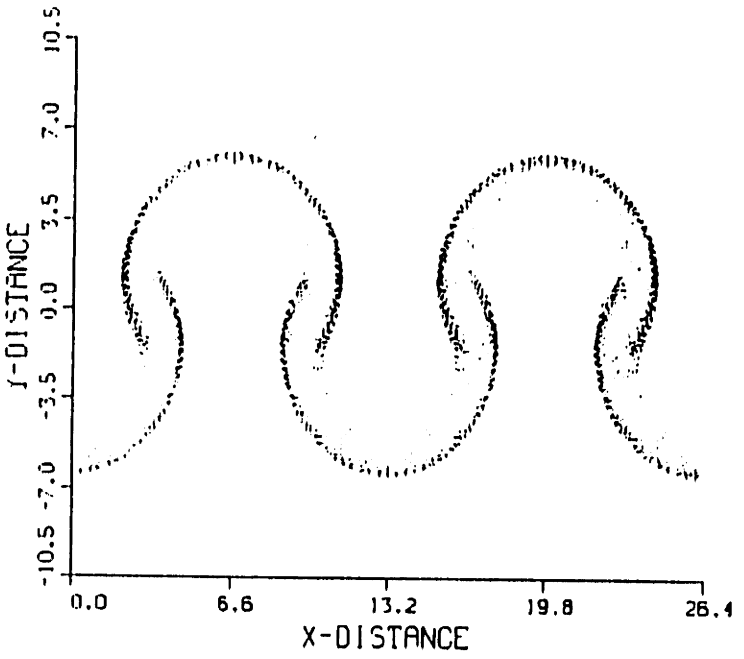

t = 7.0

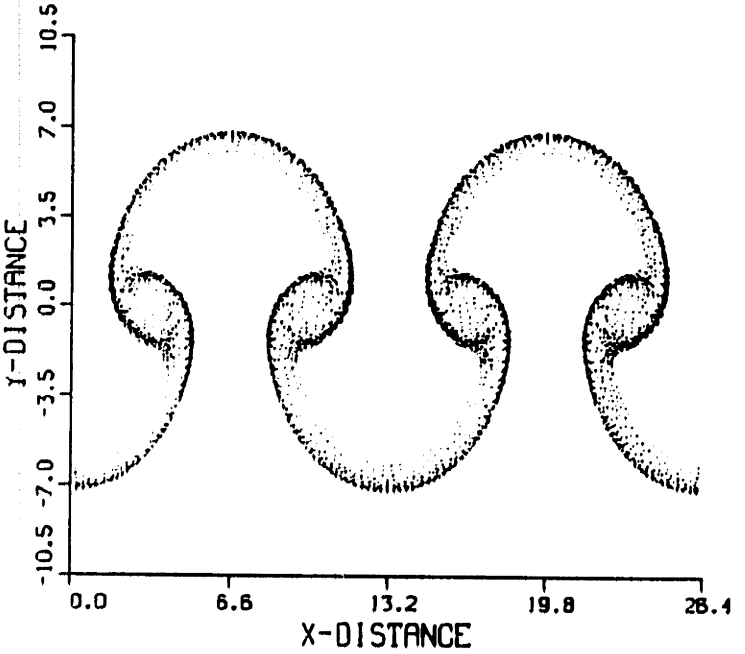

t = 7.85

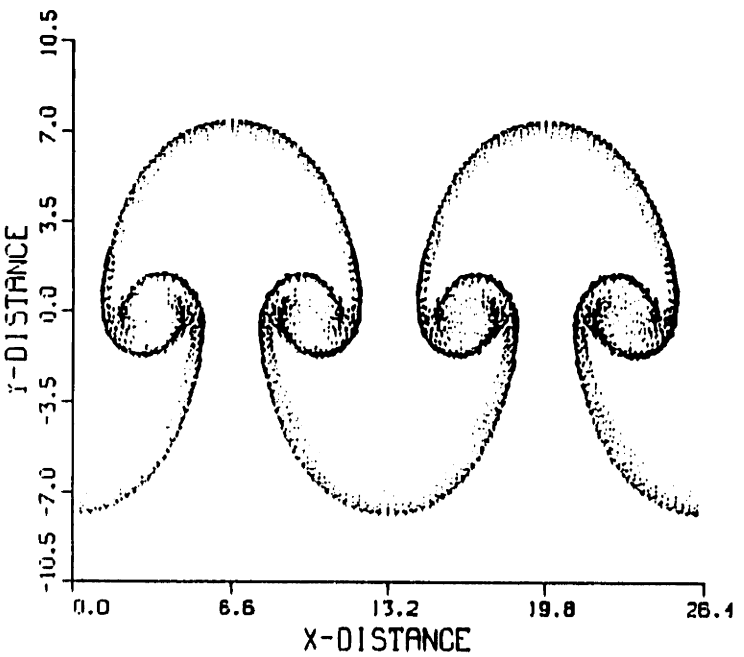

t = 8.6

Figure 60

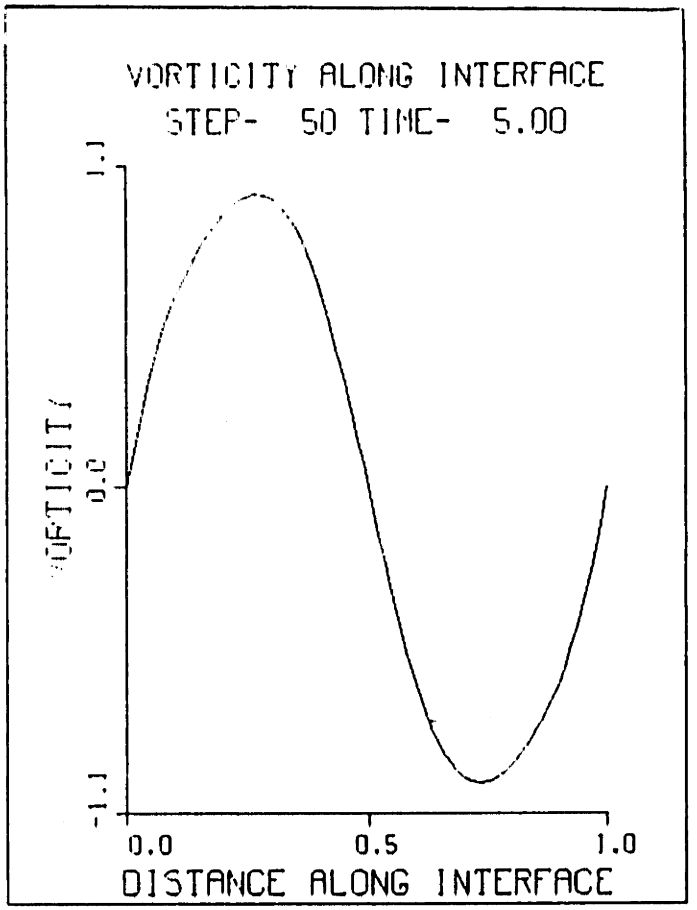
VORTICITY ALONG INTERFACE
STEP- 50 TIME- 5.00
VORTICITY
1.1
0.0
-1.1
0.0
0.5
1.0
DISTANCE ALONG INTERFACE

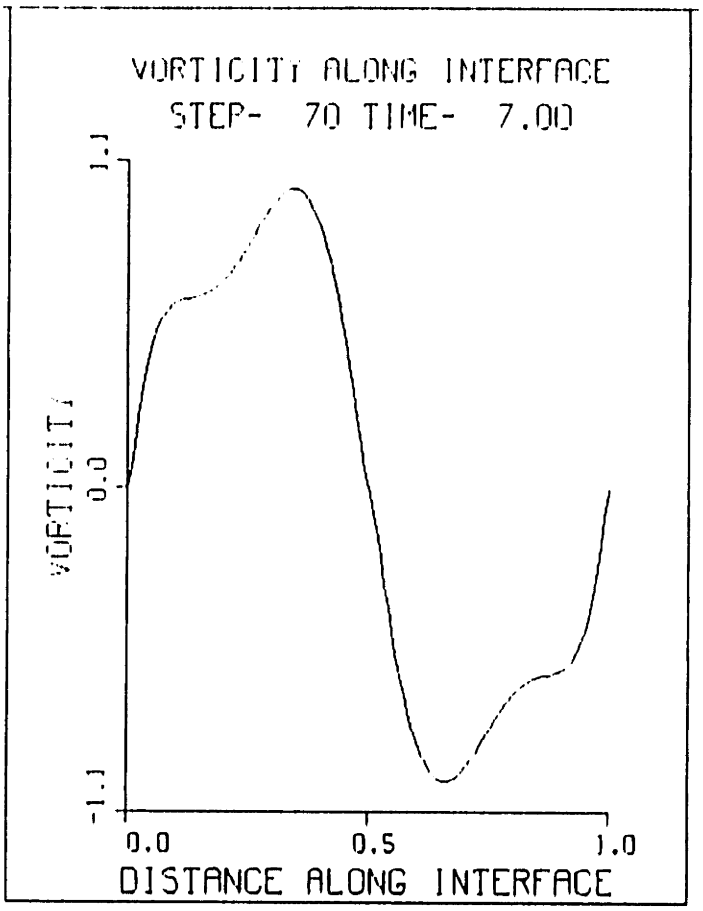
VORTICITY ALONG INTERFACE
STEP- 70 TIME- 7.00
VORTICITY
1.1
0.0
-1.1
0.0
0.5
1.0
DISTANCE ALONG INTERFACE

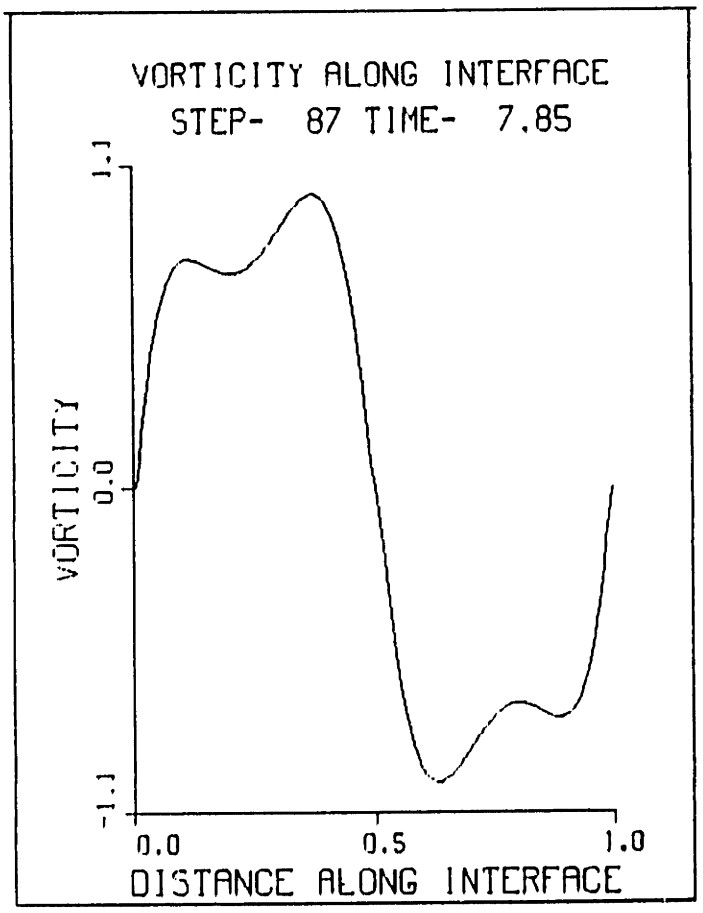
VORTICITY ALONG INTERFACE
STEP- 87 TIME- 7.85
VORTICITY
1.1
0.0
-1.1
0.0
0.5
1.0
DISTANCE ALONG INTERFACE

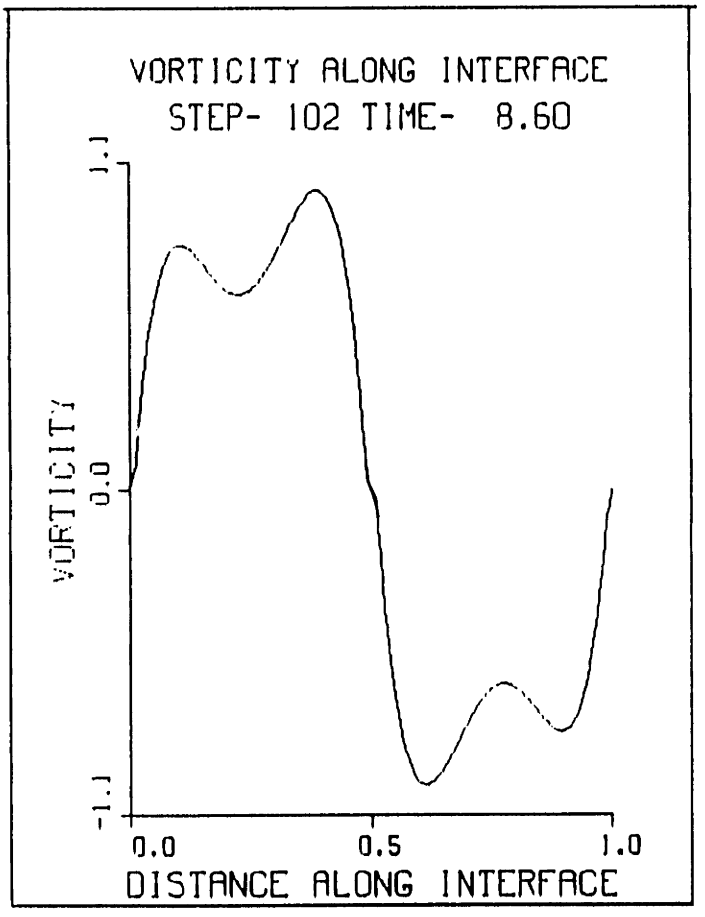
VORTICITY ALONG INTERFACE
STEP- 102 TIME- 8.60
VORTICITY
1.1
0.0
-1.1
0.0
0.5
1.0
DISTANCE ALONG INTERFACE

Figure 61

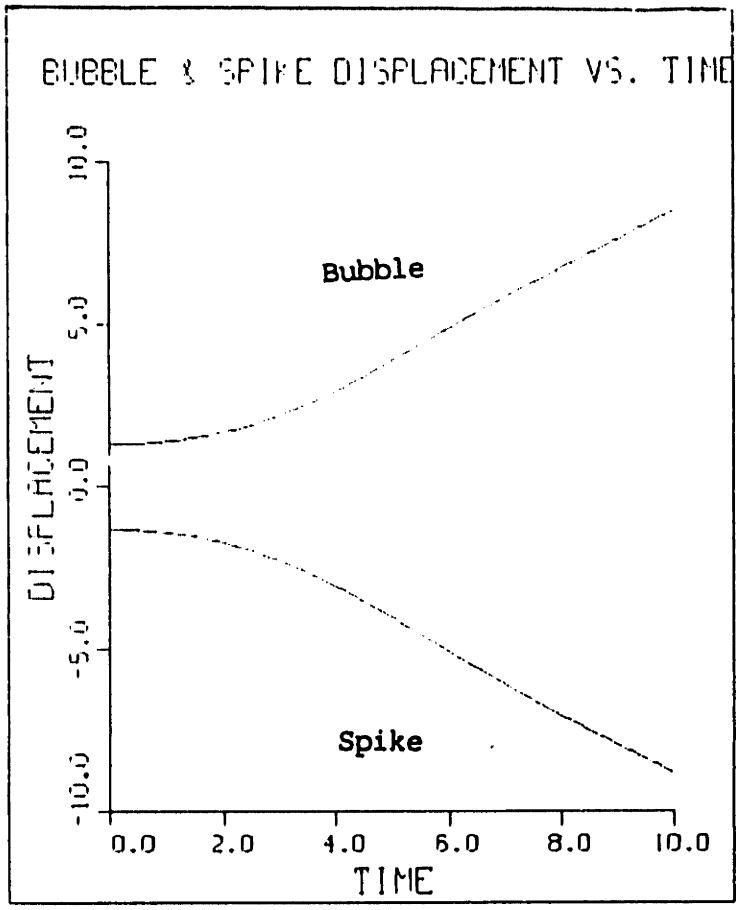

(a)

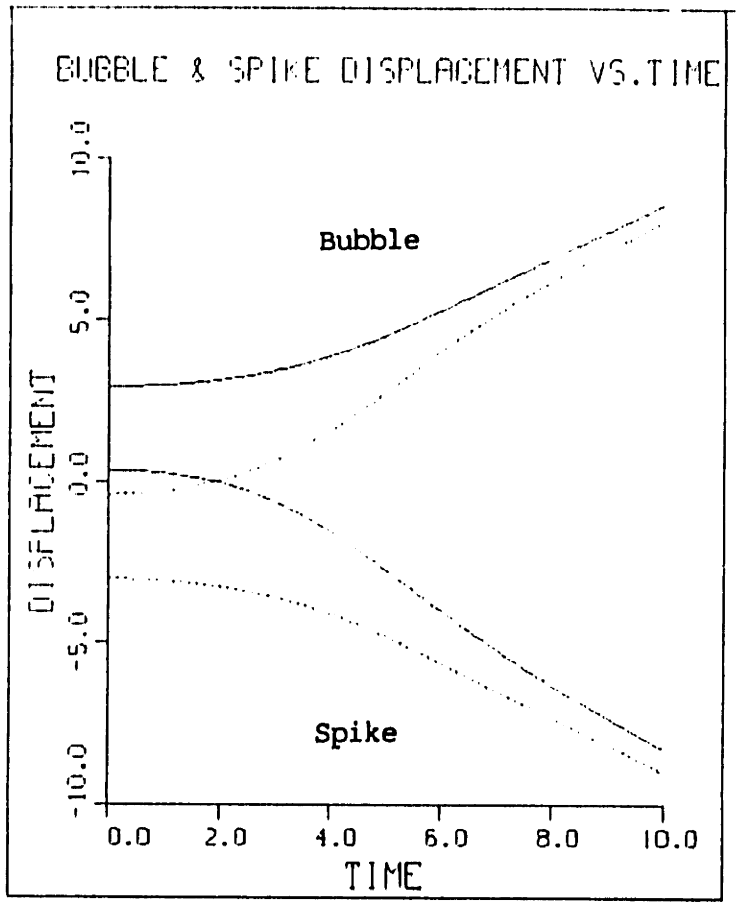

(b)

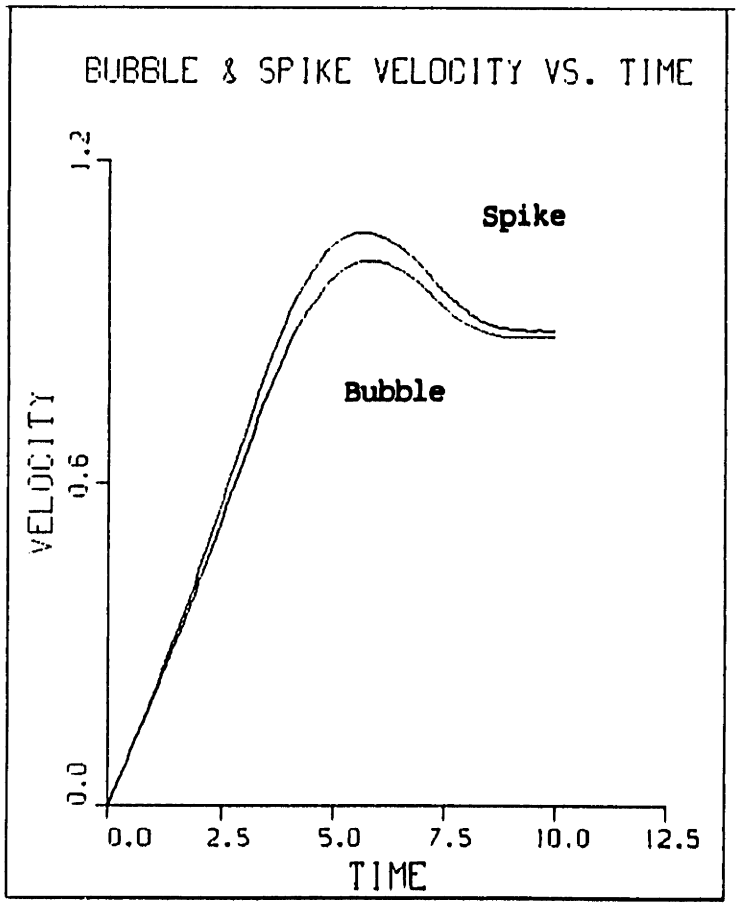

(c)

Figure 62

VI. THE STUDY OF DENSITY STRATIFIED JET FLOWS

VI. 1. INTRODUCTION

The dynamics and mixing in a turbulent heated jet emerging in a cold environment are analyzed using the results of numerical simulations conducted using the vortex/transport element method. The model is considered as a first idealization of a turbulent jet diffusion flame at moderate Reynolds number. Several cases are considered: a uniform-density jet, a density-stratified jet with infinite, finite and zero Froude number, and a density-stratified jet with unequal momentum and thermal shear layer thicknesses. The role of each dynamical process: momentum, density stratification and gravity, as well as their interactions are analyzed in detail. It is shown that density stratification and gravity play very important roles in mixing, and that the interactions between the various dynamical processes in this flow depend on physical parameters such as the density ratio, the vorticity layer and density gradient thicknesses, the Froude number and the form of perturbation.

Recent experimental observations on vertical turbulent jet diffusion flames reveal that gravity plays an important role in determining the flame structure, its stability and the rate of fuel consumption when the Reynolds number, as determined by the fuel jet conditions, is moderate (Roquemore [37], Eickhoff and Winandy [38], Strawa and Cantwell [39]). The study of turbulent jet diffusion flames is complicated by the interactions between three important mechanisms determined by the following features: (1) the velocity difference between the fuel jet and the ambient environment which

establishes a shear layer; (2) the density differential between these two streams which strongly affects the dynamics of this shear layer; and (3) the role of gravity which has a strong effect on the growth of the jet for small to moderate Froude numbers. In this study, the fuel jet is modelled as a column of high velocity hot gas surrounded by a stationary cold environment, while the ratio of the shear layer to the thermal layer thickness is varied to simulate different flame conditions.

An important mechanism in the physical model is the vorticity generation due to: (1) the interaction between the density gradient and the material acceleration, i.e., the baroclinic vorticity; and (2) the interaction between the density gradient and gravity, i.e., the gravity-generated vorticity.

VI.2. DESCRIPTION OF FLOW GEOMETRY

The schematic for the jet flow is shown in Fig. 63 (a) and (b) . It is assumed that at some point downstream of the exit of the spatial jet, the density and velocity profiles evolve from a top-hat distribution into the twin-error function distribution due to the action of viscosity. The error function profiles are used as initial conditions for the problem. The calculations are performed in a frame of reference moving with the mean velocity of the jet and the ambient. Thus, the growth of the jet is observed in a temporal frame. Periodic boundary conditions are applied in the y-direction and the domain is unbounded in the x-direction. The periodicity length is chosen as the wavelength of the perturbation that is imposed on the jet shear layers. The density of the jet fluid is assumed to be lower than that of the ambient fluid. This problem is analyzed for two kinds of perturbations (1) The varicose mode, where the perturbation is symmetric

across the centerline of the jet, i.e., it is equivalent to imposing a no flow boundary condition across the center of the jet [40], and (2) The sinuous mode, where all the material layers are perturbed in the same manner.

VI.3. GOVERNING EQUATIONS

The non-dimensional governing equations for this problem are as given in Eqns. (91) and (92). The flow is isentropic and at a very low Mach number. Thus the density is conserved along the material path. All the other assumtions made with regard to the K-H and the R-T instabilities apply to this problem as well.

$$\frac{d\rho}{dt} = 0 \tag{91}$$

$$\frac{d\omega}{dt} = -\frac{\nabla\rho}{\rho} \times \left(\frac{du}{dt} + \frac{1}{F_r} j \right) \tag{92}$$

The flow variables are non-dimensionalized with the characteristic values U_o for velocity, L_o for length and ρ_o for density. For the jet flow, $U_o = U_1/2$ where U_1 is the velocity at the centre of the jet, L_o is taken as ΔS where ΔS is the vorticity thickness and ρ_o is the ambient density (Fig. 63). The Froude number is defined as $F_r = U_o^2/(g_r L_o)$ where g_r is the gravitational acceleration. j is the unit vector in the y-direction. Therefore, the Froude number can be thought of as the ratio of the existing vorticity in the jet shear layers to that generated due to the action of gravity. Thus, for low Froude numbers, gravitational effects will be expected to dominate the physics of the problem. As F_r becomes higher, the jet flow becomes momentum dominated.

VI.4. RESULTS OF NUMERICAL SIMULATIONS

Computations were performed to understand the mechanisms of formation of large scale structures and their role in the mixing process for the following cases: a uniform-density turbulent jet, a density-stratified turbulent jet when gravity effects are negligible, i.e., $Fr = \infty$, a density-stratified jet with negligible momentum, i.e., $Fr = 0$, and a density-stratified turbulent jet with a finite Froude number. For each case, the computations were done for two modes, the varicose and the sinuous modes, of perturbation. The purpose of partitioning the problem up in this way is to identify the role played by each single process individually and to characterize the modes of interaction between these processes when they occur simultaneously. The term "turbulent jet" is used here to describe an unstable flow which has been subjected to finite, although very small, perturbations that subsequently grow beyond their linear range and cause substantial irreversible distortion beyond the initial state of the flow.

In all cases, except for the jet with negligible momentum, the calculations are started with an initial vorticity distribution made of two Gaussians of opposite signs connected by a zero vorticity zone at the core of the jet (Fig. 63 (a)). The corresponding velocity distribution is two error functions connected with a uniform velocity zone, as shown in the figure. A density stratification such that the jet fluid is hotter than the ambient fluid is superimposed. The density distribution is shown in Fig. 63 (b), and is formed of two error functions separating the jet fluid from the ambient fluid. The density ratio is four so that $\rho_{jet} = 0.25$ and $\rho_{amb.} = 1.0$. The vorticity distribution and the density distributions initially overlap. The

same functions are used to generate the velocity distribution and the density distribution.

In all cases, the two shear layers and/or the two zones of density gradients on both sides of the jet centerline are perturbed using sinewaves with the maximum amplitude being $\varepsilon = 0.02\ \lambda$ where $\lambda = 6.6\ \Delta S$ and ΔS is the characteristic thickness of each vorticity layer. A symmetric perturbation is imposed to study the growth of the varicose mode of the jet instability which is believed to be the most important mode in the initial stages of the spread of the jet. The sinuous mode is simulated by perturbing the material layers in phase with each other on both sides of the centerline.

For all cases, the evolution of the flow is shown in terms of: (1) the instantaneous location and velocity of the vortex/transport elements; (2) the temperature contours; and (3) the vorticity contours. The locations of the computational elements are used to define the flow structure, the temperature contours are utilized to study entrainment, and the vorticity contours are employed to determine the flow dynamics and the contribution of both momentum and gravity to its evolution.

VI.4.1. THE VARICOSE MODE

The varicose or the odd mode of instability in jets is studied in this section. The material layers are perturbed in a symmetric manner across the centerline of the jet. Thus the jet centerline acts as a potential wall that does not allow any flow across it. The following four cases are considered.

(i) Case I : A Uniform-Density Jet

This is the reference case in which the jet is driven by momentum only, i.e., $Fr = \infty$. The baroclinic vorticity generation due to density

stratification is neglected and so is the gravity generated vorticity. Thus, vorticity remains constant along a particle path. Fig. 64 shows the evolution of the jet structure in terms of the locations and velocities of the vortex elements at t = 2.5, 5.0, 7.8 and 9.8. The material layers are plotted for two wavelengths in order to show the development clearly. The vorticity layers on both sides of the centerline roll up to form two large-scale structures with opposite signs, generating strong entrainment currents that pull the ambient fluid into the jet core. The large eddies exhibit a strong degree of symmetry with respect to both the jet and the ambient fluids. It is also observed that the large eddies acquire a finite velocity in the direction of the jet due to the mutual interaction between the eddies across the centerline of the jet. This finite velocity, which resembles the self-induced velocity of a vortex ring in an axisymmetric jet, is small in this simulation due to the fact that the vorticity within the core of each eddy is distributed over a large area between the jet centerline and the ambient (in the case of a vortex ring, the self-induced velocity is proportional to $\ln(R/\sigma)$ where R and σ are the radii of the ring axis and the ring core, respectively). The corresponding streamline contours are shown in Fig. 65 . The streamlines show the development of the instability and the formation of the coherent structures due to the entrainment of the ambient and the jet fluids. The volumetric entrainment increases as a function of time until the instability saturates upon which fluid begins to leave the structures. The entrainment into the structures is estimated by calculating the entrainment parameter ζ defined as $\zeta = \Delta\psi-(\Delta\psi)_0$. $\Delta\psi$ is the difference between the minimum and the maximum value of ψ in the domain. $(\Delta\psi)_0$ is the value at t=0. Since the domain used for the calculation for ψ is the same for all the cases here, ζ can be used to compare volumetric entrainment between each case. The

entrainment parameter ζ is estimated from the streamline plots to be 0.5 at t=9.8.

The entrainment within the large eddies is shown more clearly in the plots of the temperature contours in Fig. 66 . In this uniform-density case, the temperature is a passive scalar. The figure indicates that with the roll-up of the vorticity layer and the formation of the large-scale structures on the two sides of the jet centerline, the ambient fluid is entrained into the cores of these eddies forming a spiral around the jet fluid. The strain field that develops during this process causes a substantial thinning of the original shear/density gradient zone in the region that separates the large eddies, the braids. The contours indicate that at the later stages of development of the varicose mode, the jet stream is formed of a series of puffs of pure jet fluid separated by lumps of well-mixed fluid in the form of symmetric mushrooms (assuming that the entrainment will be followed by molecular diffusion to complete the mixing process within these mushrooms). This situation gives rise to the experimentally observed phenomenon of intermittency in which widely disparate values of the mixture quality can be measured at the same point in space at very close moments in time. Clearly, this instability mode is unable to achieve full mixing between the jet and the ambient fluids and pure jet fluid can be detected far dowstream of the nozzle.

The dynamics leading to the establishment of these mixing contours can be revealed by inspecting the vorticity contours shown in Fig. 67 . A zone of strong concentration of vorticity forms at the center of the initial perturbation and acts as a focus for attracting vorticity which is initially distributed in the streamwise direction. This focus is transported slowly in the original direction of the jet due to the mutual interaction between the

eddies on the two opposite sides of the centerline. By the end of roll-up, the large eddies span the zone between the centerline and the ambient. Curve 1 of Fig. 80 (a) shows the circulation in the flow field as a function of time. Since there is no generation of vorticity in this case, the circulation in the field remains the same as at t=0, i.e., the curves are horizontal. The positive and the negative circulation are shown separately. Curve 1 of Fig. 80 (b) shows the mean length of the material interface as a function of time. The material length is calculated as an average over the length of all the material layers used in the calculations. The length is normalized by the length at t=0. It is observed that the length of the interface increases with the growth of the instability and the final length is more than twice the initial length. The linear growth rate of the instability is estimated by calculating the initial slope of the curve of log I versus time where $I = \int\int u\, dx\, dy$ and u is the fluctuating transverse velocity component. The linear growth rate for Case I is shown in Fig. 81 as a function of wavenumber. The shape of the curve is similar to what was obtained for the shear layer.

(ii) Case II : A Density-Stratified Hot Jet Without Gravity

The second case that is considered is the same jet as in Case I, same initial vorticity distribution, however, the density gradient is allowed to affect the dynamics of the flow. Gravitational effects are still neglected, i.e., $Fr = \infty$. Vorticity generation in this case is due to the interaction between the fluid acceleration and the density gradient, i.e., due to baroclinic effects. The locations and velocities of the vortex elements are shown in Fig. 68 at time t = 2.5, 5.0, 7.8 and 9.8. Here, the large eddies do not exhibit the same symmetry with respect to the jet and the ambient fluid as in the uniform-density case. To the contrary, the large eddies

entrain more of the hot jet fluid by volume than the cold ambient fluid as indicated by the fact that there is a deeper penetration of the jet fluid than that of the ambient fluid into the eddies. The large eddies propagate in the direction of the ambient cold fluid contrary to Case I in which they propagate in the direction of the jet fluid. This is consistent with the behavior of a density-stratified shear layer and is due to the baroclinic generation of vorticity. It is also seen that each large eddy structure contains a smaller structure within it, which rotates in the same direction as the large structure. Results show that the rate of generation of elements is much higher within the smaller structure than outside it. This is the first sign that a double structure may be observed when density stratification is dynamically significant. Fig. 69 shows the corresponding streamline contours. The value of the streamfunction at the core of the structure is $\zeta = 2.6$ at $t=9.8$. It is observed that the total volumetric entrainment of fluid into the structures has increased with respect to the uniform density jet. This is again consistent with the results obtained for the density stratified shear layer.

Entrainment in this case can be studied from the temperature contours plotted in Fig. 70. The motion of the structures in the direction of the cold fluid is seen clearly in these plots (in a frame of reference fixed to the jet nozzle, the structures propagate at a slower velocity than the mean jet velocity). The structures are slightly larger in the streamwise direction than those in Case I, but they are also smaller in the cross-stream direction. This indicates that the rate of spread of the jet is reduced in the density-stratified case as compared to the uniform density case. The structures are also more biased towards the hot jet fluid, i.e., each structure contains more hot jet fluid than cold ambient fluid. This bias is

similar to the mixing asymmetry due to density stratification which was observed in the shear layer experiments and calculations [26,27]. The ambient fluid still reaches the centerline of the jet squeezing the jet fluid to the outer edges of the large structures. It is observed that the small structure which exists within the large structure is formed of cold ambient fluid which penetrates the jet and establishes a density gradient within the large structure. The inside of the large eddies is less convoluted than in the uniform density case. It is also observed that there is less of the jet fluid by volume in the region between the eddies in the streamwise direction. This is consistent with the observation that more of the jet fluid has been entrained into the eddies. The vorticity contours, shown in Fig. 71 , exhibit a substantial deviation from those of a uniform density jet. The plots show that as soon as roll-up starts, the rate of depletion of vorticity within the braids exceeds that for the uniform density case. This depletion is actually a result of the generation of vorticity of the opposite sign to the initial vorticity within the layer. This baroclinically-generated vorticity, expressed by the term $-\nabla\rho/\rho \times \mathbf{a}$ in the vorticity transport equation, leads to a quick destruction of the vorticity in the braids. The same process occurs on the outer edges of the large structure, forming a vortex rotating in the direction opposite to that of the large eddy. Meanwhile, vorticity of the same sign as the initial vorticity is generated within the core of the eddy, leading to the formation of a stronger eddy than in the uniform density case. Most of the vorticity generation within the large eddies occurs around the density gradient, giving rise to the small structure seen within the large structure in Fig. 71 . The redistribution of vorticity within the large structures is what leads to the downward motion of the large eddies.

Curve 2 of Fig. 80 (a) shows the total circulation in the field as a function of time. The positive and the negative components are summed separately. The curves show that the generation is very small for $t < 3.0$. Beyond this time equal amounts of positive and negative circulation are generated in the flowfield. Therefore the net circulation in field is conserved and is the same as in the uniform density case. The elongation of the material interface with time is shown in Curve 2 Fig. 80 (b) . It is observed that the mean length of the interface is longer than that of Case I in the non-linear range. This is consistent with the observation that the density stratified jet is more unstable (due to vorticity generation) than the uniform density jet. The same phenomenon was observed in density stratified shear layers. Fig. 81 shows the linear growth rate of the instability over different wavenumbers for Case II. It is observed that the maximum growth rate is shifted to the right with respect to the uniform density jet. Again, this behavior is similar to what was observed for the density stratified shear layer.

(iii) Case III : A Very Slow Hot Jet in a Gravitational Field

The effect of gravity on the development of a hot jet is studied in this section. The initial momentum of the jet is assumed to be negligibly small, i.e., Fr = 0.0. Computations were performed for a stationary vertical column of hot, low-density gas surrounded by a cold, high-density environment. The velocity and the vorticity are zero everywhere at t=0. The density distribution is the same as shown in Fig. 63 (b) . Since $U_o = 0$ in this case, the velocity scale is taken as $U_o = \sqrt{L_o g_r}$, and the time scale is $t_o = \sqrt{L_o/g_r}$, where g_r is the gravitational acceleration. Gravity induces an upward motion of the hot fluid with respect to the cold fluid. This relative

motion between the fluid elements also produces vorticity, gravity-generated vorticity, as will be seen in the results. The generation of vorticity due to gravity represents the conversion of potential energy in the field into kinetic energy of the flow.

Fig. 72 shows the vortex elements and their velocities at time t = 3.75, 5.37 , 5.75 and 6.0. During the early stages, the density gradient is perpendicular to the direction of gravity and the source term in Eqn. (92), $\nabla\rho/\rho \times j$, is at its maximum value giving rise to strong gravity-generated vorticity within the density gradient zones with opposite signs on the two sides of the jet. With the applied perturbation, the generated vorticity rolls up and two symmetric eddies form as the buoyant column continues to accelerate upwards under the influence of gravity. The large-scale structures resemble those formed in the momentum-driven jet and they propagate in the direction of the accelerating hot jet. The structures also exihibit a high degree of symmetry with respect to the hot and cold gases. It is interesting to observe that there are two zones of high concentration of elements inside each large eddy, one near the leading edge and one near the center of the structure. These structures are more spread out in the streamwise direction as compared to the uniform density case. The plots also show that there are zones of very strong shear between the inner edges of the structures and the hot jet; this is due to the continuous acceleration of the buoyant jet. The streamline plots at the corresponding times are shown in Fig. 73 . Since the initial velocity is zero everywhere in the computational domain and the heavy ambient fluid is always stationary, the streamlines exist only in the region affected by the jet fluid.

The entrainment of cold fluid in this case is shown by the plot of the temperature contours in Fig. 74 . The large eddies, initially formed of jet

fluid, grow by entraining fluid from the ambient towards the core of the jet and then towards the eddy center. The inner spirals observed in Cases I and II are only seen in the early stages. As soon as the cold fluid reaches the center of the eddy, it traps a blob of hot fluid inside the large eddy and the overall structure tends to continue its motion upwards. Moreover, the contours show that more hot fluid by volume than cold fluid is entrained within the large eddy and although in a geometrical sense the structures are symmetric, their composition is certainly asymmetric with bias towards the hot fluid. This is similar to the case of a density-stratified flow without gravity, i.e., Case II. In order to investigate the dynamics of this jet, the vorticity contours are plotted in Fig. 75 . As expected, vorticity is continuously being generated due to the gravity term in Eqn. (92). As the material acceleration in the direction normal to the density gradient becomes finite due to roll-up, baroclinic vorticity is also generated. However, as apparent from the plots, except for small areas within the domain, the gravity term dominates and the vorticity generated maintains one sign on each side of the jet centerline. Roll-up leads to the formation of the observed large structures. At later stages, the vorticity within the large structure accumulates within two smaller eddies, one at the leading edge and the other at the center of the large structure. These structures are, however, much more spread out than before and small-scale roll-ups are observed everywhere. It is interesting to observe that the intense vorticity generation at the leading edge of the large structure is associated with the motion of the cold fluid blob into the hot jet fluid there. Gravity-generated vorticity tends to render the large eddy very spotty and somewhat incoherent generating a large structure more stratified than observed before.

The generation of circulation with time is shown in Curve 3 of Fig. 80 (a). The initial circulation in the field is zero. Equal amounts of positive and negative circulation are generated for $t>0$. It is observed that the magnitude of the gravity generated vorticity is considerably higher than that of the baroclinic vorticity in Case II. For $t>5.0$, the slope of the circulation curve is very large indicating that the instability is extremely strong in the non-linear stages of its growth. The mean length of the interface is plotted as a function of time in Curve 3 of Fig. 80 (b) . Again it is observed that the development of this instability is highly non-linear. For $t< 4.0$, the interface elongation is negligible. In the time interval, $4< t < 6$, the interface undergoes considerable elongation and the final slope of the curve is much larger than those observed in Cases I and II. This indicates that the rate of elongation is much larger which once again ascertains that the effect of gravity is highly destabilizing.

(iv) Case IV : A Density-Straitified Hot Jet at Moderate Froude Number

This case combines the complexities of all the previous cases. The initial distributions of vorticity and density are as shown in Fig. 63 (a) and (b), and the effects of gravity are considered as well. The thicknesses of the shear layers and the density gradient layers are the same. The Froude number used in these calculations is $Fr = 4.0$. Thus, momentum should play the dominant role but with finite contribution from gravity. The results of this case are compared with those of Case II in which gravity was neglected. Fig. 76 shows the vortex elements and their velocities at $t = 2.5, 5.0, 6.8$ and 7.8. The calculations for this case were stopped at an earlier time of $t=7.8$ as compared with $t=9.8$ for Case II. This is because the inclusion of gravity destabilizes the jet to a greater extent (see previous section) and

the instability develops faster and saturates at an earlier time. The large eddies are moving upwards in the direction of the hot fluid in this case, similar to the gravity driven jet in Case III, and contrary to Case II in which they were moving downwards in the direction of the cold fluid. The downward motion in Case II is due to the generation of baroclinic torque while in Cases III and IV, the upward motion is due to the buoyancy effects associated with the hot jet fluid. Similar to Case II, however, there is an outer large structure which contains an inner smaller structure that becomes more intense as the jet continues to rise due to the gravitational acceleration of the jet core fluid. The intensification of the inner structure is similar to what was seen in Case III where gravity-generated vorticity around the inner density gradients was found to be responsible for this development. The inner structure exists close to the leading edge of the outer structure, indicating that its fluid is hotter than that of the outer structure. The streamline contours for this case are shown in Fig. 77 . The entrainment parameter ζ is calculated as 6.4 . Thus the entrainment into the structure has increased substantially due to the added destabilizing effect of gravity.

The entrainment enhancement due to the generation of these large scales is shown by the contours of the temperature depicted in Fig. 78. There is more entrainment in this case than in any previous case and the entrainment is more strongly biased towards the hot fluid than in Case II. The entrainment bias towards the hot fluid was observed in Cases II and III, and is stronger here since the two effects are present. The figure shows that the mixing structures are bigger and more convoluted than before. The convolution results from the successive entrainment of blobs of hot fluid and cold fluid as gravity-generated vorticity roll-up follows the roll-up of the

initial vorticity. It is observed once again that the amount of hot fluid between the eddies in the streamwise direction is much less compared to Cases I and II. This indicates that more of the jet fluid by volume is entrained into the eddies. The vorticity contours shown in Fig. 79 reveal the strong generation of vorticity around the convoluted surfaces where density gradients are highest. At the early stages, the vorticity rolls up in a coherent form leading to the establishment of strong entrainment currents observed in Fig. 77 . At later stages, baroclinic vorticity becomes important supporting the formation of small scale structures within this large eddy. The presence of small scales explain the very patchy look of the mixing structures at the later stages.

The generation of circulation with time is shown in Curve 4 of Fig. 80 (a). Comparing Cases II and IV, it is immediately observed that the effect of gravity is very dominant even at a Froude number of 4. The amount of circulation generated is considerably larger than in Case II and perhaps more important is the final slopes of the curves. The slope of the curve for Case IV at t=7.8 is orders of magnitude larger than that for Case II at t=9.8. The mean material length plot in Curve 4 of Fig. 80 (b) shows that the length of the interface increases in a dramatic manner in the non-linear stages. The final length of the interface is about six times the initial length as compared to a factor of 2 for Case II. Also, the final slope of the curve for Case IV is greater than that for Case II. Fig. 81 shows the linear growth rate as a function of wavenumber for Case IV. It is observed that the inclusion of gravity makes the jet more unstable. As the Froude number goes to infinity, the curve for Case IV approaches that of Case II. Thus, the presence of gravity is highly destabilizing.

(v) Case V : The Double Structure

In many cases of interest, as in the case of a vertical jet diffusion flame, the vorticity layer forms as the jet boundary layer separates at the nozzle lip while the density gradient forms as a results of the presence of the flame which exists outside the vorticity layer. This situation can be modeled by the vorticity and density profiles shown schematically in Fig. 82 . The thickness of the density profile is twice that of the velocity profile, a case which is encountered when the heat from the flame zone diffuses at a faster rate into the ambient. The momentum-vorticity layer is perturbed by its corresponding most unstable mode which amounts to three waves. Meanwhile, the density gradient layer is perturbed by a single wave and the evolution of the flow is followed as before. Both perturbations are symmetric around the jet centerline. The Froude number in these simulations is two.

Fig. 83 shows the locations and velocities of the vortex elements at t=5.0, 6.07 and 6.57. It is observed that the momentum vorticity layer rolls up into three structures drawing both the hot jet fluid and hot fluid from the "flame" zone into the eddy core. Since both zones are at the same temperature, these small structures are symmetric as seen before in the simulations of the uniform-density jet. These small structures are moving upwards in the direction of the jet, as seen in Case I. Meanwhile, the interaction between the density-gradient zone and gravity produces a gravity-generated vorticity layer outside the momentum vorticity layer. The rollup of this layer into a large-scale structure is observed just outside the jet vorticity layer. This is a gravity-generated structure which resembles that observed in Case III. At later times, however, the gravity driven vorticity layer appears to dominate the flow field by distorting the inner small

structures and then entraining them into the core of the large structure. This results in a complicated double structure which strongly resembles experimental observations (Roquemore[37].) The acceleration of the hot fluid produced by the action of gravity is clearly observed from the upward convective motion of the large structures. In an experimental realization of this flow, the jet fluid must be clearly marked by seeding, if these structures are to be visualized (Vandsburger et al. [41] and Chen & Roquemore [42]). Fig. 84 shows the streamline contours at the corresponding time frames. It is observed that all of the entrainment is completetly dominated by the large scale gravity driven structure. The smaller momentum driven eddies do not appear in the streamline plots.

The temperature contours are shown in Fig. 85 . Since the temperature gradient is well outside the momentum vorticity layer, the small eddies do not leave a trace on these contours. The rollup of the gravity-generated vorticity over the zone of finite density gradient is responsible for the convolution of the temperature gradients into the large outside structure. This structure is formed of hot fluid from the flame zone and cold ambient fluid. As observed before in all cases with a density gradient, there is an entrainment bias towards the light hot fluid. This bias is manifested in what appears to be a process in which the large structures swallows the small structures. The large structure, formed of more hot fluid, is moving upwards due to gravity. The dynamics of this flow can be explained by inspecting the vorticity contours in Fig. 86 . The momentum vorticity layer and the gravity-generated vorticity layer are both observed in these figures. Even though the structures associated with the rollup of the momentum vorticity layer develops quite rapidly, the values of vorticity within the density-gradient layer are consistently higher by an order of magnitude. At late

times, the rollup of the gravity-generated shear layer completely dominates the flow field.

The circulation in the flow field is plotted as a function of time in Fig. 87 . The positive and negative components of circulation are shown separately. It is observed that the initial increase in circulation is almost linear. For t> 5.5, the circulation increases at a faster rate indicating that the gravity driven structures are beginning to dominate the flow. The mean length of the interface is plotted against time in Fig. 88 . Again it is observed the elongation rate increases significantly towards the final time. The final length is about twice the initial length.

(vi) Discussion:

One of the most important phenomena in turbulent diffusion flames is the interaction between the flow field and the reaction process. Since the reaction takes place after the reactants, fuel and oxidizer, have been molecularly mixed, it is important that there exists a mechanism for enhancing the mixing process to achieve higher rates of burning. The formation of large scale structures in shear layers and jets is one such mechanism. The study of the formation and growth of these structures is thus necessary to form a clear understanding of how they form and how they affect the mixing process and how they can be manipulated.

In this work, numerical simulation has been used to study the dynamics and mixing in a vertical hot jet in a cold environment with and without the effect of gravity as an idealized model of a vertical jet diffusion flame. In order to approach this complex problem systematically, solutions were obtained for increasingly more involved models. The major observations are summarized in the following paragraph.

The results of numerical simulations have revealed some interesting consequences of the presence of density gradients in a flow field:

(1) A density gradient leads to more volumetric entrainment of the light fluid than the heavy fluid, which results in a different mixture fraction within the mixing zone than in the uniform-density case. Calculations which do not account for the density variation are likely to yield wrong predictions for the flame location, which appears at the zone of stoichiometric composition.

(2) A density gradient causes the structures to move with a velocity biased towards that of the heavy fluid. In this study, it was found that the convection velocity of the structures were less than the mean velocity of the jet.

(3) The generation of baroclinic vorticity leads to the formation of small intense eddies within the large structure which results in further mixing enhancement. The vorticity contours reveal the presence of a number of these small eddies.

(4) The effect of a density gradient was to always decrease the spread of the layer in the cross-stream direction as compared to the uniform density case.

The addition of gravity in the model gave rise to more interesting dynamics due to the generation of vorticity by gravity:

(1) Gravity-generated vorticity further increases the volumetric entrainment of the light fluid and intensifies the small scale structures within the large eddy. Therefore, one might expect an increase in mixing due to the presence of gravity.

(2) Gravity destabilizes the jet shear layers to a greater extent as seen by comparing Cases II and IV. Gravity tends to increase the growth rate of the eddies making the shear layers grow faster and hence reaching the collapse

stage earlier. Thus complete mixing and burning can be achieved for a smaller length of the combustor with the help of gravity.

(3) The hot light fluid at the center of the jet is accelerated upward with respect to the ambient cold fluid and hence the structures move upward under the influence of gravity.

Thus gravity leads to faster growth of the shear layers, enhanced mixing at the cores of the eddies and an acceleration of the structures in the streamwise direction. At low and moderate jet velocities gravity is expected to play an important role in the development of the jet.

When the density gradient occurs well outside the momentum shear layers as in Case V, it was shown that the gravity-generated shear layer develops outside the momentum shear layer. These large scale structures play an important role in transporting the ambient fluid (air) to the reaction zone which is located between the two shear layers. Since the flame is outside the momentum shear layer, the small eddies are not capable of affecting the burning rate. On the other hand the large gravity-generated structures do have a dominant effect on the flame.

The results of the numerical simulations of Case V yielded good qualitative agreement with Roquemore's experimental results [37]. More importantly, the numerical study shows that the physical parameters of the problem, such as the density ratio, the thicknesses of the jet shear layers and those of the density gradient zones, the Froude number and the forms of the perturbation play very important roles in determining the dynamics of the problem. This also indicates that these flows can be effectively controlled to yield desired results by changing these parameters.

FIGURE CAPTIONS

Fig. 63. Schematic of the initial profiles for (a) the velocity and the vorticity; (b) the density and the density gradient.

Fig. 64. The locations and velocities of the vortex/transport elements at t = 2.5, 5.0, 7.8 and 9.8 respectively for Case I.

Fig. 65. The streamline contours for Case I at t= 2.5, 5.0, 7.8 and 9.8 respectively.

Fig. 66. The normalized temperature (T = 1/ρ) contours for Case I at t= 2.5, 5.0, 7.8 and 9.8 respectively.

Fig. 67. The vorticity contours for Case I at t= 2.5, 5.0, 7.8 and 9.8 respectively. The contnuous curves represent negative vorticity and the dashed curves signify positive vorticity.

Fig. 68. The locations and velocities of the vortex/transport elements at t = 2.5, 5.0, 7.8 and 9.8 respectively for Case II.

Fig. 69. The streamline contours for Case II at t= 2.5, 5.0, 7.8 and 9.8 respectively.

Fig. 70. The normalized temperature (T = 1/ρ) contours for Case II at t= 2.5, 5.0, 7.8 and 9.8 respectively.

Fig. 71. The vorticity contours for Case II at t= 2.5, 5.0, 7.8 and 9.8 respectively. The contnuous curves represent negative vorticity and the dashed curves signify positive vorticity.

Fig. 72. The locations and velocities of the vortex/transport elements at t = 3.75, 5.37, 5.75 and 6.0 respectively for Case III.

Fig. 73. The streamline contours for Case III at t= 3.75, 5.37, 5.75 and 6.0 respectively.

Fig. 74. The normalized temperature (T = 1/ρ) contours for Case III at t= 3.75, 5.37, 5.75 and 6.0 respectively.

Fig. 75. The vorticity contours for Case III at t= 3.75, 5.37, 5.75 and 6.0 respectively. The contnuous curves represent negative vorticity and the dashed curves signify positive vorticity.
[B
Fig. 76. The locations and velocities of the vortex/transport elements at t = 2.5, 5.0, 6.8 and 7.8 respectively for Case IV.

Fig. 77. The streamline contours for Case IV at t= 2.5, 5.0, 6.8 and 7.8 respectively.

Fig. 78. The normalized temperature (T = 1/ρ) contours for Case IV at t= 2.5, 5.0, 6.8 and 7.8 respectively.

Fig. 79. The vorticity contours for Case IV at t= 2.5, 5.0, 6.8 and 7.8 respectively. The contnuous curves represent negative vorticity and the dashed curves signify positive vorticity.

Fig. 80. (a) The cumulative circulation as a function of time. The positive and negative components of circulation are represented separately; (b) The average material length as a function of time. The length is normalized by the value at t=0. Curves 1, 2, 3 and 4 represent cases I, II, III and IV respectively.

Fig. 81. The linear growth rate of the instability as a function of wavenumber for cases I, II and IV respectively.

Fig. 82. The schematic of the velocity and density profiles for Case V.

Fig. 83. The locations and velocities of the vortex/transport elements at t= 5.0, 6.07 and 6.57 respectively for Case V.

Fig. 84. The streamline contours for Case V at t= 5.0, 6.07 and 6.57 respectively.

Fig. 85. The normalized temperature (T= $1/\rho$) contours for Case V at t= 5.0, 6.07 and 6.57 respectively.

Fig. 86. The vorticity contours for Case V at t= 5.0, 6.07 and 6.57 respectively. The continuous contours represent negative vorticity and the dashed curves signify positive vorticity.

Fig. 87. The cumulative circulation as a function of time for Case V. The positive and the negative components are plotted separately.

Fig. 88. The average material length as a function of time for Case V. The length is normalized by the value at t=0.

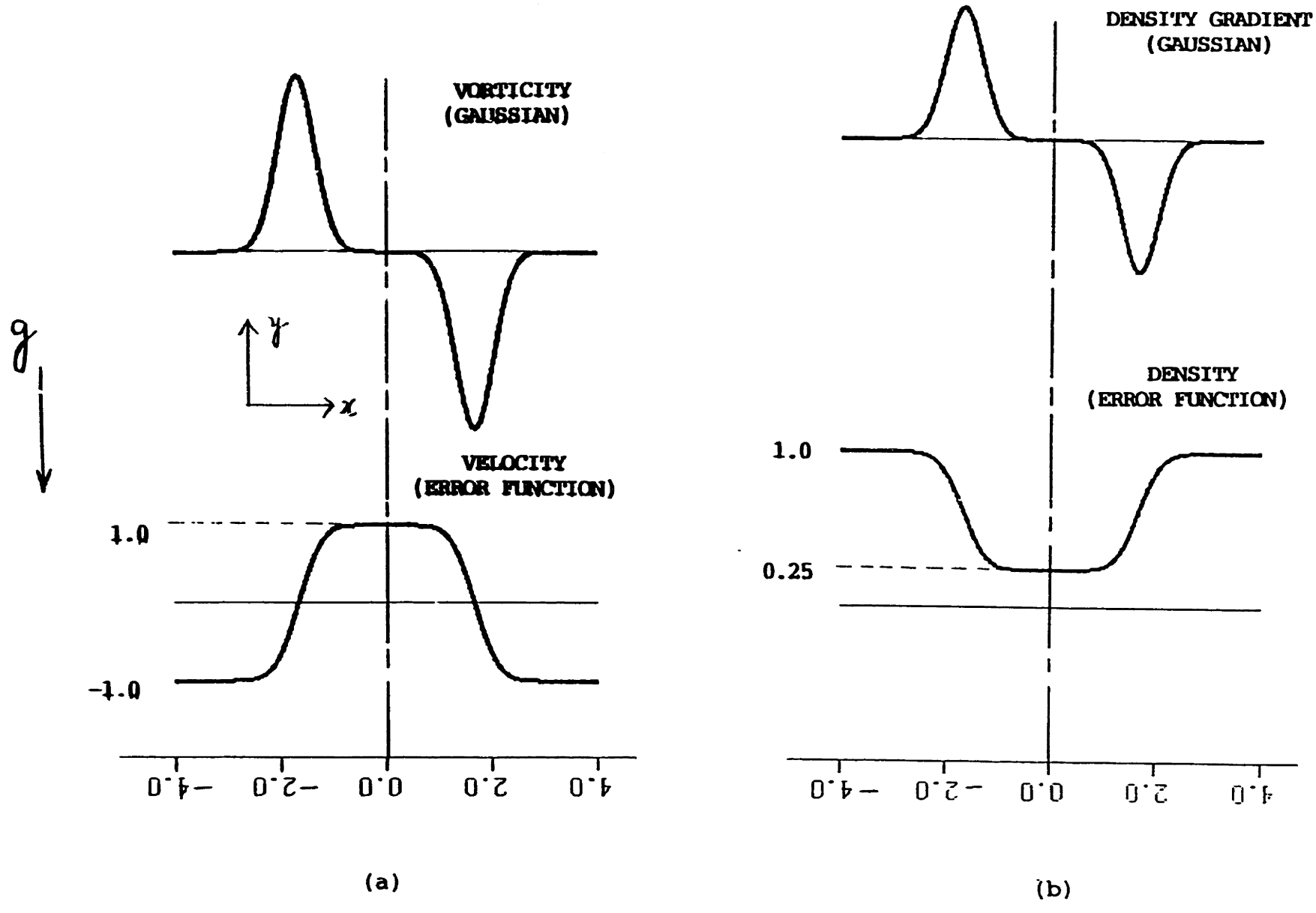
VORTICITY
(GAUSSIAN)
g
y
x
VELOCITY
(ERROR FUNCTION)
1.0
-1.0
-4.0
-2.0
0.0
2.0
4.0
(a)
DENSITY GRADIENT
(GAUSSIAN)
DENSITY
(ERROR FUNCTION)
1.0
0.25
-4.0
-2.0
0.0
2.0
4.0
(b)

Figure 63

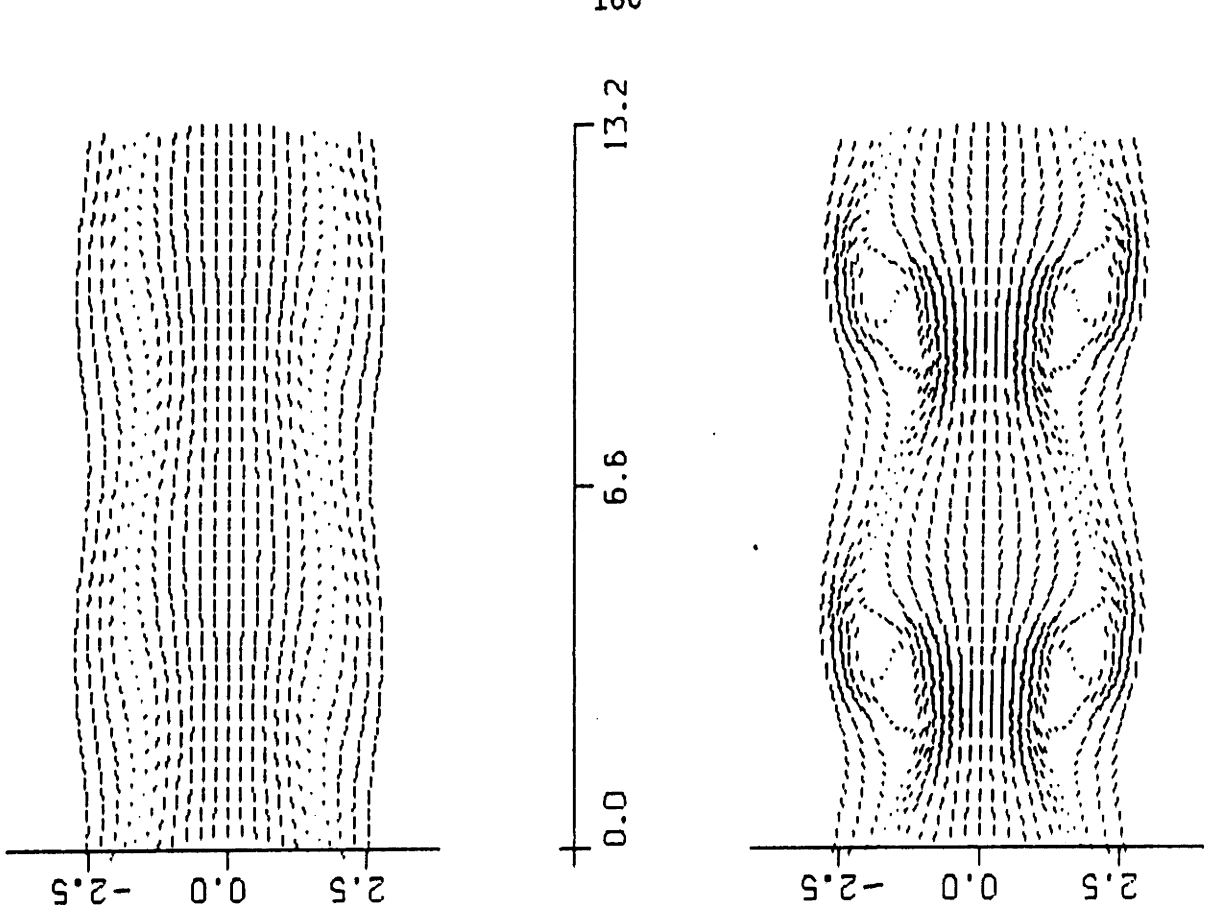

t = 2.5

t = 5.0

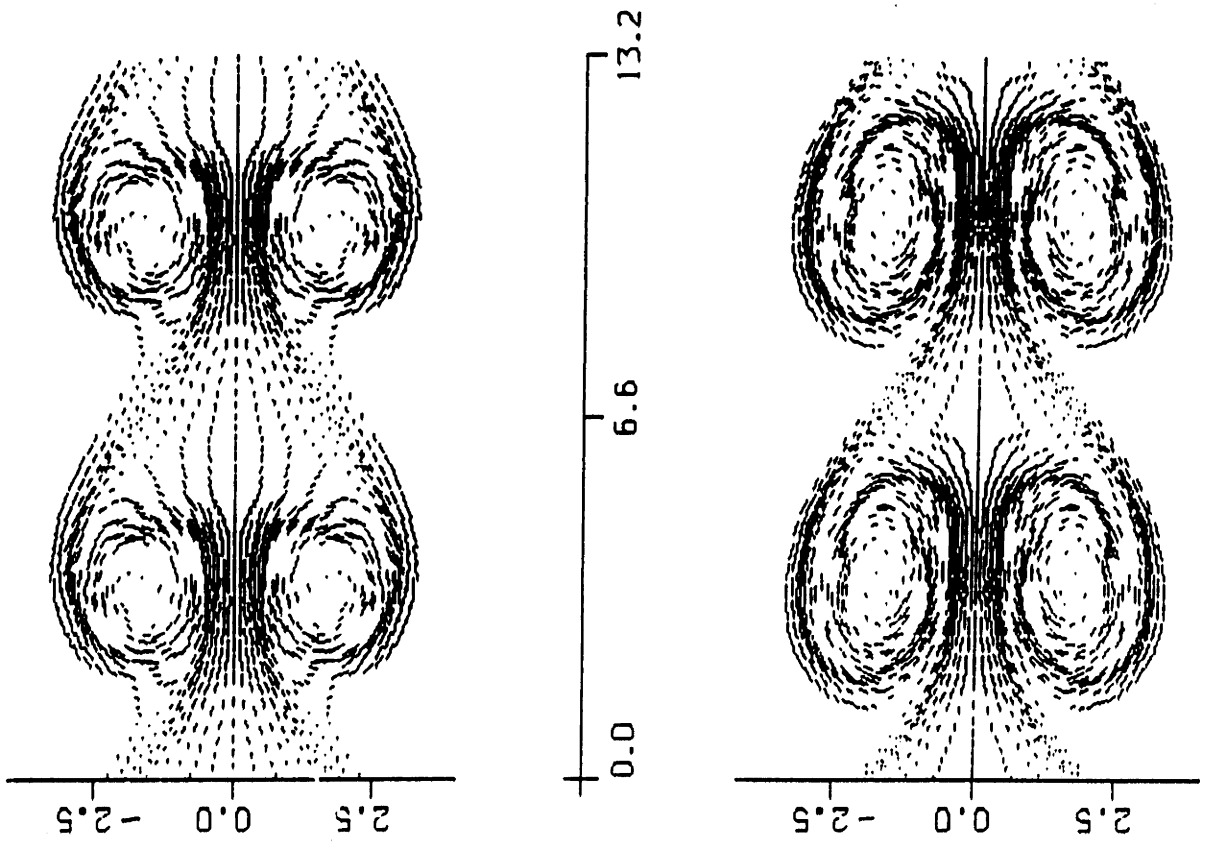

t = 7.8

t = 9.8

Figure 64

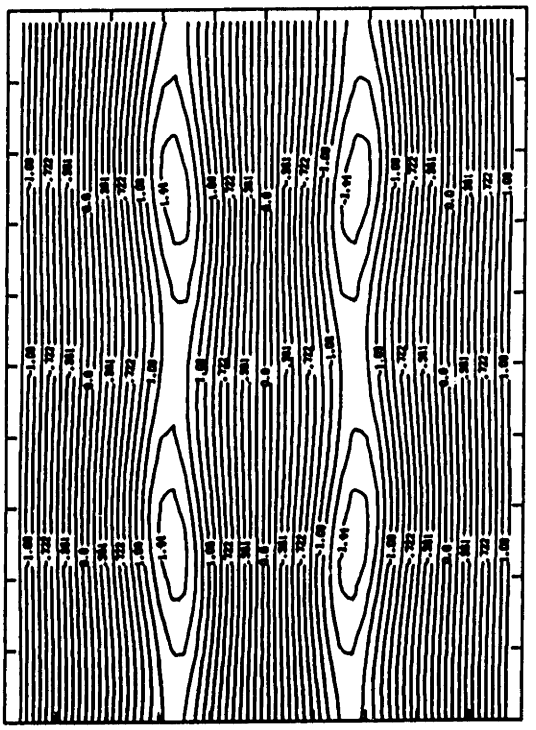

t = 2.5

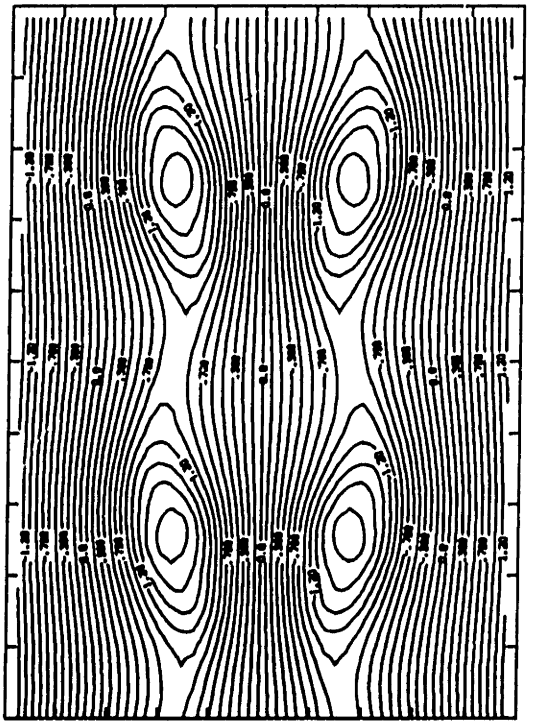

t = 5.0

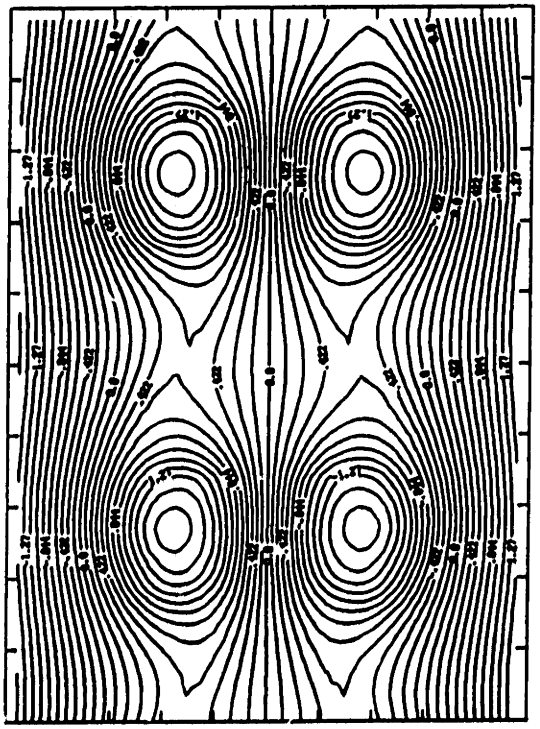

t = 7.8

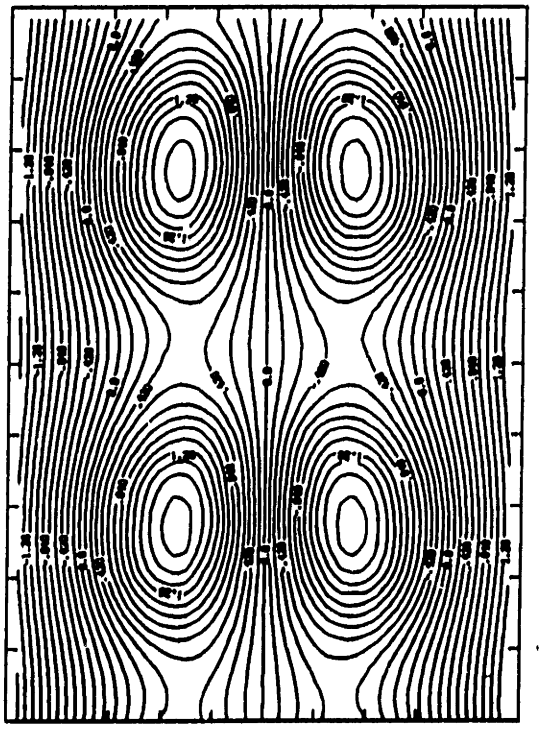

t = 9.8

Figure 65

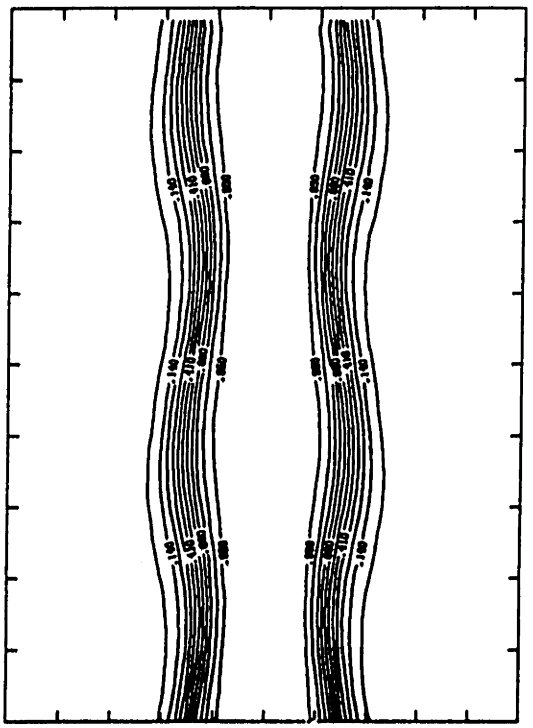

t = 2.5

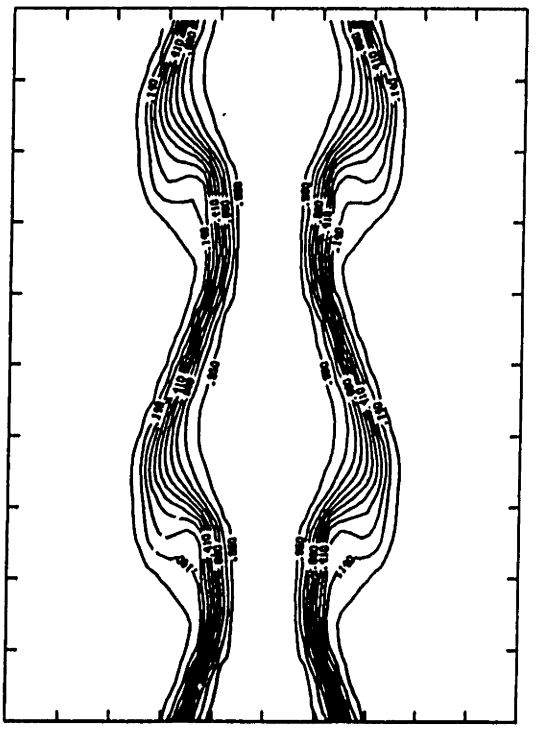

t = 5.0

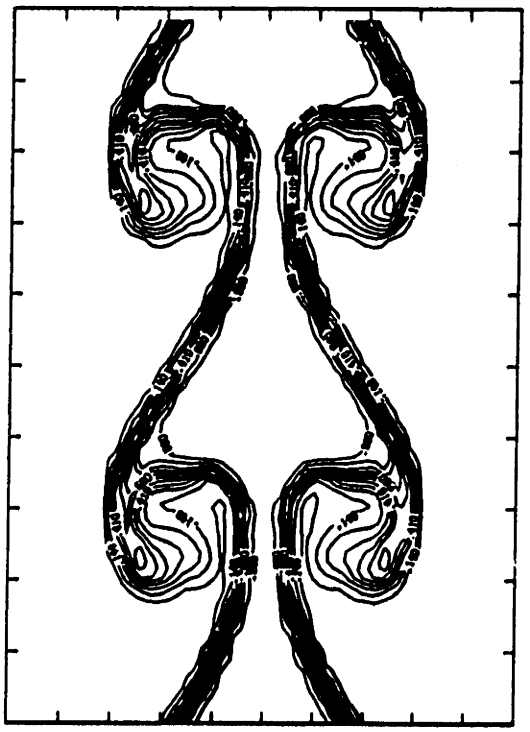

t = 7.8

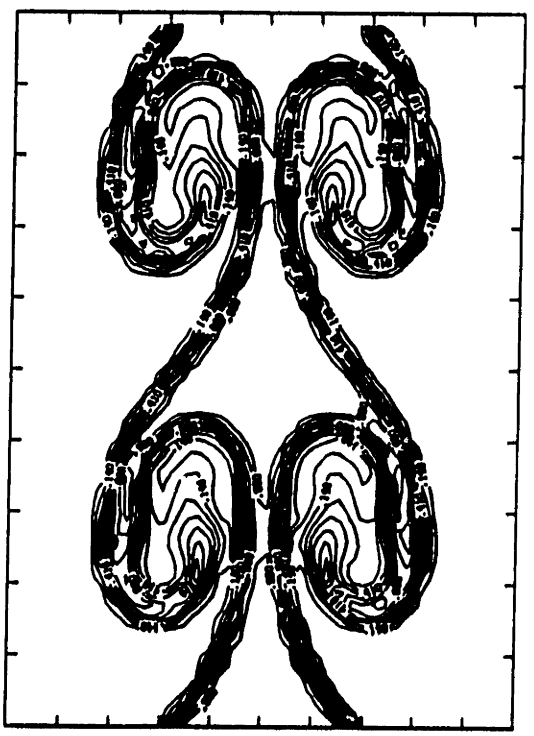

t = 9.8

Figure 66

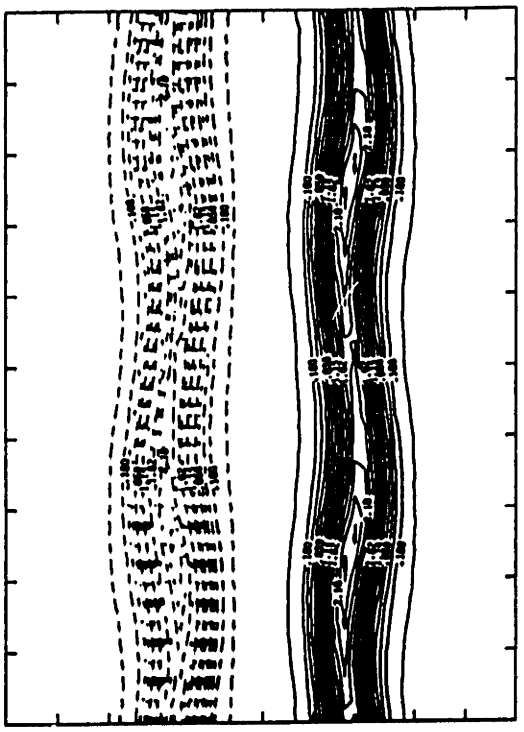

t = 2.5

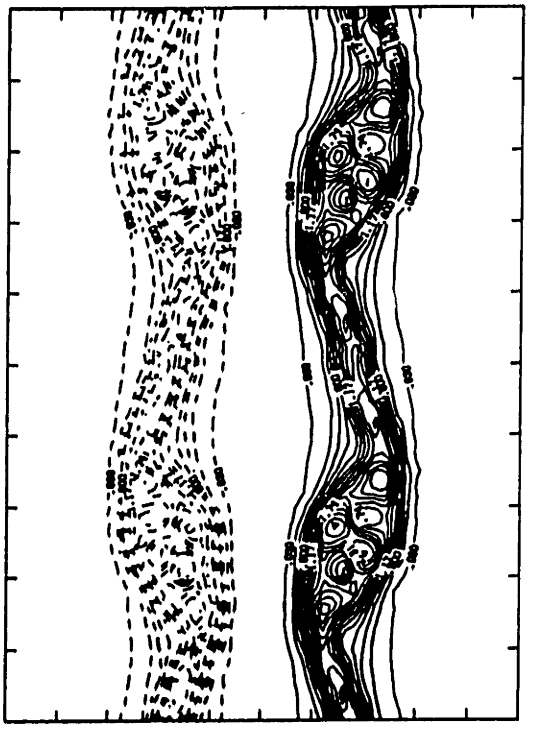

t = 5.0

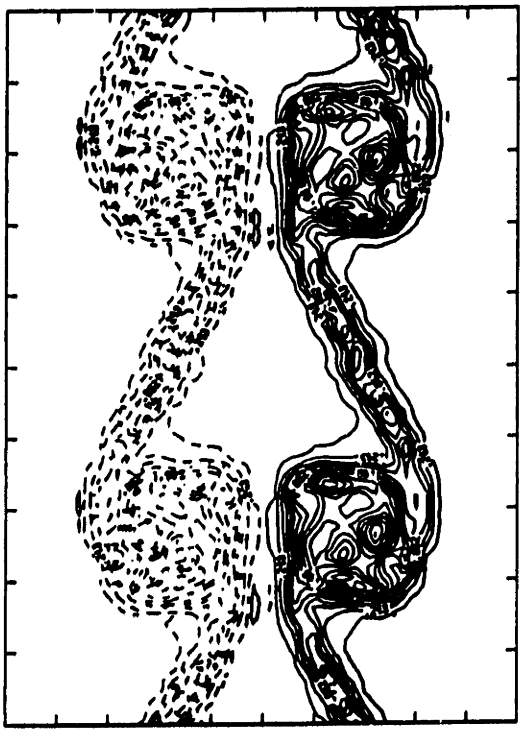

t = 7.8

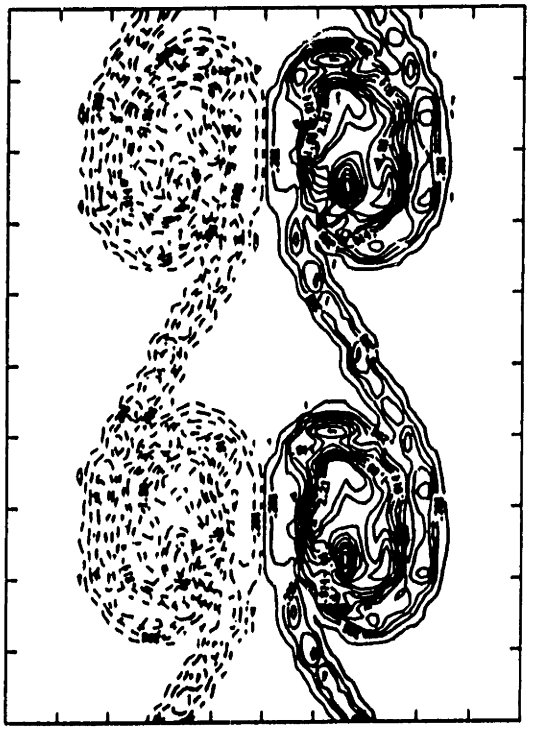

t = 9.8

Figure 67

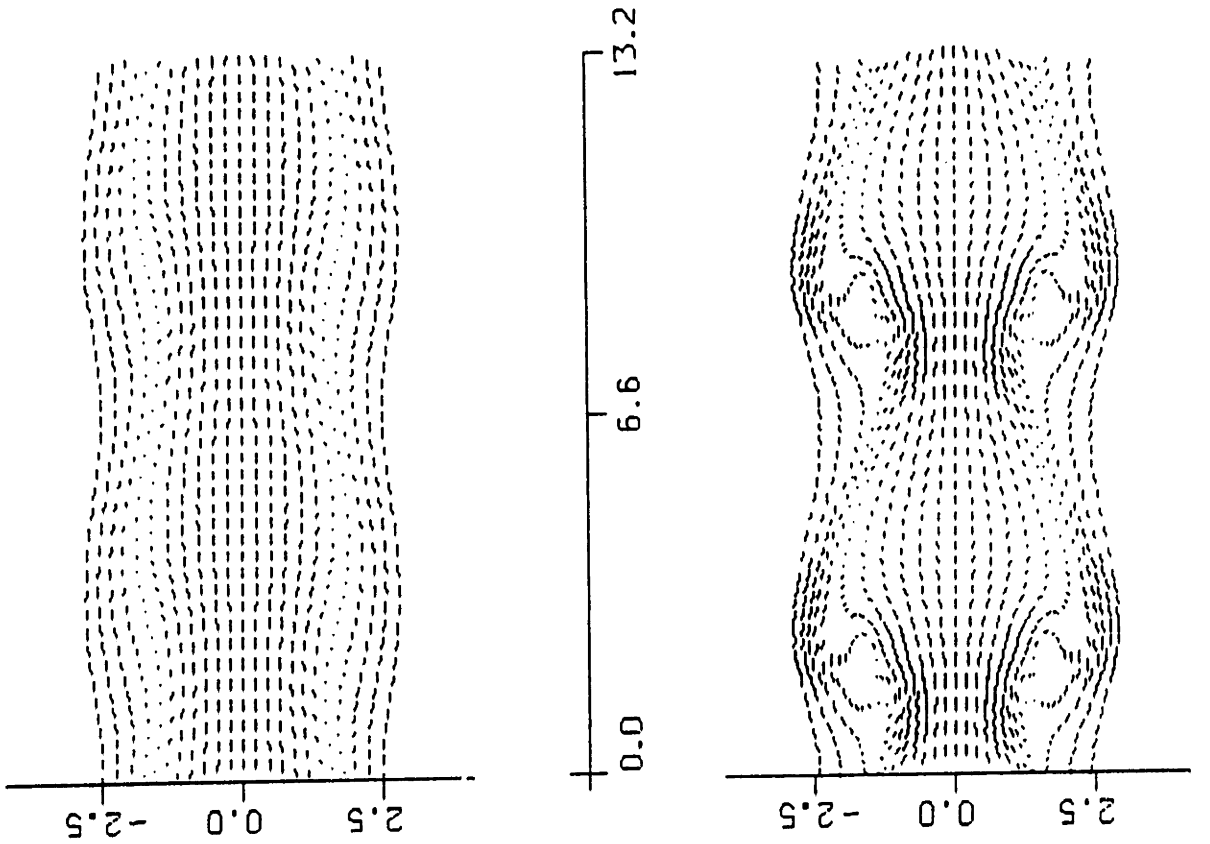

t = 2.5

t = 5.0

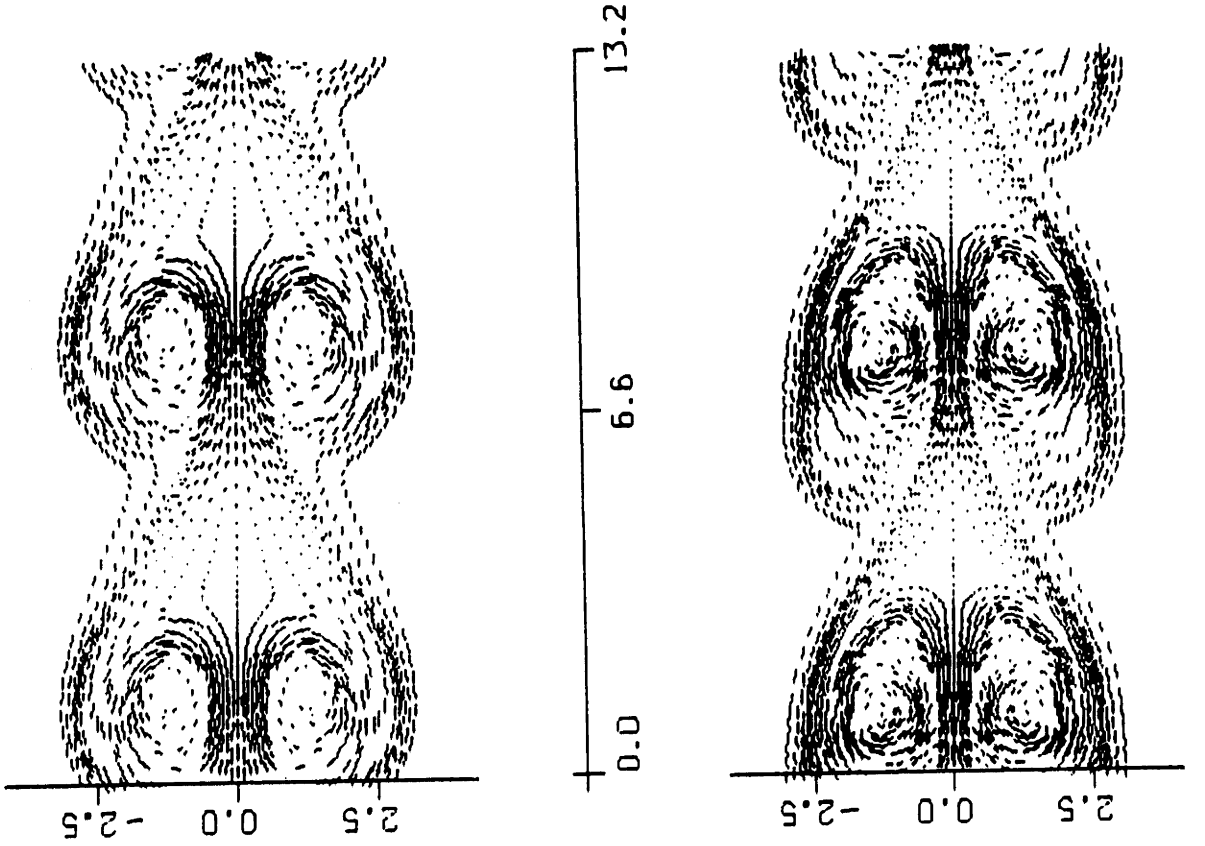

t = 7.8

t = 9.8

Figure 68

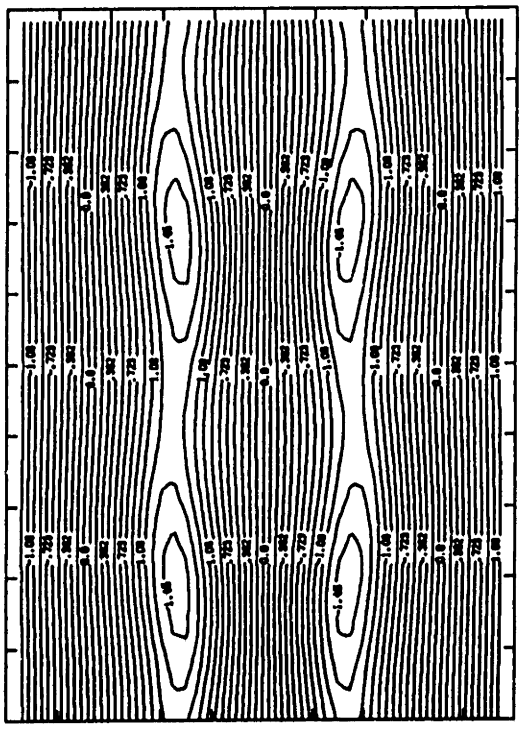

t = 2.5

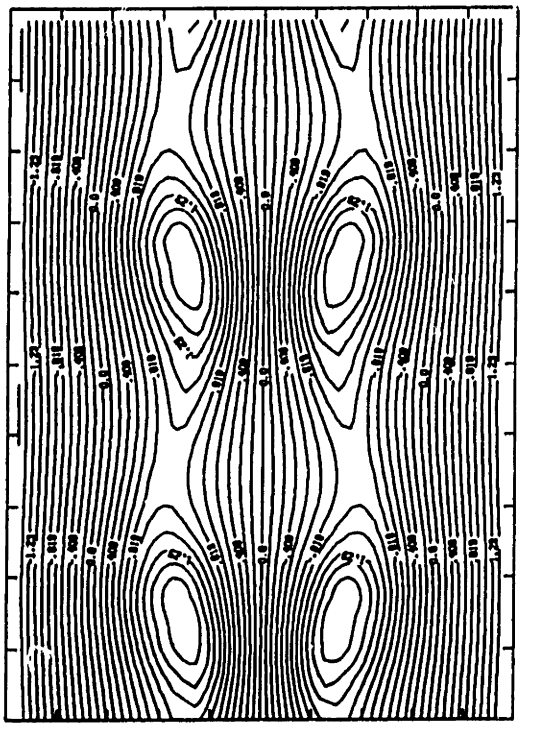

t = 5.0

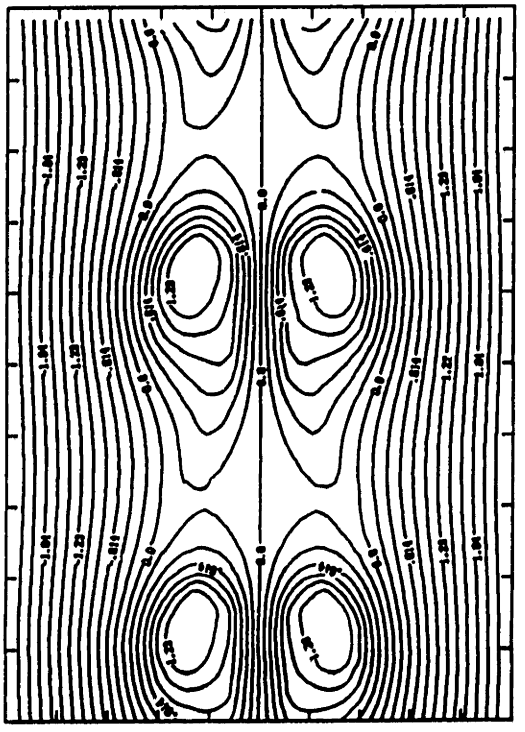

t = 7.8

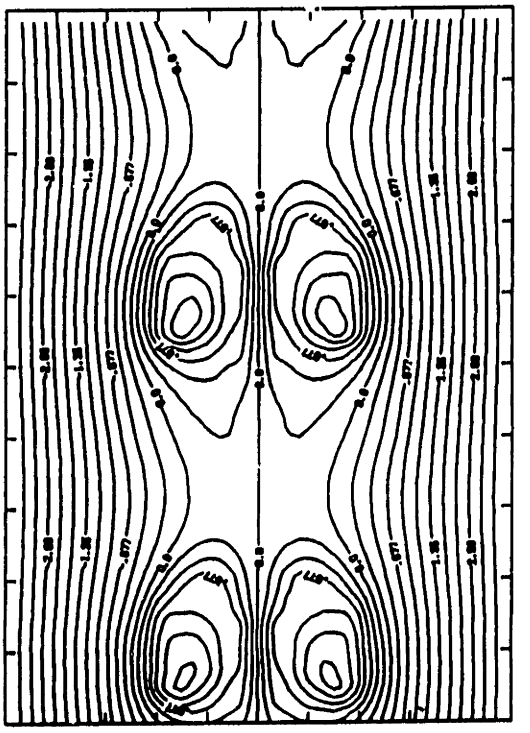

t = 9.8

Figure 69

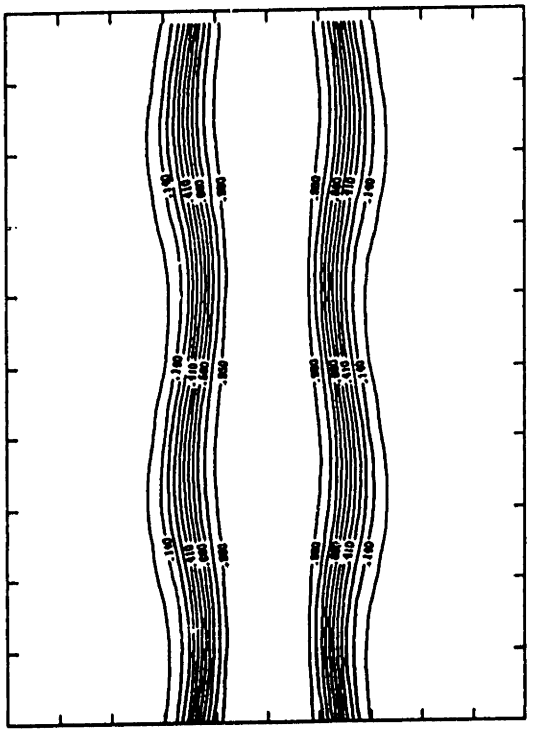

t = 2.5

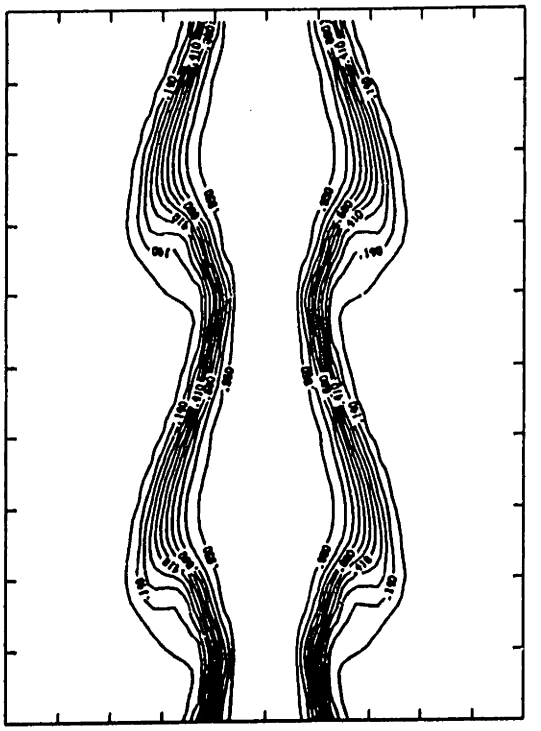

t = 5.0

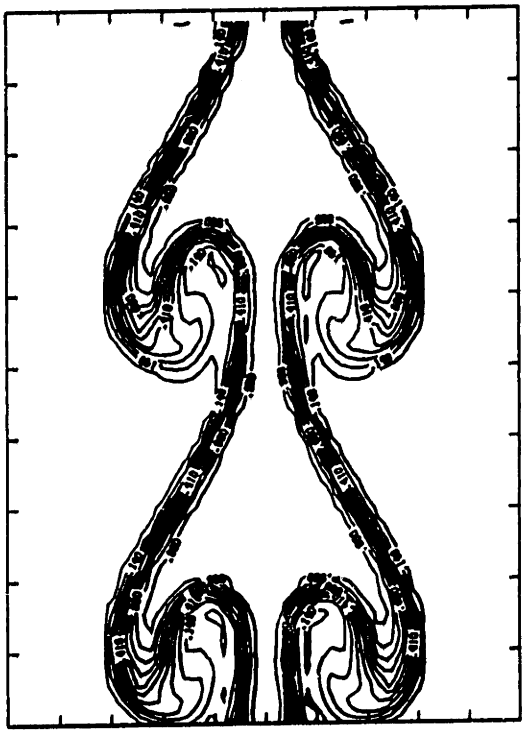

t = 7.8

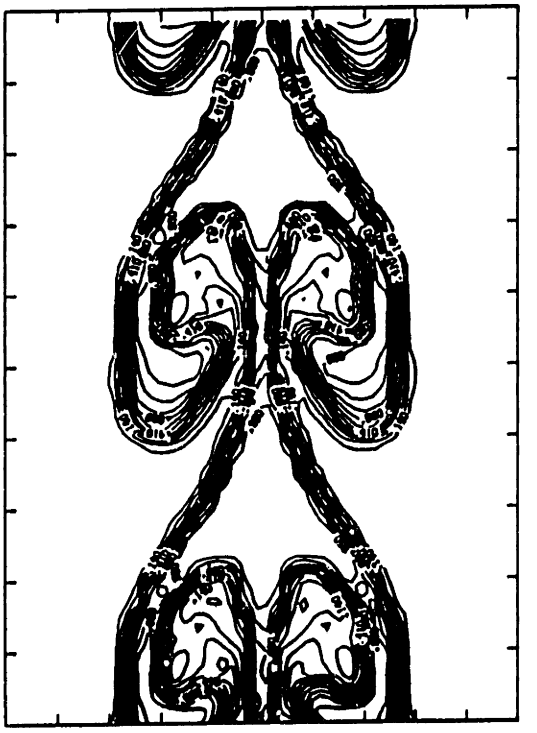

t = 9.8

Figure 70

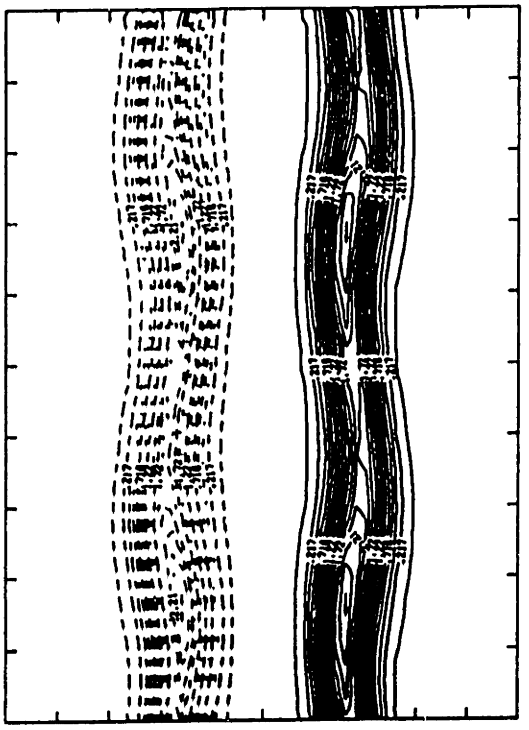

t = 2.5

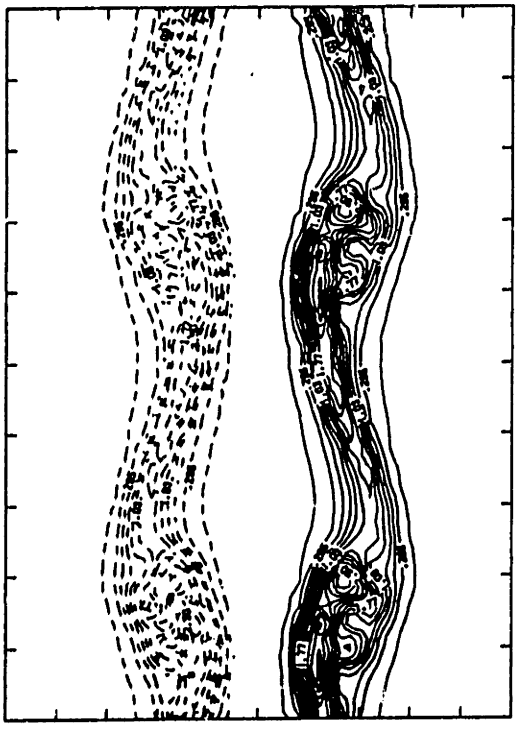

t = 5.0

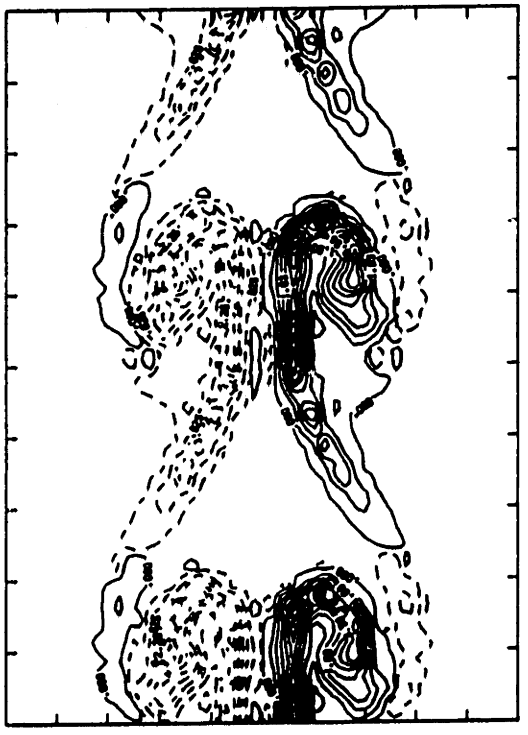

t = 7.8

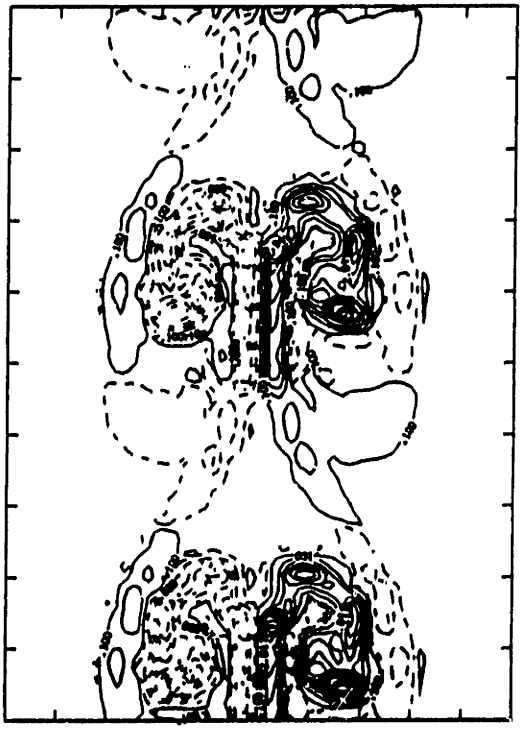

t = 9.8

Figure 71

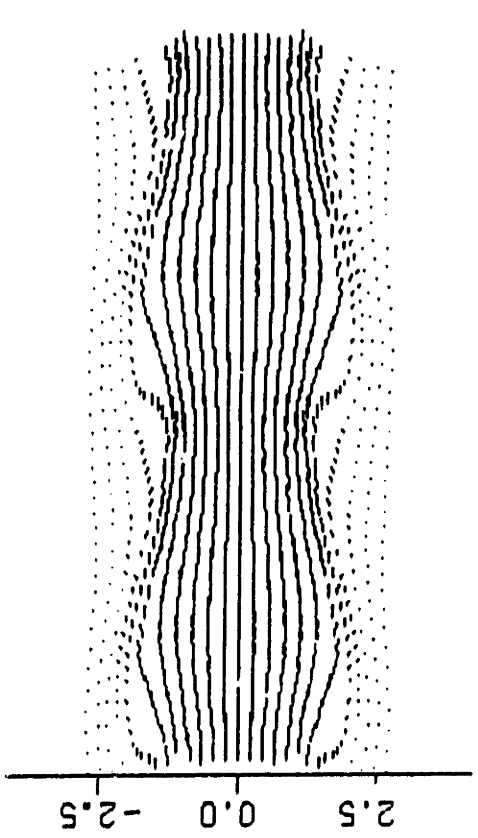

t = 3.75

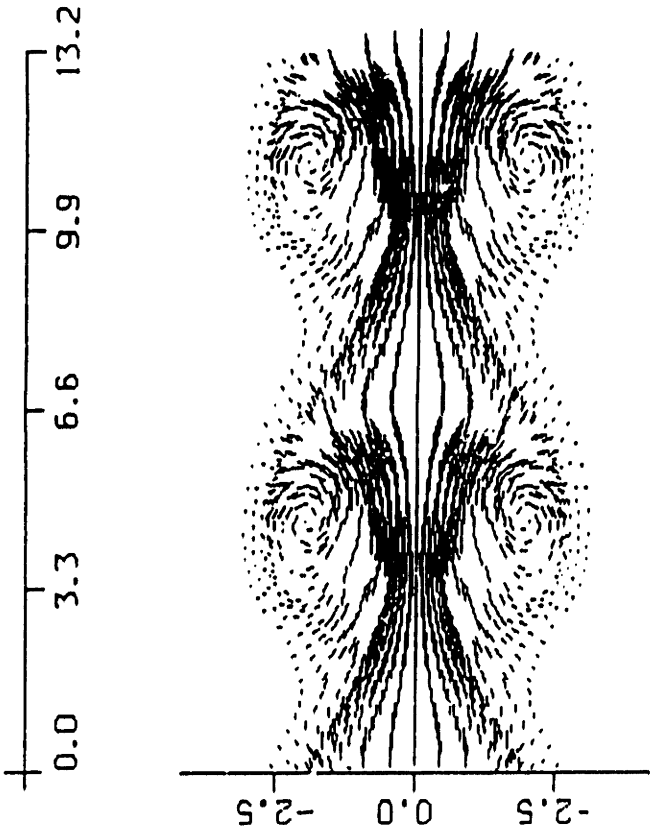

t = 5.37

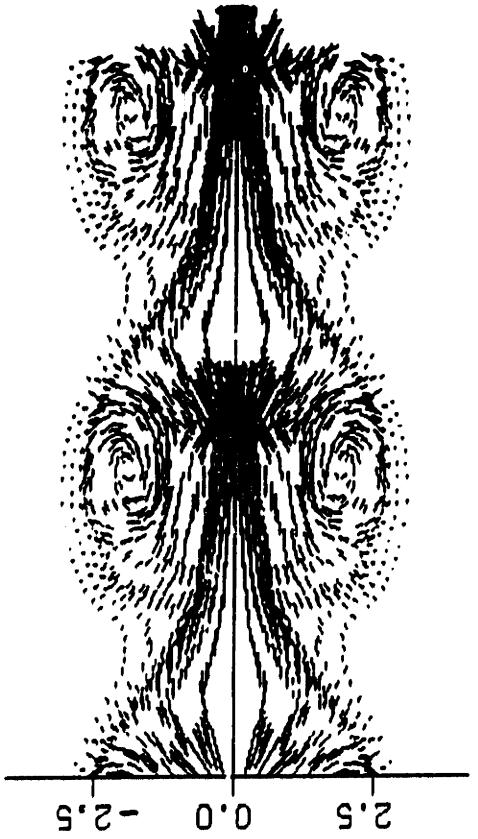

t = 5.75

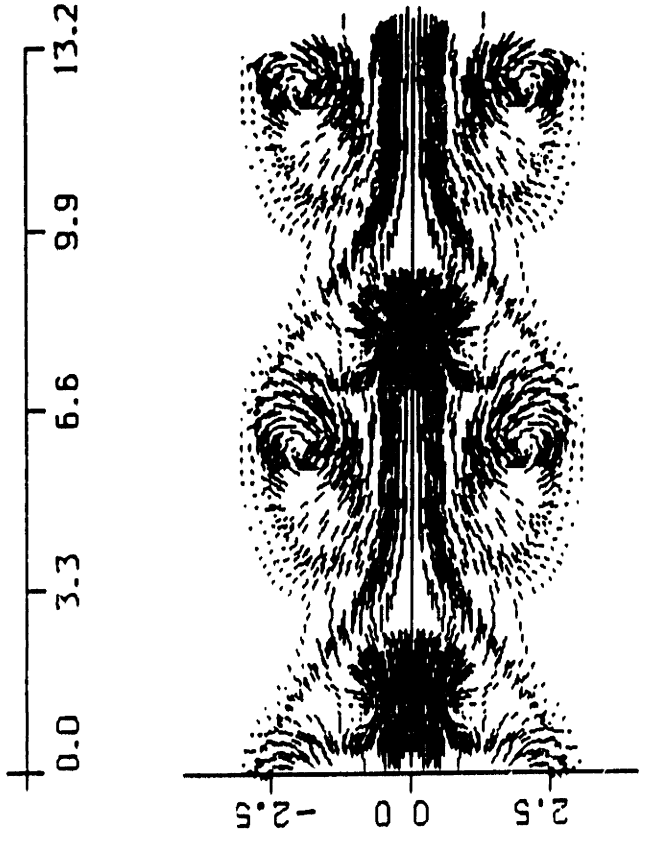

t = 6.0

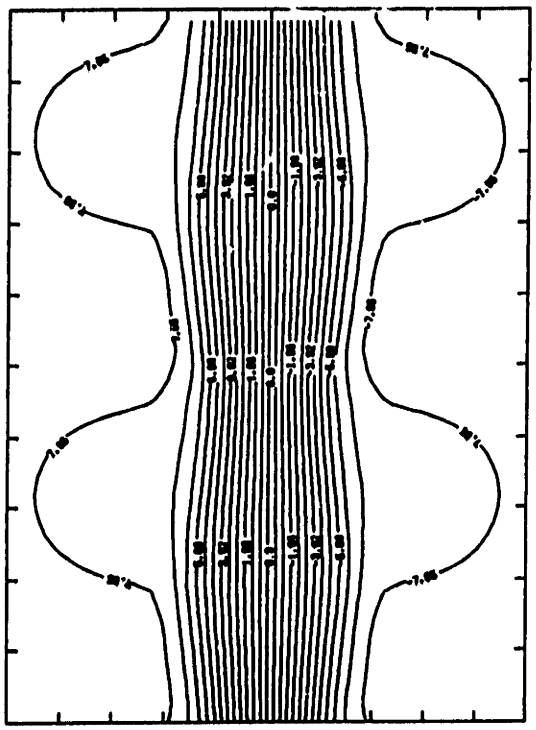

t = 3.75

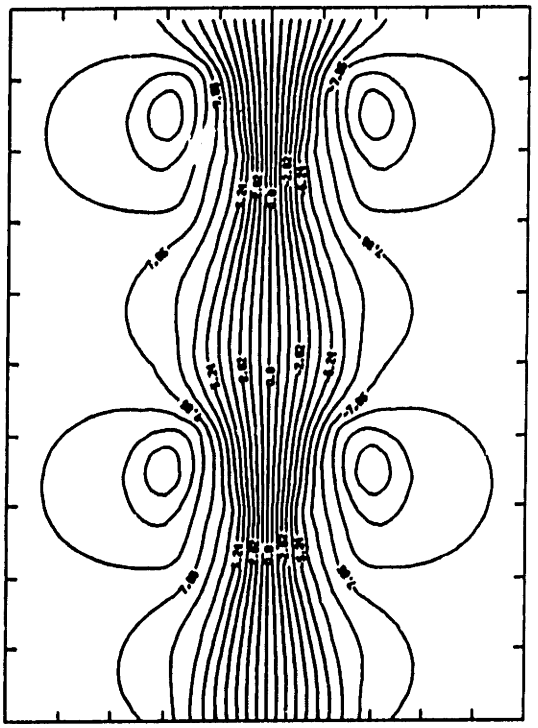

t = 5.37

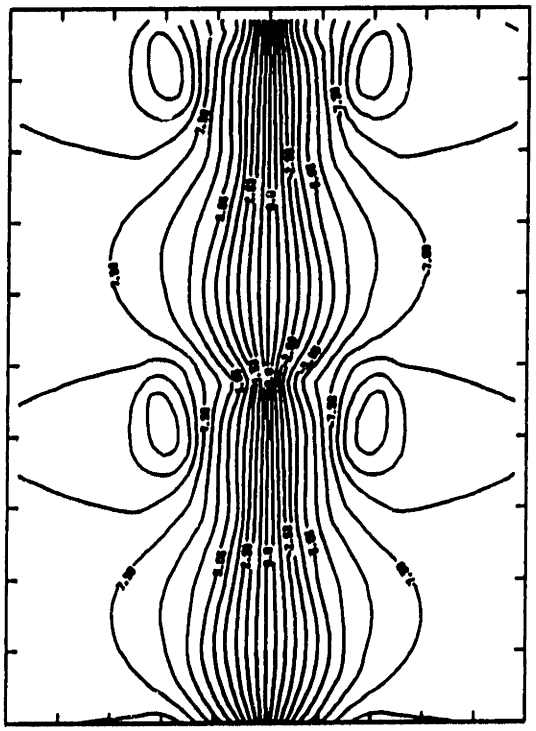

t = 5.75

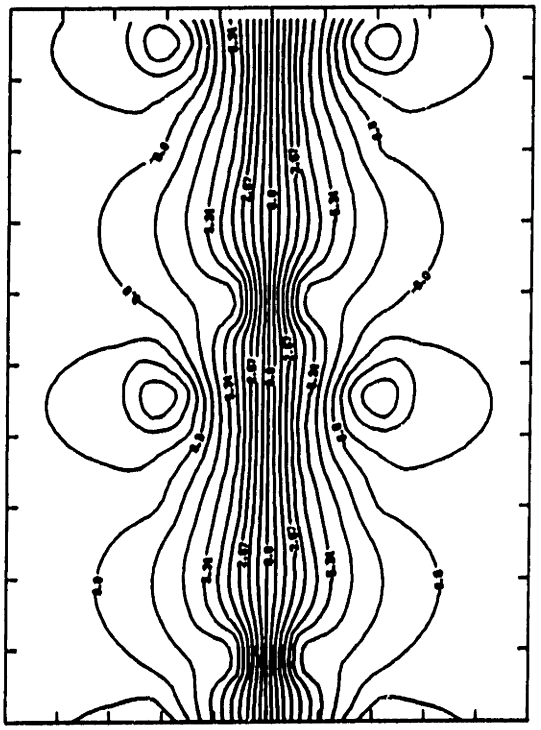

t = 6.0

Figure 73

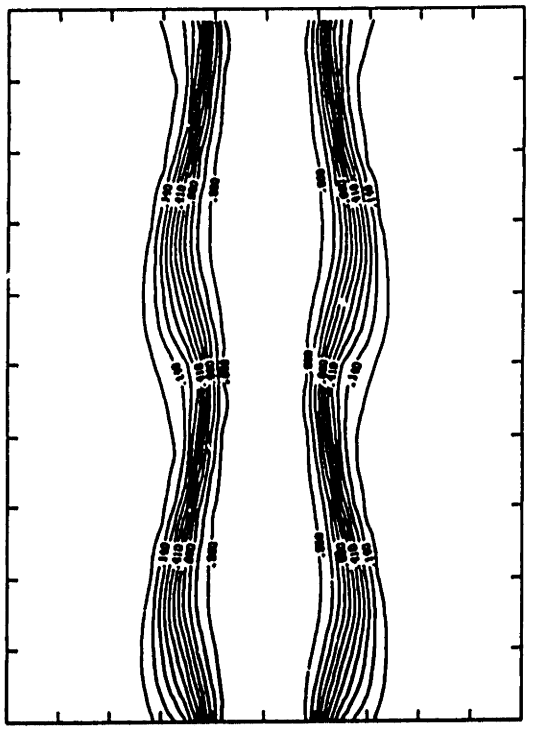

t = 3.75

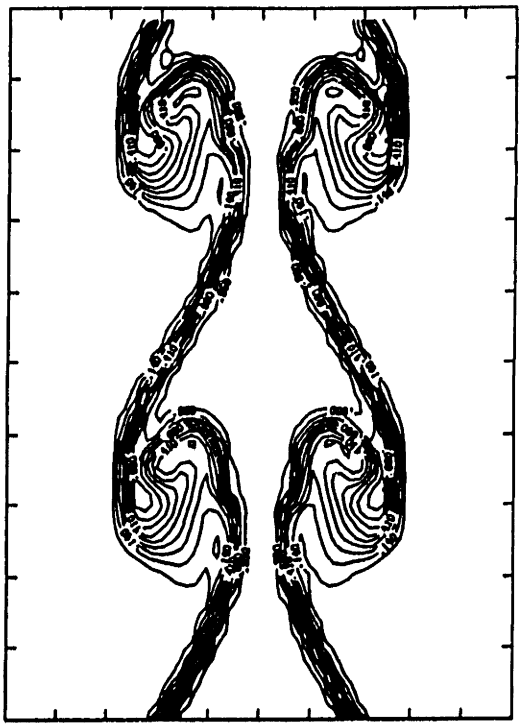

t = 5.37

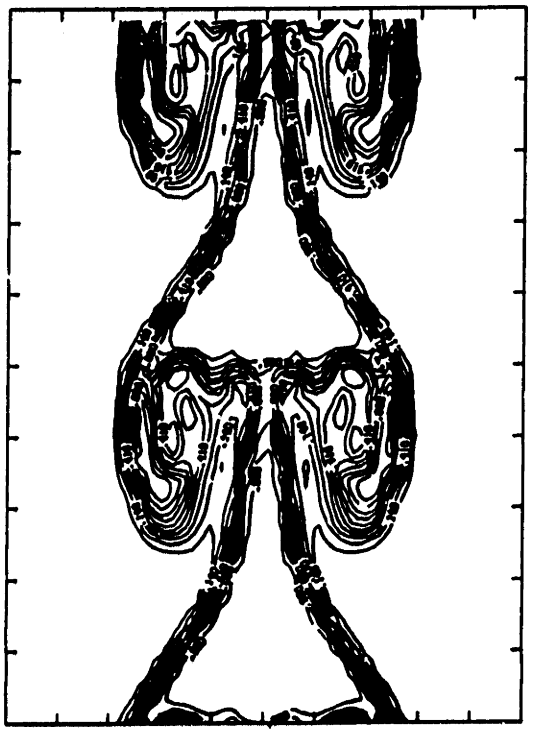

t = 5.75

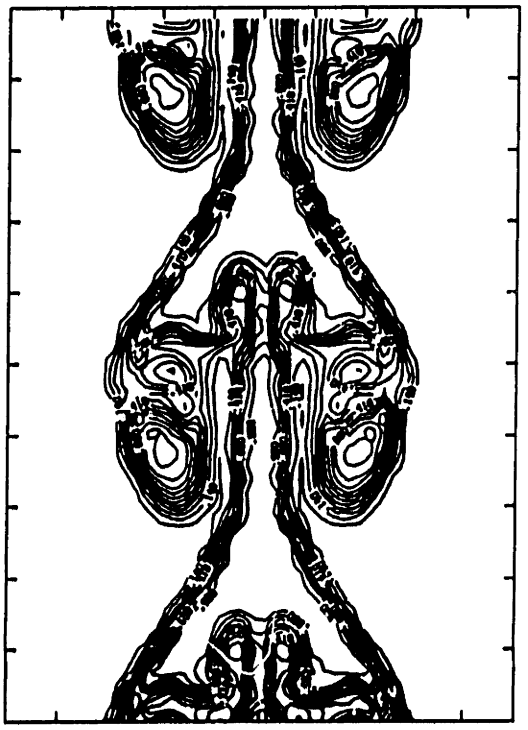

t = 6.0

Figure 74

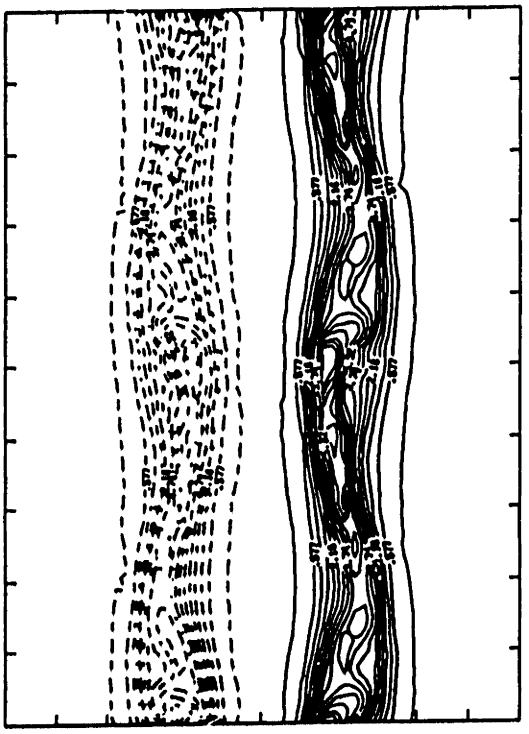

t = 3.75

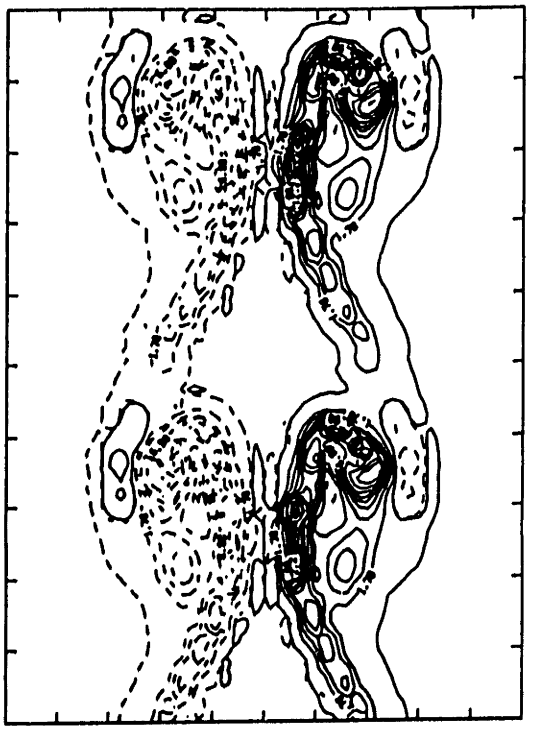

t = 5.37

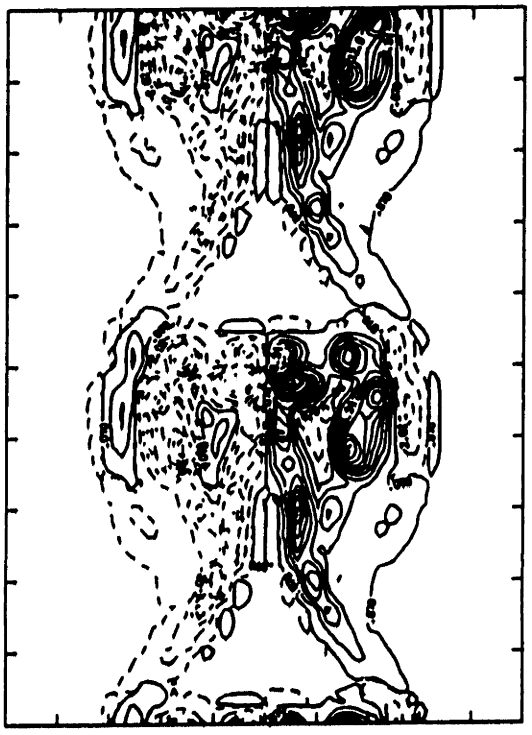

t = 5.75

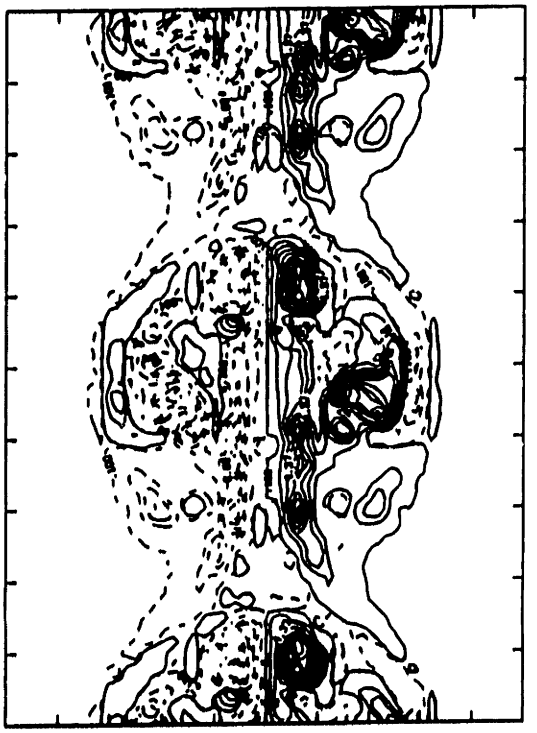

t = 6.0

Figure 75

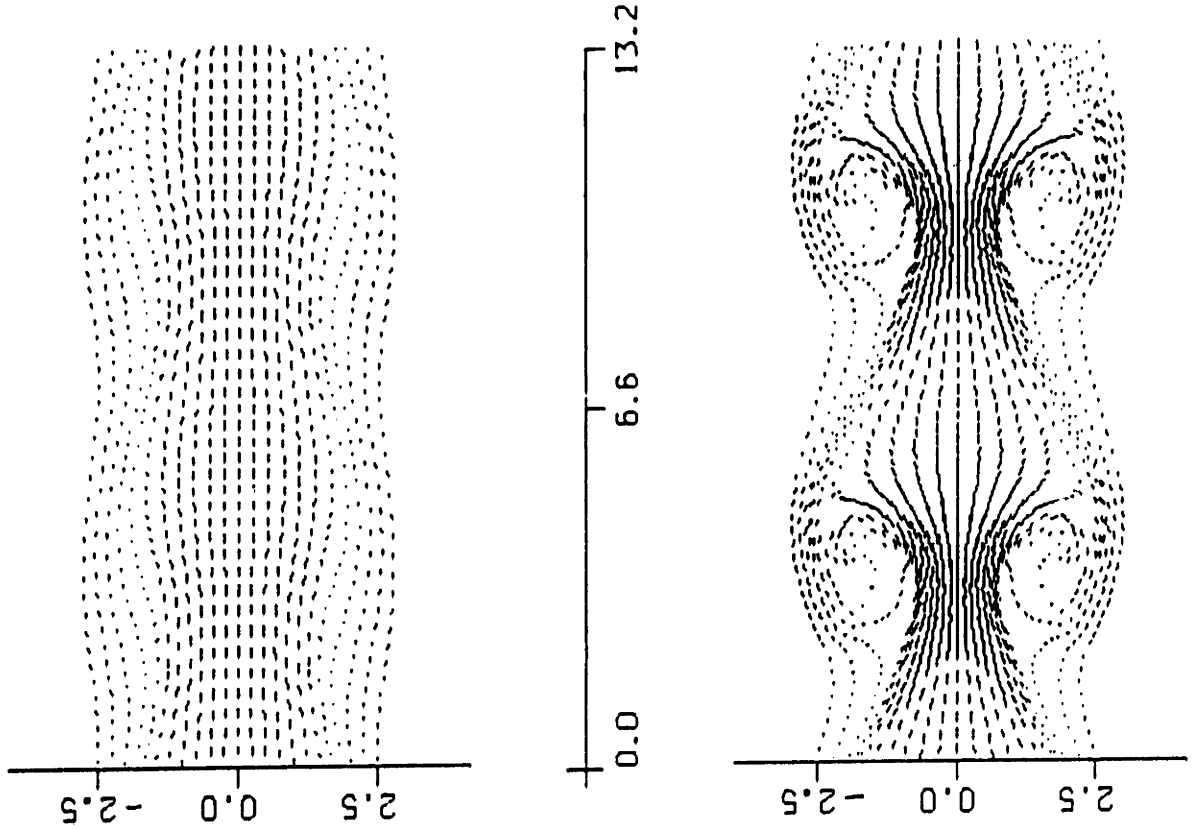

t = 2.5

t = 5.0

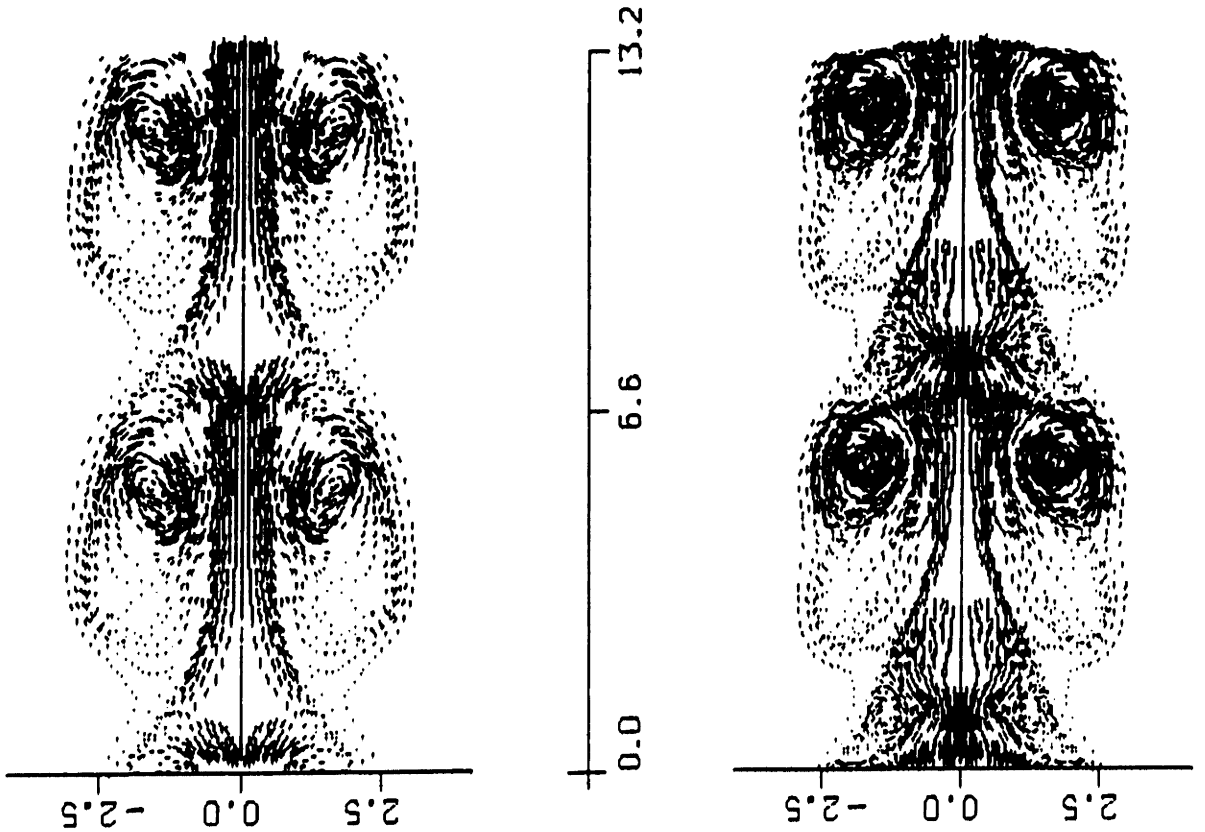

t = 6.8

t = 7.8

Figure 76

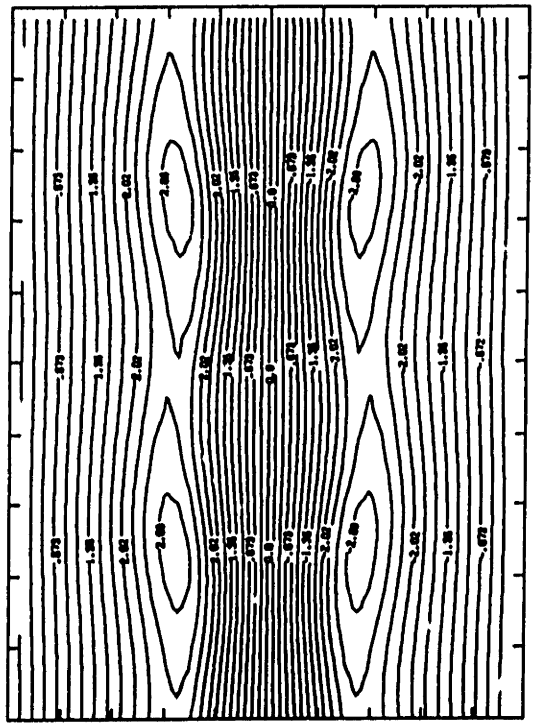

t = 2.5

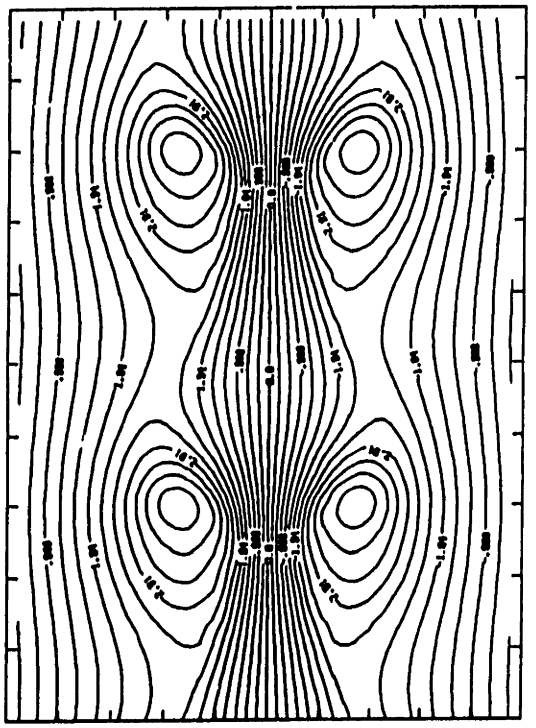

t = 5.0

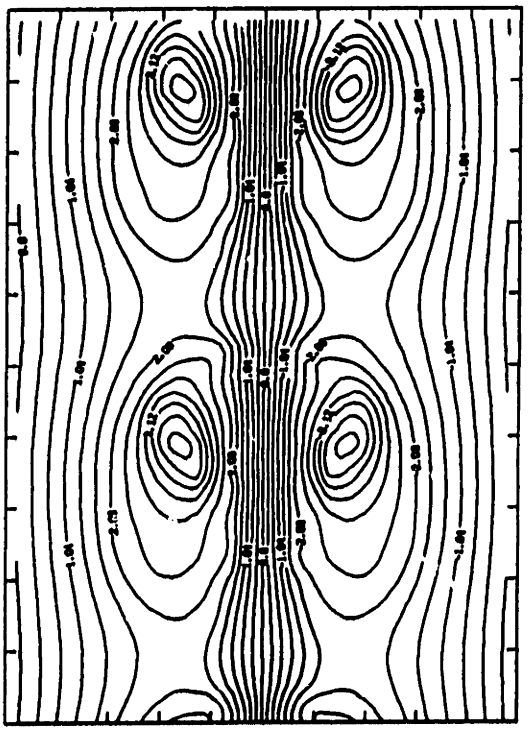

t = 6.8

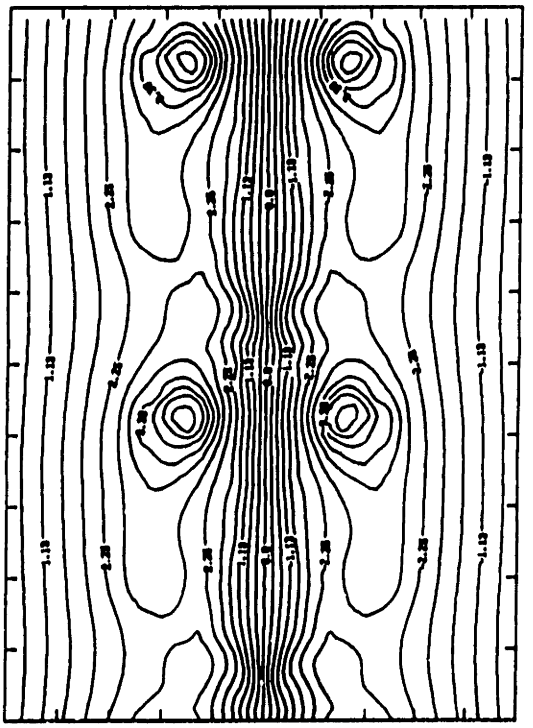

t = 7.8

Figure 77

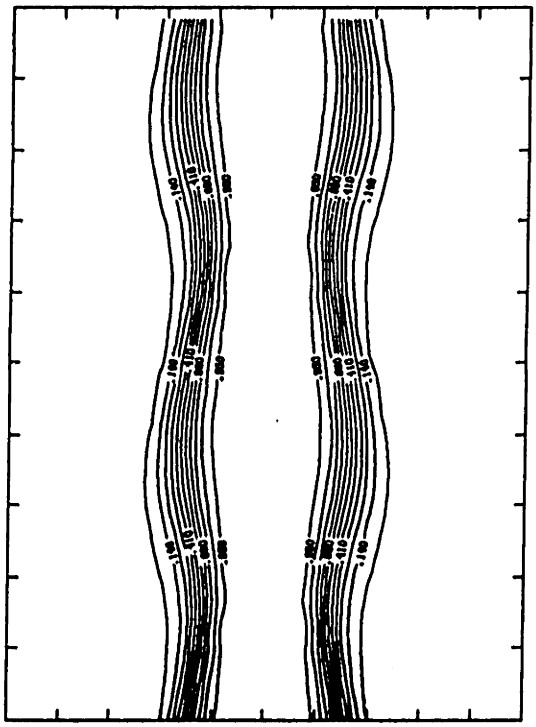

t = 2.5

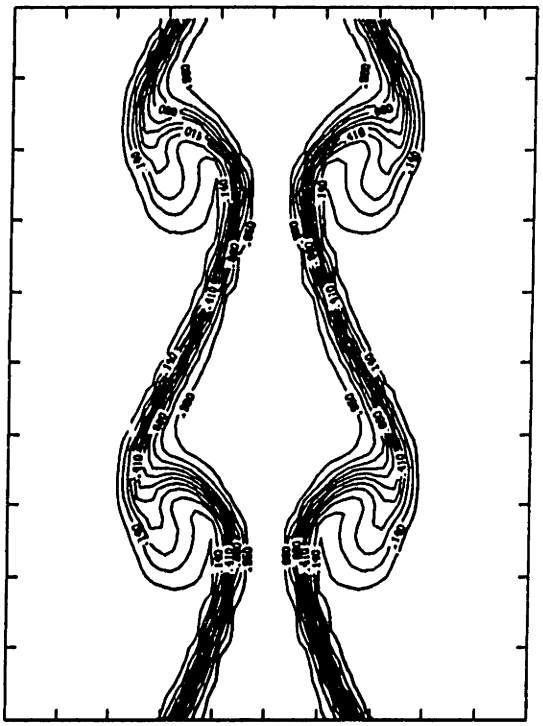

t = 5.0

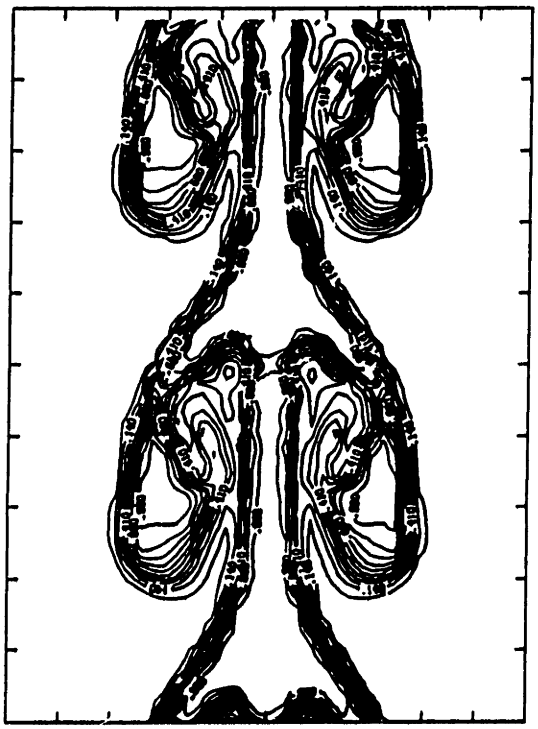

t = 6.8

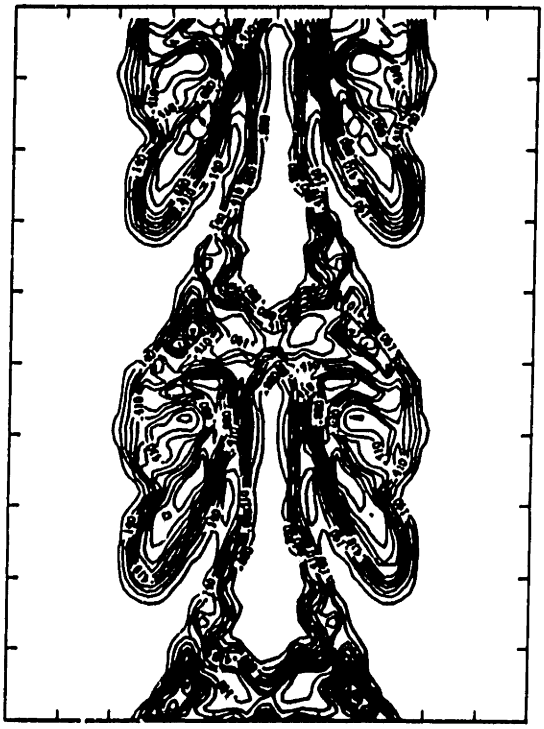

t = 7.8

Figure 78

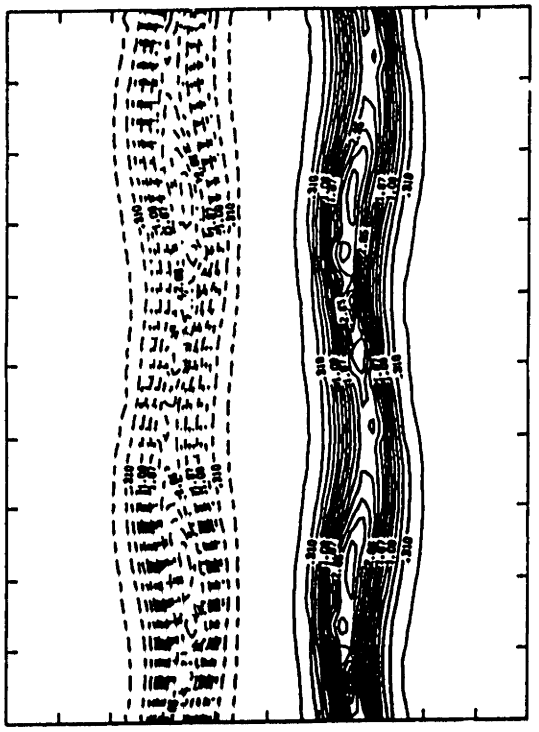

t = 2.5

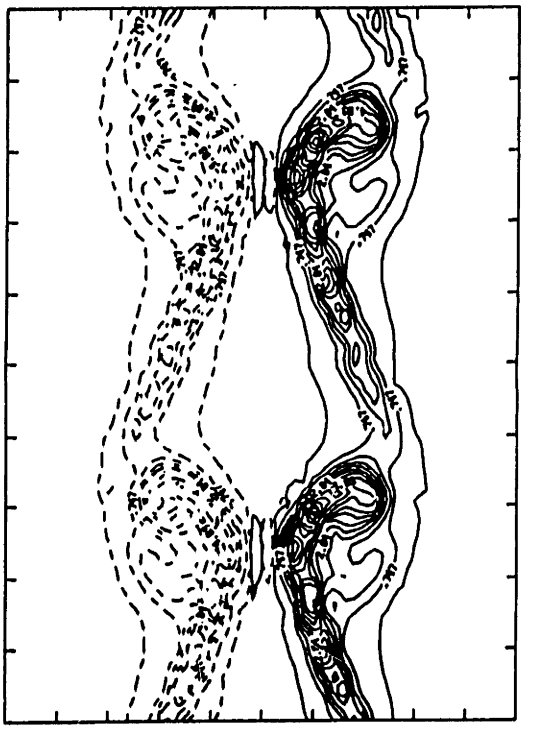

t = 5.0

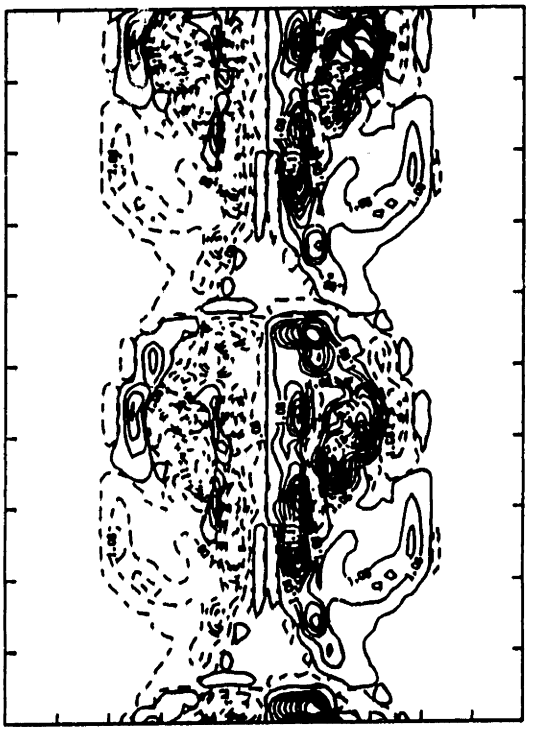

t = 6.8

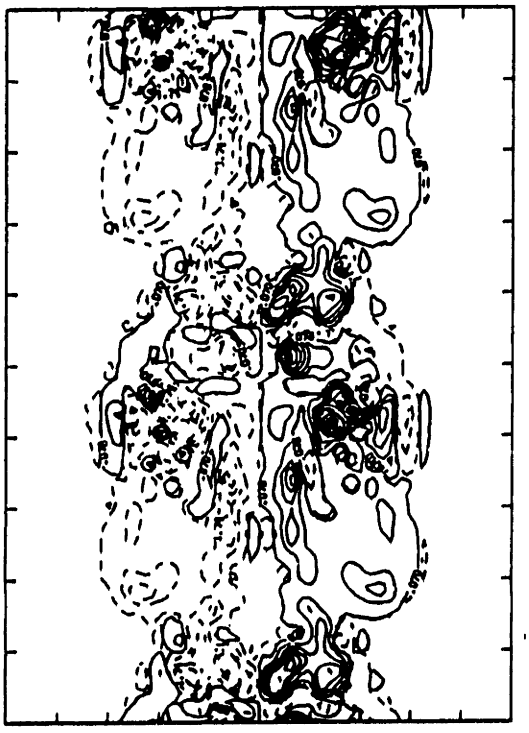

t = 7.8

Figure 79

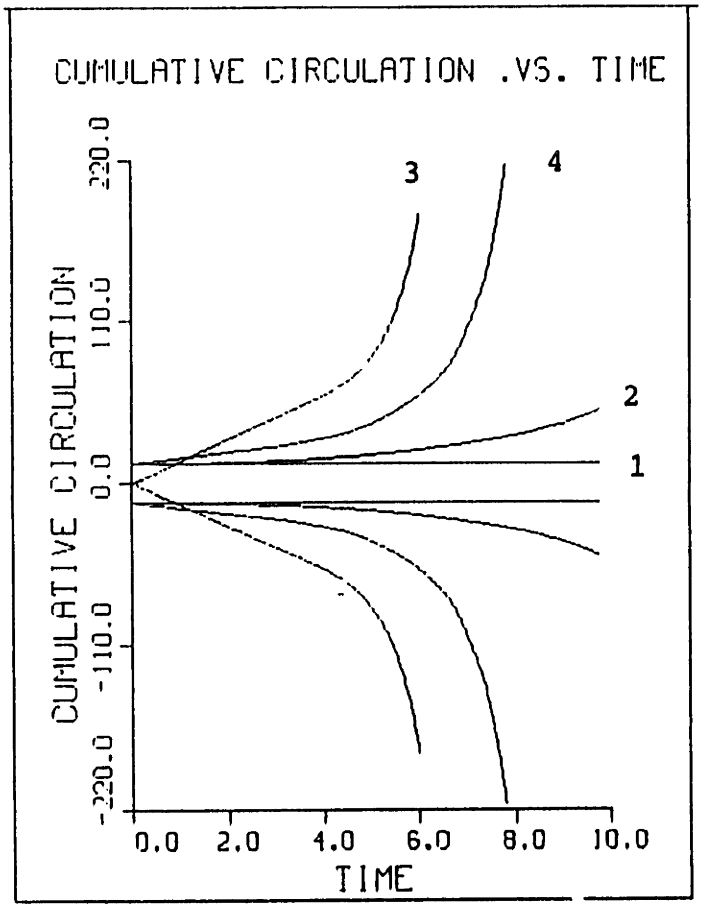
CUMULATIVE CIRCULATION .VS. TIME
CUMULATIVE CIRCULATION
220.0
110.0
0.0
-110.0
-220.0
3
4
2
1
0.0
2.0
4.0
6.0
8.0
10.0
TIME

(a)

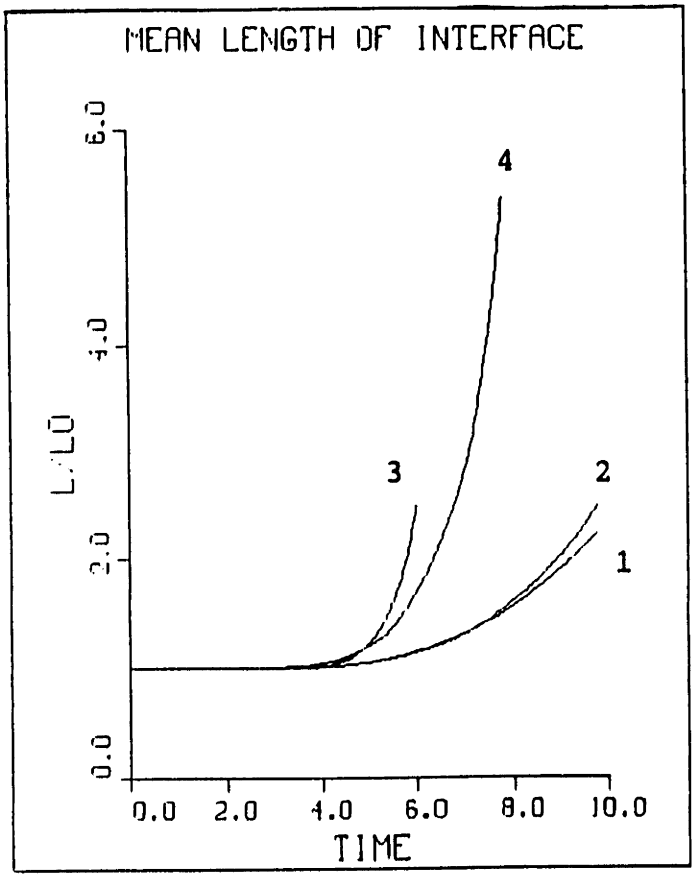
MEAN LENGTH OF INTERFACE
6.0
4.0
2.0
0.0
4
3
2
1
0.0
2.0
4.0
6.0
8.0
10.0
TIME

(b)

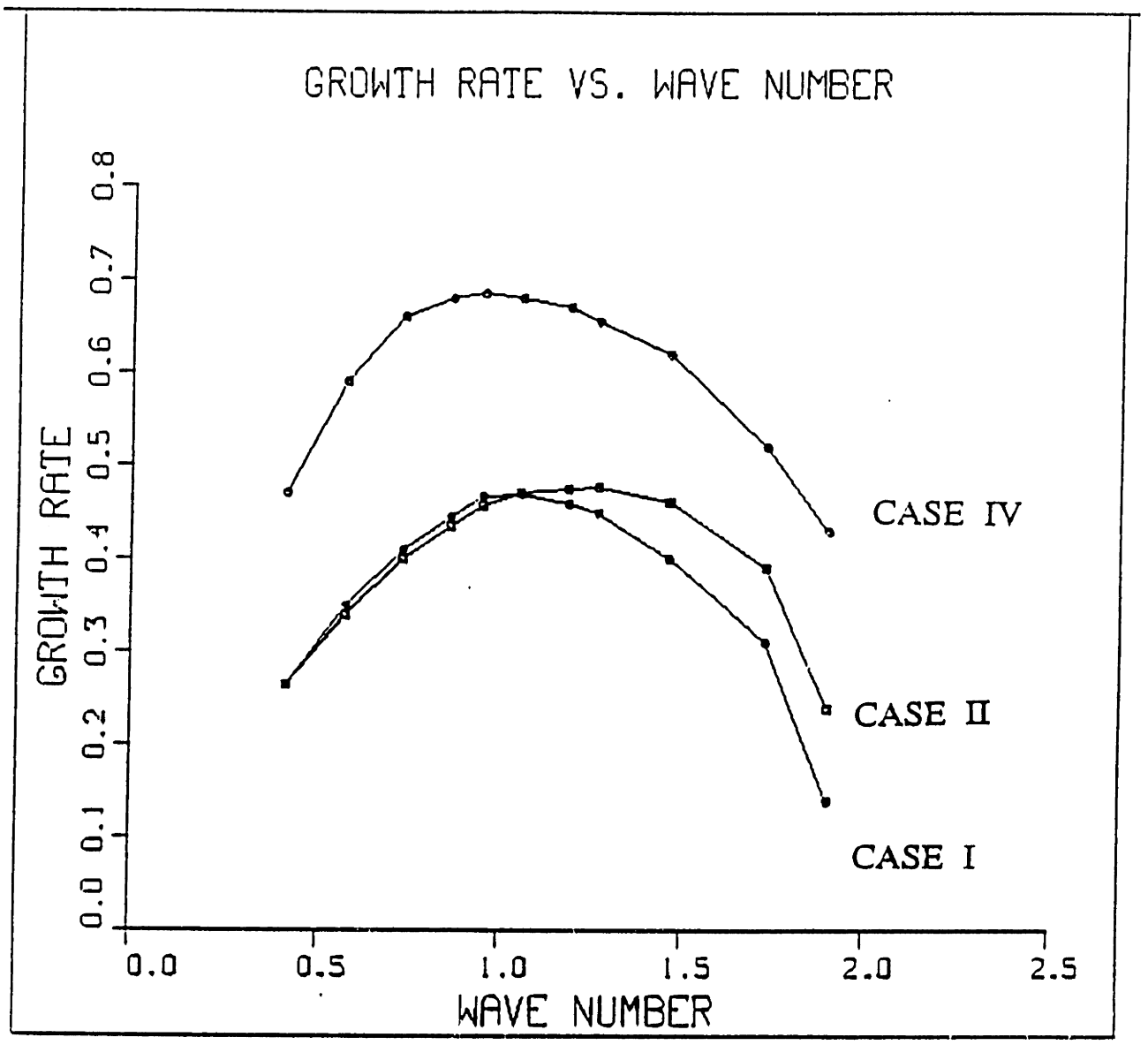
GROWTH RATE VS. WAVE NUMBER
GROWTH RATE
0.0
0.1
0.2
0.3
0.4
0.5
0.6
0.7
0.8
0.0
0.5
1.0
1.5
2.0
2.5
WAVE NUMBER
CASE IV
CASE II
CASE I

Figure 81

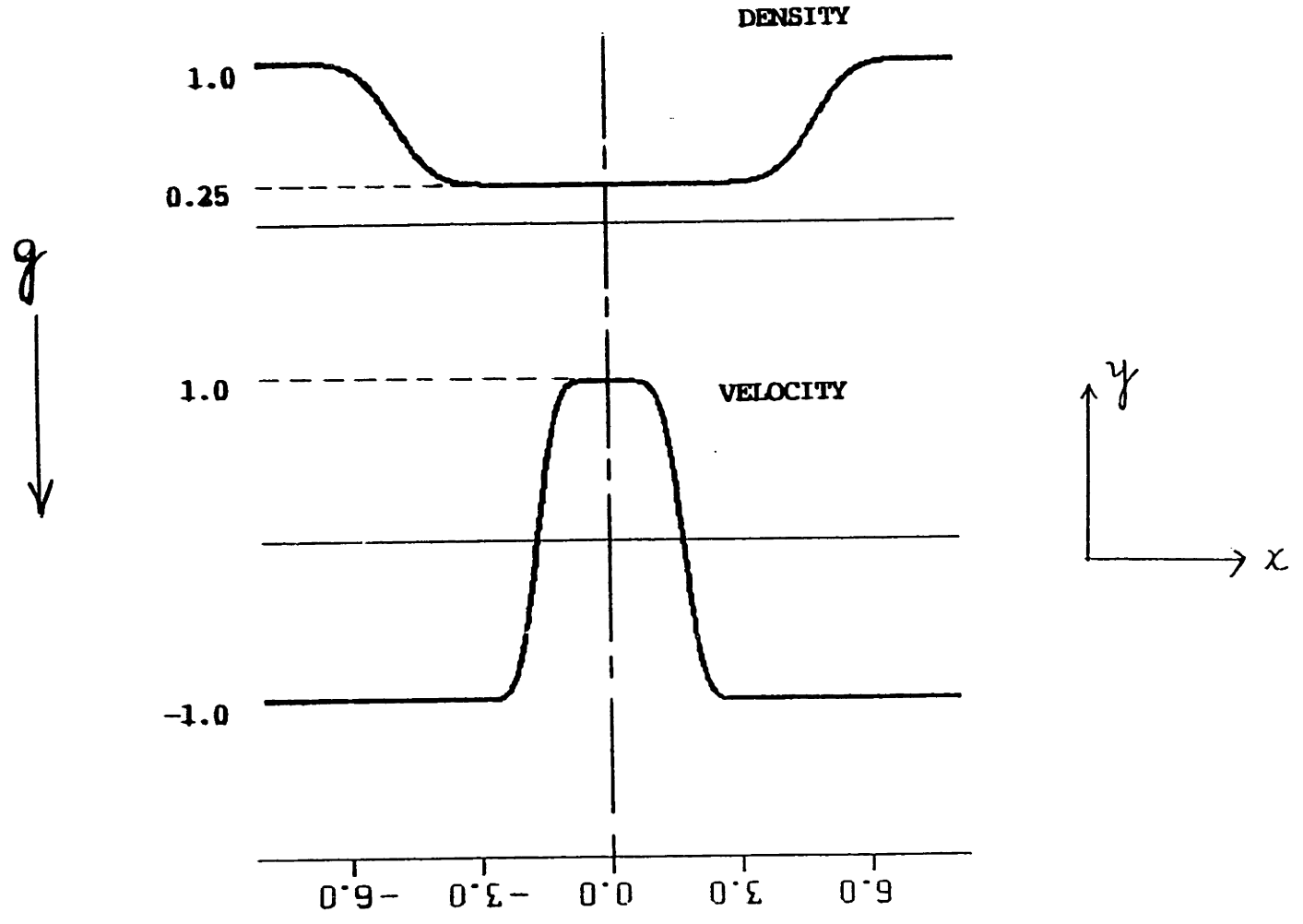

Figure 82

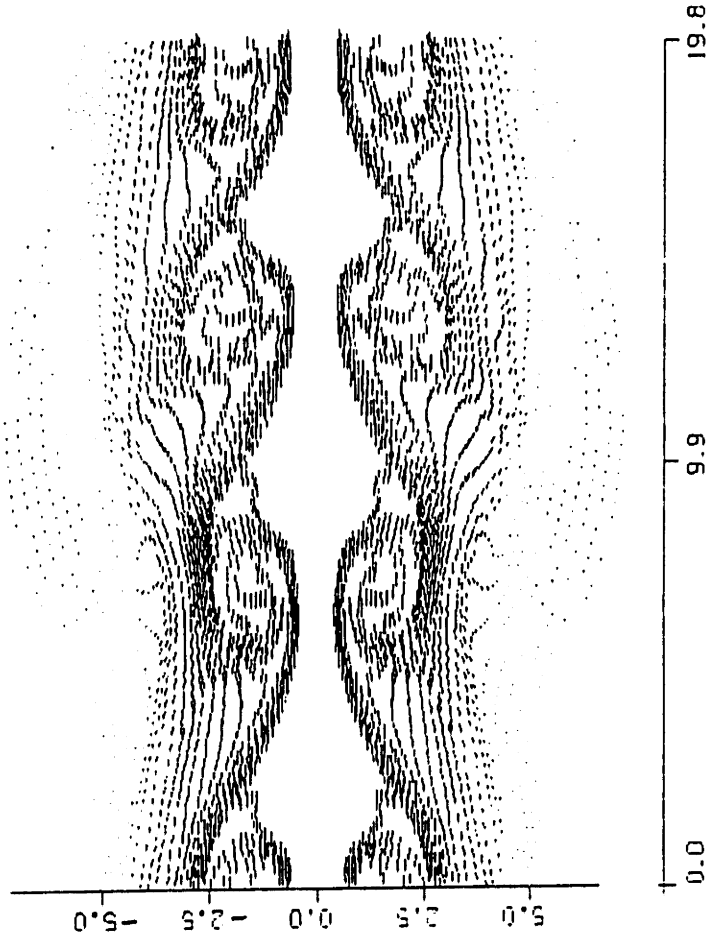

t = 5.0

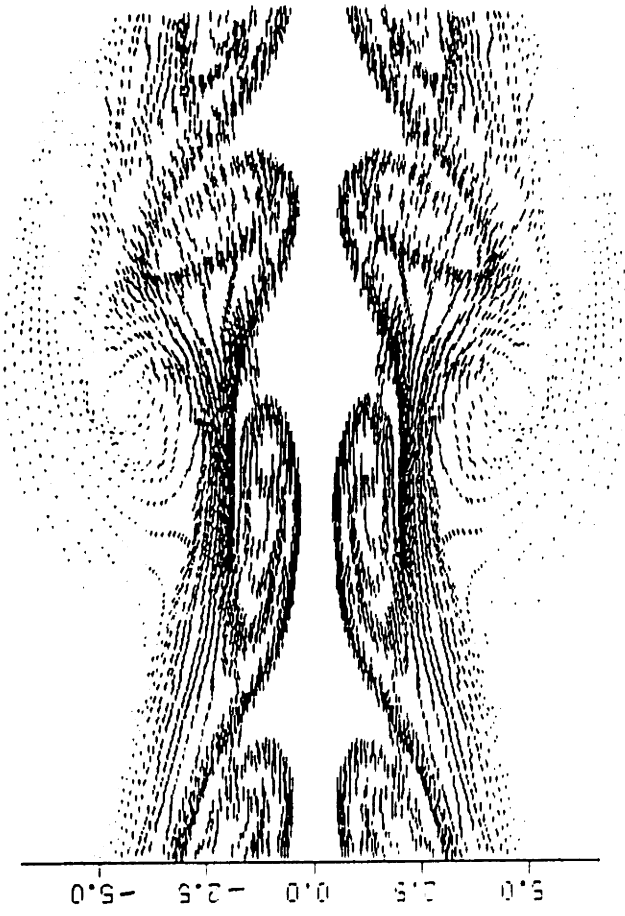

t = 6.07

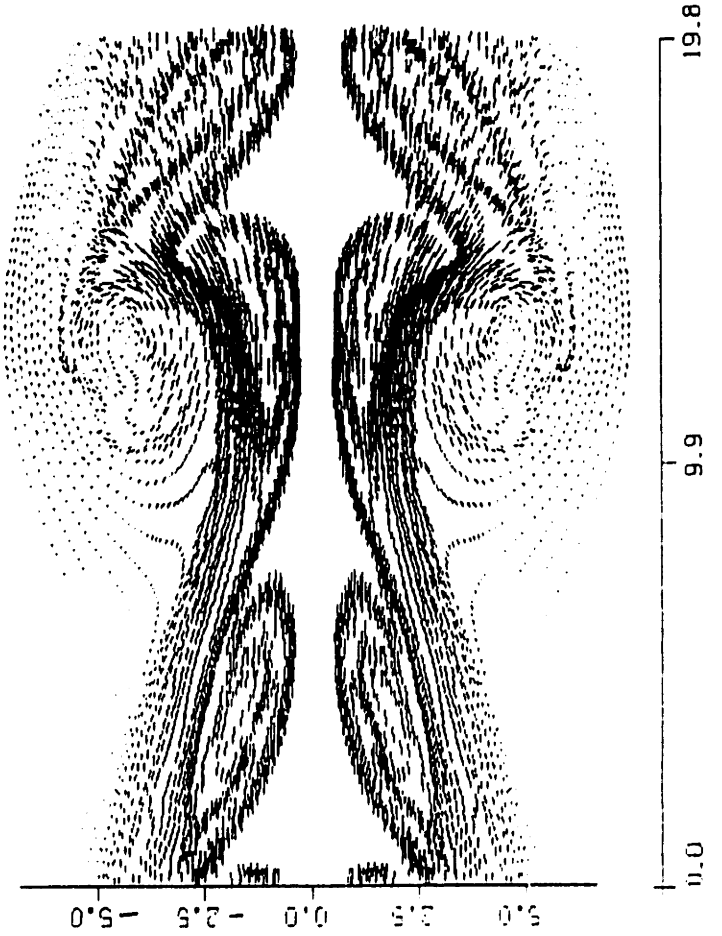

t = 6.57

Figure 83

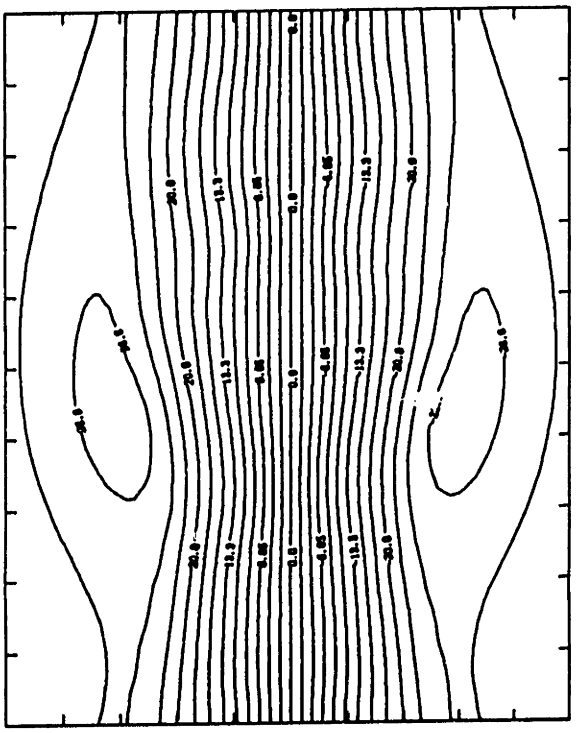

t = 5.0

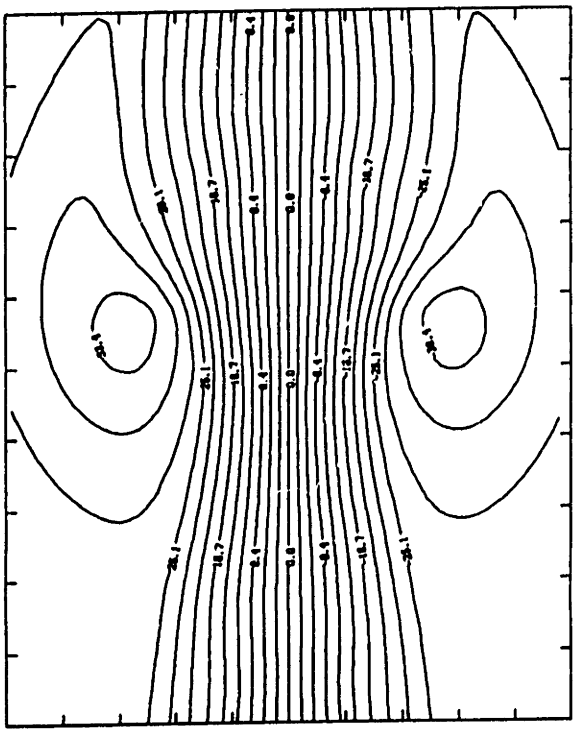

t = 6.07

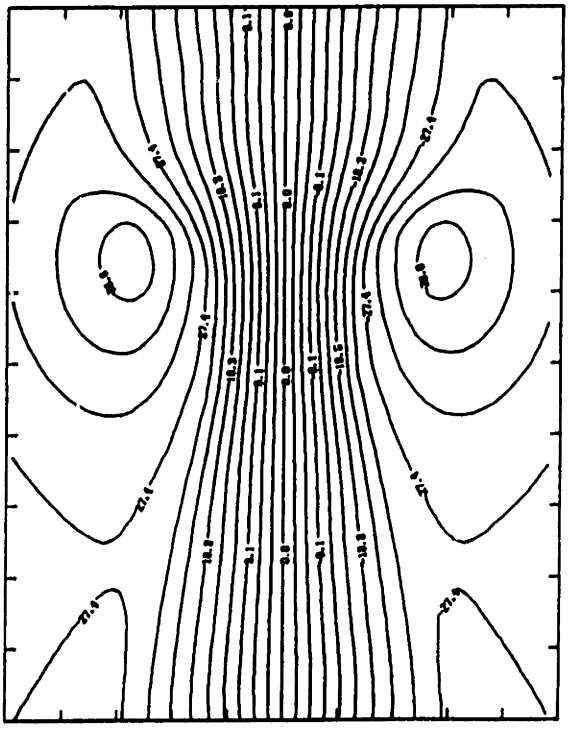

t = 6.57

Figure 84

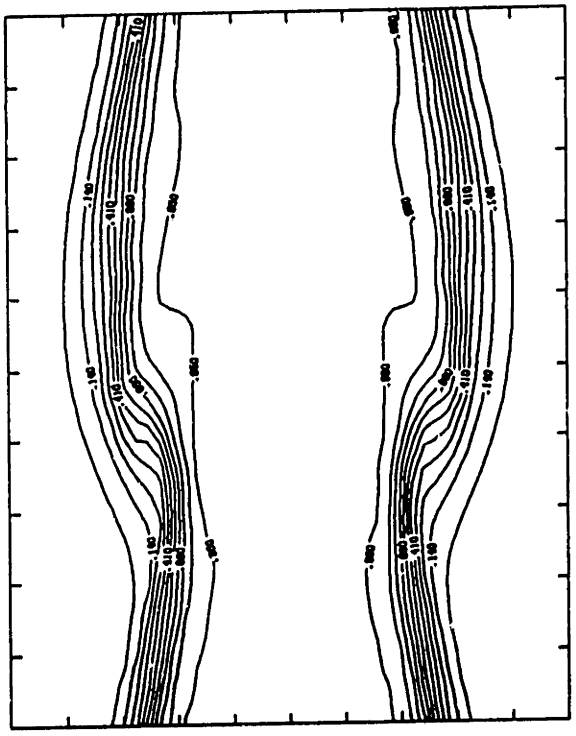

t = 5.0

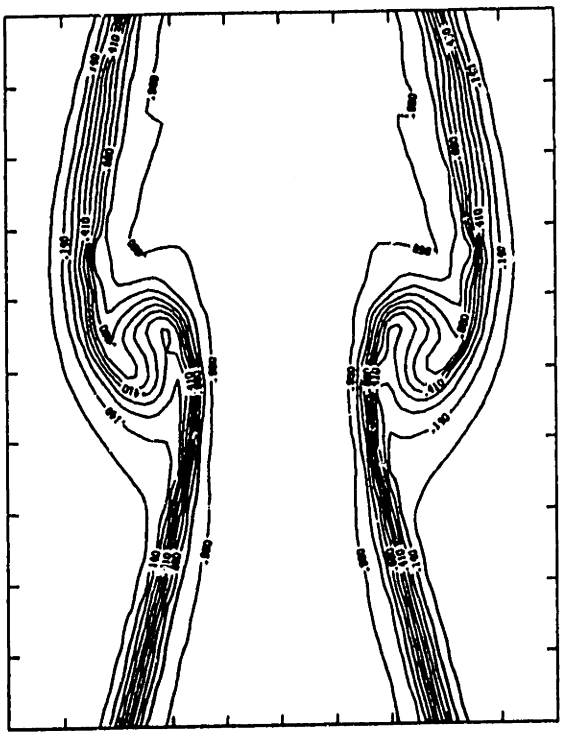

t = 6.07

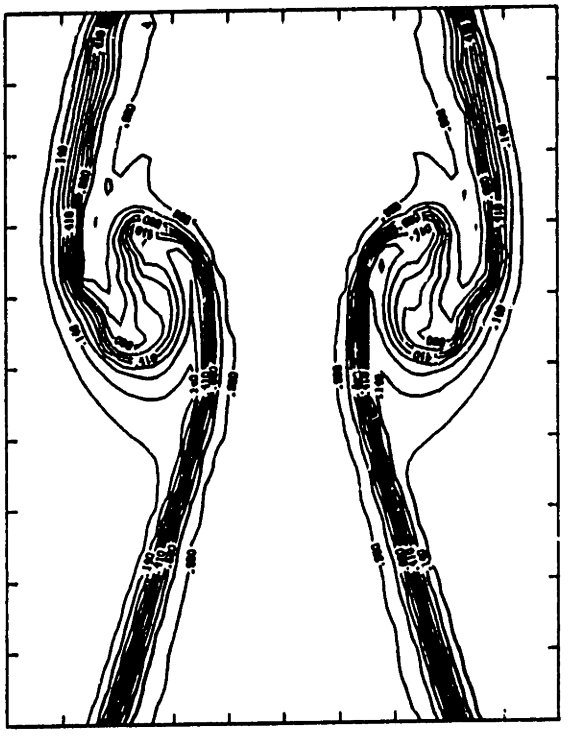

t = 6.57

Figure 85

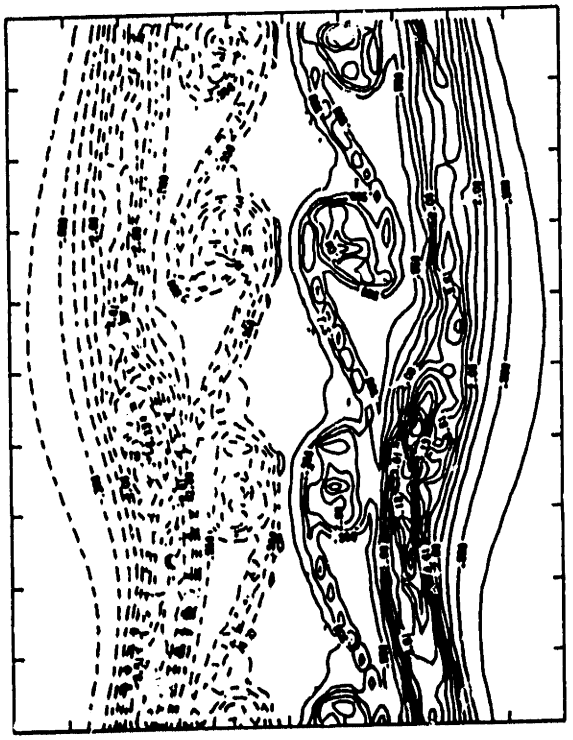

t = 5.0

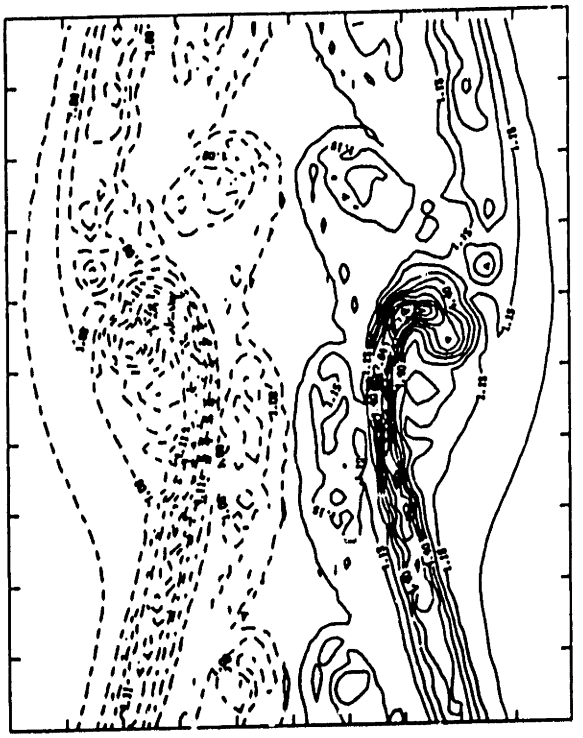

t = 6.07

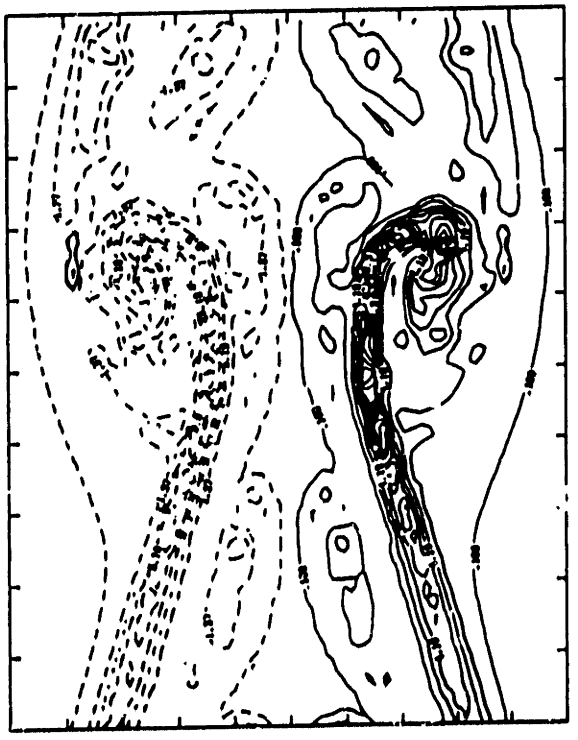

t = 6.57

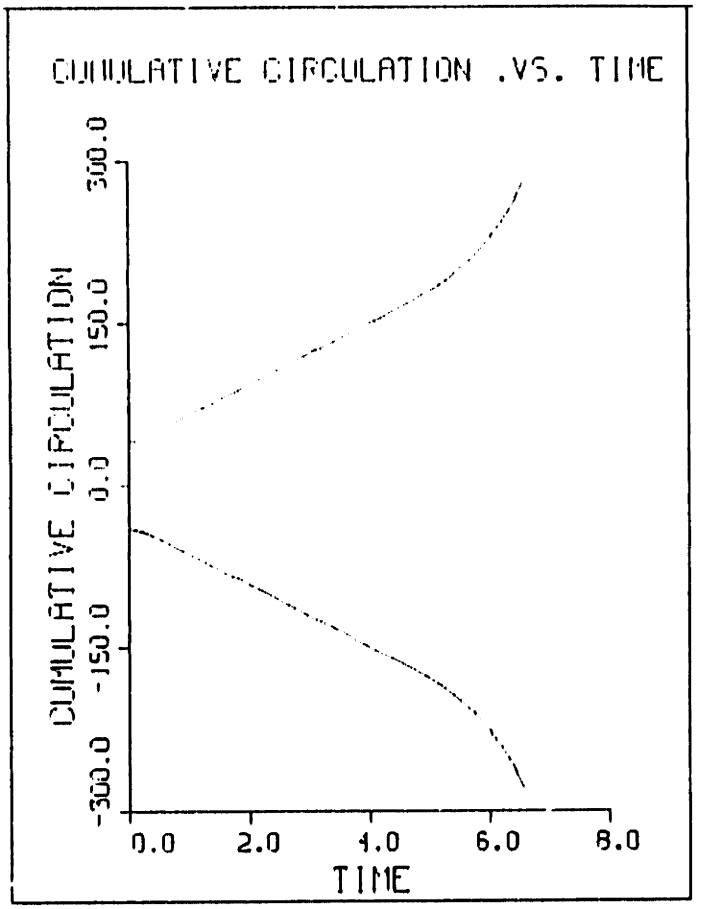
CUMULATIVE CIRCULATION .VS. TIME
CUMULATIVE CIRCULATION
300.0
150.0
0.0
-150.0
-300.0
0.0
2.0
4.0
6.0
8.0
TIME

Figure 87

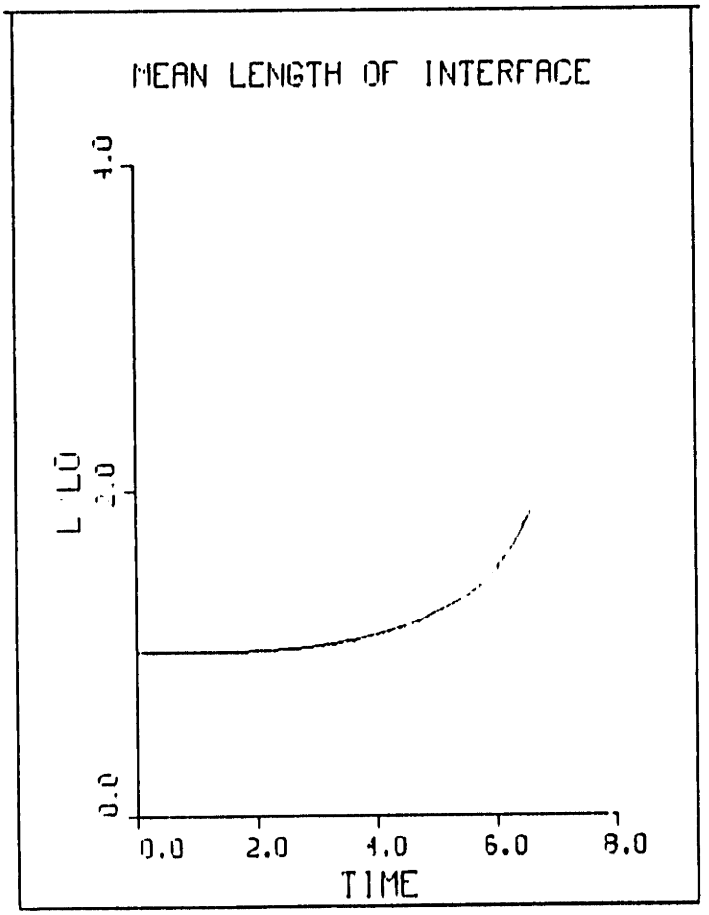
MEAN LENGTH OF INTERFACE
4.0
0.0
0.0
2.0
4.0
6.0
8.0
TIME

VI.4.2. THE SINUOUS MODE

(i) Case I : The Uniform Density Jet

The vortex/transport element plots for the sinuous mode are shown in Fig. 89 at t = 2.5, 5.0, 7.5 and 10.0 respectively. Unlike the varicose mode, the sinuous instability grows in an antisymmetric manner. The centerline of the jet in the varicose mode does not undergo any distortion. However, in the case of the sinuous instability, the core of the jet is twisted into a snakelike form and hence the name "sinuous" is used to describe this mode. It is observed that the initial perturbation of the shear layers is amplified and the resulting coherent structures resemble the Karman vortex street pattern in wake flows. The linear analysis for two-dimensional jets [25] predicts the sinuous mode of the instability to be more unstable than the varicose mode. However the growth rate of the jet shear layers depends on a number of factors such as (1) the ratio of the thickness of each shear layer to the distance of separation between the shear layers (2) the ratio of the wavelength of perturbation to the thickness of the shear layer (3) the distribution of vorticity in the shear layers and (4) the Froude number. Therefore, if the distance of separation between the shear layers is very large, the growth of one does not affect that of the other and hence the growth rate for the varicose and the sinuous mode may very well be the same. In this case, since the shear layers are close enough to influence one another, it does appear that the sinuous mode is the more unstable mode. The arguments supporting this observation are discussed below. The corresponding streamline contours for this case are shown in Fig. 90 . There exists a

direct correlation between the degree of destabilization of the flow and the amount of volumetric entrainment into the coherent structures. The volumetric entrainment is estimated by calculating the entrainment parameter ζ as was done for the varicose mode. The value of ζ at t=10.0 is found to be 0.8 which is greater than what was calculated for the varicose mode. Thus there appears to be a greater destabilization of the flow field for the sinuous mode.

The normalized temperature contours are shown in Fig. 91 for the same time frames. Tempertaure is a passive scalar in this case since the effects of baroclinic vorticity are ignored. It is interesting to note that most or all of the jet fluid is entrained into the coherent structures at late times. This is in contrast to the varicose mode, wherein most of the jet fluid at the center of the jet did not get entrained. Thus one might expect more mixing and higher burning rate for the sinuous mode. The vorticity contours for the same case, shown in Fig. 92 , reveal that most of the vorticity is accumulated within the structures. The vorticity is conserved along the particle path since generation effects are absent. Thus the two shear layers retain vorticity of the same sign as the initial vorticity.

The total circulation in the field is shown as a function of time in Curve 1 of Fig. 105 . The positive and the negative circulation are shown separately. Since there is no generation, the circulation curves are perfectly horizontal. Curve 1 of Fig. 106 shows the mean length of the interface as a function of time. It is observed that the elongation of the interface is slightly larger for the sinuous mode than the varicose mode which is consistent with the earlier observation that the sinuous mode is more unstable than the varicose mode.

(ii) Case II : The Density Stratified Jet, without Gravity

The initial velocity and density profiles are as shown in Fig. 63 . The density ratio is 4.0 . Therefore, the extra dynamic effect is the generation of baroclinic vorticity due to the interaction between the density gradient and the material acceleration. Fig. 93 shows the locations and velocities of the vortex/transport elements in the flow field at t=2.5, 5.0, 7.5 and 10.0 respectively. The convective motion of the eddies in the downward direction is clear even at very early times. A similar behavior was observed for the varicose mode and the density stratified shear layer, wherein the heavy stream tends to drag the structures along with it. At late times, it is obvious from the material interface plots that less volume of the high density fluid (in comparison with Case I)is being entrained into the structures. This observation is again consistent with what has been observed before. Denisty stratification reduces entrainment from the high density stream and increases entrainment from the low density stream. Also to be noted is the presence of an intense zone of vorticity within the large scale structures at late times leading to the formation of a 'double structure'. This inner structure is solely the result of baroclinic vorticity generation which enhances the vorticity within the core of the eddy while counteracting the vorticity at the outer edge of the eddy. Fig. 94 shows the corresponding streamline contours for Case II. The entrainment parameter ζ is calculated from the streamfunction values in the flow field. The value of ζ at t=10.0 is 3.7 . This value is higher than the ζ for Case II of the varicose mode. The greater destabilization of the flow is clearly observed from the streamline plots. It is seen that the inner zone of intense vorticity within the structure sets up stronger entrainment currents.

The normalized temperature contours ($T=1/\rho$) are shown in Fig. 95 at the corresponding time frames. In this case, the temperature is an active scalar since temperature gradients lead to the generation of vorticity. At late times, it is seen that the size of the eddy itself is larger than what was seen in Case I. This suggests increased volumetric entrainment into the structures. Fig. 96 shows the corresponding vorticity contours. The early development is similar to what was observed for Case I. At late stages, as the material acceleration becomes significant, the generation of vorticity results in the formation of a number of small scale srtuctures. It is observed that negative vorticity is being generated at the top side of the positive eddy and positive vorticity is being generated around the bottom side of the negative eddy. The intensification of vorticity in the centers of the coherent structures is clearly seen. This leads to a stronger eddy and delays the saturation of the instability.

Curve 2 of Fig. 105 shows the total circulation in the flow field as a function of time. The positive and the negative components are summed separately. The circulation increases from its initial value due to the effects of generation. Equal amounts of positive and negative circulation are generated so that the net circulation in the field remains unchanged. Curve 2 of Fig. 106 shows the mean length of the material layers as a function of time. It is observed that density stratification delays the growth of the interface initially as compared to the uniform density case. A similar phenomenon was observed in the case of the shear layer where the effect of density stratification was to decrease the linear growth rate. At late times, i.e., in the non-linear range, the density stratification produces a greater destabilizing effect. Fig. 106 shows that the density stratified curve 'catches up' with the uniform density curve at about t = 10.0. More

importantly, the final slope of the growth of the density stratified interface is larger than that of the uniform density interface. Thus the rate of destabilization is higher with density stratification.

(iii) Case III : A Very Slow Moving Density Stratified Jet

This case is similar to Case III of the varicose mode. The initial momentum in the flow field is neglected, i.e., the initial flow field is stationary under the influence of gravity. The initial density profile is as shown in Fig. 63 (b) and the flow variables are scaled in terms of the characteristic values $t_o = \sqrt{L_o/g_r}$ and $U_o = \sqrt{L_o\ g_r}$. L_o is the density gradient thickness and g_r is the gravitational acceleration. The perturbation of the density gradient interface leads to the generation of vorticity and the flow becomes unstable. Fig. 97 shows the locations and velocities of the vortex/transport elements at t=2.5, 3.75, 5.37 and 6.0 respectively. The effect of gravity is to accelerate the column of hot fluid upwards with respect to the cold ambient fluid. This is observed in the transport element plots wherein the the elements at the center of the jet possess a higher upward velocity than those on the side of the ambient. At late times, the interface goes unstable by rolling up to form the coherent structures. The structures also propagate in the upward direction due to the effect of the accelerating fluid. Once again, the development of an intense inner structure is observed within the eddies. The corresponding streamline contours are shown in Fig. 98. The initial streamlines are zero since the flow field is stationary. The flow is set into motion due to the generation of vorticity and the streamlines show the development of the flow in the initial stages and the subsequent rollup and entrainment of fluid into the structures.

Fig. 99 shows the normalized temperature contours at the corresponding times. Since the scalar is non-diffusive and conserved, the contours reflect what was observed in the material interface plots. Fig. 100 shows the vorticity contours for the same time frames. The initial generation of vorticity is due to the interaction between the density gradient and gravity. The figure shows the smooth development of the contours at the early times. As the interface goes unstable, the effects of material acceleration also become important and the vorticity distribution begins to take on a patchy appearance. The presence of a large number of small scales and large scalar gradients would lead to an efficient mixing process if molecular diffusion were allowed to be active.

Curve 3 of Fig. 105 shows the total circulation in the flow field with time. The initial circulation is zero since the flow is stationary. The rate of generation of circulation in this case is much larger than what was observed for Case II. This indicates a greater destabilizing effect of gravity with respect to material acceleration. Also, the rate of destabilization, i.e., the slope of the curve, increases with time. Curve 3 of Fig. 106 shows the mean elongation of the interface with time. The highly non-linear development of the instability is clearly observed. For $t < 4.0$, the interface elongation is negligible. But for $4.0 < t < 6.0$, the interface length increases by about three times the initial length. Also the final slope of the curve is very large compared to Cases I and II. This large degree of non-linearity is a characteristic feature of gravity dominated flows.

(iv) Case IV : A Density Stratified Jet at a Finite Froude Number

The initial velocity and density profiles for this case are as shown in Fig. 63 (a) and (b). The density ratio between the ambient and the jet fluid

is 4 and the Froude number is 4.0. Therefore, this case is the same as Case II except that gravity plays a role here. Fig. 101 shows the locations and velocities of the vortex/transport elements at t= 2.5, 5.0, 6.5 and 7.5 respectively. The calculations were stopped at an earlier time compared to Case II because gravity causes the structures to develop faster and leads to an earlier saturation of the instability. It is observed that the downward motion of the structures seen in Case II is counteracted by the effect of gravity. The structures appear to be more or less stationary. It is interesting to note that in the case of the varicose mode, gravity not only counteracted the downward motion but also propagated the structures in the upward direction at a small, but finite convection velocity. This effect of gravity is slightly diminished for the sinuous instability. The faster growth of the instability is clearly observed by comparing Cases II and IV at t=5.0 and 7.5. At late stages of development, zones of intense vorticity are observed within the large scale structures. These intense structures appear earlier in time for Case IV and are more in number as compared to Case II. Fig. 102 shows the streamline contours for the corresponding time frames. The entrainment parameter ζ as calculated from the streamfunction values turns out to be equal to 5.0 at t=7.5 . This value is less than what was observed for Case IV of the varicose mode. This phenomenon is consistent with the earlier observation that gravity is less effective for the sinuous instability. One possible explanation for this effect could be that the heated central portion of the jet in the varicose mode remains without distortion or entrainment. This provides a constant impetus for the central portion to accelerate upwards. In the case of the sinuous mode, the central portion of the jet is entrained into the eddies and is not able to provide the upward motion.

Fig. 103 shows the normalized temperature contours at the corresponding time frames. The faster development of the instability as compared to Case II leads to larger entrainment into the structures. Fig. 104 shows the vorticity contours at the same time frames. The effects of gravity generated vorticity are obvious from the plots. The intensification of vorticity in the centers of the eddies at late times is clearly observed. Thus the effect of gravity even at a moderate Froude number is to destabilize the flow to a greater extent.

Curve 4 of Fig. 105 shows the total circulation in the domain as a function of time. It is observed that the initial part of the curve for $t < 2.0$ is similar to that of Case II. But the curves begin to deviate from each other around $t = 4.0$ and the highly non-linear feature of gravitational effects becomes evident at later times. The amount of circulation being generated increases at a fast rate and the amount of circulation in the field at $t=7.5$ is about five times that for Case II at $t=10.0$. Also, the slope of the curve keeps increasing with time and is an order of magnitude larger than the final slope for Case II. Curve 4 of Fig. 106 shows the change in the mean length of the interface with time. Again, the highly non-linear development is observed. For $t < 4.0$, the length is almost equal to the initial length and in the time interval $4.0 < t < 7.5$, the interface length becomes five times its initial length.

IV. 5. CONCLUSIONS

The results for the study of the sinuous instability essentially supports all the observations made for the varicose mode. Gravity destabilizes the flow to a greater extent and leads to an earlier saturation of the

instability. The effect of baroclinicity is to produce a large number of small scales which can be very effective in enhancing mixing.

Comparing the varicose and the sinuous modes of the jet instability, it is observed that sinuous mode is more unstable in the absence of gravity. This observation is supported by the results of linear analysis for two-dimensional jets [25] wherein the sinuous mode was found to more unstable over the entire range of wavenumbers. On the other hand, when gravity is included into the simulations, it is not obvious as to whether one mode is more unstable than the other. The generation of circulation for the two modes are very similar. However, the entrainment parameters and the motion of the eddies suggest that the varicose mode might be more unstable in the presence of gravity. Unfortunately, neither experimental nor theoretical results are available to support this hypothesis.

The simulations were successful in providing qualitative insight into the effects of density stratification on jet flows. The interactions between the existing vorticity in the field and that generated due to baroclinic effects (material as well as gravitational acceleration) were studied in order to assess the amount of entrainment and mixing within the structures. It is found that entrainment is a strong function of the density ratio and gravitational effects.

FIGURE CAPTIONS

Fig. 89. The locations and velocities of the vortex/transport elements at t = 2.5, 5.0, 7.5 and 10.0 respectively for Case I.

Fig. 90. The streamline contours for Case I at t= 2.5, 5.0, 7.5 and 10.0 respectively.

Fig. 91. The normalized temperature ($T = 1/\rho$) contours for Case I at t= 2.5, 5.0, 7.5 and 10.0 respectively.

Fig. 92. The vorticity contours for Case I at t= 2.5, 5.0, 7.5 and 10.0 respectively. The contnuous curves represent negative vorticity and the dashed curves signify positive vorticity.

Fig. 93. The locations and velocities of the vortex/transport elements at t = 2.5, 5.0, 7.5 and 10.0 respectively for Case II.

Fig. 94. The streamline contours for Case II at t= 2.5, 5.0, 7.5 and 10.0 respectively.

Fig. 95. The normalized temperature ($T = 1/\rho$) contours for Case II at t= 2.5, 5.0, 7.5 and 10.0 respectively.

Fig. 96. The vorticity contours for Case II at t= 2.5, 5.0, 7.5 and 10.0 respectively. The contnuous curves represent negative vorticity and the dashed curves signify positive vorticity.

Fig. 97. The locations and velocities of the vortex/transport elements at t = 2.5, 3.75, 5.37 and 6.0 respectively for Case III.

Fig. 98. The streamline contours for Case III at t= 2.5, 3.75, 5.37 and 6.0 respectively.

Fig. 99. The normalized temperature ($T = 1/\rho$) contours for Case III at t= 2.5, 3.75, 5.37 and 6.0 respectively.

Fig. 100. The vorticity contours for Case III at t= 2.5, 3.75, 5.37 and 6.0 respectively. The contnuous curves represent negative vorticity and the dashed curves signify positive vorticity.

Fig. 101. The locations and velocities of the vortex/transport elements at t = 2.5, 5.0, 6.5 and 7.5 respectively for Case IV.

Fig. 102. The streamline contours for Case IV at t= 2.5, 5.0, 6.5 and 7.5 respectively.

Fig. 103. The normalized temperature ($T = 1/\rho$) contours for Case IV at t= 2.5, 5.0, 6.5 and 7.5 respectively.

Fig. 104. The vorticity contours for Case IV at t= 2.5, 5.0, 6.5 and 7.5 respectively. The contnuous curves represent negative vorticity and the dashed curves signify positive vorticity.

Fig. 105. The cumulative circulation as a function of time. Curves 1, 2, 3 and 4 represent cases I, II, III and IV respectively. The positive and negative components of circulation are represented separately.

Fig. 106. The average material length as a function of time. Curves 1, 2, 3 and 4 represent cases I, II, III and IV respectively. The length is normalized by the value at t=0.

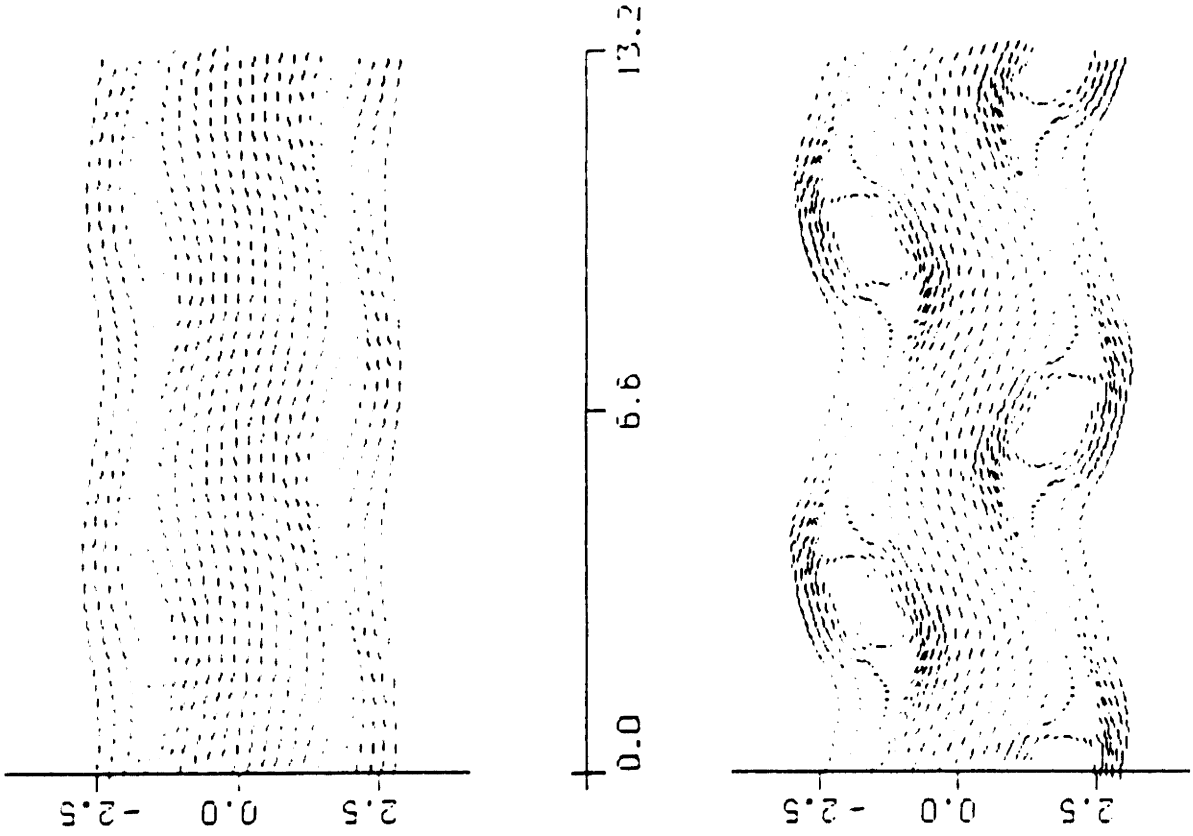

t = 2.5

t = 5.0

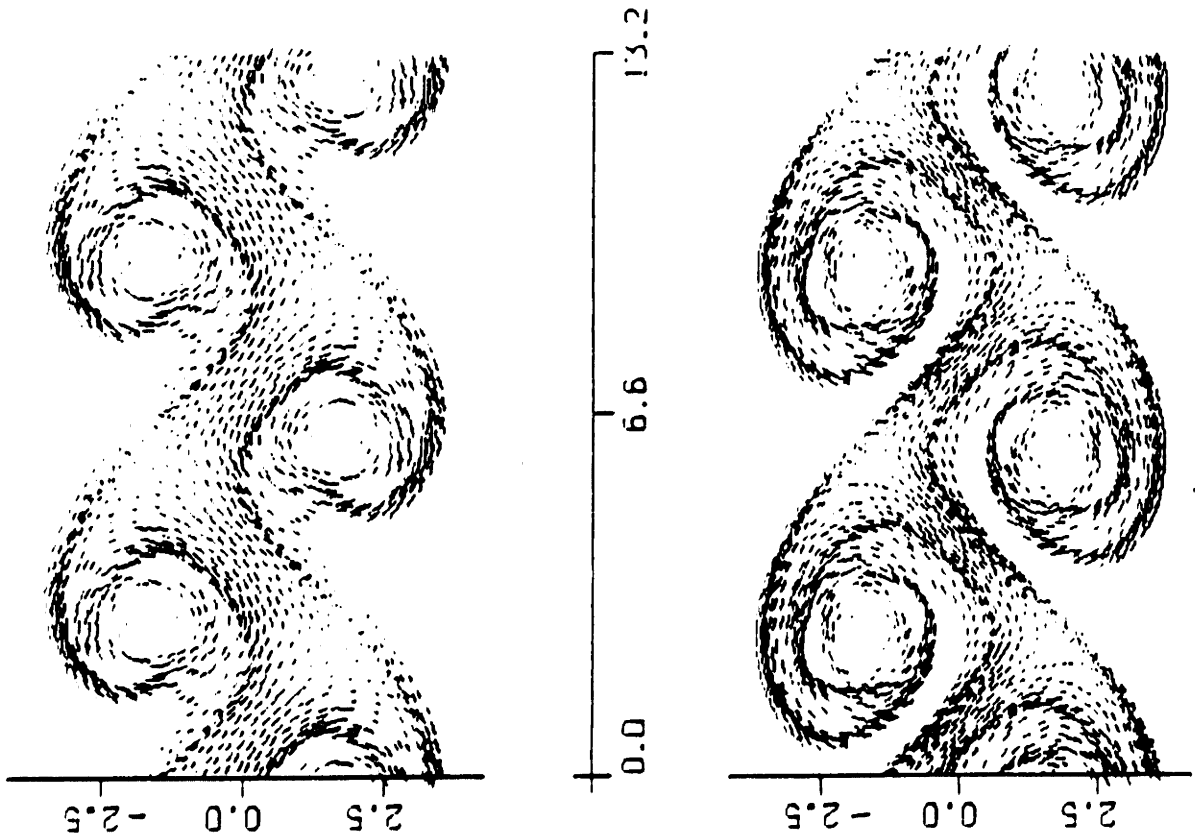

t = 7.5

t = 10.0

Figure 89

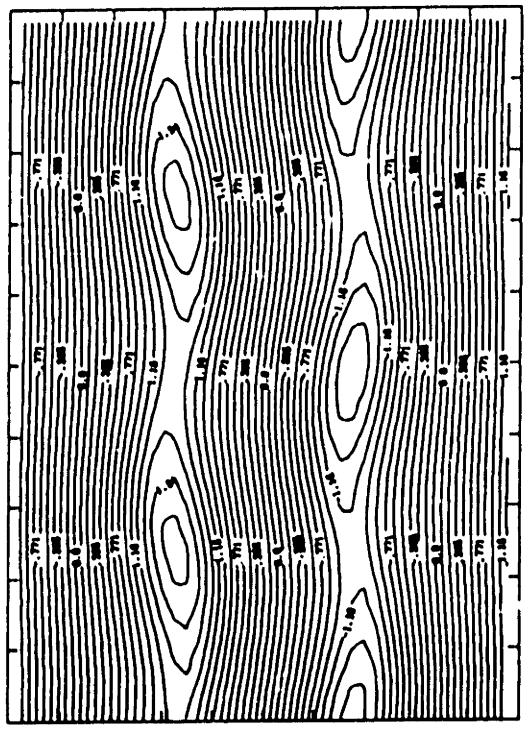

t = 2.5

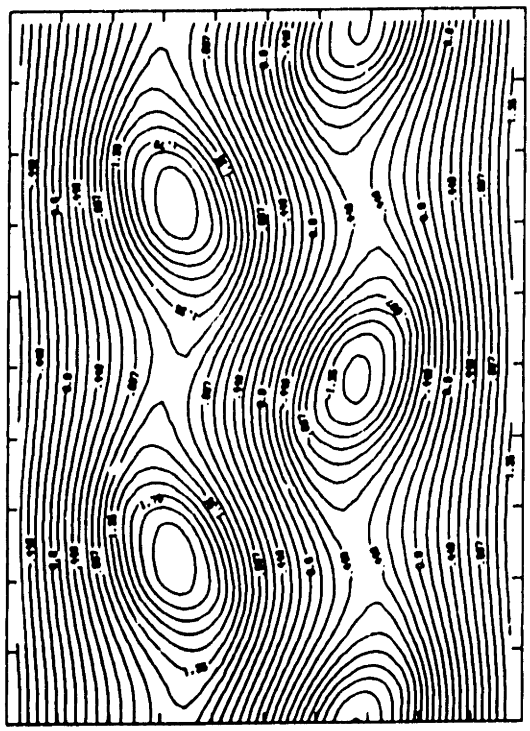

t = 5.0

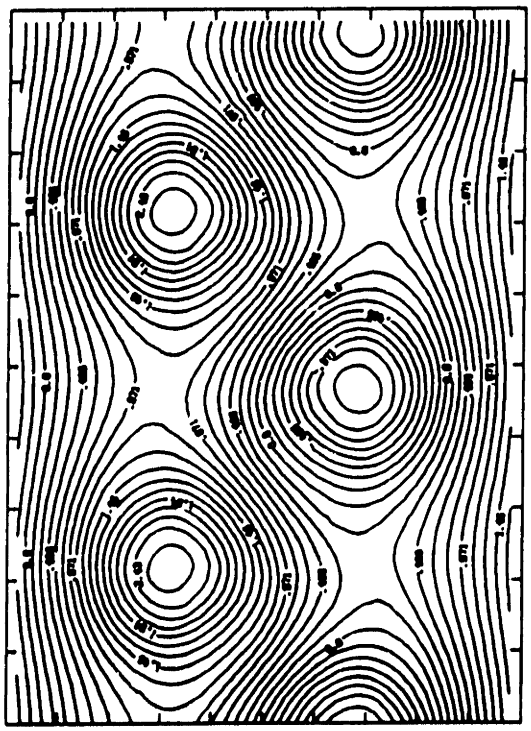

t = 7.5

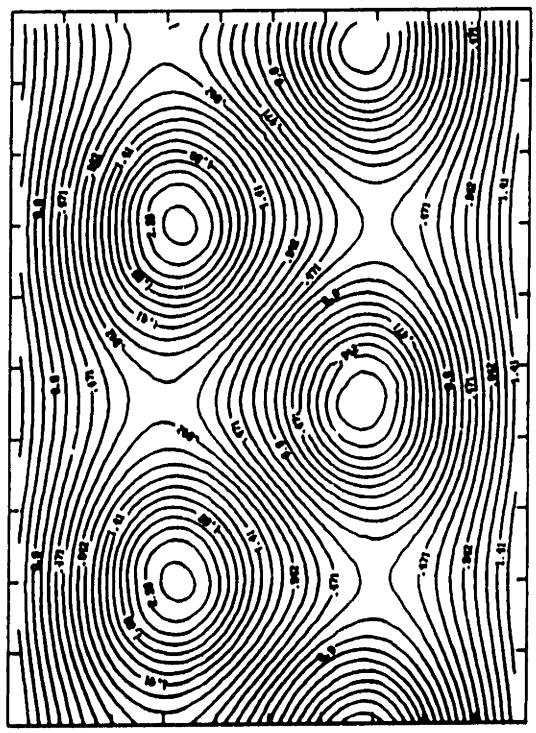

t = 10.0

Figure 90

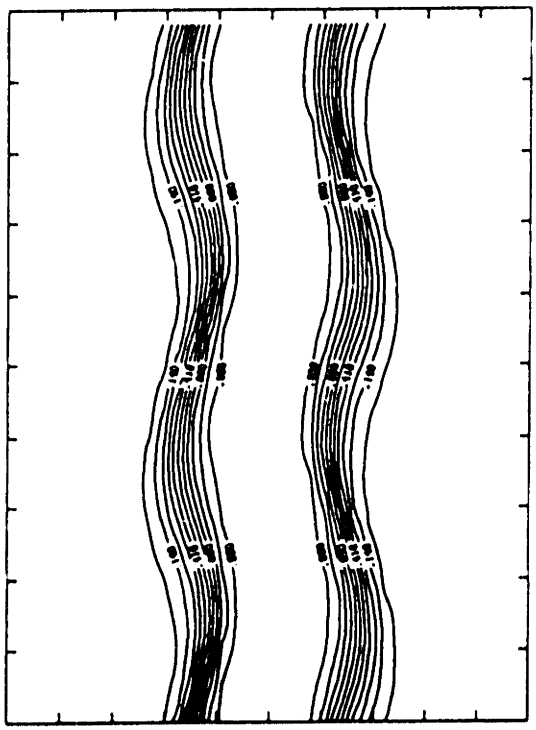

t = 2.5

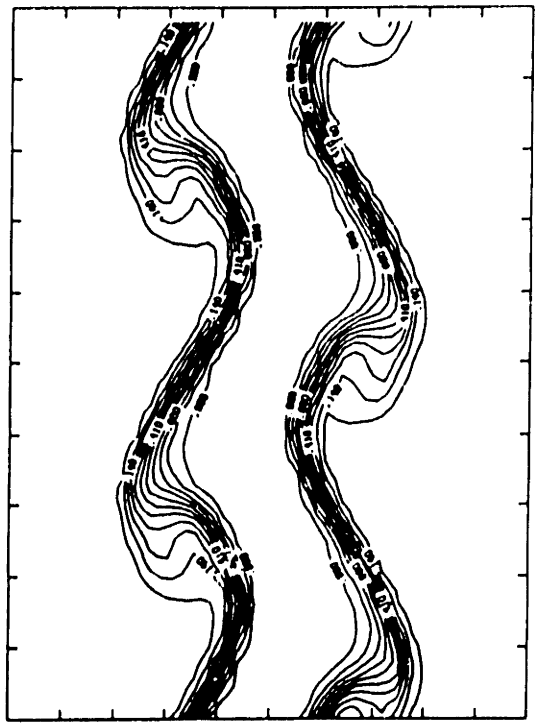

t = 5.0

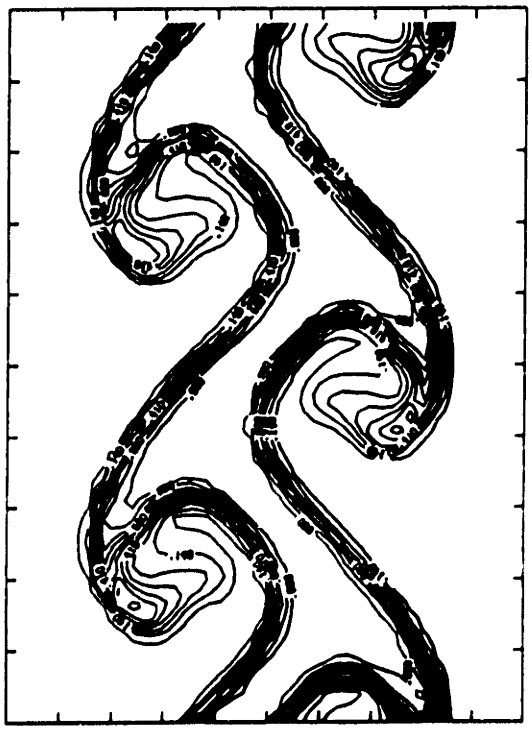

t = 7.5

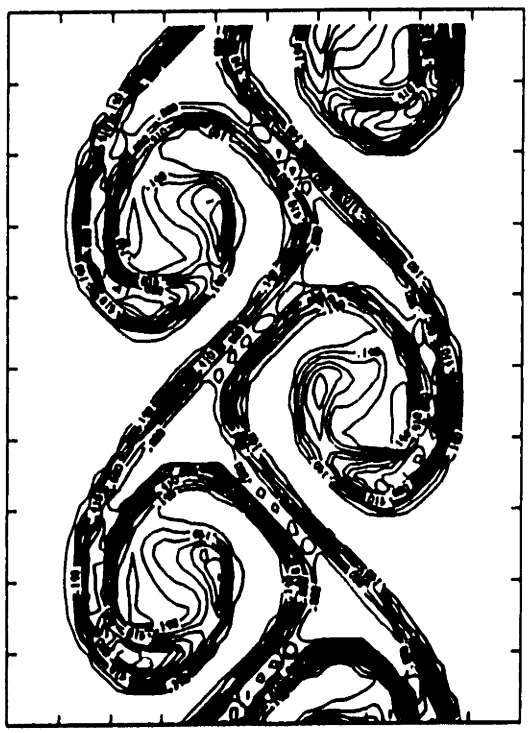

t = 10.0

Figure 91

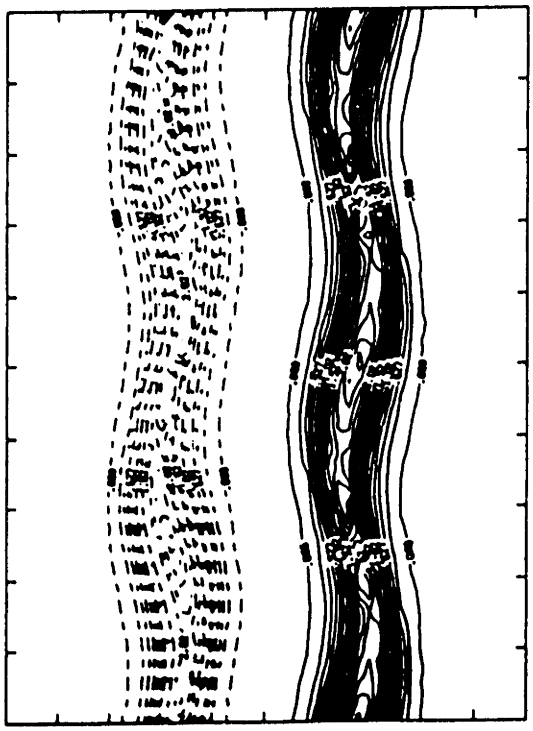

t = 2.5

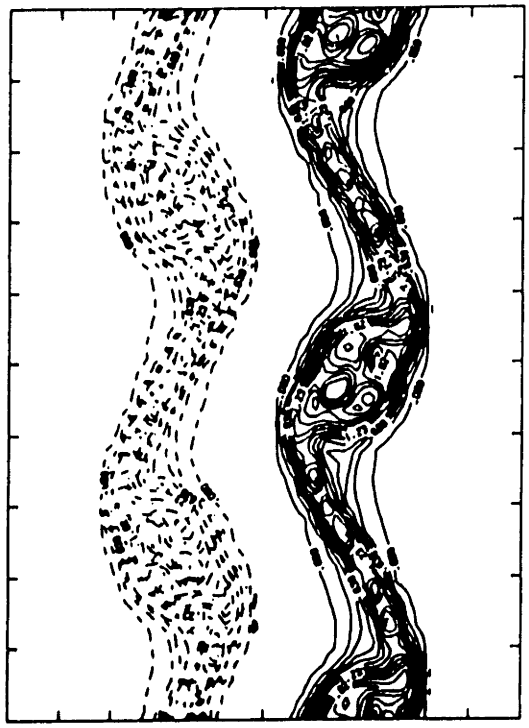

t = 5.0

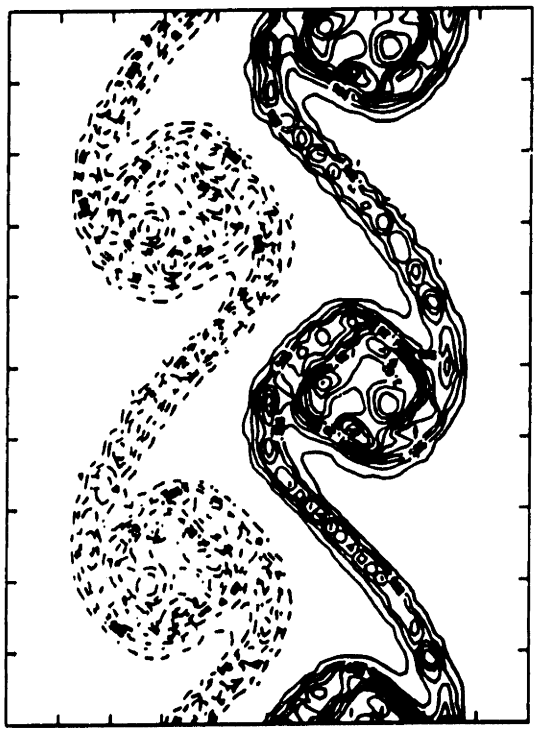

t = 7.5

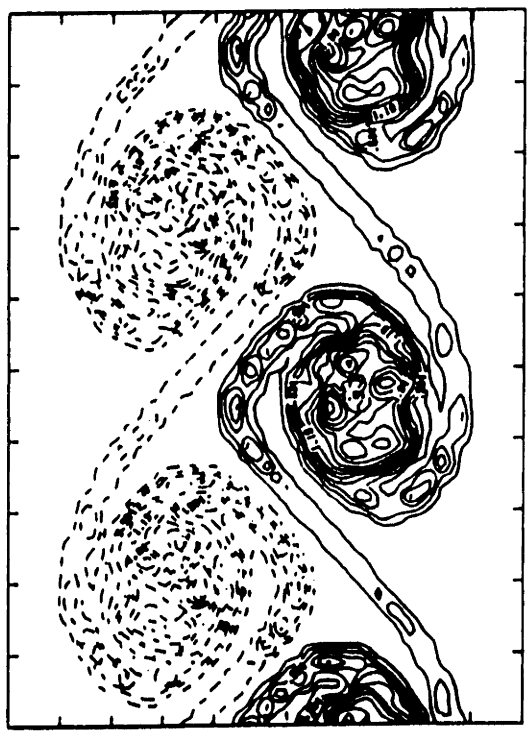

t = 10.0

Figure 92

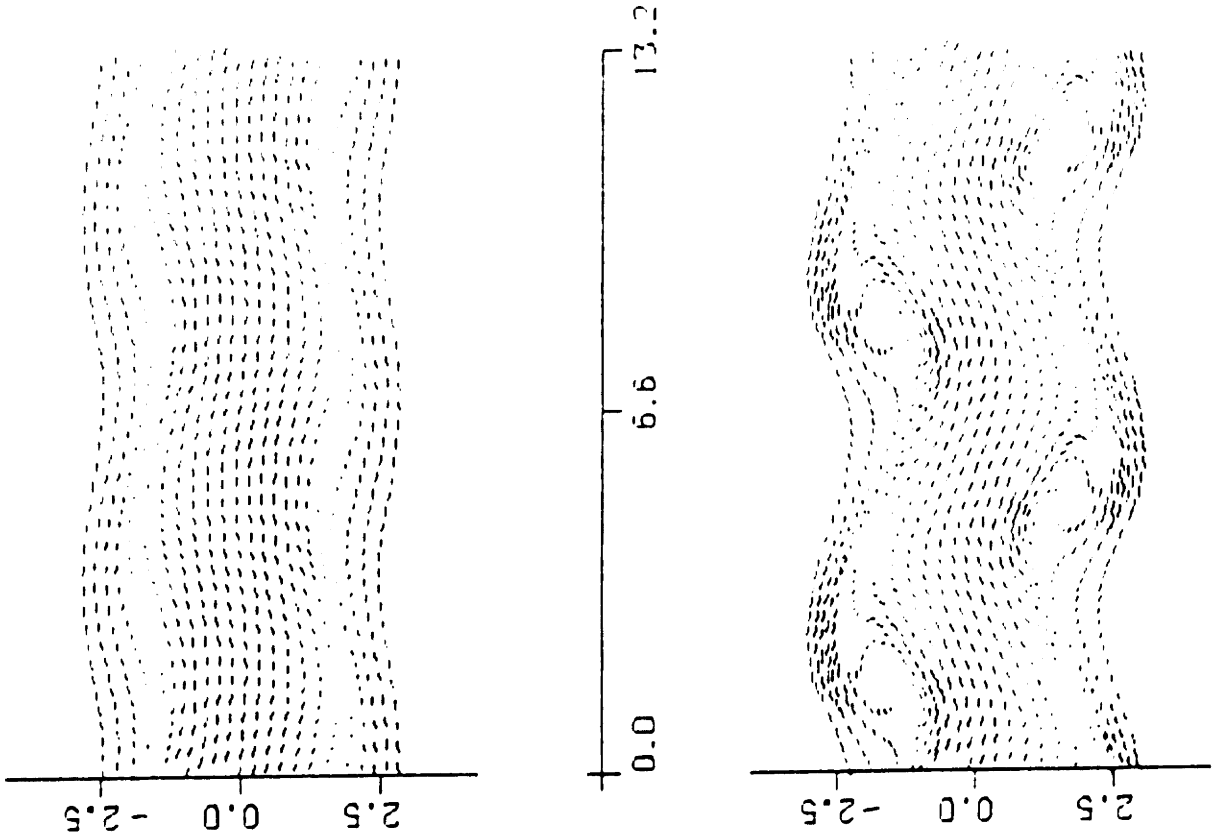

t = 2.5

t = 5.0

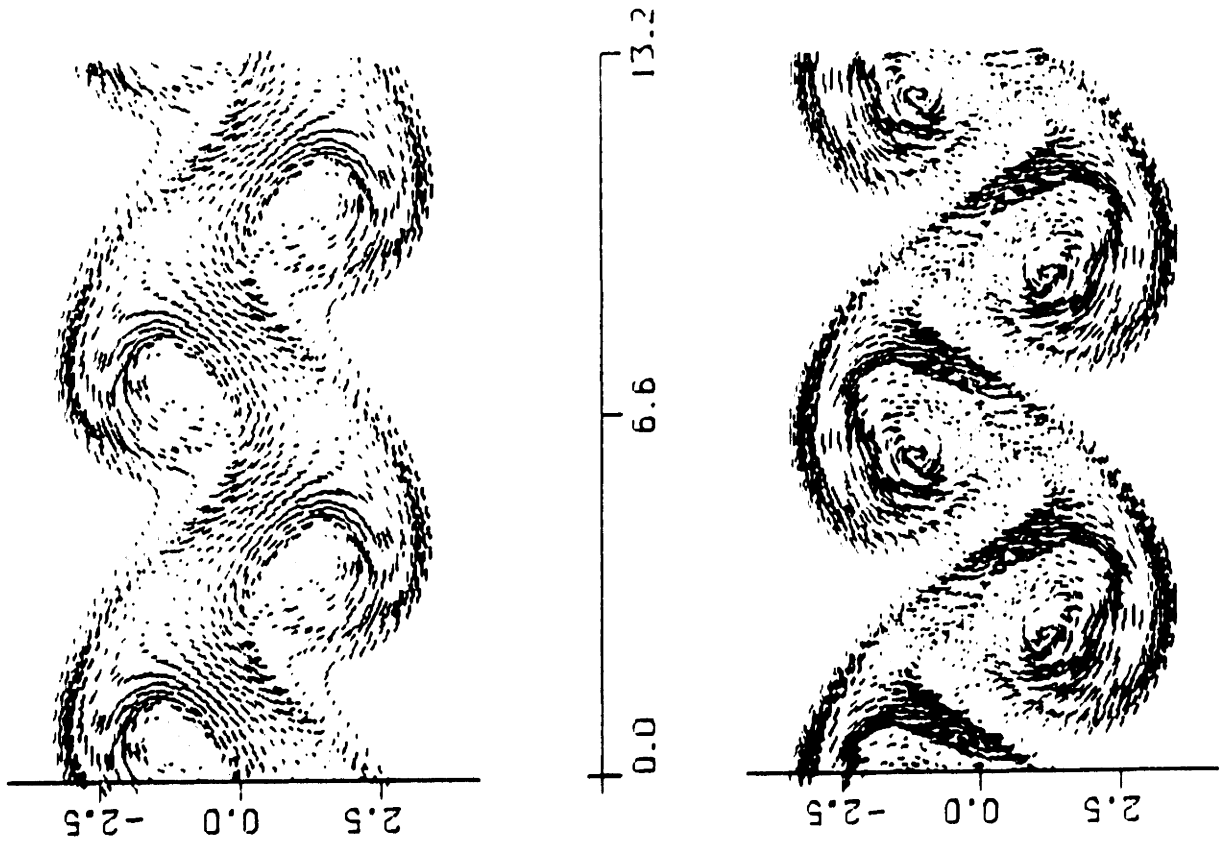

t = 7.5

t = 10.0

Figure 93

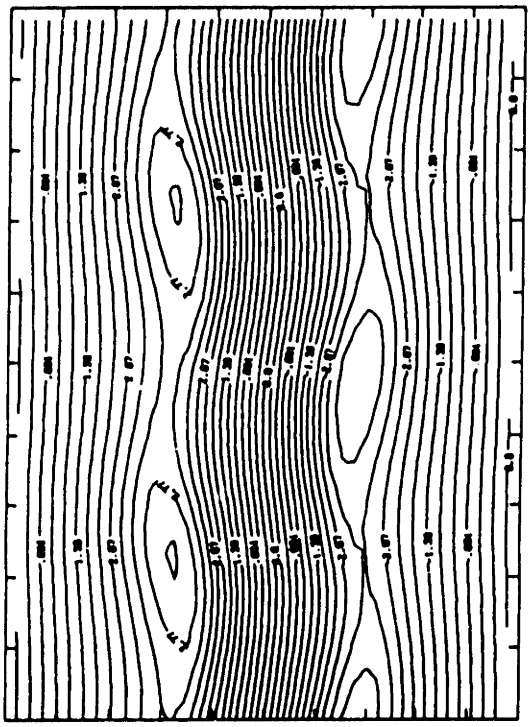

t = 2.5

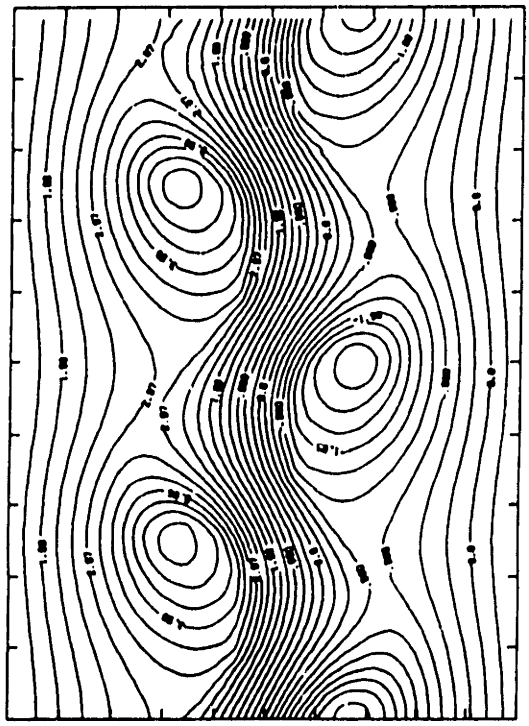

t = 5.0

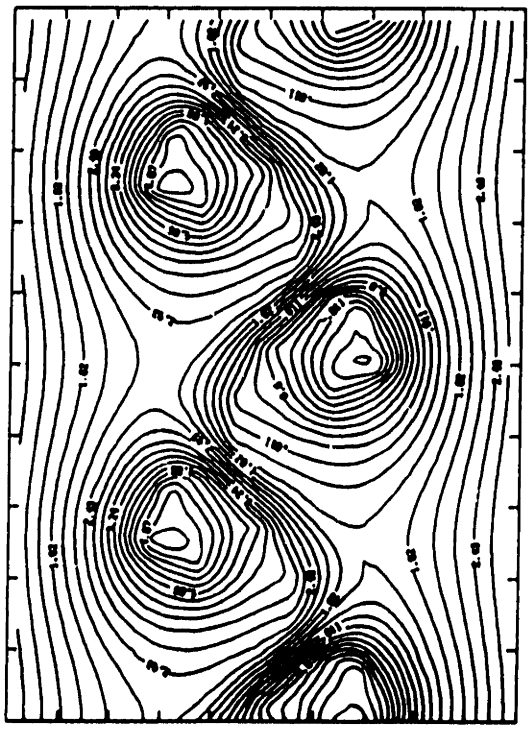

t = 7.5

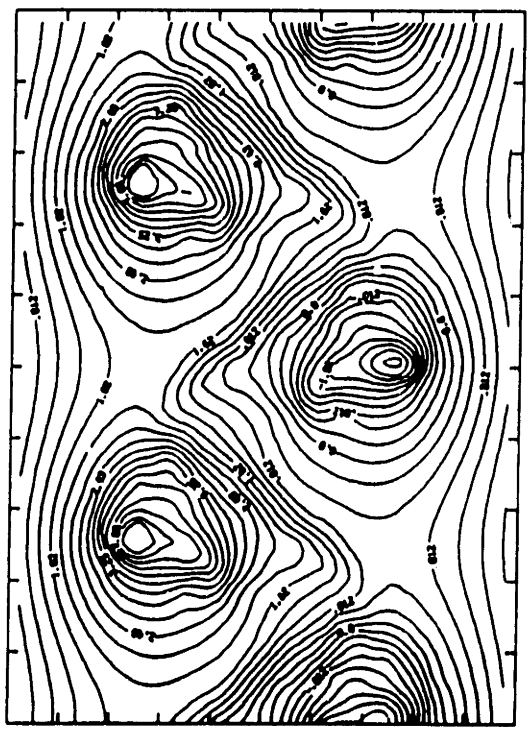

t = 10.0

Figure 94

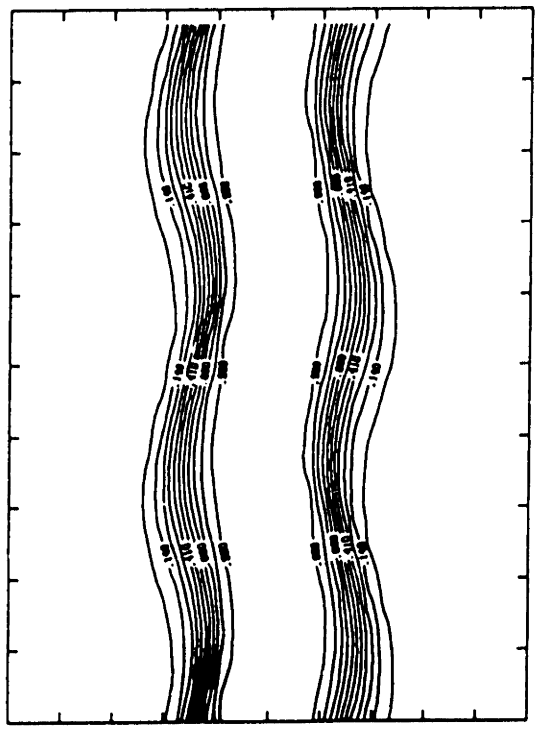

t = 2.5

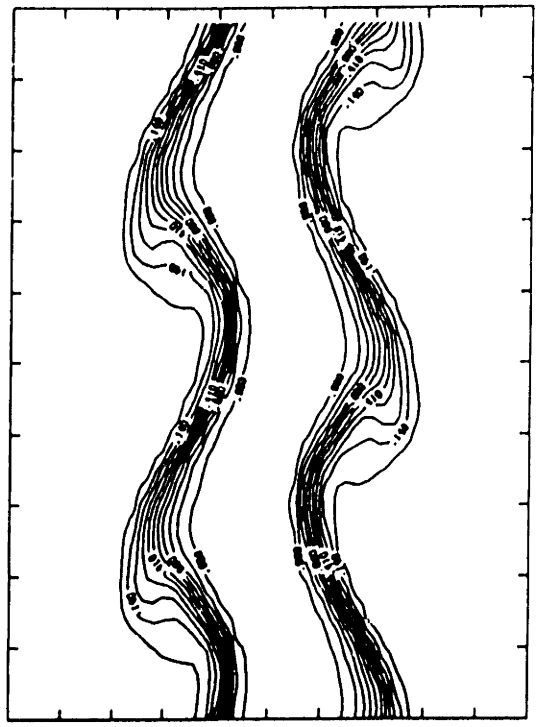

t = 5.0

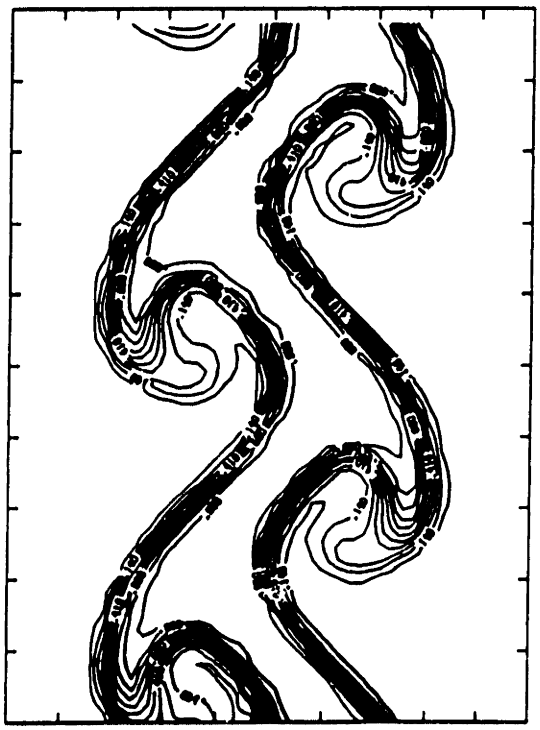

t = 7.5

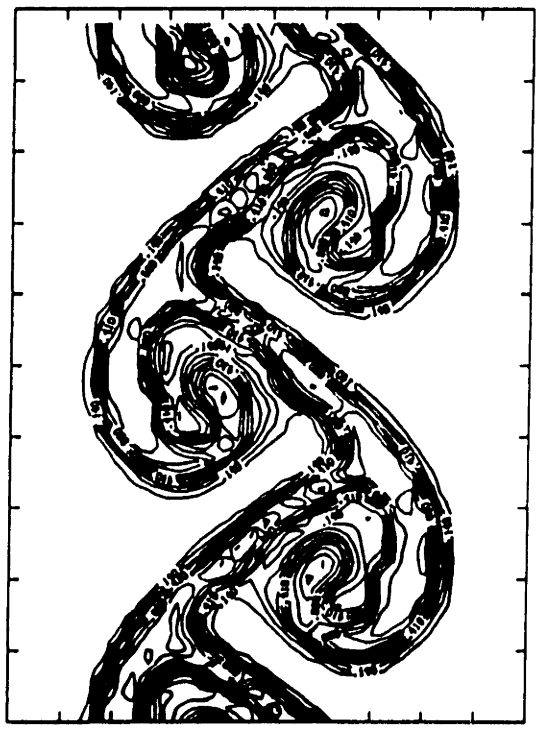

t = 10.0

Figure 95

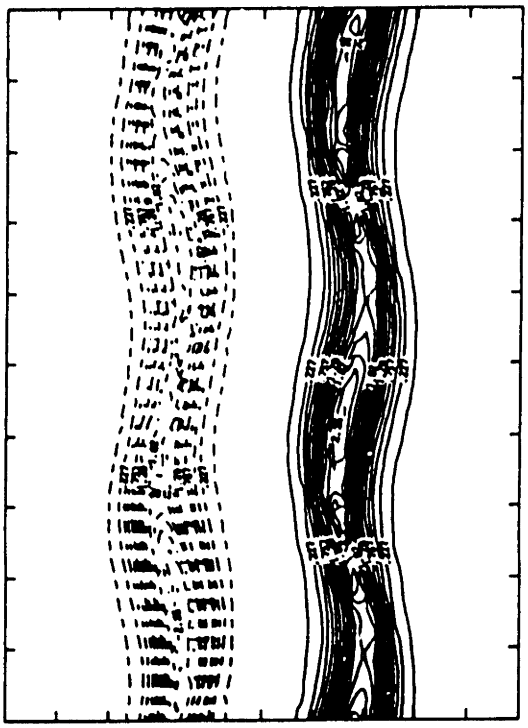

t = 2.5

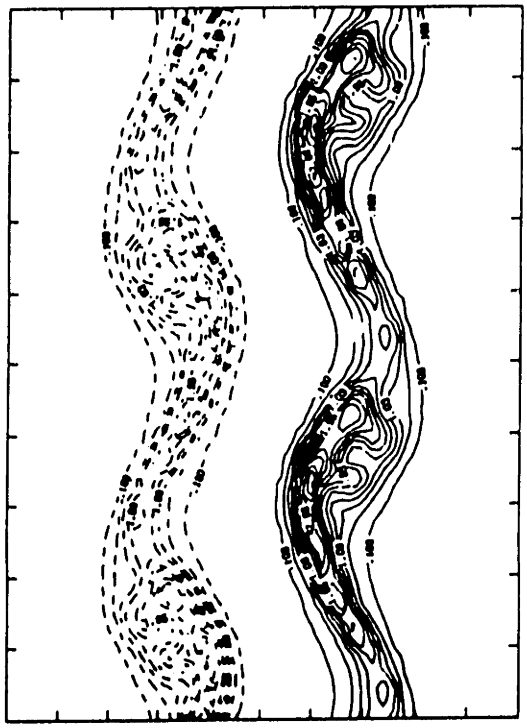

t = 5.0

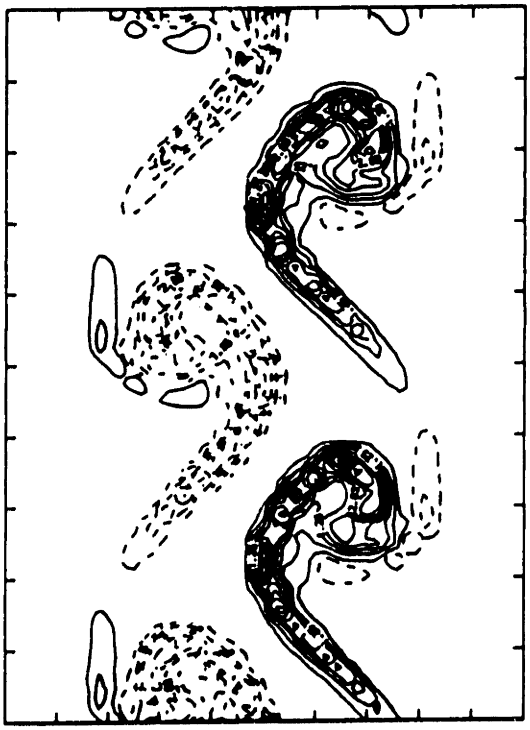

t = 7.5

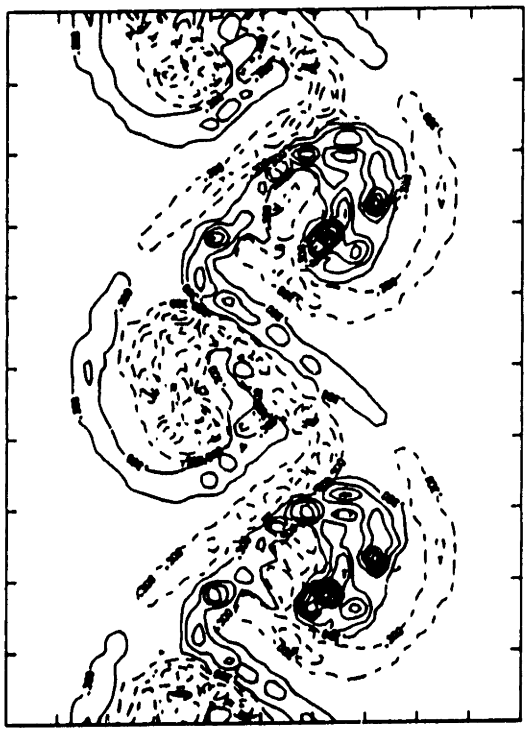

t = 10.0

Figure 96

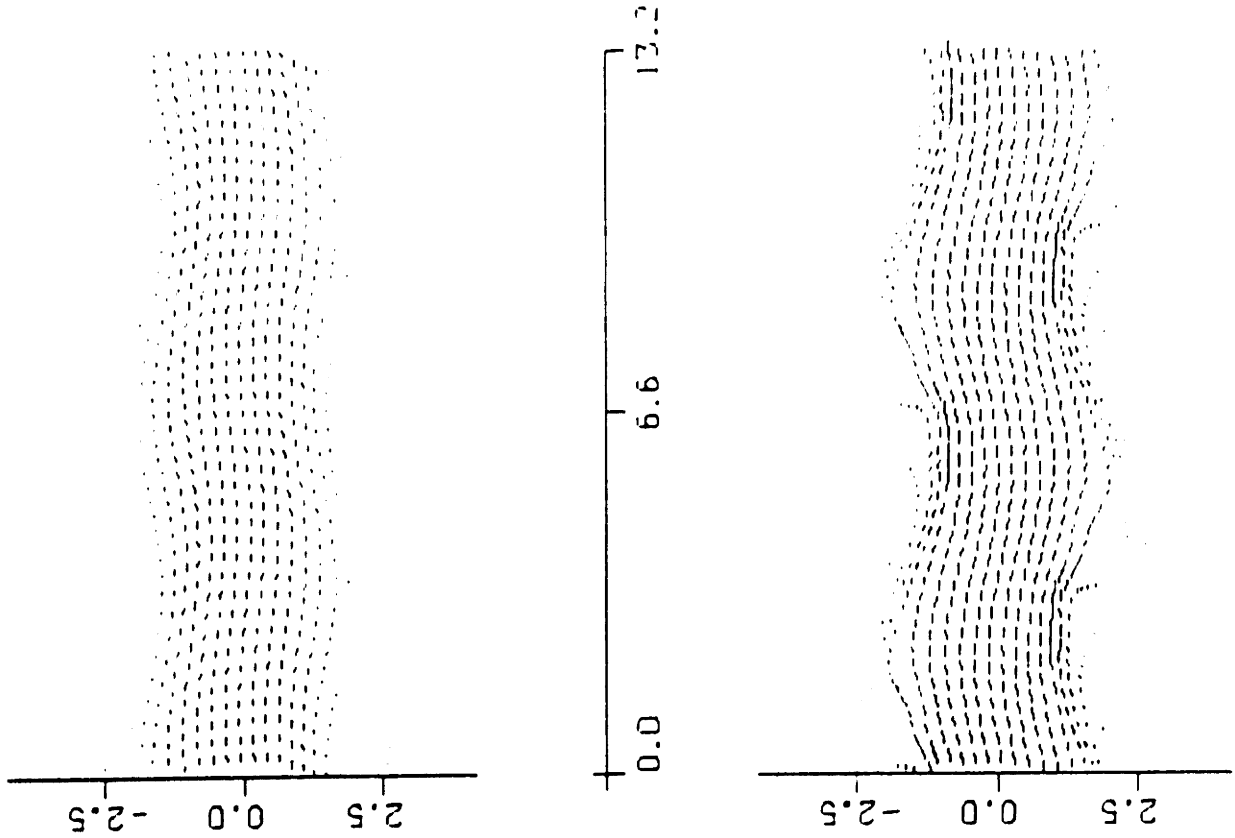

t = 2.5

t = 3.75

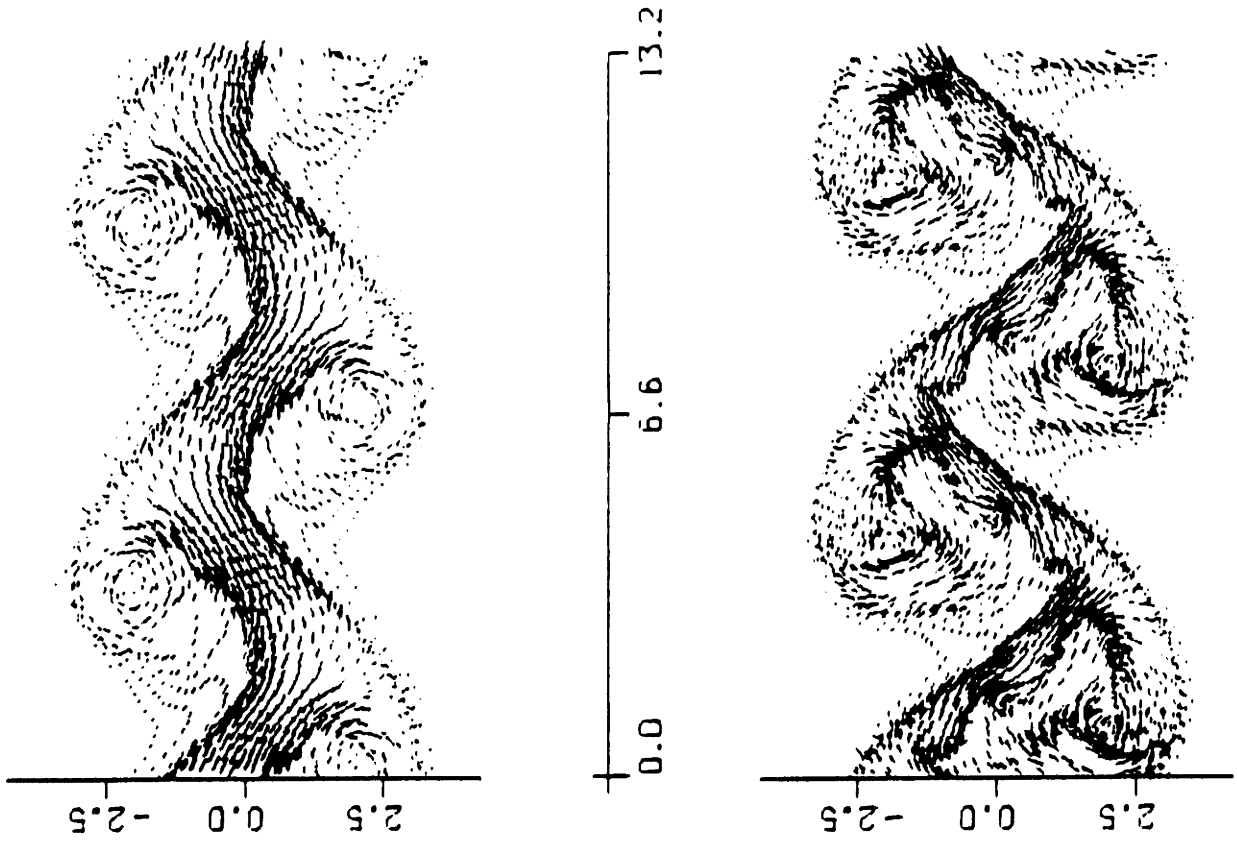

t = 5.37

t = 6.0

Figure 97

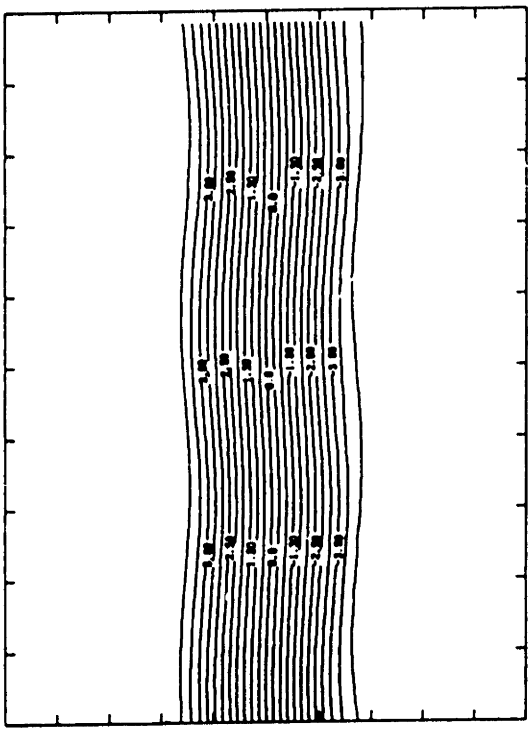

t = 2.5

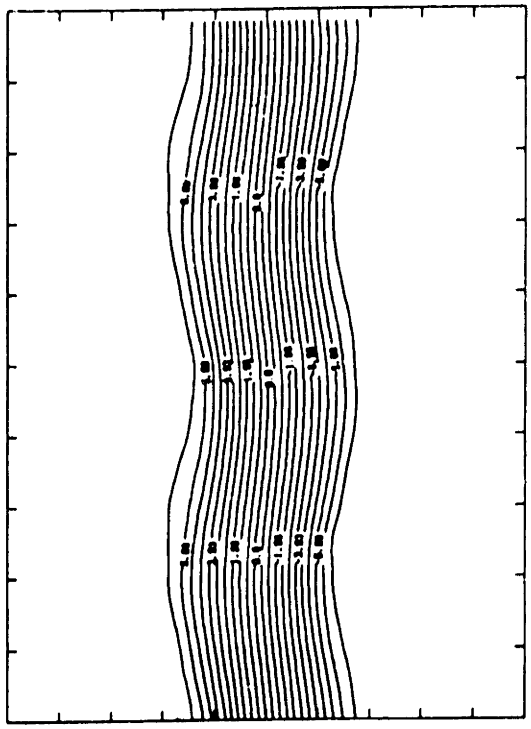

t = 3.75

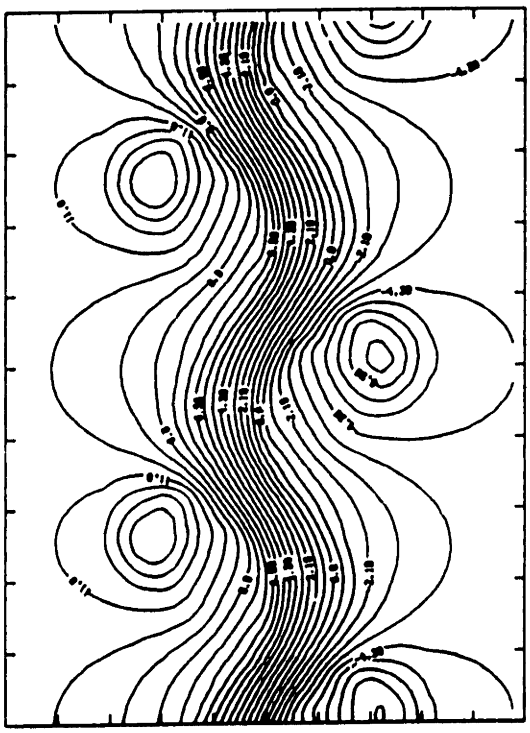

t = 5.37

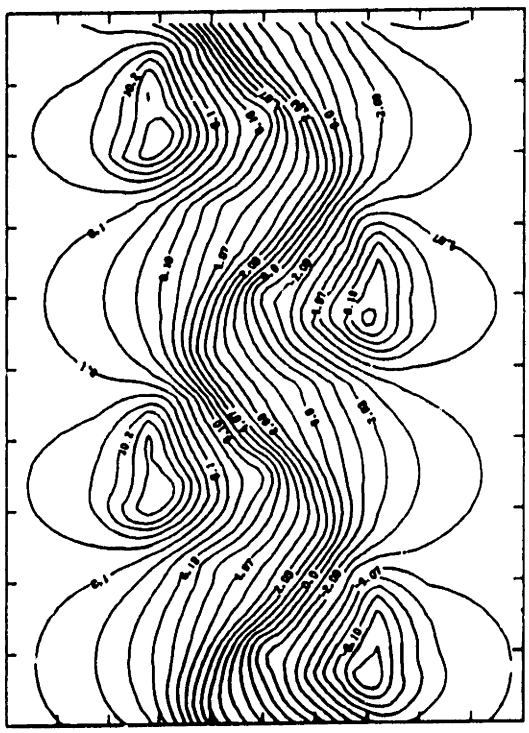

t = 6.0

Figure 98

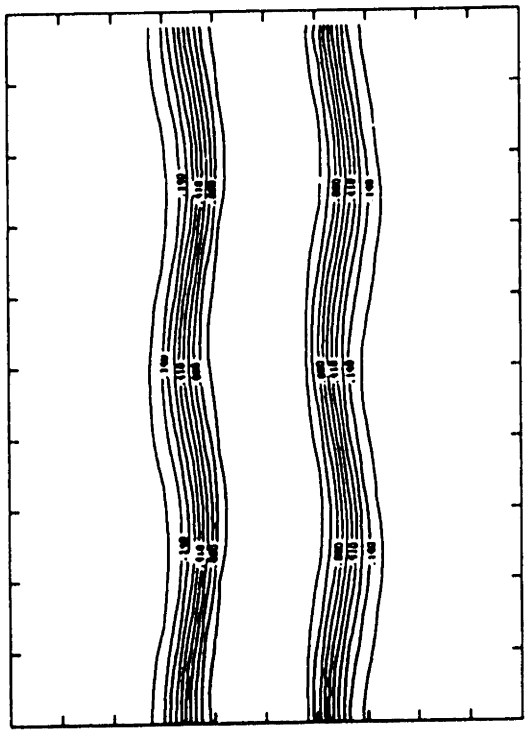

t = 2.5

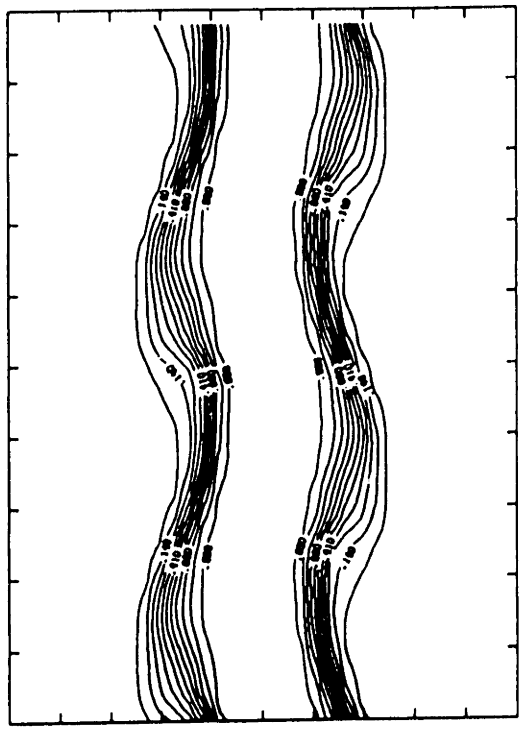

t = 3.75

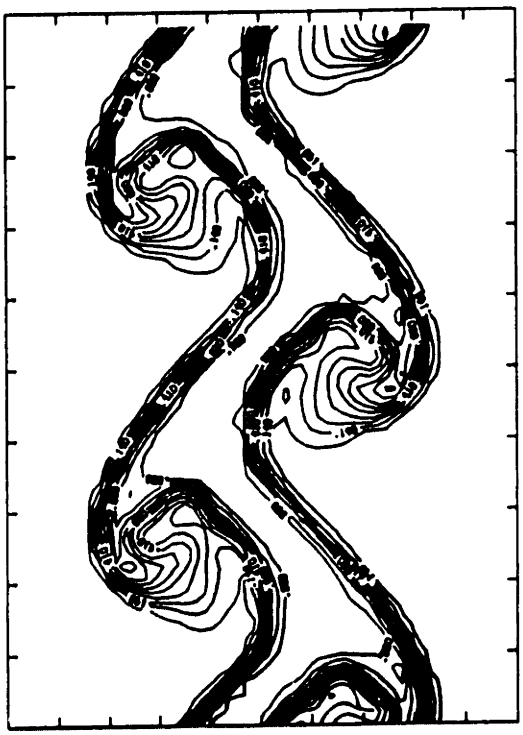

t = 5.37

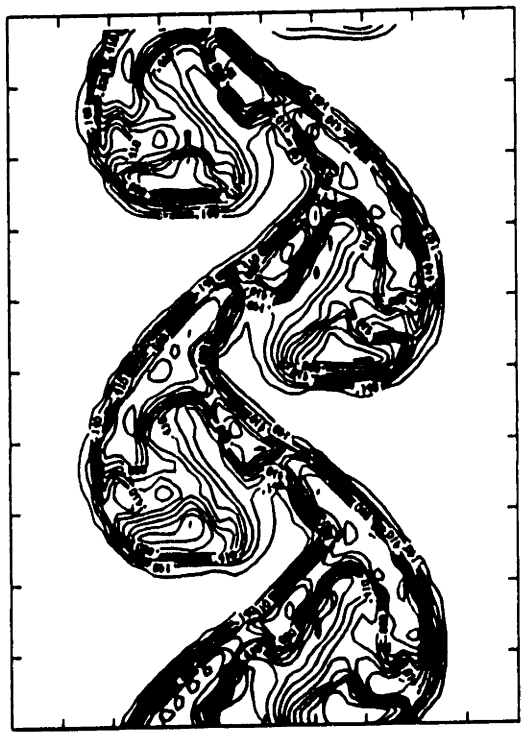

t = 6.0

Figure 99

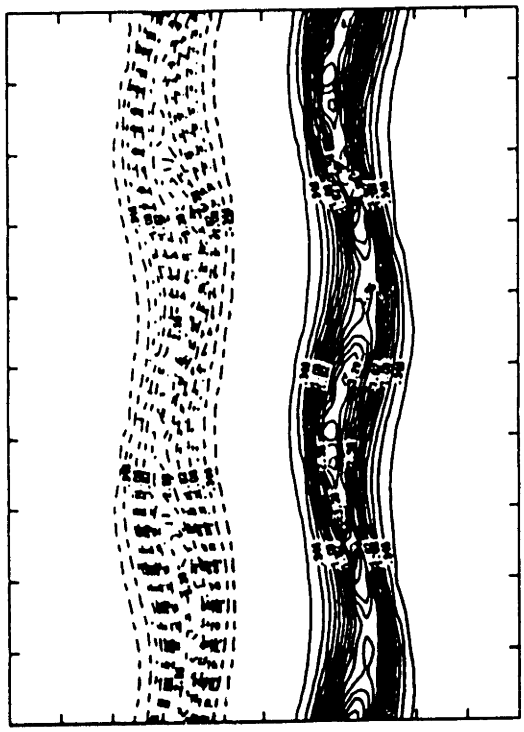

t = 2.5

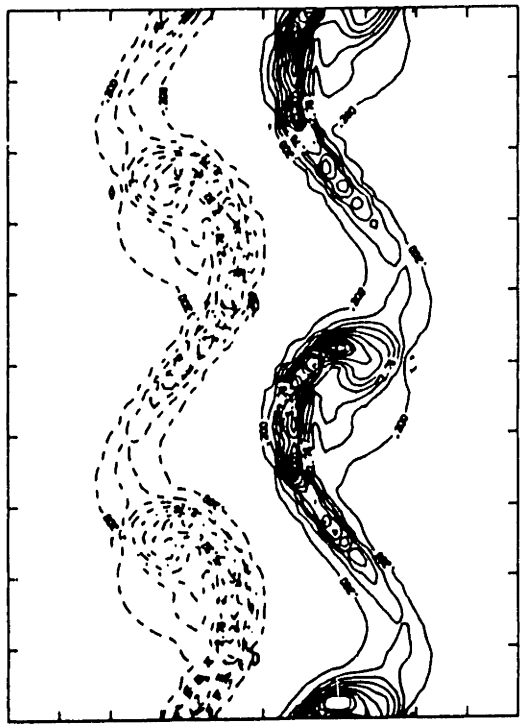

t = 3.75

t = 5.37

t = 6.0

Figure 100

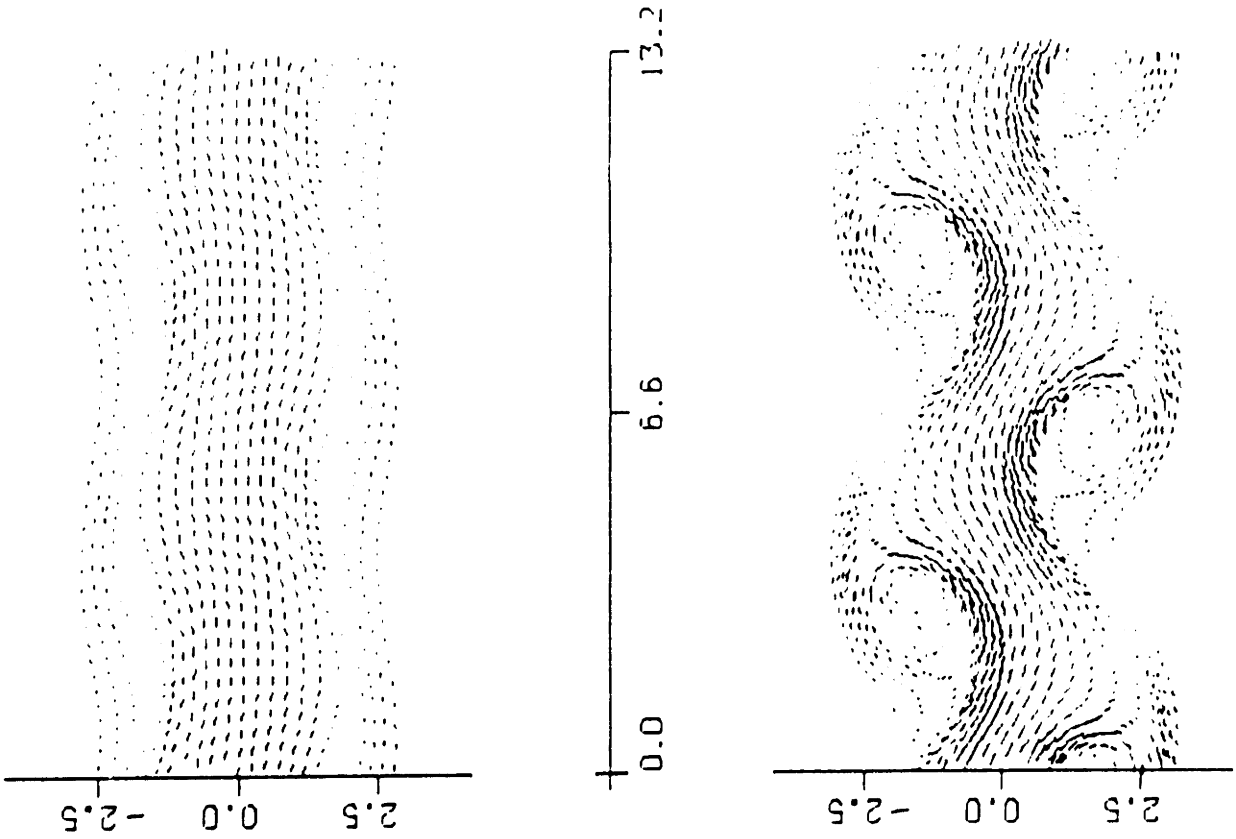

t = 2.5

t = 5.0

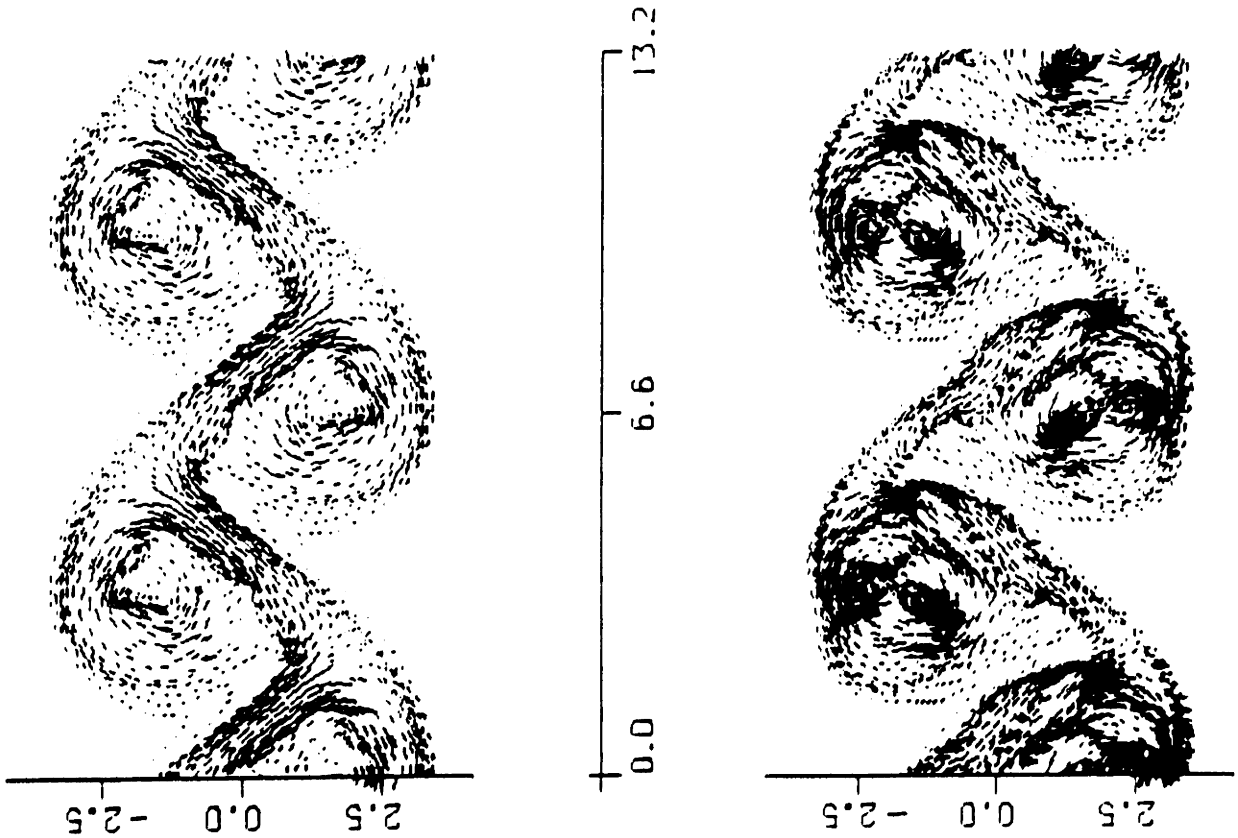

t = 6.5

t = 7.5

Figure 101

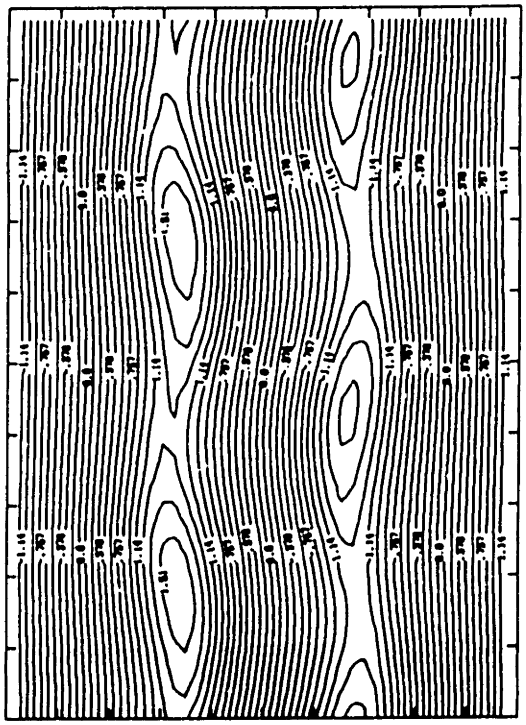

t = 2.5

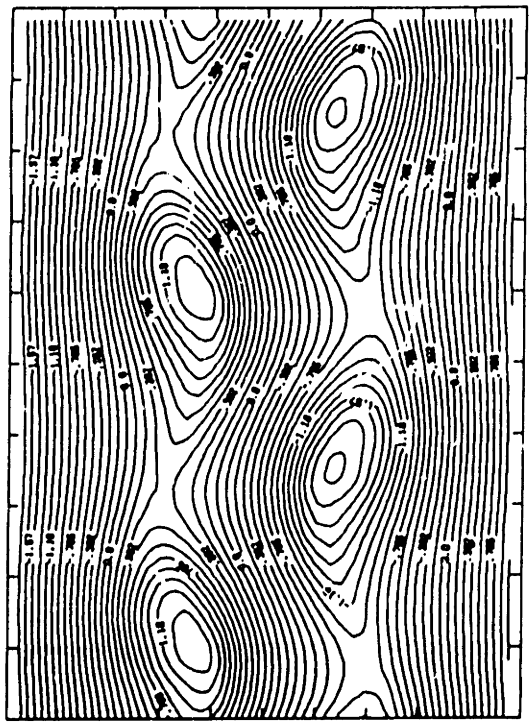

t = 5.0

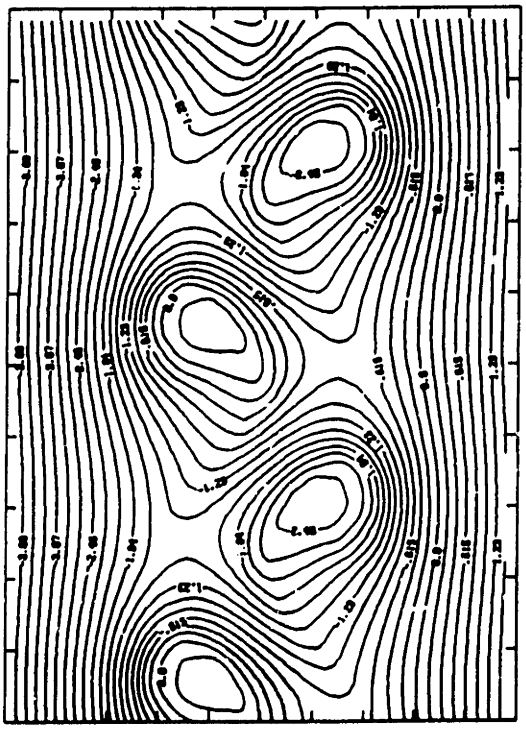

t = 6.5

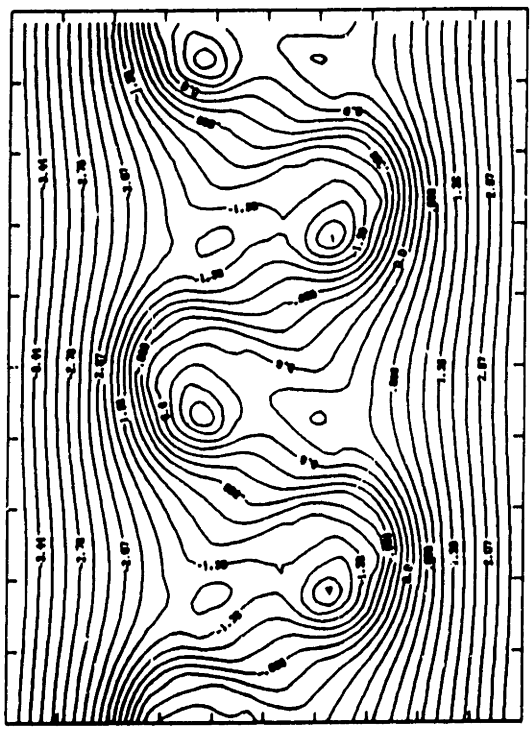

t = 7.5

Figure 102

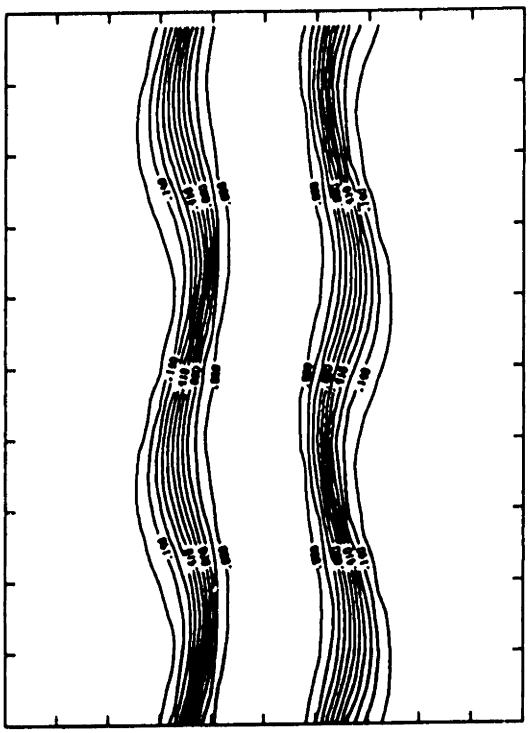

t = 2.5

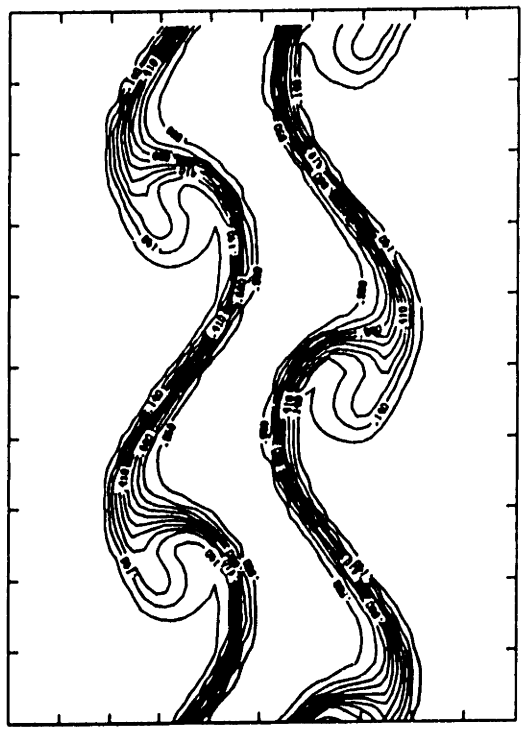

t = 5.0

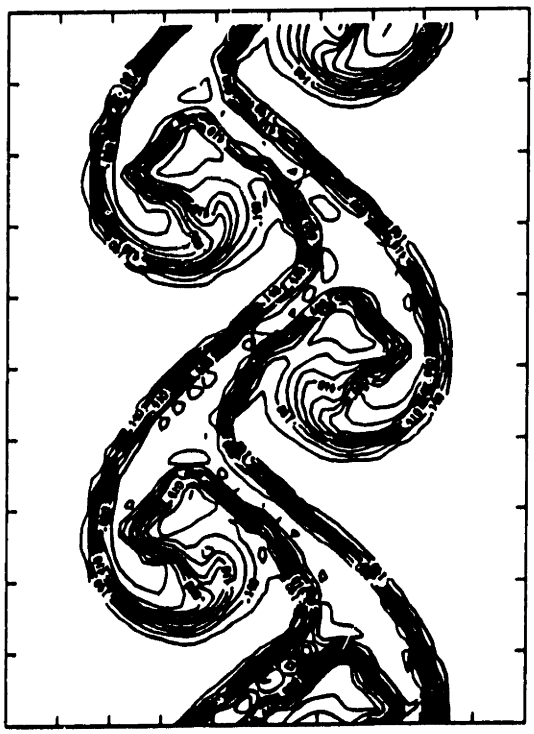

t = 6.5

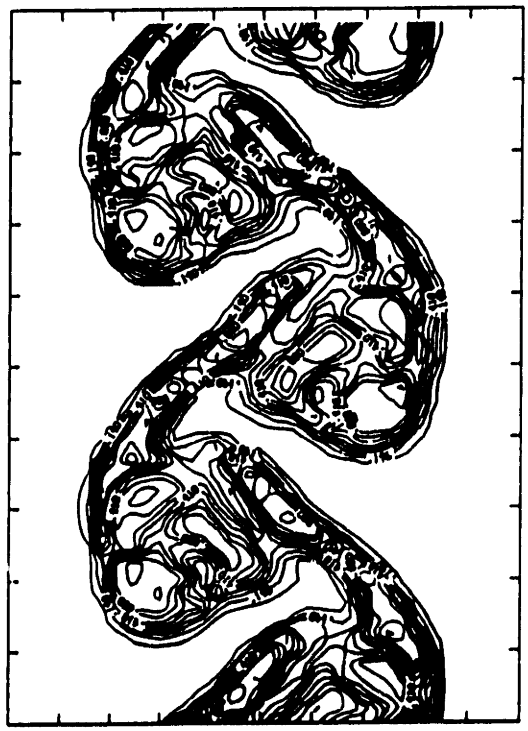

t = 7.5

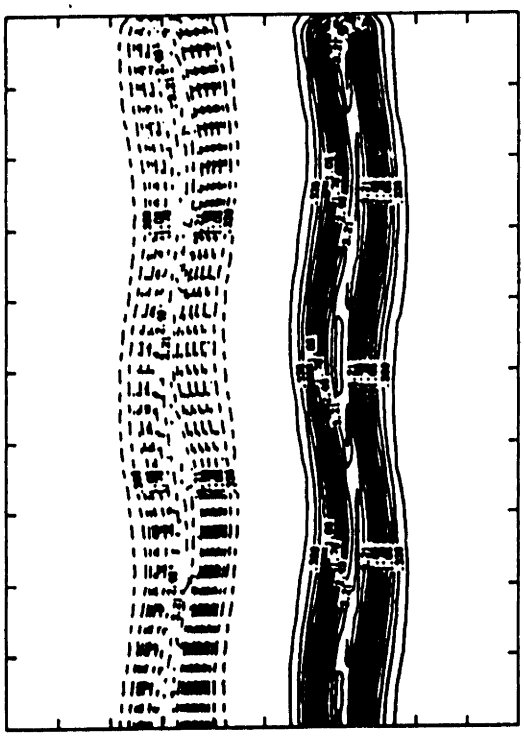

t = 2.5

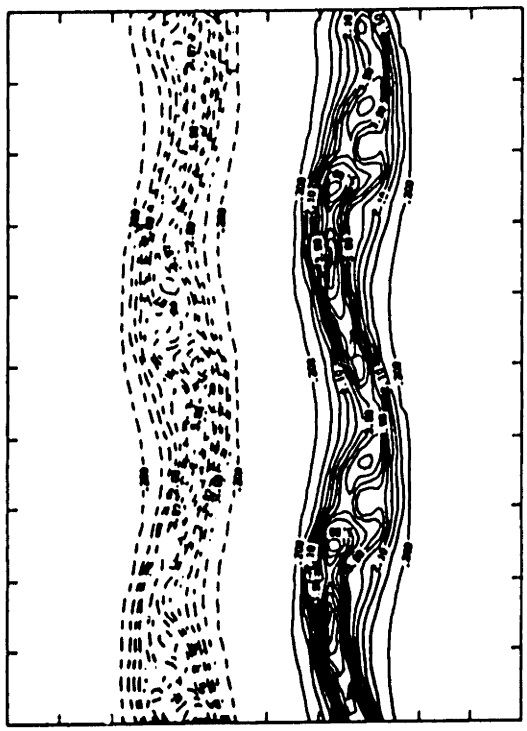

t = 5.0

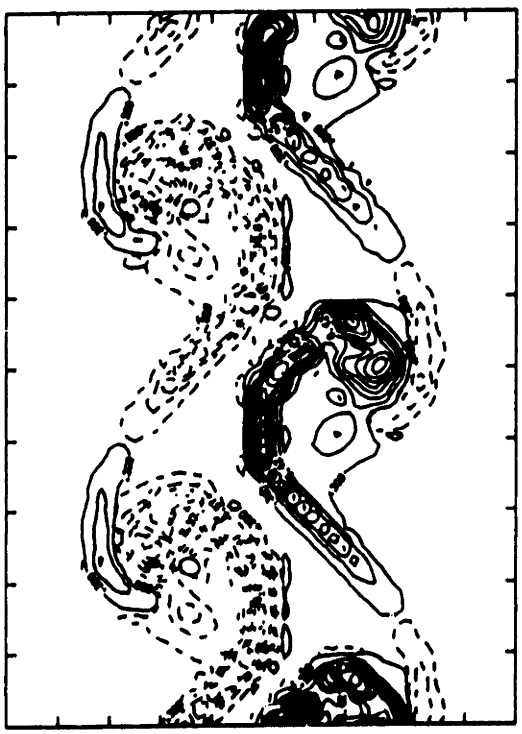

t = 6.5

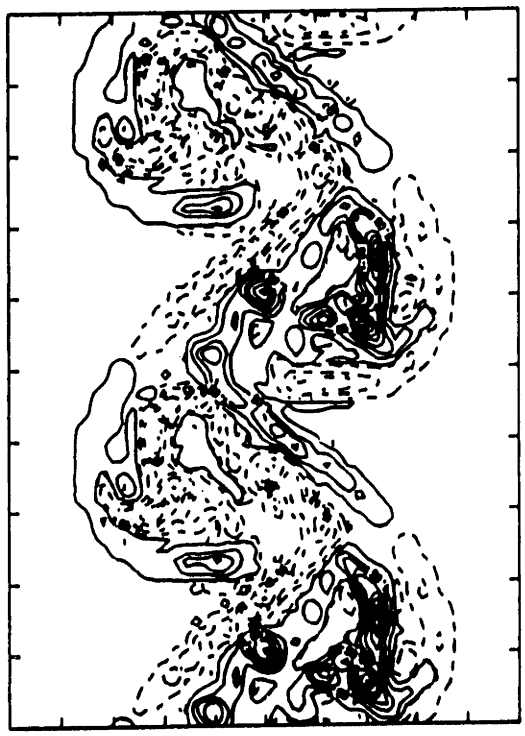

t = 7.5

Figure 104

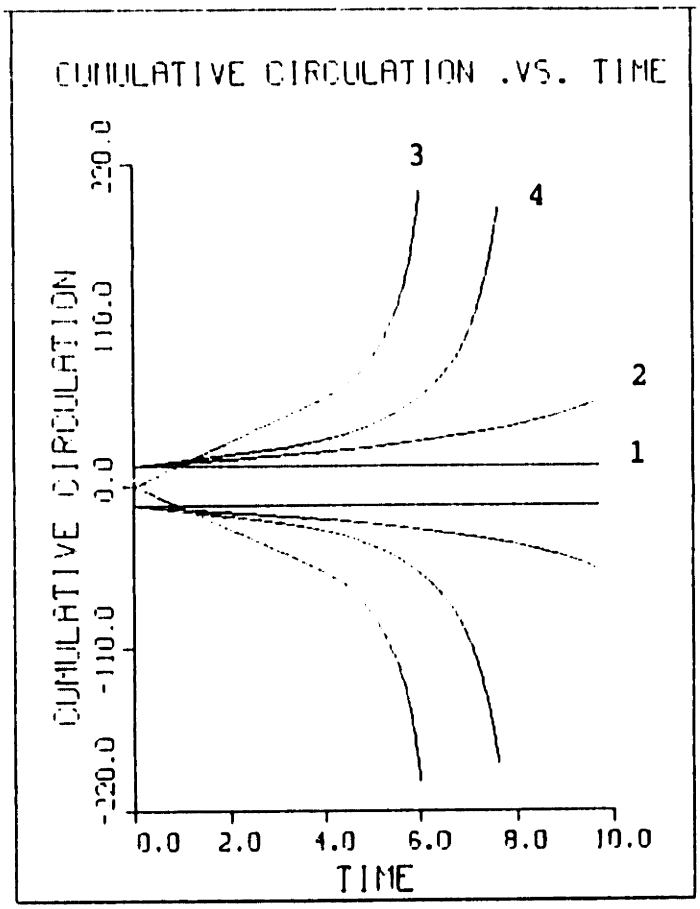

Figure 105

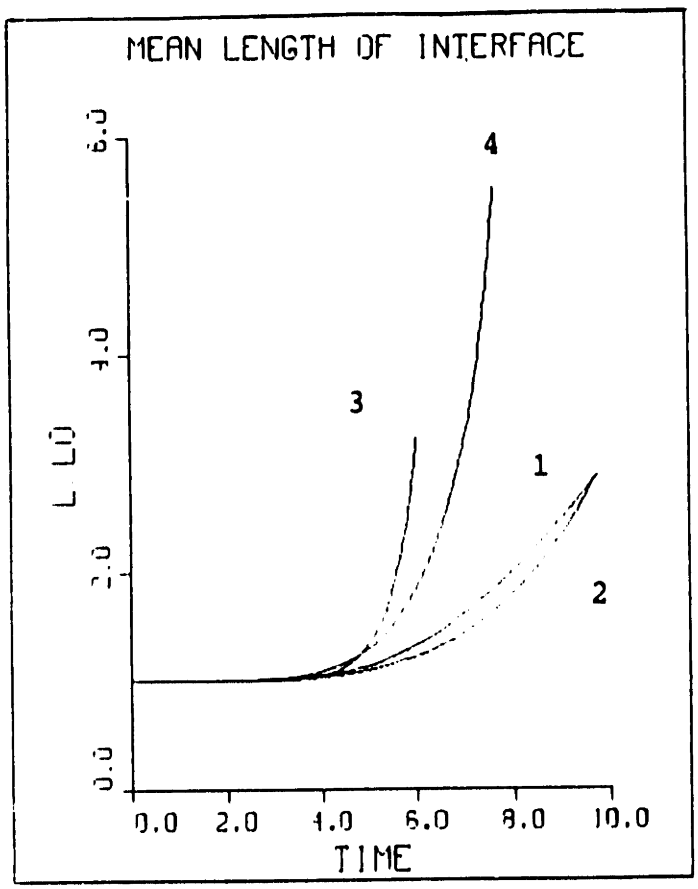

Figure 106

VII. THE NUMERICAL SIMULATION OF A JET DIFFUSION FLAME

VII. 1. INTRODUCTION

A generic example of a diffusion flame is that of a fuel jet issuing out of a nozzle and mixing with the ambient air followed by chemical reaction and heat release. The diffusion flame is therefore governed by the amount of mixing that can be accomplished between the fuel and the oxidizer. From this point of view, it is crucial to understand the dynamics of mixing in a turbulent flow field in order to improve the burning efficiency. Also, the effects of turbulence-combustion interactions are very important. It is necessary to understand how the heat release affects the flow and consequently the mixing process. The effects of buoyancy are also considered in the physical model. The role of large scale structures in enhancing mixing and chemical reaction has been the subject of a number of studies [43,44]. Recently, the effect of buoyancy on jet diffusion flames has attracted a great deal of attention [37,45].

VII. 2. DESCRIPTION OF FLOW GEOMETRY

The schematic of the flow is shown in Fig. 107. The velocity profile is similar to the one used in the study of the non-reacting jet. However, the initial temperature, or the density, is the same throughout the flowfield since the fuel as well as the oxidizer are at room temperature before the onset of reaction. The low velocity stream is the oxidizer and the high

velocity stream is the fuel. The shear layer between the two streams goes unstable and rolls up to form the large scale structures. The role played by these coherent structures in enhancing mixing and promoting chemical reaction is studied in detail. For the sake of simplicity, only the varicose mode of the jet instability is analyzed.

VII. 3. GOVERNING EQUATIONS

The non-dimensional governing equations for the jet diffusion flame are given below.

$$\frac{d\omega}{dt} = \frac{1}{\rho^2}(\nabla\rho \times \nabla p) - \omega\,(\nabla \cdot \mathbf{u}) \tag{93}$$

$$\text{Reactants } (1) + \text{Oxidizer } (r) \xrightarrow{k} \text{Products } (1+r) \tag{94}$$

$$\frac{dT}{dt} = \frac{1}{P_e}\nabla^2 T + \frac{A_f}{r} Q \dot{W} \tag{95}$$

$$\frac{dC_F}{dt} = \frac{1}{P_e L_e}\nabla^2 C_F - \frac{A_f}{r} \dot{W} \tag{96}$$

$$\frac{dC_O}{dt} = \frac{1}{P_e L_e}\nabla^2 C_O - A_f \dot{W} \tag{97}$$

$$\dot{W} = \rho C_F C_O \tag{98}$$

$$\dot{W} = \rho C_F C_O \exp(-T_a/T) \tag{99}$$

The chemistry is governed by a single step, second order reaction wherein a single unit of mass of fuel reacts with r mass units of oxidizer to form (1+r) units of products. r is assumed to be unity in all the cases considered

in this study. The vorticity equation has an additional term that includes the effect of flow divergence. The equations are non-dimensionalized by the characteristic values U_o for velocity, L_o for length, T_o for temperature and C_∞ for concentration. U_o is given as $U_o = \Delta U/2$, ΔU being the velocity difference between the jet and the ambient; L_o is the characteristic thickness of the shear layer given by $L_o = 2\sqrt{2}\ \sigma$, σ being the standard deviation of the Gaussian vorticity distribution. T_o is the room temperature and C_∞ is the free stream concentration of the species. A_f is the pre-exponential factor and is given by $A_f = (A\ L_o\ \rho_o)/U_o$. A is the constant in the Arrhenius rate expression. The non-dimensional activation energy is defined as $T_a = E/(R\ T_o)$ where E is the dimensional activation energy and R is the universal gas constant. The non-dimensional heat release parameter Q is the enthalpy of reaction normalized by $C_p\ T_o$ and signifies the increase in temperature caused by the complete burning of one mass unit of fuel. Simulations are conducted for two source terms; one without exponential dependence , Eqn.(98) and one with exponential dependence on temperature, Eqn.(99).

VII. 4. RESULTS OF NUMERICAL SIMULATIONS

The flow field is perturbed symmetrically in order to simulate the varicose mode. The amplitude of perturbation is 0.05 λ, λ being the wavelength of perturbation. Simulations were conducted for the non-reacting as well as reacting flow fields in order to draw appropriate comparisons. The initial set of simulations for the reacting flow are done without temperature dependence. The Peclet number for all the reacting cases is assumed to be equal to 1000 and the non-dimensional heat release parameter Q is 3.0 .

VII. 4. 1. ZERO ACTIVATION ENERGY MODEL ($W = \rho C_F C_O$)

(i) Case I : Non-Reacting Flow:

The velocities and locations of the vortex/transport elements at t=2.5, 5.0, 7.5 and 10.0 respectively are shown in Fig. 108. The development of the flow is very similar to what was observed for the uniform-density jet flow in section IV. However, in this case, the amplitude of perturbation ($\varepsilon = 0.05\lambda$)is higher than what was used in section IV. The instability grows by entraining fluid from both streams and ultimately saturates upon which fluid begins to rejoin the free streams. The structures appear to be convecting in the streamwise direction due to the effect of the induced velocity across the line of symmetry. Fig. 109 shows the corresponding streamline contours. The volumetric entrainment within the structure increases with time until the instability saturates. This is indicated by the increasing number of streamlines that form closed contours around the structure. The motion of the centers of the eddies is also clearly shown by the streamline plots.

Since the temperature is uniform throughout the flow field, the normalized temperature contours are not shown for this case. Fig. 110 shows the fuel concentration contours for the different time frames although there is no reaction in the flow field. Thus, the fuel concentration can be thought of as a passive, conserved scalar in this case. By tracing the $C_F = 0.5$ contour, it is found that more of the jet fluid by volume is being entrained into the eddies. Fig. 111 shows the vorticity contours at the corresponding times. Since the flow has no density gradients, the vorticity is conserved along the material path. Therefore, the total circulation in the flow field in unaltered and the vorticity contours essentially follow the material line

plots. Therefore, the cumulative circulation curves are horizontal as shown in Curve 1 of Fig. 132. Curve 1 of Fig. 133 shows the mean length of the interface as a function of time. The mean length is obtained as an average over the length of all the material layers used in the calculations. The final length is about three times the initial length.

(ii) Case II : A_f =0.0625, W = ρ C_F C_O

The source term for the reaction is proportional to the concentrations of fuel and oxidizer and is independent of the temperature. The Damkohler number or A_f is assumed to be small, i.e., the flow is fast compared to the speed of reaction. Fig. 112 shows the location and velocities of the vortex/transport elements at t=2.5, 5.0, 7.5 and 10.0 respectively. Since the speed of reaction is very slow compared to the flow, the growth of the structures is very similar to what was observed in the non-reacting case. Although, after close inspection of the material lines, some effects of chemical reaction do become clear. The eddies appear to have expanded due to the heat release taking place inside. The vorticity at the center of the structures appears to be diffuse in contrast to the concentrated structures in Case I. From observing the material lines at the late stages of development, it is clear that heat release has slowed down the growth of the instability. There is less entrainment of the ambient fluid into the eddies due to the effects of the expansion field. Fig. 113 shows the product concentration contours at the corresponding time frames. Due to the nature of the source term, the initial reaction takes place in zones where concentrations of fuel and oxidizer both exist. Since the reaction rate is independent of the temperature, the initial reaction is very strong inspite of the reactants being cold, i.e., there is

no ignition delay. As the structures begin to rollup, a strong strain field is generated in the flow. It is observed that the product formation in zones of large positive strain is inhibited. At late times, all of the products are present in the cores of the eddies and the braids are completely devoid of reaction. The srong strain in the flow field blows out the flame and the reaction proceeds in zones of negative strain, i.e., the centers of the eddies. Also, the maximum amount of mixing takes place in the cores and since the reaction rate of the diffusion flame is critically dependent on mixing, most of the combustion is limited to the cores. Fig. 114 shows the corresponding fuel concentration contours. It is observed that some of the fuel in the center of the structure has been consumed as a result of the reation.

Fig. 115 shows contours of the source term W for a single structure at the same time frames. The contors are shaded to indicate the magnitude of the source term. The darkest shade indicates a value between 66% and 100% of the maximum value of W. The lighter shade indicates a value between 33% and 66% of the maximum value of W. The magnitude of the source term can be thought of as a potential for chemical reaction. It is interesting to note that the source term always has a finite value even in regions of high strain although there is no product formation. This can be explained by looking at the governing equations for the species concentrations. The amount of reactants consumed at a point in the flow field is a sum of the convective, diffusive and the source terms. Although the source term may have a finite value in regions of high positive strain, the convective and the diffusion may counteract the effect of the source. Thus there is no net effect on the formation of products. The reaction appears to be taking place in a distributed zone inside and around the large scale structures. The turbulence

in the field has resulted in an increase in the burning area or reaction zone. From Fig. 115, it is observed that the magnitude of the source term is smaller in the centers of the eddies as compared to the edges of the structures. This is because the cores have already reacted to form products and the reaction rate in these regions are smaller. The vorticity contours for this case are shown in Fig. 116. The initial development of the vorticity field is very similar to what was seen in Case I. The effects of vorticity generation are insignificant since both halves of the jet more or less maintain their initial signs of vorticity. However, at late times, it is observed that the magnitude of vorticity within the structures is smaller with respect to Case I. This is because the expansion field within the structures tends to weaken the local vorticity. In this case, the magnitude of reaction being small, the effects of expansion are not very obvious.

Curve 2 of Fig. 132 shows the cumulative circulation in the flow field as a function of time for this case. The initial density gradients in the field are zero. Therefore, the generation of circulation takes place only after a certain amount of products have formed. It is interesting to note that the magnitude of generation for the jet diffusion flame is much smaller than that for the non-reacting density stratified jet studied in section IV. Curve 2 of Fig. 133 shows the mean length of the jet shear layers as a function of time. The effects of expansion are more obvious in this plot. It is observed that the reacting eddy grow slowly compared to Case I. The expansion within the structures stabilizes the flow and leads to less elongation of the material layers. Fig. 134 shows the mass of products formed as a function of time for the turbulent and the laminar flame. The laminar product formation is calculated as the amount of products formed if the flow field were to remain completely stable and planar, i.e., the instability is completely suppressed.

Therefore any differences between the laminar and the turbulent product formation rates are due to effects of turbulence in the field. Curve 1 represents the laminar flame and Curve 2 represents the turbulent flame. The initial product formation rate for the laminar flame is very large and at late times the slope of the curve approaches zero. This is because the source term for the reation is maximum at t=0 and as the reaction proceeds, less of the fuel and oxidizer are present for the reation. At very late times, all of the fuel and the oxidizer are consumed and the reaction rate goes to zero. Hence the slope of the curve keeps decreasing with time until it approaches zero. As is expected, the initial product formation is identical for both the turbulent and the laminar flame. However, as time progresses, it is observed that the amount of products formed by the turbulent flame becomes smaller than that of the laminar flame. This is because the developing strain field blows out or extinguishes the flame in regions of positive strain. However at late times, the amount of mixing due to entrainment within the structures increases and the turbulent flame curve increases beyond the laminar curve. Thus the two contradictory effects of flow turbulence is observed here. One is that of the strain field extinguishing the flame and another is that of turbulence enhancing mixing and hence the burning rate.

(iii) Case III : $A_f = 0.25$

The speed of the reaction in this case is increases by a factor of 4 compared to Case II. Fig. 117 shows the locations and velocities of the vortex/transport elements at t=2.5, 5.0, 7.5 and 10.0 respectively. The effects of the chemical reaction are very apparent in this case. The volumetric expansion within the cores of the eddies inhibits the rollup to a great extent and the structures appear to be expanding out at late times. The

cores of the eddies appear to be more diffuse than those in Cases I and II. It is also observed that the total volumetric entrainment into the structures is decreased considerably. Fig. 118 shows the product concentation contours at the corresponding time frames. Again, most of the product formation appears to be within the cores of the eddies. The strain field extinguishes the flame in regions of large positive strain. In this case, however, the magnitude of the strain field is much smaller compared to those in cases I and II due to the effect of the volumetric expansion stabilizing the flow field. The fuel concentration contours are shown in Fig. 119. It is observed that the values of the fuel concentration are smaller in the cores of the eddies than around the circumference of the structures. The consumption of reactants within the structures is shown clearly by the contours.

Fig. 120 shows the contours for the source term at the corresponding time frames. Again, it is observed that the source term has finite values in zones of large positive strain inspite of the product formation being very small. Although the reaction takes place in distributed zones at the early stages of development, the reaction zone at late times is in the form of a sheet around the eddies. The circumference of the eddies are zones of large positive strains and the reaction is especially sensitive to strain at this stage. The centers of the eddies are comprised mainly of products and hence the value of the source term in these regions is very small. The vorticity contours for this case are shown in Fig. 121. The stabilizing effect of volumetric expansion is clearly observed in these plots. The peak values of vorticity at late times are smaller compared to those in cases I and II indicating the reduction in vorticity due to expansion. The damping of the instability due to heat release has been observed in experiments [45,46,47].

The cumulative circulation in the field is plotted as a function of time in Curve 3 of Fig. 132 . It is interesting to note that although the flow is more stable in this case, the amount of circulation generated is slightly more than what was observed for Case II. This is due to that fact that the higher heat release in this case leads to larger values for $\nabla\rho$ although the value of ∇p is decreased due to the inhibition of rollup. The net effect is a small increase in the amount of circulation generated. The mean length of the material layers is plotted as a function of time in Curve 3 of Fig. 133 . The curve for the mean length is below the curves for cases I and II. The effect of a larger source term is to stabilize the flow and to decrease the elongation of the material layers.

Fig. 135 shows the laminar and the turbulent product formation rates for this case. Since the magnitude of the souce term is larger, the initial slopes of the curves are larger than in Case II. However, the same qualitative features are observed here. The development of the strain field causes the turbulent product formation curve to decrease below that of the laminar curve. It is observed that the decrease below the laminar flame is larger in this case compared to that in Case II. This is because the reaction zone aligns itself with the strainfield and the reaction rate becomes very sensitive to the local value of strain. At late times, the increased mixing due to the instability causes the turbulent curve to increase above the laminar product formation.

(iv) Case IV : $A_f = 0.5$

The magnitude of the chemical source term is increased by a factor of two as compared to case III. The locations and velocities of the vortex/transport elements are shown in Fig. 122 at t=2.5, 5.0, 7.5 and 10.0 respectively. Due

to the large degree of heat release, the rollup is almost completely inhibited. The volumetric entrainment from both streams into the structures is very small compared to the previous cases. The volumetric expansion within the cores leads to a very diffuse appearance of the structure as a whole. The product concentration contours at the corresponding time frames are shown in Fig. 123 . It is immediately obvious that the strain field is very weak due to the stabilization of the flow. Most of the product formation takes place in the centers of the structures with a negligible amount in the braids between the eddies. The fuel concentration contours for this case are shown in Fig. 124. It is observed that the higher value of the Damkohler number has resulted in greater consumption of the fuel within the eddies.

Fig. 125 shows the contours for the source term at different times. The maximum values of the source term occur at the edges of the eddies. This is because the cores of the eddies are comprised mainly of products and the value of the source term is close to zero in these regions. Thus, most of the reaction zone is present in regions of strong strain. The vorticity contours for this case are shown in Fig. 126. The inhibition of the flow field due to the local dilatation of the flow is clearly observed. The vorticity values in the domain are smaller than in the previous cases. The generation of circulation in the domain is plotted as a function of time in Curve 4 of Fig. 132 . Again, it is surprising to see that the circulation generated is slightly more than in Cases II and III despite the fact that there is very little rollup in Case IV. However, a stronger chemical source term leads to larger values for $\nabla\rho$ which counteracts the decrease in ∇p to produce a small increase in the generation of circulation. The elongation of the material layers is plotted as a function of time in Curve 4 of Fig. 133. The degree of

elongation is much smaller than what was observed in the previous cases. The stabilization of the flow field leads to smaller strain rates.

The amount of products formed is plotted as a function of time in Fig. 136 for both the laminar and the turbulent flame. The initial slopes of the curves are very large due to the larger magnitude for the source term. Although the strain field in this case is considerably weaker than in the previous cases, it is observed that the turbulent flame is almost completely extinguished at about t=6.0 . The slope of the product formation curve is almost zero in this region. The reason for this phenomenon is that the large initial reaction rates quickly depletes the amount of reactant and oxidizer in the reaction zone which then aligns itself with a strong strainfield that thins and stretches out the area of reaction. Therefore, the value of the source term in these zones is very small and even a relatively weak strain field is able to cause a blow out of the flame. At late times, however, due to the enhanced mixing within the cores, the turbulent product formation increases above that of the laminar flame.

(v) Case V : $A_f = 0.5$, Fr = 2.0

It is quite clear from the previous simulations that any increase in the effective Damkohler number beyond that of Case IV is going to completely damp the instability in the flow field. In order to destabilize the flow at this high value of the chemical source term, buoyancy is included in the simulations in the form of a finite Froude number of 2. The locations and velocities of the vortex/transport elements are shown in Fig. 127 at t=2.5, 5.0, 7.5 and 10.0 respectively. During the early stages, the flow develops quite similar to what was observed for Case IV. However, as more and more

products are formed due to the reaction, buoyant forces become active and lead to an increased destabilization of the flow field. It is clear that at the late stages, the eddies are entraining more fluid from the free streams leading to increased mixing and enhanced reaction within the cores. The structures have an expanded appearance at late times due to the volumetric expansion taking place within. The precise mechanism for the extra destabilization of the flow is the gravity generated vorticity. Fig. 128 shows the product concentration contours at the corresponding time frames. At the late stages of development, inspite of the large strain rates, some amount of product concentation is observed in the braids. Due to the Damkohler number being high, the flame is able to survive the effects of a stronger strain field. Higher values for the product concentration are observed within the structures indicating that more amount of products have been formed relative to Case IV. The fuel concentration contours are shown in Fig. 129. It is observed that most of the fuel within the eddies is consumed in the reaction and the fuel concentration is the highest in the braids between the eddies.

The contours for the source term are plotted in Fig. 130 at the corresponding times. Most of the initial burning takes place within the cores of the eddies and at late times the value of the source term in the cores goes to zero. Large values for the source term are observed around the edges and the braids of the eddies. Fig. 131 shows the corresponding vorticity contours for Case V. The generation of vorticity is quite apparent even in the early stages of development. Vorticity of opposite signs is being generated on both halves of the flow domain. This leads to an additional destabilization of the flow. The vorticity values within the structures are considerably larger than what was observed for Cases II, III and IV. The

cumulative circulation in the domain is plotted as a function of time in Curve 5 of Fig. 132. It is observed that the generation of circulation takes place at a higher rate compared to the previous cases. The final circulation in the field is about twice that for Case IV. However, the total circulation in the flow field is zero because of the symmetry across the center line. The mean length of the material layers is shown as a function of time in Curve 5 of Fig. 133. Initially, the curve is quite similar to Curve 4 of Case IV. At late stages, however, the effect of buoyancy becomes dominant and the elongation rate of the material layers increases even beyond that of the non-reacting eddy.

Fig. 137 shows the product formation as a function of time for the laminar and the turbulent flame. The initial stage of development resembles closely that of Case IV. The enhanced entrainment and mixing due to buoyancy at the late stages leads to additional product formation as is seen in Fig. 137. Thus buoyancy is very effective in destabilizing the flow field and generating more amount of products due to enhanced turbulent mixing.

(vi) Discussion :

The above simulations of the jet diffusion flame under conditions of different Damkohler numbers have brought out some rather interesting physics regarding the interaction between the flow and the reaction. It is observed that for large values of the reaction rate, the combined effects of baroclinicity and volumetric expansion in the flow field tends to dampen the growth of the instability. To separate the effects of baroclinicity and volumetric expansion, simulations were conducted for case IV ($A_f = 0.5$), one with baroclinicity but without expansion and one with expansion but without

baroclinicity. The results for the mean material length are shown in Fig. 138. The mean material length is an indicator of the degree of instability in the flow field. Curves 1 and 4 are reproduced for cases I and IV respectively. Curve 2 represents the simulation without heat release and curve 3 represents the case without baroclinicity. It is observed from curve 2 that baroclinicity by itself tends to stabilize the flow to a small degree. However, it is obvious from curve 3 that most of the stabilization of the flow is due to the volumetric expansion term which reduces the local concentration of vorticity.

Also, the product formation in a diffusion flame is very sensitive to the local strain rate. At large values of the strain rate, the convective and the diffusion terms counteract the production term and the flame is locally extinguished. However, the mixing in the cores of the eddies is greatly enhanced due to stretch and diffusion and most or all of the reaction takes place in these zones. At high Damkohler numbers, the addition of buoyancy counteracts the stabilization of the flow due to volumetric expansion and greatly increases the degree of instability in the flow field. Under these conditions, the turbulent flame produces significantly more products than the laminar flame. However, in cases II, III and IV , the turbulent flame product formation is more or less equal to that of the laminar flame. It is to be noted that the nature of the source term that has been used in these calculations is not very realistic since the reation rate is completely independent of temperature. This may lead to some rather erroneous predictions of the flow-combustion interactions.

FIGURE CAPTIONS

Fig. 107. Schematic of the jet diffusion flame. (a) the initial velocity and vorticity profiles; (b) the initial oxidizer and fuel concentration profiles.

Fig. 108. The locations and velocities of the vortex/transport elements at t= 2.5, 5.0, 7.5 abd 10.0 respectively for Case I.

Fig. 109. The streamline contours for Case I at t= 2.5, 5.0, 7.5 and 10.0 respectively.

Fig. 110. The fuel concentration contours at t = 2.5, 5.0, 7.5 and 10.0 respectively for Case I.

Fig. 111. The vorticity contours for Case I at t= 2.5, 5.0, 7.5 and 10.0 respectively. The continuous contours represent negative vorticity and the dashed contours signify positive vorticity.

Fig. 112. The locations and velocities of the vortex/transport elements at t= 2.5, 5.0, 7.5 and 10.0 respectively for Case II.

Fig. 113. The product concentration contours at t= 2.5, 5.0, 7.5 and 10.0 respectively for Case II.

Fig. 114. The fuel concentration contours at t= 2.5, 5.0, 7.5 and 10.0 respectively for Case II.

Fig. 115. The source term contours for Case II at t= 2.5, 5.0, 7.5 and 10.0 respectively.

Fig. 116. The vorticity contours for Case II at t= 2.5, 5.0, 7.5 and 10.0 respectively. The continuous contours represent negative vorticity and the dashed contours signify positive vorticity.

Fig. 117. The locations and velocities of the vortex/transport elements at t= 2.5, 5.0, 7.5 and 10.0 respectively for Case III.

Fig. 118. The product concentration contours at t= 2.5, 5.0, 7.5 and 10.0 respectively for Case III.

Fig. 119. The fuel concentration contours at t= 2.5, 5.0, 7.5 and 10.0 respectively for Case III.

Fig. 120. The source term contours for Case III at t= 2.5, 5.0, 7.5 and 10.0 respectively.

Fig. 121. The vorticity contours for Case III at t= 2.5, 5.0, 7.5 and 10.0 respectively. The continuous contours represent negative vorticity and the dashed contours signify positive vorticity.

Fig. 122. The locations and velocities of the vortex/transport elements at t= 2.5, 5.0, 7.5 and 10.0 respectively for Case IV.

Fig. 123. The product concentration contours at t= 2.5, 5.0, 7.5 and 10.0 respectively for Case IV.

Fig. 124. The fuel concentration contours at t= 2.5, 5.0, 7.5 and 10.0 respectively for Case IV.

Fig. 125. The source term contours for Case IV at t= 2.5, 5.0, 7.5 and 10.0 respectively.

Fig. 126. The vorticity contours for Case IV at t= 2.5, 5.0, 7.5 and 10.0 respectively. The continuous contours represent negative vorticity and the dashed contours signify positive vorticity.

Fig. 127. The locations and velocities of the vortex/transport elements at t= 2.5, 5.0, 7.5 and 10.0 respectively for Case V.

Fig. 128. The product concentration contours at t= 2.5, 5.0, 7.5 and 10.0 respectively for Case V.

Fig. 129. The fuel concentration contours at t= 2.5, 5.0, 7.5 and 10.0 respectively for Case V.

Fig. 130. The source term contours for Case V at t= 2.5, 5.0, 7.5 and 10.0 respectively.

Fig. 131. The vorticity contours for Case V at t= 2.5, 5.0, 7.5 and 10.0 respectively. The continuous contours represent negative vorticity and the dashed contours signify positive vorticity.

Fig. 132. The cumulative circulation in the flow field as a function of time. The positive and the negative components are shown separately. Curves 1, 2, 3, 4 and 5 represent Cases I, II, III, IV and V respectively.

Fig. 133. The mean length of the material layers as a function of time. Curves 1, 2, 3, 4 and 5 represent cases I, II, III, IV and V respectively.

Fig. 134. The mass of products formed as a function of time for Case II. Curves 1 and 2 represent the laminar and the turbulent product formation respectively.

Fig. 135. The mass of products formed as a function of time for Case III. Curves 1 and 2 represent the laminar and the turbulent product formation respectively.

Fig. 136. The mass of products formed as a function of time for Case IV. Curves 1 and 2 represent the laminar and the turbulent product formation respectively.

Fig. 137. The mass of products formed as a function of time for Case V. Curves 1 and 2 represent the laminar and the turbulent product formation respectively.

Fig. 138. The mean material length versus time. Curves 1 and 4 represent cases I and IV respectively. Curve 2 is the result of the simulation without heat release and curve 3 that of the simulation without baroclinicity.

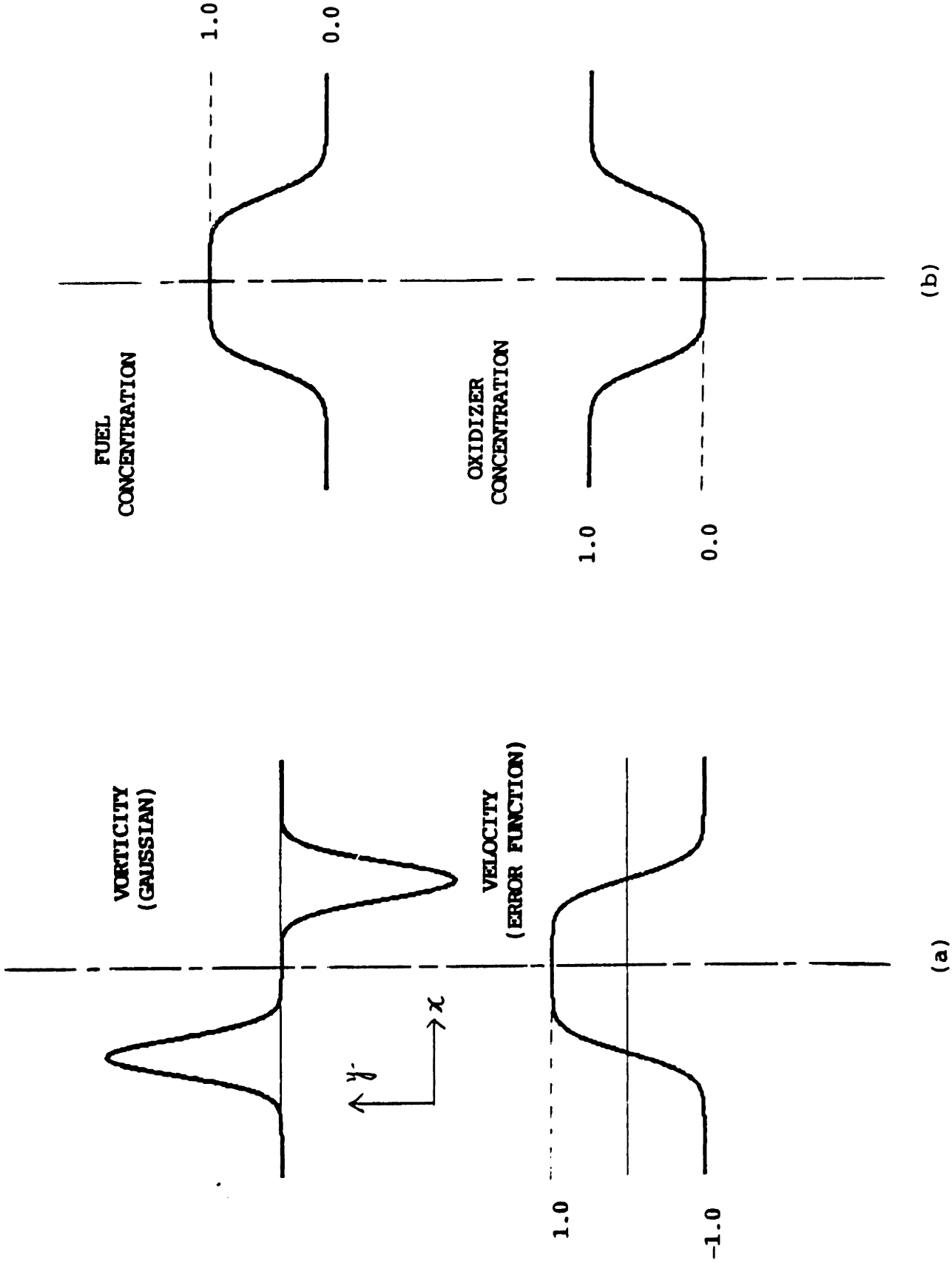
VORTICITY
(GAUSSIAN)
VELOCITY
(ERROR FUNCTION)
1.0
-1.0
y
x
(a)
FUEL
CONCENTRATION
1.0
0.0
OXIDIZER
CONCENTRATION
1.0
0.0
(b)

Figure 107

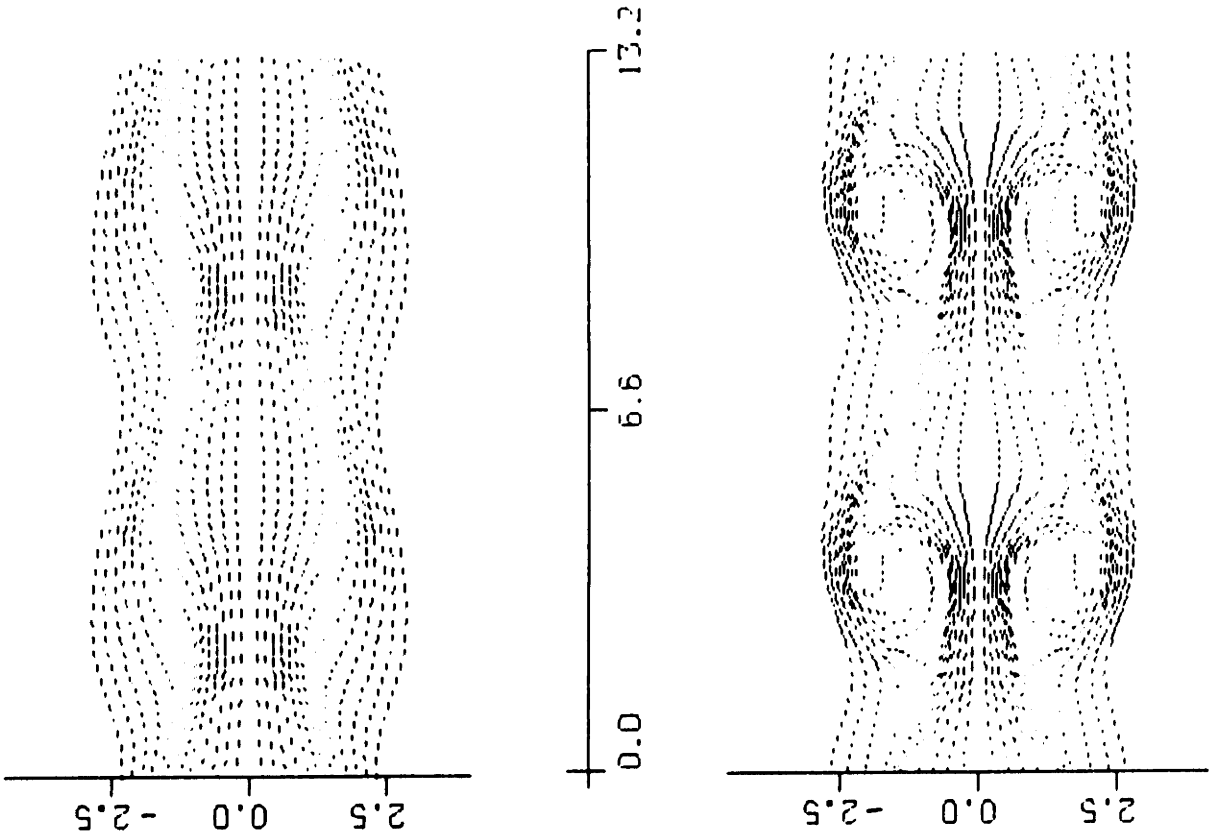

t = 2.5

t = 5.0

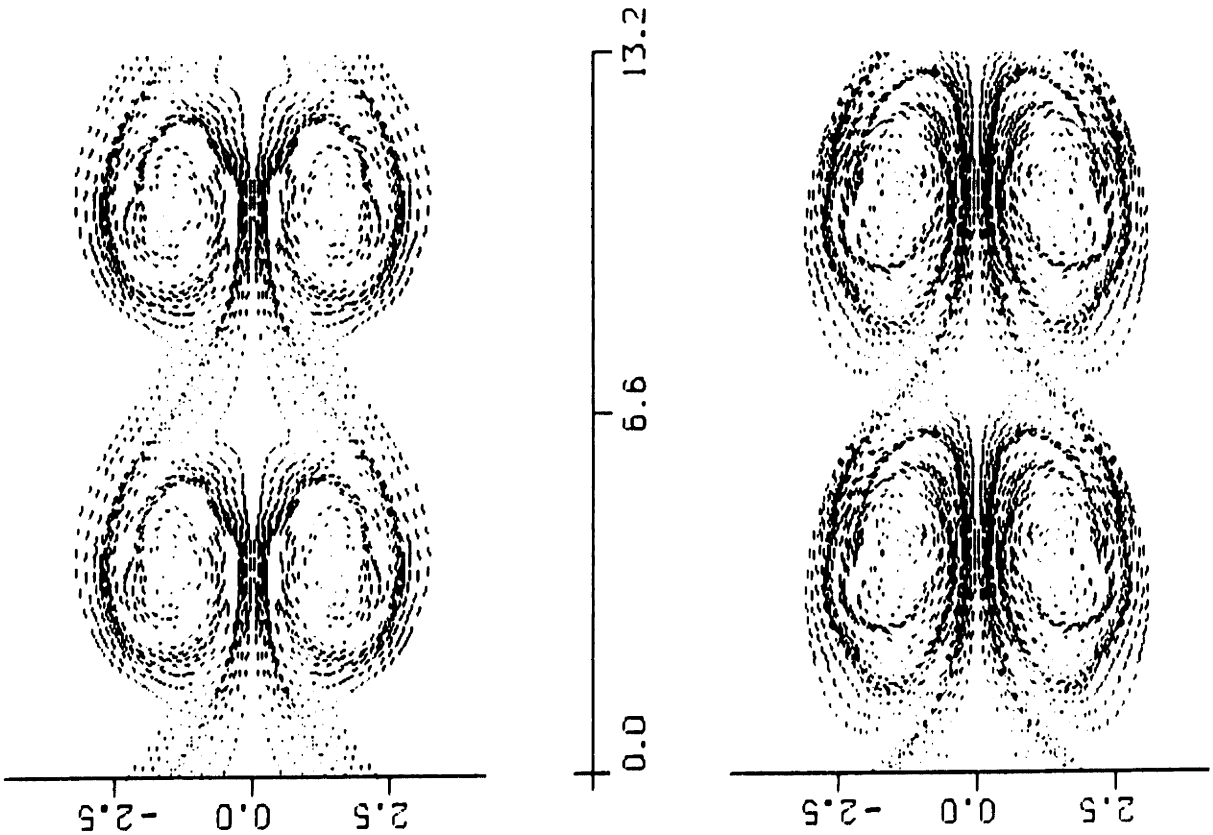

t = 7.5

t = 10.0

Figure 108

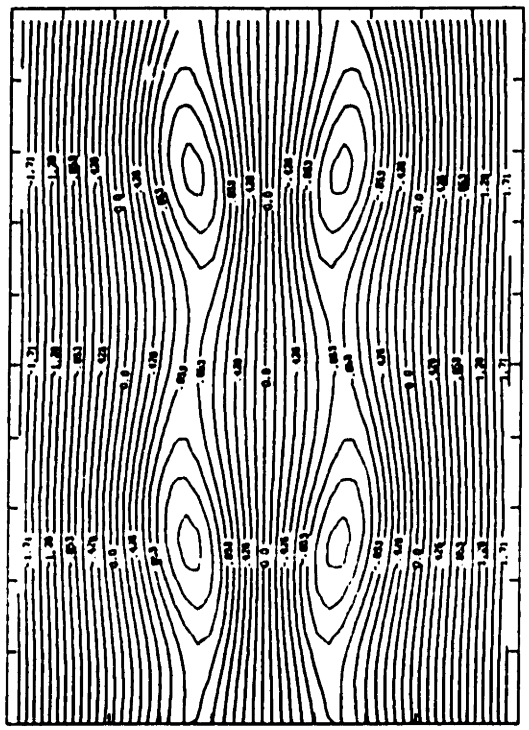

t = 2.5

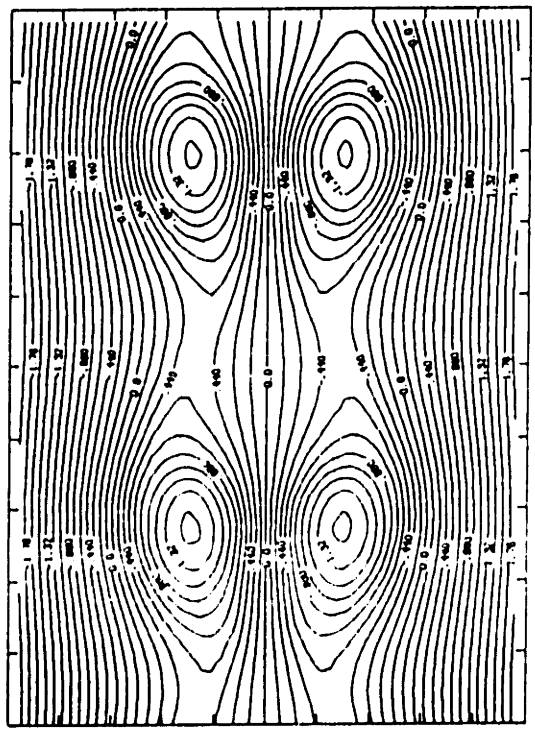

t = 5.0

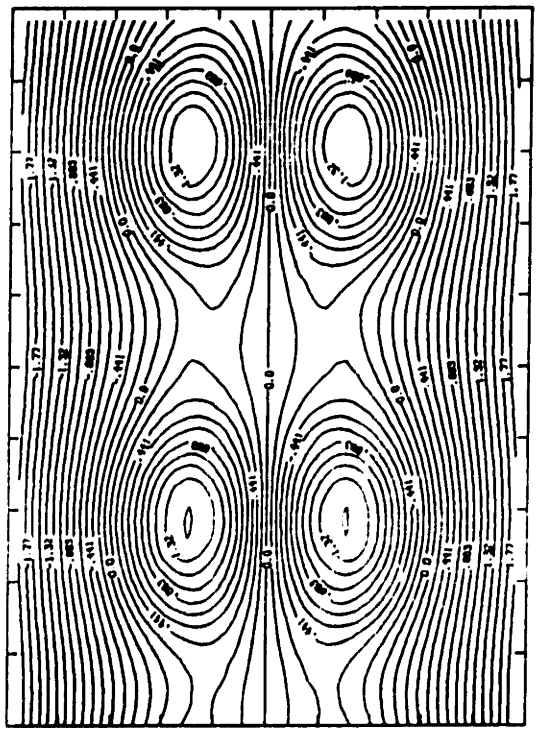

t = 7.5

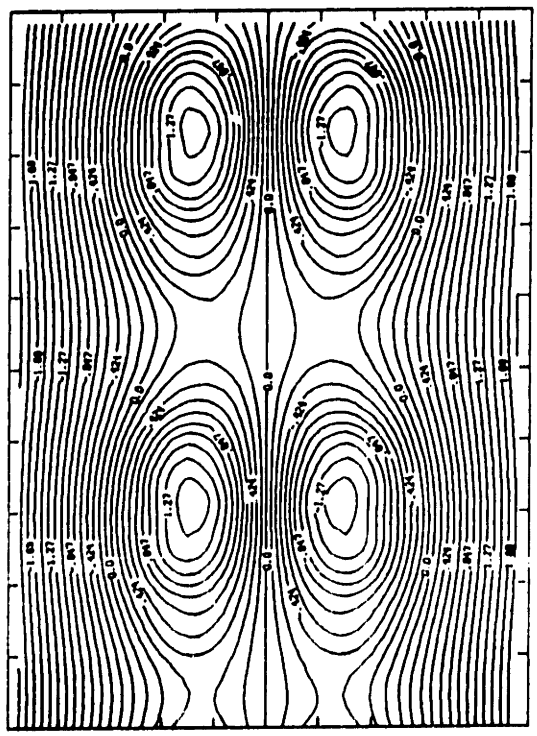

t = 10.0

Figure 109

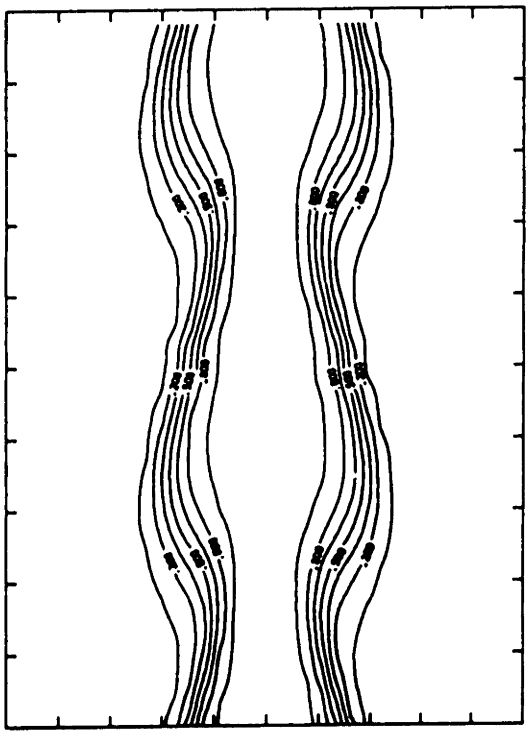

t = 2.5

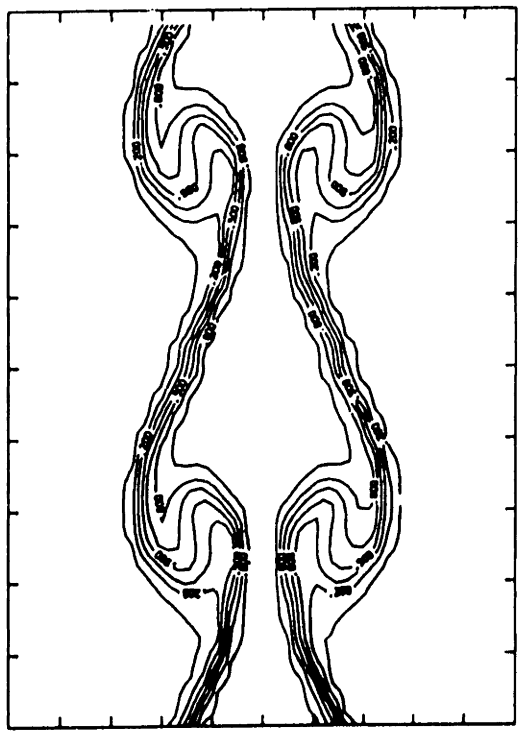

t = 5.0

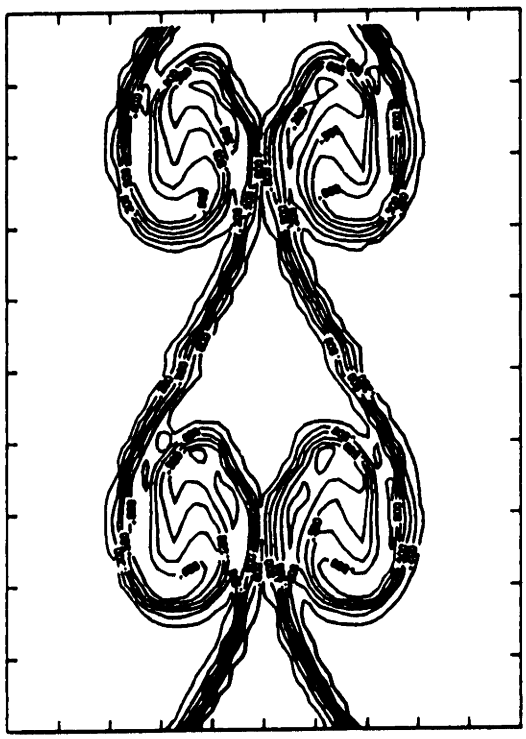

t = 7.5

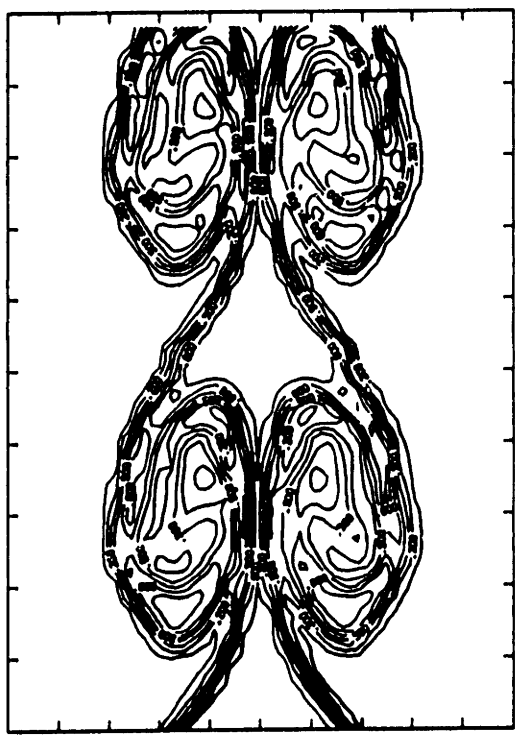

t = 10.0

Figure 110

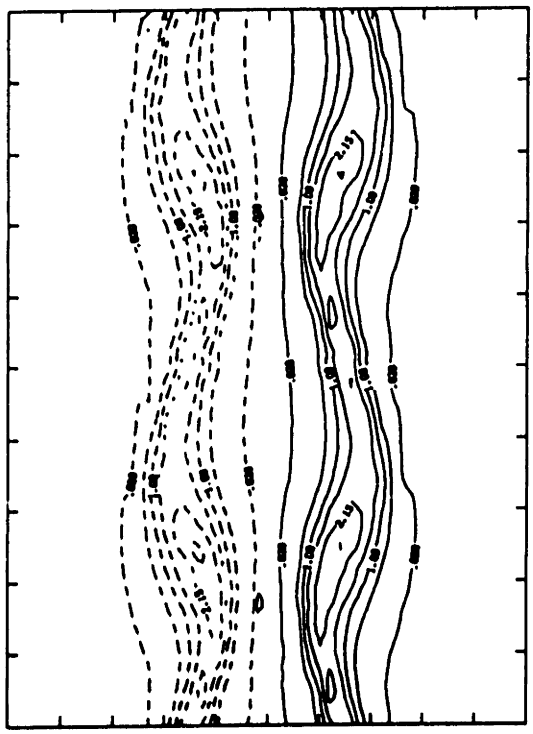

t = 2.5

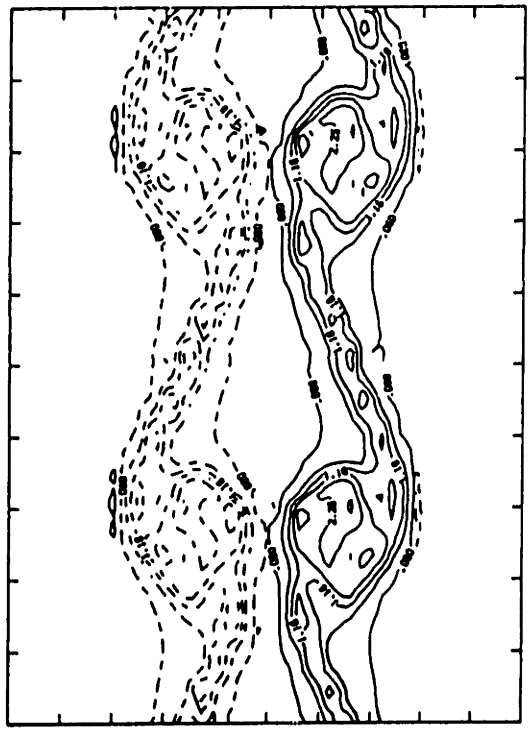

t = 5.0

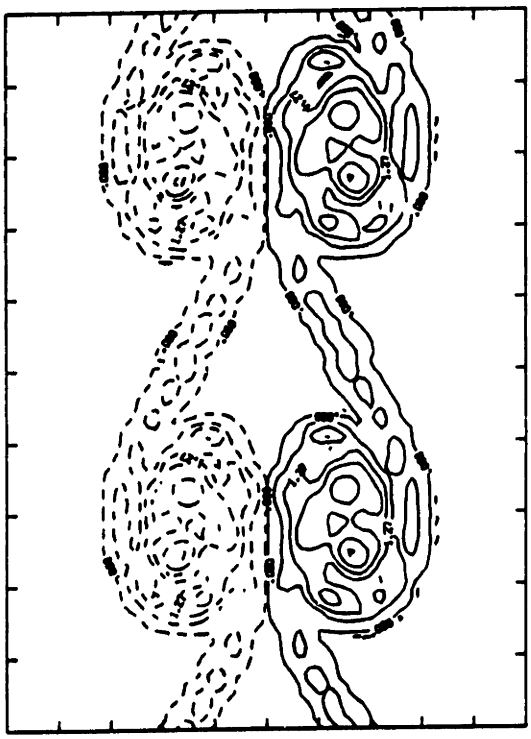

t = 7.5

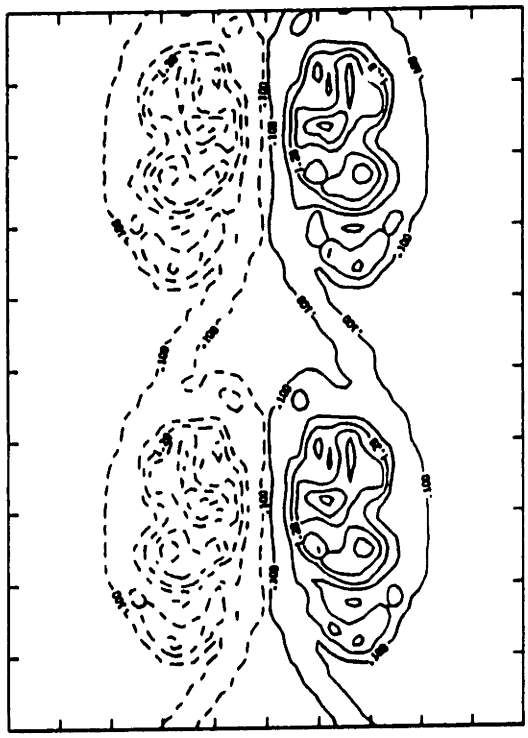

t = 10.0

Figure 111

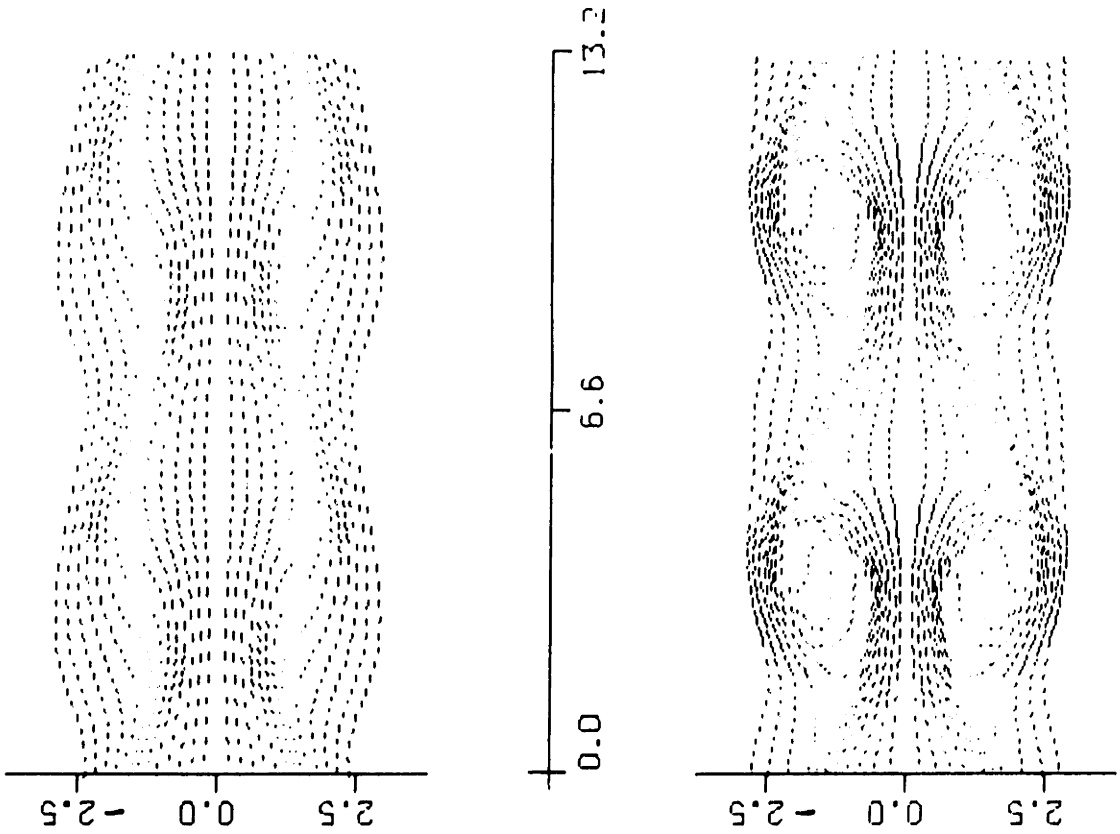

t = 2.5

t = 5.0

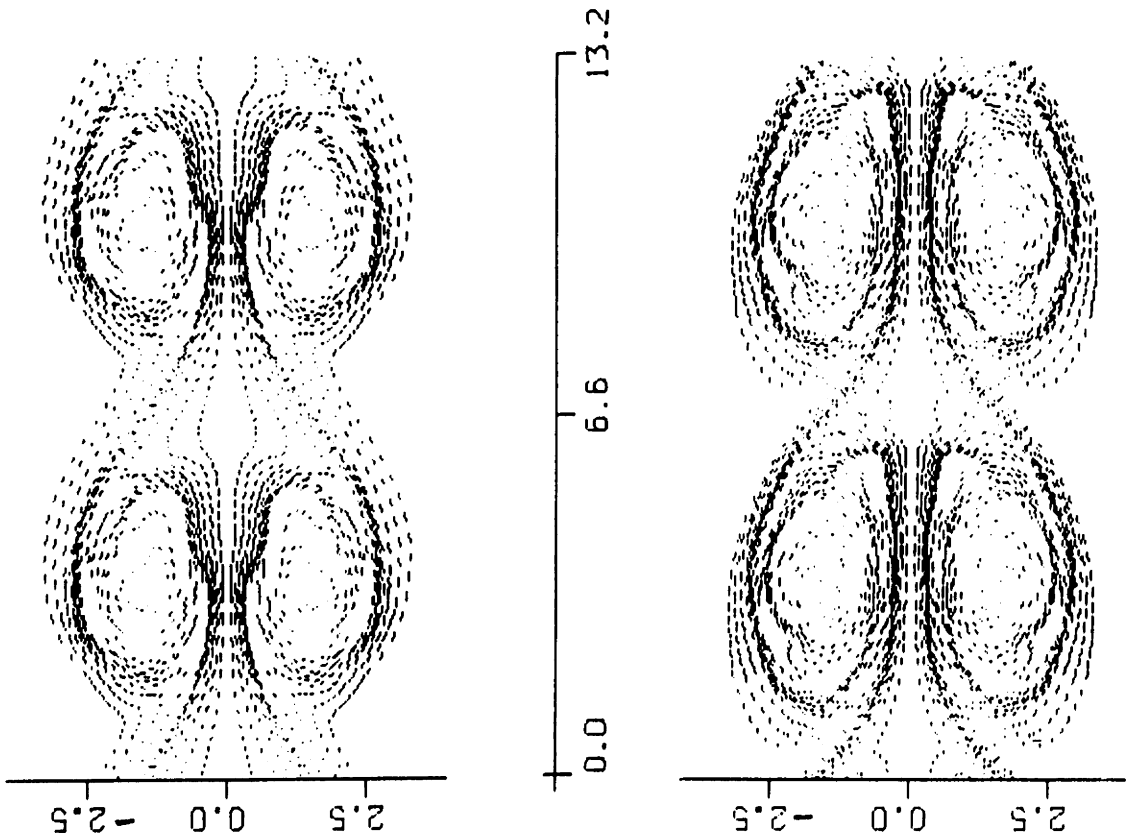

t = 7.5

t = 10.0

Figure 112

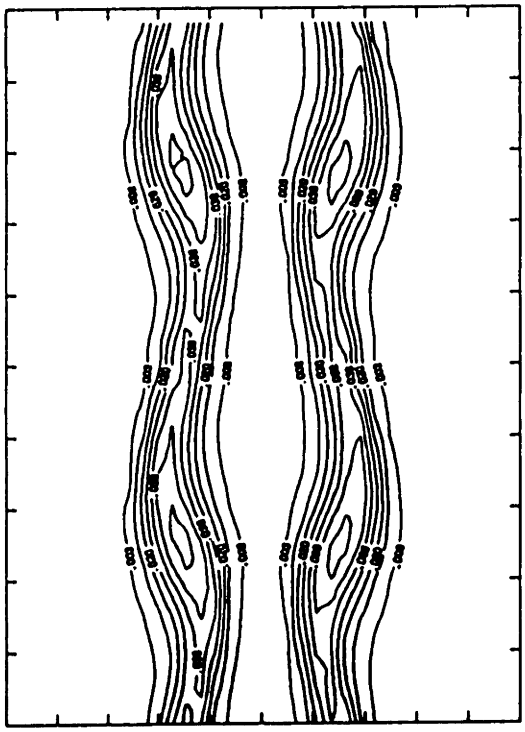

t = 2.5

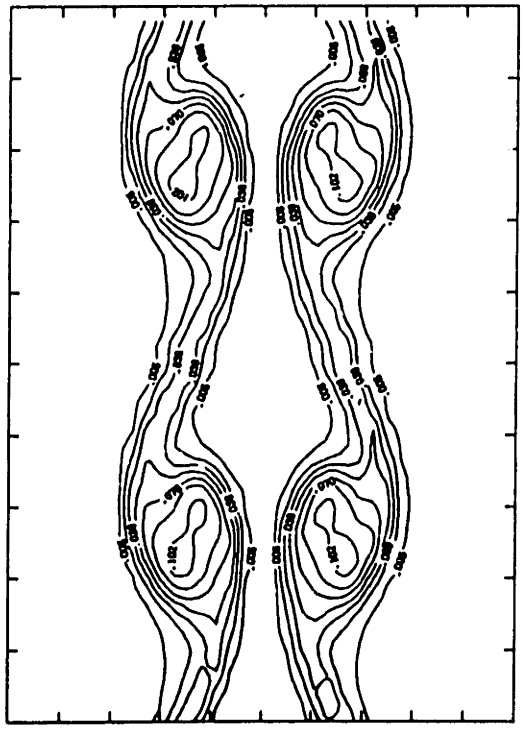

t = 5.0

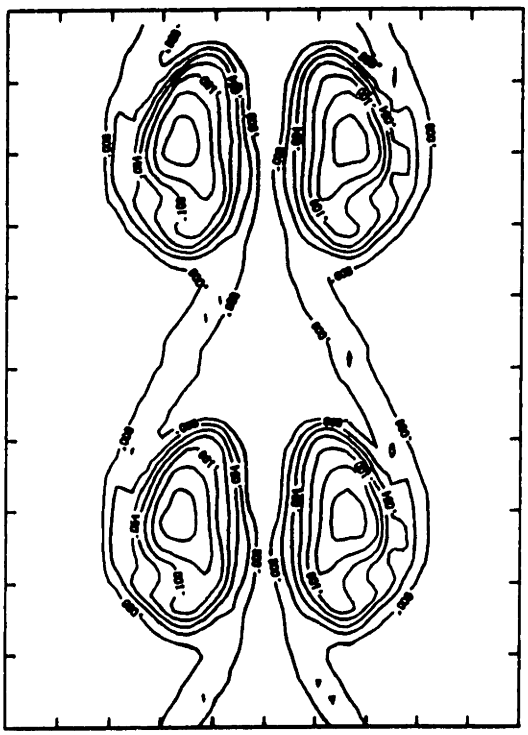

t = 7.5

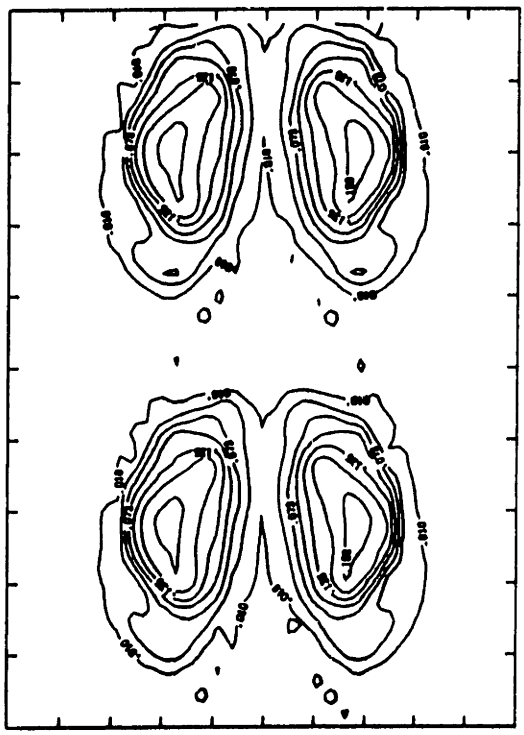

t = 10.0

Figure 113

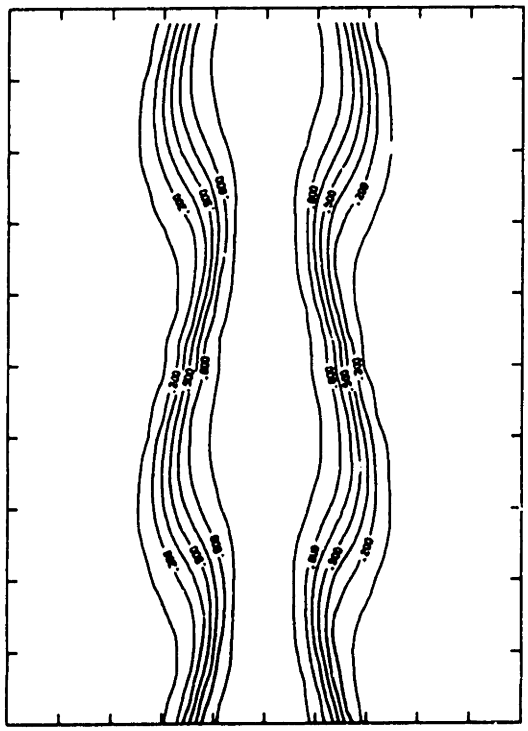

t = 2.5

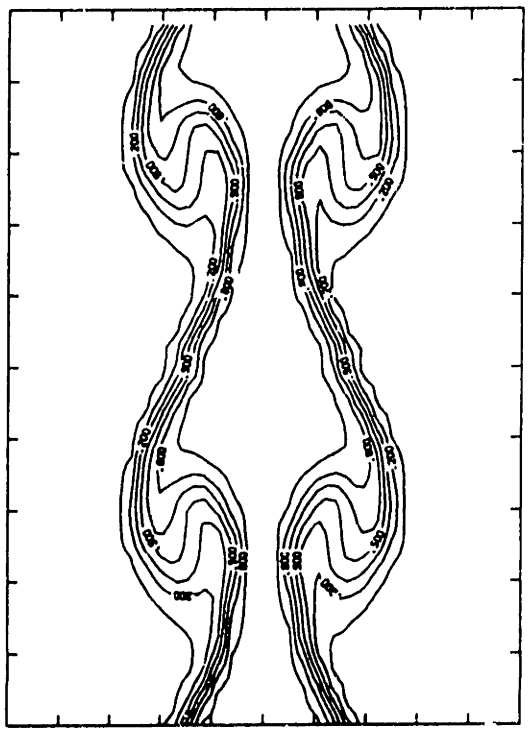

t = 5.0

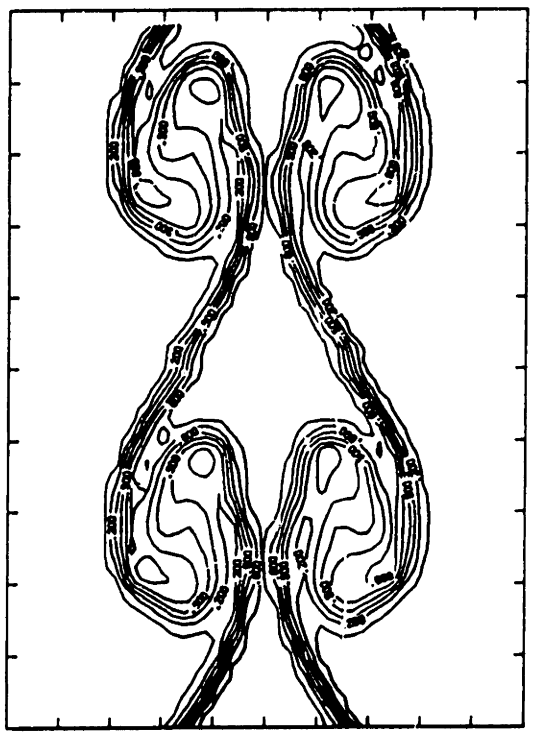

t = 7.5

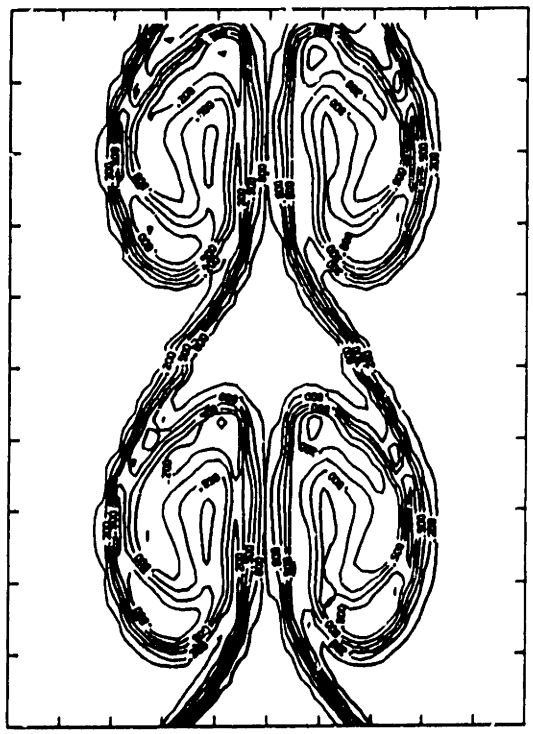

t = 10.0

Figure 114

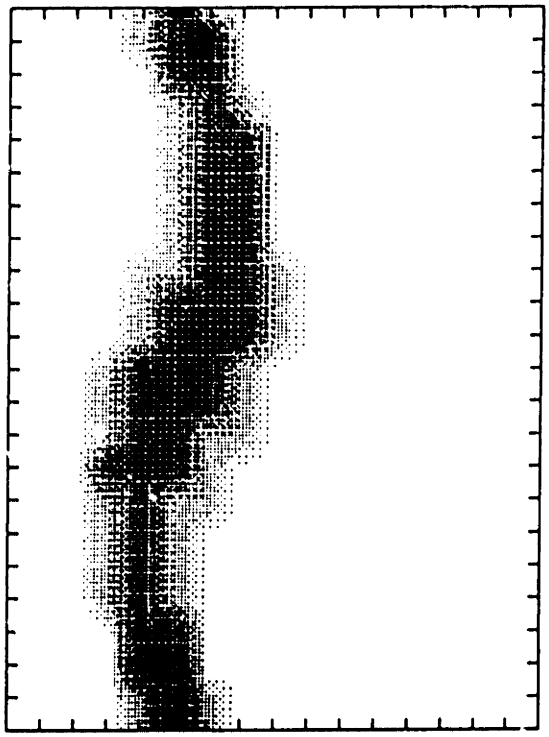

t = 2.5

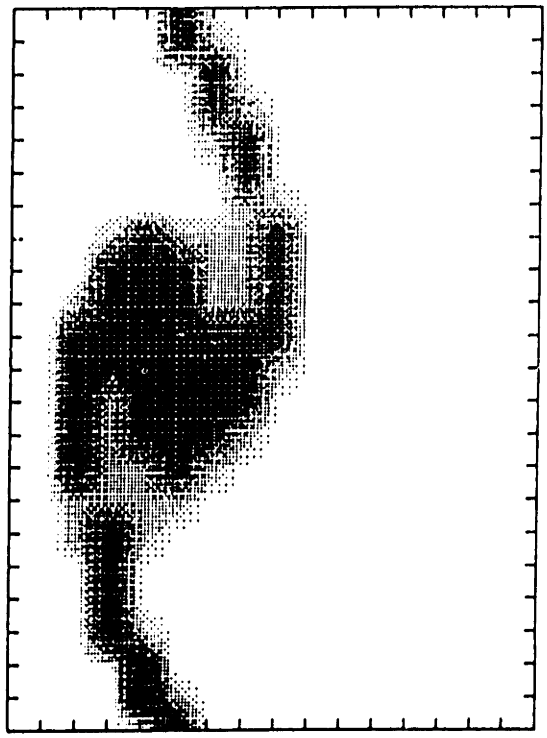

t = 5.0

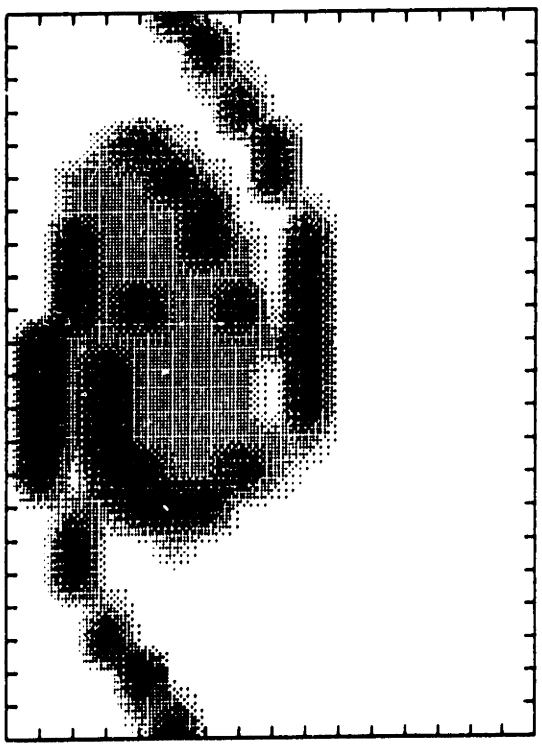

t = 7.5

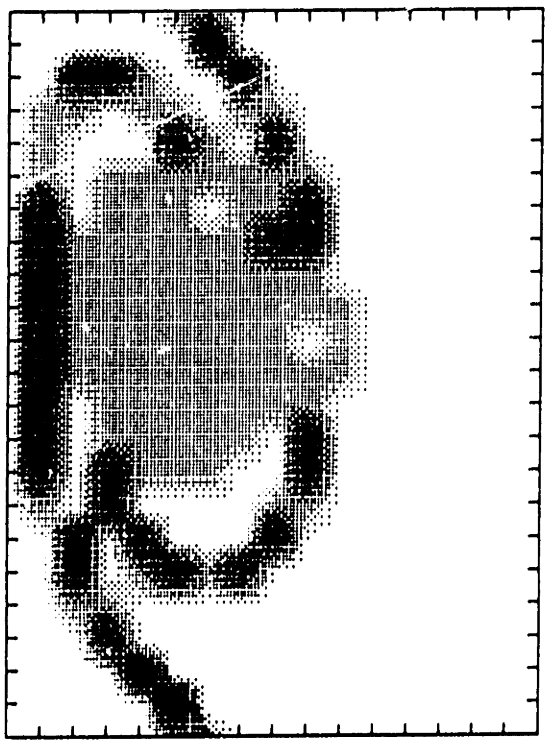

t = 10.0

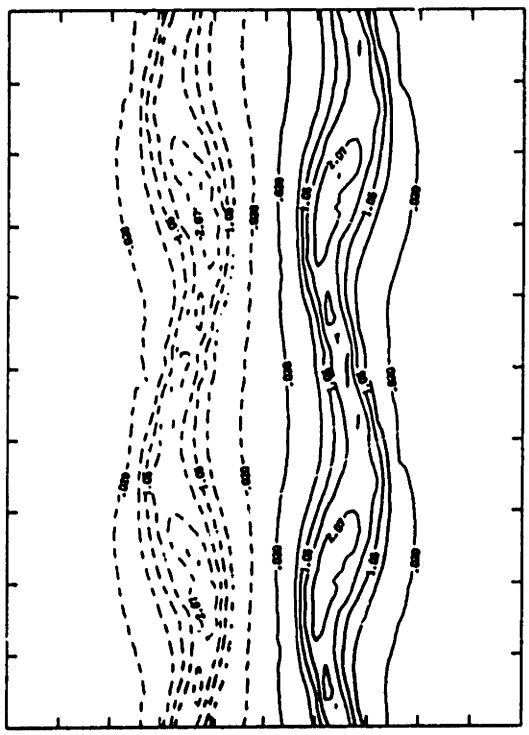

t = 2.5

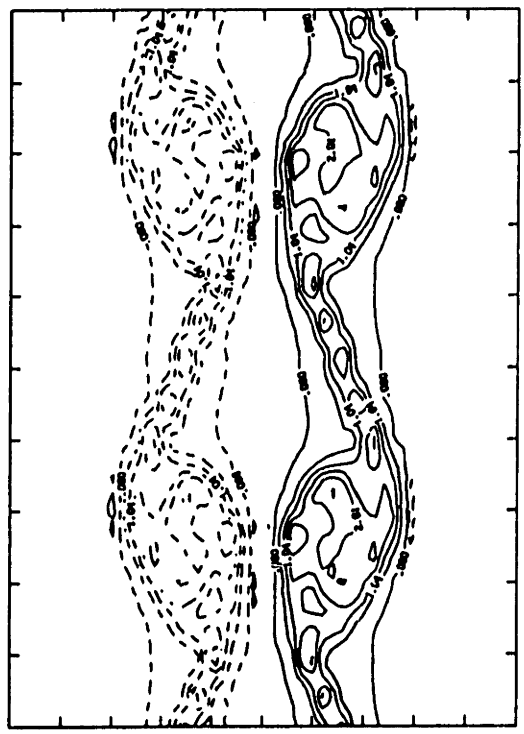

t = 5.0

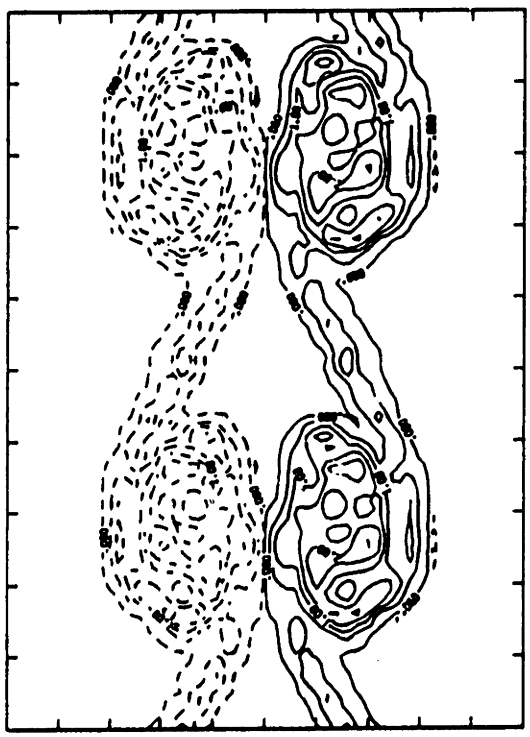

t = 7.5

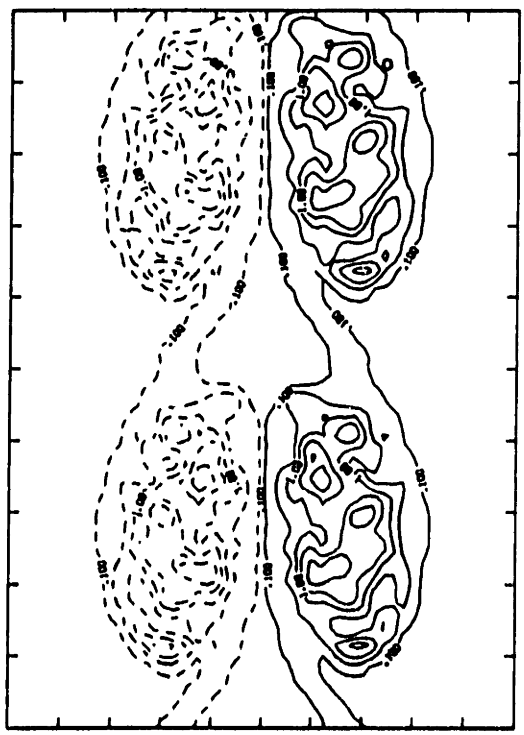

t = 10.0

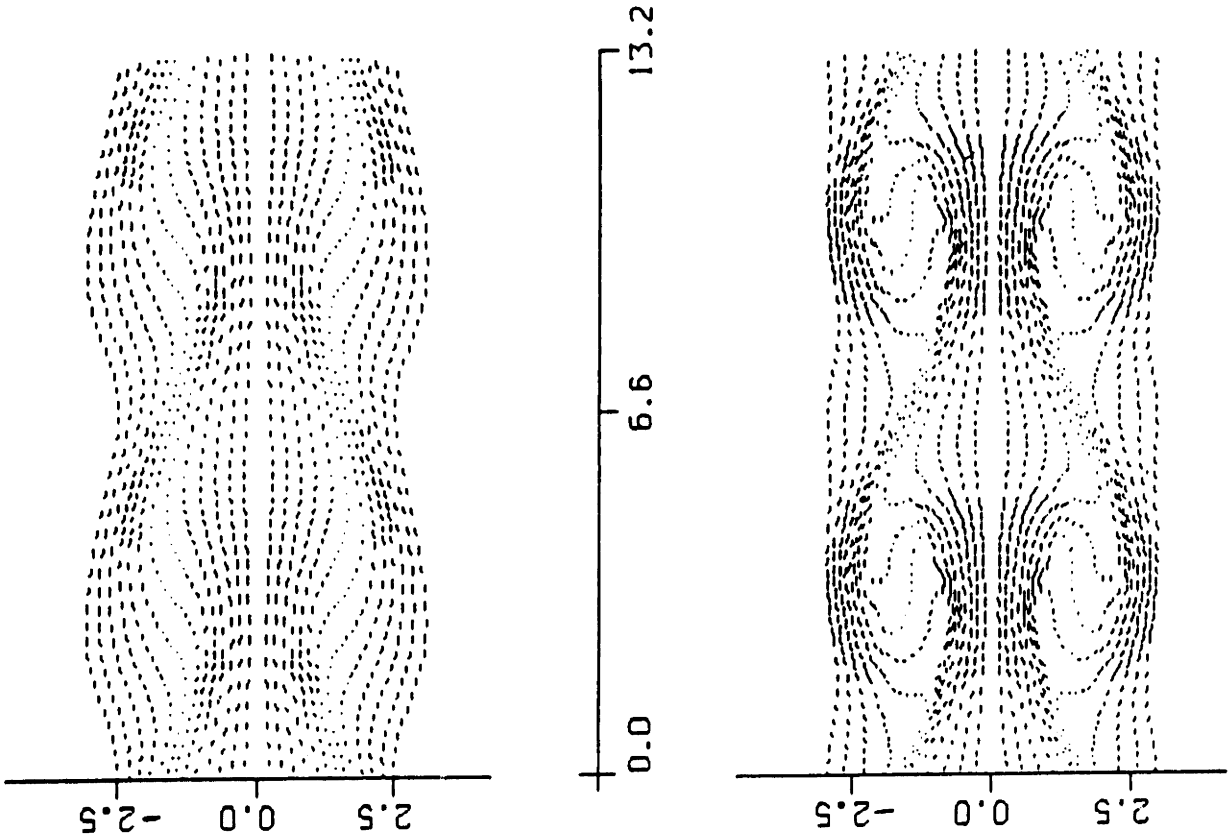

t = 2.5

t = 5.0

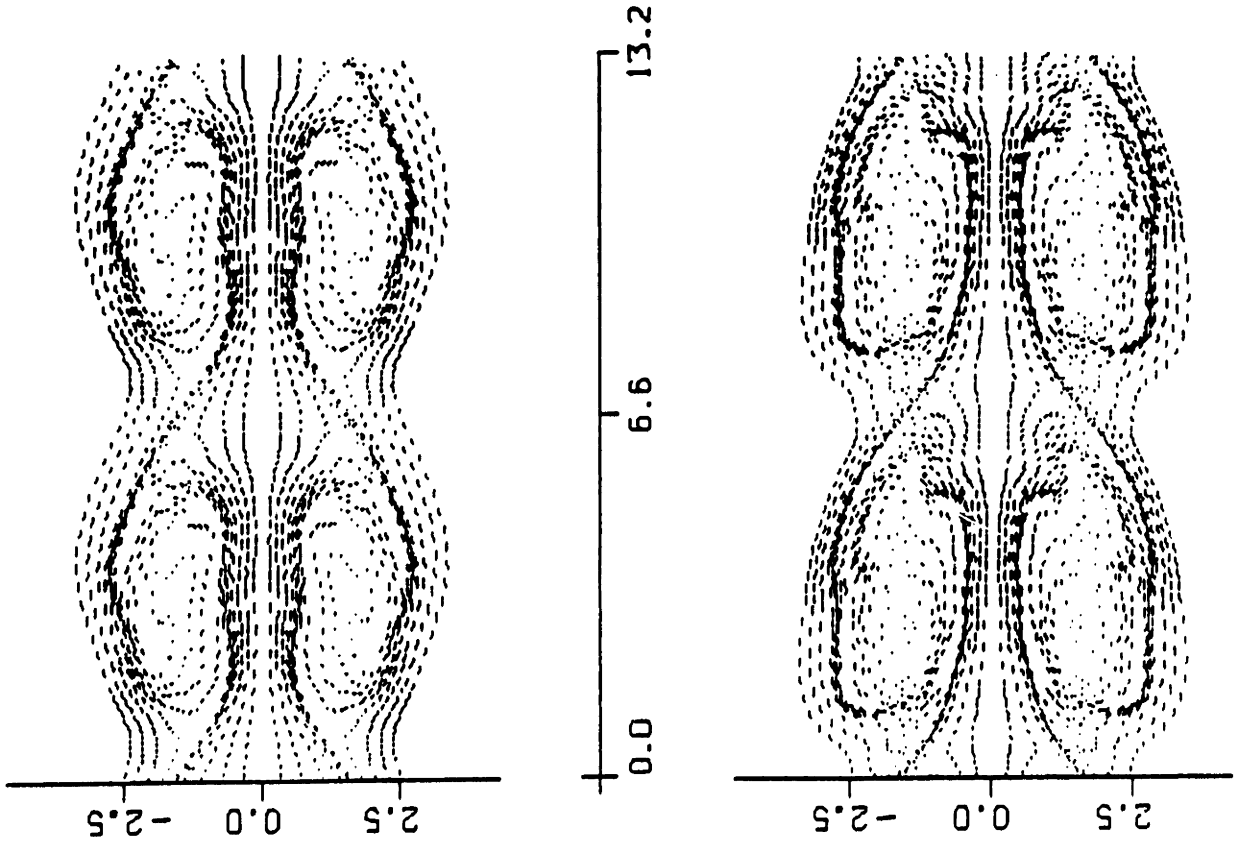

t = 7.5

t = 10.0

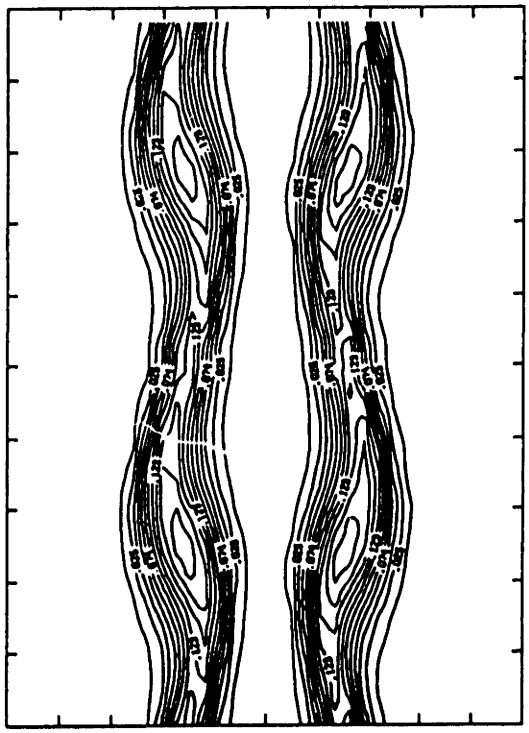

t = 2.5

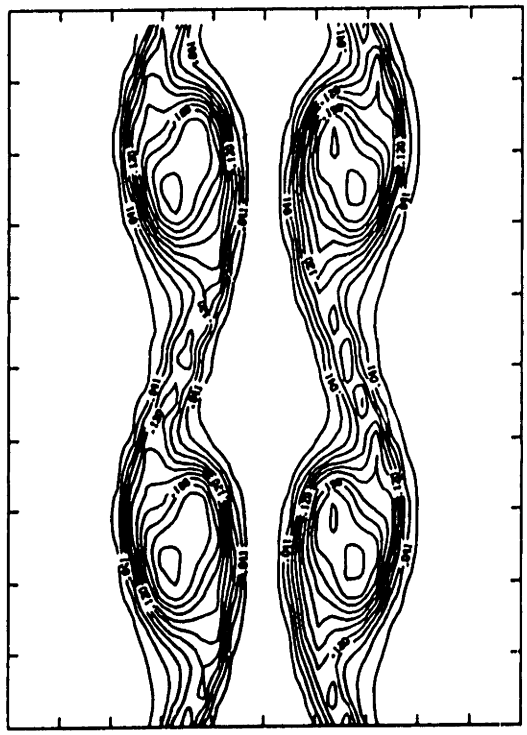

t = 5.0

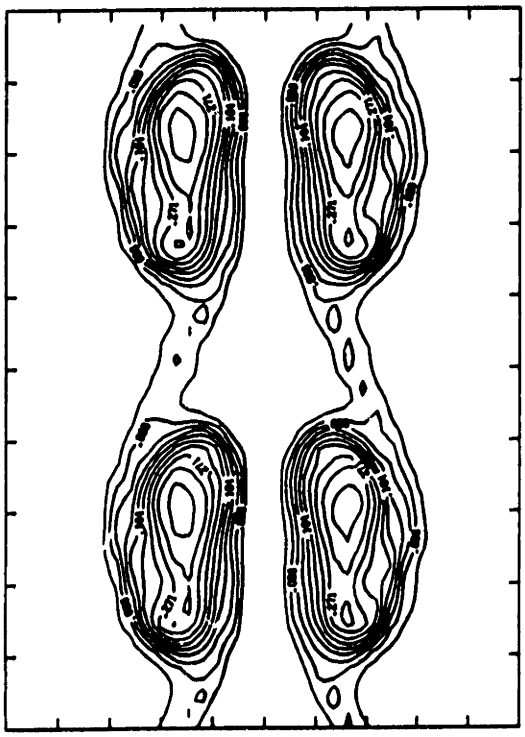

t = 7.5

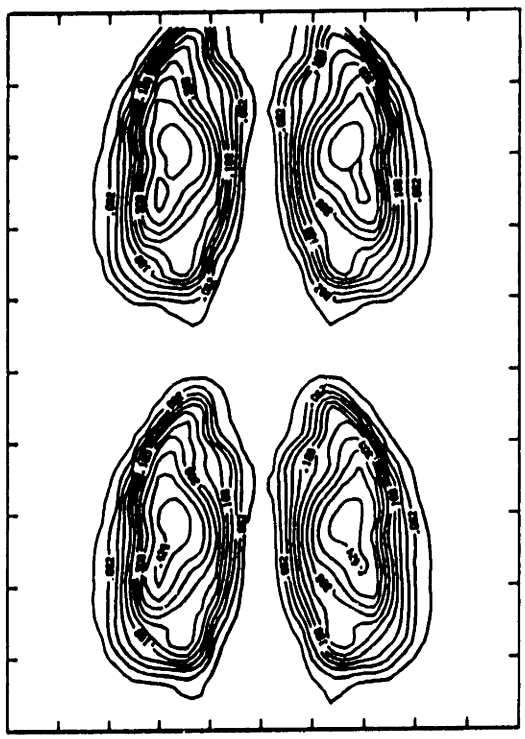

t = 10.0

Figure 118

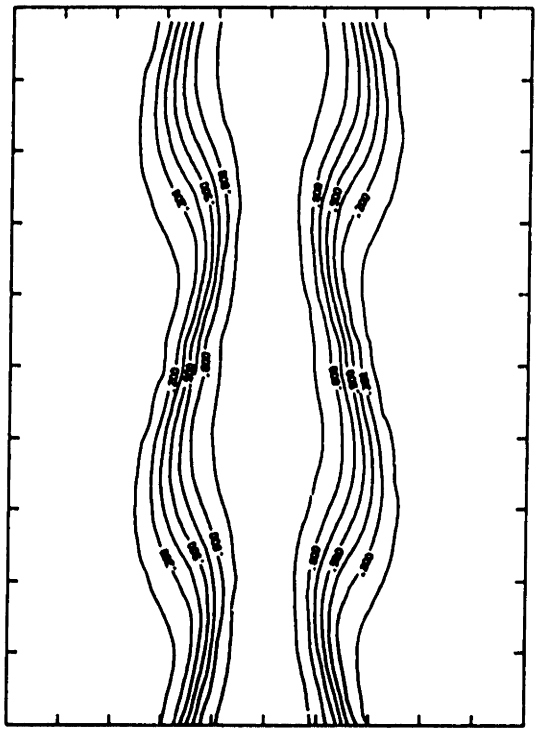

t = 2.5

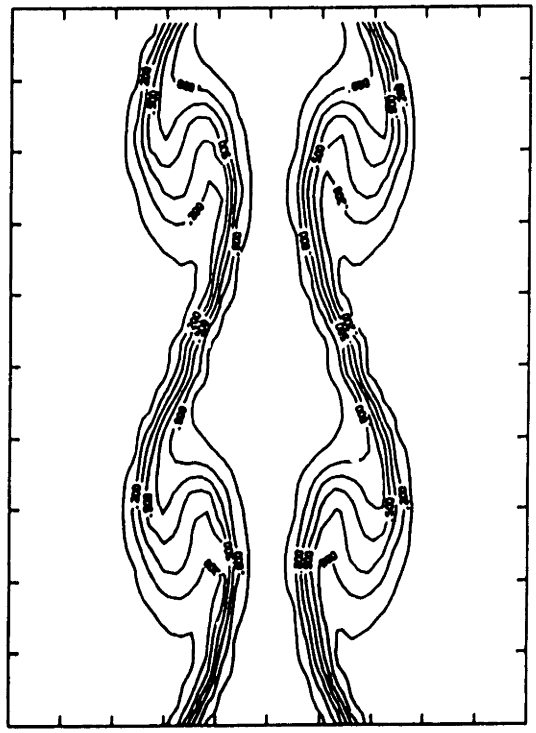

t = 5.0

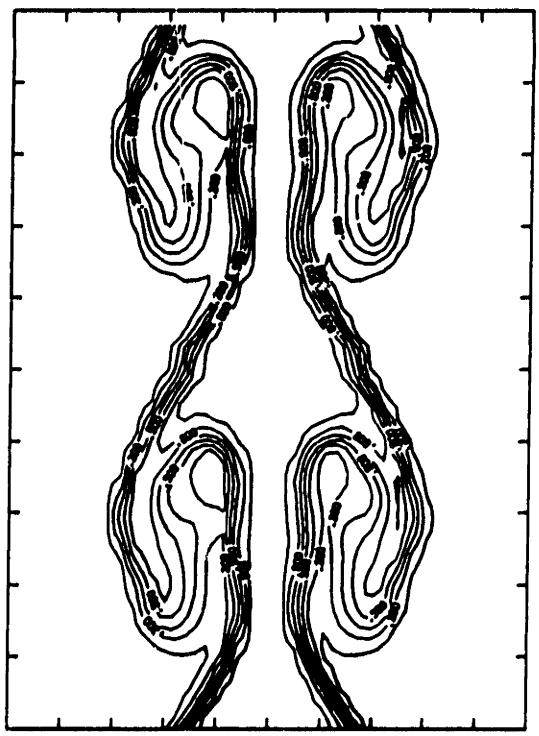

t = 7.5

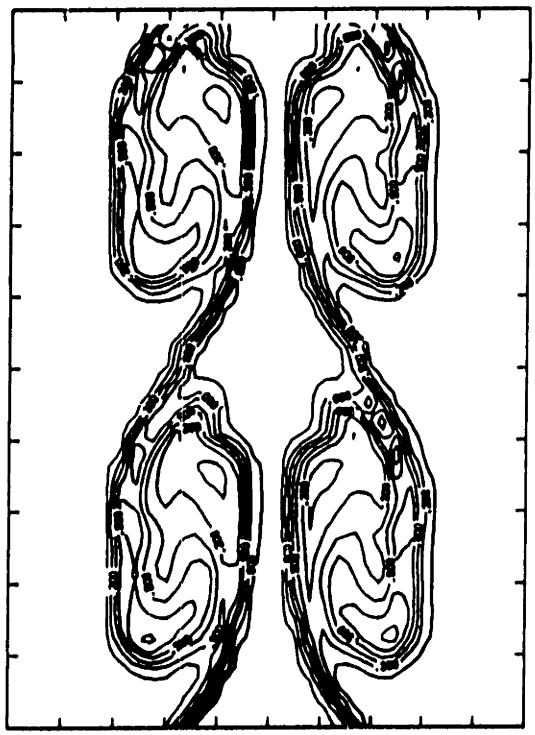

t = 10.0

Figure 119

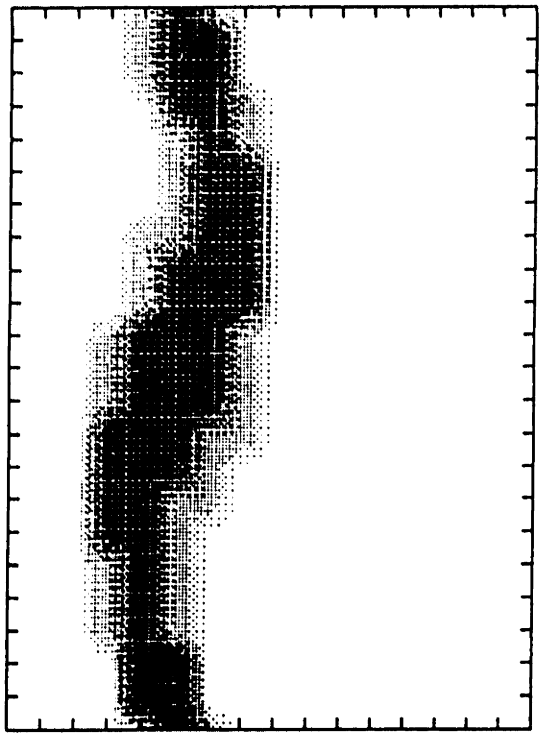

t = 2.5

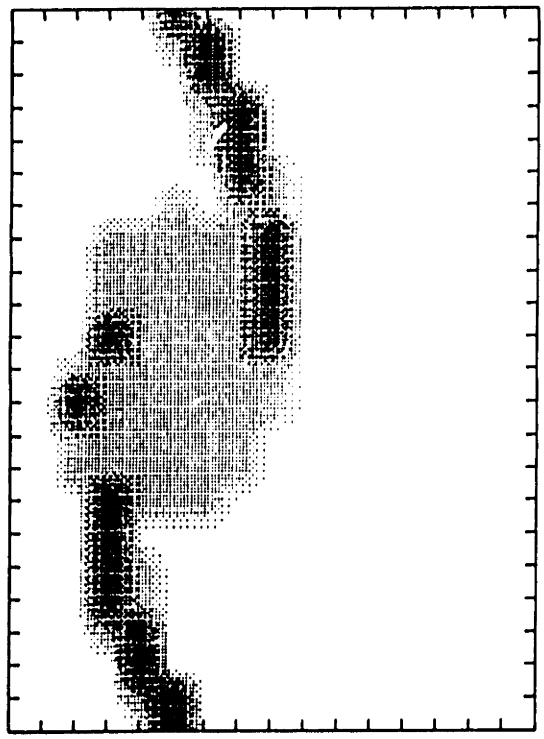

t = 5.0

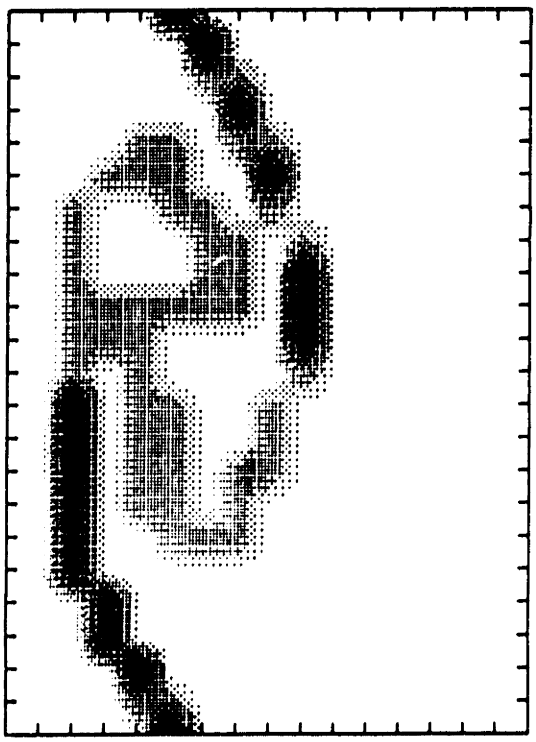

t = 7.5

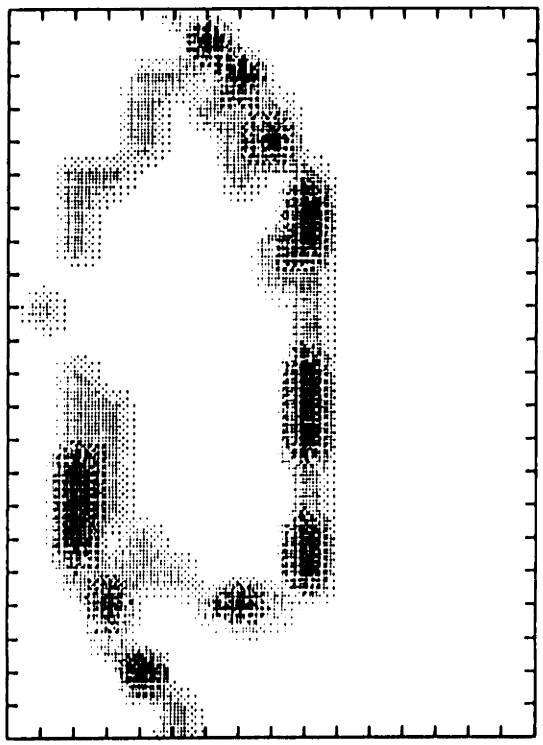

t = 10.0

Figure 120

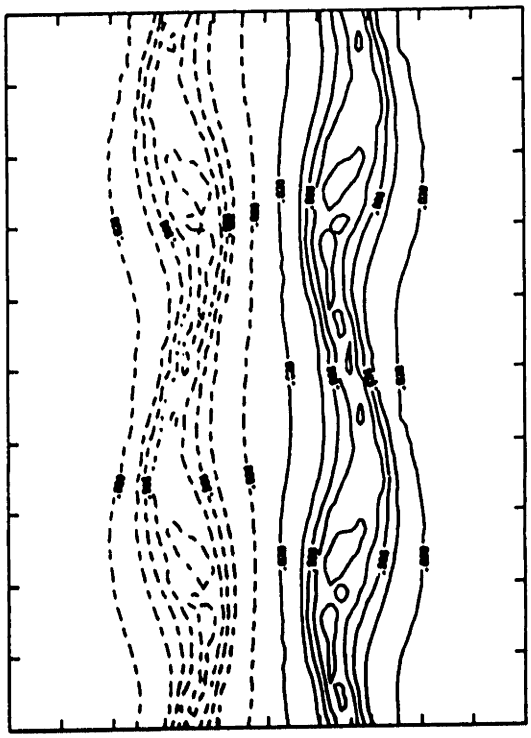

t = 2.5

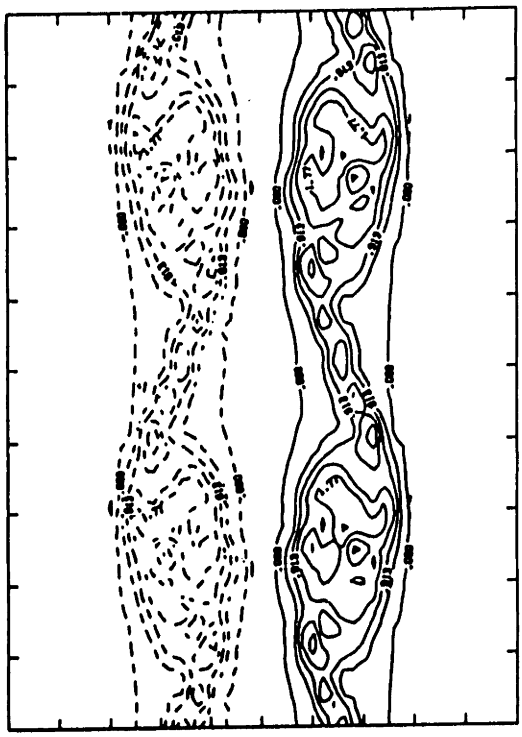

t = 5.0

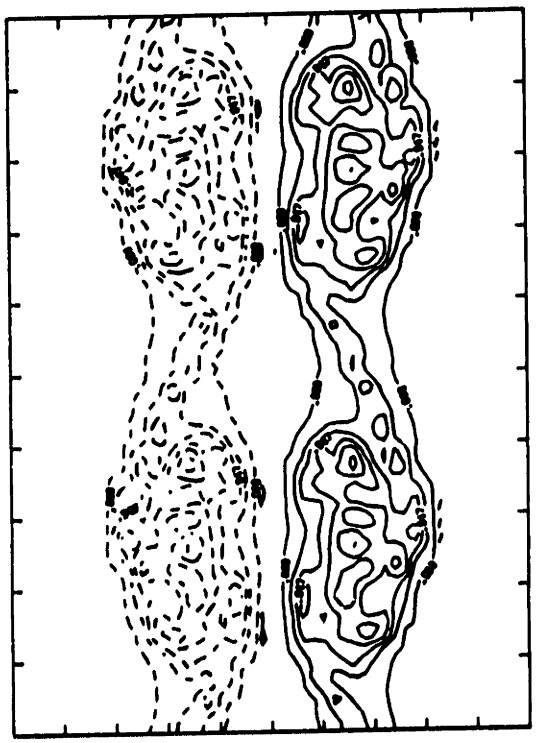

t = 7.5

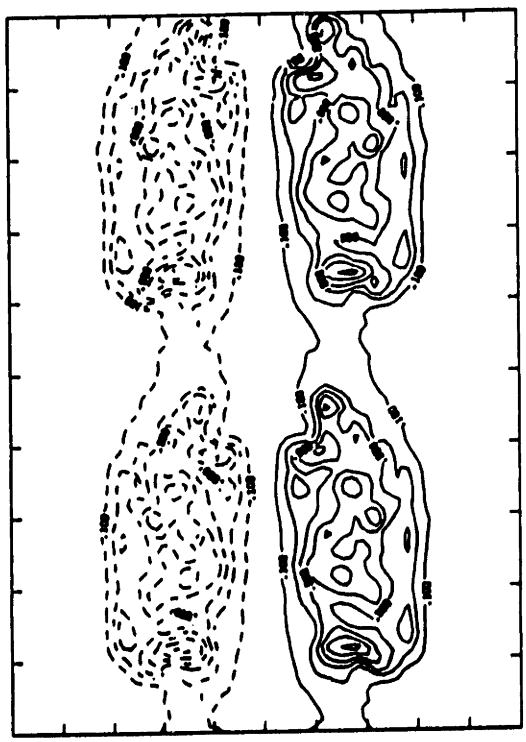

t = 10.0

Figure 121

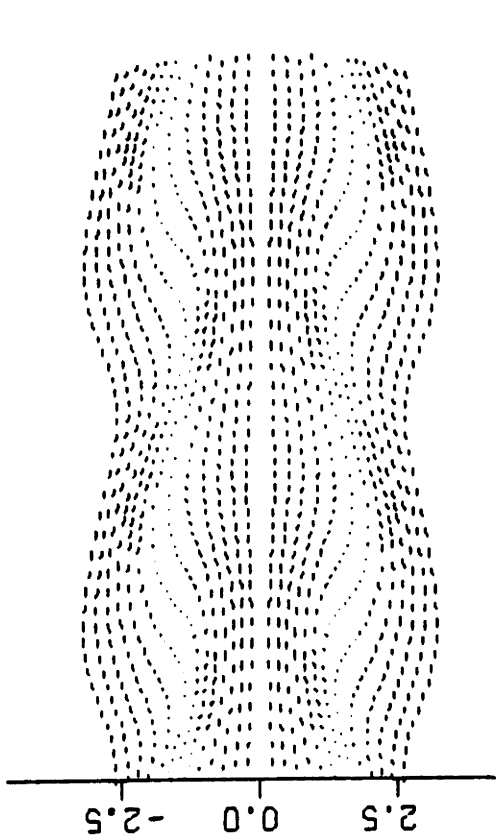

t = 2.5

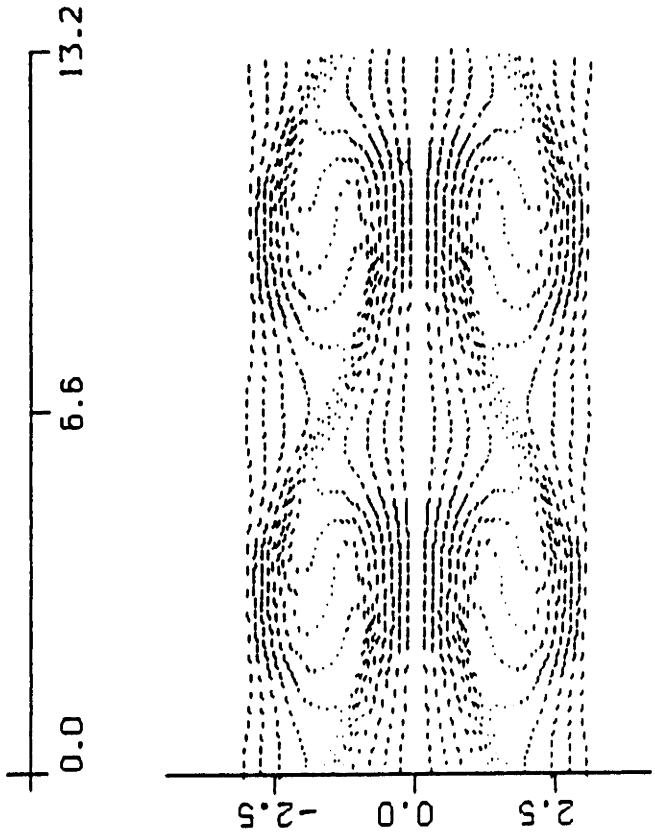

t = 5.0

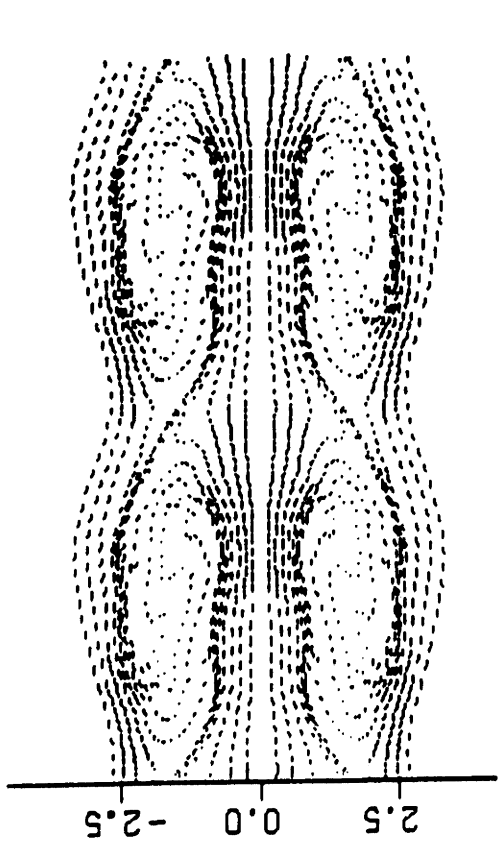

t = 7.5

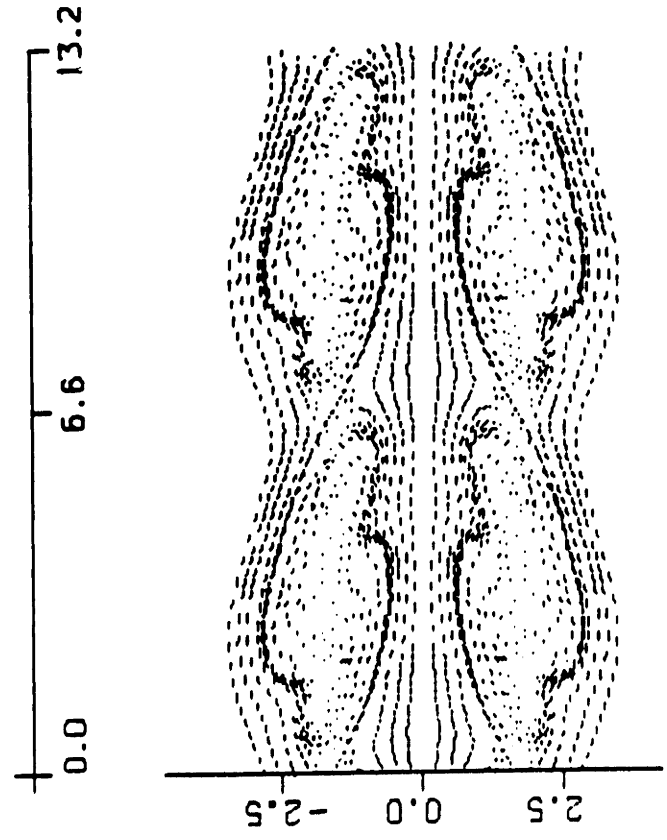

t = 10.0

Figure 122

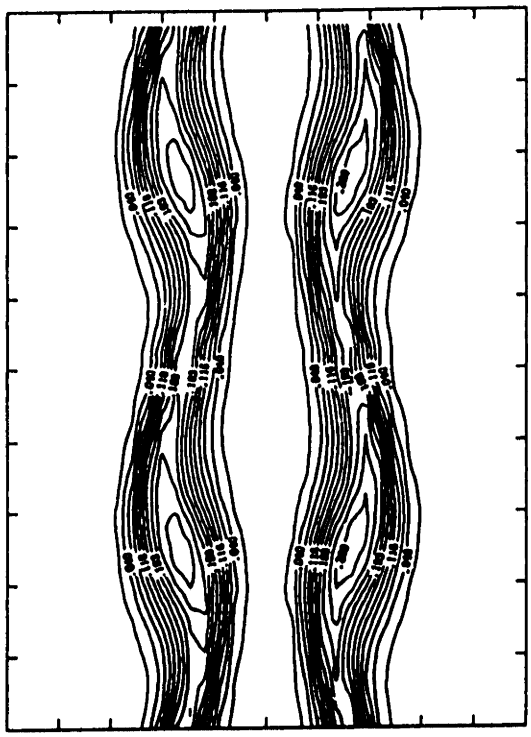

t = 2.5

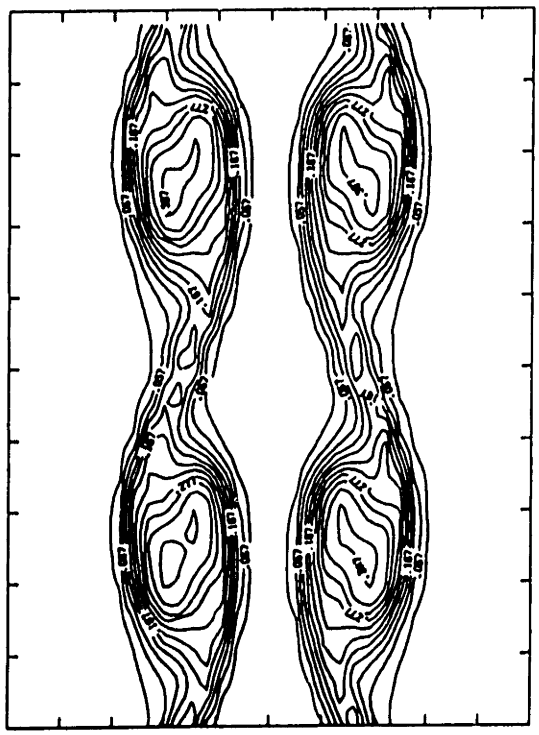

t = 5.0

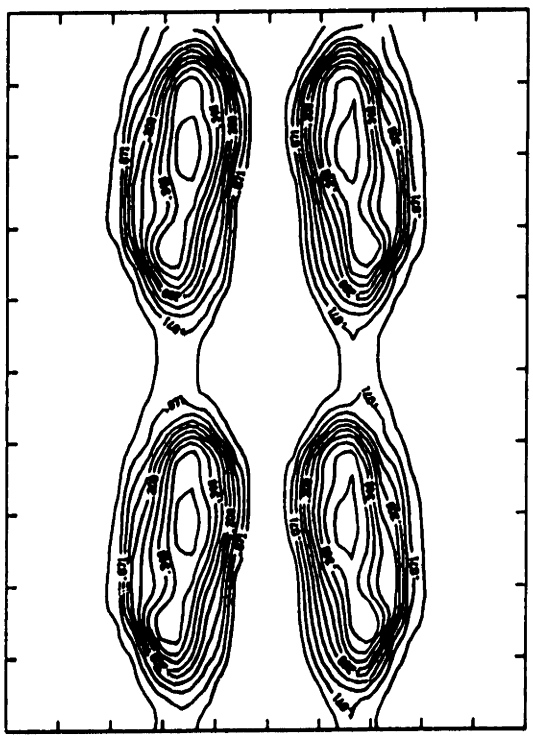

t = 7.5

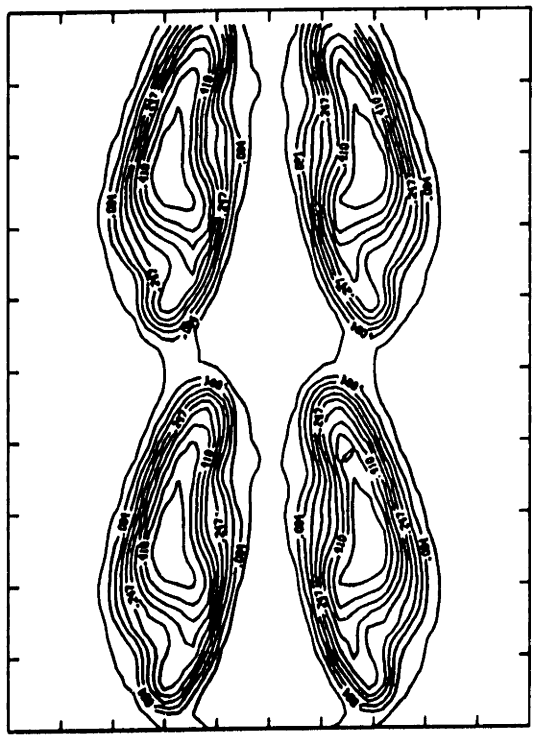

t = 10.0

Figure 123

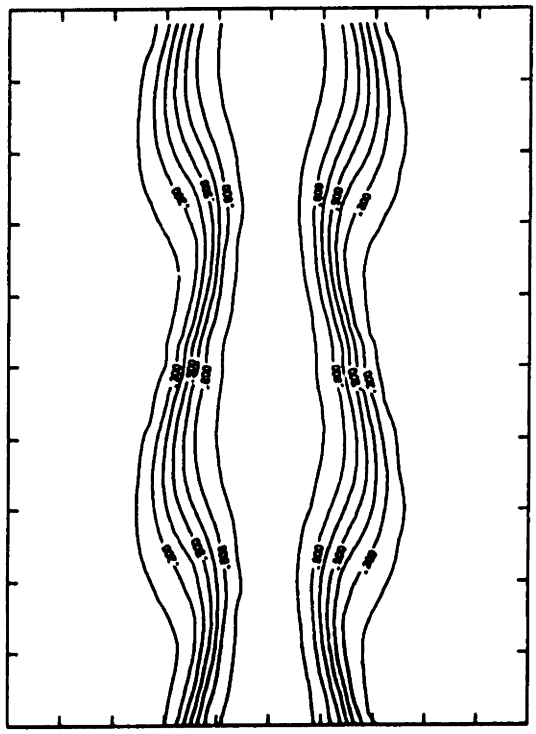

t = 2.5

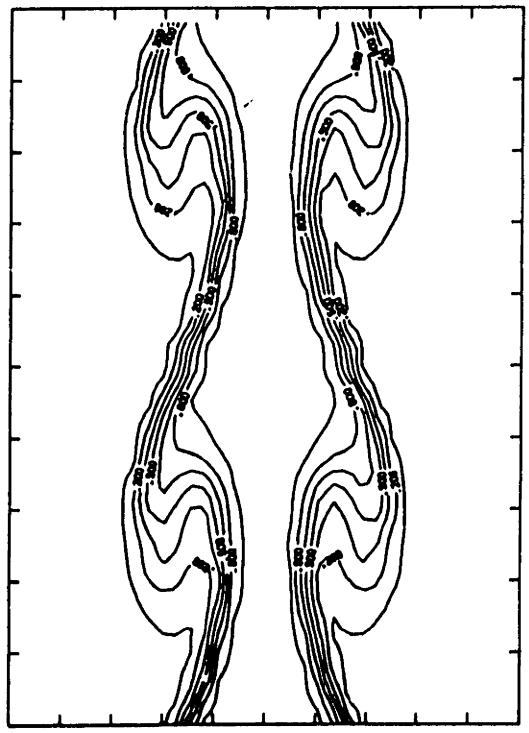

t = 5.0

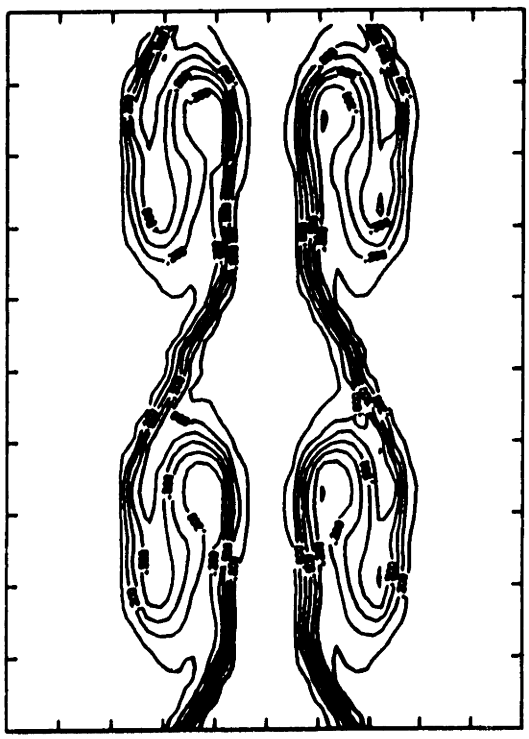

t = 7.5

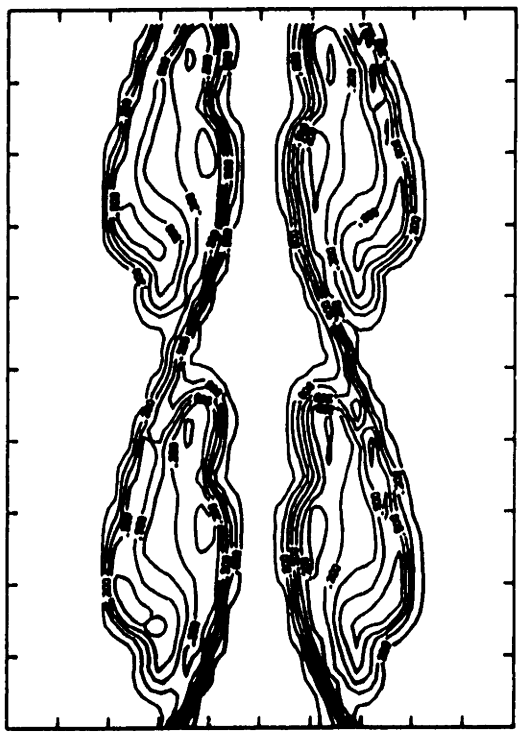

t = 10.0

Figure 124

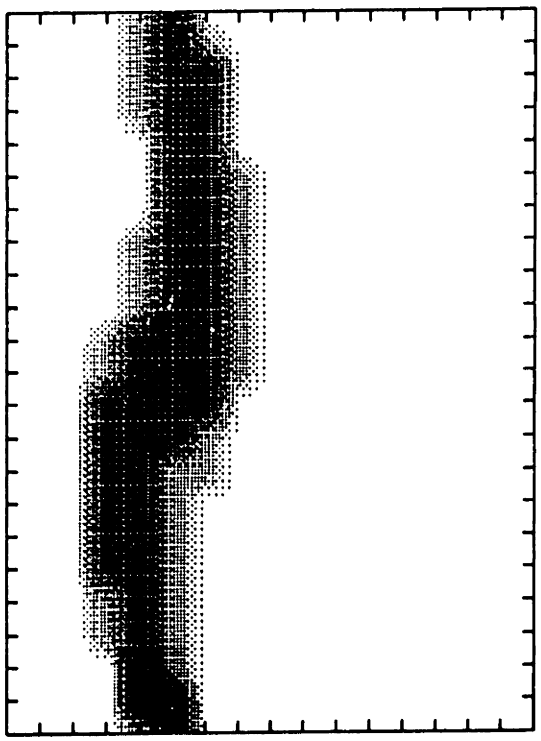

t = 2.5

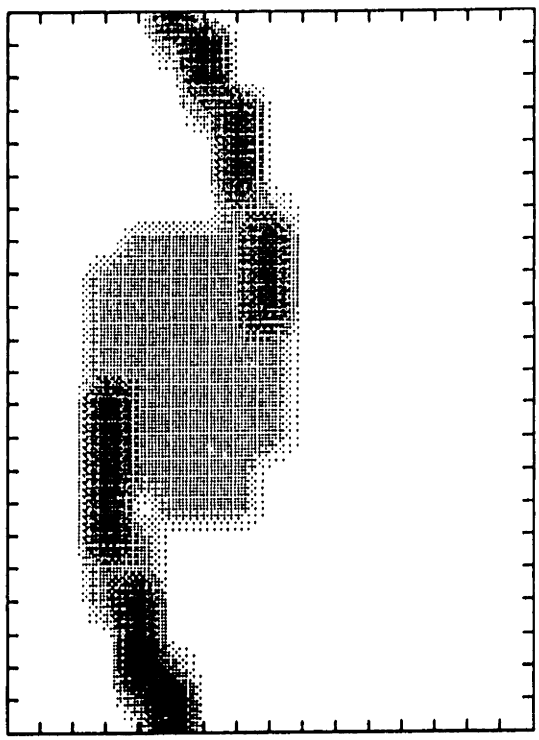

t = 5.0

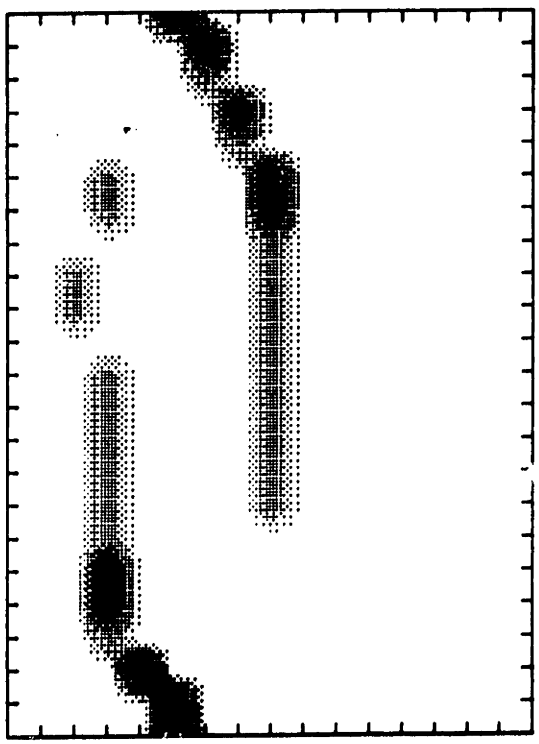

t = 7.5

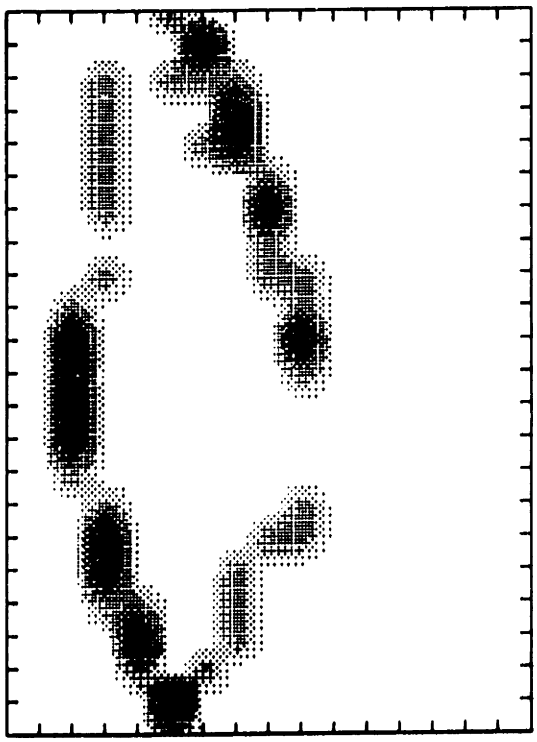

t = 10.0

Figure 125

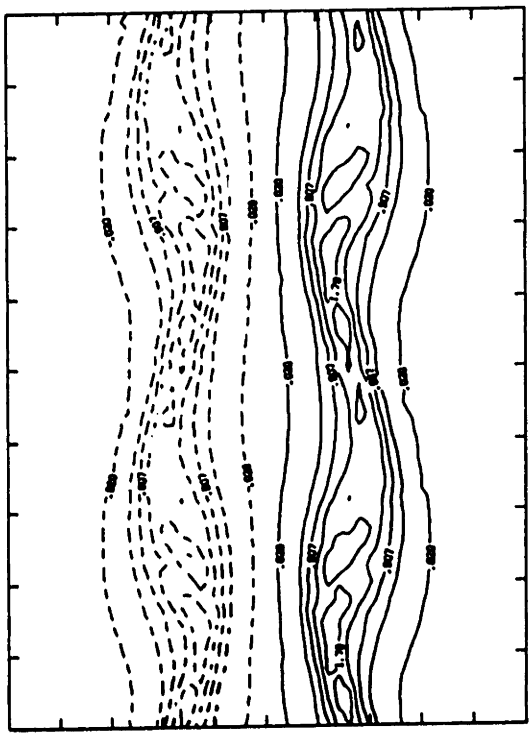

t = 2.5

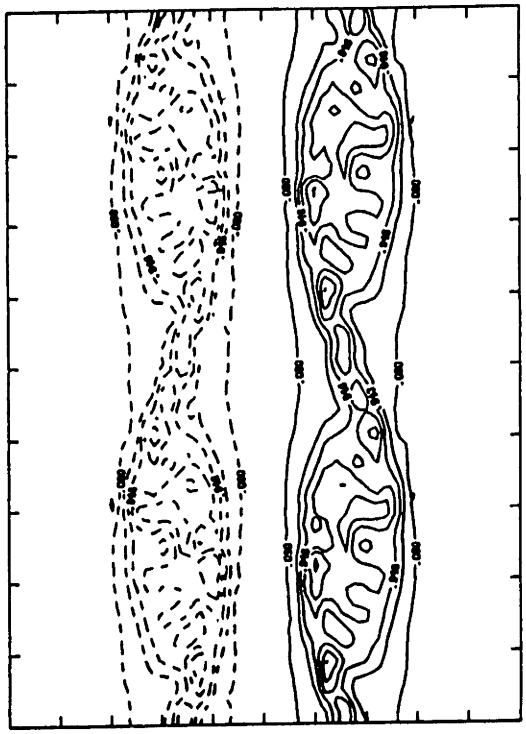

t = 5.0

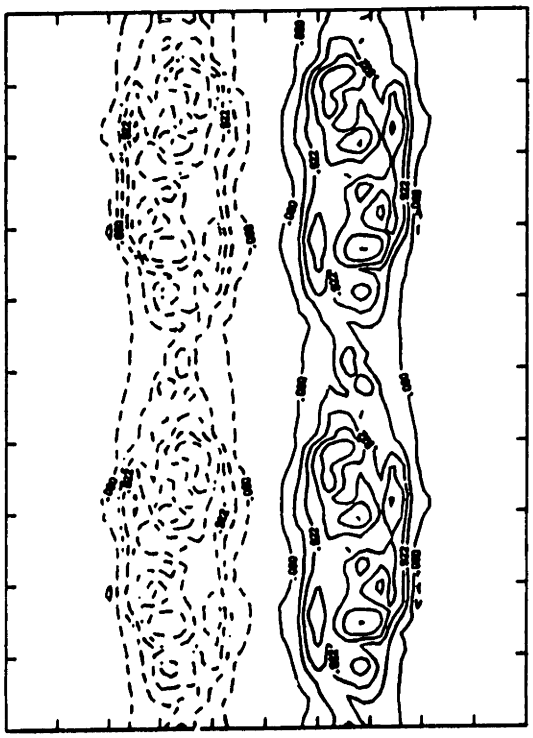

t = 7.5

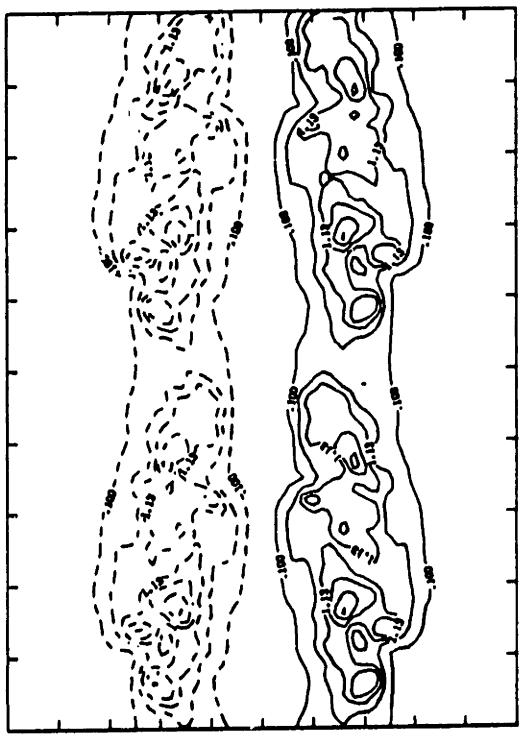

t = 10.0

Figure 126

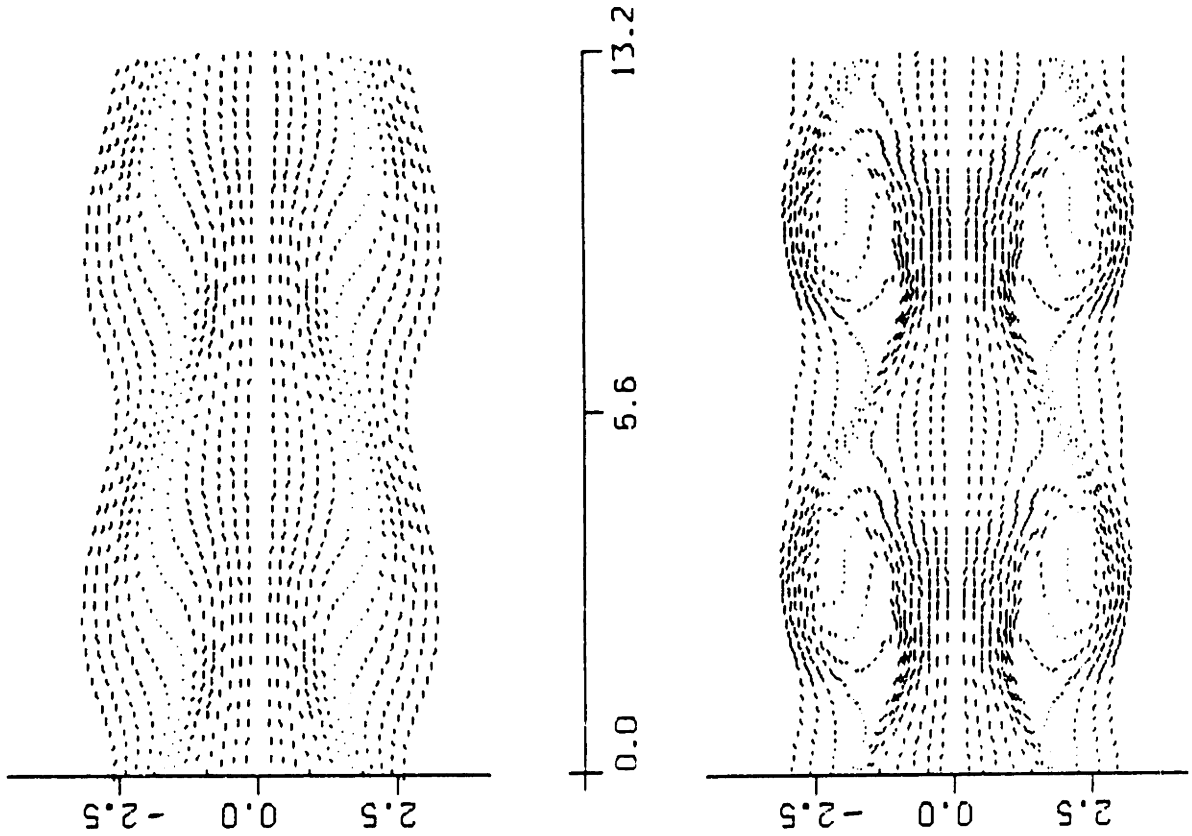

t = 2.5

t = 5.0

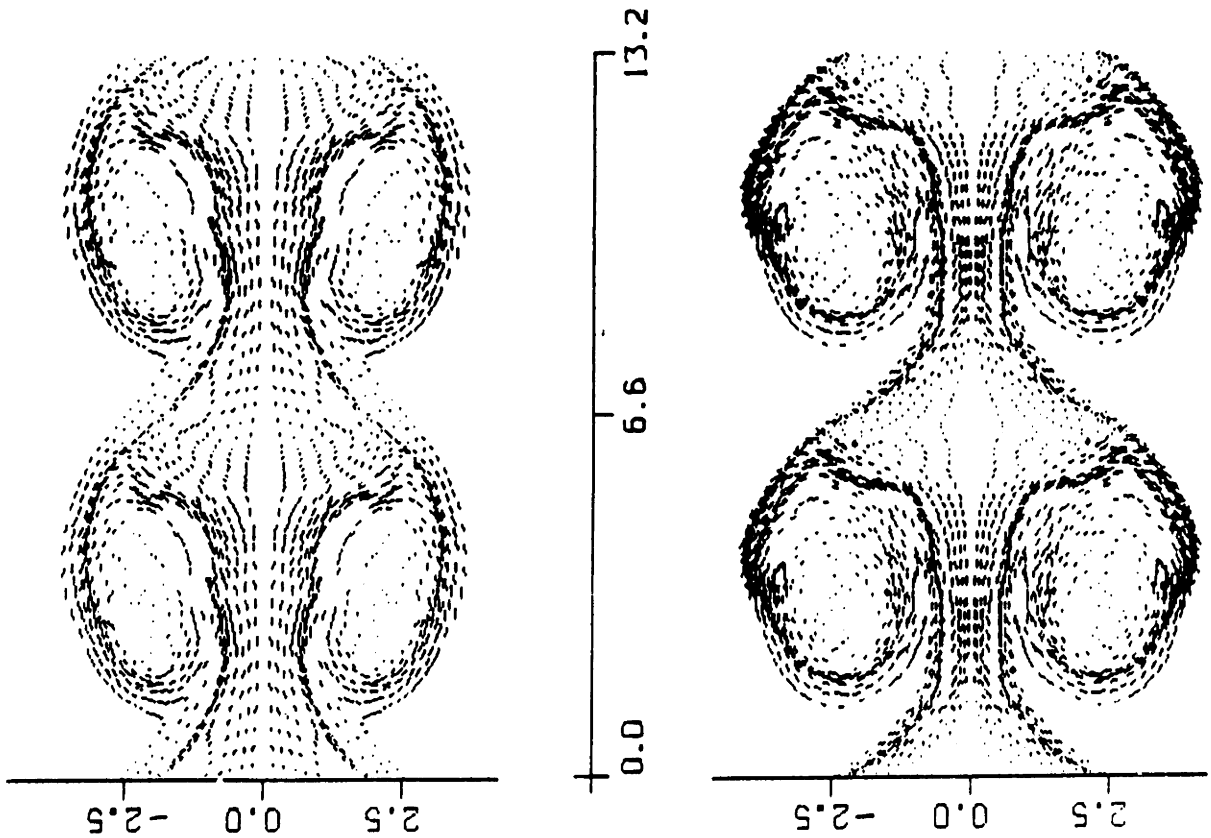

t = 7.5

t = 10.0

Figure 127

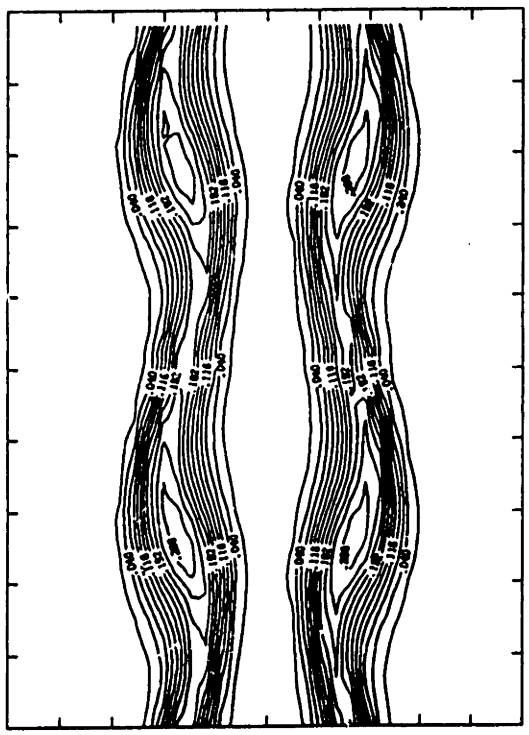

t = 2.5

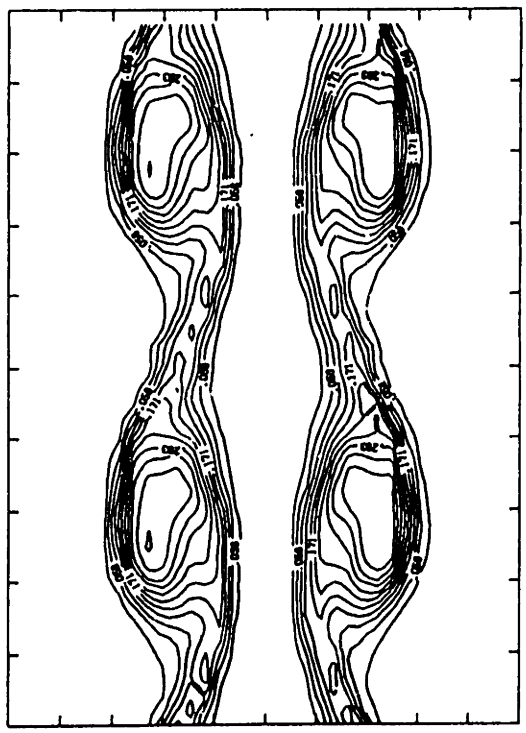

t = 5.0

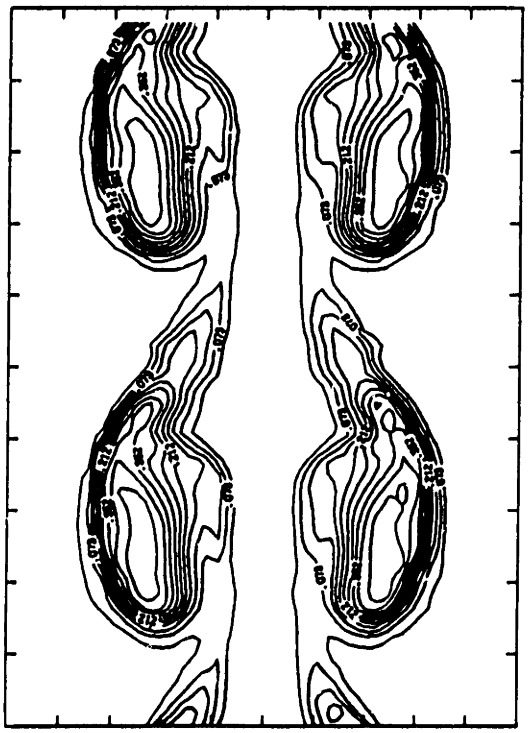

t = 7.5

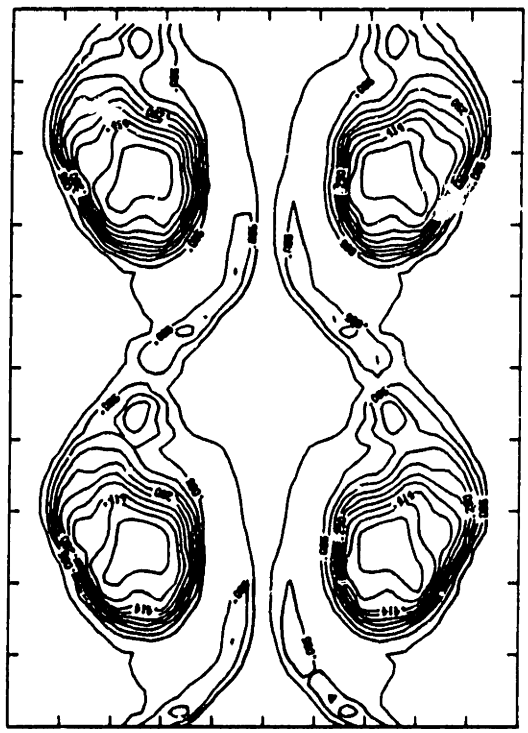

t = 10.0

Figure 128

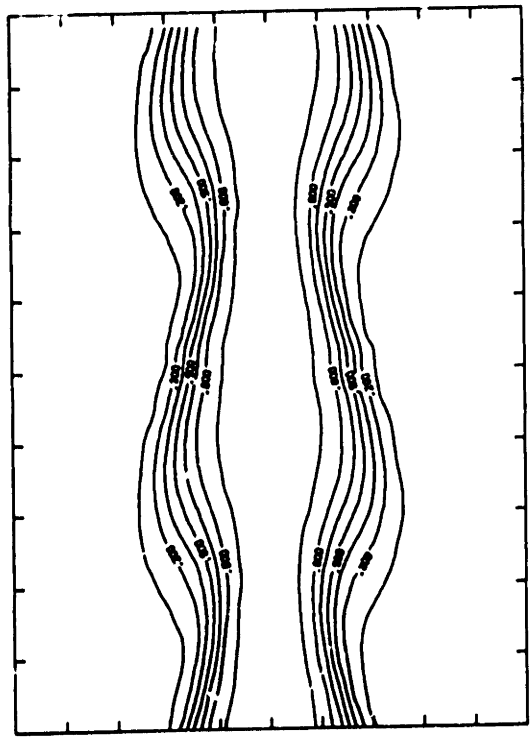

t = 2.5

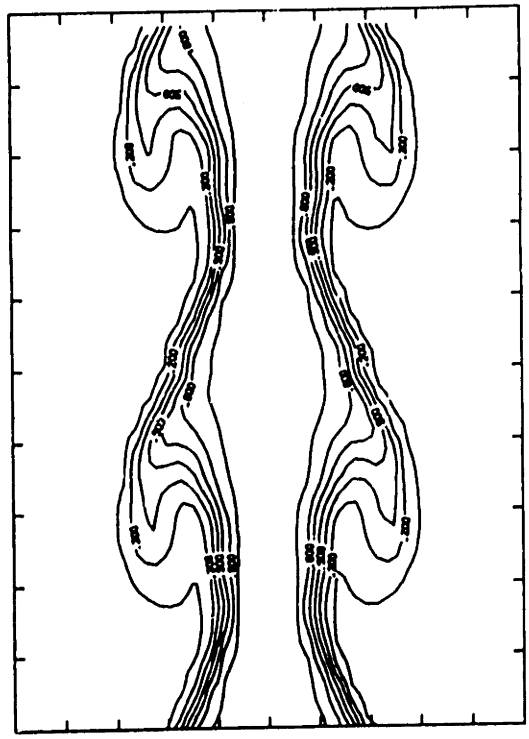

t = 5.0

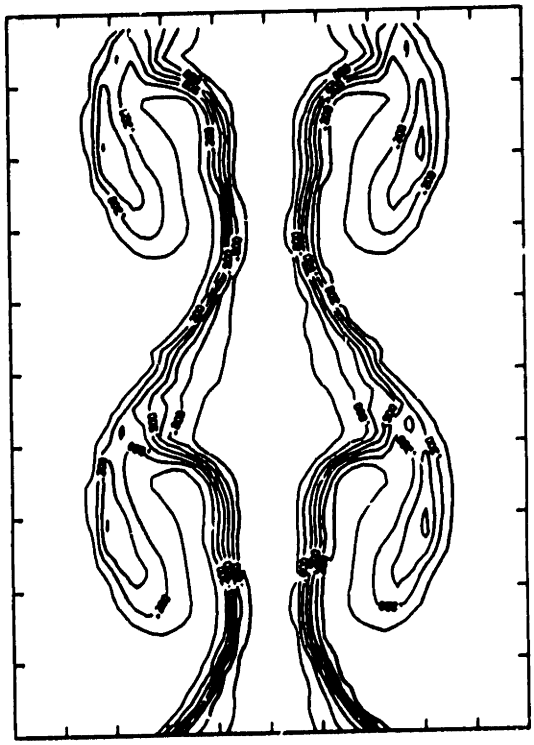

t = 7.5

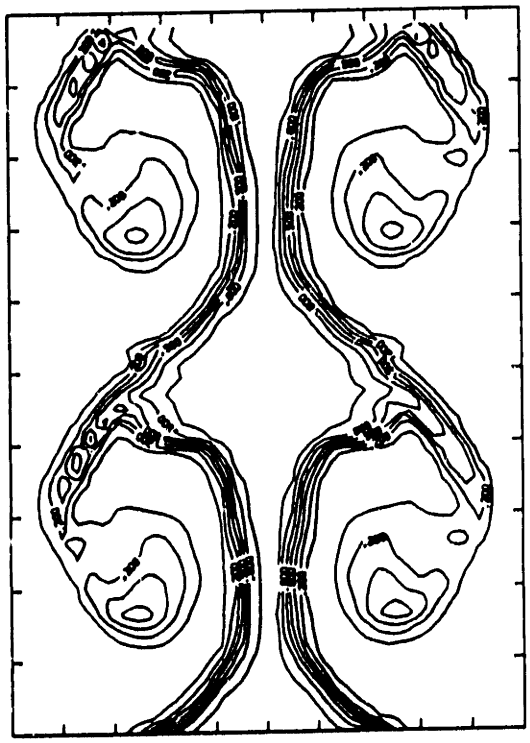

t = 10.0

Figure 129

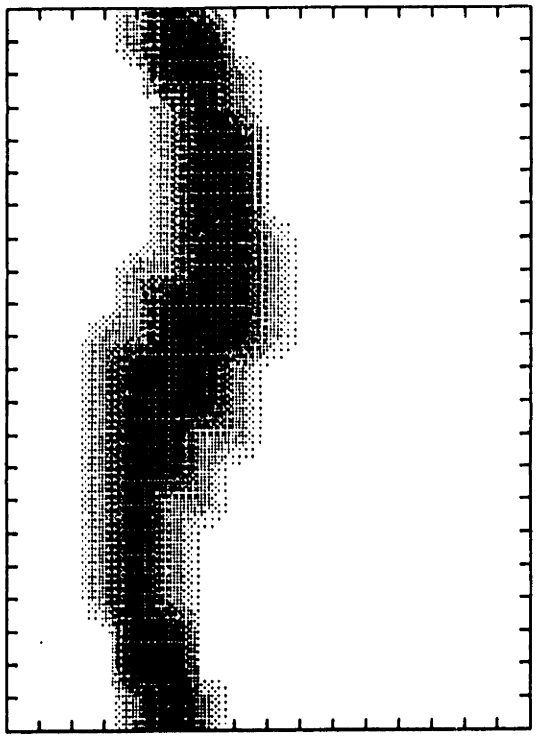

t = 2.5

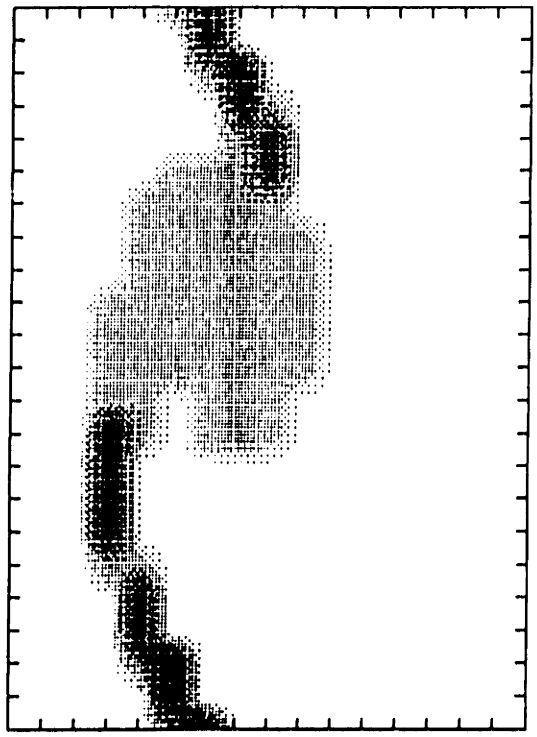

t = 5.0

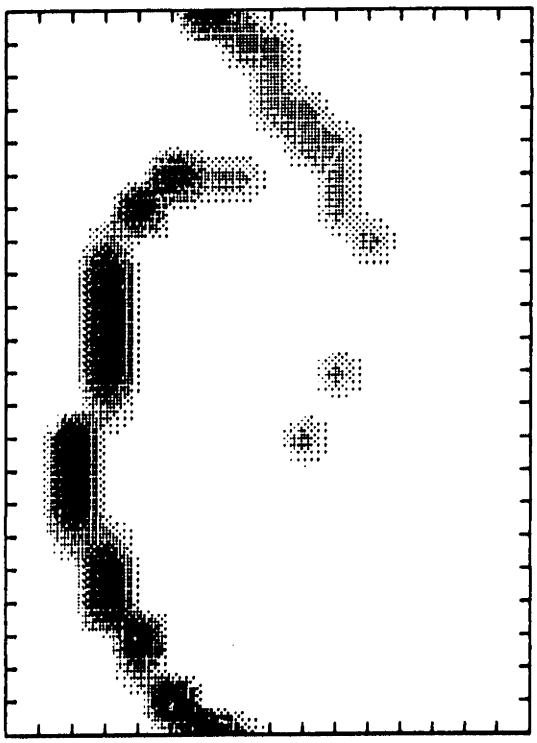

t = 7.5

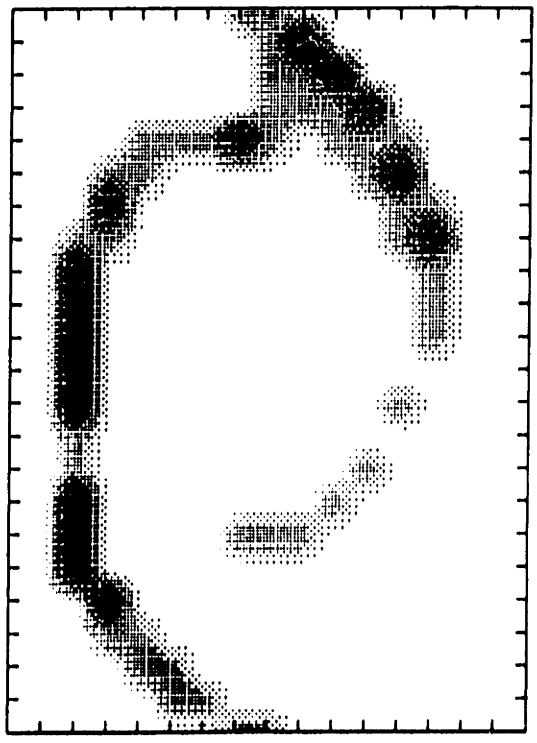

t = 10.0

Figure 130

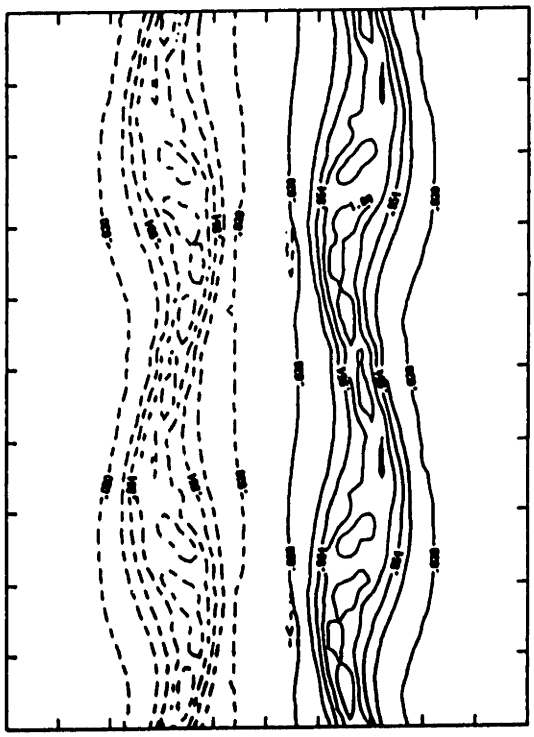

t = 2.5

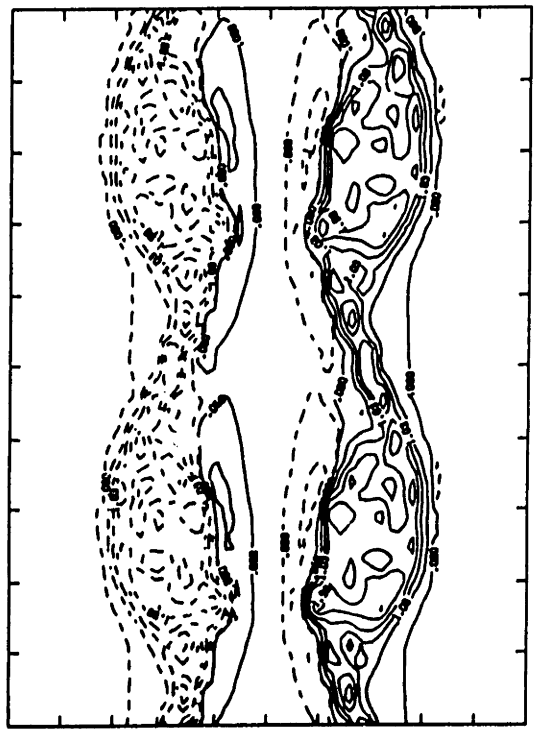

t = 5.0

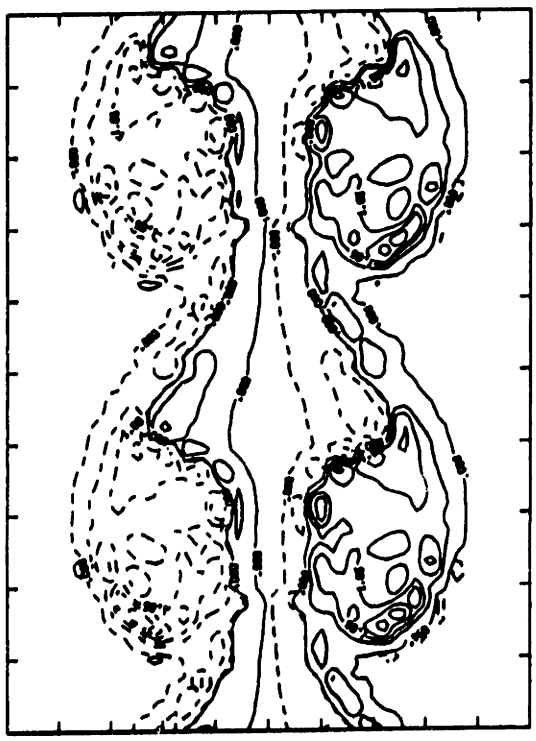

t = 7.5

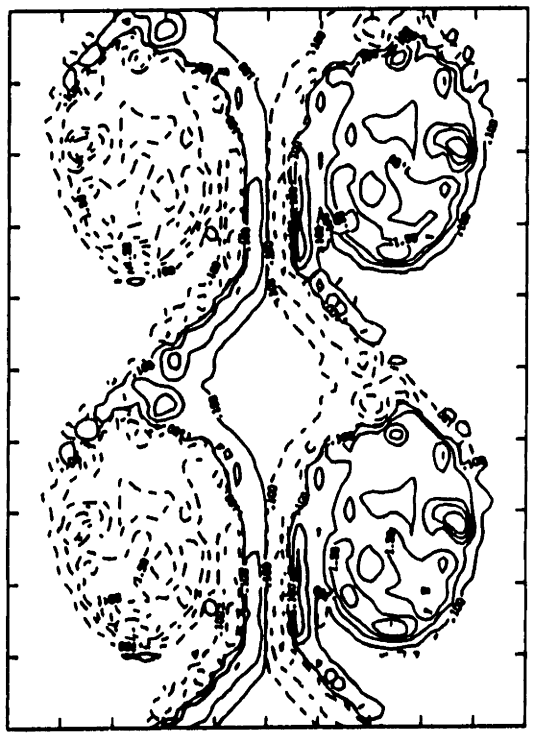

t = 10.0

Figure 131

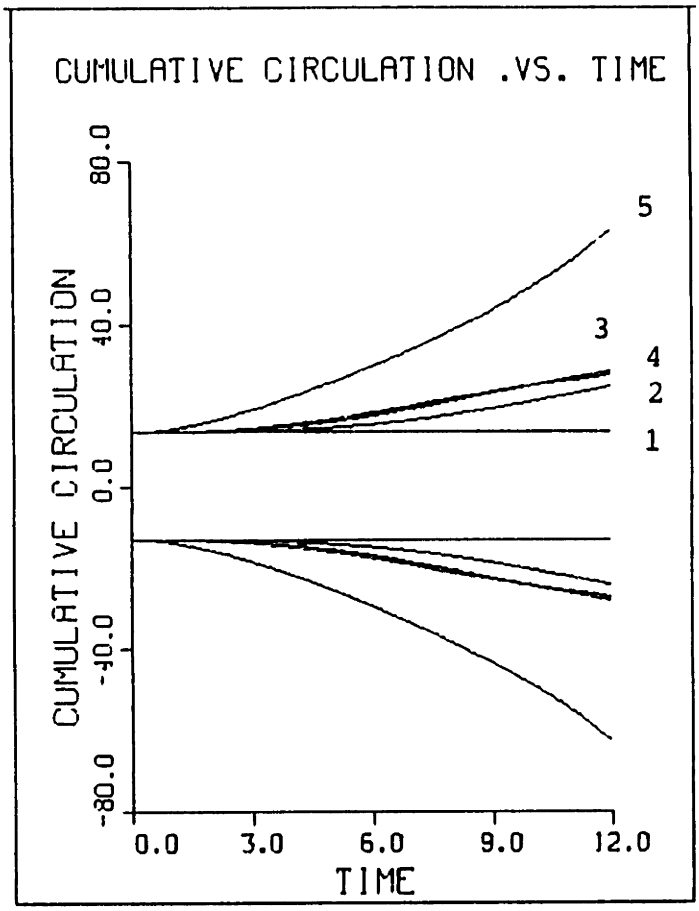

Figure 132

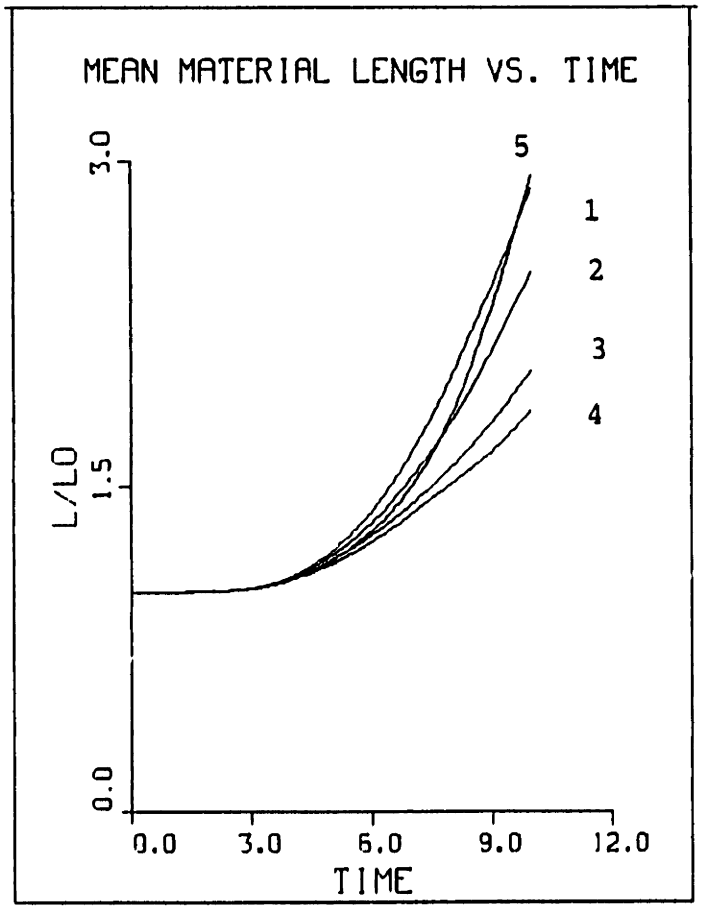

Figure 133

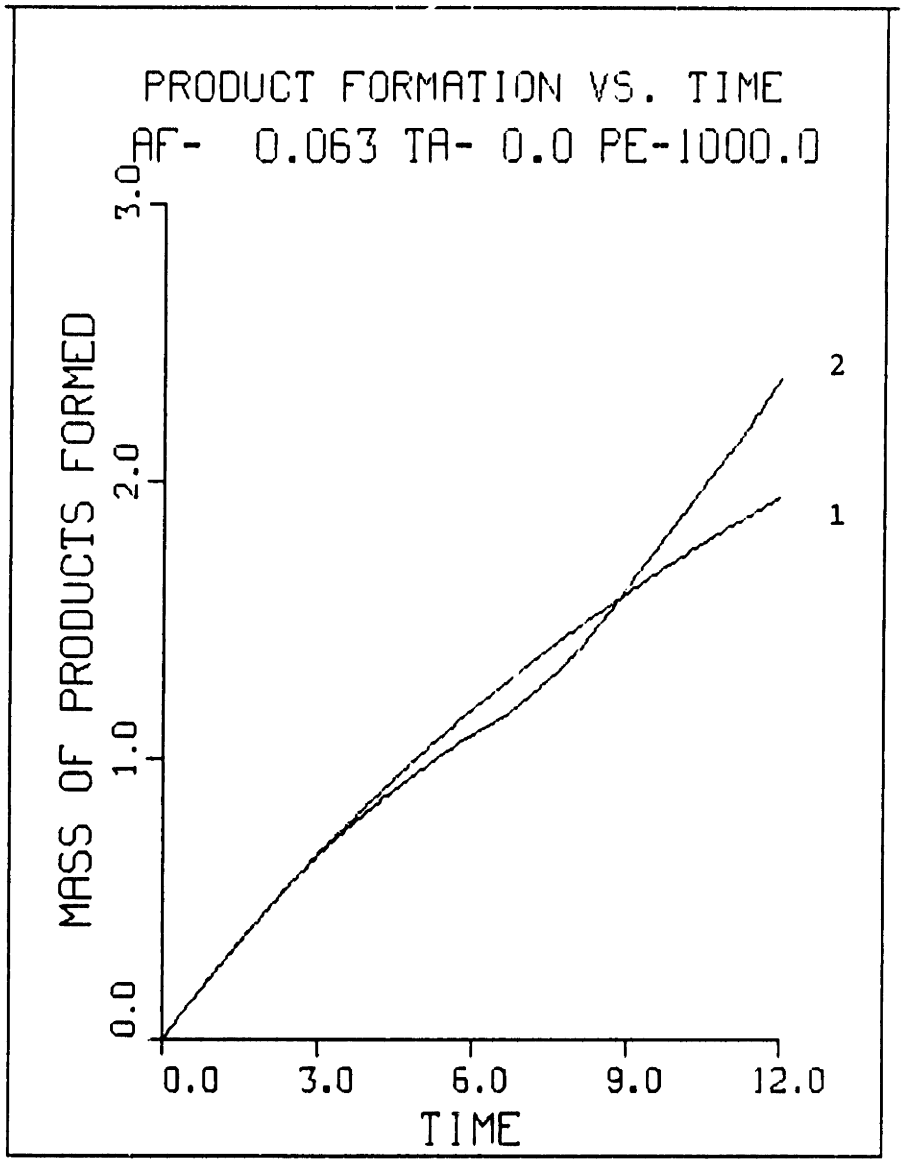
PRODUCT FORMATION VS. TIME
AF- 0.063 TA- 0.0 PE-1000.0
MASS OF PRODUCTS FORMED
3.0
2.0
1.0
0.0
2
1
0.0
3.0
6.0
9.0
12.0
TIME

Figure 134

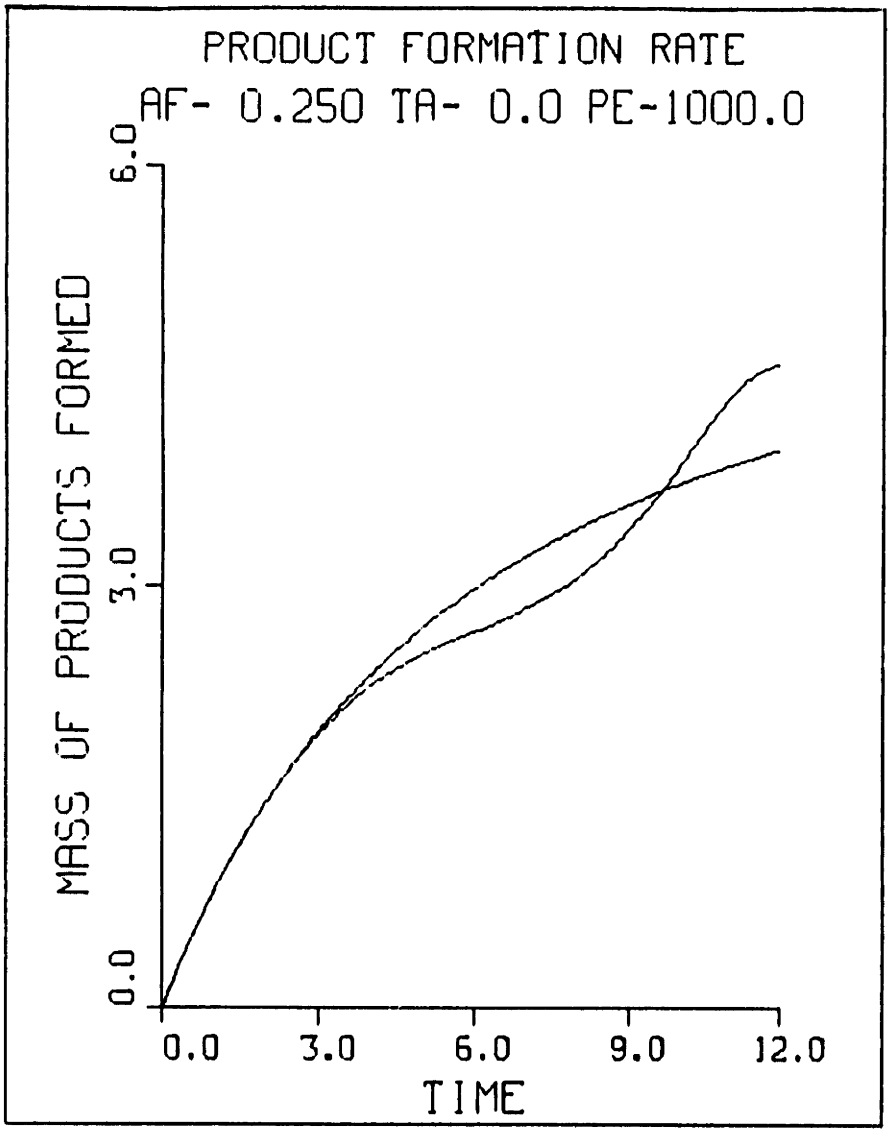
PRODUCT FORMATION RATE
AF- 0.250 TA- 0.0 PE-1000.0
MASS OF PRODUCTS FORMED
6.0
3.0
0.0
0.0
3.0
6.0
9.0
12.0
TIME

Figure 135

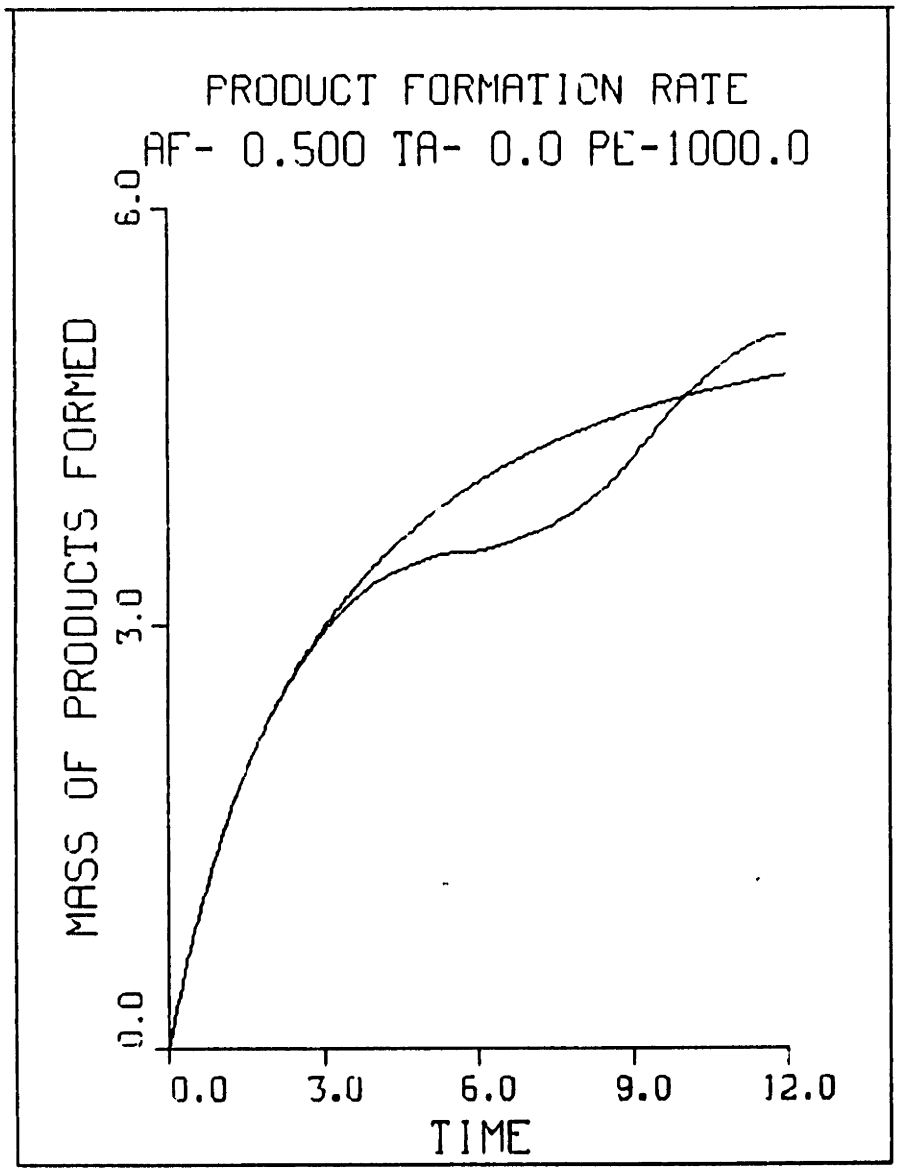
PRODUCT FORMATION RATE
AF- 0.500 TA- 0.0 PE-1000.0
MASS OF PRODUCTS FORMED
6.0
3.0
0.0
0.0
3.0
6.0
9.0
12.0
TIME

Figure 136

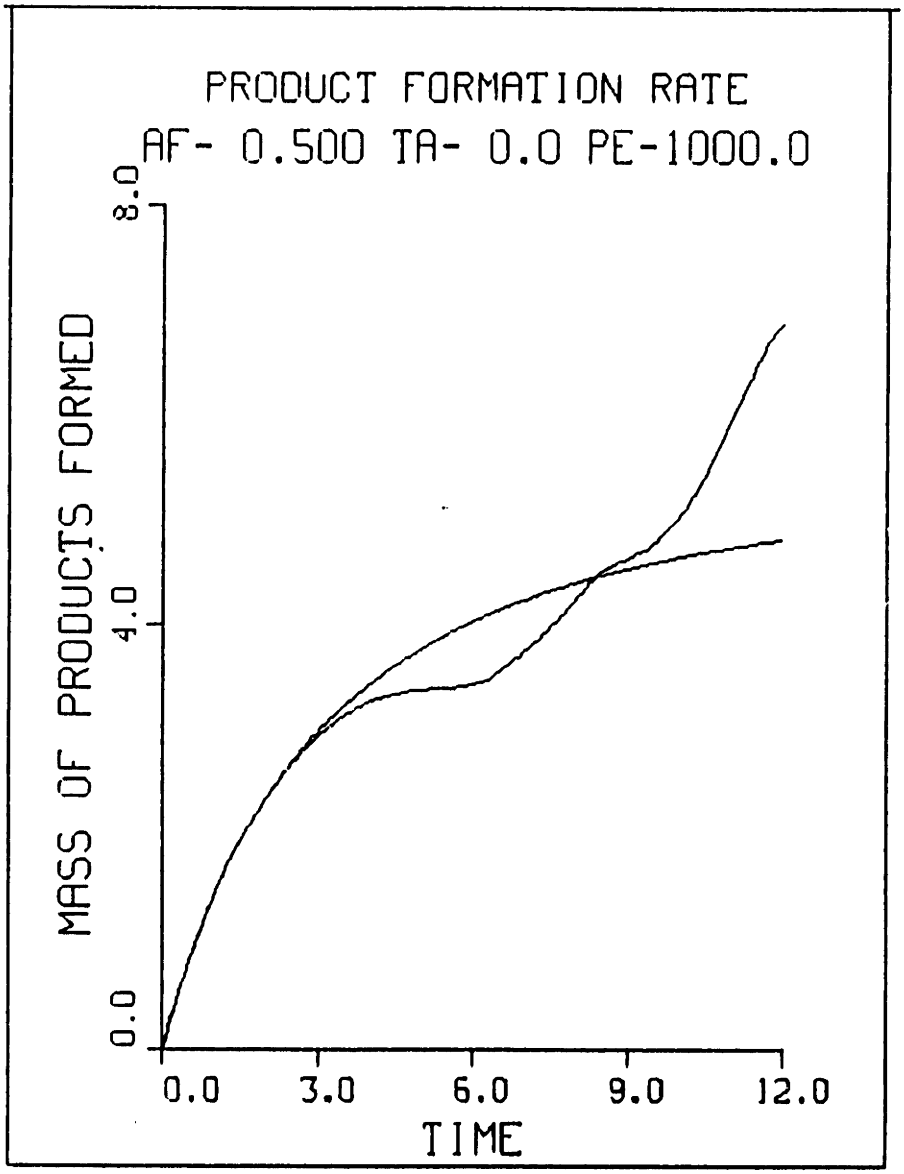
PRODUCT FORMATION RATE
AF- 0.500 TA- 0.0 PE-1000.0
MASS OF PRODUCTS FORMED
8.0
4.0
0.0
0.0
3.0
6.0
9.0
12.0
TIME

Figure 137

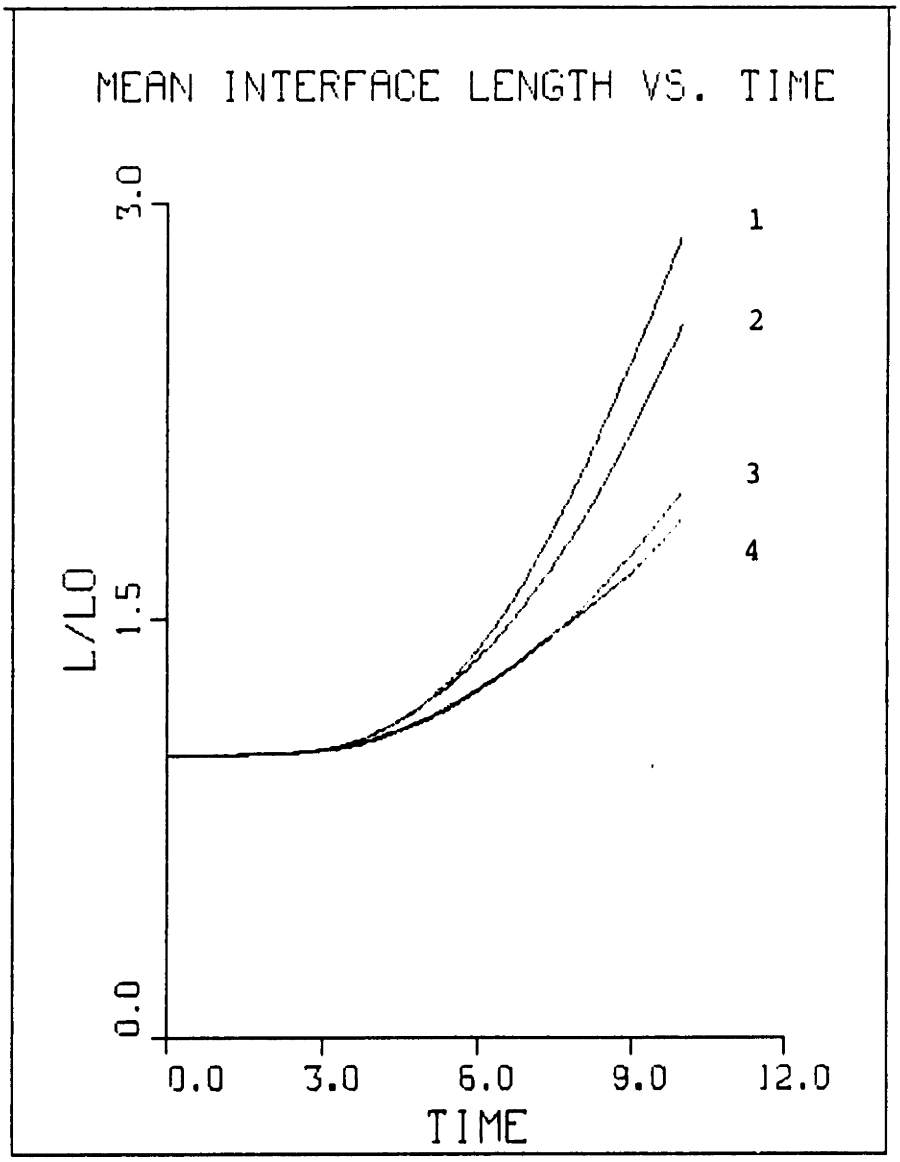
MEAN INTERFACE LENGTH VS. TIME
3.0
1.5
0.0
L/LO
0.0
3.0
6.0
9.0
12.0
TIME
1
2
3
4

Figure 138

VII. 4. 2. FINITE ACTIVATION ENERGY MODEL

The simulations were conducted using a Arrhenius chemical source term of the type shown in Eqn.(99). The non-dimensional activation energy for all the cases is taken to be 10.0 . Since the presence of the exponential greatly reduces the magnitude of the source term, the pre-exponential factor, A_f is increased in order to obtain significant product formation. Results were obtained for A_f = 150.0, 300.0 and 750.0 . Again, the results are compared against the non-reacting case in the previous section.

(i) Case I : A_f = 150.0

The locations and velocities of the vortex/transport elements are shown in Fig. 139 at t=2.5, 5.0, 7.5 and 10.0 respectively. Since the rate of reaction is exponentially dependent on the temperature, the initial product formation is very small, i.e., there is an ignition delay. In fact for this low value of A_f, the growth of the shear layers is exactly similar to that of the non-reacting flow. There is very little volumetric expansion in the field as is evidenced from the material line plots. The product formation contours at the corresponding time frames are shown in Fig. 140. The initial product formation is very small as shown by the very small values for the product concentration in the plots. Again, it is observed that the product formation is very sensitive to the local strain rate. Most of the reaction is taking place inside the eddies and there is very little product formation in the braids between the structures. The fuel concentration contours are shown in Fig. 141. It is observed that there is very little difference between the

reacting fuel concentration and the non-reacting fuel concentration contours in the previous section. Again, the small value of the Damkohler number and the ignition delay result in a very small amount of reaction taking place within the structures.

The contours for the magnitude of the source term are shown in Fig. 142. It is observed that the source term has a finite magnitude in the braids although the product formation in this region is zero. Most of the reaction zone is concentrated within the structure even at the late stages of development. This is unlike what was observed in the zero activation energy model wherein most of the reaction zone at the late stages was concentrated around the circumference of the eddies. The initial reaction increases the temperature in the core and since the reaction is temperature dependent, the reaction rate increases within the core. At the braids, the cooling effect caused due to the strainfield reduces the magnitude of the source term in these regions. Fig. 143 shows the vorticity contours at the corresponding time frames. It is observed that there is very little difference in the vorticity distribution between this case and the non-reacting case. Since the product formation is very low, the volumetric expansion and the generated vorticity are very small thus leading to negligible change in the vorticity distribution.

The cumulative circulation in the domain is plotted as a function of time in Curve 2 of Fig. 154. A finite amount of circulation is generated as seen from the plot but the magnitude is too small to significantly alter the dynamics of the flow. Curve 2 of Fig. 155 shows the mean length of the layers as a function of time. This curve is slightly below that of the non-reacting case indicating that the growth of the layer has been slightly reduced due to the reaction. The amount of product formation is plotted as a function of

time for the laminar and the turbulent flame in Fig. 156. Curves 1 and 2 represent the laminar and the turbulent product formation respectively. Unlike, the zero activation energy model used in the previous simulations, it is seen that the Arrhenius model with finite activation energy predicts very little product formation in the initial stages. This period is known as the ignition delay. As the strain field develops, the flame is extinguished in certain regions of the flow resulting in the turbulent product formation becoming smaller than that of the laminar flame. However, at late stages of the flow, due to the enhanced mixing and reaction within the eddies, the turbulent product formation increases above that of the laminar flame.

(ii) Case II : $A_f = 300.0$

The magnitude of the source term is increased by a factor of two compared to Case I. The locations and velocities of the vortex/transport elements are shown in Fig. 144 at t=2.5, 5.0, 7.5 and 10.0 respectively. The development of the flow field closely resembles that of the previous case indicating that the effects of reaction are still negligible. A close inspection of the cores of the eddies reveals the effects of volumetric expansion, but its magnitude is too small to affect the large scale dynamics of the flow field. The product concentration contours at the corresponding time frames are shown in Fig. 145. Again, the major qualitative features are similar to what was observed in the previous case. Larger values for the product concentration are seen in the cores of the eddies as compared to Case I. This is due to the magnitude of the source term being larger in this case. Once again, most or all of the reaction is within the cores of the eddies and the flame is extinguished in regions of large positive strain. The contours for the fuel

concentration are shown in Fig. 146. Increased fuel consumption within the structure is observed as a result of the increased Damkohler number.

Fig. 147 shows the contours for the magnitude of the source term at the corresponding times. It is interesting to note that the magnitude of the source term appears to be decreasing in regions of positive strain. This is because of the temperature dependence in the source term. In regions of positive strain, the cooling effect due to diffusion is very strong and as the temperature decreases, the magnitude of the source term decreases exponentially. Therefore, with an arrhenius model for the chemical reaction, it is expected that the reaction rate will be extremely sensitive to the local strain field. The vorticity contours at the corresponding time frames are shown in Fig. 148. Again, the development of the vorticity field is very similar to that of the previous case, although the small but finite volumetric expansion leads to smaller values for the vorticity at the centers of the structures. However the feedback from the reaction to the flow field is very small in this case.

The cumulative circulation in the flow field is plotted as a function of time in Curve 3 of Fig. 154. The curve is slightly above that of Case I indicating that the larger product formation leads to a small increase in the amount of circulation generated. The mean length of the material layers is plotted as a function of time in Curve 3 of Fig. 155. It is seen that the increased volumetric expansion slows down the growth of the layer as compared to Case I. From Figs. 154 and 155, it is clear that the amount of reaction is not sufficient to cause any significant changes in the flow field. The mass of products formed with time is shown in Fig. 157 for the laminar and the turbulent flame. The same qualitative features observed before are seen here too. The developing strain field causes the turbulent product formation

to decrease below that of the laminar flame and at the late stages, the turbulent curve increases above the laminar curve due to increased product formation in the cores of the eddies. It is to be noted that the decrease in turbulent product formation with respect to the laminar flame is less in Case II than in Case I. This indicates that the flame is more resistant to strain at higher Damkohler numbers.

(iii) Case III : $A_f = 750.0$

The magnitude of the source term is increased by a factor of 2.5 compared to Case II. It is to be remembered that the source term is highly non-linear and an increase in its magnitude by a small factor can lead to an order of magnitude increase in product formation. Fig. 149 shows the locations and velocities of the vortex/transport elements at t=2.5, 5.0, 7.5 and 10.0 respectively. The initial development of the flow field is similar to that of the previous cases, however, at the late stages, it is observed that a strong volmetric expansion is taking place inside the eddies. The non-linear nature of the interaction is clearly obvious from the plots. All or most of the reaction takes place in the time interval $7.5<t<10.0$. This is because the flow field is very cold initially and the chemical reaction is very small. As the temperature increases due to the reaction, the magnitude of the source term increases exponentially which leads to greater heat release and rise in temperature. Thus, the cycle goes on with the source term and the temeprature increasing exponentially. The central zones of the eddies look very diffuse due to the effects of expansion. Although the heat release in the final stages of the flow is quite large, the instability is not damped due to the expansion. This is because of the ignition delay that occurs in the initial

stages of development during which expansion effects are negligible. Thus the flow develops strongly and is not affected by the reaction. The effects of reaction become significant only after the fluids have been entrained into the structures. The contours for the product concentration are shown in Fig. 150 at the corresponding time frames. It is observed that the product formation rate is very sensitive to strain and flame blows off in regions of positive strain. Very large values for the product concentration are observed at the final stages of development of the eddies indicating that a large amount of reaction has taken place. The contours for the fuel concentration are shown in Fig. 151. The increased value of the Damkohler number results in complete consumption of all the fuel within the structure.

Fig. 152 shows the contours for the magnitude of the source term at the corresponding times. It is observed that most of the eddy is comprised of products and the value of the reaction rate in the regions within the eddy are nearly zero. The reaction zone is concentrated around the circumference of the large scale structures. The value of the source term in the braids is very small due to the cooling effect of the cold reactant streams. Fig. 153 shows the vorticity contours at t=2.5, 5.0, 7.5 and 10.0 respectively. The values of the vorticity in the initial stages are not affected due to the ignition delay and hence the flow field is not damped by the reaction. At the late stages, the large volmetric expansion within the eddies causes a substantial weakening of the vorticity field.

The cumulative circulation in the domain with time is shown in Curve 4 of Fig. 154 . It is observed that the greater product formation at the late stages leads to higher values for $\nabla\rho$ in the field which in turn leads more generation of circulation compared to the previous cases. Curve 4 of Fig. 155 shows the mean length of the material layers with time. The curve is

below those of the previous cases indicating that the volumetric expansion has a stabilizing effect on the flow field, particularly at the late stages. The mass of products formed with time is shown in Fig. 158 for the laminar and the turbulent flame. Although the development of the strain field does lead to the flame blowing off in certain regions of the flow, the enhanced reaction in other regions make up for it and the turbulent product formation curve never decreases below that of the laminar flame. At the late stages, the turbulent product formation increases rapidly compared to the laminar flame and the final products ratio between the turbulent and the laminar flame is almost two. Comparing cases I and III, it is seen that a factor of 5 increase in the source term leads to a factor of 25 in the final amount of products formed. This illustrates the highly non-linear dependence of product formation on the source term.

VII . 5. CONCLUSIONS

Simulations were conducted for the jet diffusion flame with two source terms, one with a zero activation energy source term and one with a finite activation energy source term. Both sets of simulations yielded a great deal of insight into the outcome of turbulence-combustion interactions. For the zero activation energy model, it is seen that the effect of heat release is always to stabilize the flow field and if the Damkohler number is too large, the instability is completely damped. Due to this phenomenon, the turbulent product formation never increases significantly above that of the laminar flame.

With the Arrhenius temperature dependence, the turbulent product formation at low Damkohler numbers is almost the same as that of the laminar

flame. At large values of the Damkohler number, the turbulent flame produces an order of magnitude increase in product formation above that of the laminar flame. This behavior is more in agreement with experimental observations and thus the Arrhenius model for the reaction is more accurate. When turbulence-combustion interactions are significant, the assumtion of a source term without temperature dependence can lead to large errors in the predictions of the reaction rate.

In both cases, it is observed that at low Damkohler numbers, the reaction takes place in a distributed zone within the large scale structures. In this regime, the flame or reaction is not very sensitive to the strain field. At large Damkohler numbers, however, the flame exists as a reaction sheet around the circumference of the eddies. Since the reaction zone is more or less aligned with the strainfield, the reaction rate becomes sensitive to the local value of strain. It is interesting to note that the product formation curves for the diffusion flame are in stark contrast to what is observed in the case of the premixed flame. For the premixed flame, the turbulent product formation curve approaches that of the laminar flame as the Damkohler number increases. On the other hand, for the diffusion flame, the two curves approach each other as the Damkohler number decreases.

FIGURE CAPTIONS

Fig. 139. The locations and velocities of the vortex/transport elements at t= 2.5, 5.0, 7.5 and 10.0 respectively for Case I.

Fig. 140. The product concentration contours at t= 2.5, 5.0, 7.5 and 10.0 respectively for Case I.

Fig. 141. The fuel concentration contours at t= 2.5, 5.0, 7.5 and 10.0 respectively for Case I.

Fig. 142. The source term contours for Case I at t= 2.5, 5.0, 7.5 and 10.0 respectively.

Fig. 143. The vorticity contours for Case I at t= 2.5, 5.0, 7.5 and 10.0 respectively. The continuous contours represent negative vorticity and the dashed contours signify positive vorticity.

Fig. 144. The locations and velocities of the vortex/transport elements at t= 2.5, 5.0, 7.5 and 10.0 respectively for Case II.

Fig. 145. The product concentration contours at t= 2.5, 5.0, 7.5 and 10.0 respectively for Case II.

Fig. 146. The fuel concentration contours at t= 2.5, 5.0, 7.5 and 10.0 respectively for Case II.

Fig. 147. The source term contours for Case II at t= 2.5, 5.0, 7.5 and 10.0 respectively.

Fig. 148. The vorticity contours for Case II at t= 2.5, 5.0, 7.5 and 10.0 respectively. The continuous contours represent negative vorticity and the dashed contours signify positive vorticity.

Fig. 149. The locations and velocities of the vortex/transport elements at t= 2.5, 5.0, 7.5 and 10.0 respectively for Case III.

Fig. 150. The product concentration contours at t= 2.5, 5.0, 7.5 and 10.0 respectively for Case III.

Fig. 151. The fuel concentration contours at t= 2.5, 5.0, 7.5 and 10.0 respectively for Case III.

Fig. 152. The source term contours for Case III at t= 2.5, 5.0, 7.5 and 10.0 respectively.

Fig. 153. The vorticity contours for Case III at t= 2.5, 5.0, 7.5 and 10.0 respectively. The continuous contours represent negative vorticity and the dashed contours signify positive vorticity.

Fig. 154. The cumulative circulation in the flow field as a function of time. The positive and the negative components are shown separately. Curves 1, 2, 3 and 4 represent the non-reacting case and cases I, II and III respectively.

Fig. 155. The mean length of the material layers as a function of time. Curves 1, 2, 3 and 4 represent the non-reacting case and cases I, II and III respectively.

Fig. 156. The mass of products formed as a function of time for Case I. Curves 1 and 2 represent the laminar and the turbulent product formation respectively.

Fig. 157. The mass of products formed as a function of time for Case II. Curves 1 and 2 represent the laminar and the turbulent product formation respectively.

Fig. 158. The mass of products formed as a function of time for Case III. Curves 1 and 2 represent the laminar and the turbulent product formation respectively.

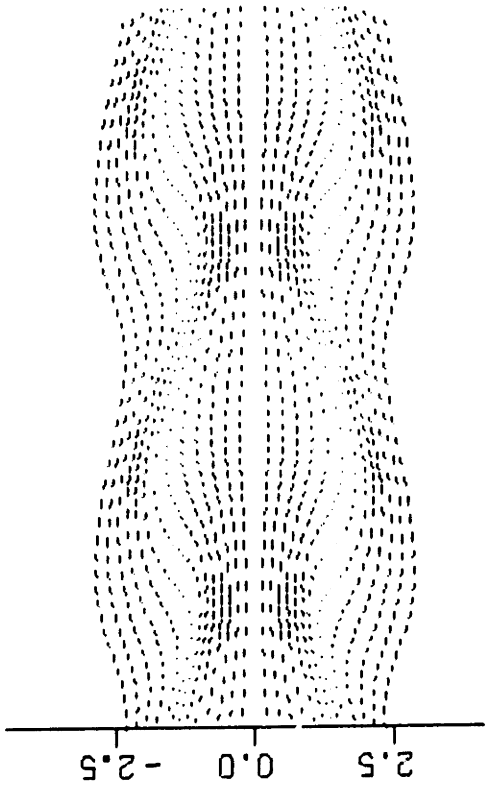

t = 2.5

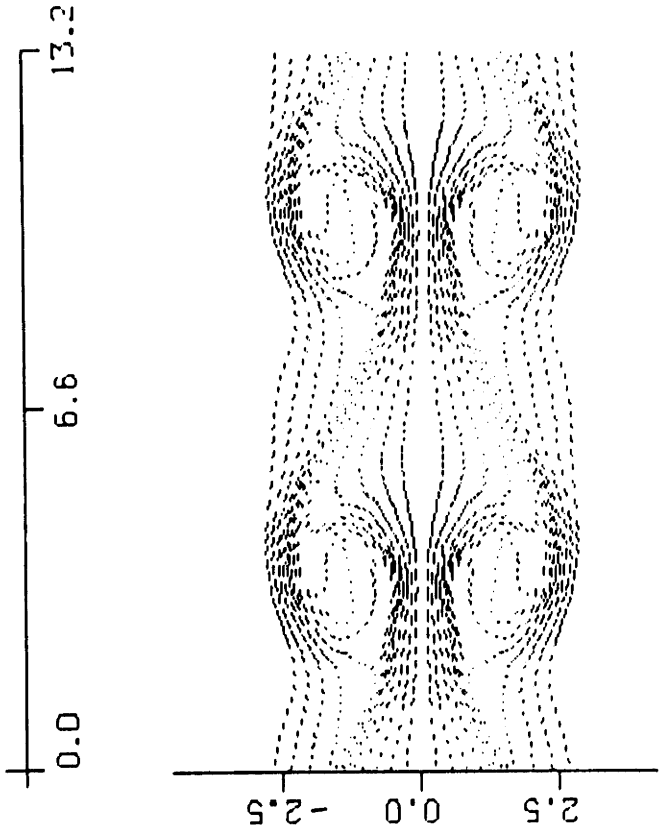

t = 5.0

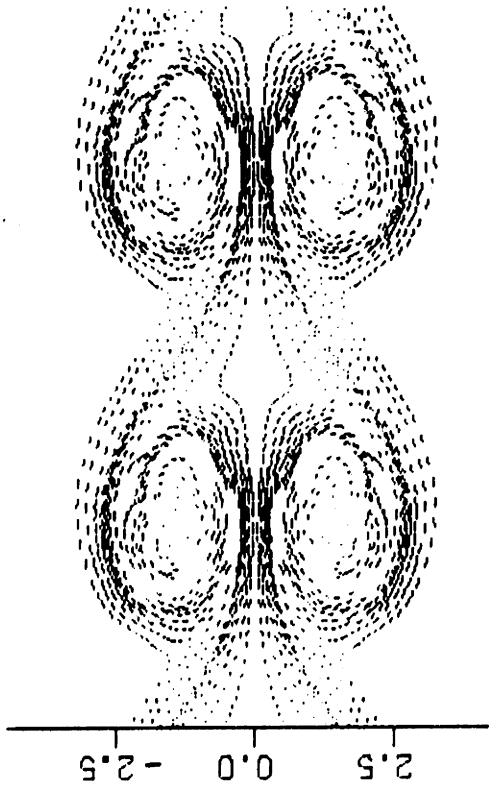

t = 7.5

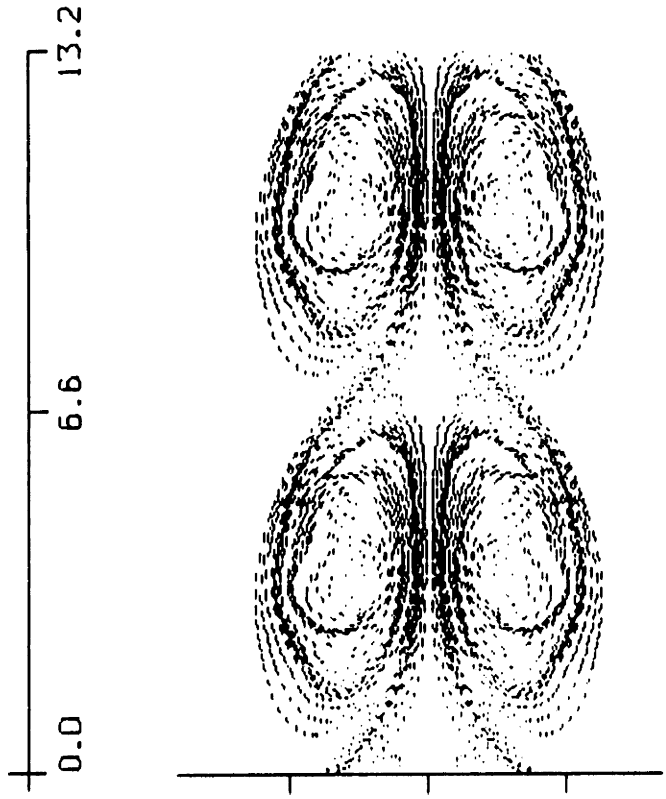

t = 10.0

Figure 139

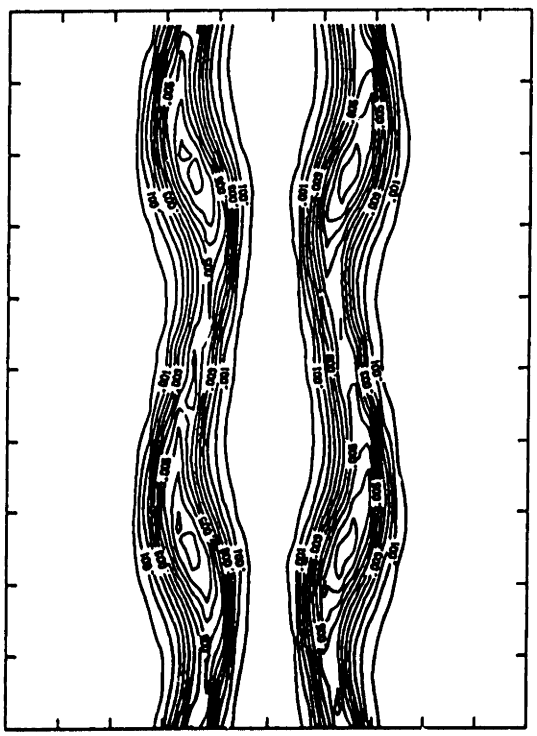

t = 2.5

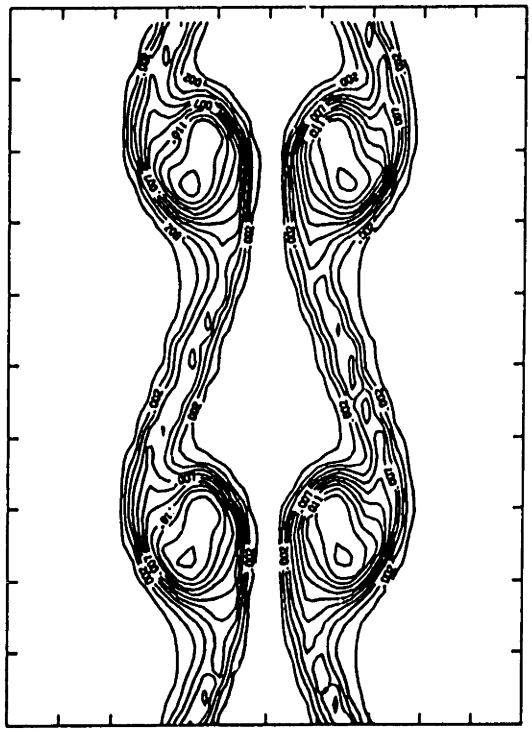

t = 5.0

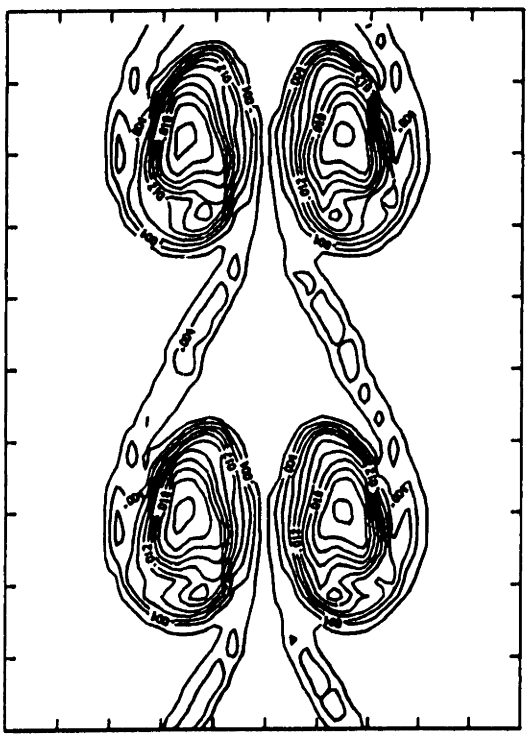

t = 7.5

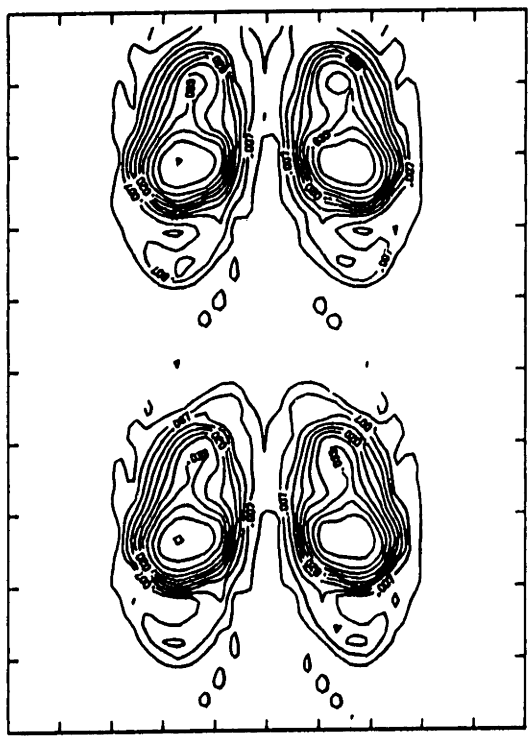

t = 10.0

Figure 140

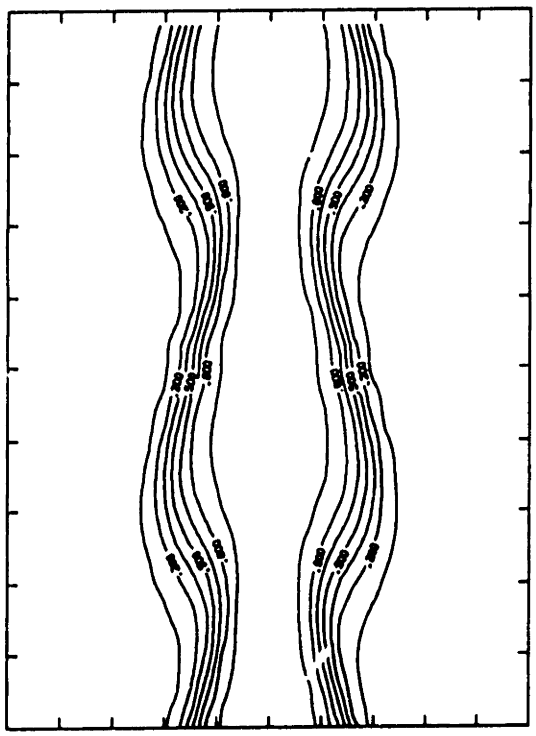

t = 2.5

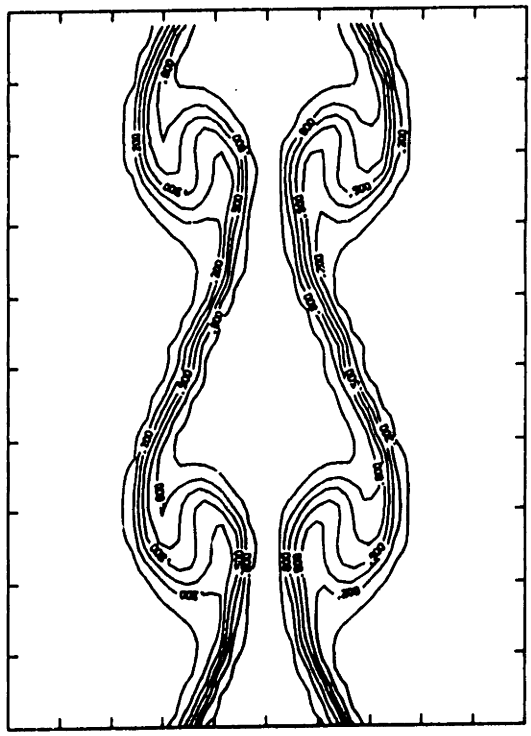

t = 5.0

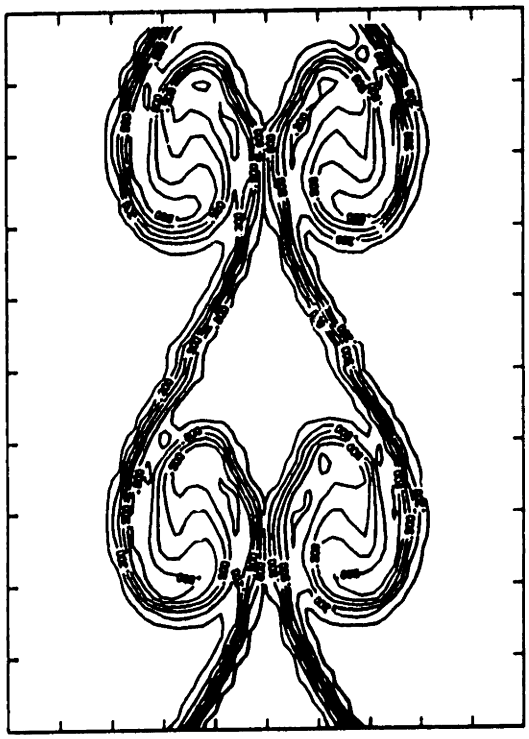

t = 7.5

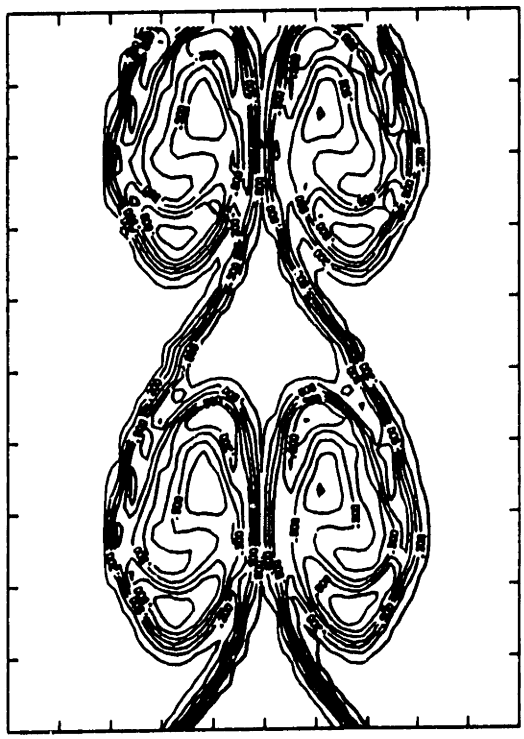

t = 10.0

Figure 141

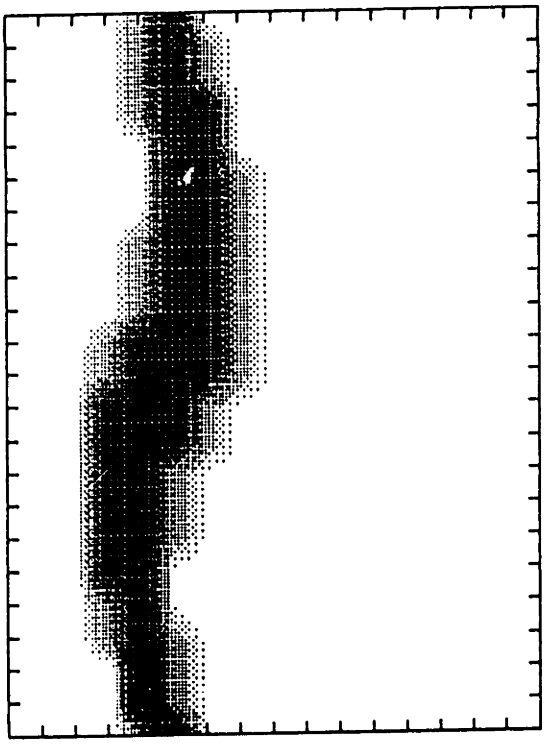

t = 2.5

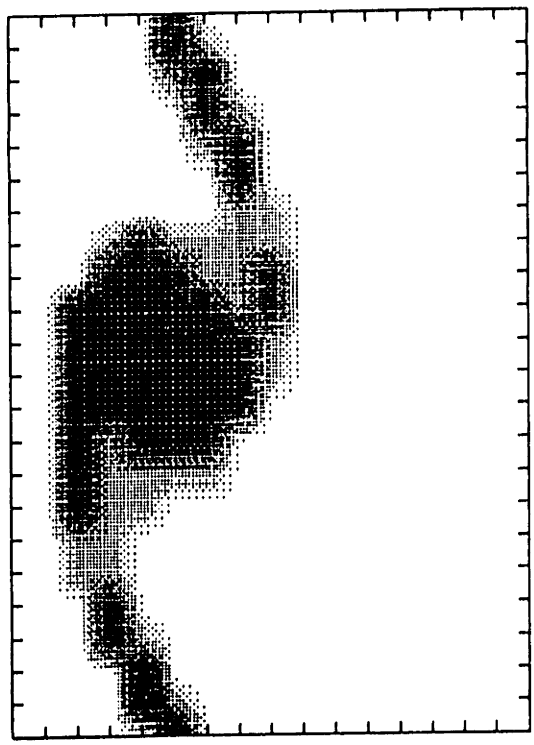

t = 5.0

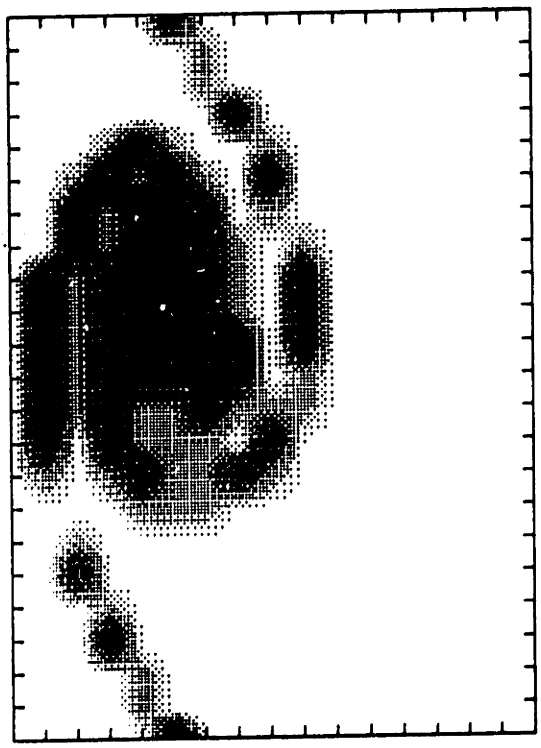

t = 7.5

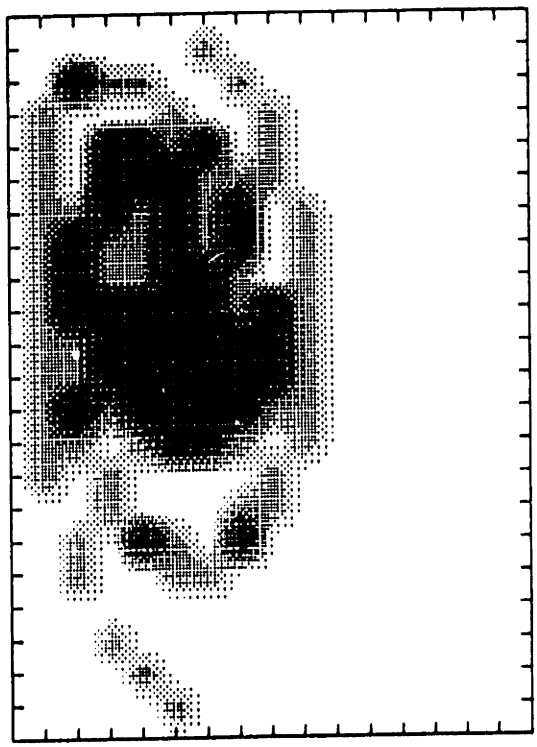

t = 10.0

Figure 142

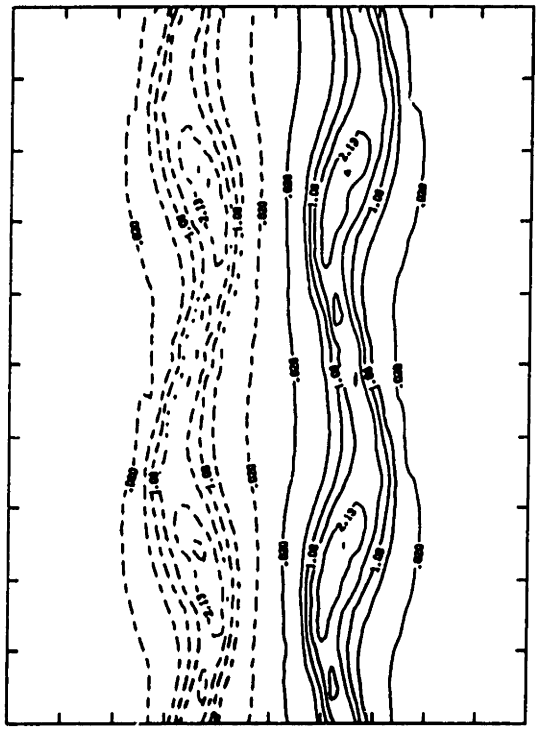

t = 2.5

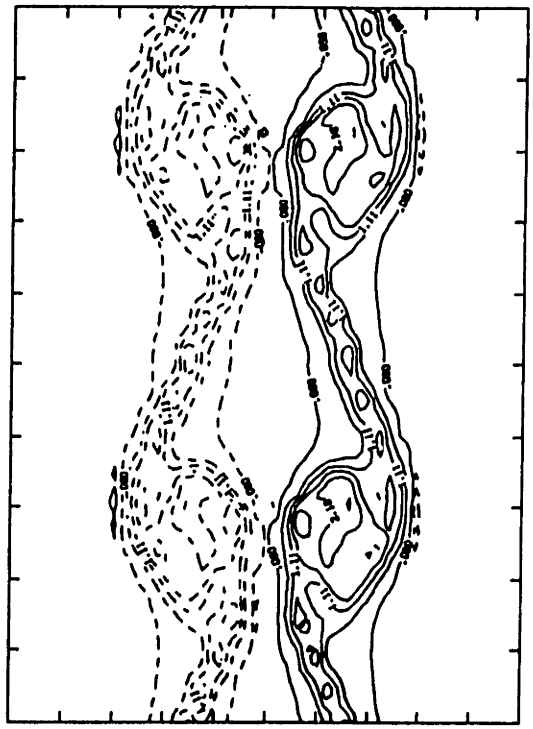

t = 5.0

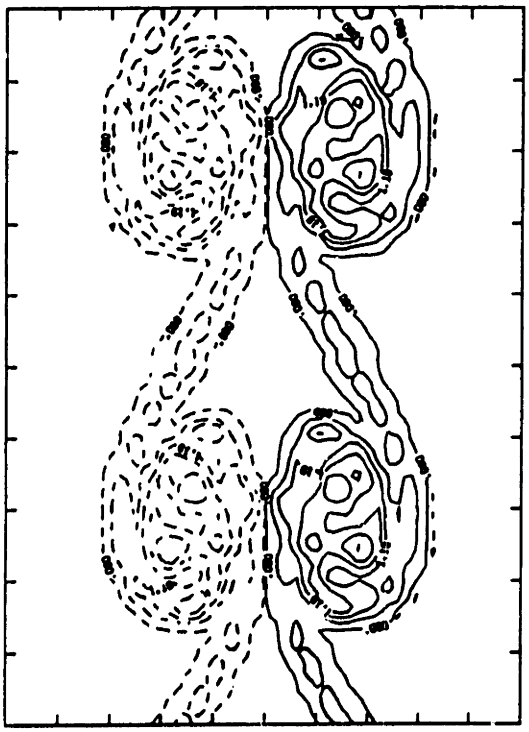

t = 7.5

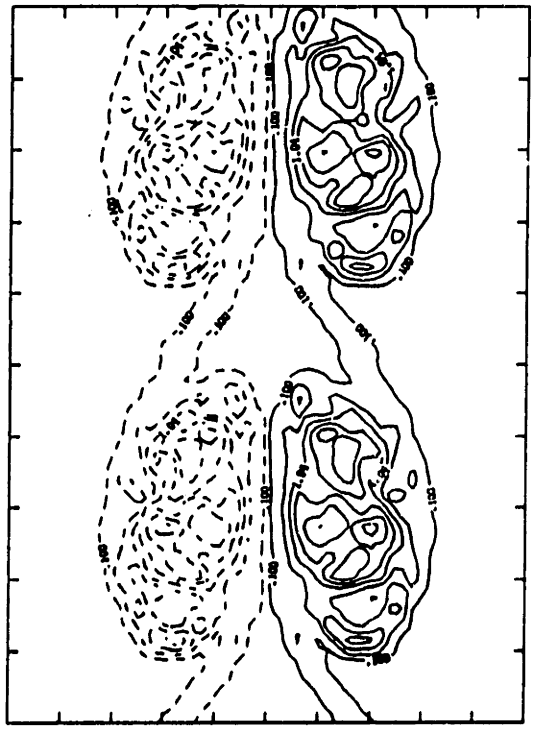

t = 10.0

Figure 143

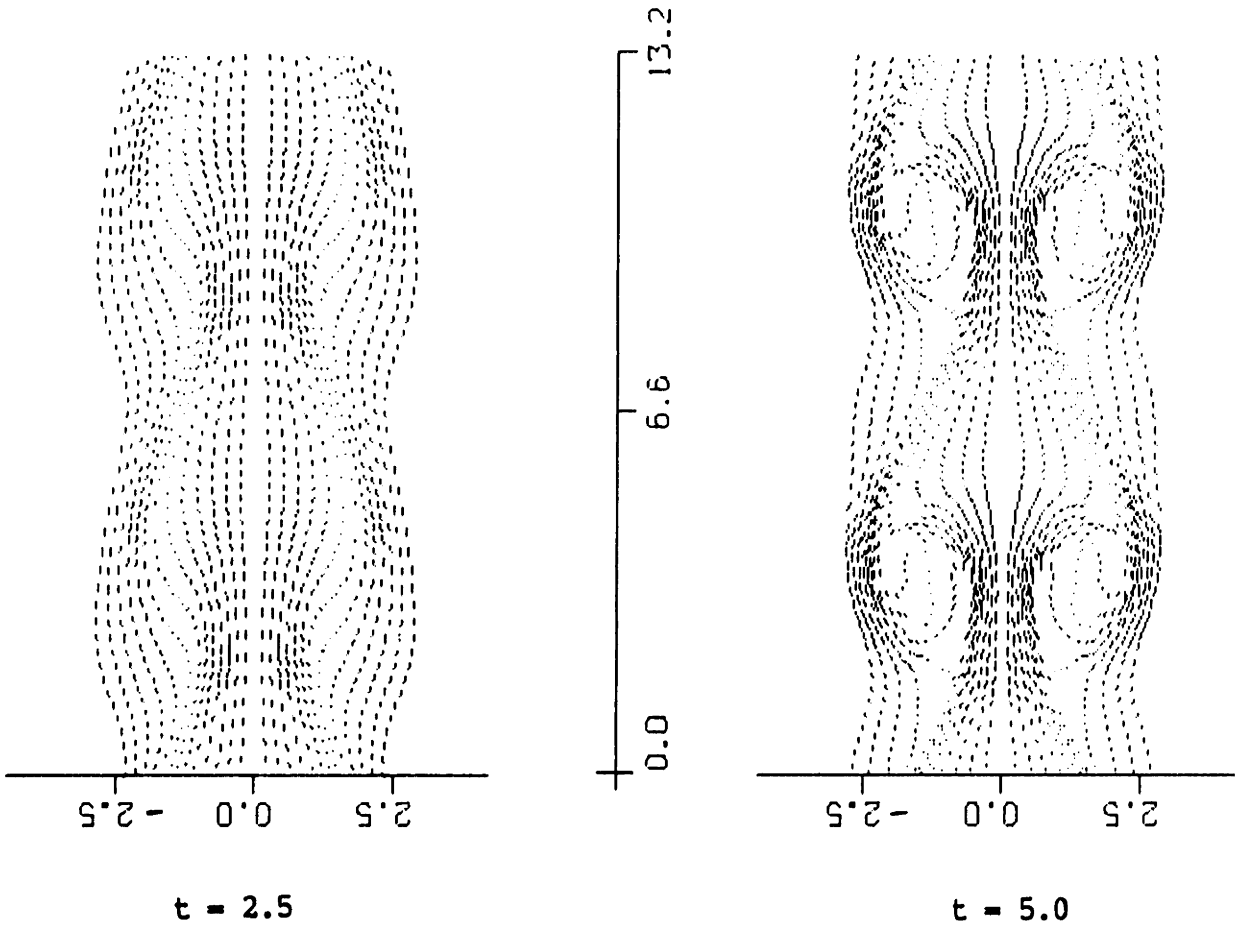

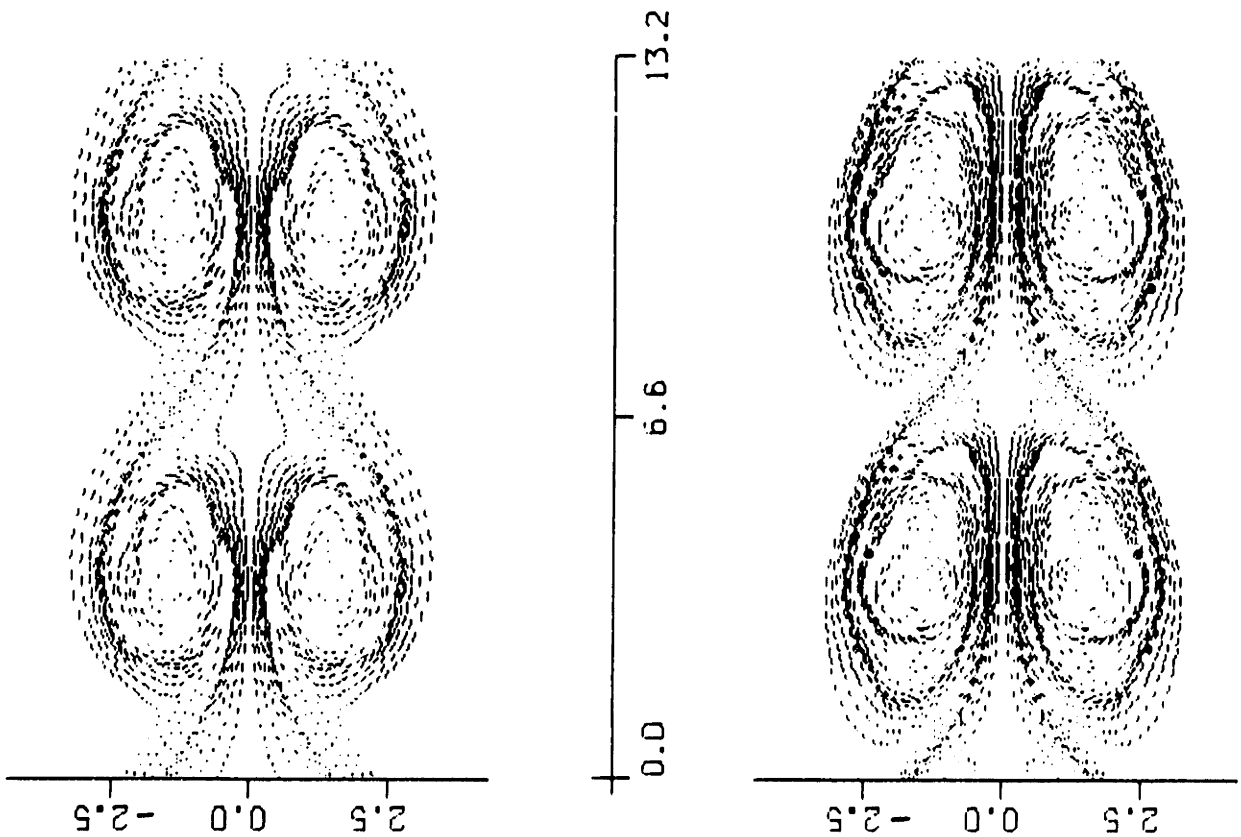

Figure 144

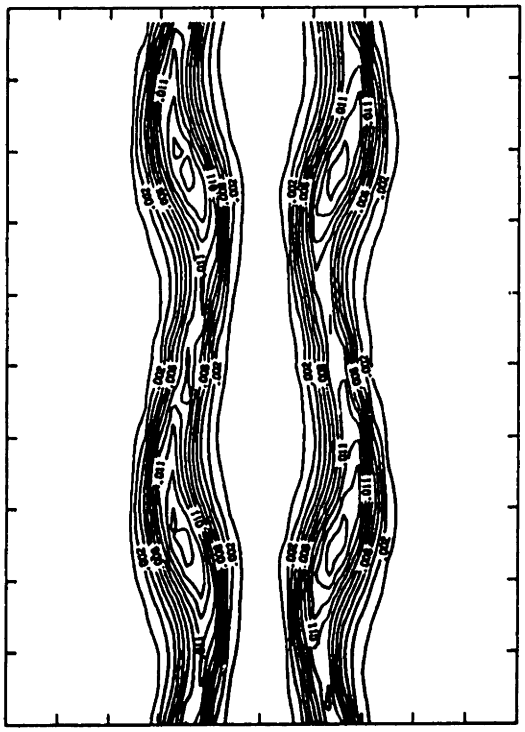

t = 2.5

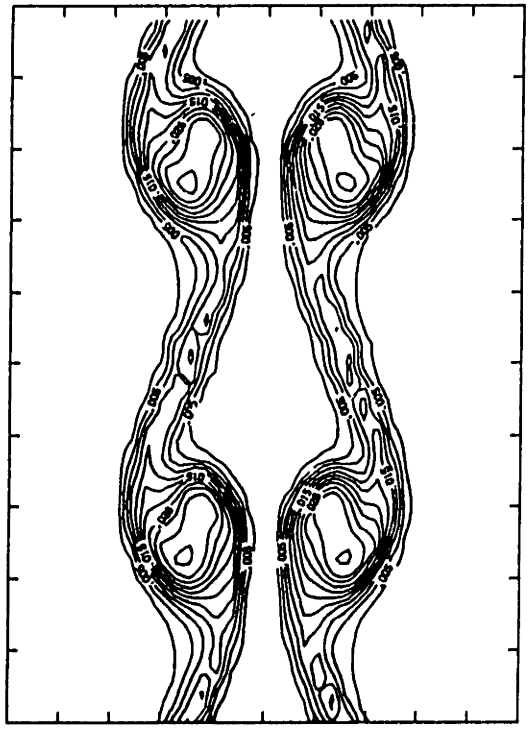

t = 5.0

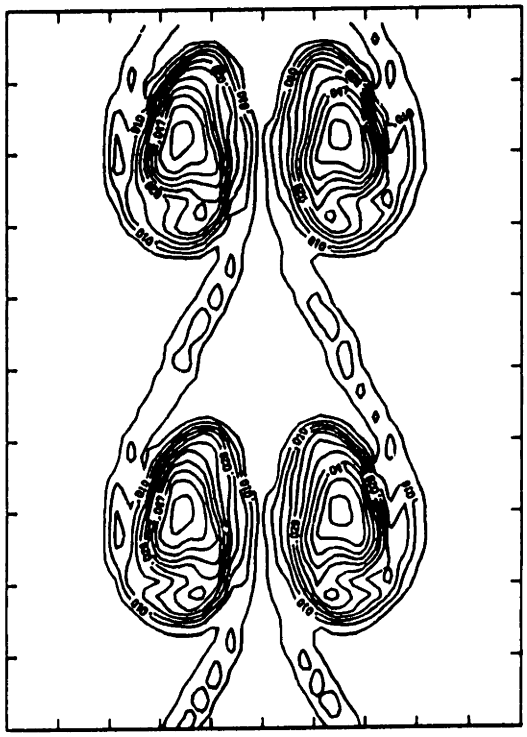

t = 7.5

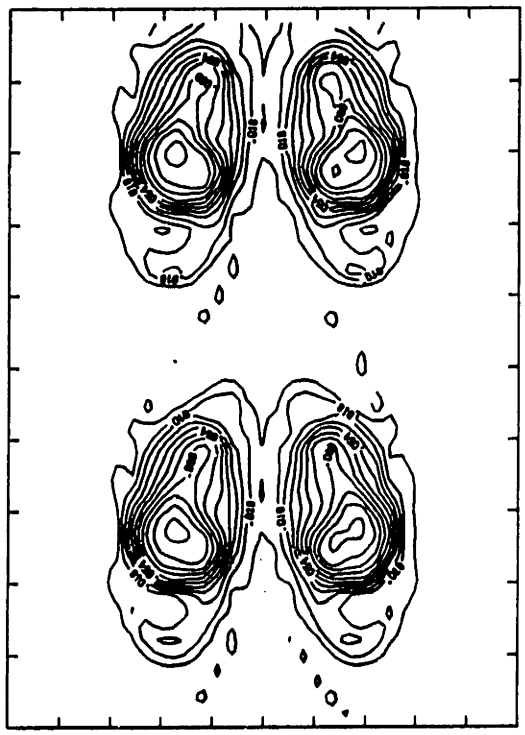

t = 10.0

Figure 145

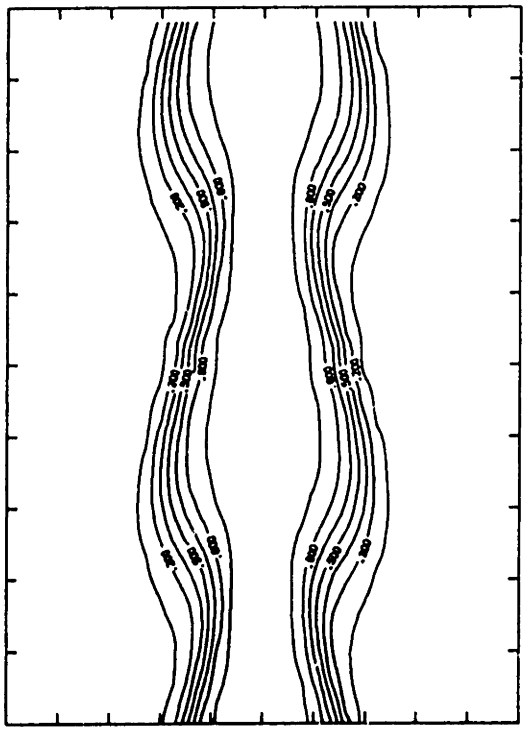

t = 2.5

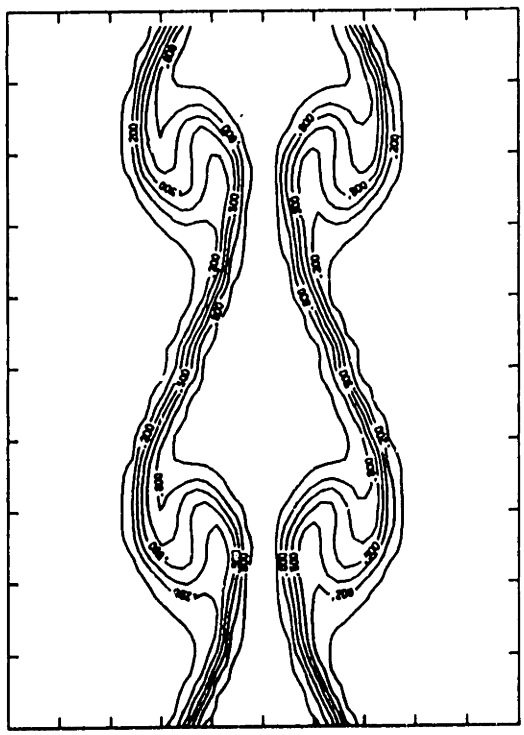

t = 5.0

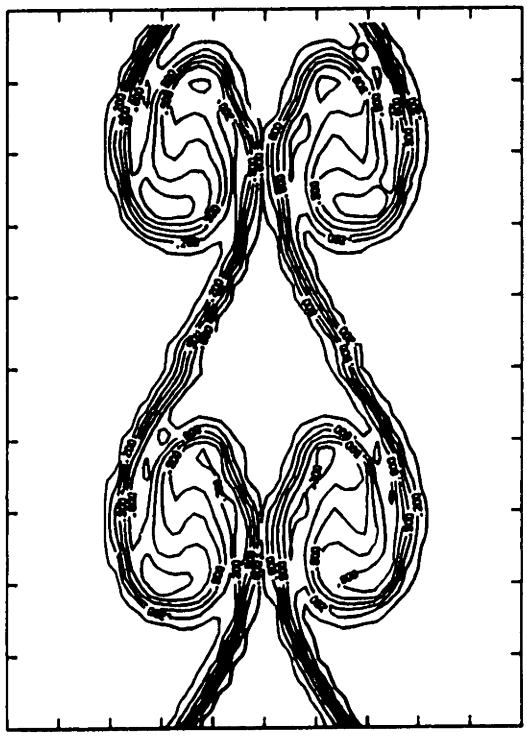

t = 7.5

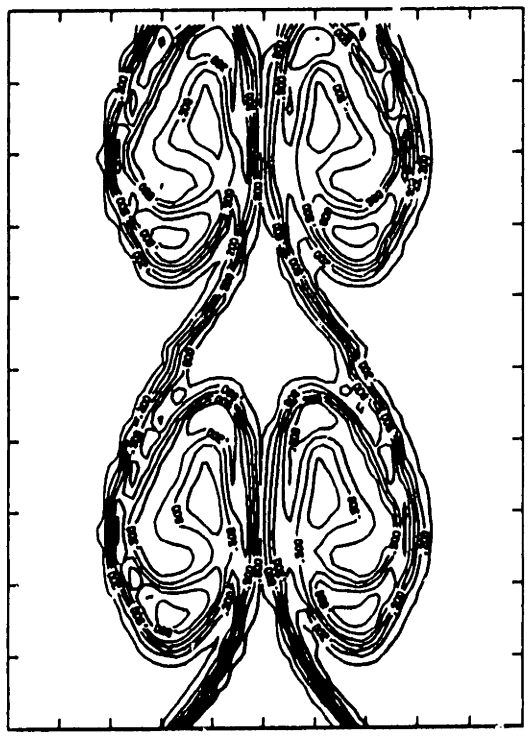

t = 10.0

Figure 146

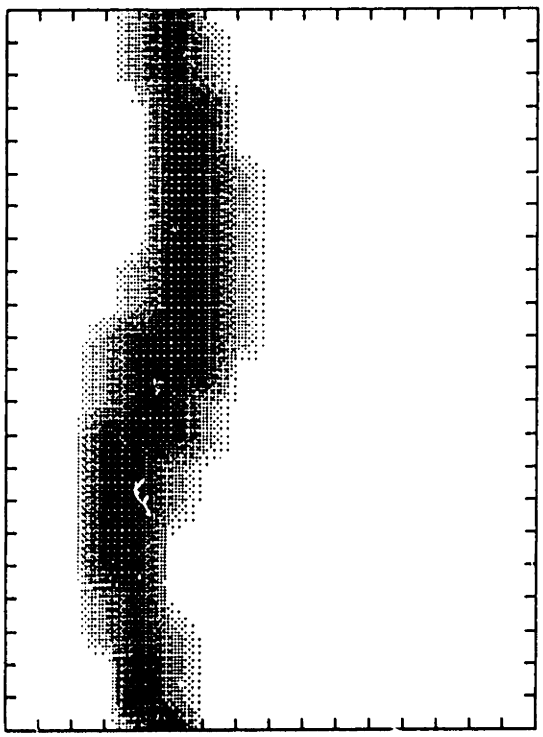

t = 2.5

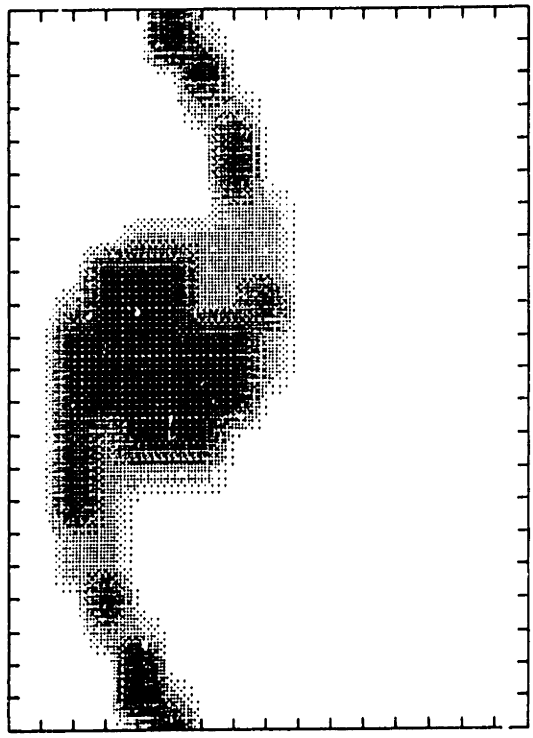

t = 5.0

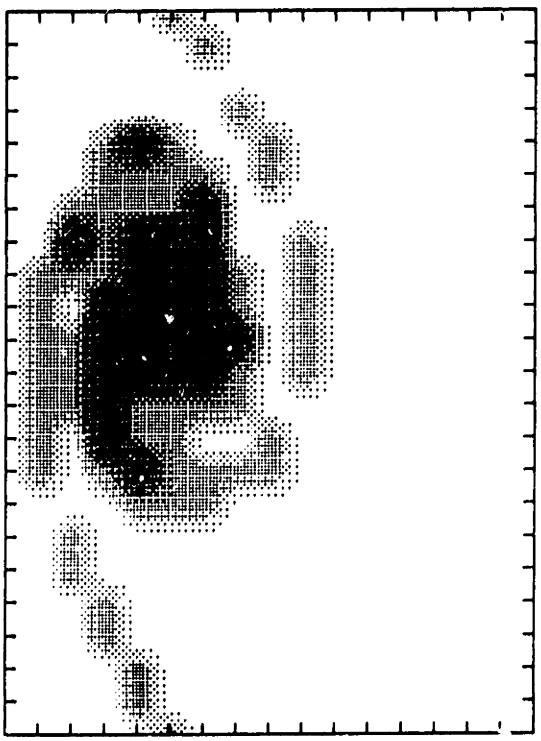

t = 7.5

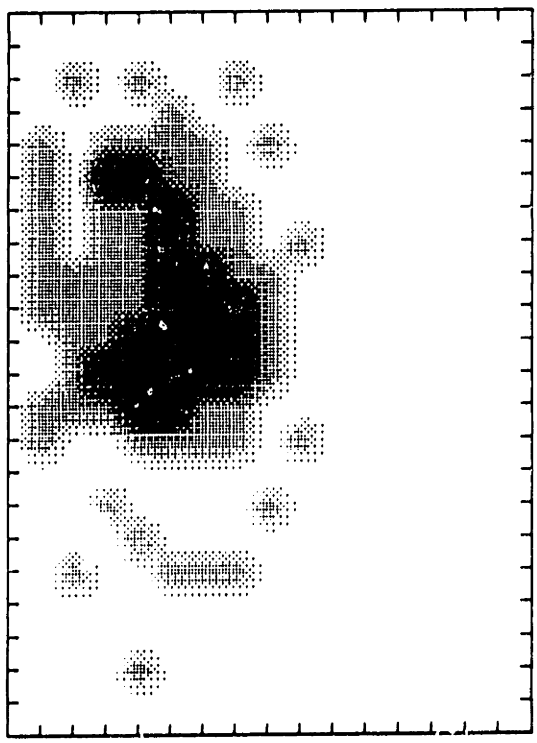

t = 10.0

Figure 147

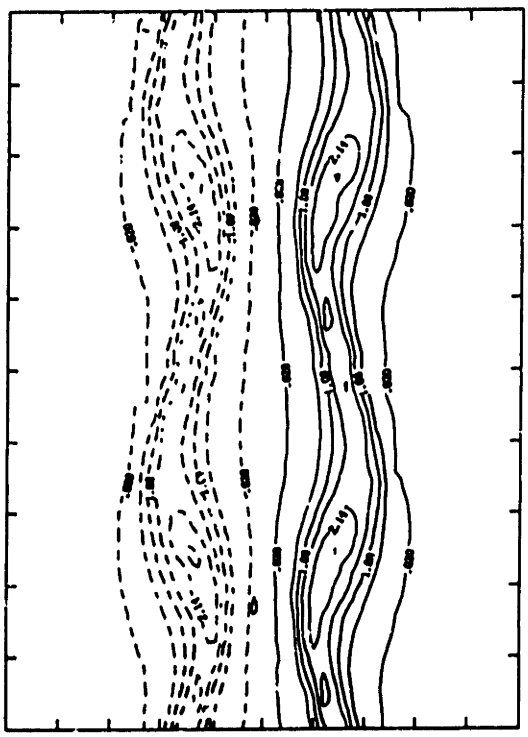

t = 2.5

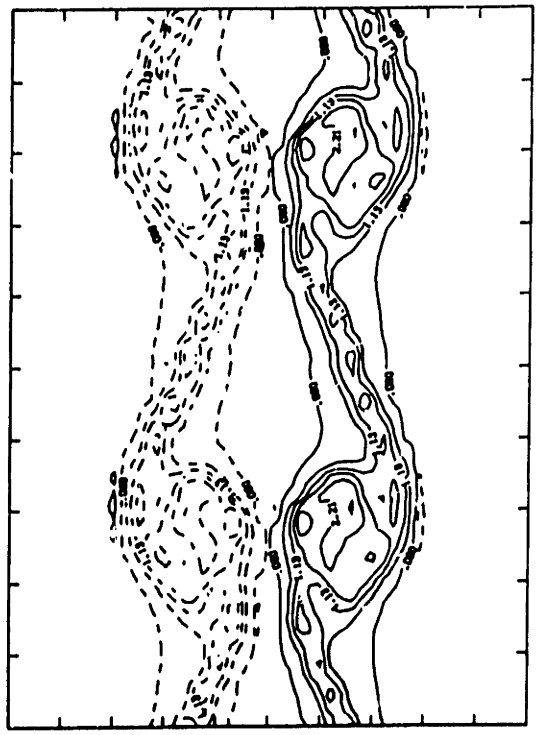

t = 5.0

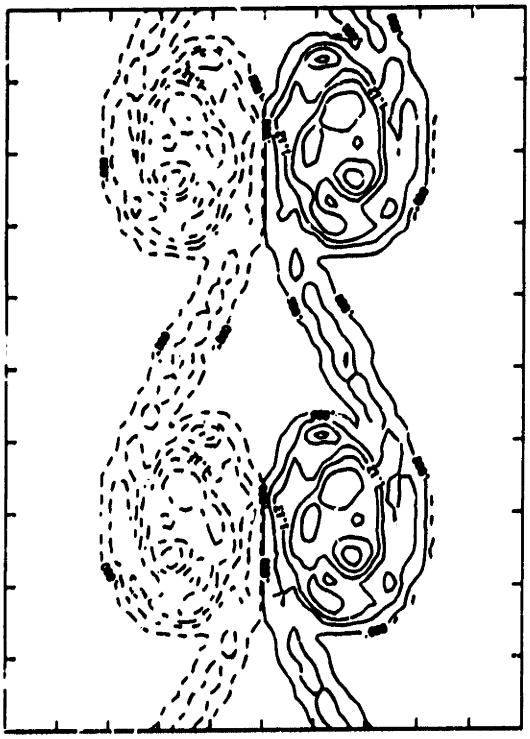

t = 7.5

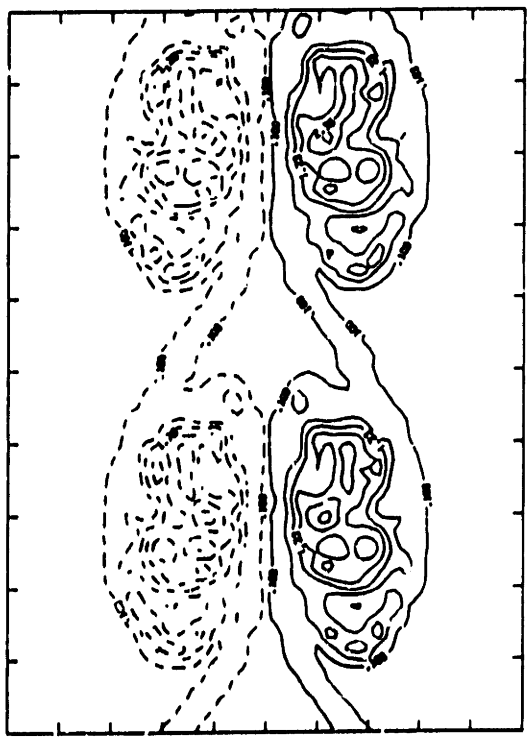

t = 10.0

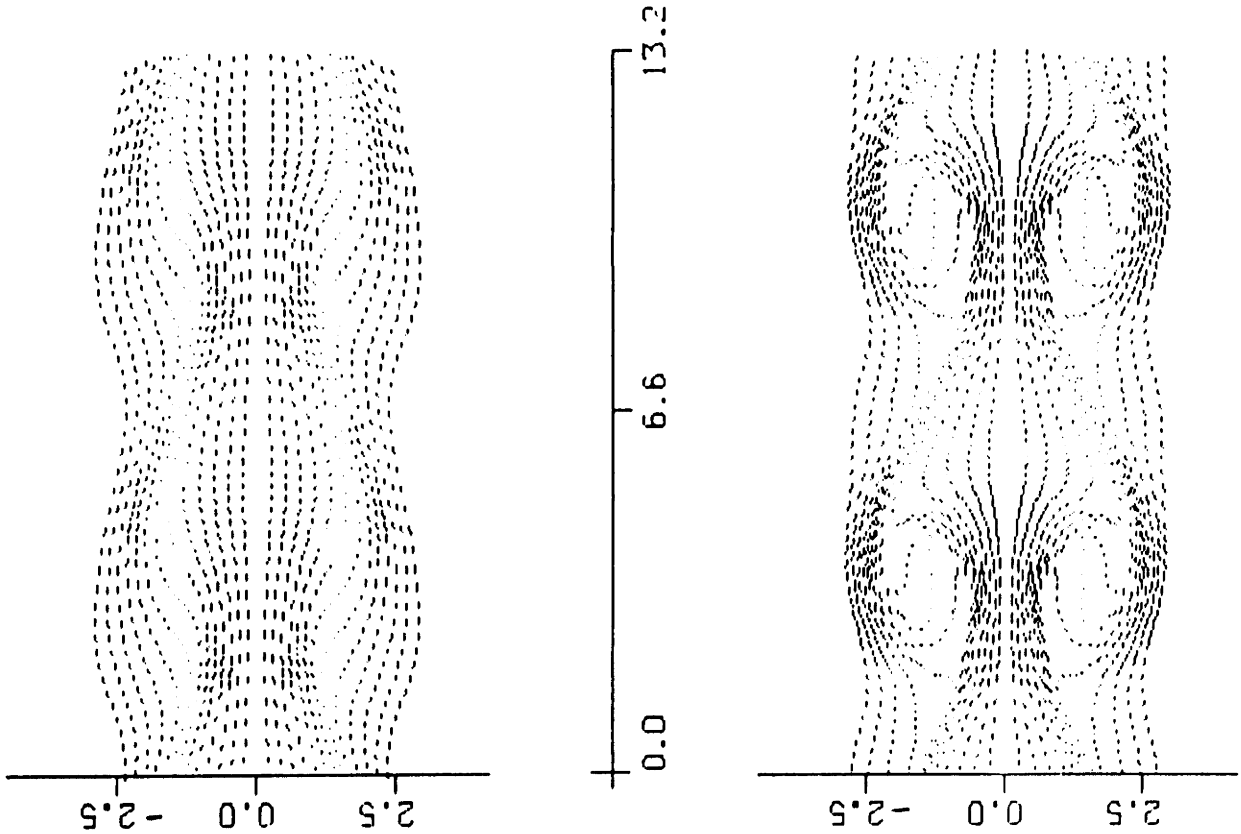

t = 2.5

t = 5.0

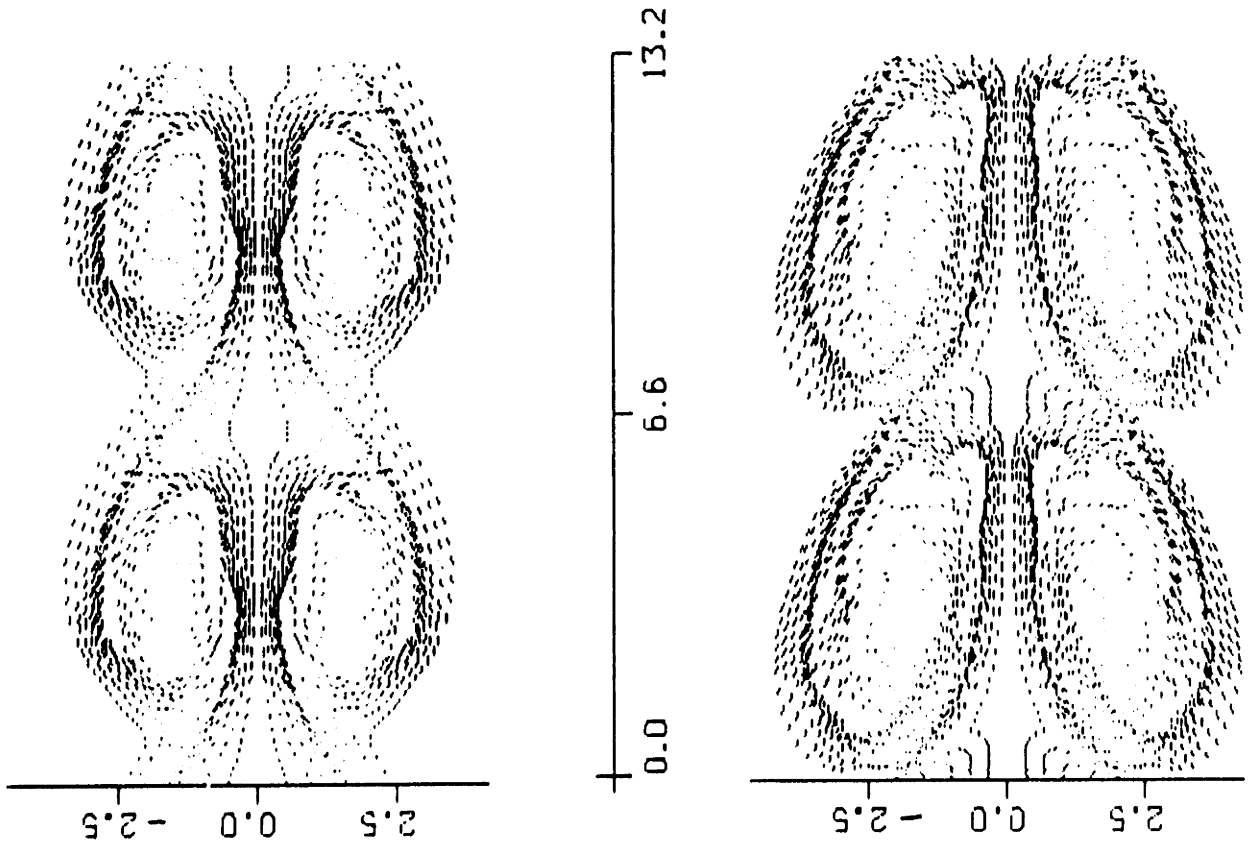

t = 7.5

t = 10.0

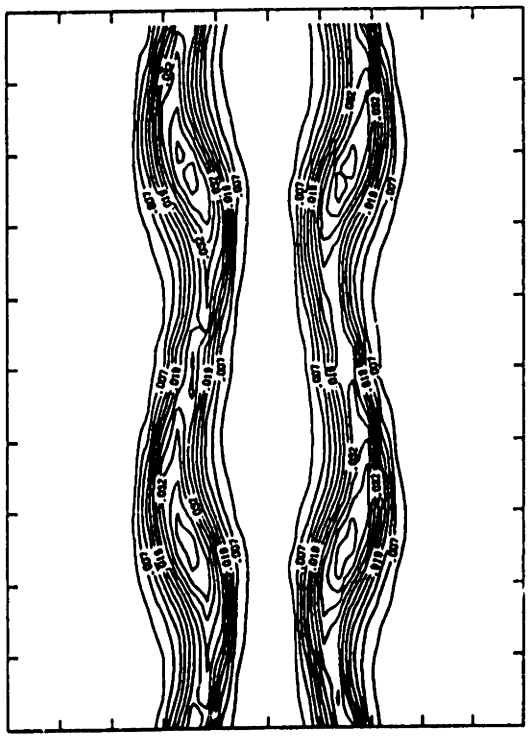

t = 2.5

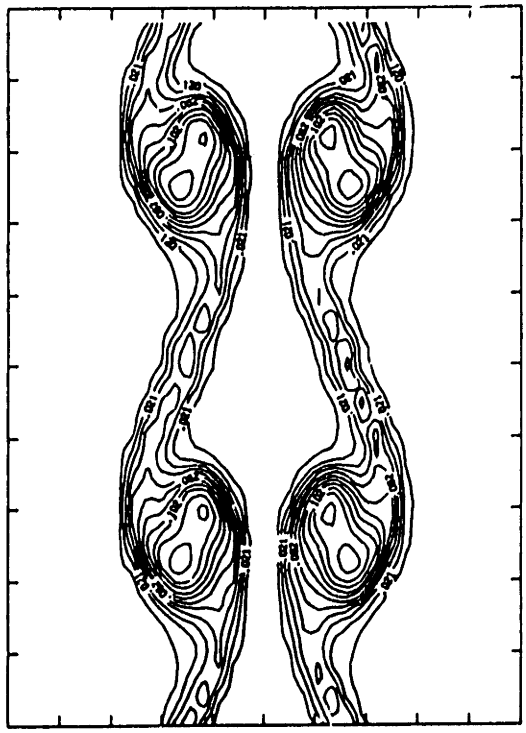

t = 5.0

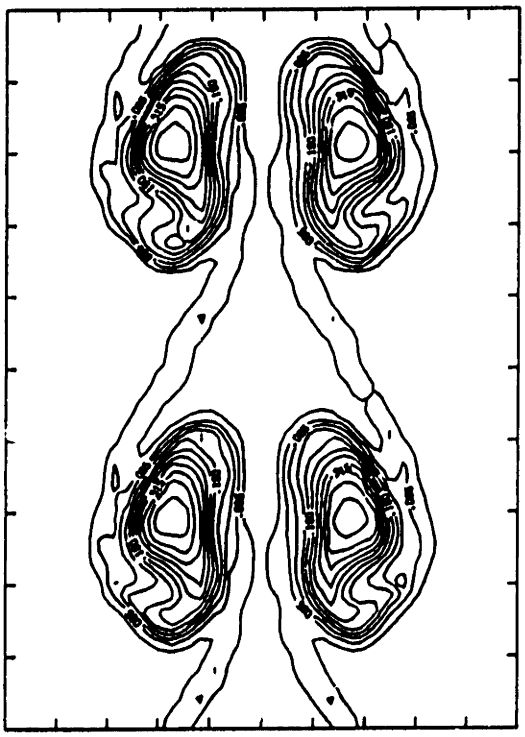

t = 7.5

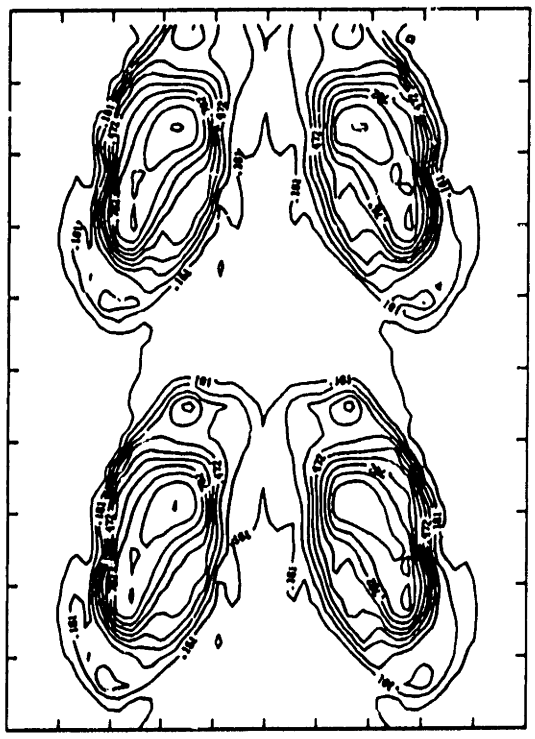

t = 10.0

Figure 150

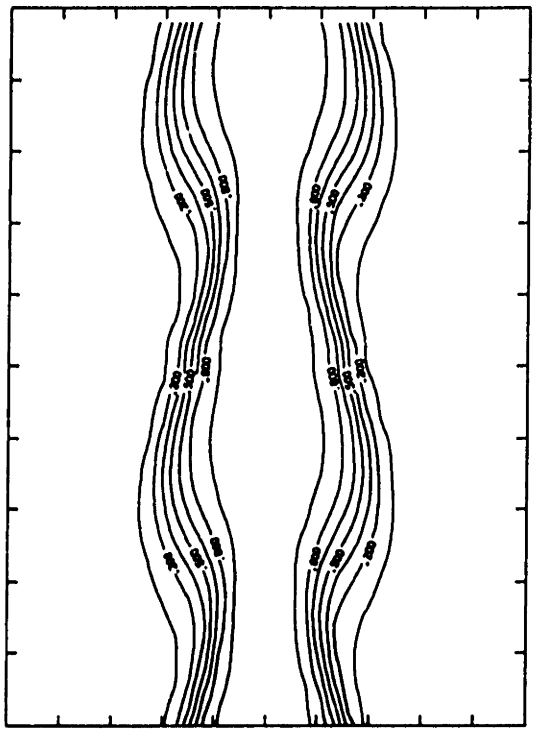

t = 2.5

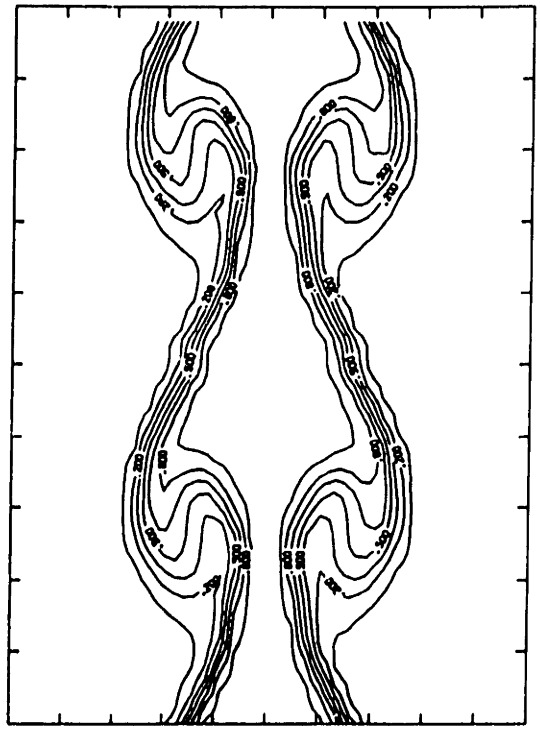

t = 5.0

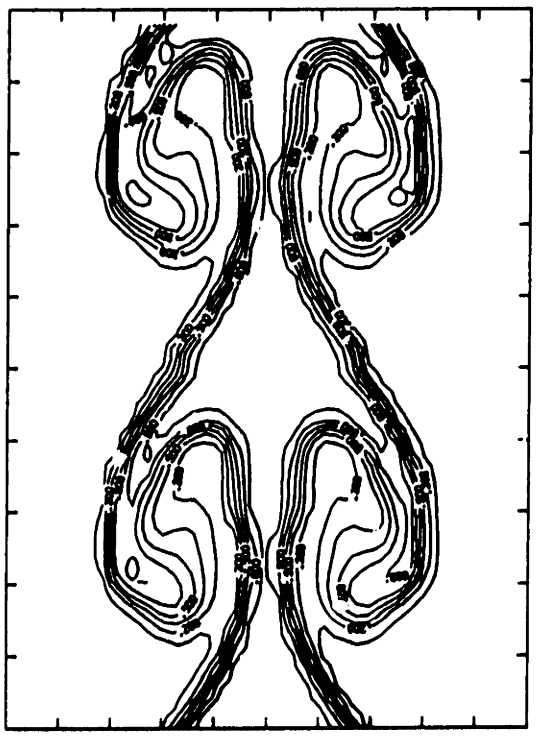

t = 7.5

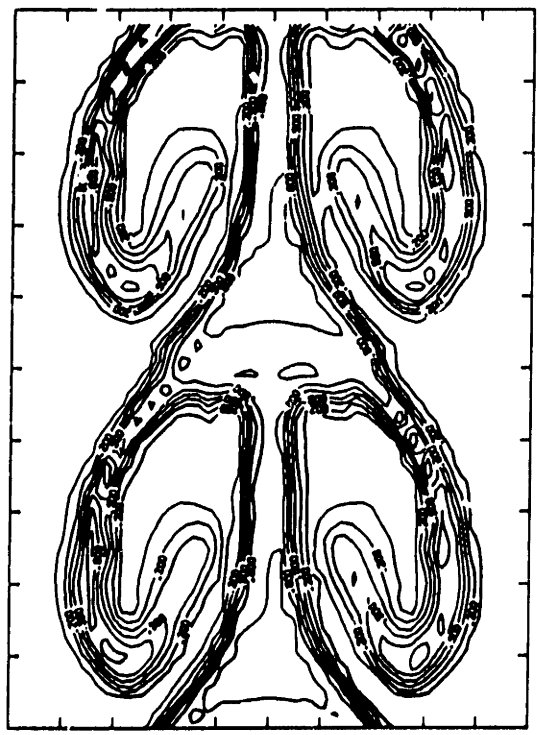

t = 10.0

Figure 151

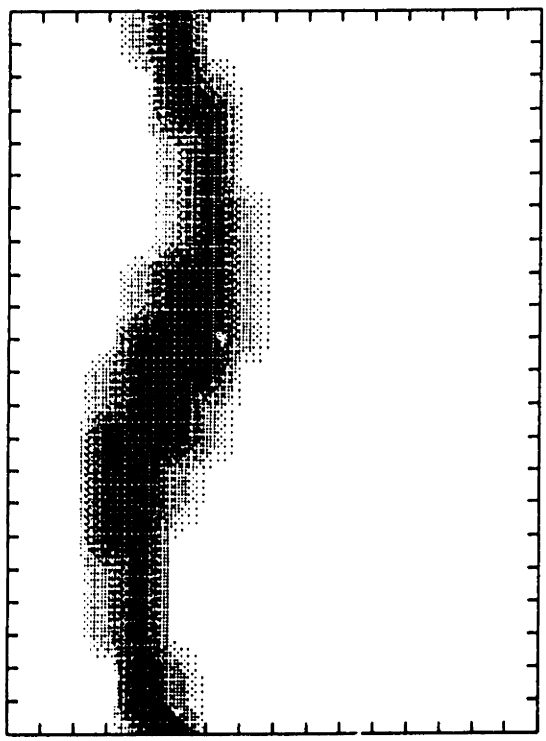

t = 2.5

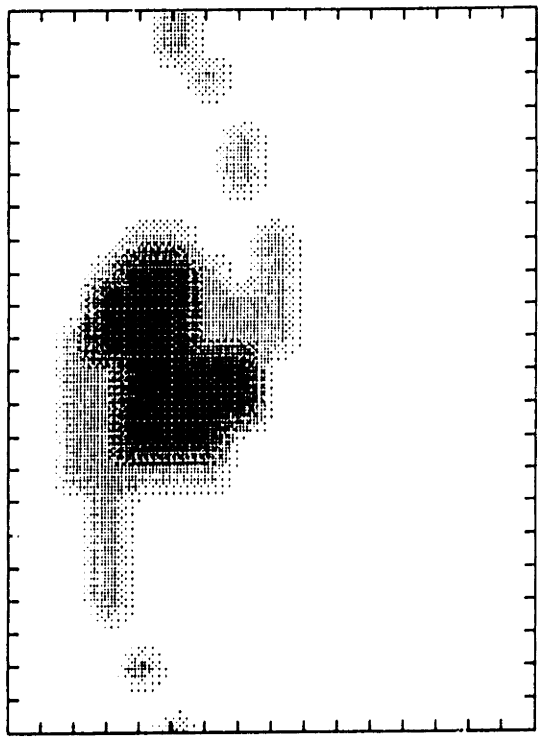

t = 5.0

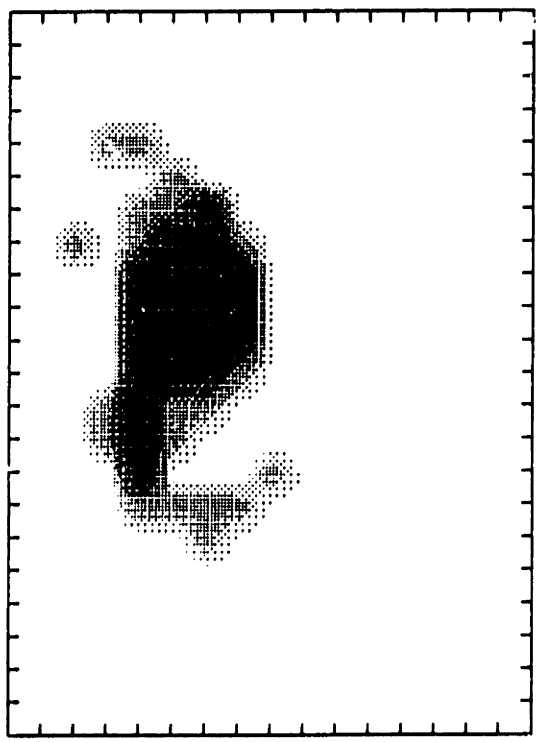

t = 7.5

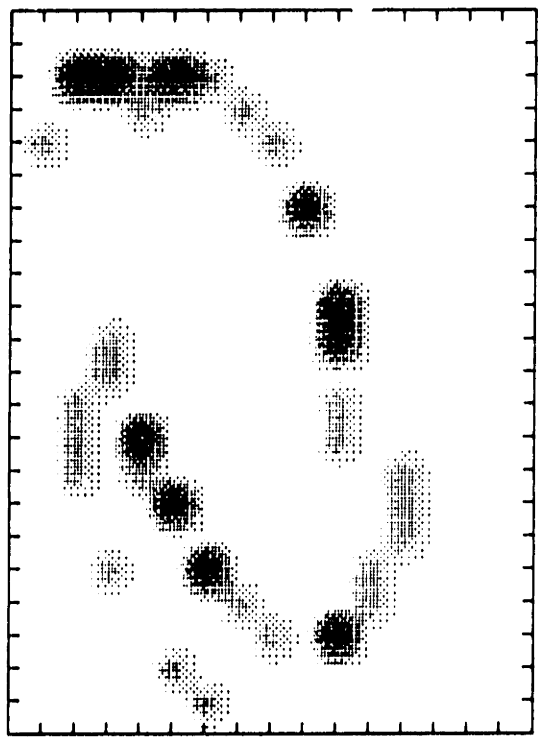

t = 10.0

Figure 152

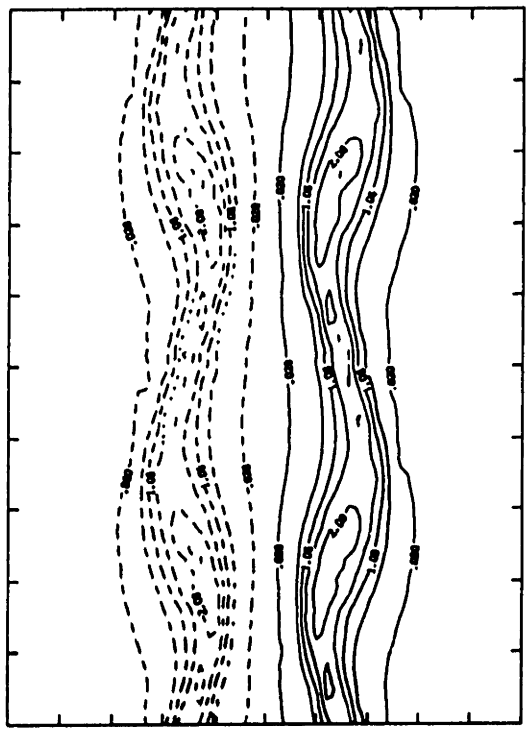

t = 2.5

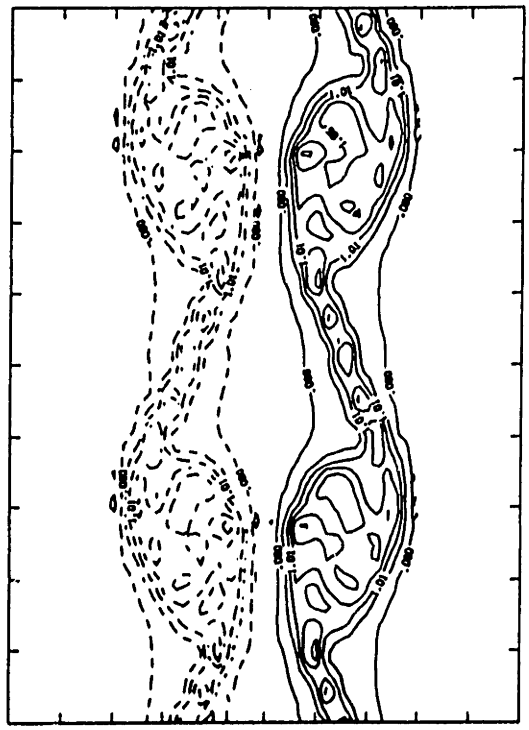

t = 5.0

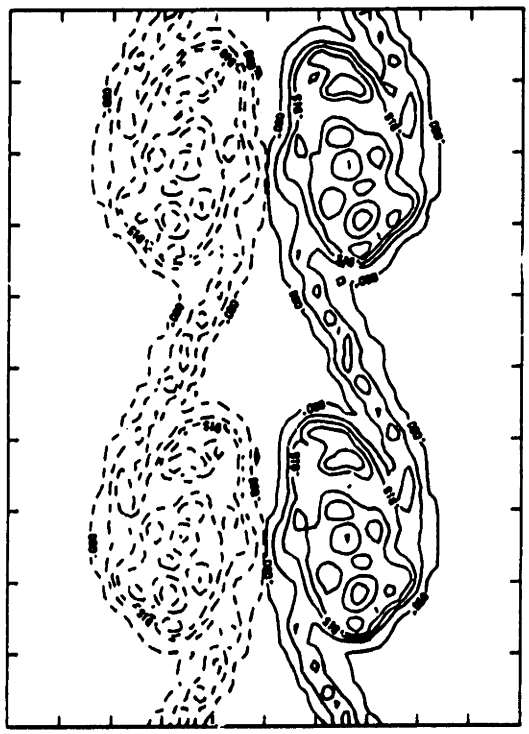

t = 7.5

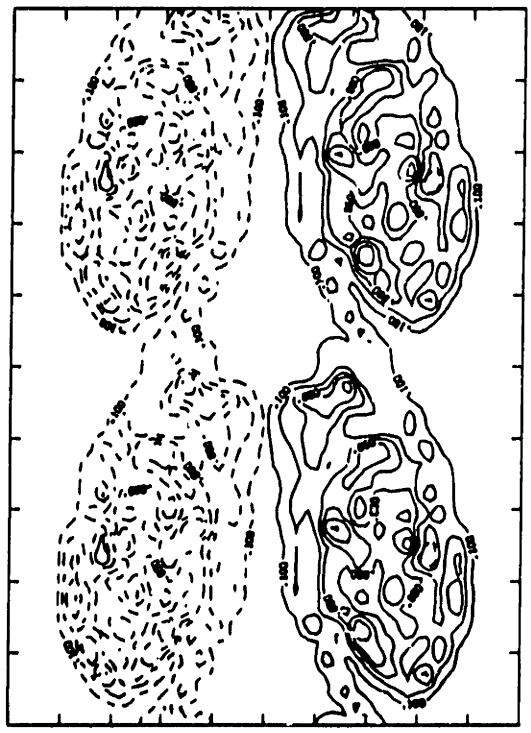

t = 10.0

Figure 153

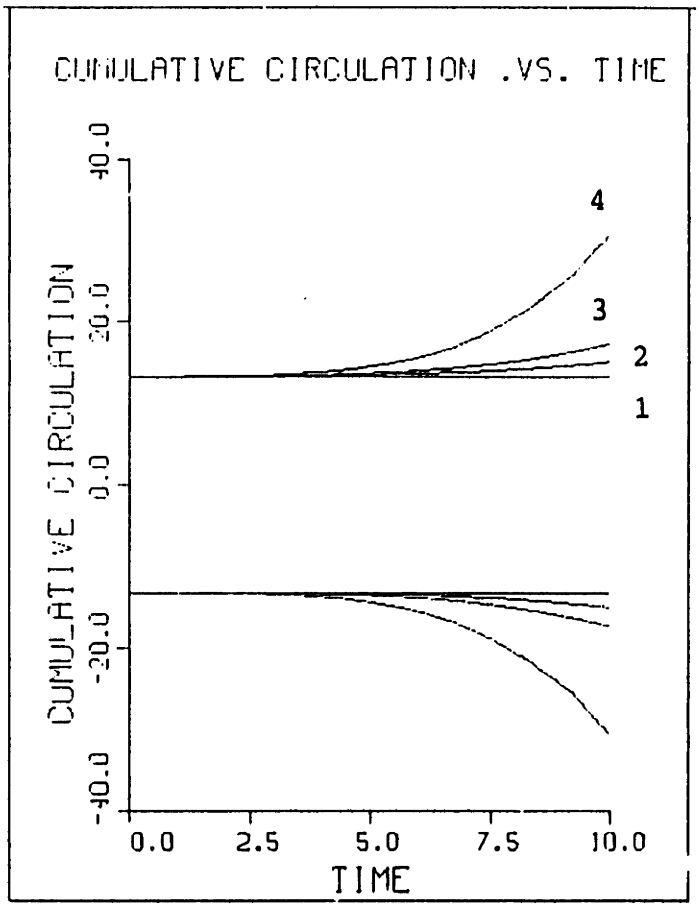

Figure 154

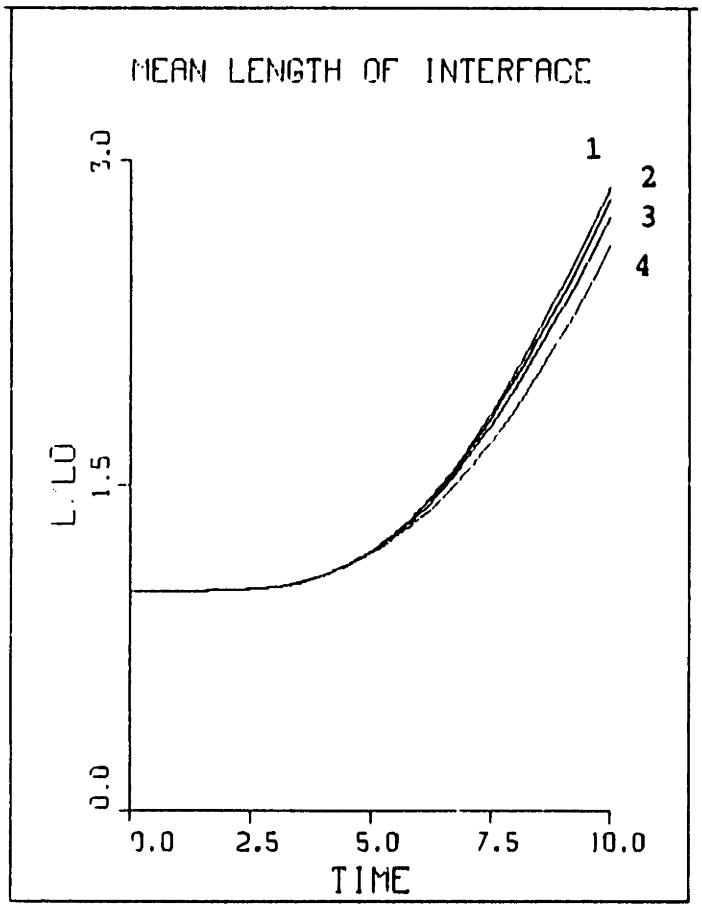

Figure 155

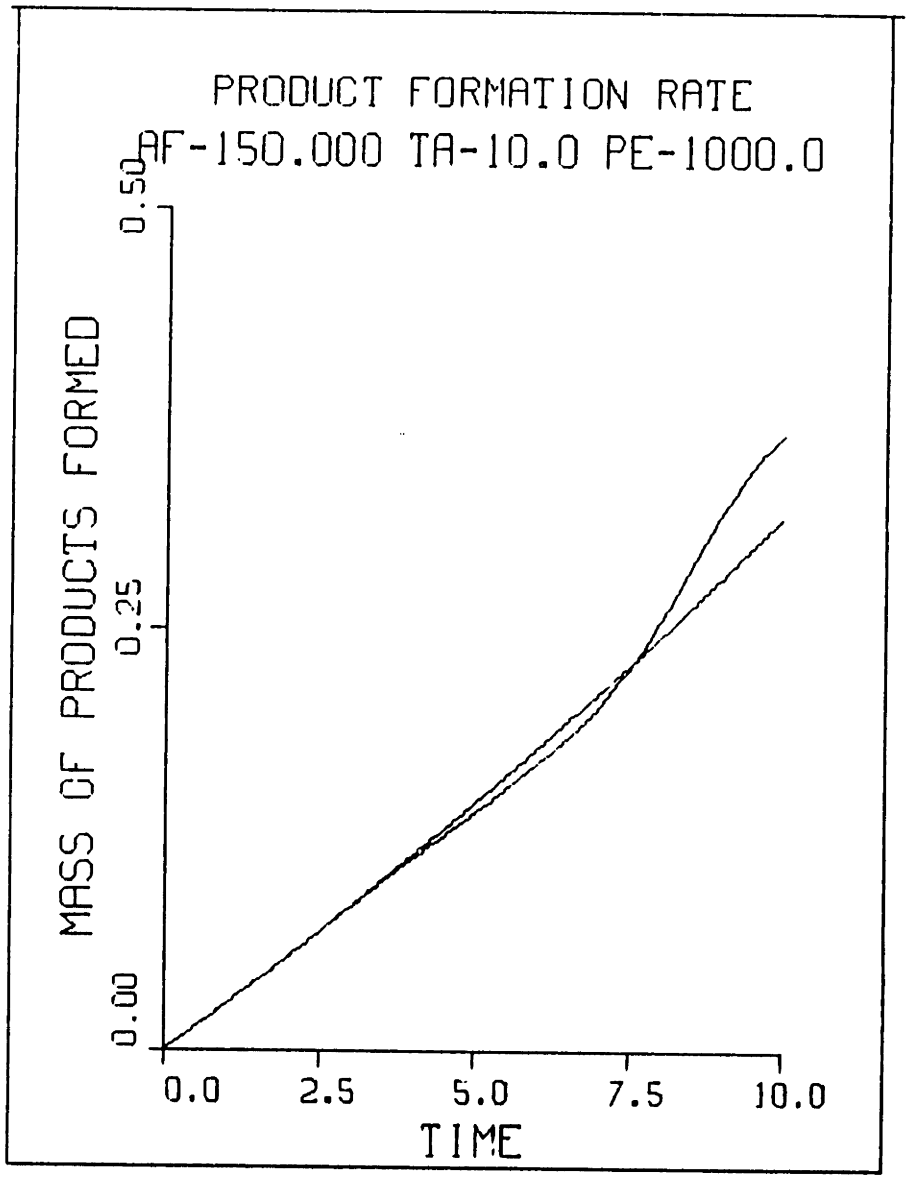
PRODUCT FORMATION RATE
AF-150.000 TA-10.0 PE-1000.0
MASS OF PRODUCTS FORMED
0.50
0.25
0.00
0.0
2.5
5.0
7.5
10.0
TIME

Figure 156

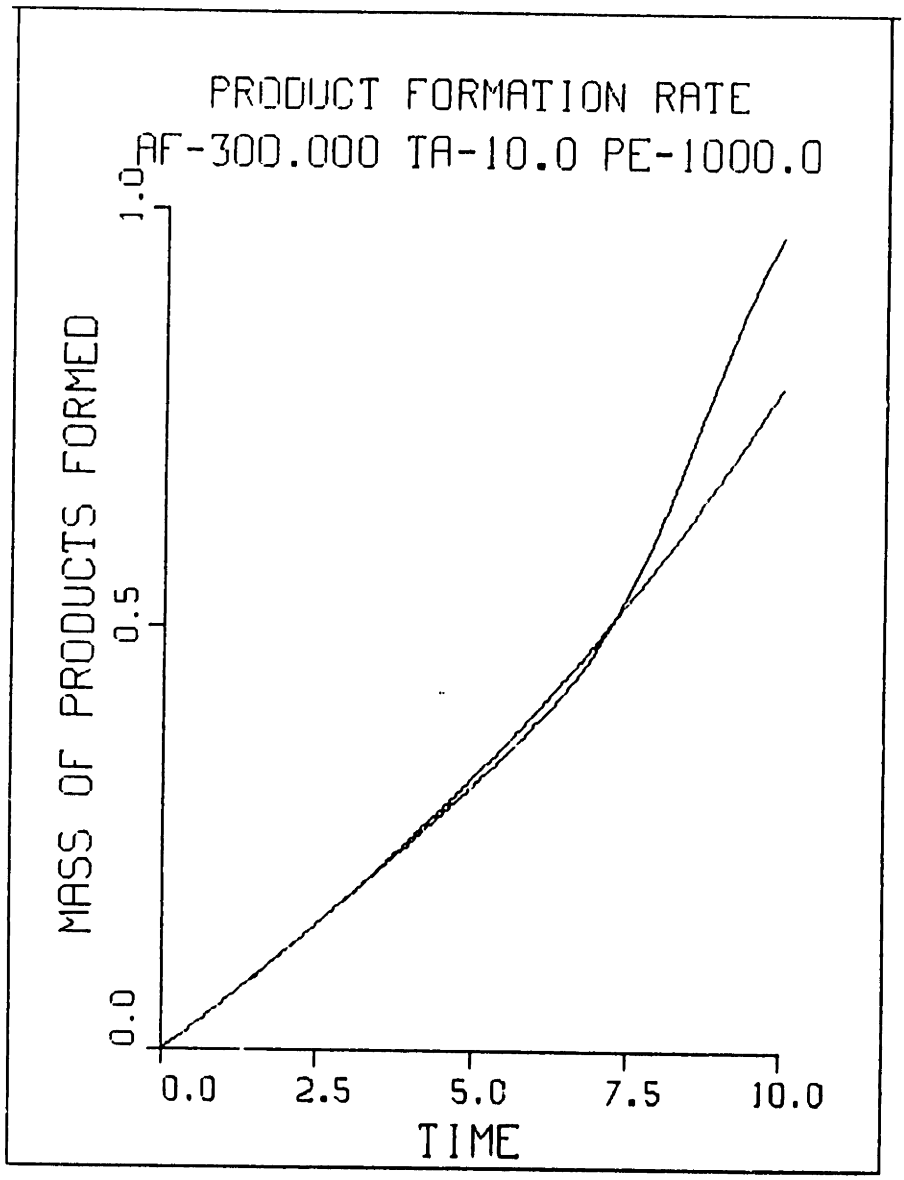
PRODUCT FORMATION RATE
AF-300.000 TA-10.0 PE-1000.0
MASS OF PRODUCTS FORMED
1.0
0.5
0.0
0.0
2.5
5.0
7.5
10.0
TIME

Figure 157

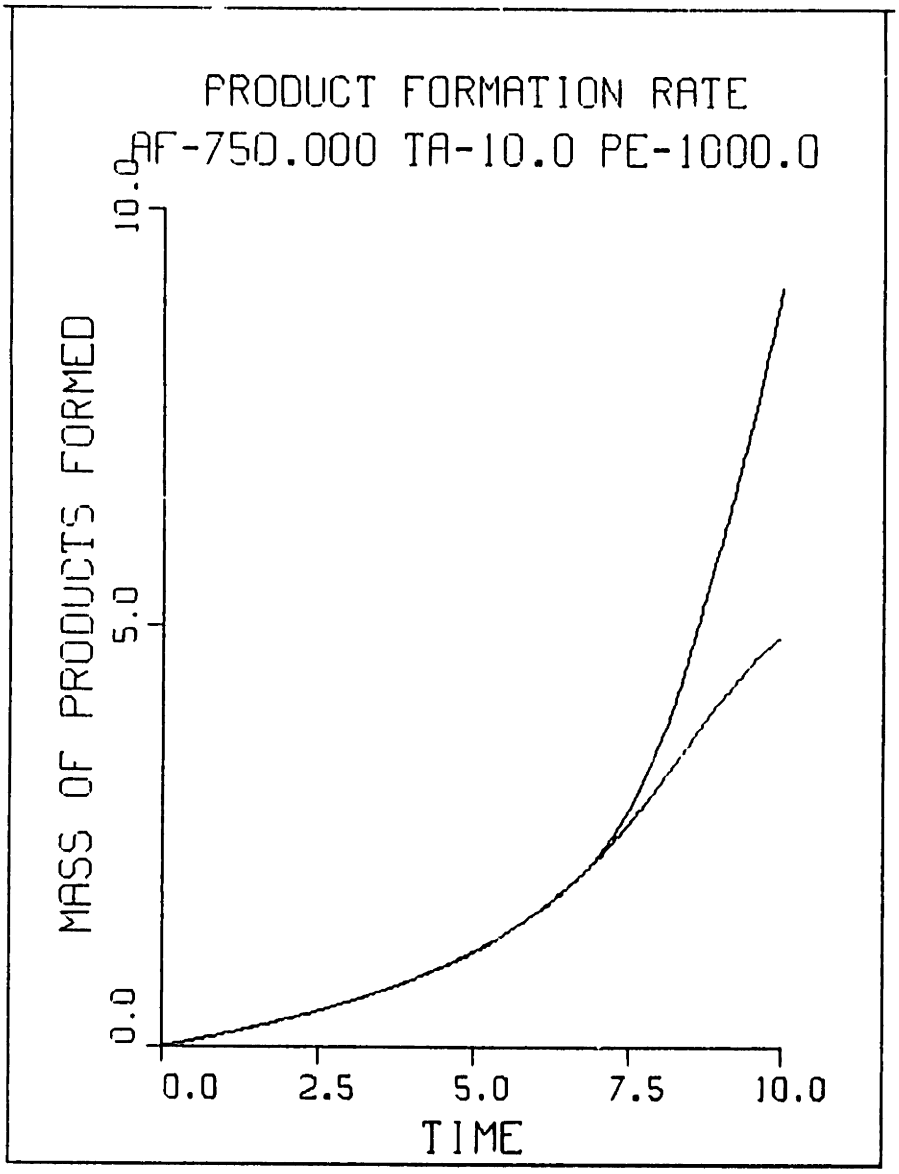
PRODUCT FORMATION RATE
AF-750.000 TA-10.0 PE-1000.0
MASS OF PRODUCTS FORMED
10.0
5.0
0.0
0.0
2.5
5.0
7.5
10.0
TIME

Figure 158

VIII. THE STUDY OF PREMIXED COMBUSTION IN A SHEAR LAYER

VIII. 1. INTRODUCTION

Premixed combustion is of great importance both from practical as well as fundamental considerations. From a practical standpoint, the understanding of premixed flames is crucial in order to improve burning efficiency in automotive and jet engines and to reduce pollutant formation. Fundamentally, the study of turbulent-combustion is a complex and challenging problem because of the inherent feedback between the flow and the reaction. The flow field affects the burning rate through the mechanism of flow stretch and curvature while the reaction in turn affects the flowfield through volumetric expansion and flame generated vorticity [48,49]. Moreover, experiments [50, 54] and simulations [51] have revealed that the nature and magnitude of these interactions are a function of the relative speed of the reaction with respect to the flow as defined by an appropriate Damkohler number. Other dimensionless parameters that govern this problem are the Peclet number, the Lewis number, the Activation Energy and the Enthalpy of Reaction. Thus the solution to this problem can be interpreted on a five dimensional space, one for each of the afore-mentioned non-dimensional groups.

VIII. 2. DESCRIPTION OF FLOW GEOMETRY

Fig. 159 shows the schematic for the reacting shear layer. The velocity field is similar to the one considered for the study of the density stratified shear layer. The initial vorticity is distributed in the form of a Gaussian and the velocity distribution is an error function. The initial

temperature profile is also an error function as shown in the figure. The bottom stream is the product stream and the top stream consists of reactants. The movement of the flame is in the upward direction, i.e., towards the reactants. Thus the flame that is considered here is a thick flame whose length scale, as estimated from the thickness of the temperature gradient profile, is of the same order as the scale of the flow. As the flame moves upwards, the flow (or the vorticity field) is allowed to become unstable due to the Kelvin-Helmholtz instability. This leads to the formation of a turbulent eddy producing a strong strain field. The effects of the strain field and curvature on the burning rate of the flame and the reverse effects of volumetric expansion and baroclinic vorticity on the flow are studied in detail. Previous investigations of the effect of strain on the premixed flame iniclude the stagnation point flow model [52,53] wherein a steady, planar strain is imposed on the flame. Although, a relation was established between the strain rate and the flame speed as a result of this work, these results cannot be directly extended to a turbulent flow field in which the strain rate is highly unsteady and curvature effects are important. The present model is closer to simulating these effects since the physics of the highly unsteady flow field is already built into the model. Computations are also done for a laminar flame (i.e., the flow field is stationary except for the flow generated due to expansion) in order to understand the effects of stretch on the reaction.

VIII. 3. GOVERNING EQUATIONS

The governing equations for the premixed shear layer are given below and in Table 1. The reaction is a one step, first order irreversible reaction in

which reactants go to products. The chemical souce term is of the Arrhenius form and is a function of the reactant concentration and the temperature.

$$\text{(PREMIXED FLAME)} \quad \text{Reactants} \xrightarrow{k = A \exp(-E/RT)} \text{Products} \tag{100}$$

$$\frac{dT}{dt} = \frac{1}{P_e} \nabla^2 T + A_f Q \dot{W} \tag{101}$$

$$\frac{dC_R}{dt} = \frac{1}{P_e L_e} \nabla^2 C_R - A_f \dot{W} \tag{102}$$

$$\frac{dC_P}{dt} = \frac{1}{P_e L_e} \nabla^2 C_P + A_f \dot{W} \tag{103}$$

$$\dot{W} = C_R \exp(-T_a/T) \tag{104}$$

The variables are non-dimensionalized by the characteristic values U_o for velocity , L_o for length, T_o for temperature and C_∞ for concentration. U_o is given by $\Delta U/2$ where ΔU is the velocity difference between the free streams and $L_o = \sqrt{2}\,\sigma$ where σ is the standard deviation of the initial Gaussian vorticity distribution. T_o and T_p are the temperatures of the reactant and the product streams respectively and C_∞ is the reactant concentration in the reactant stream. A_f is the pre-exponential factor and is given by $A_f = (A\,L_o)/U_o$. A is the constant in the Arrhenius rate expression. The non-dimensional activation energy is defined as $T_a = E/(R\,T_o)$ where E is the dimensional activation energy and R is the universal gas constant. The non-dimensional enthalpy of reaction is given by $Q = (T_p - T_o)/T_o$ and signifies the increase in temperature due to the complete burning of one mass unit of reactant.

VIII. 4. RESULTS OF NUMERICAL SIMULATIONS

The shear layer is perturbed sinusoidally at a wavelength $\lambda = 13.2\ L_o$. This is close to the most unstable mode for a non-reacting layer. However, in this case, the additional effect of heat release is present and this modifies the dynamics of the growth of the instability. The temperature ratio between the products and the reactants is 5. The non-dimensional activation energy is taken to be equal to 10.

(i) Case I : $A_f = 2.0,\ \varepsilon = 0.01\ \lambda$

The first case that is considered is that of the reacting shear layer that is initially perturbed at an amplitude equal to 0.01 λ. The Peclet number is 1000 and the Lewis number is unity. This case can therefore be compared to the non-reacting density stratified shear layer for $r_\rho = 5$. Fig. 160 shows the locations and velocities of the vortex/transport elements at t= 5.5, 11.0, 16.5 and 22.0 respectively. These correspond to the same time frames that were considered for the non-reacting layer. Comparing the two, it is immediately obvious that the the growth of the instability in the reacting shear layer is diminished. The layer remains more or less flat with some rollup in the center. The only extra dynamic effect in the physical model is the inclusion of the flow divergence term in the vorticity equation. The effect of volumetric expansion or flow dilatation due to combustion is to weaken the concentration of vorticity. This effect has been observed during experiments on reacting mixing layers wherein the volumetric expansion stabilizes the flow and leads to delayed growth and pairing [46]. Although

the vorticity in the field is reduced due to expansion, the area integral of the vorticity, i.e., the circulation, is conserved during this process. This is because the vorticity decreases by the same factor as the increase in the fluid area (or volume in a three dimensional sense) and hence the product, the circulation. is unchanged.

Fig. 161 shows the normalized temperature (or product concentration) contours at the corresponding times. Again, it is obvious from the contours that the degree of rollup is very small compared to non-reacting shear layer. The area of burning is more or less equal to that of the laminar flame, i.e., the effects of flow stretch are very small. Fig. 162 shows the corresponding vorticity contours at the same time frames. It is clear from the first time frame that the vorticity layer is much thicker than that of the non-reacting layer. This is a consequence of the volumetric expansion in the flow field. Also, for this thick layer, the imposed perturbation may no longer be the most unstable one. The growth rate of the layer, as inferred from the linear theory, is smaller for a layer that is thinner or thicker than the one correspnding to the most unstable mode. Therefore, the instability for the thicker layer grows at a slower rate. It is also observed that the amount of vorticity generation in the flow field is very small. This is because the layer undergoes very little distortion and the magnitude of the ($\nabla\rho \times \nabla p$) term is very small. Towards the late stages of growth, some amount of positive circulation is generated on the top side of the eddy as seen from the plots. Fig. 163 (a) shows the cumulative circulation in the domain as a function of time. The positive and the negative components are summed separately. Comparing the amount of circulation generated for a non-reacting density stratified shear layer for $r_\rho = 5$ and the reacting shear layer, it is clear that the inhibition of the rollup has reduced the amount of circulation

generated. Density stratification in the non-reacting shear layer leads to greater destabilization in the non-linear range, but with reaction, the generation effects are suppressed leading to further stabilization of the flow. Fig. 163 (b) shows the mean length of the material layers as a function of time. It is observed that the final length of the interface is about 1.6 times the initial length. This value is smaller than what was obtained for the non-reacting shear layer. Thus the elongation of the flame or the vorticity layers is suppressed due to the expansion field.

Therefore, it is obvious from the above simulation that the effect of heat release is to stabilize the shear layer instability. This is highly undesirable since the mixing efficiency is greatly reduced which in turn leads to a lower burning rate. One way of avoiding this problem is to perturb this layer at a higher amplitude. This causes the shear layer to grow and rollup at a faster rate. The destabilization of the flow field leads to improved mixing and a larger burning rate. The effect of the instability on the burning rate can be estimated by comparing the total mass of products formed in a turbulent flame to that in a laminar flame. In case of the laminar flame, the shear layer is not allowed to grow, i.e., the flame remains flat and planar and propagates into the reactants at the laminar flame speed. The laminar flame problem is an eigenvalue problem with the flame speed being the eigenvalue that satisfies the differential equation and the boundary conditions. The laminar flame speed is a function of the Damkohler number, the Peclet number, the Lewis number, the enthalpy of reaction and the activation energy. Therefore, once the above parameters are specified, there is one and only one flame speed that satisfies all the constraints. In the present case, an initial temperature and concentration distribution are specified along with all the dimensionless groups. These

distributions may not be the steady state distributions of the laminar flame. As the integration in time proceeds, the distributions converge to that of the steady state laminar flame. Once this condition is reached, the problem essentially reduces to one of steady state in a frame of reference moving with the flame. Therefore, depending on the initial conditions, the flame may not initially propagate at the laminar flame speed. However, the speed of the flame converges to the eigenvalue solution in time. This is very similar to starting the problem with an arbitrary solution and iterating to get the correct solution.

The fact that the laminar flame solution is not known a priori may cause some complications in the solution of the turbulent flame problem. The effect of stretch is to change the local speed of propagation of the flame. Thus, if the initial conditions are arbitrarily specified, two kinds of transient behavior may be observed; one due to the effects of flow stretch and another due to the laminar flame converging to its eigenvalue solution. The interactions between these two transient modes may further complicate the physics of the problem. Since this study is an effort to understand the effect of the flow field on the burning rate, it would be desirable to eliminate the transient due to the convergence of the laminar flame speed. This can be done by starting with the laminar flame profile (as obtained from the solution of the laminar flame problem) as the initial condition to the turbulent flame problem. This approach is adopted in the next few cases to be studied.

It is found that the initial distributions of temperature and concentration correspond to the solution of the laminar flame problem for the parameters A_f =0.125, L_e=1.0, P_e =10000.0, Q= 4.0 and T_a = 10.0 . In order to make appropriate comparisons, the same laminar flame is used for all the

cases to be studied. The relative speed of the reaction with respect to the flow can be varied either by changing the speed of the flow or by changing the speed of the reaction. The speed of the reaction is controlled by A_f and since the source term is highly non-linear, the reaction rate is not directly proportional to A_f. The speed of the flow can be changed by scaling the magnitude of circulation in the flow field. Therefore, if the circulation is scaled down by a factor of five, the flow develops five times as slow and vice versa. Thus, in order to make appropriate comparisons, the effective Damkohler number of the problem is changed by merely changing the speed of the flow. C_f is the factor that indicates the ratio of total circulation in the flow field to that in Case I.

(ii) Case II : $A_f = 0.125$, $C_f = 0.25$

The magnitude of the toatl circulation in the flow field is four times less than in Case I. Therefore, the speed of the flow is reduced by a factor of four. In order to avoid the suppression of the instability due to the volumetric expansion, the shear layer is perturbed at a higher amplitude of $\epsilon = 0.05\ \lambda$ so that the instability grows quickly. Fig. 164 shows the locations and velocities of the vortex/transport elements at t= 16.87, 33.75, 50.62 and 68.75 respectively. The instability develops rapidly and the interface rolls up to form the large scale structure. The characteristic features of the growth of the instability for density stratified shear layers are observed here too. The structure propagates at a finite convection velocity in the direction of the heavier reactant stream. Also, the eddy entrains more of the low density products by volume. At the late stages of growth, the appearance of concentrated small scale structures is observed. Fig. 165 shows

the product concentration contours for the corresponding time frames. Since the Damkohler number is realtively small in this case, the amount of product formation is also small. The product concentration contours can also be used to identify the flame area or the region over which combustion is taking place. It is observed that at the initial stages, the flame is more or less flat and planar. As the strain field develops, the flame becomes thinner in the braid region and thicker in the core of the eddy. At late times, most of the burning takes place in the core of the structure. Fig. 166 shows the shaded contours for the magnitude of the source term W over the flow field. The darkest shade indicates a value between 75% and 100% of the maximum value of W and the lighter shade indicates a value between 50% and 75% of the maximum value of W. It is observed that the burning area becomes very thin in the braids where the strain rate is positive. However, the combination of entrainment and diffusion within the core increases the net burning area and at late times it is observed that the burning is taking place in a distributed zone within the structure.

Fig. 167 shows the vorticity contours at the corresponding times. The initial vorticity in the flow field is negative and as time proceeds, positive vorticity is generated due to baroclinic effects. Since the Damkohler number is small, the effects of volumetric expansion do not appear to be significant. The total circulation in the flow field is a conserved quantity. Therefore the generation of positive circulation is offset by an equal amount of negative circulation generated elsewhere in the flow field. Fig. 176 (a) shows the amounts of positive and negative circulation generated in the domain as a function of time. The generation effects increase with the growth of the instability. Figs. 177 and 178 show the mean material length and the flame length respectively as a function of time. The flame length is

calculated as the length of the interface corresponding to the maximum reaction zone, i.e., the contour at which the Arrhenius term is maximum. Curve 1 in Figs. 177 and 178 represent the results of this case. It is observed that the mean material length increases by a factor of 3.9 with respect to the initial length. It is observed that the flame length also increases by a similar factor. In fact the final slopes of material and flame curves are almost equal suggesting that the flame is experiencing almost the same strain and elongation as the material layers. Thus, the instability is very effective in increasing the burning area and hence the product formation rate. This was already observed in Fig. 166 where the final burning area is much larger than the initial area.

Curve 2 of Fig. 179 shows the mass of products formed with time. Curve 1 is the product formation for the corresponding laminar flame. It is observed that the initial product formation in the turbulent flame is very similar to that in a laminar flame. As the flow becomes unstable, the strain field elongates the flame thereby increasing the burning area and hence the product formation rate. At the final time, it is observed that the turbulent flame has produced twice the amount of products compared to the laminar flame. Curve 2 of Fig. 180 shows the slope of the product formation curve as a function of time. Curve 1 is the slope of the laminar flame. It is observed that the slope of the turbulent flame decreases below that of the laminar flame in the initial stages. During this stage most of the flame is experiencing positive strain and the rate of product formation is reduced due to thinning of the flame. At late stages, however, the slope of the turbulent product curve is about four times greater than that of the laminar product curve. This correlates directly with the increase in burning area observed in Fig. 166.

(iii) Case III : $A_f = 0.125$, $C_f = 0.125$

The speed of the flow is reduced by a factor of two compared to Case II, i.e., the effective Damkohler number is increased by a factor of two. Fig. 168 shows the locations and velocities of the vortex/transport elements at t= 33.75, 67.5, 101.25 and 137.5 respectively. These time frames correspond to those in Case II with regard to the development of the flow field. The flow becomes unstable with time and leads to the development of the coherent structure. At late stages of the flow, more number of small scale eddies appear on the edges of the large structure. Fig. 169 shows the product concentration contours at the corresponding time frames. The effect of the increased Damkohler number is immediately obvious. The contours in the central region of the structure are very sparse indicating that the core consists essentially of the products formed due to reaction. Again, the flame is thinner in the braid region and thicker in the core of the eddy. The flame appears to exist on the edges of the structure and the burning area at late times is much larger compared to the initial flame area. Fig. 170 shows the contours for the source term W. The characteristic features observed here are similar to what was observed in case II. However, the chemistry being faster than the flow, the turbulence is not able to stretch and entrain the flame as much and is thus less effective in increasing the total burning area inside the eddy. Although the burning at the final stages takes place in a distributed zone, the amount of burning area generated is less compared to that in case II.

Fig. 171 shows the vorticity contours for this case. The development of the vorticity field is very similar to what was observed before. Positive

vorticity is generated on the top side of the structure and an equivalent amount of negative vorticity is generated in the center and on the under side of the eddy. Fig. 176 (b) shows the cumulative circulation in the domain as a function of time. The positive and the negative components are shown separately. The circulation curves are very similar to those of Case II. Curve 2 in Figs. 177 and 178 show the elongation of the material layers and the flame as a function of time. From Fig. 177, it is observed that the final length of 3.78 for Case III is slightly smaller than that for Case II. If there were no feedback between the reaction and the flow, the final lengths would be exactly the same. However, in this case, due to the increased Damkohler number and the subsequent volumetric expansion, the flow field experiences a small degree of stabilization. Hence the final material length for Case III is smaller than that of Case II. From Curve 2 of Fig. 178, it is seen that the elongation of the flame does not follow the elongation of the material layers. At any given time, the slope of the material length curve is greater than that of the flame length curve. This indicates that the strain field is less effective in stretching the flame as compared to Case II. At higher Damkohler numbess, the flame is stronger and is able to resist the effects of the flow field to a greater degree.

Curve 3 of Fig. 179 shows the product formation curve for Case III. The initial product formation is similar to the laminar flame. At late times, the effects of the strainfield become apparent as the turbulent product formation increases above that of the laminar flame. At the final time, the turbulent flame has produced about 1.6 times the amount of products as the laminar flame. This factor is smaller than what was obtained for Case II, indicating that the turbulence in the flow was less effective in increasing the amount of products. Curve 3 of Fig. 180 shows the slope of the product formation

curve as a function of time. The initial decrease below the laminar burning rate due to strain is again observed; however, the decrease in this case is smaller than in case II. This may be due to the flame being more resistant to strain as a result of the increased Damkohler number. Although the rate of burning increases in the later stages, it is observed that the increase is smaller than what was seen for case II. This correlates well with the earlier observation that the turbulence is not successful in generating as much of the burning area as was done for the lower Damkohler number.

(iv) Case IV : $A_f = 0.125$, $C_f = 0.0625$

The speed of the flow is further reduced by a factor of two in this case, i.e., the effective Damkohler number is again increased by a factor of two. Fig. 172 shows the locations and velocities of the vortex/transport elements at t= 67.5, 135.0, 202.5 and 275.0 respectively. The effects of increased reaction and volumetric expansion are more obvious in this case. Close inspection of the development of the instability reveals that the flow field grows at a slower rate and at late times, the center of the structure looks more diffuse indicating that chemical reaction has occurred in these zones. The structure has an expanded appearance due to the local dilatation of the flow field as a result of reaction. Fig. 173 shows the product concentration contours for the corresponding time frames. It is immediately obvious that more amount of chemical reaction is taking place inside the eddies. The center of the structure looks very sparse since it is comprised essentially of products. The flame exists on the edges of the structure and there is very little burning at the core of the eddy. Fig. 174 shows the shaded contours for the source term W. It is observed that the burning area at the late

stages exists on the circumference of the eddy. Unlike the distributed burning zone that was observed for the lower Damkohler numbers, the flame zone appears to be in the form of a reaction sheet. Although, the burning area appears to have increased compared to the initial flame area, it is observed that this increase is smaller for Case IV as compared to Cases II and III, i.e., the turbulence is not able to generate more burning area due to the flame being much faster than the flow.

Fig. 175 shows the vorticity contours for this case. It is observed that the vorticity in the center of the structure is very sparse. This is due to the effect of volumetric expansion which tends to weaken the local vorticity. Fig. 176 (c) shows the generation of circulation with time. The circulation generation is very similar to what was observed for cases II and III.

Curve 3 in Figs. 177 and 178 show the mean material length and the flame length as a function of time.. It is observed that the final material length of 3.28 in this case is less than those obtained for cases II and III. The stronger volumetric expansion in this case causes the flow field to develop at a slower rate. Curve 3 of Fig. 178 shows that the slope of the flame length curve is smaller than the slope of the material length curve at any given time. This indicates that the flame itself is experiencing less elongation than the material layers, i.e., the flow field is not very effective in stretching the flame.

Curve 4 of Fig. 179 shows the product formation with time for Case IV. The initial mass of products formed by the turbulent flame is slightly less than that of the laminar flame. The developing strain field thins the flame in regions of positive strain thus reducing the flame propagation speed in these zones. Although the flame speed increases above the laminar flame value in regions of negative strain, this increase does not completely counteract

the decrease in flame speed due to positive strain. The reason for this behavior is the highly unsteady nature of the flow-combustion interactions and the highly non-linear source term. However, at late times, the turbulent product formation increases above that of the laminar flame. It is to be observed that the amount of products formed at the final time is only about 1.23 times that of the laminar flame. Also, the final slopes of the two curves are almost equal. Curve 4 of Fig. 180 shows the rate of product formation as a function of time. It is observed that the initial decrease due to strain is smaller than what was observed for the earlier cases. Thus, at this high value for the Damkohler number, the flame is very resistant to the strain field. Although, the slope of product formation does increase, this increase is much smaller as compared to the lower Damkohler number cases. Thus the turbulence in the flow is unable to increase the burning area of the flame due to the flow being much slower than the chemistry. It is quite obvious that the product formation for higher Damkohler numbers can be approximated very well by the laminar flame.

VIII. 5. CONCLUSIONS

The simulation of premixed combustion in a shear layer has revealed some rather interesting outcomes of turbulence-combustion interactions. First and foremost, it is observed that the growth of the instability is completely damped for low amplitudes of perturbation. The reason for this phenomenon is the local dilatation of the flow which weakens the local vorticity concentration and inhibits the roll up of the shear layer. The amplitude of perturbation had to be increased to a higher value in order for the flow field to become unstable. Secondly, it is observed that the effect of the

growth of the instability is to increase the product formation in the shear layer relative to the planar laminar flame. The precise mechanism by which flow stretch increases product formation is discussed below.

A flat planar flame of length L and thickness δ is considered. For simplicity, a constant strain rate 'k' in the horizontal direction is imposed on the flame. Therefore, the length of the flame increases as a function of time due to the longitudinal strain. Since the strain rate is constant, the expression for L is obtained from:

$$\frac{1}{L}\frac{dL}{dt} = k \tag{105}$$

which implies

$$L = L_o \exp(kt) \tag{106}$$

where L_o is the initial length.

Assuming that the thickness of the flame decreases as the length increases, i.e., $L\delta \sim$ constant, the above expression can be written as :

$$\delta \sim \delta_o \exp(-kt) \tag{107}$$

where δ_o is the initial thickness of the flame. Therefore, the thickness of the flame decreases exponentially with time. However, at some value of δ, say δ_d, the effect of diffusion becomes dominant and prevents the decrease of the flame thickness below this value. Therefore, the flame thickness remains constant at δ_d while the length L is increasing exponentially according to Eqn. (). Thus, the total burning area ($=L\delta_d$) also increases exponentially with time causing an increasing in the product formation rate. Therefore, the effect of flow stretch in the presence of diffusion leads to increased burning rates. However, in a turbulent flow field, the strain rate at any

point is highly unsteady and the above arguments may not hold precisely. But the basic mechanism by which strain increases the burning rate is still the same.

A third feature of turbulence-combustion interaction that is observed in the simulations is that the flow field is very effective in increasing product formation above that of the laminar flame at low Damkohler numbers. This is not the case at higher values of the Damkohler number. This is because, at high Damkohler numbers, the flame is more resistant to the strain field and the flow is not able to strain the flame to a great degree. Hence the observed increase in product formation above that of the laminar flame is very small. As the Damkohler number goes to infinity, the turbulent product formation curve converges to the laminar flame curve, i.e., the flame is so fast that it hardly feels the perturbations in the flow field.

In order to separate the effects of baroclinicity and the heat release, simulations were conducted for case III, one without heat release and one without baroclinicity. The degree of instability in each case was measured by calculating the mean material length as a function of time. The results are shown in Fig. 181. Curve 1 stands for the non-reacting uniform density shear layer, curve 2 represents the case with baroclinicity but without volumetric expansion, curve 3 represents the case with heat release but without baroclinicity and curve 4 are the results reproduced for case III (with both baroclinicity and heat release). It is interesting to note that for the premixed shear layer, baroclinicity by itself is highly destabilizing. Heat release or volumetric expansion results in the stabilization of the shear layer due to the decrease in local vorticity.

FIGURE CAPTIONS

Fig. 159. The schematic for premixed combustion in a shear layer.

Fig. 160. The locations and velocities of the vortex/transport elements at t= 5.5, 11.0, 16.5 and 22.0 respectively for Case I.

Fig. 161. The product concentration contours for Case I at t= 5.5, 11.0, 16.5 and 22.0 respectively.

Fig. 162. The vorticity contours for Case I at t= 5.5, 11.0, 16.5 and 22.0 respectively. The continuous curves represent negative vorticity and the dashed contours signify positive vorticity.

Fig. 163. (a) Cumulative circulation versus time for Case I. The positive and negative components are shown separately. (b) The mean material length as a function of time.

Fig. 164. The locations and velocities of the vortex/transport elements at t= 16.87, 33.75, 50.62 and 68.75 respectively for Case II.

Fig. 165. The product concentration contours for Case II at t= 16.87, 33.75, 50.62 and 68.75 respectively.

Fig. 166. The source term contours for Case II at t= 16.87, 33.75, 50.62 and 68.75 respectively.

Fig. 167. The vorticity contours for Case II at t= 16.87, 33.75, 50.62 and 68.75 respectively. The continuous curves represent negative vorticity and the dashed contours signify positive vorticity.

Fig. 168. The locations and velocities of the vortex/transport elements at t= 33.75, 67.5, 101.25 and 137.5 respectively for Case III.

Fig. 169. The product concentration contours for Case III at t= 33.75, 67.5, 101.25 and 137.5 respectively.

Fig. 170. The source term contours for Case III at t= 33.75, 67.5, 101.25 and 137.5 respectively.

Fig. 171. The vorticity contours for Case III at t= 33.75, 67.5, 101.25 and 137.5 respectively. The continuous curves represent negative vorticity and the dashed contours signify positive vorticity.

Fig. 172. The locations and velocities of the vortex/transport elements at t= 67.5, 135.0, 202.5 and 275.0 respectively for Case IV.

Fig. 173. The product concentration contours for Case IV at t= 67.5, 135.0, 202.5 and 275.0 respectively.

Fig. 174. The source term contours for Case IV at t= 67.5, 135.0, 202.5 and 275.0 respectively.

Fig. 175. The vorticity contours for Case IV at t= 67.5, 135.0, 202.5 and 275.0 respectively. The continuous curves represent negative vorticity and the dashed contours signify positive vorticity.

Fig. 176. Cumulative circulation as a function of time for (a) Case II, (b) Case III and (c) Case IV. The positive and negative components are shown separately.

Fig. 177. The mean material length as a function of time. Curves 1,2 and 3 represent cases II, III and IV respectively.

Fig. 178. The flame length as a function of time . Curves 1, 2 and 3 represent cases II, III and IV respectively.

Fig. 179. The mass of products formed as a function of time. Curve 1 represents the laminar flame. Curves 2, 3 and 4 represent cases II, III and IV respectively.

Fig. 180. The rate of product formation as a function of time. Curve 1 represents the laminar flame. Curves 2, 3 and 4 represent cases II, III and IV respectively.

Fig. 181. The mean material length versus time. Curve 1 represents the non-reacting uniform density shear layer, curve 2 represents the case with baroclinicity but without heat release, curve 3 represents the case with heat release but without baroclinicity and curve 4 is reproduced from the results of case III.

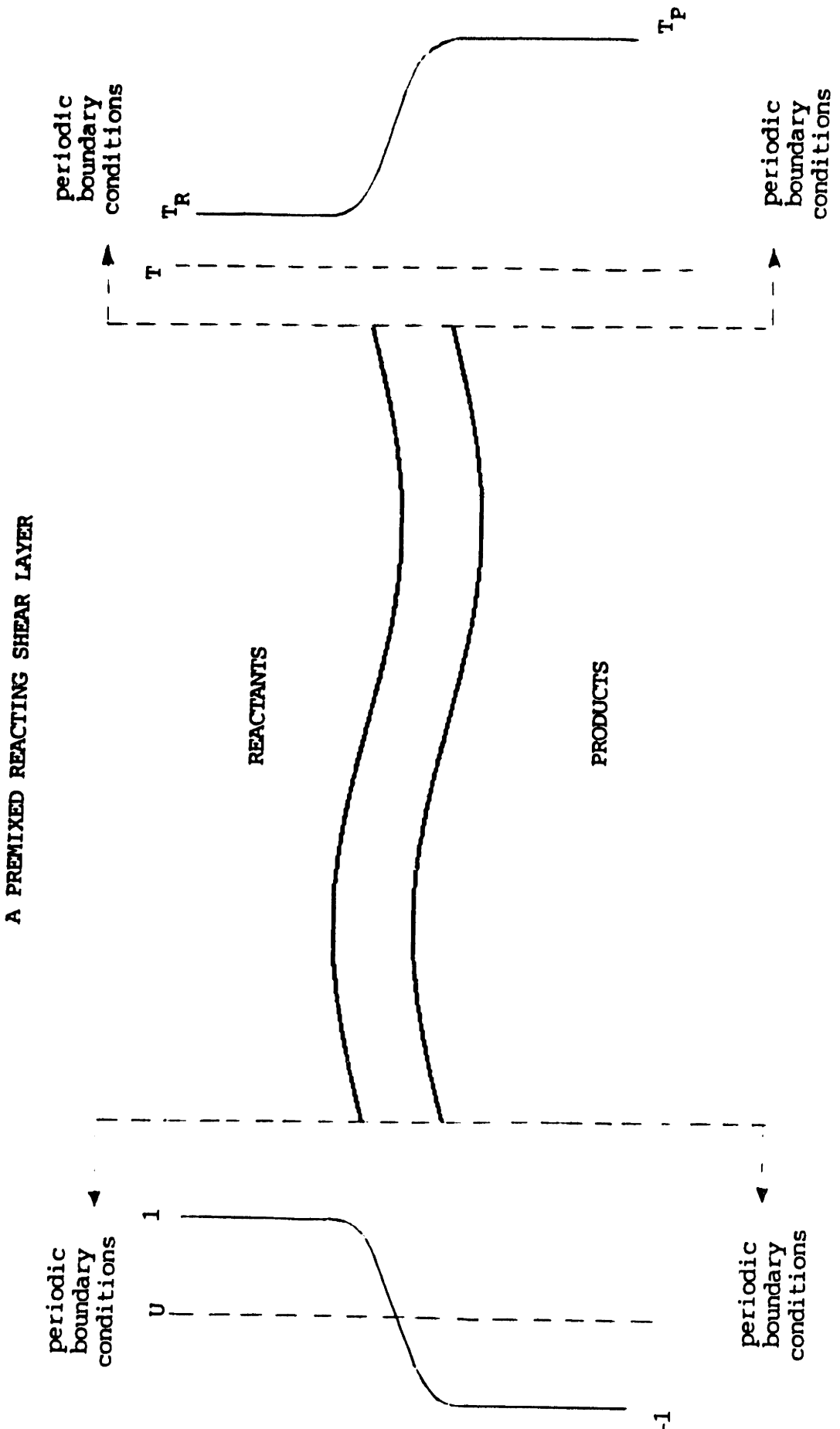
A PREMIXED REACTING SHEAR LAYER
periodic boundary conditions
periodic boundary conditions
periodic boundary conditions
periodic boundary conditions
T_R
T_P
T
U
1
-1
REACTANTS
PRODUCTS

Figure 159

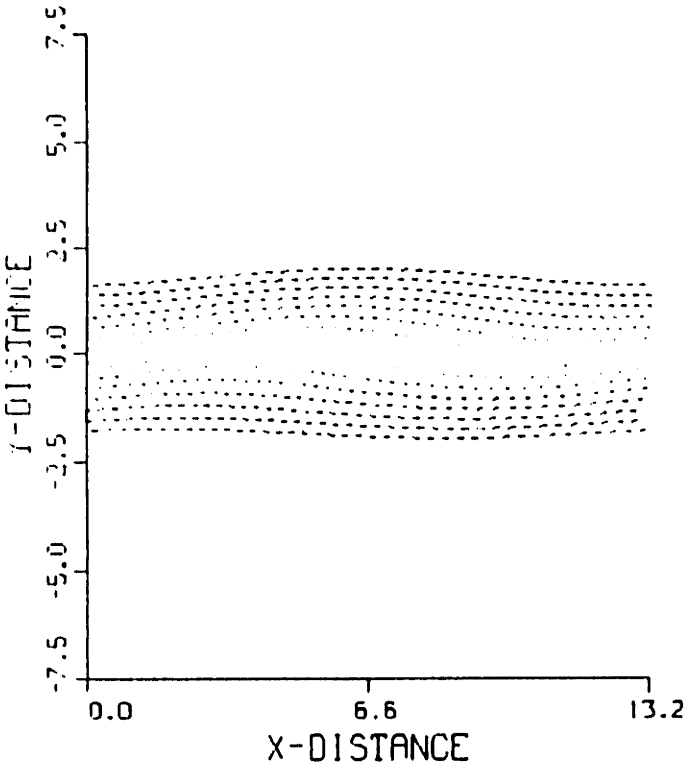

t = 5.5

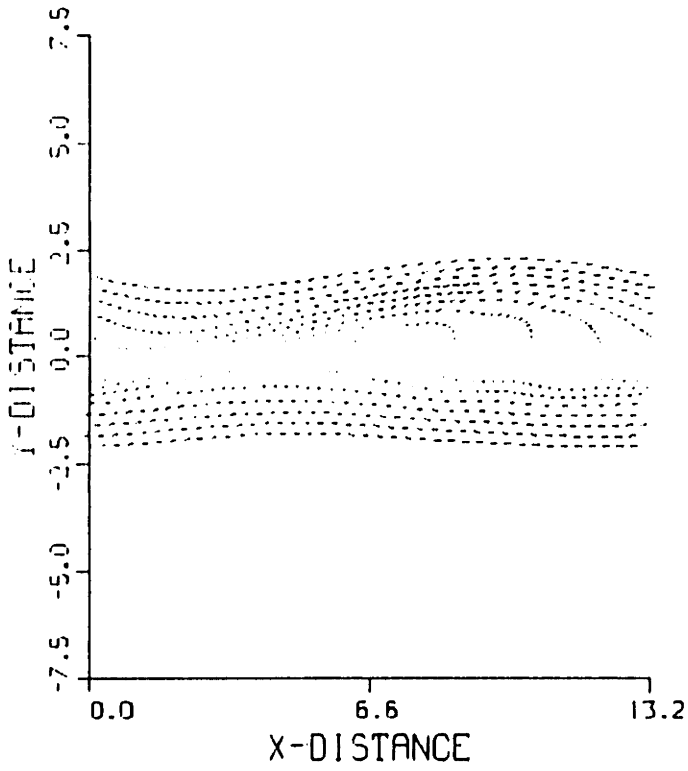

t = 11.0

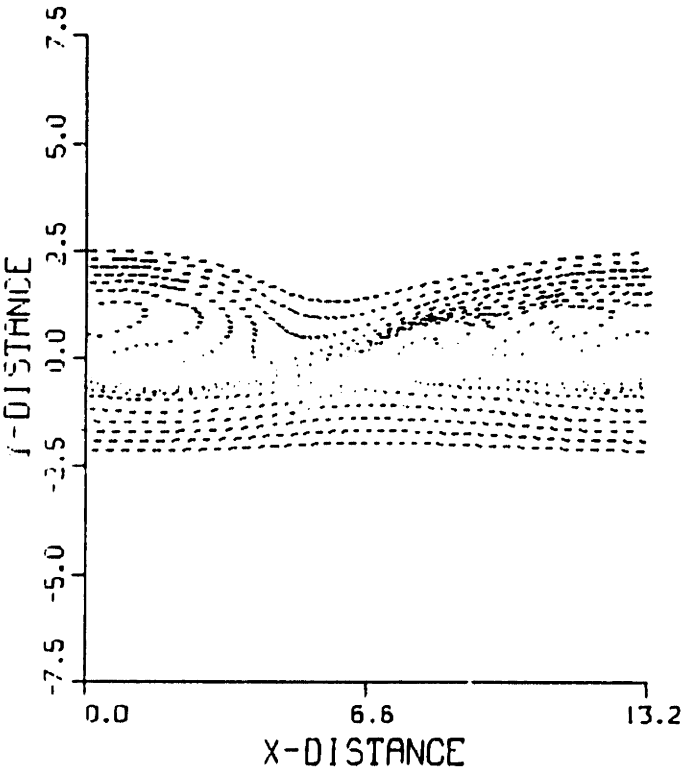

t = 16.5

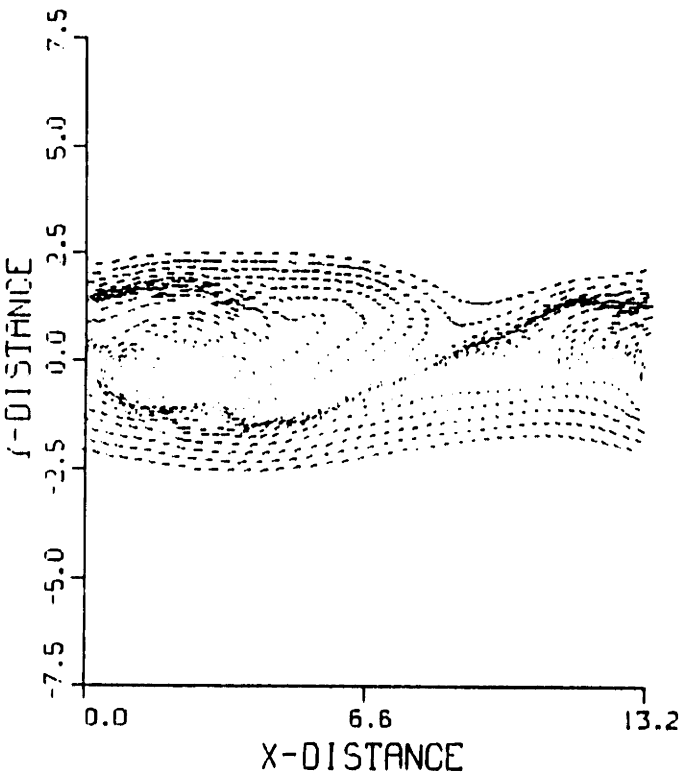

t = 22.0

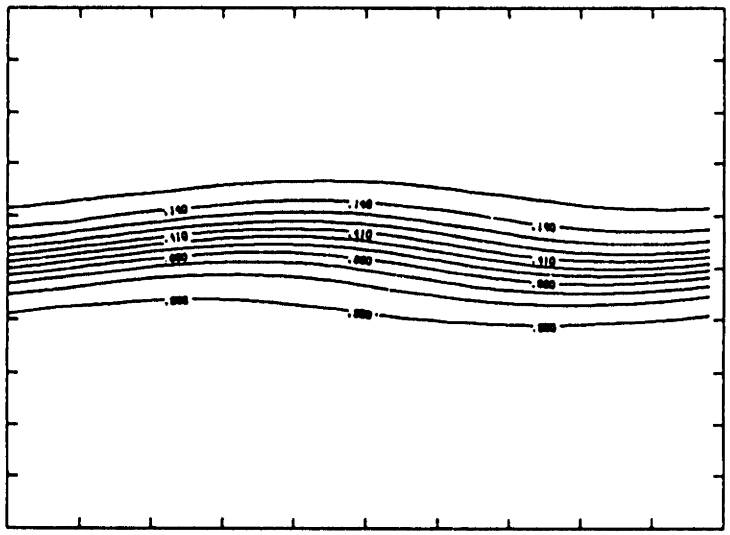

t = 5.5

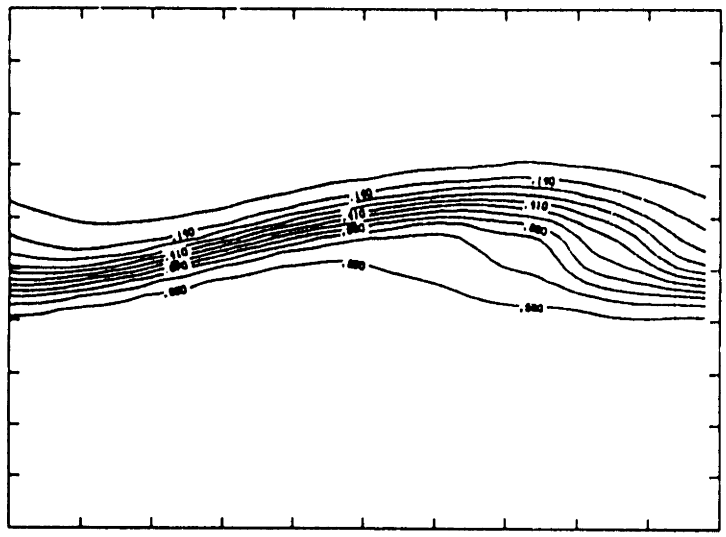

t = 11.0

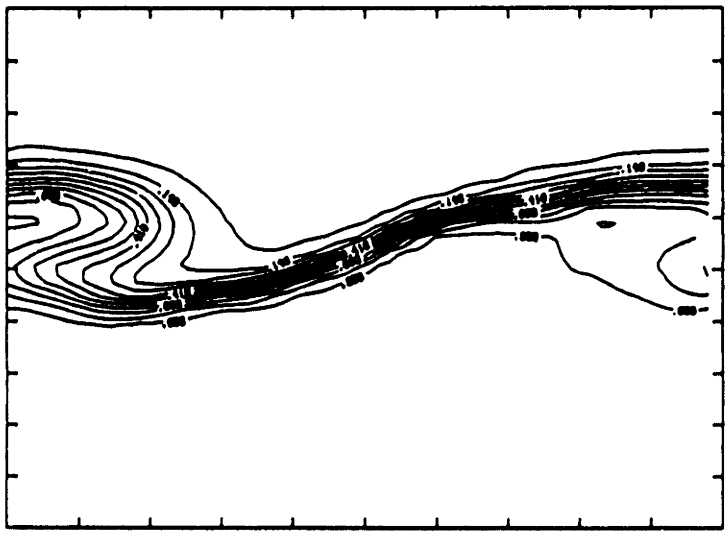

t = 16.5

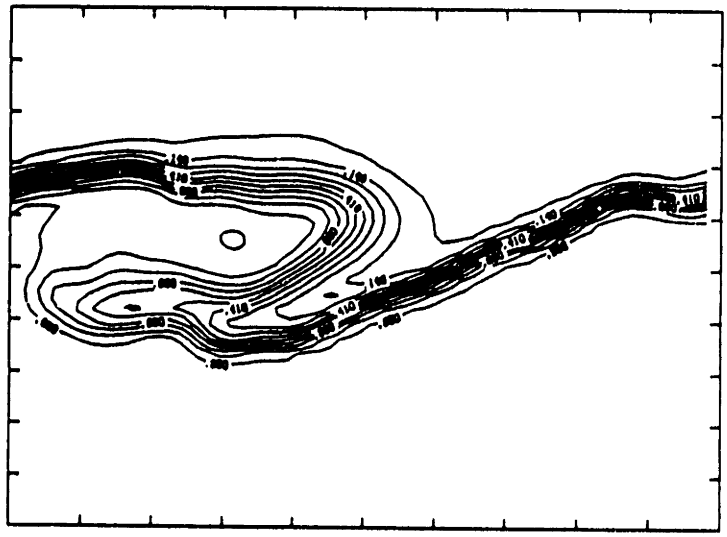

t = 22.0

Figure 161

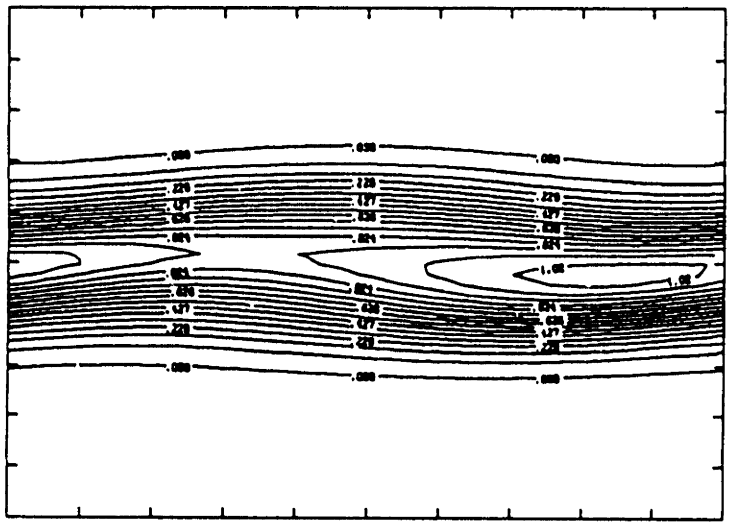

t = 5.5

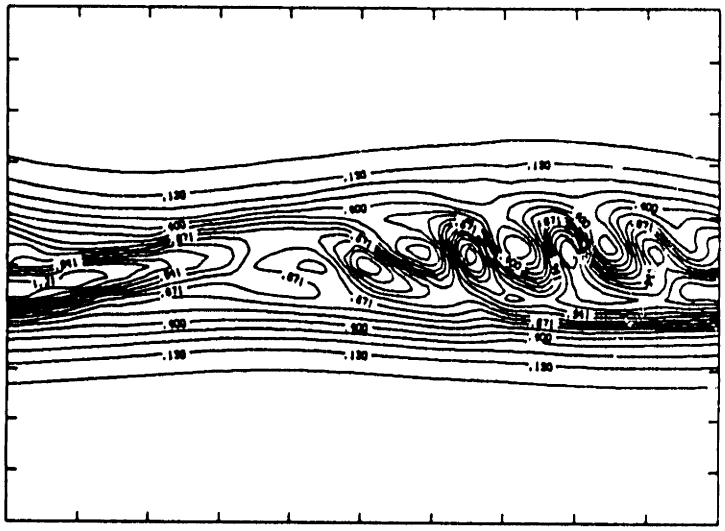

t = 11.0

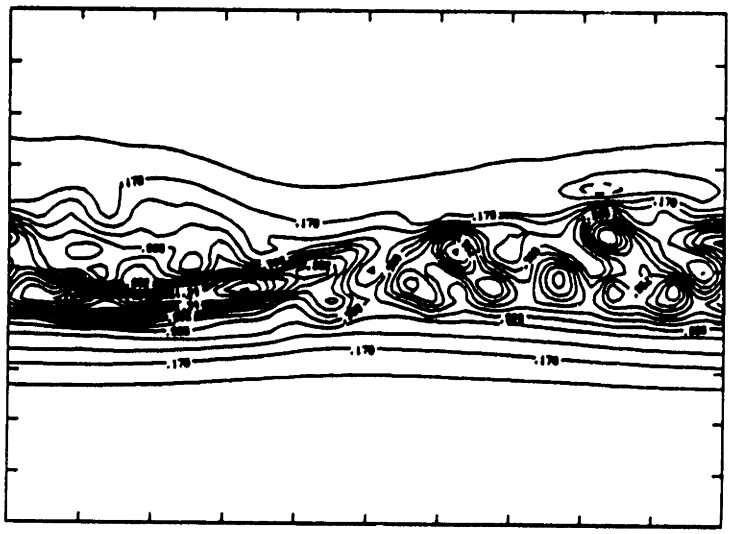

t = 16.5

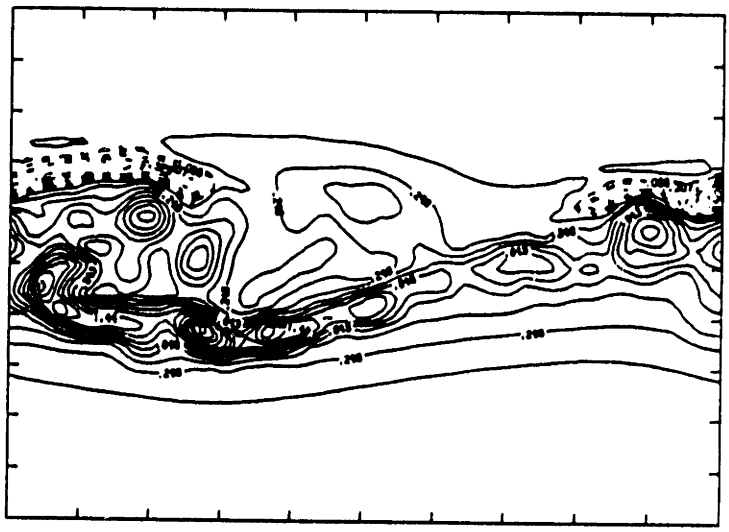

t = 22.0

Figure 162

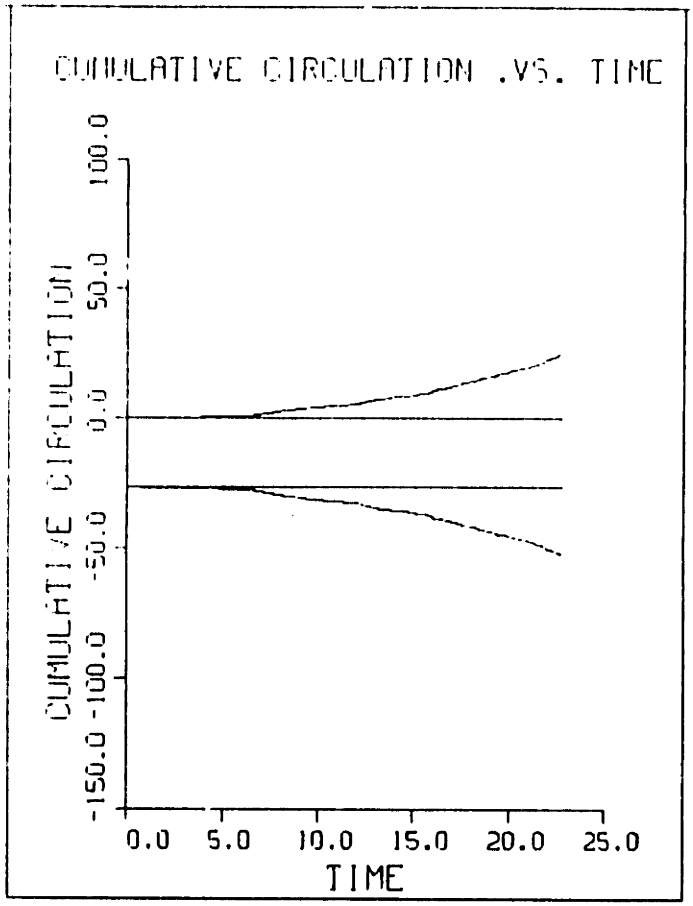
CUMULATIVE CIRCULATION .VS. TIME
CUMULATIVE CIRCULATION
100.0
50.0
0.0
-50.0
-100.0
-150.0
0.0
5.0
10.0
15.0
20.0
25.0
TIME

(a)

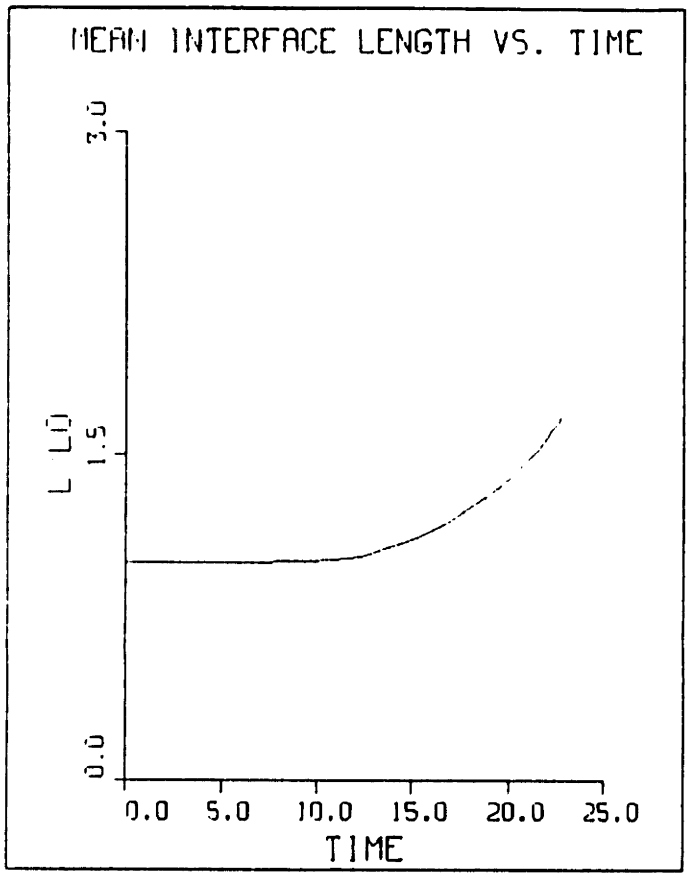
MEAN INTERFACE LENGTH VS. TIME
L LD
3.0
1.5
0.0
0.0
5.0
10.0
15.0
20.0
25.0
TIME

(b)

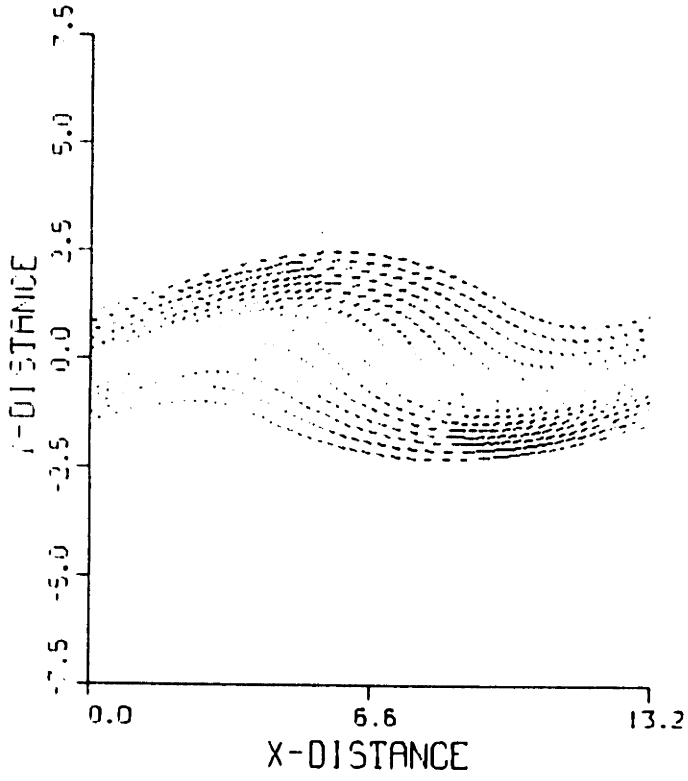

t = 16.87

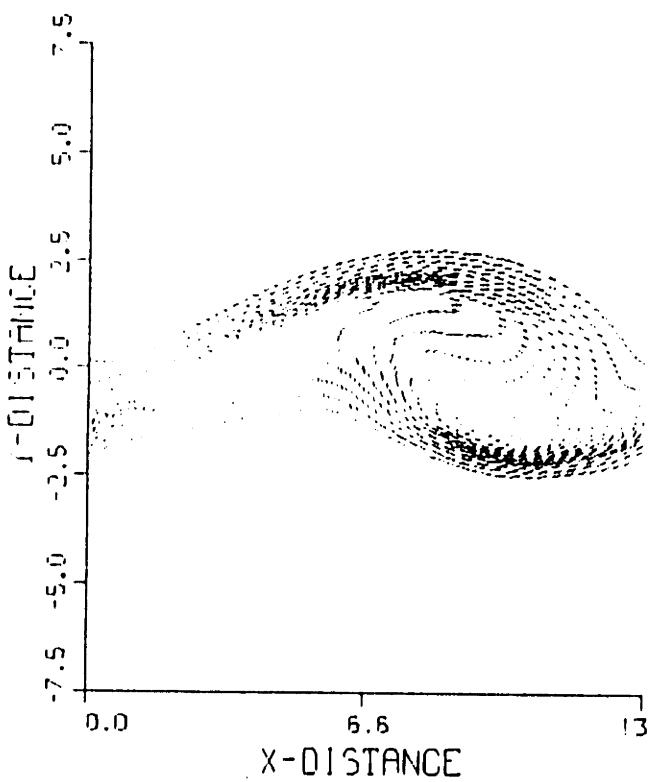

t = 33.75

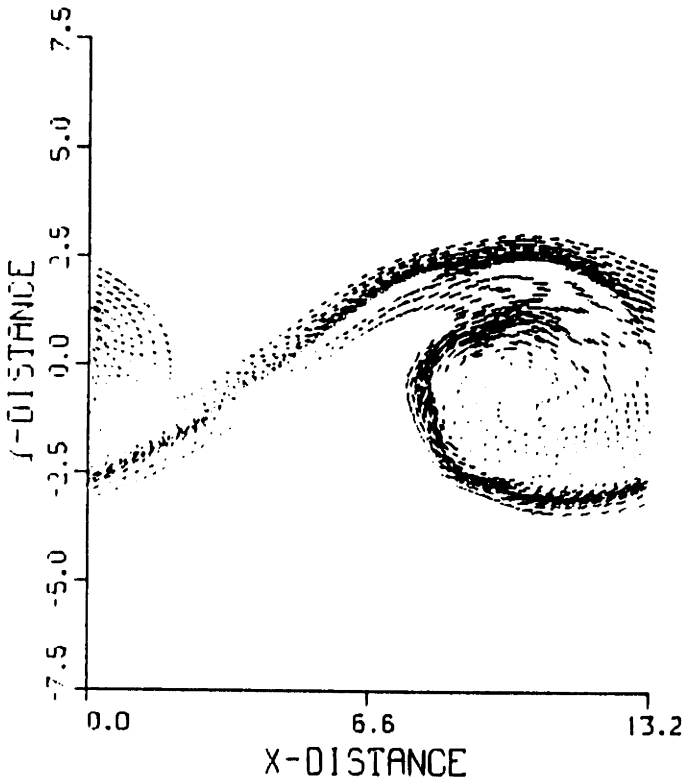

t = 50.62

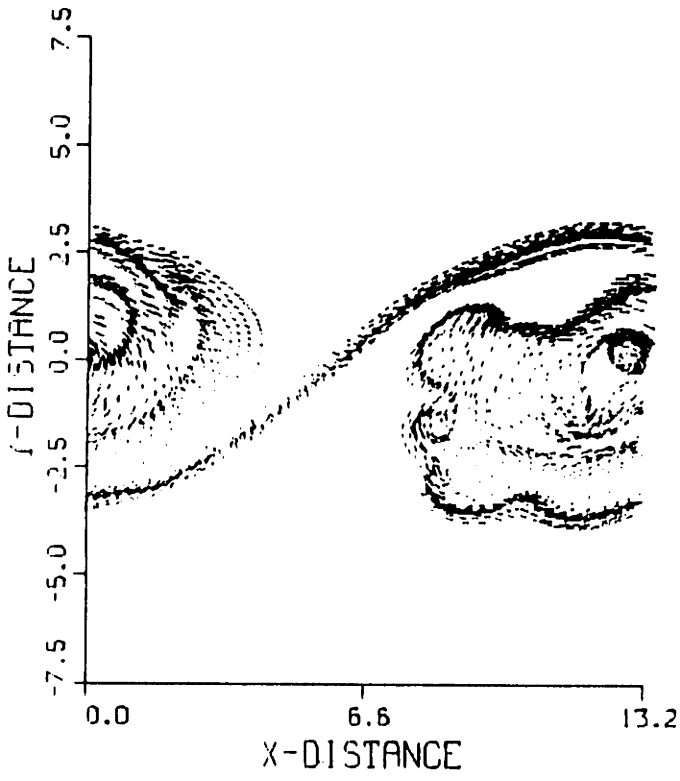

t = 68.75

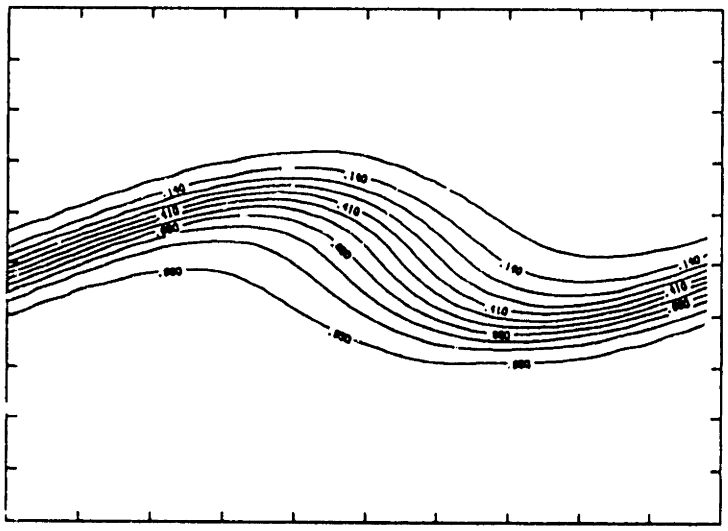

t = 16.87

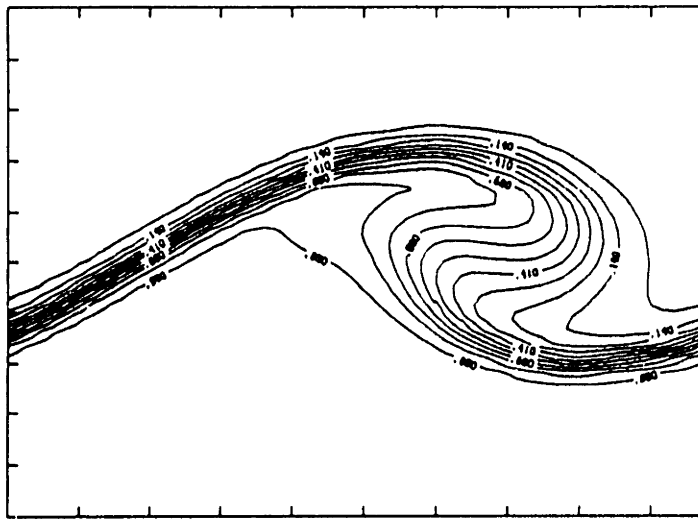

t = 33.75

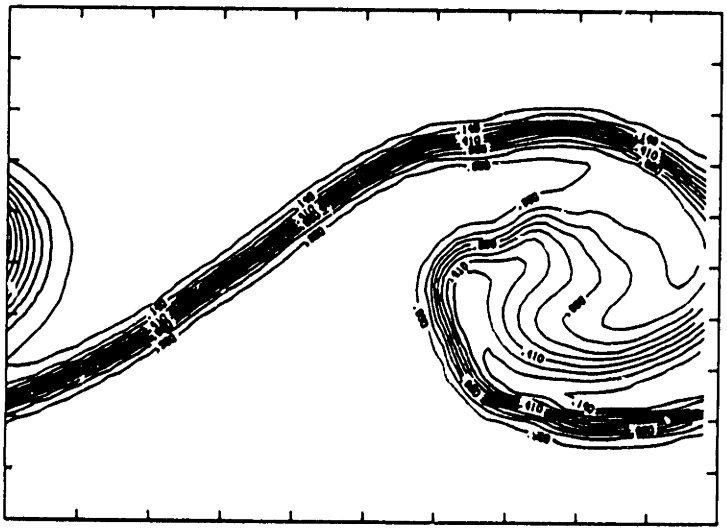

t = 50.62

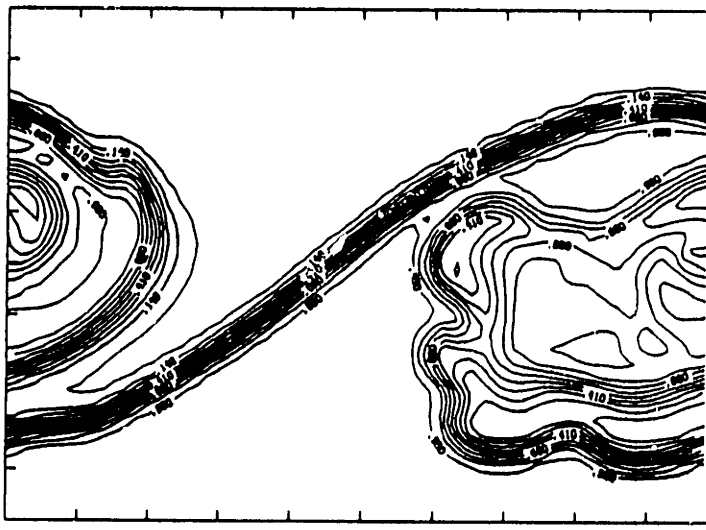

t = 68.75

Figure 165

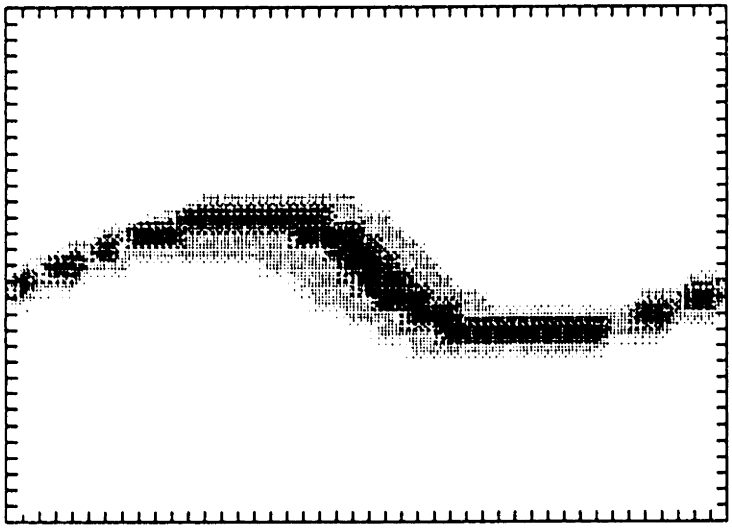

t = 16.87

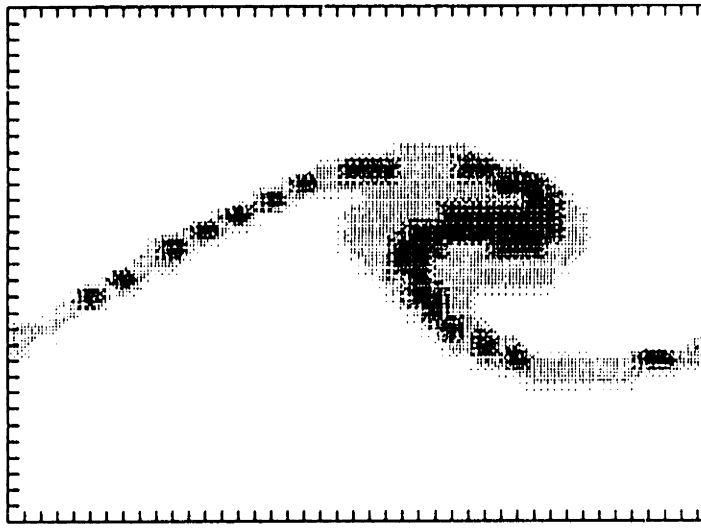

t = 33.75

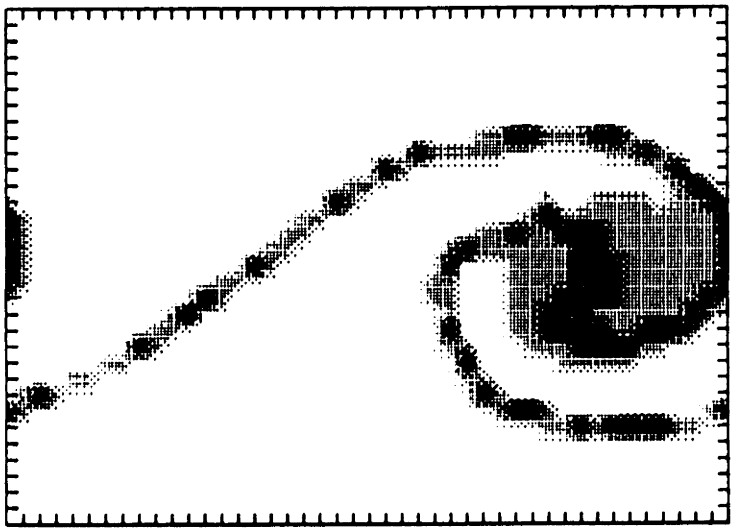

t = 50.62

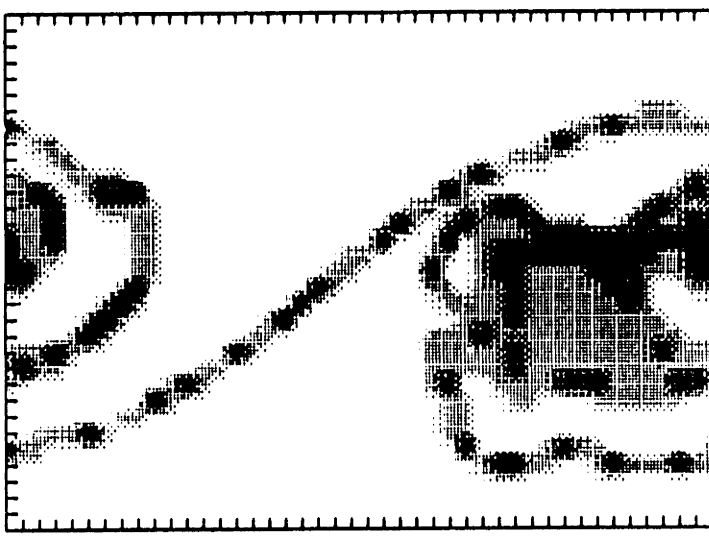

t = 68.75

Figure 166

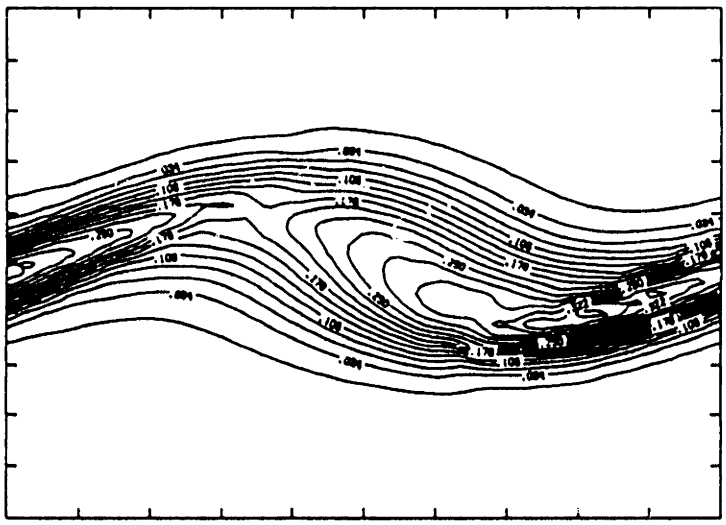

t = 16.87

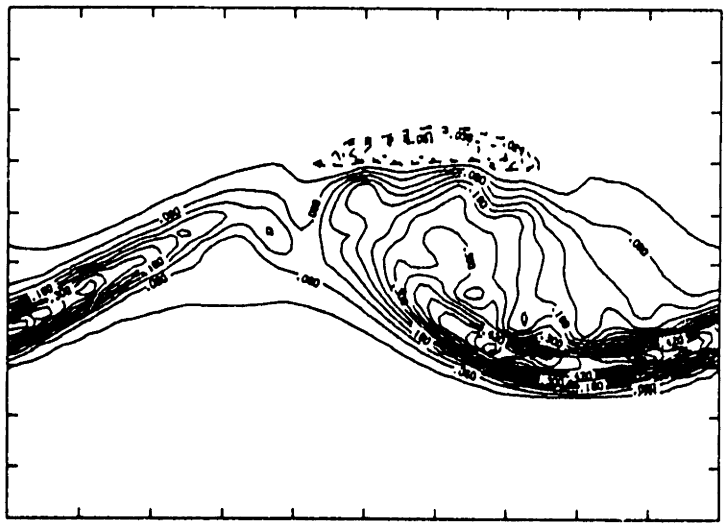

t = 33.75

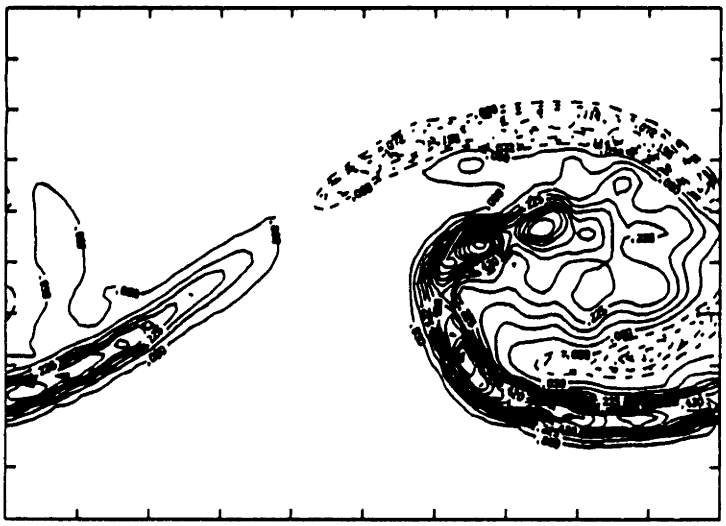

t = 50.62

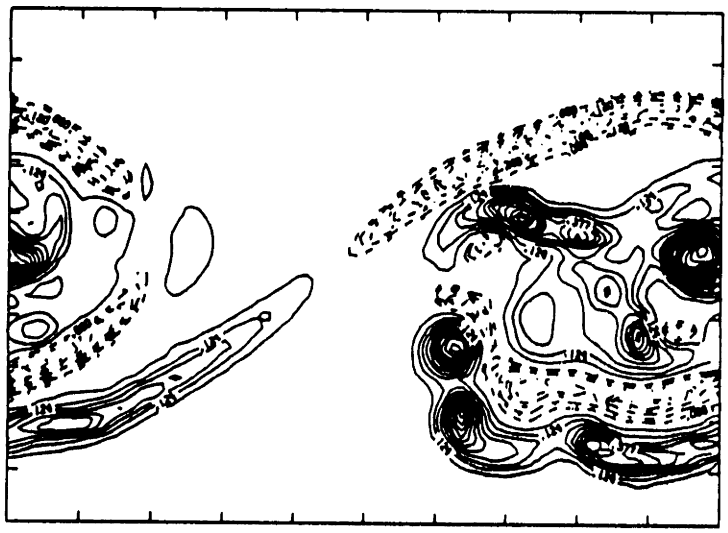

t = 68.75

Figure 167

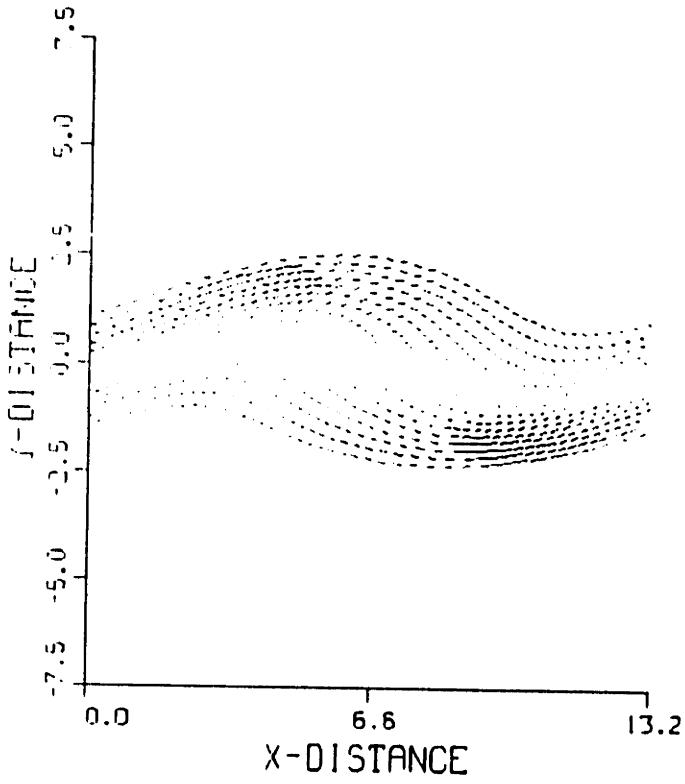

t = 33.75

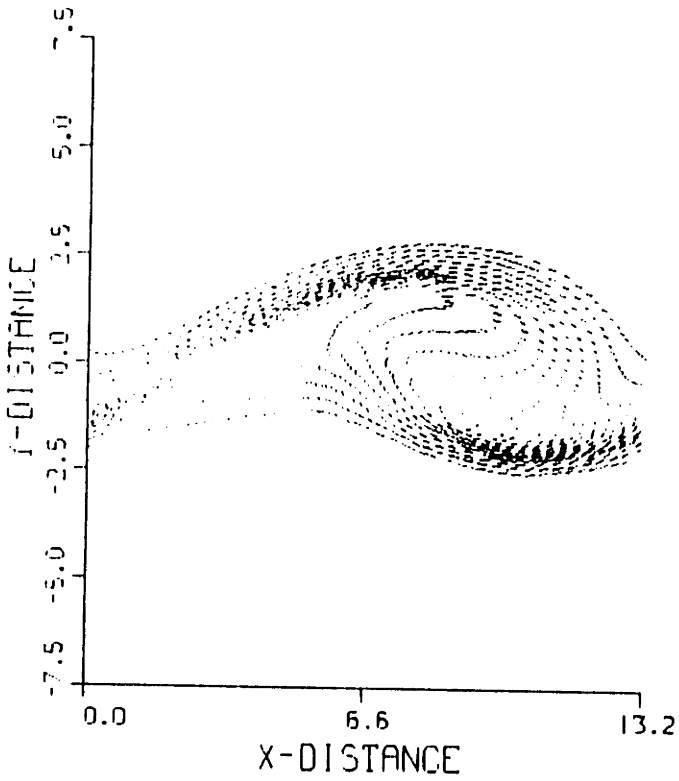

t = 67.5

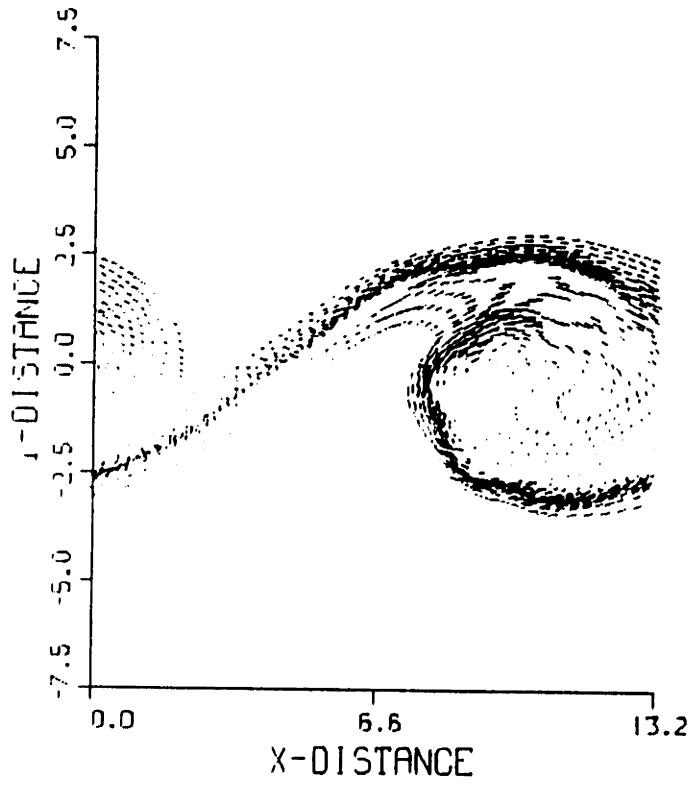

t = 101.25

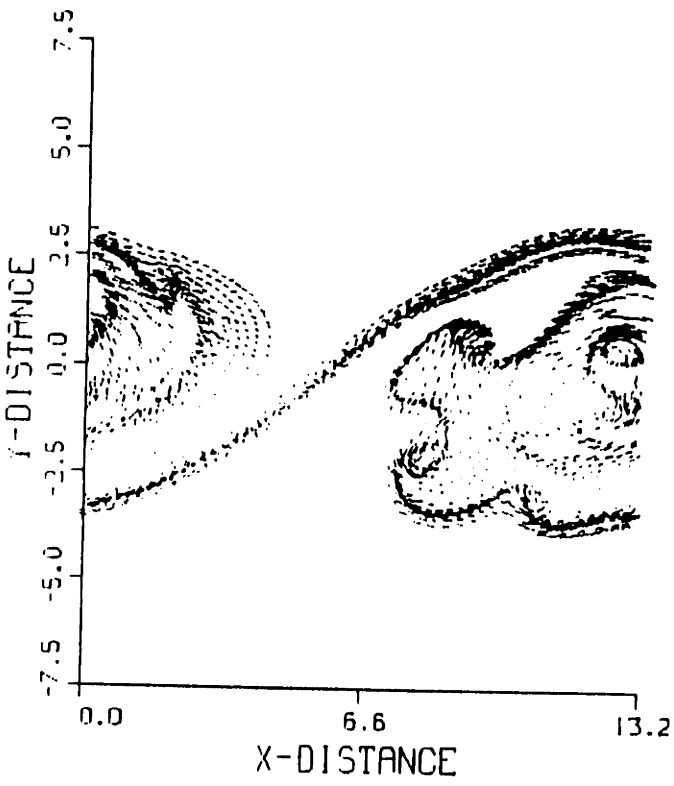

t = 137.5

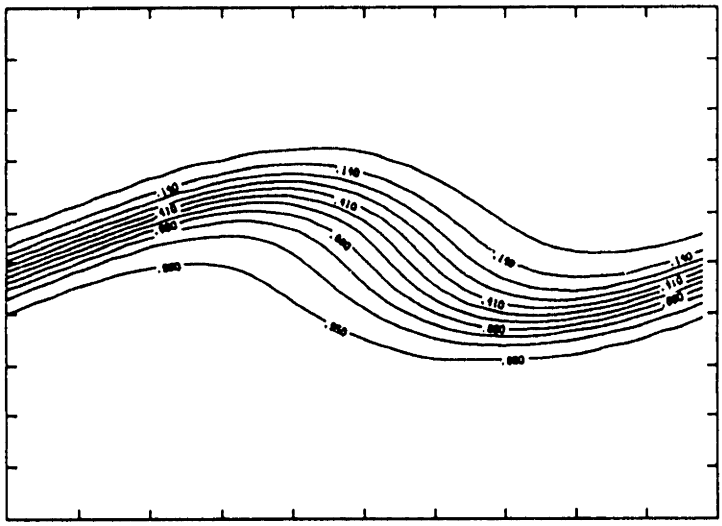

t = 33.75

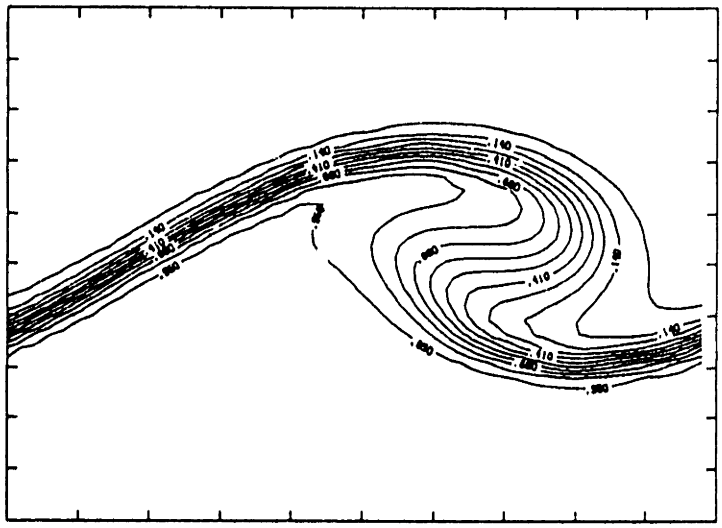

t = 67.5

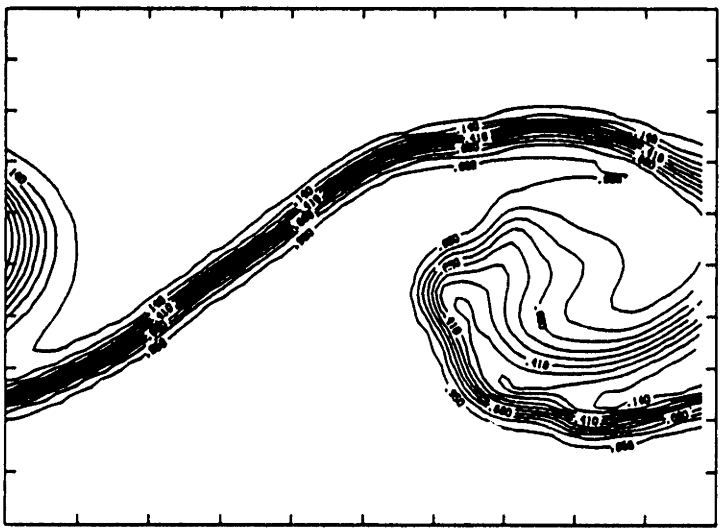

t = 101.25

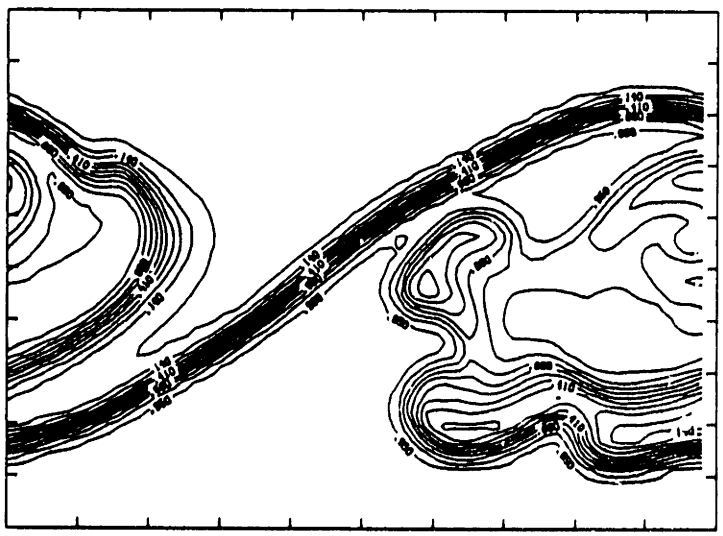

t = 137.5

Figure 169

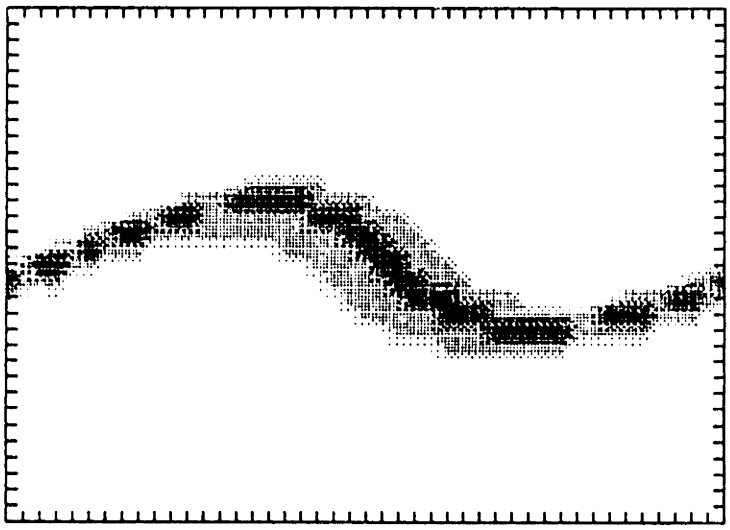

t = 33.75

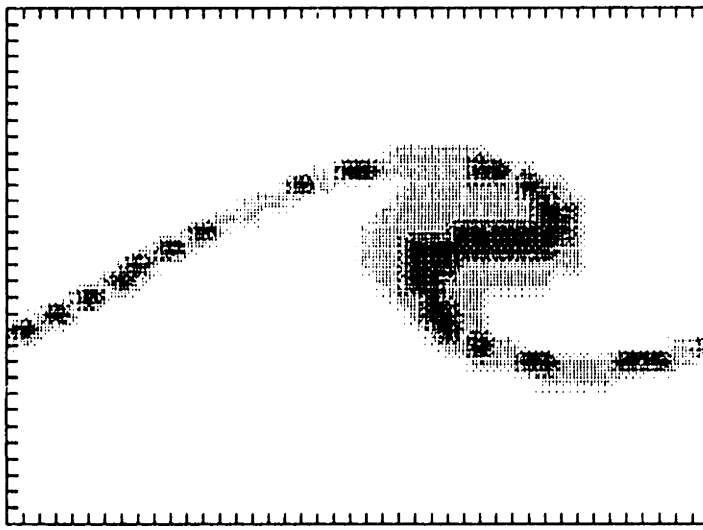

t = 67.5

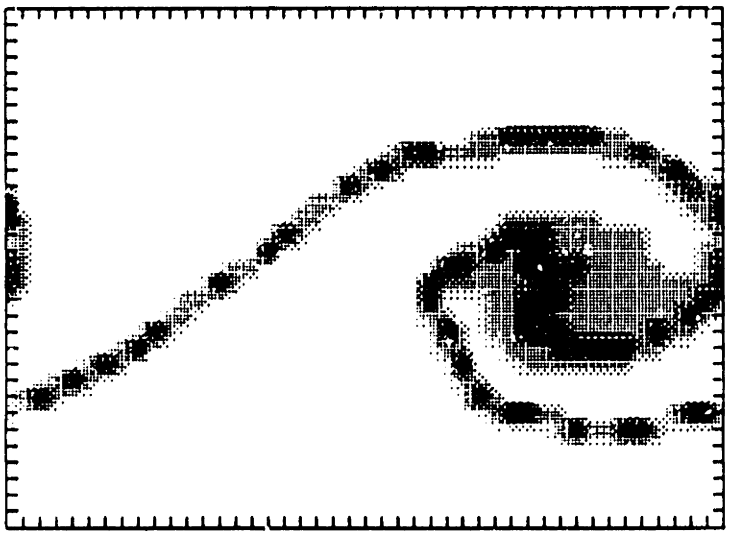

t = 101.25

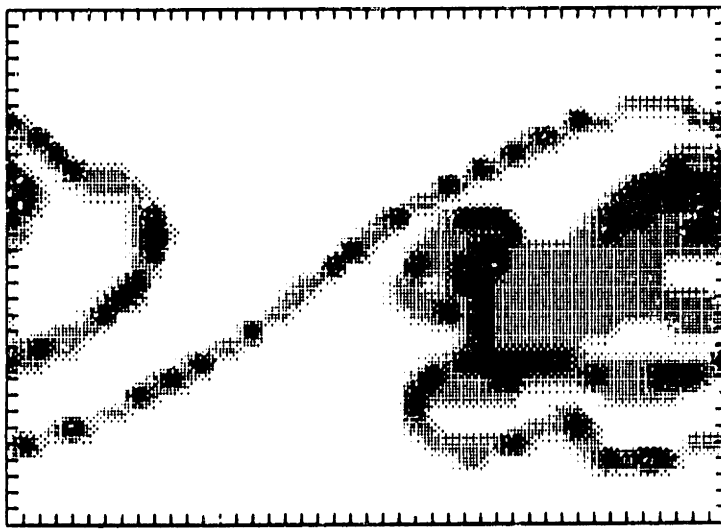

t = 137.5

Figure 170

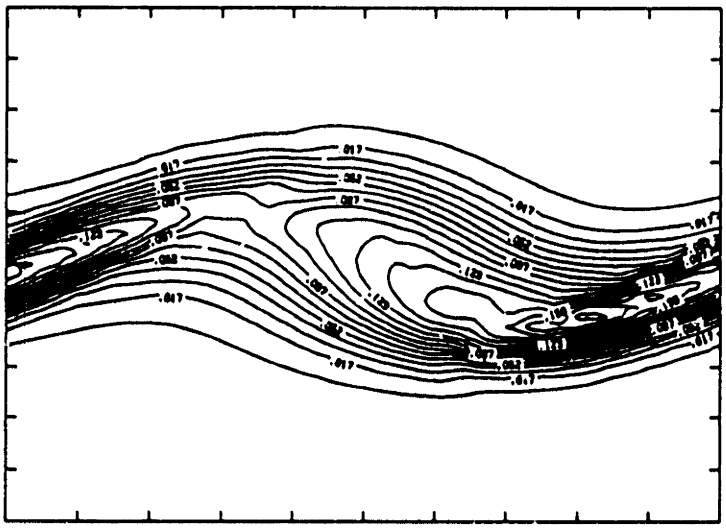

t = 33.75

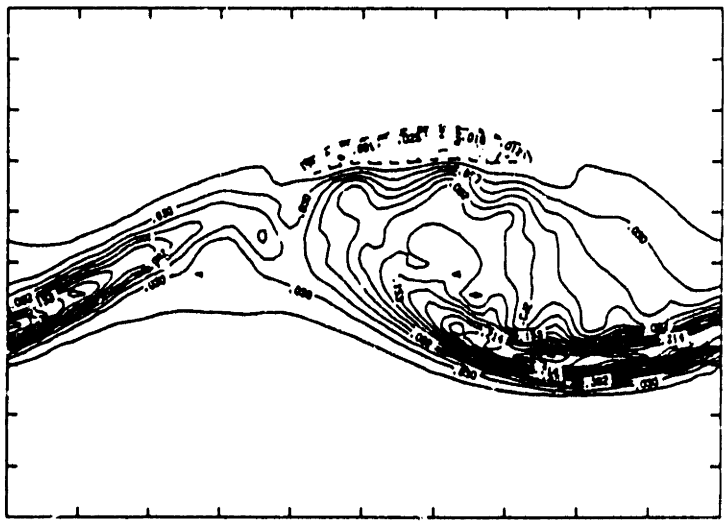

t = 67.5

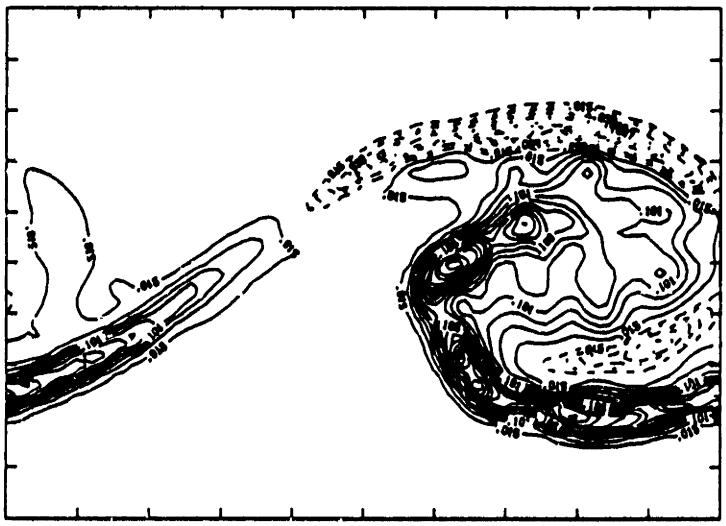

t = 101.25

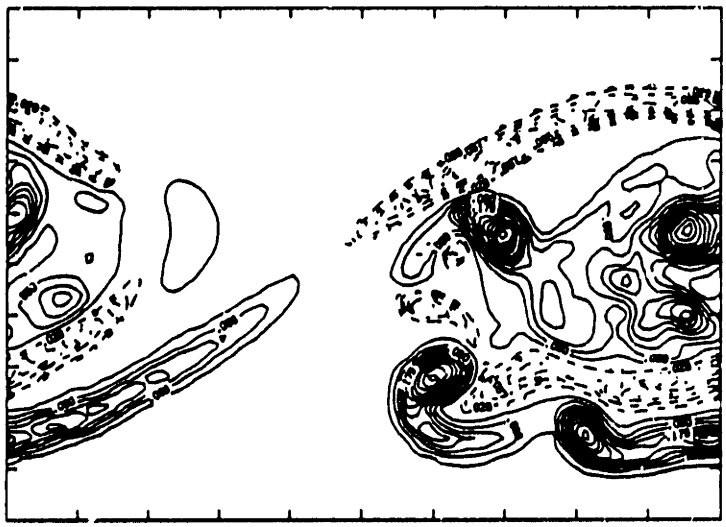

t = 137.5

Figure 171

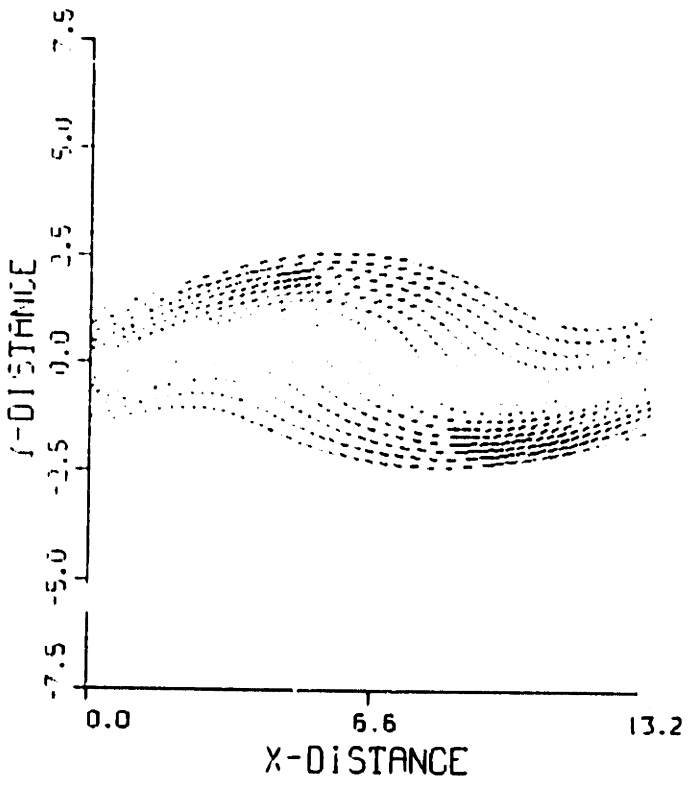

t = 67.5

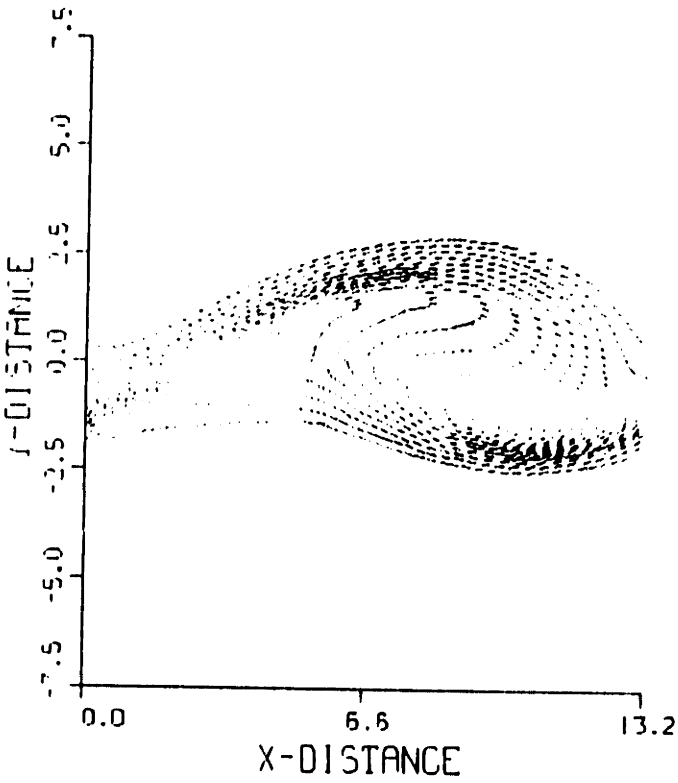

t = 135.0

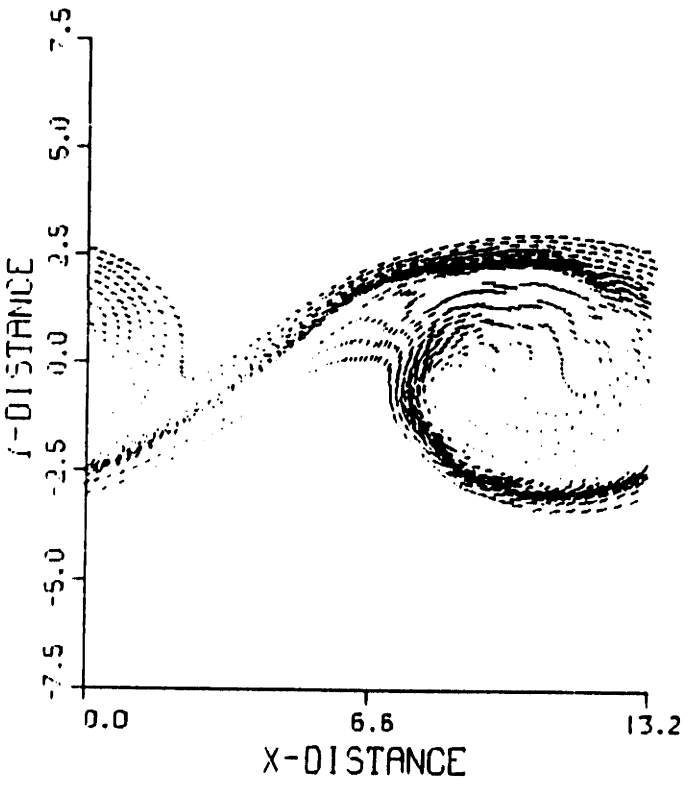

t = 202.5

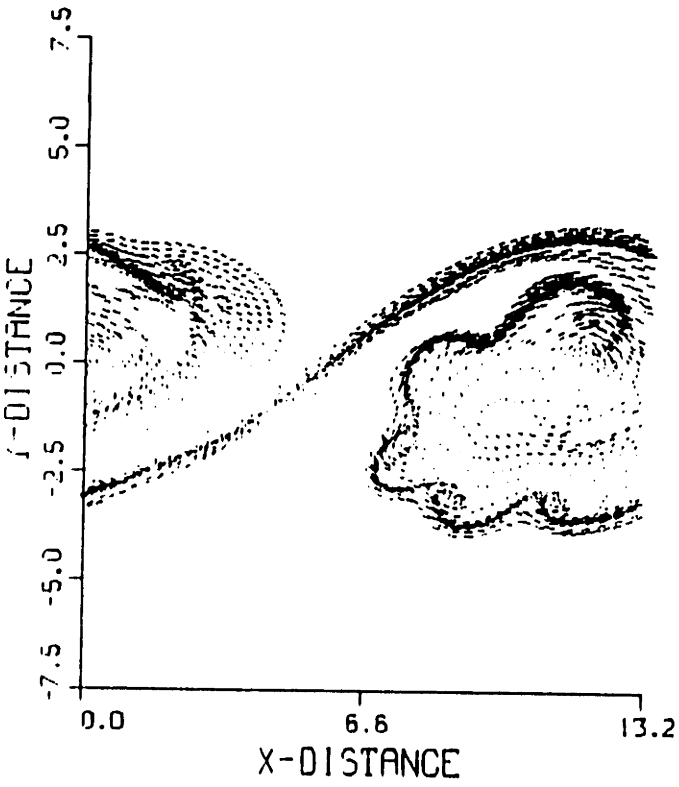

t = 275.0

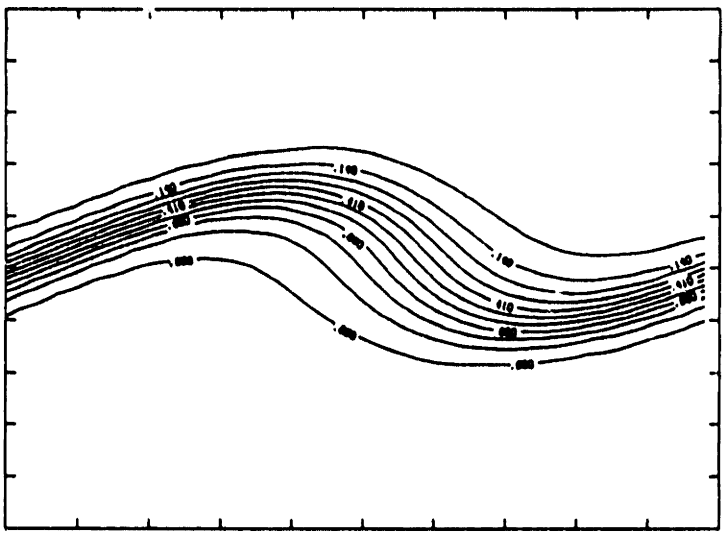

t = 67.5

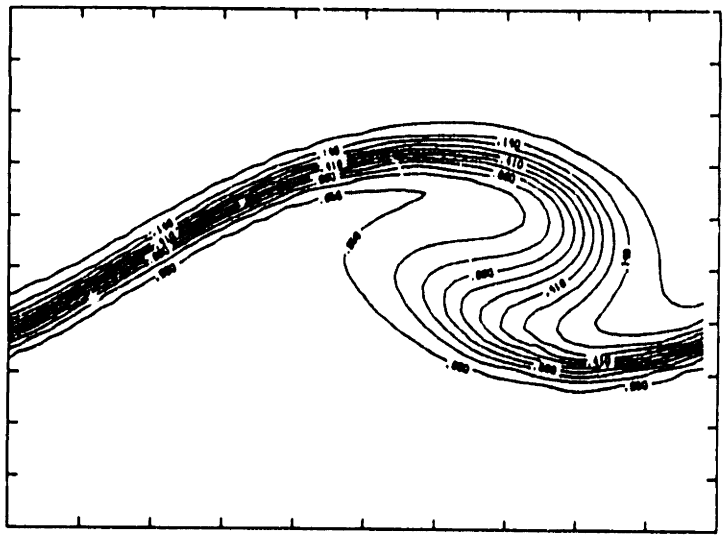

t = 135.0

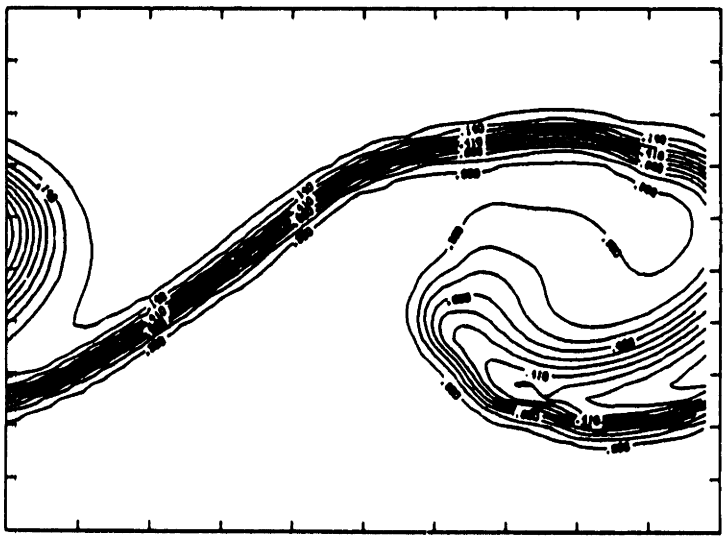

t = 202.5

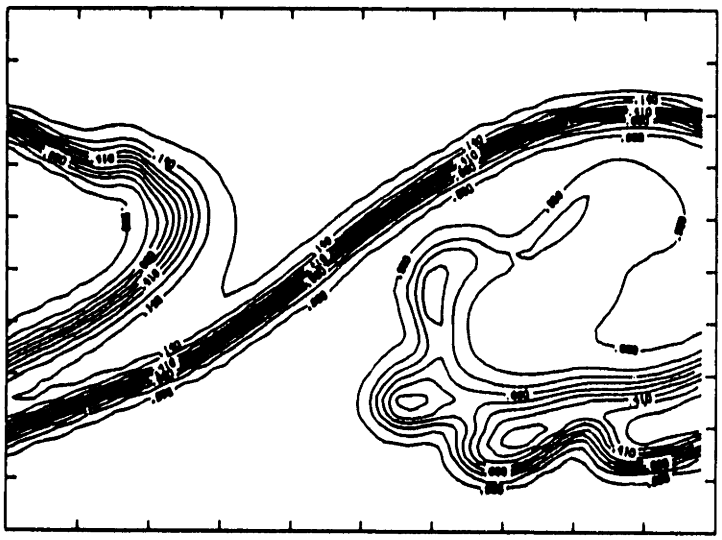

t = 275.0

Figure 173

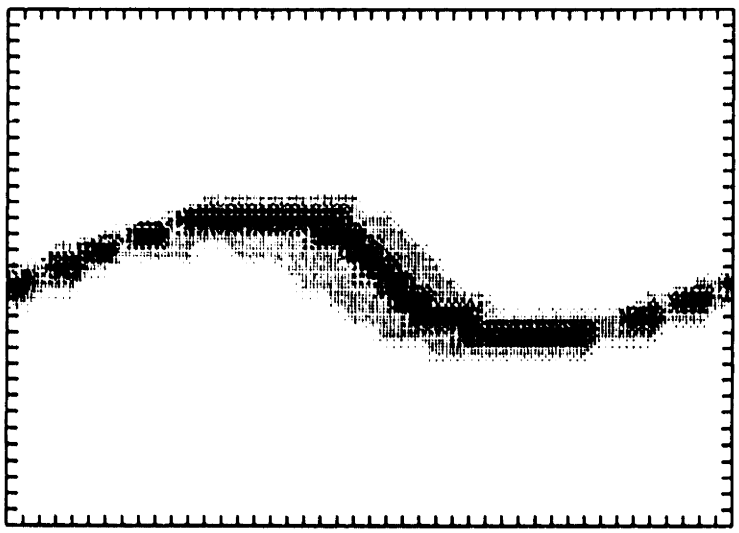

t = 67.5

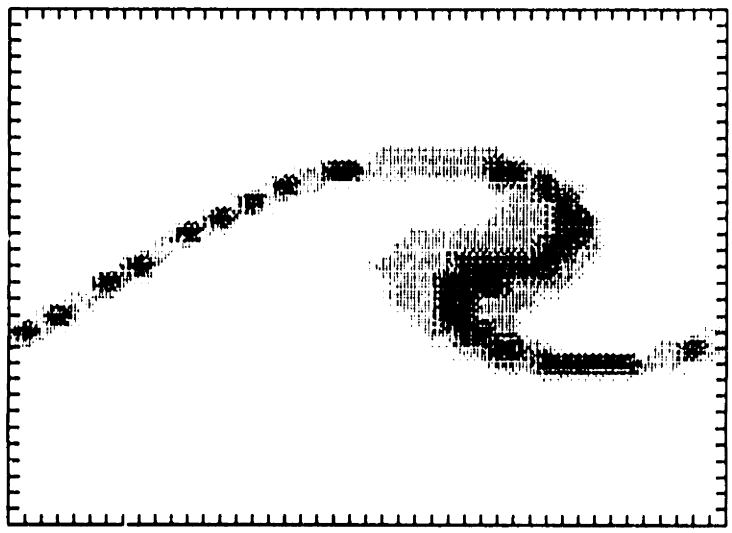

t = 135.0

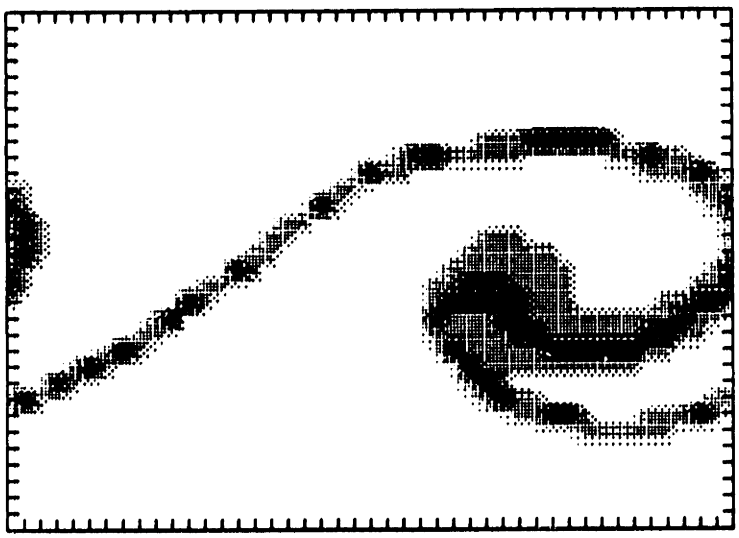

t = 202.5

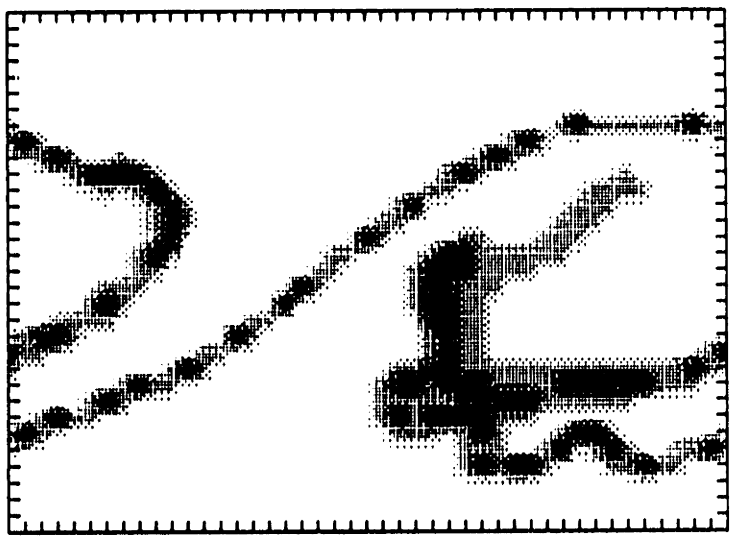

t = 275.0

Figure 174

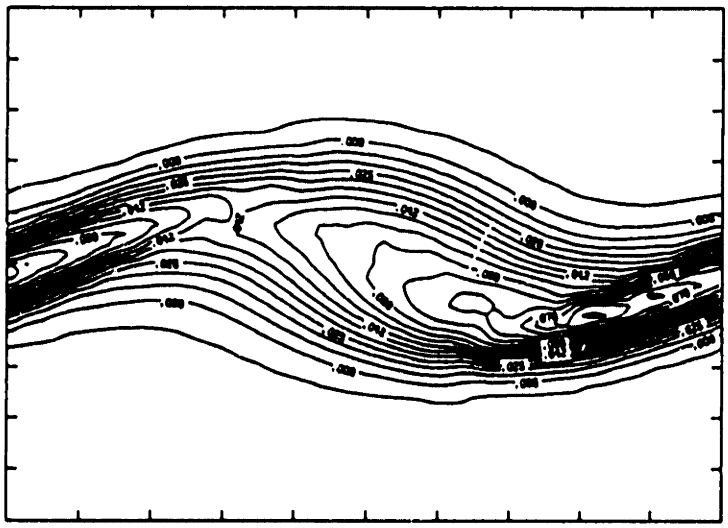

t = 67.5

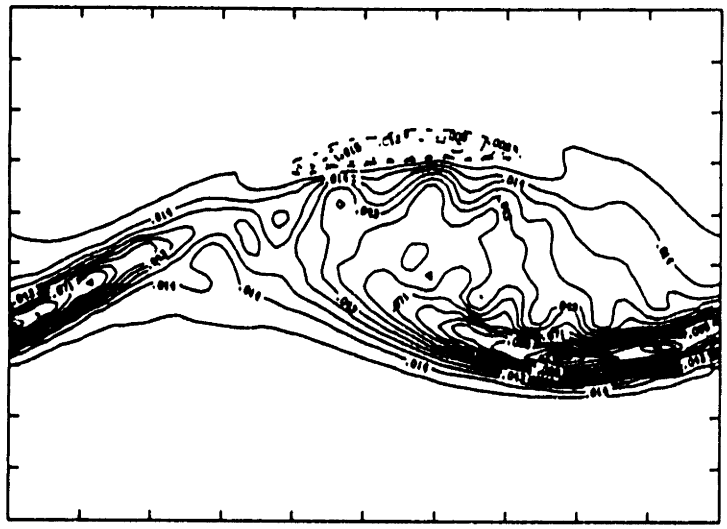

t = 135.0

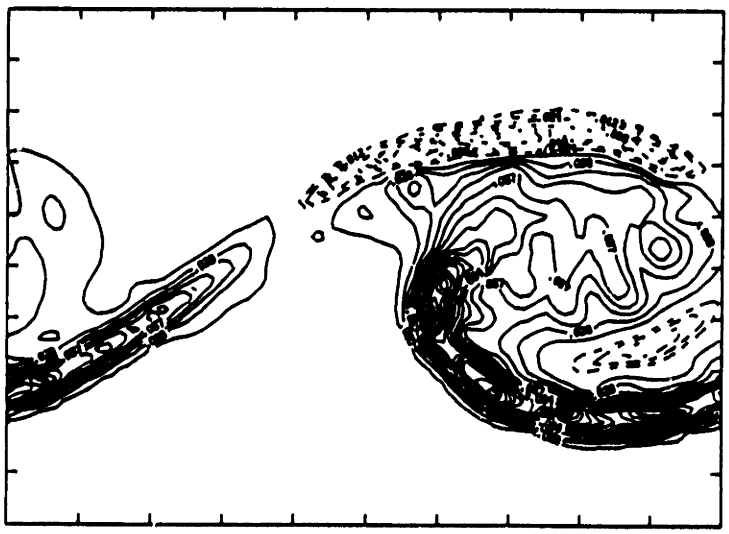

t = 202.5

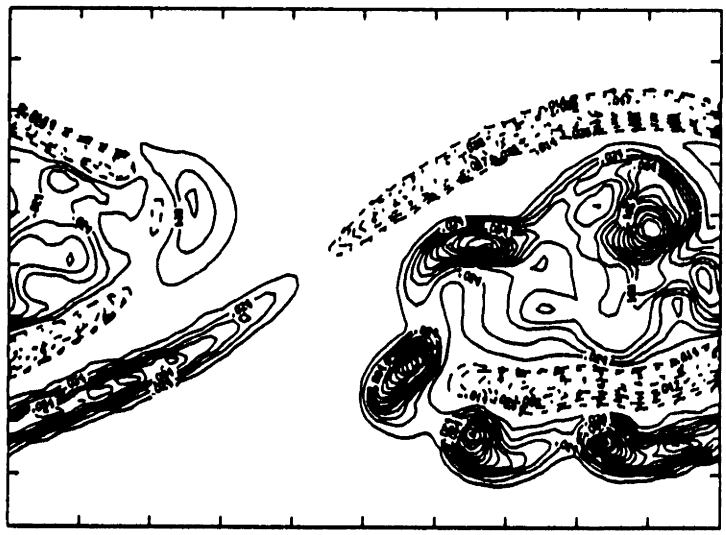

t = 275.0

Figure 175

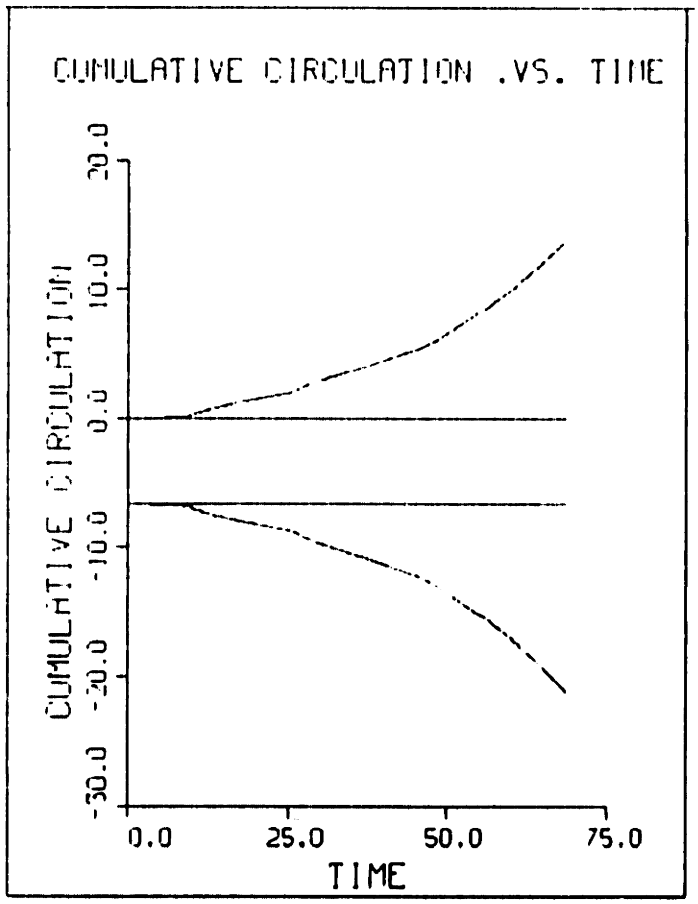

(a)

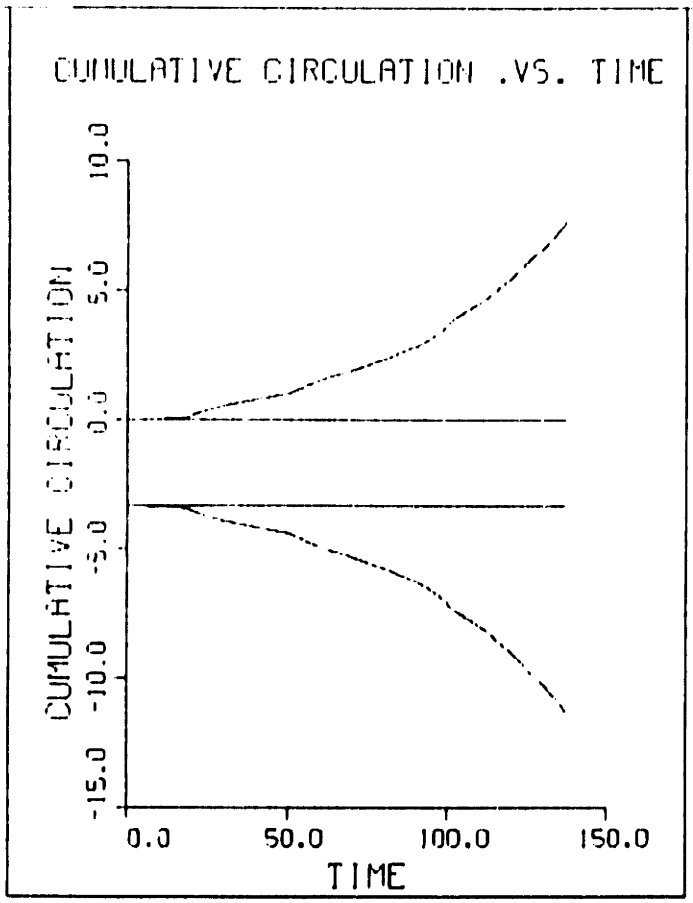

(b)

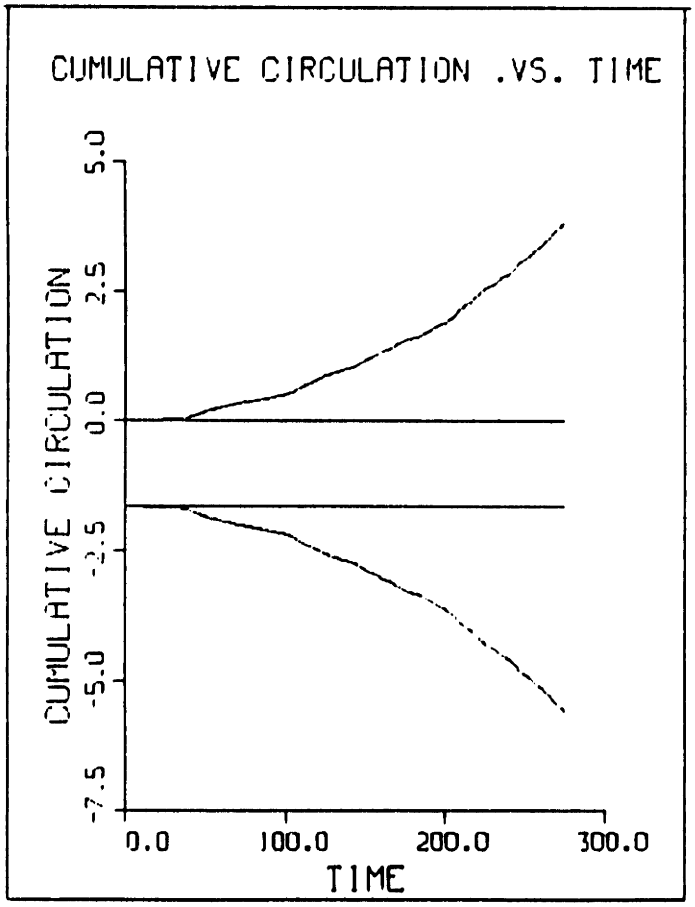

(c)

Figure 176

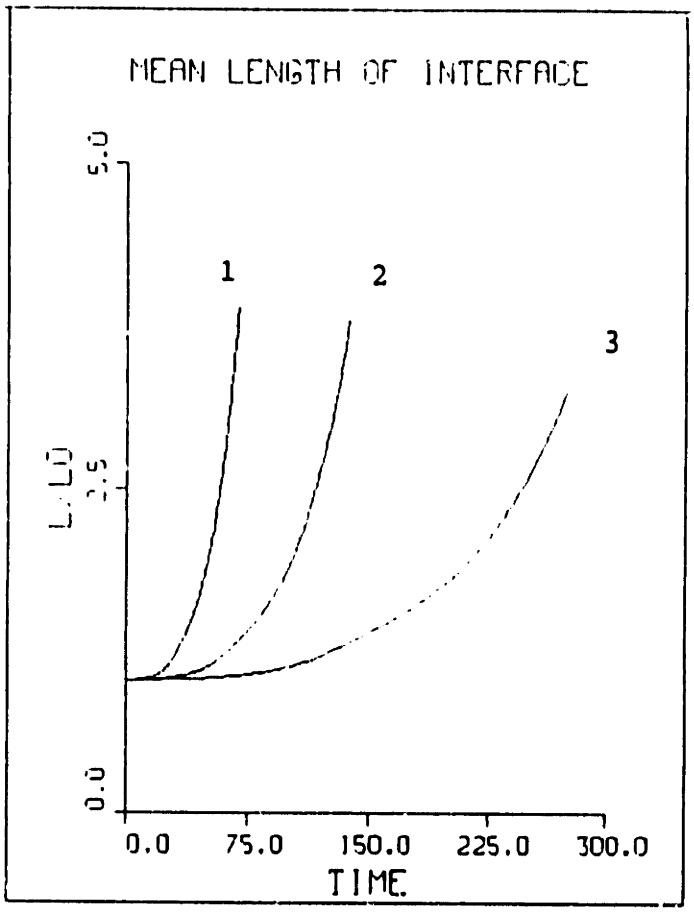

Figure 177

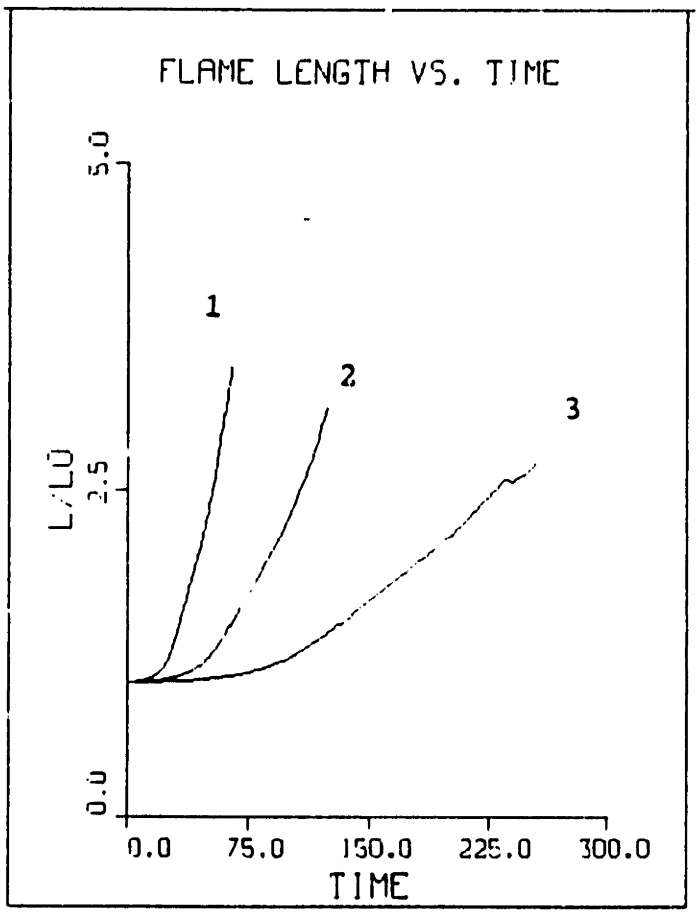

Figure 178

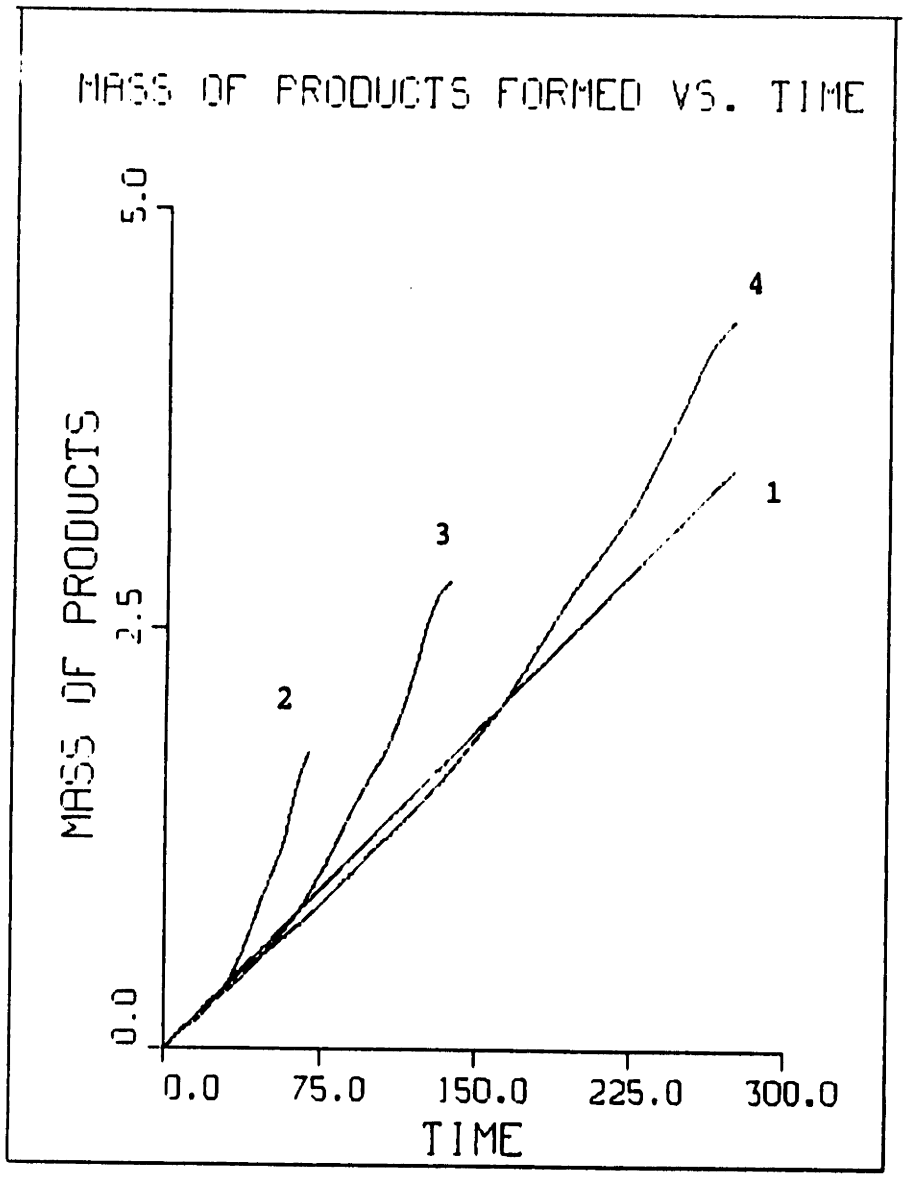
MASS OF PRODUCTS FORMED VS. TIME
MASS OF PRODUCTS
5.0
2.5
0.0
0.0
75.0
150.0
225.0
300.0
TIME
1
2
3
4

Figure 179

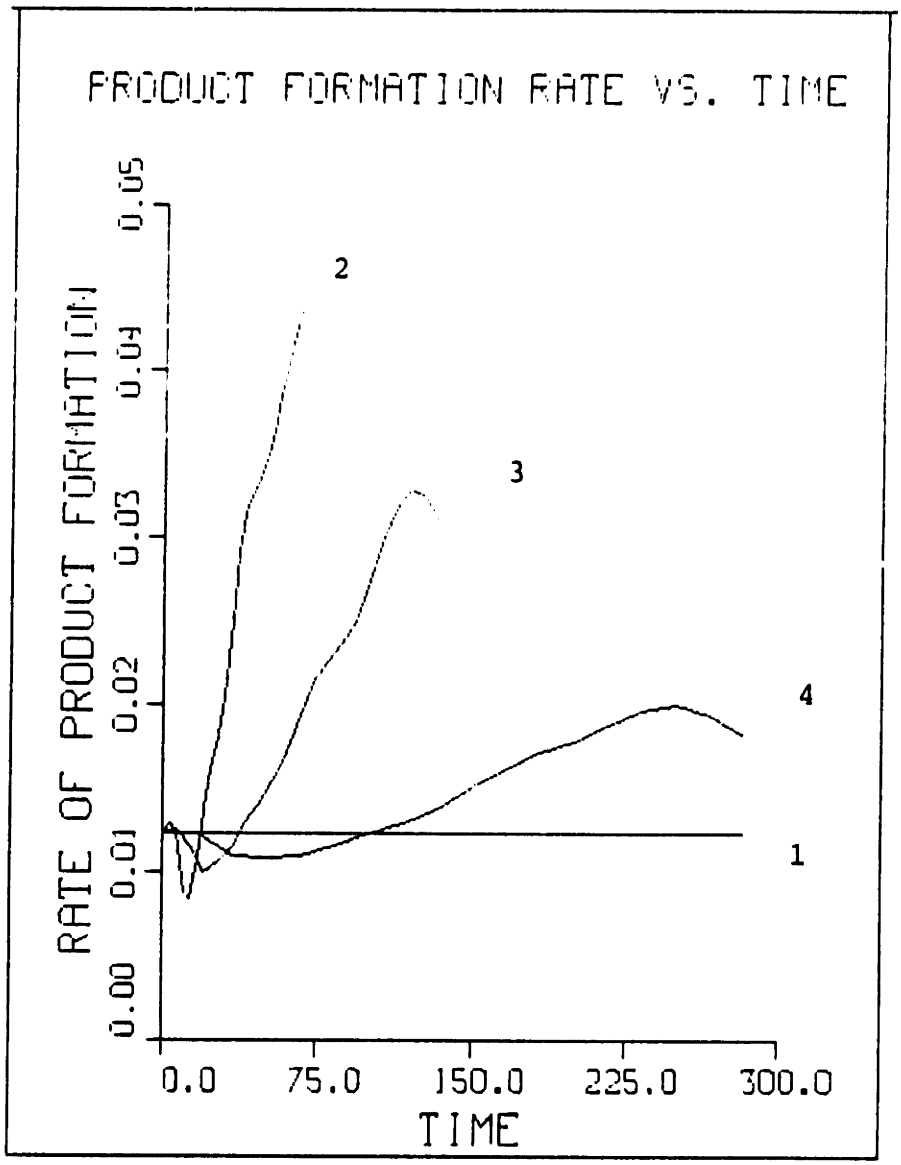
PRODUCT FORMATION RATE VS. TIME
RATE OF PRODUCT FORMATION
0.00
0.01
0.02
0.03
0.04
0.05
0.0
75.0
150.0
225.0
300.0
TIME
1
2
3
4

Figure 180

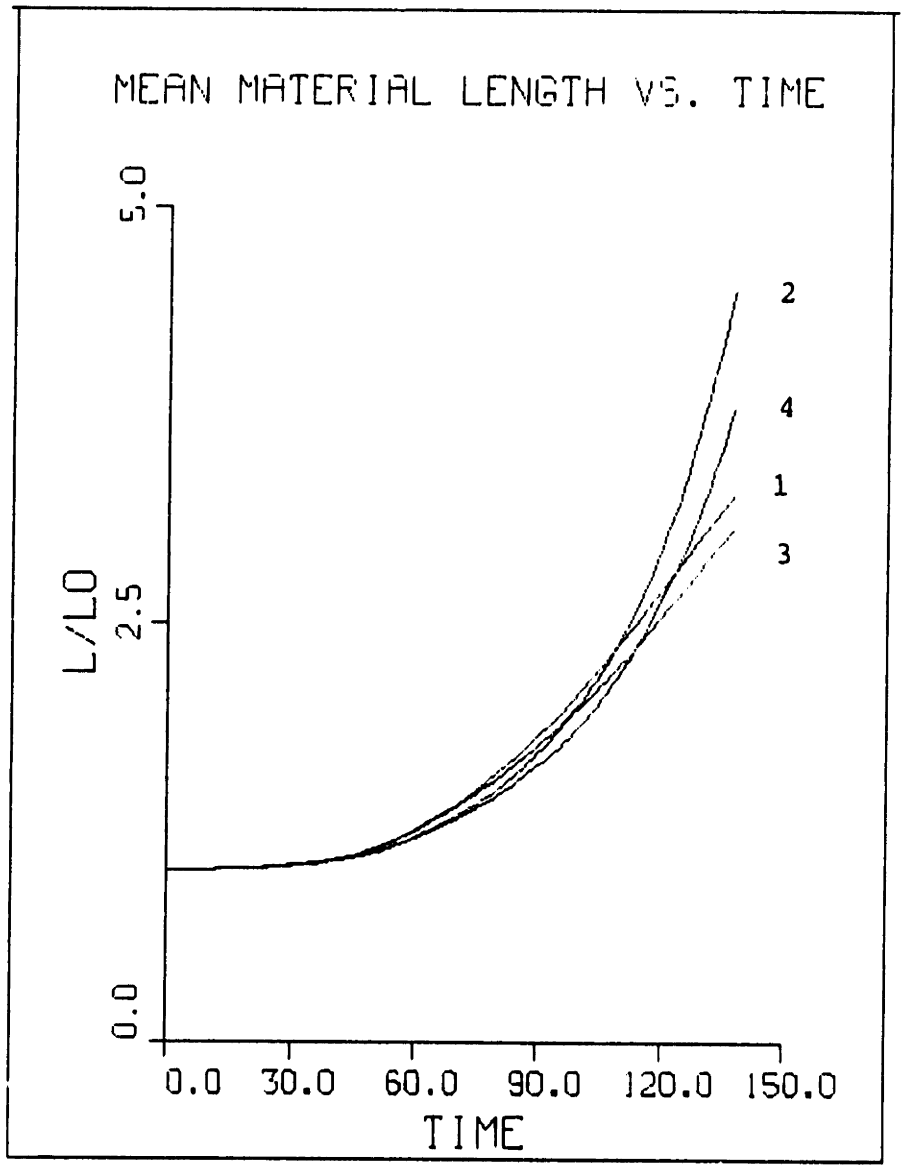
MEAN MATERIAL LENGTH VS. TIME
5.0
2.5
0.0
L/LO
2
4
1
3
0.0
30.0
60.0
90.0
120.0
150.0
TIME

Figure 181

IX. DISCUSSIONS AND CONCLUSIONS

The vortex/transport element method was applied to study five typical problems in turbulent flows. The scheme was developed from first principles and validated by applying it to study the density stratified Kelvin-Helmholtz instability and the Rayleigh-Taylor instability in a gravitational field. Validation was done by comparing the results of the simulations with the predictions of the linear theory in the initial stages of growth of the instability. In the non-linear range, the results of the calculations were compared with experimental and previous theoretical results. On both counts, the results of the simulations yielded accurate results. Once validation was complete, the scheme was used to study problems such as the density stratified jet, the jet diffusion flame and the premixed shear layer.

It was shown that density stratification has a negligible impact on the linear growth rate of the most unstable mode. However, the effects of density stratification is particularly important in the non-linear stages of growth. The presence of a density field destabilizes the flow to a much greater extent in the non-linear range. Also, the effects of buoyancy play a very important role in destabilizing the flow field. It was found that flow developed in a highly non-linear manner under the influence of gravity, more so than with pure baroclinic effects. For the density stratified K-H instability, comparisons were made with empirical results for the convection velocity of the structure and the entrainment ratio. The numerical simulations were able to predict with great accuracy both the above quantities for a shear layer. The asymptotic velocities of the bubble and the spike for the R-T instability were compared with those obtained by other

investigators and again it was found that the numerical results were in good agreement with those of the other investigations.

The study of the jet diffusion flame revealed that the effect of heat release is to weaken the vorticity field and to damp the growth of the instability. The diffusion flame, with temperature dependence, was found to be very sensitive to the local strain rate in the flow field. The flame was extinguished in regions of large positive strain and the reaction was confined to zones of negative strain. At low Damkohler numbers, the product formation in a turbulent diffusion flame is very similar to that of a laminar flame. For high Damkohler numbers, the turbulent product formation at the late stages of growth showed a significant increase above that of the laminar flame. A contrasting behavior was obtained for the premixed flame. At low values of the Damkohler number, the turbulent premixed flame yielded a large amount of products compared to the laminar flame. As the Damkohler number was increased, the turbulent product formation curve converged to that of the laminar flame. In a qualitative sense, all of the above features have been observed in experiments.

The numerical method was able to resolve the complex non-linear interaction between the flow field and the reaction. The future extension to this work lies in applying it to study three dimensional instabilities and more realistic flow fields with boundaries.

REFERENCES

1. Williams, F.A., Theory Of Combustion in Laminar Flows, Ann. Rev. Fluid Mech., 3 (1971), pp.171-188.

2. Buckmaster, J.D. and Ludford, G.S.S., Theory of Laminar Flames, Cambridge University Press, 1981.

3. Peters, N., Discussion of Test Problem A, GAMM - Workshop on Numerical Methods in Laminar Flame Propagation, pp. 1-14.

4. Ludford, G.S.S., Activation-Energy Asymptotics of the Plane Premixed Flame, GAMM - Workshop on Numerical Methods in Laminar Flame Propagation, pp. 15-28.

5. Williams, F.A., Asymptotics Methods in Turbulent Combustion, AIAA Preprint, 84-0475, 1984.

6. Riley, J.J., Metcalfe, R.W. and Orszag, S.A., Direct Numerical Simulations of Chemically Reacting Turbulent Mixing Layers, Phys. Fluids, 29, 1986, pp. 406-422.

7. McMurtry, P.A., Jou, W.H., Riley, J.J., and Metcalfe, R.W., Direct Numerical Simulations of a Reacting Mixing Layer with Chemical Heat Release, AIAA Journal, 24, No: 6, 1986, pp. 962-970.

8. Ghoniem, A.F., Computational Methods in Turbulent Reacting Flow, Lectures in Applied Mathematics, 24, 199-265 (1986).

9. Majda, A. and Sethian, J.A., The Derivation and Numerical Solution of the Equations for Zero Mach Number Combustion, Comb. Sci. Tech., 42, 185-205 (1987).

10. Kuo, K. K., Principles of Combustion, John Wiley & Sons, 1986.

11. Ghoniem, A.F., Heidarinejad, G. and Krishnan, A., Numerical Simulation of a Thermally Stratified Shear Layer Using the Vortex Element Method, J. Comput. Phys., 75, (1988), pp. 135-166.

12. Ghoniem, A.F. and Krishnan, A., Baroclinic Effects in Stratified Flows, Submitted to J. Fluid Mech., 1989.

13. Ghoniem, A.F., Heidarinejad, G. and Krishnan, A., Turbulence-Combustion Interactions in a Reacting Shear Layer, Proceedings of the Joint France-USA Workshop on Turbulent Reactive Flows, Rouen, France, July 1987.

14. Chorin, A. and Bernard, P., Discretization of a Vortex Sheet With an Example of Roll-up, J. Comput. Phys., 13, pp.423-428 (1973).

15. Hald, O.H., Convergence of Vortex Methods for Euler's Equations, SIAM J. Num. Anal., 16, 726-755 (1979).

16. Beale, T.J. and Majda, A., Vortex Methods II: Higher Order Accuracy in Two and Three Dimensions, Math. Comput., 39, 159, pp. 28-52 (1982).

17. Leonard, A., Vortex Methods for Flow Simulation, J. Comput. Phys., 37, pp. 289-335 (1980).

18. Anderson, C. and Greengard, C., On Vortex Methods, SIAM J. Num. Anal., 22, pp. 417-444 (1985).

19. Krasny, R., Desingularization of Periodic Vortex Sheet Rollup, J. Comput. Phys., 65, pp. 292-313 (1986).

20. Zabuski, N.J. and Overman, E.A., Regularization of Contour Dynamical Algorithms, J. Comput. Phys., 52, pp. 351-373 (1983).

21. Batchelor, G.K., An Introduction to Fluid Dynamics, Cambridge University Press (1967).

22. Brown, G.L. and Roshko, A., On Density Effects and Large Structures in Turbulent Mixing Layers, J. Fluid Mech., 64 (4), 775-816 (1974).

23. Corcos, G.M. and Sherman, F.S., The Mixing Layer: Deterministic Models of Turbulent Flow. Part I: Introduction and the Two-Dimensional Flow, J. Fluid Mech., 139, pp. 29-65 (1984).

24. Pozrikidis, C. and Higdon, J.L., Non-Linear Kelvin-Helmholtz Instability of a Finite Vortex Layer, J. Fluid Mech., 157, 225-263 (1985).

25. Betchov, R. and Criminale, W.O., Stability of Parallel Flows, Academic Press, 1967.

26. Dimotakis, P.E., Two Dimensional Shear Layer Entrainment, AIAA Journal, 24, pp.1791-1796 (1986).

27. Dimotakis, P.E., Turbulent Free Shear Layer Mixing, AIAA Paper, AIAA-89-0262, Reno, Nevada (1989).

28. Corcos, G. and Lin, S., The Mixing Layer: Deterministic Models of a Turbulent Flow. Part 3. The Effect of Plane Strain on the Dynamics of Streamwise Vortices, J. Fluid Mech., 141, pp.139-178 (1984).

29. Ghoniem, A.F. and Krishnan, A., Mixing Patterns and the Generation of Vorticity in a Density Stratified Shear Layer, The Workshop on Physics of Compressible Turbulent Mixing, Princeton University, October 1988.

30. Riley, J.J. and Metcalfe, R.W., Direct Numerical Simulation of a Perturbed, Turbulent Mixing Layer, AIAA Paper, AIAA-80-0274 (1980).

31. Anderson, C. A Vortex Method for Flows with a Slight Density Variation, J. Comput. Phys., 61, pp. 417 (1985).

32. Daly, B. J., Numerical Study of Two Fluid Rayleigh-Taylor Instability, Phys. Fluids, 10, 297-307 (1967).

33. Tryggvason, G., Numerical Simulations of the Rayleigh-Taylor Instability, J. Comput. Phys., 75, 253-282 (1988).

34. Kerr, R. M., Simulation of Rayleigh-Taylor Flows Using Vortex Blobs, J. Comput. Phys., 76, 48-84 (1988).

35. Baker, G. R., Meiron, D. I. and Orszag, S. A., Vortex Simulations of the Rayleigh-Taylor Instability, Phys. Fluids, 23, pp. 1485 (1980).

36. Turner, J.S., Buoyancy Effects in Fluids, Cambridge University Press, 1973.

37. Roquemore, W.M., Chen, L.D., Goss, L.P. and Lynn, W.F., The Structure of Jet Diffusion Flames, United States-France Joint Workshop on Turbulent Reactive Flows, July 6-10, 1987, Rouen, France.

38. Eickhoff, H. and Winandy, A., Visualization of Vortex Formation in Jet Diffusion Flames, Combustion and Flame, 60, pp.99-101, (1985).

39. Strawa, A.W. and Cantwell, B.J., Visualization of the Structure of a Pulsed Methane-Air Diffusion Flame, Phys. Fluids, 28(8), pp:2317-20, 1985.

40. Krishnan, A. and Ghoniem, A.F., Numerical Simulation of the Structure of a Heated Jet in a Cold Environment, AIAA Paper, AIAA-89-0485, January 9-12, 1989, Reno, Nevada.

41. Vandsburger, U., Lewis, G., Seitzman, J.M., Allen, M.G., Bowman, C.T. and Hanson, R.K., Flame-Flow Structure in an Acoustically Driven Jet Flame, Western States Section/ The Combustion Institute Fall Meeting, 27-28 October 1986, University of Arizona, Tucson, AZ.

42. Chen, L.D. and Roquemore, W.M., Visualization of Jet Flames, Combustion and Flame, 66, pp:81-86, 1986.

43. Peters, N. and Williams, F.A., Coherent Structures in Turbulent Combustion, The Role of Coherent Structures in Modelling Turbulence and Mixing, edited by J. Jimenez, Springer-Verlag Lecture Notes in Physics, 136, pp. 364-393 (1981).

44. Masutani, S.M. and Bowman, C.T., The Structure of a Chemically Reacting Plane Mixing Layer, J. Fluid Mech., 172, pp.93-126 (1986).

45. Hosangadi, A., Merkle, C.L. and Turns, S.R., Analysis of Forced Combusting Jets, AIAA Paper, AIAA-89-0662, Reno, Nevada (1989).

46. Hermanson, J.C., Mungal, M.G. and Dimotakis, P.E., Heat Release Effects on Shear Layer Growth and Entrainment, AIAA Paper, AIAA-85-0142 (1985).

47. Mungal, M.G. and Dimotakis, P.E., Mixing and Combustion with Low Heat Release in a Turbulent Shear Layer, J. Fluid Mech., 148, pp.349-382 (1984).

48. Ghoniem, A.F. and Krishnan, A., Origin and Manifestation of Flow-Combustion Interactions in a Premixed Shear Layer, 22nd Symposium (International) on Combustion, August 13-16, 1988, Seattle, Washington.

49. Ghoniem, A.F., Heidarinejad, G. and Krishnan, A., On Mixing, Baroclinicity and the Effect of Strain in a Chemically Reacting Shear Layer,

AIAA 26th Aerospace Sciences Meeting, January 11-14, Reno, Nevada AIAA-88-0729.

50. Keller, J. and Daily, J.W., The Effects of Highly Exothermic Chemical Reaction on a Two-Dimensional Mixing Layer, AIAA Journal, 23, pp.1937-45 (1985).

51. Ghoniem, A.F., Effect of Large Scale Structures on Turbulent Flame Propagation, Comb. Flame, 64: 321-336 (1986).

52. Darabiha, N., Candel, S.M. and Marble, F.E., The Effect of Strain Rate on a Premixed Laminar Flame, Combustion and Flame, 64: 203-217 (1986).

53. Libby, P.A. and Williams, F.A., Strained Premixed Laminar Flames Under Nonadiabatic Conditions, Comb. Sci. Tech., 31, 1-42 (1983).

54. Pitz, R.W. and Daily, J.W., Experimental Study of Combustion in a Turbulent Free Shear-Layer Formed at a Rearward-Facing Step, AIAA Journal, 21, pp.1565-70 (1983).